Observational Study of X-ray Spectra of Binary Pulsars with Ginga

Tatehiro MIHARA
The Institute of Physical and Chemical Research (RIKEN)
Hirosawa, Wako, Saitama 351-01, Japan

A thesis submitted for
the requirements of the degree of
DOCTOR OF SCIENCE (Physics)
at the
UNIVERSITY OF TOKYO

May 31, 1995

Contents

Chapter 1

Introduction

A neutron star is formed as an end product of a massive star evolution. On the core surface of a normal star nuclear fusion generates a large amount of heat continuously. The heat emitted from the surface of the star to the vast space by visible photons prevents the stellar body from collapsing gravitationally. In the case of the sun the luminosity of $L_\odot = 4 \times 10^{33}$ erg/s supports the mass of $M_\odot = 2 \times 10^{33}$ g to the radius of $R_\odot = 7 \times 10^{10}$ cm. Nuclear reactions of microscopic scale generate the immense amount of radiation from a star which supports the huge body.

When the star core uses up the nuclear energy, the reduced emission can no longer balance the gravity. The core begins to collapse until degenerate pressure of electrons can support the gravity. If the core mass is less than 1.4 $M_\odot$, degenerate electrons can keep the core at a radius of 10^9 cm, and the star becomes a white dwarf. When the mass is 1.4~2 $M_\odot$, electrons and protons merge into neutrons, degenerate neutron pressure supports the body to a radius of 10^6 cm, and the star becomes a neutron star. In this case, too, elementary particles of small scales play a main role. If the core mass is larger than about 2 $M_\odot$, there is no known force to prevent it from collapsing further to become a black hole.

Nowadays large particle colliders are build on the Earth, but the available energy is nearly at the limit. Celestial bodies offer natural laboratories for physics at a scale of a number of magnitudes larger. A neutron star has a large size, but the properties are dominated by the small scale of elementary physics and physics of condensed matter. The measurement of the properties of degenerate stars has become one of the most advanced physical experiments.

The possibility of the existence of a neutron star was first pointed out by Baade and Zwicky (1934), two years after the discovery of the neutron by Chadwick in 1932. However, a neutron star with a radius of 10 km is too small to be observed in optical light. The first detection of emission from a neutron star was from a compact X-ray binary Sco X-1

in 1962. Later on, the discovery of a radio pulsar in 1967 and an X-ray pulsar in 1971 confirmed the existence of neutron stars. Now many kinds of celestial objects are found to be neutron stars including radio pulsars, millisecond radio pulsars, X-ray pulsars, X-ray bursters, γ-ray burst sources and so on.

Radio and X-ray pulsars are generally believed to be rotating neutron stars with strong magnetic fields. There are several methods available to estimate their magnetic field intensity. One of these methods is used for radio pulsars. The radio waves from radio pulsars are considered to be emitted by magnetic dipole radiation using the rotational energy of the neutron star. Observations of the period and its derivative find the dipole components of the magnetic fields to be $10^{11} \sim 10^{13}$ Gauss. The recently discovered millisecond pulsars indicate much weaker magnetic fields, $10^{9} \sim 10^{10}$ G, and are often considered to be 'recycled' pulsars (§2.2.4). Another method is used for accreting X-ray pulsars. If an accreting neutron star is in a rotational equilibrium state, the accretion torque theory predicts a certain relation between the rotational period, magnetic field and X-ray luminosity (§2.3.4). Using this relation, one can estimate the magnetic fields of some X-ray pulsars to be $10^{12} \sim 10^{13}$ G, although the results are somewhat uncertain.

The only method to measure the magnetic field of a neutron star directly is to use electron cyclotron resonance lines in their X-ray spectra. The resonance energy is proportional to the magnetic fields intensity, and a magnetic field of 10^{12} G corresponds to the resonance energy of 12 keV, which is just within the X-ray region. Before the *Ginga* satellite was launched, cyclotron lines had been reported only from two X-ray pulsars, Her X-1 and 4U 0115+63 (§2.4). Therefore cyclotron structures were considered to be rare phenomena.

Recently, however, *Ginga* GBD has found cyclotron absorption structures in γ-ray bursts and revealed that at least some, if not all, γ-ray bursts originate from neutron stars (§2.4.3). Moreover, the good sensitivity of the *Ginga* LAC has led to discoveries of cyclotron resonance structures from 11 X-ray pulsars (§5). These new discoveries have shown that the cyclotron structure is a common feature of accreting pulsars and that resonance structure contributes significantly to the X-ray spectrum. The continuum spectrum and the resonance structure are strongly coupled with each other. In the analysis of this thesis, a new continuum model (NPEX) is introduced, which can fit all the spectra of X-ray pulsars very well together with the CYAB function describing the resonance structure. A possible physical meaning of the NPEX model is a Comptonized spectrum, which gives a new information about the emission mechanism of the X-ray pulsars.

In this thesis, brief reviews about X-ray sources and cyclotron structures are given in Chapter 2. Description of *Ginga* satellite is in Chapter 3. The Observations are described in Chapter 4 for each source. Data Analysis and Results are in Chapter 5. The Discussion and prospects are given in the last Chapter 6.

Chapter 2

Reviews

In this chapter, after a brief summary of the history of X-ray astronomy, X-ray pulsars and radio pulsars are reviewed with particular emphasis upon their magnetic fields. A review is also given on the energy spectra of binary X-ray pulsars, and on the cyclotron resonance structure which is the main subject of this thesis.

2.1 A Brief History of X-ray Astronomy

On 1962 June 18, an Aerobee rocket carrying Geiger counters was launched to measure fluorescent X-rays from the moon (Giacconi *et al.* 1962). Unfortunately they did not detect any X-ray emission from the moon, but more fortunately they discovered celestial X-ray emission from a sky direction near the Galactic center. The X-rays they detected were emission from the brightest cosmic X-ray source now known as Sco X-1, a typical low-mass X-ray binary (LMXB) source in which mass accretion onto a neutron star from a low-mass companion star is thought to produce a huge amount of X-rays. With subsequent observations using rockets and balloons, more than 40 X-ray sources were discovered by the end of the 1960's.

On 1970 December 12, the first X-ray astronomy satellite *UHURU* was launched by NASA. *UHURU* had a long slit collimator and performed an all-sky survey for X-ray sources utilizing the satellite spin. It finally discovered 339 cosmic X-ray sources, listed as the 4U catalog. Since then, the number of cosmic X-ray sources has been growing rapidly, due to observations from a series of X-ray astronomy satellites of progressively improved sensitivities, such as *OSO-7*, *Ariel-5*, *OSO-8*, *HEAO-1*, *the Einstein Observatory*, *EXOSAT*, *ROSAT* and so on. Important contributions have also been made by three Japanese satellites, *Hakucho* launched in 1979, *Tenma* launched in 1983, and *Ginga* launched in 1987 whose data provide the basis for the present thesis.

Various galactic and extragalactic objects have so far been catalogued as cosmic X-ray sources. The galactic X-ray sources comprise neutron star binaries, super nova remnants,

normal stars and so on, while extragalactic X-ray sources include normal galaxies, clusters of galaxies, and active galactic nuclei such as Seyfert galaxies and quasars. Today it is known that most celestial objects more or less emit X-rays, although relative dominance of the X-ray emission varies significantly among different classes of objects. For example, the X-ray to optical luminosity ratios of normal stars and normal galaxies are only 10^{-4} to 10^{-7}, while those of galactic neutron star binaries and active galactic nuclei range over $1 - 10^3$.

One of the most dramatic discoveries in the history of X-ray astronomy was the *UHURU* detection of a regular 4.8 s X-ray pulsation from the galactic X-ray source Cen X-3 (Giacconi *et al.* 1971). It was 4 years after the discovery of the radio pulsar (Hewish *et al.* 1968) which established the existence of neutron stars. The pulsation of Cen X-3 was interpreted as a rotation of a mass-accreting magnetized neutron star. X-rays from Cen X-3 disappeared periodically every 2.1 days, and the pulse period showed modulation at the same 2.1 day period. These phenomena were interpreted that Cen X-3 forms an eclipsing binary system, and the pulse period is Doppler modulated due to orbital motion of the neutron star. The binary nature of Cen X-3 was then confirmed by optical identification of its companion with an O-type star (Krzemiński 1974). Using the orbital parameters and the eclipse information, the mass function of the system was derived, and the mass of the neutron star was thereby determined to be about 1.4 $M_\odot$(Avni and Bahcall 1974, 1975). Since then, about 30 similar objects, including a number of transient sources, have been discovered within our Galaxy and in the Magellanic clouds. These objects are now called accretion-powered pulsars, or (binary) X-ray pulsars. Timing observations of about a dozen X-ray pulsars have indicated neutron star mass in the range 1–2 $M_\odot$, typically 1.4 $M_\odot$(Joss and Rappaport 1976, Rappaport and Joss 1983). The X-ray pulsars are reviewed in more detail in §2.3.3.

Another important progress in our understanding of neutron stars was initiated in 1975 by the discovery of X-ray bursts from the bright LMXB named 4U1820-30 with the *ANS* satellite (Grindlay *et al.* 1976). Since then more than 20 LMXBs have been recognized as X-ray burst sources, from observations with various satellites including *Hakucho*. The X-ray burst phenomenon has been understood as a thermonuclear flash on the surface of a mass-accreting neutron star without a strong magnetic field (Lamb and Lamb 1978). By applying the Stefan-Boltzmann law to the observed X-ray burst spectra which are roughly of blackbody shape, and by equating the observed burst luminosity with the Eddington limit, distances and radii of these neutron stars have been determined. These observations have established that the neutron stars in these sources have a typical radius of 10 km. The LMXB sources are reviewed in more detail in §2.3.2.

Thus X-ray astronomy has made valuable contributions to our contemporary knowledge of basic parameters, particularly mass and radius, of the neutron star. However, the

third important parameter of the neutron star, i.e. the magnetic field, has remained much less understood. Through measurements of electron cyclotron effects in the spectra of about 10 X-ray pulsars, in the present thesis an attempt is made for the first time to make a comprehensive contribution from X-ray astronomy to the understanding of magnetic fields of neutron stars.

2.2 Rotation-powered neutron stars

There are about 800 known neutron stars in our Galaxy. They are grossly divided into about 700 rotation powered objects and about 100 accretion powered ones, according to whether their electromagnetic radiation is powered by rotational energy of the neutron star or by gravitational energy release of matter accreting onto the neutron star, respectively. In this section, rotation-powered neutron stars are reviewed.

2.2.1 Radio pulsars

A neutron star is believed to be born with a rapid rotation in a supernova explosion, because a fraction of the angular momentum of the progenitor is transferred to the neutron star. These fast-rotating neutron stars are mostly young ($< 10^7$ yr) objects distributed mainly along the Galactic disk (figure 2.2.1). Using rotational energies and magnetic fields, they accelerate charged particles and emit non-thermal electromagnetic radiation which is pulsed at their rotation periods. These objects are classified as rotation-powered neutron stars, and usually called radio pulsars (Manchester and Taylor 1977) because their pulsed emissions usually come out in the radio wavelengths.

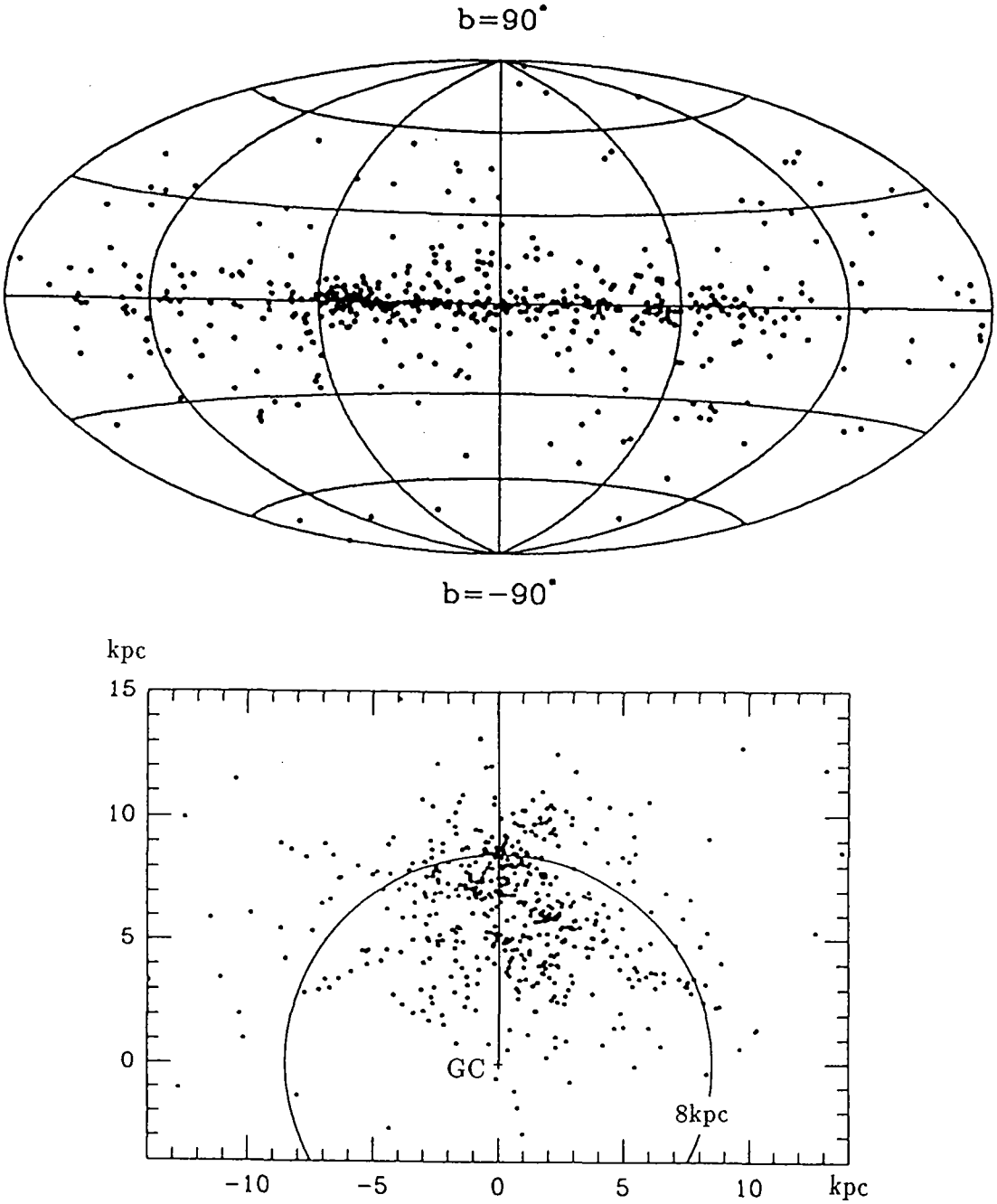

Figure 2.2.1: Galactic distribution of the radio pulsars (Lyne 1995)

The rotation-powered neutron stars always exhibit spin down, as they convert their rotational energy into radiation and particle energy through magnetic dipole radiation and other processes. Aged pulsars are therefore supposed to be rotating slowly, and their emission is thought to be weak because the magnetic dipole luminosity L_{md} scales as B^2P^{-4}, where B is the surface magnetic field (assuming dipole configuration) and P is the pulse period. Employing a standard value $I \sim 10^{45}$ g cm^2 for the moment of inertia of a neutron star, the spin-down rate $\dot{P}$ observed for a radio pulsar is readily converted into its rotational energy loss rate $L_{loss} = -I\dot{P}P^{-3}$. Then L_{loss} can be equated with L_{md} to obtain an estimate (more properly, an upper limit) on B, as

$$\frac{B}{10^{12}\mathrm{G}} = 3.1 \left(\frac{\dot{P}}{10^{-14}\ \mathrm{s\ s^{-1}}}\right)^{\frac{1}{2}} \left(\frac{P}{1\mathrm{s}}\right)^{\frac{1}{2}}. \tag{2.1}$$

As shown in figure 2.2.2, this estimate gives $B = 10^{11}$ to 10^{13} G for most radio pulsars.

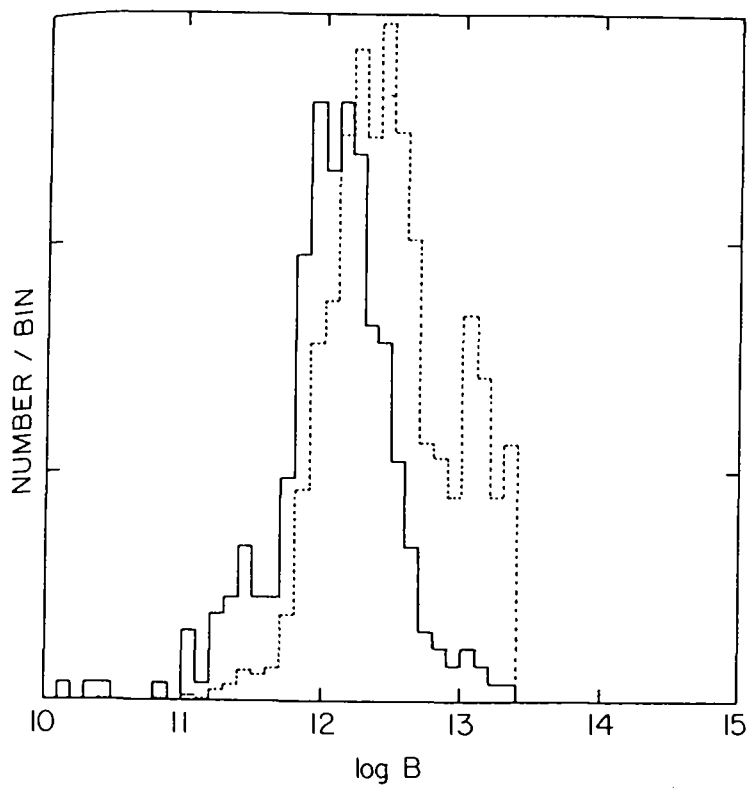

FIG. 2.16. Distribution of pulsar magnetic fields. The observed pulsars (295) are in solid while the corrected distribution taking into account the number versus magnetic field scaling for dipole spin-down is shown dashed. The secondary "peak" is probably just a statistical fluctuation.

Figure 2.2.2: Magnetic fields of radio pulsars (Michel 1991)

2.2.2 Very active radio pulsars

Although radio pulsars usually exhibit steeply falling radio spectra towards higher frequencies, the most active of them emit exceptional pulsed radiation in optical, X-ray, and even up to γ-ray ranges. These objects are exclusively found in supernova remnants (SNRs), and conversely they form a major fraction of the neutron stars for which physical associations with SNRs are established or suggested. These examples include the Crab pulsar (0531+21, 33 ms period) in the Crab nebula, the Vela pulsar (0833-45, 89 ms period) in the Vela SNR, the 50ms pulsar 0540-69.3 in the LMC, the 150 ms pulsar PSR1509-58 in the SNR called MSH15-52, the 39.5 ms pulsar PSR1951+32 in the SNR CTB80, and so on. These objects have short 'characteristic age' defined as

$$\tau = P/\dot{P}, \tag{2.2}$$

and are actually very young, as evidenced by their association with SNRs.

2.2.3 Hypothesis of magnetic field decay

Through statistical treatment of the radio pulsar data, a number of authors have claimed that the magnetic fields of radio pulsars (and of neutron stars in general) decay exponentially on time scales of 10^{6-7} years (Ostriker and Gunn 1969, Manchester and Taylor 1977, Lyne *et al.* 1985). The simplest reason for this hypothesis is that the magnetic field estimated through eq.(2.1) is apparently anticorrelated with the characteristic age defined by eq.(2.2). Another support to the hypothesis is the fact that radio pulsars with larger distances from the Galactic plane tend to exhibit smaller values of B; note that older pulsars are thought to be distributed with a larger scale height over the Galactic plane, since pulsars are usually 'runaway' objects with high proper motions.

Extreme care is however needed here, because eq.(2.1) strictly speaking gives only upper limits on B, and τ may be significantly different from the true age of the object. Moreover, the radio pulsar data are severely biased with selection effects. In fact, some authors have been arguing against the rapid field-decay scenario. Sang and Chanmugam (1990) proposed that non-exponential decay is consistent with the current pulsar statistics. Furthermore, recent re-analysis of the pulsar statistics by Wakatsuki *et al.* (1992) show that all the available data on radio pulsars are consistent with the 'no field decay' hypothesis. As shown later, the present thesis will give an impact upon the issue of the pulsar magnetic field decay.

2.2.4 Millisecond pulsars

Recently about 15 radio pulsars with peculiar characteristics have been discovered. This class of objects, called 'millisecond pulsars', are very fast rotators with pulse periods

< 0.1 s. They also exhibit extremely small spin-down rate, indicating that their magnetic fields are extremely small; typically $B < 10^9$G in terms of eq.(2.1). The fastest pulsar PSR1937+21, with $P = 1.56$ ms, $\dot{P} = 10^{-19}$ s s^{-1}, and $B = 4 \times 10^8$ G, belongs to this class. In sharp contrast to the ordinary radio pulsars, the millisecond pulsars are found preferentially in the Galactic bulge region, particularly in globular clusters, that is, among old population objects. Therefore the millisecond pulsars are no doubt very aged objects even though they are rotating rapidly. Another characteristic of these objects is that about one third of them are found in binary systems, whereas the ordinary radio pulsars are mostly single objects with only a few exceptions.

A popular scenario accounting for the millisecond pulsars describes them as 'recycled' objects (van den Heuvel 1991,1992). The scenario assumes that they are very old ($> 10^9$ years) neutron stars, which had lost their strong magnetic fields according to the 'field decay' hypothesis, before they were captured by nearby stars to form LMXBs. The neutron stars were then spun up gradually by the accretion torque as the companions evolved off the main sequence. After the mass accretion terminated, the neutron stars were left as fast-spinning objects. This scenario can explain a number of important features of the millisecond pulsars. However a serious difficulty is that the population of millisecond pulsars estimated from the current detections seems too large compared with the estimated LMXB population. As the above scenario is closely tied with the assumed magnetic field decay, this issue will be discussed again later in §6.4.

2.3 Accretion-powered neutron stars

2.3.1 Mass accretion onto neutron stars

At the surface of a neutron star with a radius of 10 km and a mass of 1.4 $M_\odot$, the gravitational potential energy reaches $\sim$ 20 % of the rest mass energy, or numerically about 200 MeV/nucleon. This is about 30 times larger than the nuclear energy released in hydrogen-to-helium nuclear fusion. Therefore, when a neutron star is in an environment where sufficient amount of matter is available for accretion, it becomes a very efficient radiation emitter, namely an accretion powered neutron star. The matter accreting onto a neutron star acquires large specific kinetic energy, which is somehow converted into thermal energy. However the temperature of the accreting matter does not normally reach the free-fall temperature (which is of order 10^{12} K for protons), because of the efficient radiative cooling. The thermal energy is emitted from the neutron star predominantly in the form of X-ray radiation, thus making the X-ray band most suitable for the study of these objects.

Efficient mass accretion is realized in a mass-exchanging close binary system composed of a mass-accreting neutron star and a mass-donating non-degenerate star. Therefore

essentially all the accretion-powered neutron stars are close binaries. The mass accretion occurs when the companion star fills its Roche lobe so that the matter of the companion flows onto the neutron star through the inner Lagrange point. Such a form of mass transfer is called Roche lobe overflow accretion, or sometimes disk-fed accretion, because in such a case the accreting matter usually has specific angular momentum large enough to form an accretion disk around the neutron star. Even when the companion star does not fill the Roche lobe, the neutron star can be activated by gravitationally capturing stellar wind from the companion on condition that the wind is dense enough. Such a process is called wind-fed accretion. In the wind-fed accretion, an accretion disk does not necessarily form around the neutron star.

If the neutron star has an elliptical orbit, the Roche lobe filling condition or the stellar wind density changes with the orbital phase. In either case, the X-ray intensity is significantly modulated with the orbital period. Furthermore in some systems, the neutron star is occulted by the companion star for a certain part of the orbit, thus producing periodic X-ray eclipses. The accretion-powered neutron star is observed as a transient X-ray source when there is a large change in the accretion rate, due to accretion disk instabilities, activity cycles in the companion star, resonance with a nearby third body, and so on.

As described below, the accretion powered neutron stars can be classified into low-mass X-ray binaries (LMXBs) and high-mass X-ray binaries (HMXBs).

2.3.2 Low mass X-ray binaries (LMXBs) and X-ray burst sources

A good fraction of the accretion-powered neutron stars, including the brightest persistent cosmic (non-solar) X-ray source Sco X-1, form a class called low-mass X-ray binaries (LMXBs). A LMXB is primarily defined as a mass-exchanging binary system composed of a neutron star and a low mass (late-type) normal star. Since a low mass star lacks strong stellar wind, the mass accretion is thought to take place via Roche-lobe overflow, hence the primary star is thought to fill the Roche lobe. Similar to the millisecond pulsars, the LMXBs are loosely concentrated in the galactic bulge region, in particular in rich globular clusters.

X-ray signals from LMXBs generally lack pulsations, implying that the neutron stars in these systems have weak ($< 10^9$ G) magnetic fields so that the accretion flow is not significantly affected by the magnetic pressure. Strictly speaking, a few X-ray emitting binaries with low-mass companions exhibit clear X-ray pulsations indicating that they involve strongly magnetized neutron stars. These examples include Her X-1, 4U1626-67 and GX 1+4. In the present thesis, such exceptional objects are conventionally excluded from the definition of LMXB and classified as X-ray pulsars.

Normally LMXBs exhibit X-ray luminosities of order 10^{37-38} ergs s^{-1}, which can

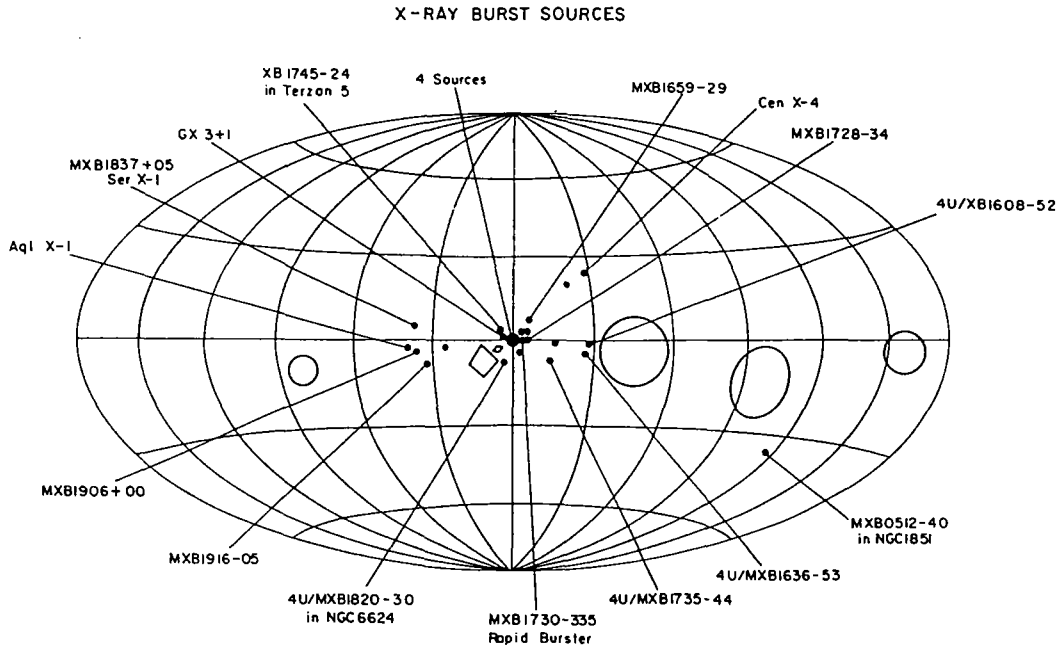

Figure 2.3.1: Galactic distribution of LMXBs (Lewin and Joss 1983)

be explained by a mass accretion onto a neutron star with a rate of $\sim 10^{-9}\ M_{\odot}\mathrm{y}^{-1}$. Their X-ray spectra resemble a thermal Bremsstrahlung spectrum with temperature in the range of a few keV. However, Mitsuda *et al.* (1984) revealed that the LMXB spectrum is much better described as a superposition of a multi-color blackbody emission and a blackbody emission, both having characteristic temperatures in the range 1–2 keV. The former component can be identified with emission from an optically thick (geometrically thin) accretion disk, while the latter can be interpreted as an optically thick emission from the neutron star surface.

Instead of periodic pulses, a LMXB generally exhibits irregular intensity variability on time scales from a fraction of a second up to hours. These variations sometimes involve quasi-periodic components, called quasi-periodic oscillations (QPOs), over a typical frequency range of 5–100 Hz. By extensive investigations from *EXOSAT* and *Ginga*, an instability model of the accretion disk is proposed for the QPO. Some LMXBs exhibit long-term (months to years) variations with such a large amplitude that they are regarded as transient sources or recurrent transients. An outburst in a transient LMXB is also thought to be triggered by an accretion disk instability.

An outstanding feature common to a major fraction of LMXBs is the X-ray burst phenomenon, which is thought to be a manifestation of an unstable thermonuclear reaction on the surface of an accretion-powered neutron star without strong magnetic field. As

already mentioned in §2.1, the X-ray bursts have provided a valuable means to estimate the size of the neutron star in LMXBs. When matter accretes slowly onto a weakly magnetized neutron star, the matter spreads over the whole surface of the neutron star. If the pressure at the bottom of the accreted matter reaches a threshold, an unstable thermonuclear flash occurs and blows up the accreted matter, which is observed as a X-ray burst. The brightest LMXBs normally lack burst activity, which can be explained if the surface temperature of such a neutron star becomes high enough so that the nuclear fusion in the accreting matter takes place continuously without leading to an unstable flash.

2.3.3 High mass X-ray binaries (HMXBs) and X-ray pulsars

When a neutron star forms a mass-exchanging close binary with a massive (early type) star, the system is called a high mass X-ray binary (HMXB); these make up the other subclass of accretion-powered neutron stars. The neutron star in a HMXB is normally powered via the wind-fed accretion, because early type stars produce intense stellar winds. The HMXBs are young ($< 10^7$) objects distributed along the galactic plane (figure 2.3.2) Because of a large radius of the primary star, a HMXB often exhibits X-ray eclipses.

With a very high probability, the neutron star in a HMXB has a strong surface magnetic field in excess of 10^{10} G. In such a case, the accretion flow is funneled onto magnetic polar caps and form two localized X-ray emission regions. When the rotation and magnetic axes of the neutron star are not identical, the emission regions appear and disappear according to the rotation producing periodic intensity modulations which are observed as X-ray pulses. These objects, including Cen X-3 as introduced in §2.1, are called binary X-ray pulsars, or simply X-ray pulsars. Therefore the concept of X-ray pulsars is nearly identical to that of HMXBs, although there are several important exceptions. The three objects, Her X-1, 4U 1626-67 and GX 1+4 (see §2.3.2), are clearly X-ray pulsars but are not HMXBs. On the other hand, an X-ray source called 4U 1700-37 is a typical HMXB but not recognized as an X-ray pulsar because its X-ray pulses are yet to be discovered.

The HMXBs are divided into two subtypes of somewhat different properties. One of them is characterized by a massive (typically 15–35 $M_\odot$) OB type companion star, a relatively short ($<$ 10 days) binary period implying a relatively small ($<$ 150 lt-s) binary separation, a nearly circular orbit with eccentricity ≤ 0.1, a relatively steady X-ray intensity, and normally well-defined X-ray eclipses. Their X-ray spectra often exhibit variable low-energy absorption features and strong fluorescent iron-K lines, which indicate that the entire binary system is immersed in relatively dense cool matter (i.e. a stellar wind). These examples include Cen X-3, SMC X-1, LMC X-4, Vela X-1, 4U 1538-52, 4U 1700-37 and so on, all of which are discussed in this thesis. Among them the former two or three objects with high luminosities are possibly powered via disk-fed accretion, while

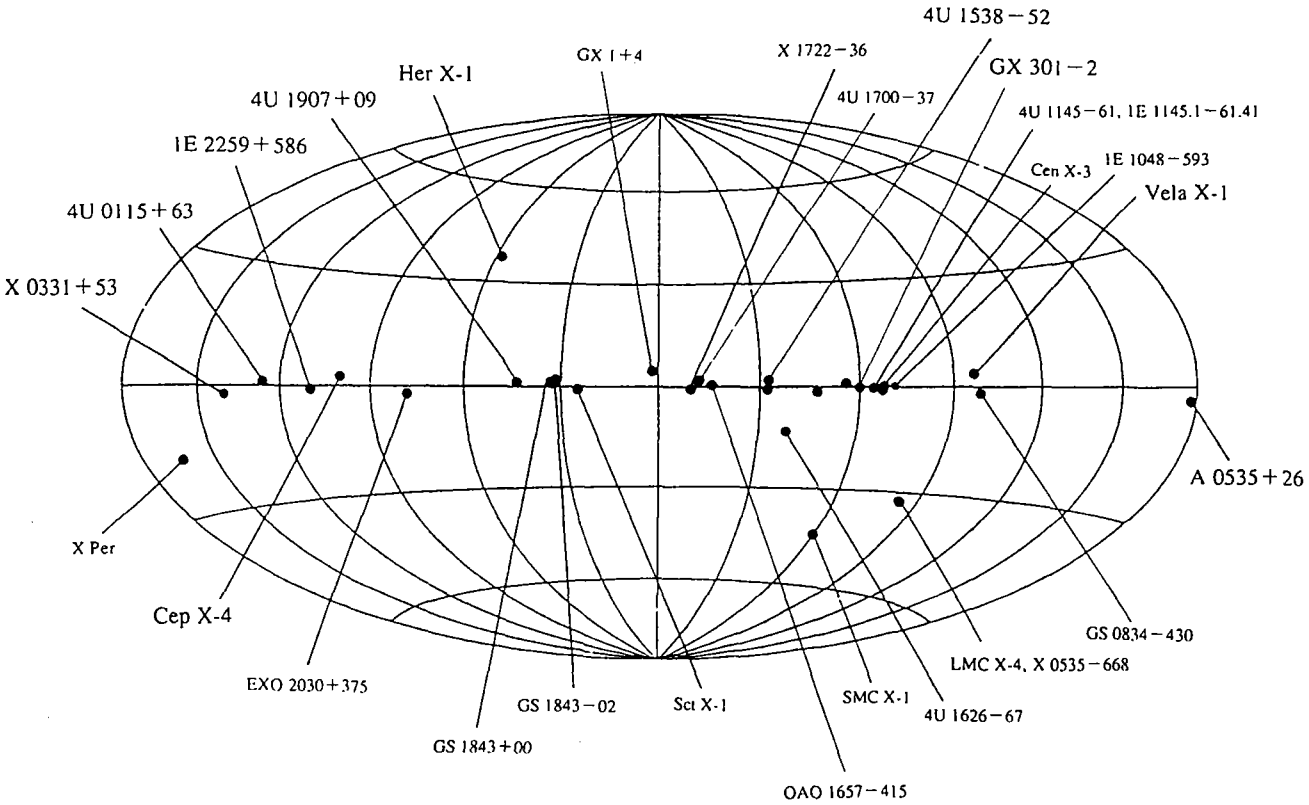

Figure 2.3.2: Galactic distribution of X-ray pulsars.

the others are powered by the wind-fed process.

The other subtype of HMXB is characterized by a Be-type companion star (a B-type star with strong emission lines), a long (> 10 days) orbital period, a significant orbital eccentricity, lack of X-ray eclipses, and a high degree of intensity variations on time scales from a fraction of the orbital period up to many years. These objects, called Be-pulsars, are mostly transient X-ray sources that are dormant for a significant fraction of the time. Recurrent transient pulsars dealt with in this thesis, namely A0535+26, 4U 0115+63, X0331+53, Cep X-4 and so on, all belong to this subclass. A Be star is thought to be rotating rapidly, and to possess a variable disk-like envelope along its rotational equatorial plane which becomes the source of both the optical emission lines and the mass accretion. The transient nature of Be-pulsars can be explained in terms of long-term evolution of the envelope. A few HMXBs, including GX301-2 and 4U 1907+09, have hybrid characteristics

in between the two subtypes introduced above.

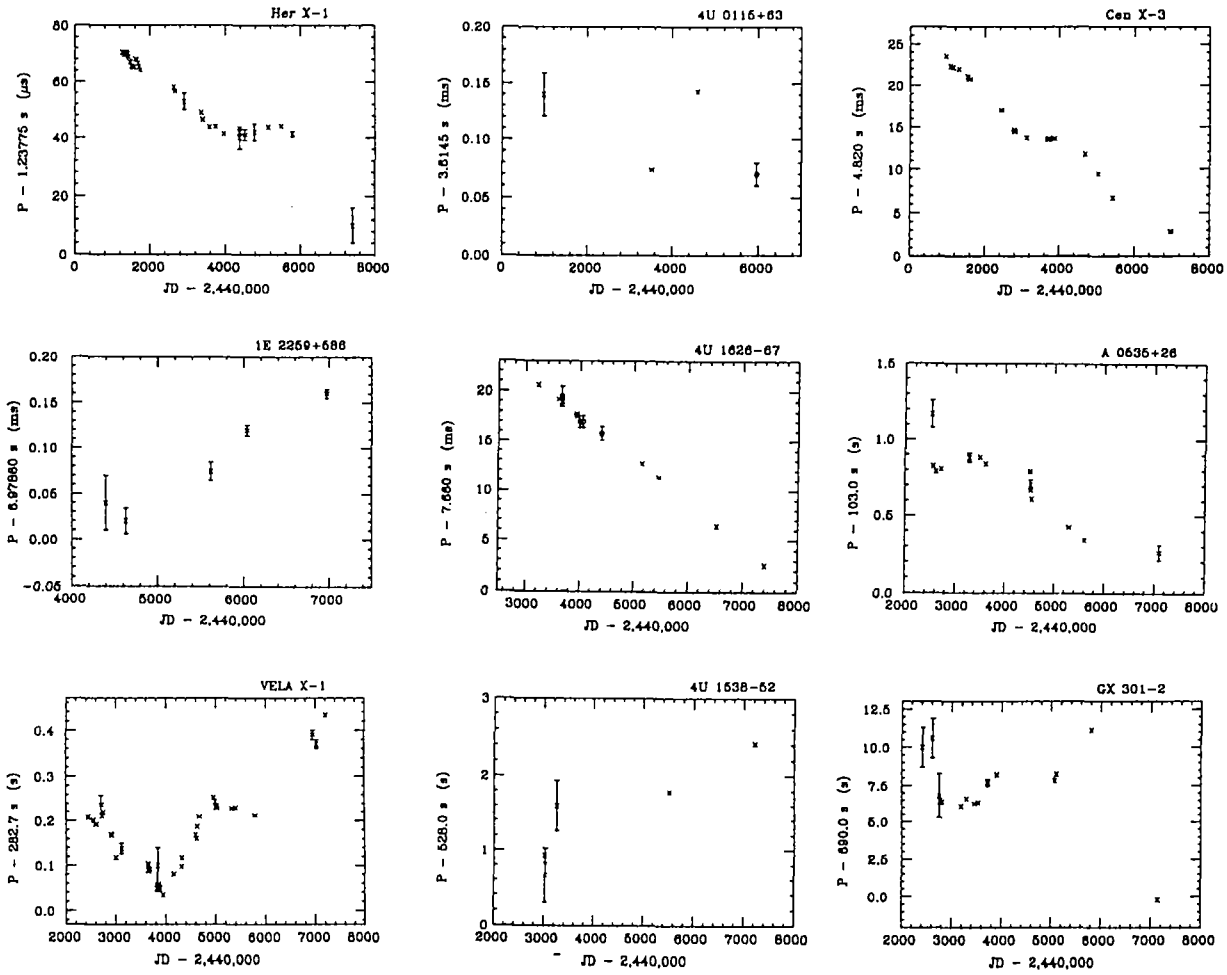

Figure 2.3.3: Long-term changes of the pulse periods of some X-ray pulsars (Nagase 1989).

Unlike the radio pulsars, the binary X-ray pulsars exhibit a variety of pulse periods ranging from 0.07 s to 800 s. Moreover, pulse periods of some X-ray pulsars decrease monotonically, while those of the others can increase with time or fluctuate randomly (figure 2.3.3). This is because the neutron star interacts strongly with the accreting matter via the magnetic field, exchanging angular momentum in a complex manner. Theoretical treatment of such an interaction has been formulated by Ghosh and Lamb (1978, 1979a, b) which will be reviewed briefly in the next subsection. Unlike the radio pulsars, the binary X-ray pulsars exhibit a variety of pulse periods ranging from 50 ms to 700 s. Moreover, pulse periods of some X-ray pulsars decrease monotonically, while those of the others can increase with time or fluctuate randomly (figure 2.3.3). This is because the neutron star

interacts strongly with the accreting matter via the magnetic field, exchanging angular momentum in a complex manner. Theoretical treatment of such an interaction has been formulated by Ghosh and Lamb (1978, 1979a, b) which will be reviewed briefly in the next subsection.

2.3.4 Accretion torque theory

The accretion torque theory developed by Ghosh and Lamb attempts to find a relationship between the magnetic dipole moment of the pulsar, the mass accretion rate onto it, the rotation period P (or angular frequency Ω_s) of the pulsar, and its time derivative $\dot{P}$. As illustrated in figure 2.3.4, the theory assumes that the accreting matter forms an accretion disk outside a certain radius r_0 (called effective Alfvén radius) from the neutron star which rotates with the Keplerian law of angular velocity

$$\Omega_K(r) = (GM/r^3)^{1/2}$$

where M is the mass of the neutron star and G is the constant of gravity. Because the magnetic field strength increases in the vicinity of the pulsar as $B \propto r^{-3}$, the theory assumes that the magnetic pressure dominates over the gravitational pull for $r < r_0$, where r_0 is a certain radius, and that the accreting matter in this region flows along the magnetic field lines onto the neutron star.

A quantitative treatment gives

$$r_0 = 0.52\ r_A, \tag{2.3}$$

where

$$r_A = 3.2 \times 10^8\ \mu_{30}^{4/7}\ \dot{M}_{17}^{-2/7}\ (M/M_\odot)^{-1/7} \quad \text{cm}$$

is the characteristic Alfvén radius for spherical accretion, which is derived from the condition $B^2/8\pi = \rho v_{ff}^2$. Here μ_{30} is the magnetic dipole moment in unit of 10^{30} G cm^3, $\dot{M}_{17}$ is the mass accretion rate in units of 10^{17} g s^{-1}, B is the local magnetic field, ρ is the density of the matter, and v_{ff} is the free-fall velocity. The difference between r_0 and r_A is due to the fact that the magnetic field lines threading the disk far from the neutron star are dragged inward by the radial drift velocity of the matter in the disk.

Basic idea of the theory is that the pulsar can spin up if the Keplerian angular velocity Ω_K of the matter near $r = r_0$ is higher than the angular velocity Ω_s with which the magnetic fields rotate rigidly with the pulsar, because in such a case the magnetic stress decelerates the Keplerian flow of matter and the angular momentum is transferred from the accreting matter to the pulsar. In other words, the pulsar can spin up if $r_0 < r_c$, in which r_c is 'corotating radius' defined as a radius where the Keplerian angular velocity $\Omega_K(r)$ equals Ω_s;

$$r_c = (GM/\Omega_s^2)^{1/3}. \tag{2.4}$$

If $r_0 > r_c$ on the contrary, due either to a very strong magnetic field or a reduced accretion rate, the pulsar is expected to show a spin down. Furthermore, matter can no longer accrete onto the neutron star if this condition is extreme, because the centrifugal force exerted by the field will blow off the matter. This is called the propeller effect, and in this case the source is expected to emit almost no X-rays.

The condition of a rotational equilibrium of a pulsar can be expressed as $r_0 = r_c$. Substituting eq.(2.3) and eq.(2.4), and converting the mass accretion rate into the X-ray luminosity L_{37} in 10^{37} erg s^{-1}, the equilibrium rotation period P_{eq} is expressed as

$$P_{eq} = 1.35\ \mu_{30}^{6/7}\ L_{37}^{-3/7}\ R_6^{-3/7}\ (M/M_\odot)^{-2/7} \quad \text{sec}$$

where R_6 is the radius of the neutron star in 10^6 cm. For example, Her X-1, with $P = 1.24$ s and $L_{37} \sim 1$, is near the rotational equilibrium, indicating $\mu_{30} \sim 1$. Since the surface magnetic field B is related as $R^3 B = \mu$ for a perfect dipole field, the theory implies $B \sim 10^{12}$ G. This is in a good agreement with the surface magnetic field estimated for the radio pulsars.

When $r_0 < r_c$, the theory can further predict the torque exerted from the accreting matter to the pulsar, and relate it to the rotational period change $\dot{P}$ as

$$-\dot{P} = 5.0 \times 10^{-5}\ n(\omega_s)\ \mu_{30}^{2/7}\ R_6^{6/7}\ (M/M_\odot)^{-3/7}\ I_{45}^{-1}\ (P L_{37}^{3/7})^2 \quad \text{s/yr.}$$

Here I_{45} is the moment of inertia of the pulsar in 10^{45} g cm^2, $\omega_s = \Omega_s/\Omega_K(r_0)$ is called fastness parameter, and the function $n(\omega_s) = (1-\omega_s/\Omega_s)/(1-\omega_s)$ is called torque function. Since P, $\dot{P}$ and L_{37} are observable quantities, the magnetic field can be calculated if R_6, M, I_{45} are assumed.

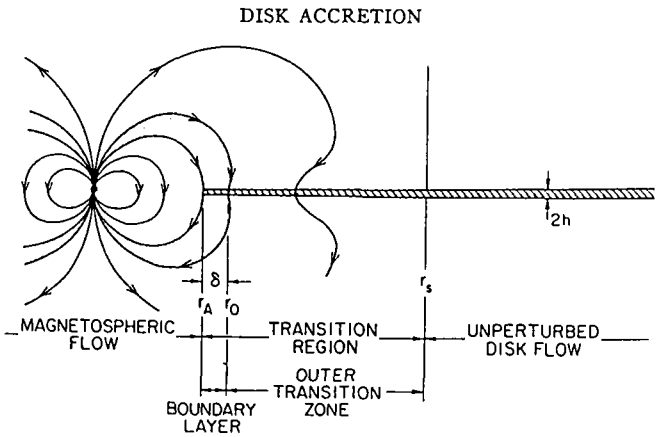

Figure 2.3.4: Accretion disk with a strong magnetic field (Ghosh and Lamb 1979b).

The magnetic fields thus derived through the accretion torque theory are shown in table 2.3.1 together with the observational parameters used for the calculation. However,

the derived field intensities become unrealistically large for some sources, particularly for wind-fed long-period sources such as GX 301-2. This would suggest that the accretion torque theory is not applicable to all the X-ray pulsars.

Table 2.3.1: Surface magnetic field strengths of some X-ray pulsars estimated from the accretion torque theory (Ghosh and Lamb 1979b).

Sources	P [s]	Mean L [10^{37} erg/s]	$\tau_S^{(a)}$ [yr]	$r_0^{(b)}$ [10^8 cm]	$B^{(c)}$ [10^{12} G]
SMC X-1	0.71	50	1.3×10^3	0.36	0.50
Her X-1	1.24	1	3.3×10^5	1.1	0.47
4U0115+63	3.6	$\geq$0.9	3.1×10^4	2.0	1.4
Cen X-3	4.84	5	3.6×10^3	2.4	4.5
A0535+26	104	6	2.9×10^1	17	148
GX 1+4	121	4	5.0×10^1	21	170
Vela X-1	283	0.1	1.0×10^4	40	86
GX 301-2	700	0.3	1.2×10^2	70	394
X Per	836	4×10^{-4}	5.9×10^3	38	4.8

a : The spin-up time scale, defined by eq.(2.2).
b : The calculated effective Alfvén radius (see text).
c : Surface magnetic field, derived from μ_{30} assuming $B = \mu_{30}/(10\text{km})^3$.

2.3.5 Photon flux spectra of binary X-ray pulsars

Among various cosmic X-ray sources, the accretion-powered pulsars are generally characterized with very flat X-ray spectra. A typical X-ray pulsar spectrum is approximated with a power-law form up to 10–20 keV, above which the spectrum exhibits a steep turn over. Moreover the spectrum often exhibits photoelectric absorption below several keV by cold matter which is located around the pulsar. Thus the photon flux spectrum $F(E)$ of an X-ray pulsar has been fitted traditionally with 'power-law times exponential cutoff (ECUT)' model (White, Swank and Holt 1983), of the form

$$F(E) = AE^{-\alpha} \exp(-N_H \sigma(E)) \times \begin{cases} 1 & (E < E_c) \\ \exp\{-(E - E_c)/E_f\} & (E > E_c). \end{cases}$$

Here E is the X-ray energy, α is the photon index which is typically in the range 0.2–1.0, E_c (typically 10–20 keV) is the energy where the high-energy cutoff starts, E_f (typically

5–30 keV) represents the steepness of the cutoff. N_H is the equivalent hydrogen column density, and $\sigma(E)$ is the cross section of photoelectric absorption due to cold matter of cosmic abundance (Morrison and McCammon 1983). In addition to the continuum, the X-ray pulsar spectrum very often shows fluorescent iron K-lines (Kα at 6.40 keV and Kβ at 7.05 keV) (Makishima 1986).

The high-energy spectral break had been established, by the end of the 1970's, as a phenomenon common to a majority of X-ray pulsars. However except for several very early investigations from purely theoretical aspect (Pravdo *et al.* 1978; Bonazzola *et al.* 1979), there was surprisingly no attempt to search for origin and physical meaning of the high-energy break in the pulsar spectra. Tanaka (1986) was probably the first to suspect that the spectral break is a direct consequence of the electron cyclotron resonance in the accretion column of the X-ray pulsars. Meantime, as the high-quality pulsar spectra became available from the *Tenma* SPC experiment (Tanaka *et al.* 1984; Koyama *et al.* 1984), the 'power-law times exponential cutoff' model became gradually unable to reproduce the observed data because of too abrupt a break at $E = E_c$ and too convex a model curvature above E_c (Makishima *et al.* 1990a).

These circumstances have led Tanaka (1986) and Makishima *et al.* (1990a) to propose two improved spectral models to represent the X-ray pulsar spectrum. One is called 'Fermi-Dirac cutoff (FDCO)' model, given as

$$F(E) = AE^{-\alpha} \exp(-N_H\sigma(E)) \frac{1}{1 + \exp\{(E - E_c)/E_f\}}$$

in terms of the Fermi-Dirac distribution function. However, this is of purely empirical one, without particular physical meaning related to any aspect of degenerate Fermi gas.

2.4 Cyclotron Resonances in Celestial Objects

Although the electron cyclotron resonance is a phenomenon widely seen in laboratory experiments in plasma physics as well as in condensed matter physics, before the *Ginga* era there were only a limited number of reports on observations of electron cyclotron resonances from celestial objects. As reviewed in this section, these reports concerns two X-ray pulsars (Her X-1 and 4U 0115+63), three gamma-ray bursts, and several magnetized white dwarfs. Theories of the electron cyclotron resonance are reviewed in §2.6.

2.4.1 Cyclotron resonance features in Her X-1

The 1.24 s pulsar Her X-1 is the second discovered X-ray pulsar (Tananbaum 1972) following Cen X-3, and the first pulsar from which the cyclotron resonance effect was observed (Trümper *et al.* 1978). Below, basic properties of this prototype object will be reviewed first, followed by a summary of observations of its cyclotron structure.

The orbital period of Her X-1 is 1.70 d, which involves a well defined eclipse and a Doppler modulation of the pulse arrival times. Unlike most X-ray pulsars, the companion star, HZ Her, is of rather late-type and has an estimated mass of about 2 $M_{\odot}$. Its spectral type changes between A and B with the orbital period, because over a certain orbital phase the surface facing the pulsar, heated up by the X-rays, is visible. This system is thought to be a Roche lobe overflow system because the X-ray luminosity of 2×10^{37} erg/s cannot be sustained by a weak stellar wind from an A type star. The persistent luminosity suggests that a stable accretion disk is formed around the pulsar.

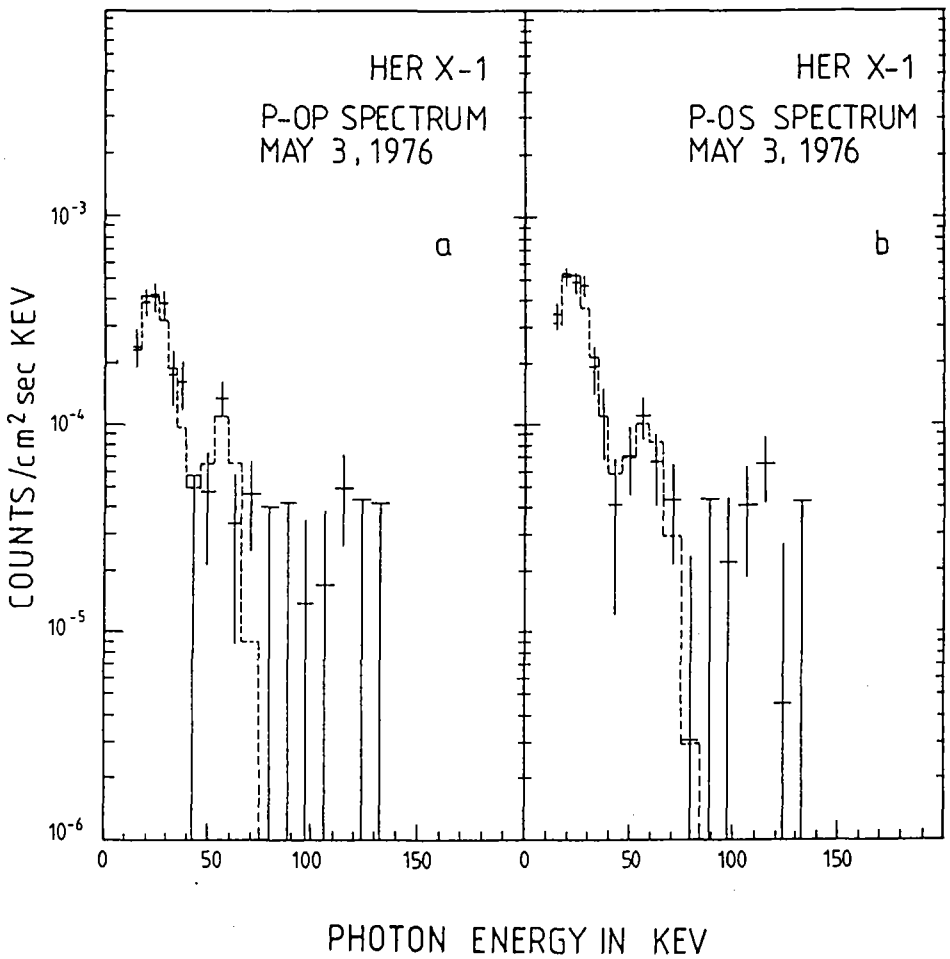

Figure 2.4.1: The deconvolved spectra of Her X-1 with scintillation counters on board balloon experiment (Trümper *et al.* 1978). This is the first discovery of the cyclotron structure in the X-ray pulsars.

The X-ray intensity of Her X-1 shows a clear modulation with a 35 day period, which begins with a sudden X-ray brightening up to 100 mCrab (main-on) followed by a gradual decrease in about 10 days down to 4 mCrab (low-state). Her X-1 brightens up again for a while at the middle of the 35 d period up to 30 mCrab (short-on), and gradually returns to the low state level in 7 d. During the main-on state, another phenomenon called pre-

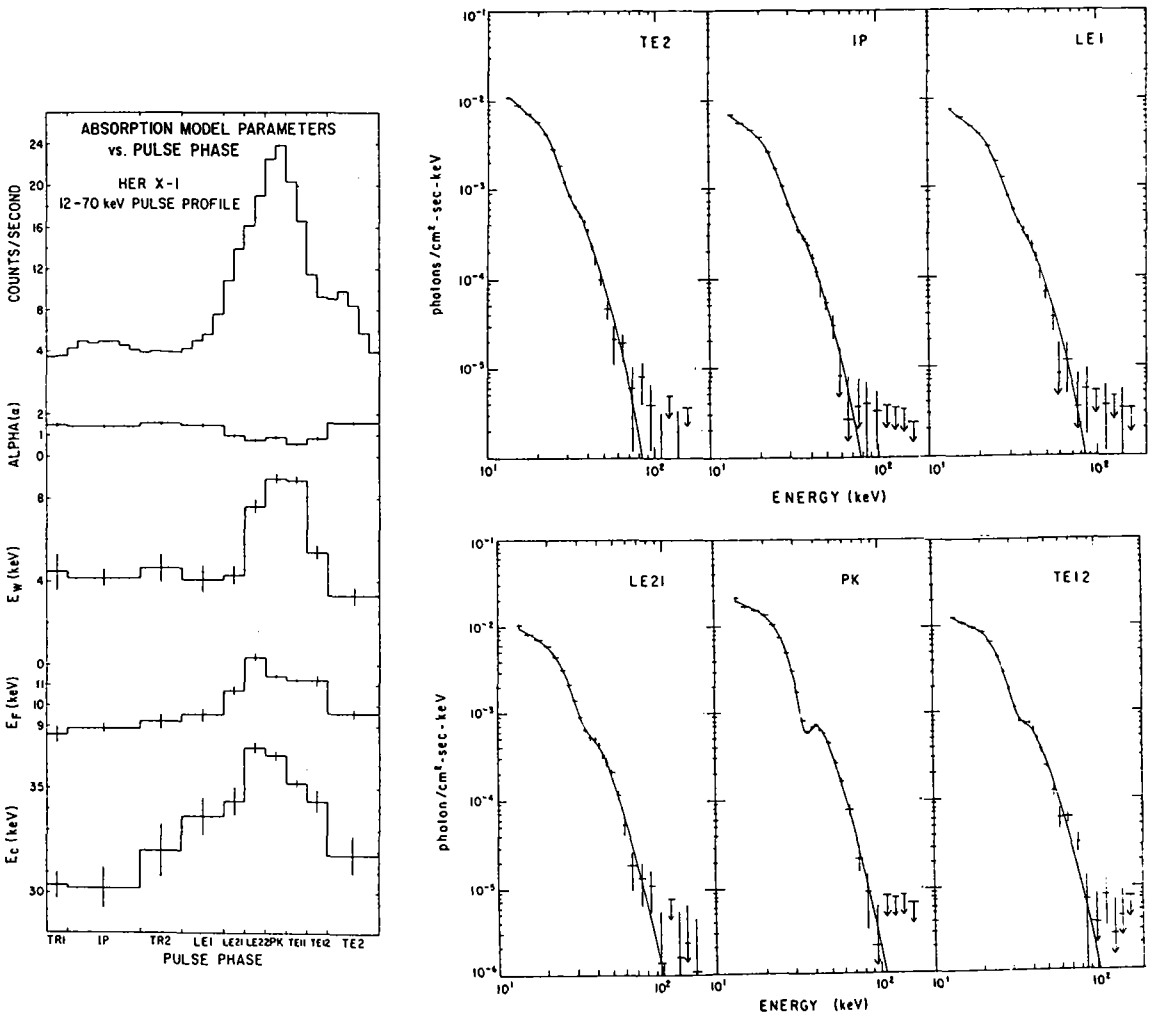

Figure 2.4.2: The phase-resolved deconvolved spectra of Her X-1 with *HEAO-1* A4 (Soong *et al.* 1990).

eclipse dip, which is a sudden increase in the X-ray absorption, recurs with a 1.6 d period. This cycle is probably a beat between 1.70 d and 35 d. The X-ray pulsation is present in the main-on and short-on, but absent in the low state (Mihara *et al.* 1991a). On the other hand, the X-ray heating effect on HZ Her persists through the 35 d cycle implying that the mass accretion rate stays rather constant (Bahcall 1972, 1978). Therefore the 35 d modulation and the pre-eclipse dips are probably a result of partial or total obscuration of the pulsed X-rays, by thick material which is very likely to be associated with the accretion disk. The residual flux during the low state can be interpreted as reprocessed X-rays (Mihara *et al.* 1991a). The origin of the 35 d modulation is often attributed to

a precession of the accretion disk or precession of the neutron star, but this is still very controversial.

The 35 d phase of Her X-1 is subject to a jitter by a few days. Moreover, Her X-1 stayed in a low-state continuously from 1983 June to 1984 February. As the optical archival data since 1890 indicate occasional darkening of HZ Her, such an extended low state is likely to be a result of a real decrease in the mass accretion rate.

The cyclotron resonance structures in the hard X-ray spectrum from Her X-1 were first discovered by Trümper *et al.* (1978) in a balloon observation using NaI scintillators. The observed spectrum of the pulse peak is shown in figure 2.4.1b. It was interpreted as showing either two absorption lines at 42 and 80 keV, or instead two emission lines at 58 and 110 keV. The same features were also observed in 'pulse peak minus pulse bottom' spectrum (figure 2.4.1a). These results were later confirmed by the same group (Voges *et al.* 1982), who performed detailed pulse-phase resolved analysis. Furthermore, follow-up observations were performed by many other experiments, including *Ariel-5* (Coe *et al.* 1977), *HEAO-1* A4 (Figure 2.4.2, Soong *et al.* 1990), and so on. Although these observations mostly reconfirmed the presence of cyclotron resonance effects in the Her X-1 spectra, it still remained uncertain whether the feature appears in absorption or in emission.

Mihara *et al.* (1990b) observed Her X-1 with *Ginga* LAC (see §4.2 and §5.2 for details), in which they introduced a new technique of expanding the energy range up to 60 keV by reducing the detector high voltage (see §3.2.3). They clearly confirmed the cyclotron features in the LAC spectra, and convincingly showed that the cyclotron effects appear as an absorption feature near 35 keV. The essence of this process will be repeated in the present thesis.

2.4.2 Cyclotron resonance features in 4U 0115+63

The second pulsar exhibiting a cyclotron resonance is 4U 0115+63. This is a typical recurrent transient source which makes X-ray outbursts with an interval of a few years.

The absorption at 20.1 keV was found with *HEAO-1* A4 as shown in figure 2.4.3*left* (Wheaton *et al.* 1979). The *HEAO-1* A4 experiment consisted of two sets of a 0.3cm thick NaI phoswich scintillation counter with an area of $\sim$ 100 cm^2. The energy band was 12–180 keV. The upper trace of figure 2.4.3 is total counts and the lower is pulsed (pulse peak – pulse bottom) counts. The pulsed spectrum shows an absorption at 20.1 keV. Since the energy resolution is about 30% at 20 keV, the width of the absorption was not resolved.

From the data taken simultaneously with the *HEAO-1* A2 experiment (proportional

counters), White *et al.* (1983) confirmed the structures at 11.5 and 23 keV which appeared in absorption at the pulse peak phase and in emission at the inter-pulse phase (figure 2.4.3*right*).

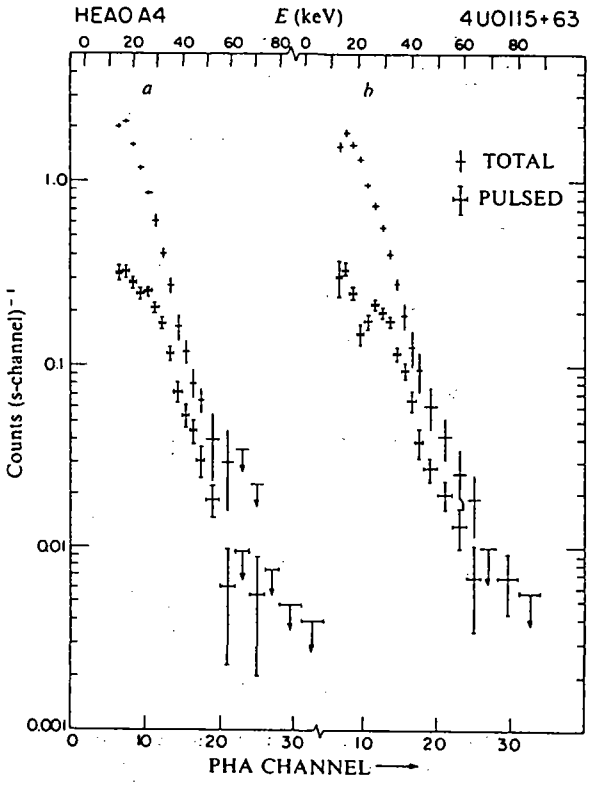

Fig. 3 Pulse height spectra of the total (upper) and pulsed (lower) counts in: *a*, LED1; and *b*, LED2. The 20 keV feature shows most clearly in LED2 in PHA channel 9. If it results from cyclotron resonance absorption, it corresponds to a surface magnetic field *B* of ~ 1.8–2.5×10^{12} G, (depending on the gravitational redshift), probably near the poles of the neutron star.

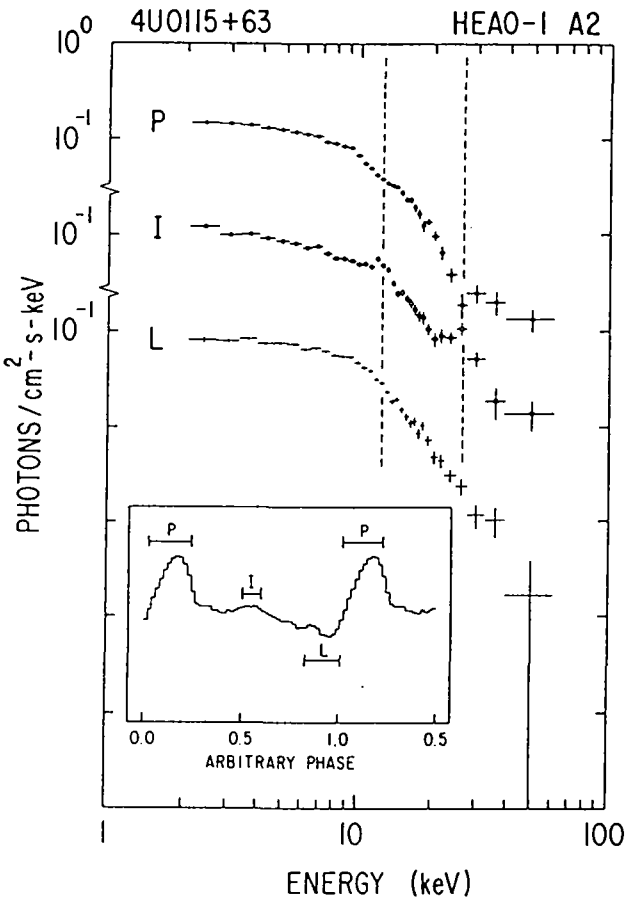

Figure 2.4.3: *Left*: The discovery of the 20 keV absorption feature in the spectrum of 4U 0115+63 with *HEAO-1* A4 (Wheaton *et al.* 1979). *Right*: The incident spectra with *HEAO-1* A2. The 11.5 and 23 keV features are found.

2.4.3 Cyclotron absorption lines from gamma-ray bursts

Evidence of cyclotron structure in the spectra of many gamma-ray bursts was first reported by Mazets *et al.* (1981) based on the Konus experiment on the Venera satellite. The report has remained controversial however, because the data statistics were generally poor and some of the claimed features could have arisen as an artifact of the spectral deconvolution.

Throughout the mission lifetime of *Ginga* , the GBD experiment detected 119 gamma-ray bursts over the 2–370 keV energy range. Among 23 events for which good spectra were obtained, at least three events, GB870303, GB880205, and GB890929 (figure 2.4.4), exhibited significant spectral dip features at 19.3, 20.4 and $\sim$ 26 keV, respectively (Murakami *et al.* 1988; Fenimore *et al.* 1988; Yoshida *et al.* 1991). Although the features did not persist over the entire burst duration and the dip energy varied considerably during one burst, all these features were detected by both the scintillator and the proportional counter with high statistical significance. Moreover, the spectrum from each event exhibited additional one or two dips whose energies were in harmonic separation from that of the main feature. Therefore the observed spectra have been interpreted as showing fundamental and higher harmonic absorptions due to electron cyclotron resonance. Since the inferred magnetic fields, of order 2×10^{12} G, are expected only on the neutron star surface, it has been revealed that some gamma-ray bursts originate in strongly magnetized neutron stars.

There have been a number of attempts to theoretically reproduce the GBD spectra by assuming that a thermal spectrum is incident upon a region where the electron cyclotron scattering takes place (Fenimore *et al.* 1988; Wang *et al.* 1989, 1993; Alexander and Meszaros 1989; Nishimura *et al.* 1992). These attempts have generally been successful, although geometrical configuration of the emission and the scattering regions is yet to be specified. In particular, Wang *et al.* (1989) compared the GB880205 spectrum with a Monte Carlo simulation and derived the physical condition of the scattering region as $B = (1.71 \pm 0.07) \times 10^{12}$ G, $N_e = (1.2 \pm 0.6) \times 10^{21}$ electrons/cm^2, and $\cos\theta = 0.31 \pm 0.05$, where B, N_e and θ are the field strength, the electron density and the observing angle, respectively.

Since 1991, many gamma-ray bursts have been observed with the BATSE experiment on board the *Compton Gamma-Ray Observatory*, revealing a number of interesting results on their spatial and flux distributions. However it is rather puzzling that there has so far been no report of BATSE confirmation of cyclotron features in any of the detected bursts (Band *et al.* 1994, Ford *et al.* 1992, Palmer *et al.* 1992).

GB870303
Graziani *et al.* 1992

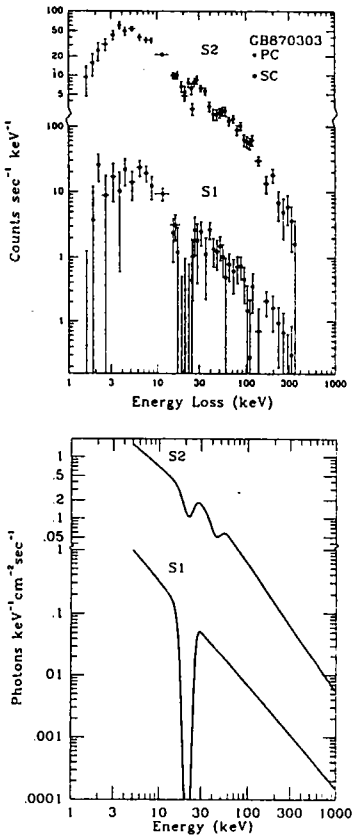

GB880205
Fenimore *et al.* 1988

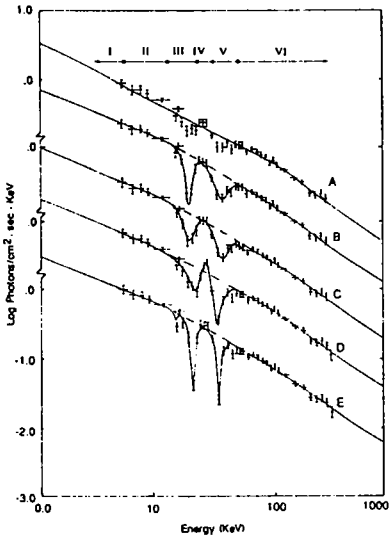

GB890929
Yoshida *et al.* 1991

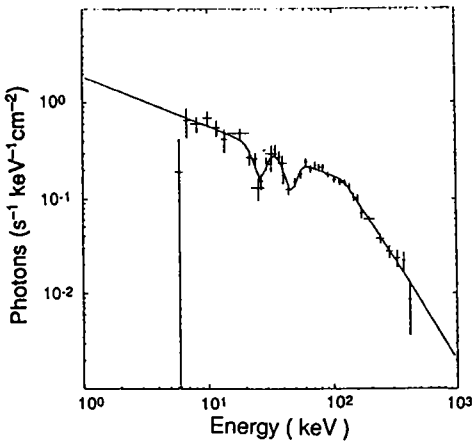

Figure 2.4.4: Cyclotron spectral features in gamma-ray burst spectra observed by the *Ginga* GBD. All the three show harmonic structures. The first two events, GB870303 and GB880205, shows a fundamental energy of about 20 keV, while the third one, GB890929, shows it at 26keV. (Murakami *et al.* 1988; Graziani *et al.* 1992; Fenimore *et al.* 1988; Yoshida *et al.* 1991)

2.4.4 Cyclotron emission lines from magnetized white dwarfs

Some white dwarfs have surface magnetic fields of order 10^{6-7} G. These field strengths have been measured by utilizing the Zeeman splitting of emission and absorption lines, and cyclotron emission lines in the optical band. The cyclotron emission lines were first discovered from VV Pup, a 'polar' source which is a class of mass-exchanging binaries involving magnetized white dwarfs (Visvanathan and Wickramasinghe 1979).

Cropper *et al.* (1988) showed that cyclotron harmonics can generally be found in the optical spectra from polar objects. As shown in figure 2.4.5, a careful subtraction of many atomic emission lines from the observed optical spectrum reveals a series of spectral humps with nearly the same interval. These humps have been interpreted as harmonic series of cyclotron emission lines, which indicate a magnetic field intensity of about 10^7 G. These effects were only seen when the accretion column was on the visible side. Therefore emission regions of the cyclotron lines are considered to be mass-accreting polar caps of the white dwarf, where hard X-rays with optically-thin Bremsstrahlung spectrum are also produced. These results have provided determinations of surface magnetic fields for a number of polars.

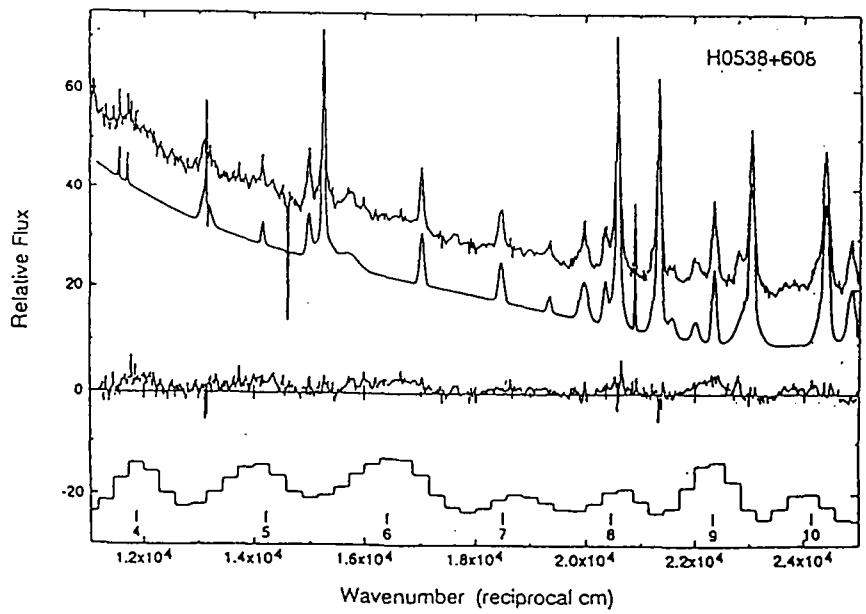

Figure 2.4.5: The spectrum of a polar H0538+608 from 4000 to 9100 Å (Cropper *et al.* 1988). The top curve shows the raw spectrum and the second one is the best fit model for a continuum and emission lines. The third one is the fit residuals. The bottom one is the appropriately binned residuals, and shows harmonics emissions.

2.5 Magnetic fields of neutron stars

2.5.1 Origin of the magnetic fields

The possible existence of strong magnetic fields in neutron stars was pointed out by Woltjer (1964) since if the surface magnetic flux is conserved in the formation of a neutron star, the neutron star may have a strong ($\sim 10^{12}$ G on the surface) magnetic field. However, the flux conservation may not occur if there is extreme turbulence in the collapse. Another origin of the magnetic field is proposed by Blandford *et al.* (1983); it is created in the crust from a weak initial seed field by thermoelectric effects after the neutron star is formed.

2.5.2 Theoretical approach

The core of the neutron star is considered to be superfluid of neutrons (a review: Lamb 1991). The superfluid continues rotating with the initial angular momentum because it does not have any friction. The supercurrent induced during supernova collapse via flux conservation also survives. The supercurrent is only decayed out via ohmic dissipation. However, electrical conductivity of the core is so high that the decay time becomes $> 10^{12}$ y, longer than the Hubble time (Sang and Chanmugam 1987). The electrical conductivity of the outer crust is 10^6 times lower, where the decay time becomes 10^7 y. Since the place which holds the magnetic fields is not known, there is no practical limitation from the theory.

2.5.3 Magnetic evolution of pulsars in binaries

Radio pulsars, ms pulsars, X-ray binary pulsars, and γ-bursts are different objects; however, all of them are neutron stars and the evolution of the magnetic fields could combine them to a single story (van den Heuvel 1991, 1992). The scenario is that a neutron star is born with intense (10^{12-14} G) magnetic field and the magnetic field decays with time, although the way of the decay may change if they have mass accretion or not. Their history makes the various objects noted above.

According to this scenario, a new-born single pulsar evolves, as radio pulsar $\rightarrow$ stop emission in the graveyard $\rightarrow$ γ-ray burst may sometimes occur $\rightarrow$ stay long and the magnetic field decays $\rightarrow$ acquire low-mass companion star $\rightarrow$ LMXB $\rightarrow$ spin-up to ms $\rightarrow$ accretion stop $\rightarrow$ ms pulsar. If the system is a detached low mass binary, the scenario is the same. Instead of catching a star, it waits for the companion to evolve and fill the Roche-lobe. If it is a high mass binary, an X-ray binary pulsar is formed and it spins up keeping the intense magnetic fields.

According to Srinivasan (1990) and Jones (1991), the magnetic fields of the accreting X-ray pulsar does not always decay. If we consider the interaction in the neutron star

core between superfluid neutron vortices carrying the rotation of the neutron star and the proton vortices carrying the magnetic fields, the strong magnetic field of Her X-1 (6×10^8 y old) becomes consistent with the 10^7 field decay of radio pulsars. This is because the decay of the magnetic field, that is the diffusion out of the proton vortex from the neutron core, is suppressed by the inward radial movement of neutron vortices in the spin-up phase by accretion. Moreover the intersection of neutron and proton vortices may occur and the flux is moved inward away from the surface of the superconductor. If the accretion does not occur as radio pulsars, the neutron vortices with magnetic field move out by ohmic diffusion and the decay time gets shorter.

Anyway these theories have not been generally accepted yet. They are one of the possibilities of the truth and must be checked by the further observations.

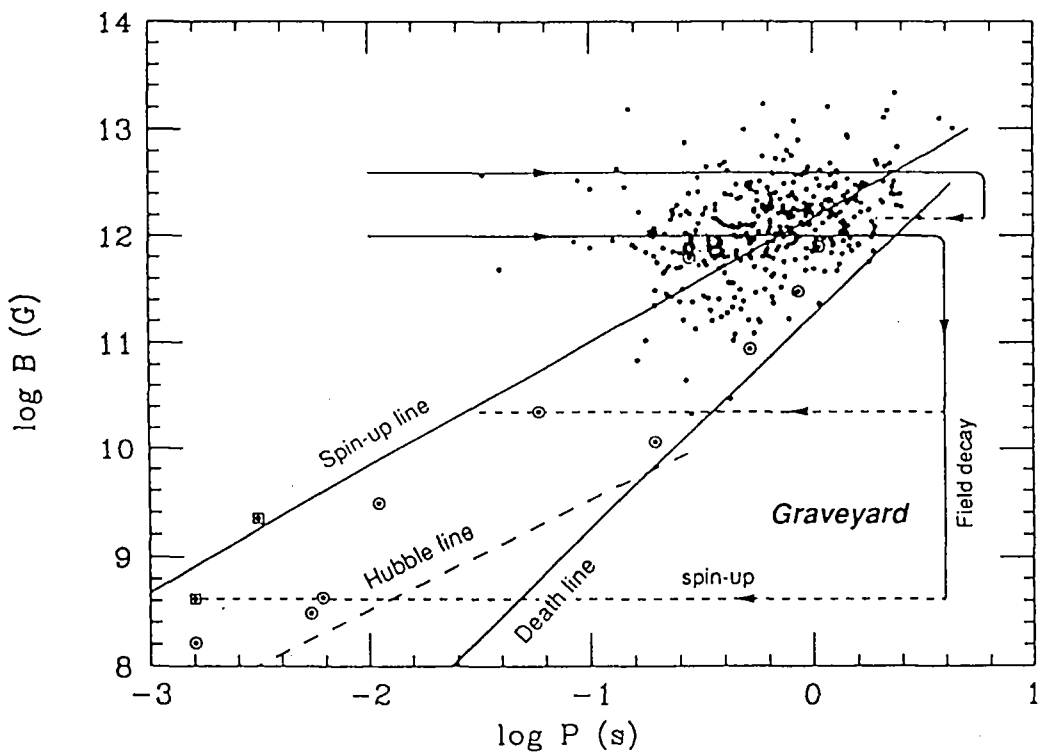

Figure 2.5.1: radio pulsar distribution on P–B plane. (van den Heuvel 1991)

2.6 Theoretical studies of Cyclotron scattering structures

The X-ray binary pulsar is considered to be an accreting neutron star with an intense magnetic field. Since accreting matter is ionized by the strong emission from the pulsar, it falls onto the magnetic poles of the neutron star only along the magnetic field. The structure of the emission column was studied eg. by Inoue (1975) for the low luminosity case but most of pulsars have too high luminosity for this model. In magnetic fields, electrons exhibit circular motion and cannot move across the field lines. Since electrons cause emission, scattering, and absorption of photons, the emergent spectrum is strongly affected by the magnetic fields. In order to explain the emission from the accretion column, there are three major problems: (1) absorption and scattering cross sections in a strong magnetic field, (2) hydrodynamical calculations giving the density and temperature profile of the accretion column, (3) solution of radiative transfer equations using cross sections obtained in (1) and geometry determined in (2). Many attempts to solve all the 3 problems under some simplifications are done by Meszaros (1992), Nagel (1980), Kii (1986), Bulik *et al.* (1992) and so on, but the situation is quite complicated and there is no satisfactory solution that solves the problems in a self-consistent manner.

2.6.1 Landau levels

Physics of electrons in an uniform magnetic field have been well studied by many authors in terms of non-relativistic as well as relativistic quantum theory (see Canuto and Ventura 1977 and the references therein; Melrose and Parle 1983). Let us consider an electron moving in an uniform magnetic field parallel to the z-axis with a strength of B. In the classical picture, it moves along a helix of a radius R given as

$$R = \frac{v_p m_e}{eB} \qquad \text{(in MKSA units)}$$

where v_p is the velocity of the electron perpendicular to the magnetic field, m_e is the electron rest mass, and e is an electronic charge.

We have to introduce the quantum mechanics if R is smaller than or comparable to the de Broglie wavelength, $\lambda_B = \hbar/mv$; in other words, $B > (v_p/c)^2 B_{cr}$, where $B_{cr} \equiv (m_e^2 c^3)/(\hbar e) = 4.41 \times 10^{13}$ G is the critical magnetic field strength.

Then the kinetic energy of an electron perpendicular to the field is quantized into Landau levels. In non-relativistic limit, that is

$$E_a < m_e c^2 = 511\text{keV}, \qquad \text{in other words,} \qquad B < B_{cr} = 4.41 \times 10^{13}\text{G},$$

the n-th Landau level is described as

$$E_n = \left(n' + \frac{1}{2} + s\right) E_a, \qquad n' = 0, 1, 2, ...,$$

Here, $s = \pm 1/2$ is the electronic spin, and $E_a = \hbar e B/m_e$ is the cyclotron energy. Then

$$E_n = nE_a, \qquad n = 0, 1, 2, ...,$$

$$E_a[\mathrm{keV}] = 11.6\ n\ \frac{B}{10^{12}[\mathrm{G}]} \tag{2.5}$$

These quantized energy levels are called Landau levels. The Landau levels are equally separated in the non-relativistic limit.

The life time of electrons in the excited level is very short, i.e., the radiative decay rate is very large, typically $\sim 10^{16}(B/10^{12}[\mathrm{G}])^2\ \mathrm{s}^{-1}$. Since the collisional decay rate is much smaller than that of radiative decay, an excited electron immediately falls to the ground level by emitting a photon with the same energy. Thus, this process is a scattering rather than an absorption, and most electrons are in the ground level ($n = 0$) with aligned spin ($s = -1/2$).

In the relativistic regime, the Landau levels are generally given as

$$E_n = mc^2 \frac{\sqrt{1 + 2n(B/B_{cr})\sin^2\theta} - 1}{\sin^2\theta}.$$

when $B/B_{cr} \ll 1$,

$$\simeq mc^2 n(B/B_{cr}),$$

where θ is the angle between the incident photon and the magnetic field. The resonance energy decreases with increasing angle θ.

If the resonance from the ground state to the first excited state is at 30 keV, the magnetic field strength is estimated to be 2.6×10^{12} G. This leads to $nB/B_{cr} = 0.06n$, so that the quantum effect should be taken into account, but non-relativistic approximation would be valid for small n.

Since a cyclotron scattering takes place near the neutron star surface, the observed resonance energy is affected by the gravitational redshift.

$$E_a^{obs} = E_a\ (1 + z)^{-1}$$

$$(1 + z)^{-1} = \left(1 - \frac{2GM_{NS}}{Rc^2}\right)^{1/2}$$

Here, M_{NS} is the mass of the neutron star and R is the distance of the scattering region from the center of the neutron star. Using $M_{NS} = 1.4\ M_\odot$ and $R = 10^6$ cm, we get $(1 + z)^{-1} = 0.76$. Thus observed B should be 20–30 % less than the real magnetic field at the surface of the neutron star.

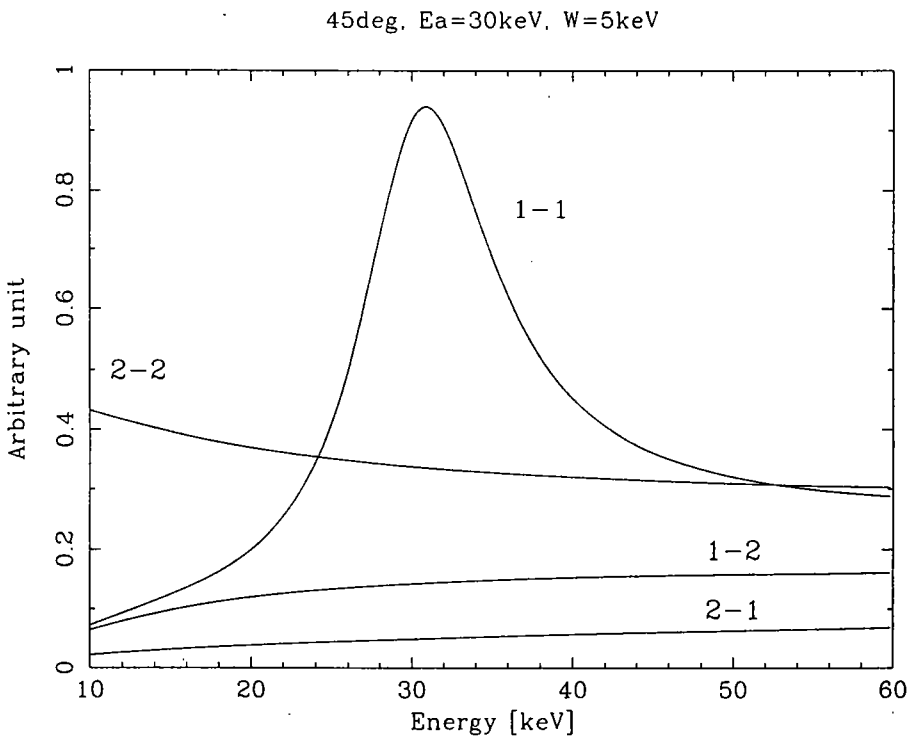

Figure 2.6.1: Energy dependences of Thomson cross section after the quantum treatment, $\theta = 45°$. See text for "1–1, 1–2, 2–1, and 2–2". The vertical axis is in an arbitrary unit.

2.6.2 The scattering cross section

The Thomson/Compton cross section in a magnetized cold plasma was derived by Ventura (1979), (see also Nagel 1980, Chap. 4 in Meszaros 1992, and Appendix 1 in Kii 1986). The cross section depends on the polarizations and directions of the incoming and outgoing photons, and whether the electron spin flip does occur or not. The polarization of the photon is represented by a linear combination of the following two modes; 1. extraordinary mode: the E-vector is perpendicular to B, and 2. ordinary mode: the E-vector is parallel to B. By integrating over outgoing angles, the scattering cross section is divided into four combinations of the polarizations of incoming and outgoing photon (Ventura 1979): 1→1, 1→2, 2→1, and 2→2, as a function of the angle θ between the incoming photon direction and the magnetic field. The four cases with $\theta = 45°$ are calculated in figure 2.6.1. Only the 1→1 case has a resonance at $E = E_a$. The 1→1 case is dominant at $\theta = 0°$, and 2→2 is dominant at $\theta = 90°$.

The remarkable point is that the 1→1 cross section at $\theta = 0°$ can be represented by a simple form

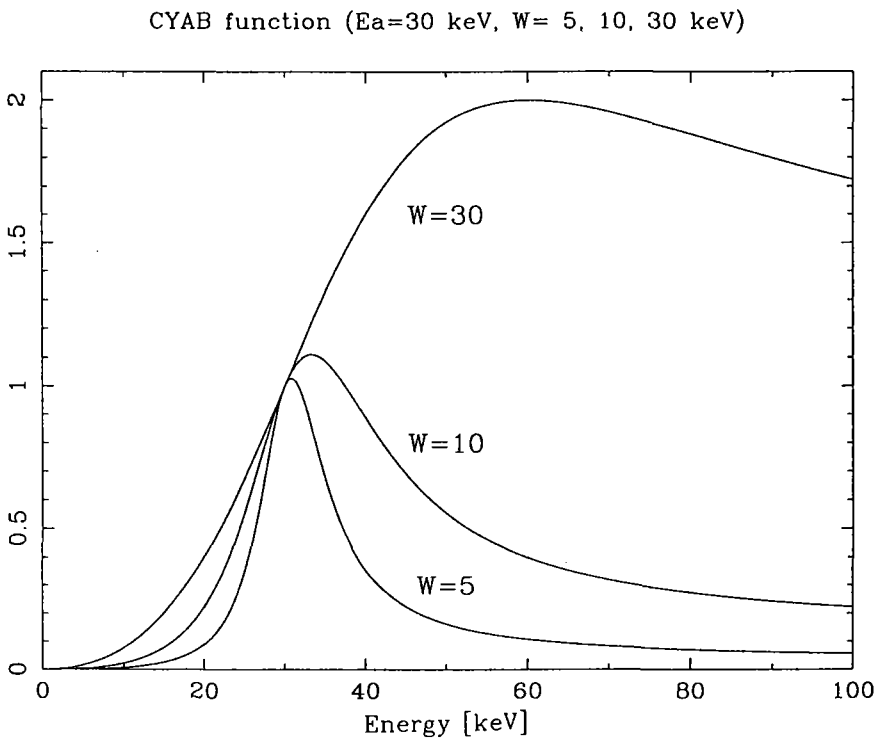

Figure 2.6.2: CYAB function for $D = 1$, E_a=30 keV and W=5, 10, 30 keV.

$$\sigma(E) = \sigma_T \frac{E^2}{(E - E_a)^2 + W^2},$$

where σ_T is the Thomson cross section, E_a is the resonance energy, and W is the width of the resonance. In a cold plasma, W is purely the natural width. The life time of an excited electron in the Landau level may be as short as 10^{-16} s (Nagel 1980). By applying $\Delta E \Delta t = \hbar$, W can be evaluated to be $\sim$ 10 eV. In real cases, however, thermal Doppler broadening and other geometrical effects are added up. When $E \to \infty$, σ approaches σ_T, which comes from that an electron with a large enough energy is free from the magnetic effect. The incident spectrum $I_0(E)$ is modified as $I_0(E)\exp(-\sigma(E)N_H)$, where N_H is the column density of the scattering plasma.

In the fitting, we replace the normalization with $D \equiv \sigma_T N_H (E_a/W)^2$, as $\sigma(E)N_H$ takes the value D at $E = E_a$. The parameter D is dimensionless and called as "Depth" in this thesis.

$$CYAB(E) = \sigma(E)N_H = \frac{D\,(\frac{W}{E_a}E)^2}{(E - E_a)^2 + W^2} \tag{2.6}$$

We cite this formula as CYAB (CYclotron ABsorption; the name comes from a historical reason) hereafter. As shown in figure 2.6.2, $\sigma(E)N_H$ has a peak around $E = E_a$, forming

a maximum at $E = E_a + W^2/E_a$, and approaches $D(W/E_a)^2$ for $E \gg E_a$. The peak drifts with W and the resonance peak is not clear for a large W.

Even when $\theta > 0°$, the absolute value of $1 \to 1$ cross section is only slightly different from CYAB function, and eq.(2.6) can give a very good approximation if the normalization is adjusted. It can be also pointed out that the non-relativistic quantum treatment of the Thomson scattering in a magnetized cold plasma leads to the exactly same cross section (see Chap. 4 in Meszaros 1992). The classical radiation power from a forced oscillator in a harmonic potential (see Chap. 3.6 in Rybicki and Lightman 1979, and Chap. 4.2 in Mihalas 1978) has a similar formula. These may justify the use of the CYAB function as the cross section of the cyclotron scattering.

Vacuum polarization becomes important in the cross section when

$$\left(\frac{\omega_p}{\omega}\right)^2 < \frac{1}{15}\frac{\alpha}{\pi}\left(\frac{B}{B_{cr}}\right)^2$$

(Ventura 1979), where $\omega_p = \sqrt{4\pi e^2 n_e/m}$ is the plasma frequency. This condition can be expressed in the following form:

$$\hbar\omega > 1.5\left(\frac{E_a}{10\ [\mathrm{keV}]}\right)^{-1}\left(\frac{n_e}{10^{20}\ [\mathrm{cm}^{-3}]}\right)^{1/2}\ [\mathrm{keV}].$$

Thus vacuum polarization may take an effect in a thin plasma.

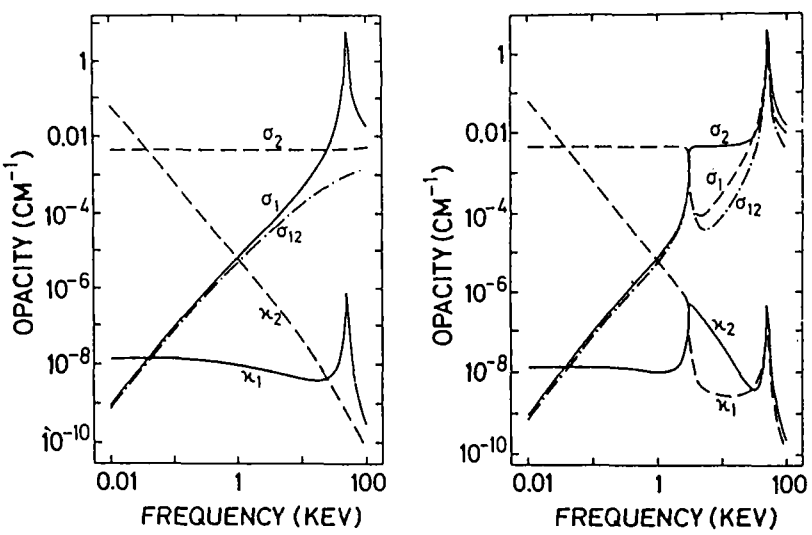

FIGURE 4.2.4 Angle-averaged scattering (σ_i) and bremsstrahlung (κ_i) opacities (cross section times density) for the ordinary and extraordinary modes for $n_e = 10^{22}$ cm^{-3} and $\hbar\omega_c = 50$ keV. The left panel is without, and the right panel is with, inclusion of vacuum effects. From J. Ventura, W. Nagel, and P. Mészáros, 1979, *Ap. J.* (*Letters*), 233, L125.

Figure 2.6.3: Taken from Meszaros (1992).

Above discussions take account of only the ground and the first excitation Landau levels, and assume a cold plasma where electron temperature is neglected. If higher Landau levels are taken into account, a multi-photon process becomes dominant in the scattering at around $nE_a(n = 2, 3, ...)$, that is an electron virtually/really excited into the second or higher Landau levels results in multiple outgoing photons. For example, in the 2 photon process, one $2E_a$ photon is absorbed and two E_a photons come out.

Moreover, in a hot plasma, the electrons have thermal motions along the magnetic field. The Doppler effect leads to a significant change in photon energy on scattering.

These two effects make the radiative transfer very complicated in a magnetized hot plasma. Some work has been done taking account of (at least one of) them; e.g. Nagel (1981a,b), Nagel (1982), Daugherty and Harding (1986), Wang *et al.* (1989), Harding and Preece (1989), and Alexander and Meszaros (1991a,b).

Alexander and Meszaros (1991a) calculated the scattering cross section in the framework of the quantum electrodynamics, as well as considering the electron thermal distribution. Their cross section shows the second and third harmonic resonances (figure 2.6.4 left). The width becomes as large as $E_a(kT/m_ec^2)^{1/2}$ by the thermal Doppler effect, where T is the temperature of electrons. Figure 2.6.4 right is the cross sections of various two photon processes. The $2E_a \rightarrow E_a + E_a$ process has a larger cross section than $2E_a \rightarrow 2E_a$ process.

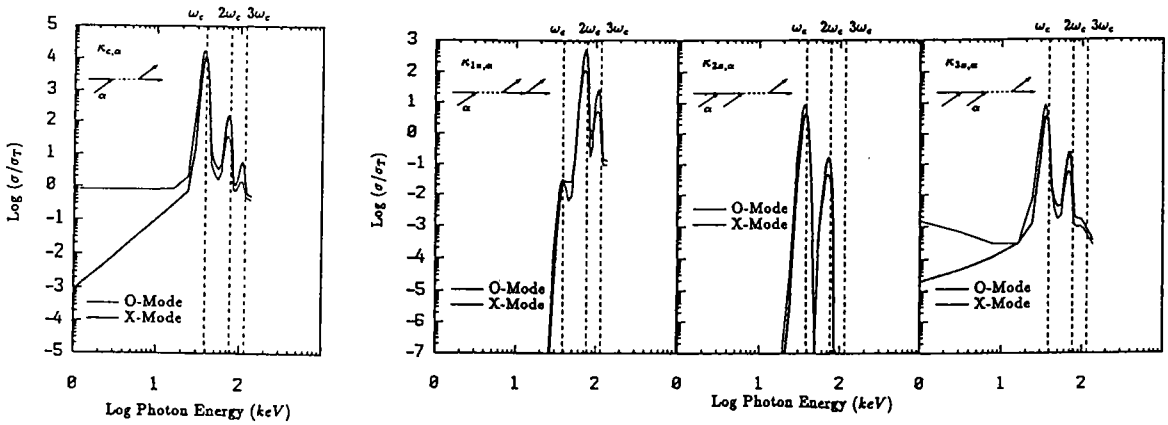

Figure 2.6.4: Cross sections of one-photon process (left) and two-photon processes (right). All the process are calculated for both extraordinary and ordinary polarization photons. Taken from Alexander and Meszaros (1991a,b).

Nagel (1981b) calculated the magnetic radiative transfer in a self free-free emitting and self Comptonizing plasma under the simplifications: using only one-photon process, averaging angular dependency of the cross section, and employing two-stream approximation. The emerging spectra for several optical depths are shown in Figure 2.6.5. When the Thomson optical depth $\tau < 1$, the spectrum accompanies an "emission" line. When $\tau > 1$, it shows an "absorption" feature.

The scattering of photons out of the core of the resonance makes an "absorption" feature, and the mechanism is similar to that of the classical Fraunhofer mechanism for the stellar absorption lines. Instead of the temperature gradient, there is an outward decreasing photon density. Near the line, we see only a short distance into the atmosphere, where the photon density is low, leading to a low intensity. Apart from the resonance, we see deeper, where the larger photon density leads to a higher intensity.

The shape of the continuum after repeated Compton scatterings resembles the non-magnetic Comptonized spectra such as Sunyaev and Titarchuk (1980). In addition to the cyclotron "absorption" feature modifying the Wien hump, there is a difference in the low-energy spectra, where the extraordinary cross section is very different from the Thomson cross section.

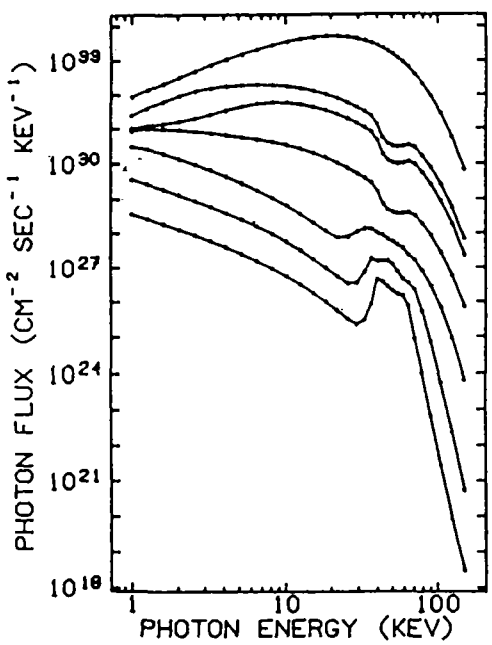

Figure 2.6.5: Spectra of magnetized slabs of increasing Thomson optical depth $\tau = 10^{-2}, 10^{-1}, ..., 10^{3}$, from bottom to top, showing the total flux in both polarizations. E_a = 50 keV, $\rho = 10^{-2}$ g cm^{-3}, and kT = 10 keV are assumed. The top curve is the Wien spectrum of kT = 10 keV. Taken from Nagel (1981b).

Alexander and Meszaros (1991b) studied the magnetic radiative transfer using the cross section including two-photon processes, and compared a calculated spectra with those observed by Trümper *et al.* (1978) and by Mihara *et al.* (1990) for Her X-1 (figure 2.6.6). The simulated spectra are similar to the observed one, but since they are numerical calculations with many parameters, the model fitting to the real data has not been performed.

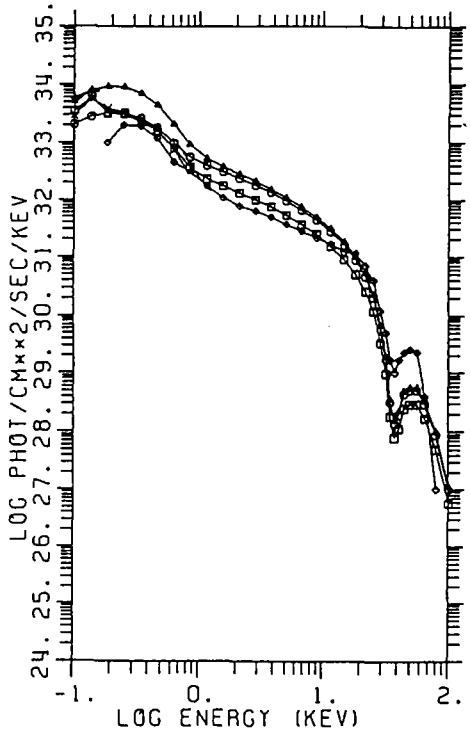

FIGURE 7.6.1 Angle-averaged spectrum of a static homogeneous atmosphere with a soft-photon source compared to the observations of Her X-1 (*diamonds*). Three models are shown with $\hbar\omega_c$ = 38 keV, kT = 7 keV, and $\rho = 1.67 \times 10^{-4}$ g cm^{-3}. The triangles and circles are for a soft photon source at the outer (inner) boundary, no escape at the inner boundary, and τ_T = 6.6, while the squares are for a soft photon source at the inner boundary, free escape from both outer and inner boundary, and twice the previous optical depth. From P. Mészáros and W. Nagel, 1985, *Ap. J.*, 298, 147.

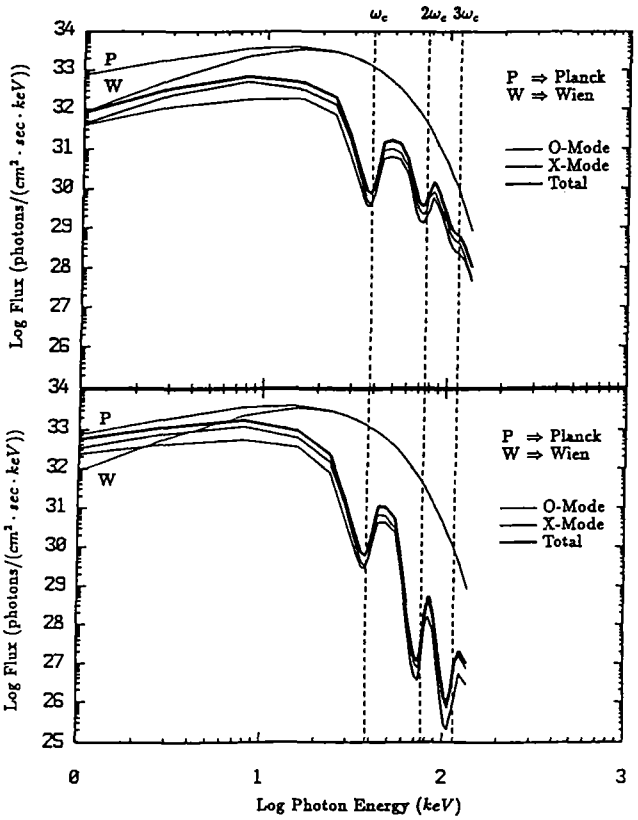

FIGURE 6.5.2 A calculation of the continuum and cyclotron line spectrum including three harmonics for ρ = 0.5 g cm^{-3}, kT = 9 keV, $\tau_T = 2 \times 10^4$, and $\hbar\omega_c$ = 38 keV. The top panel includes only the linear one-photon scattering processes, while the bottom panel includes all the one- and two-photon scattering and emission processes discussed in Chap. 5.2 These calculations use fully relativistic cross sections and one angle of scattering. The curves marked P and W are the Planck and Wien spectra. From S. Alexander and P. Mészáros, 1991, *Ap. J.*, 372, 554.

Figure 2.6.6: Taken from Meszaros (1992).

Chapter 3

Instrumentation

3.1 The *Ginga* satellite

The X-ray observatory *Ginga* (figure 3.1.1) is the third X-ray astronomical satellite of Japan following *Hakucho* and *Tenma*. The body weighing 417 kg had a rectangular shape of about 1 m × 1 m wide and 1.4 m high and four solar paddles. It was launched on 1987 February 5, just before the splendid super nova explosion of SN1987a (1987 Feb. 25), from the KSC (Kagoshima Space Center) of ISAS (Institute of Space and Astronautical Science) into an orbit of 31 degree inclination by the M-3SII rocket. The initial orbit of *Ginga* was nearly circular, with 670 km apogee, and 520 km perigee height from the ground. The orbital period was ~96 min. The height of the orbit gradually decreased since the launch, particularly after 1988 when the solar activity increased, until it reentered the atmosphere on 1991 November 1. *Ginga* continued observations without any critical trouble through the mission life of 4 years and 9 months. Having spent its first three years as the only X-ray observatory in the world, the satellite carried out many important collaborative observations in the last years of its mission life. Contributions of *Ginga* to astronomy and astrophysics are still continuing.

3.1.1 Orbit and Operation

Ginga was operated from the ground station at the KSC. The orbit of the satellite was almost fixed with respect to the solar co-ordinates, but the earth rotates. Therefore, the satellite passed over the KSC only for 5 consecutive orbits out of the daily 15 revolutions. They are called 'contact orbits'. Communication with the satellite was available only for about 10 minutes in each contact orbit. Figure 3.1.2 shows that the contact orbit passes rather high particle regions, especially, through the South Atlantic Anomaly.

On the other hand, we cannot make contact in the other ten orbits, which are called 'remote orbits'. *Ginga* does not pass through the SAA during the remote orbits. Therefore

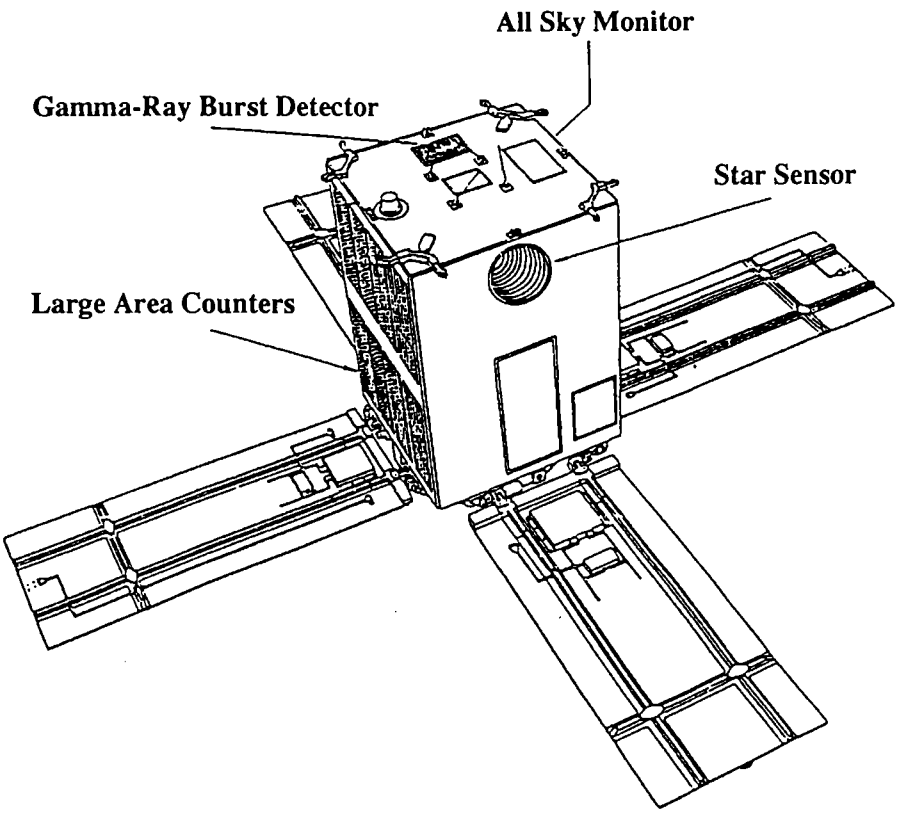

Figure 3.1.1: Instruments of the *Ginga* satellite (Turner *et al.* 1989)

the background is lower in the remote orbits than in the contact orbits.

The data obtained with the instruments, and the information of attitude, house keeping *etc.* were edited by the on-board data processor (DP) and stored in the bubble data recorder (BDR; capacity of 41.9 Mbit) while the satellite was out of contact. These stored data were then transmitted to the ground during spacecraft passages over the KSC. During these ground contacts, the two duty scientists in KSC send various instructions (so called commands) to the satellite and also check the status of the instruments.

3.1.2 Attitude control

Definition of three axes (X, Y, Z) of *Ginga* is also shown in figure 3.1.3. The Z-axis coincides with the thrust direction of the rocket, as well as the direction of the spacecraft angular momentum.

Ginga was a three-axis stabilized satellite, and its attitude was automatically controlled to meet with instructions from the ground. The attitude control system of *Ginga* utilized a bias momentum wheel and three magnetic torquers as actuators. The wheel carried the

Omni-directional flux in electrons cm^{-2} s^{-1}. (Adapted from Stassinopoulos, E. G., *World Maps of Constant B, L, and Flux Contours*, NASA SP-3054, 1970.)

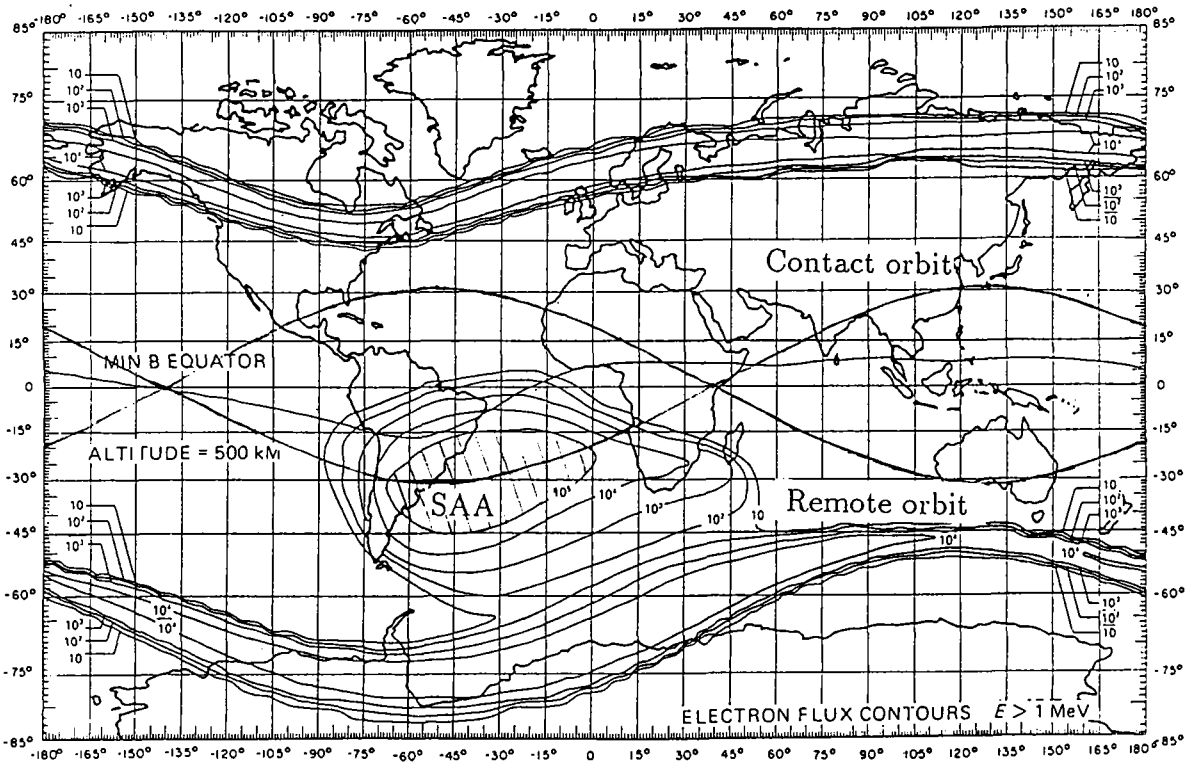

Figure 3.1.2: Orbits of *Ginga* satellite and the South Atlantic Anomaly

bias angular momentum to stabilize the spacecraft attitude. The wheel also controlled the spacecraft direction around the Z-axis (called 'slew'). The magnetic torquers controlled the Z-axis direction ('maneuver'). Because of this hybrid design of the attitude control system, the maneuvability around the Z-axis was $\sim$ 170 times more efficient than that around X- and Y-axes. That is, the speed of the slew and the maneuver was $\leq 14°$/min and $\leq 5°$/h, respectively.

The spacecraft attitude was measured on-board in reference to four gyros (X, Y, Z and skew). Differences between the instructed and measured attitudes were fed back, through an on-board closed loop, to the attitude control actuators in order to minimize the discrepancy down to an accuracy of $\sim 0.1°$. Furthermore, based on data from the gyros as well as from two (X and -Y directed) star sensors and a two-dimensional sun sensor, the spacecraft attitude and the aspect of the on-board instruments were finally determined later on ground with a typical accuracy of $\sim 0.02°$. Gradual drifts of the gyros were calibrated occasionally through this sort of data analysis on ground.

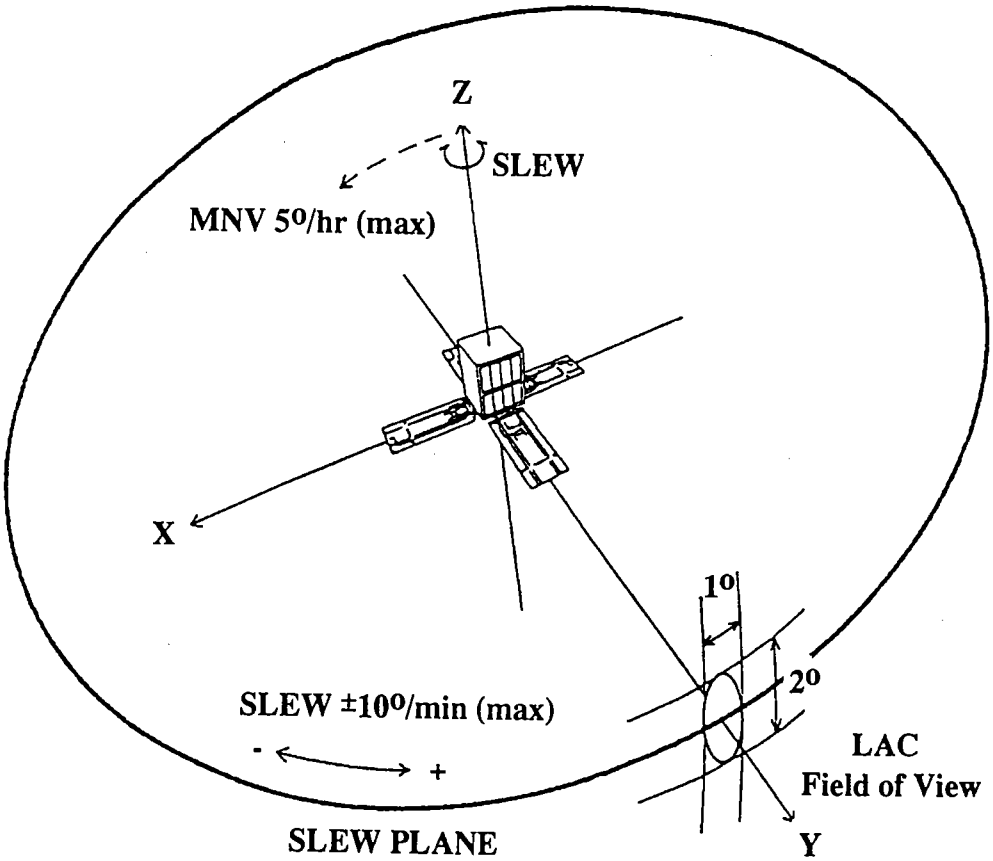

Figure 3.1.3: Definition of the three axes of *Ginga* . The LAC is mounted on the Y-face of the spacecraft. (Turner *et al.* 1989)

3.1.3 On-board instruments

Ginga carried three on-board instruments, Large Area Counter (LAC; Turner *et al.* 1989), All Sky Monitor (ASM; Tsunemi *et al.* 1989), and Gamma Burst Detector (GBD; Murakami *et al.* 1989). The main instrument, LAC, will be described in detail in 3.2.

The ASM usually monitors the X-ray sources in about 2/3rds of the sky once in a day when *Ginga* rotated 360 degrees around its Z-axis. The long fields of view are approximately directed opposite to the LAC. The ASM is composed of a pair of proportional counter arrays each of which had three independent electrodes with different fields of view. Each of the 6 counters had an effective area of about 70 cm^2 and a field of view of a narrow rectangle (2 × 80 degree) shape. They were each tilted by about 16 degree and could determine the position of the X-ray source. The detection limit was 50 mCrab for the perpendicular direction to the counters. The discovery of X-ray novas and the long-term monitoring of the intensity of the bright sources were reported by Tsunemi *et al.* (1991).

The ASM was made by Osaka University and Osaka City University.

The GBD was a wide energy range detector for γ-ray bursts, which is a phenomenon that strong γ-ray emission suddenly comes from one direction of the sky. The burst duration is from 100 ms to a hundred seconds. The source is not yet identified and the origin is not yet clear though γ-ray bursts were discovered in 1973, an early stage of X and γ-ray astronomy. The GBD consists of a xenon-filled proportional counter with effective area of 100 cm^2 and a NaI scintillation counter with effective area of 60 cm^2, covering the energy range of 2 - 30 keV and 20 - 400 keV respectively, and both have wide fields of view directed in the spacecraft Z-axis. The GBD was designed to perform observations concurrently with the LAC or the ASM. It was a joint experiment of Los Aramos National Laboratory and ISAS. It detected hundreds of γ-ray bursts in the life of *Ginga* . The discovery of a cyclotron harmonic structure in the spectra of three γ-ray bursts revealed that some γ-ray bursts occur on the neutron stars (Murakami *et al.* 1988).

3.2 The Large Area Counter

The LAC experiment was built under ISAS (Japan) – Leicester University (UK) collaboration to observe faint objects, from nearby stars to remote active galactic nuclei, and to study the fast time variability of Galactic compact objects. The experiment consisted of eight identical sealed-off multi-wired proportional counters with a total effective area of 4000 cm^2, and an electronic processing system. With its large effective area and a low internal noise, the LAC had the highest sensitivity so far achieved for cosmic X-rays in the 2–60 keV energy band.

3.2.1 The LAC detectors

Each of the eight LAC detectors was provided with its own internal guard counters, anticoincidence, pre-amplifiers, housekeeping monitoring channels, and high voltage supply which was operated normally at $\simeq$ 1830 volts. Design of each proportional counter is illustrated in figure 3.2.1. The gas vessel is made of stainless steel with an active depth of 39 mm, and the volume was filled with gas composed of 75% argon, 20% xenon and 5% carbon-dioxide (quenching mixture) at a pressure of 1.86 atm (at 273K). Beryllium entrance windows were 62μm thick and were divided into six blocks. In front of the entrance windows, the collimators were assembled using 25μm thick stainless steel sheets to achieve a field of view of $1.^\circ1 \times 2.^\circ0$ (FWHM). The collimators also served as a window support. The top 15 mm and bottom 15 mm of the collimator were coated with silver paint to prevent contamination of the spectrum by K fluorescence lines of iron, nickel, and chrome. Though this caused a fluorescent line of silver at 22.1 keV, there are no important lines from the celestial sources around this energy and it was used as an energy calibration

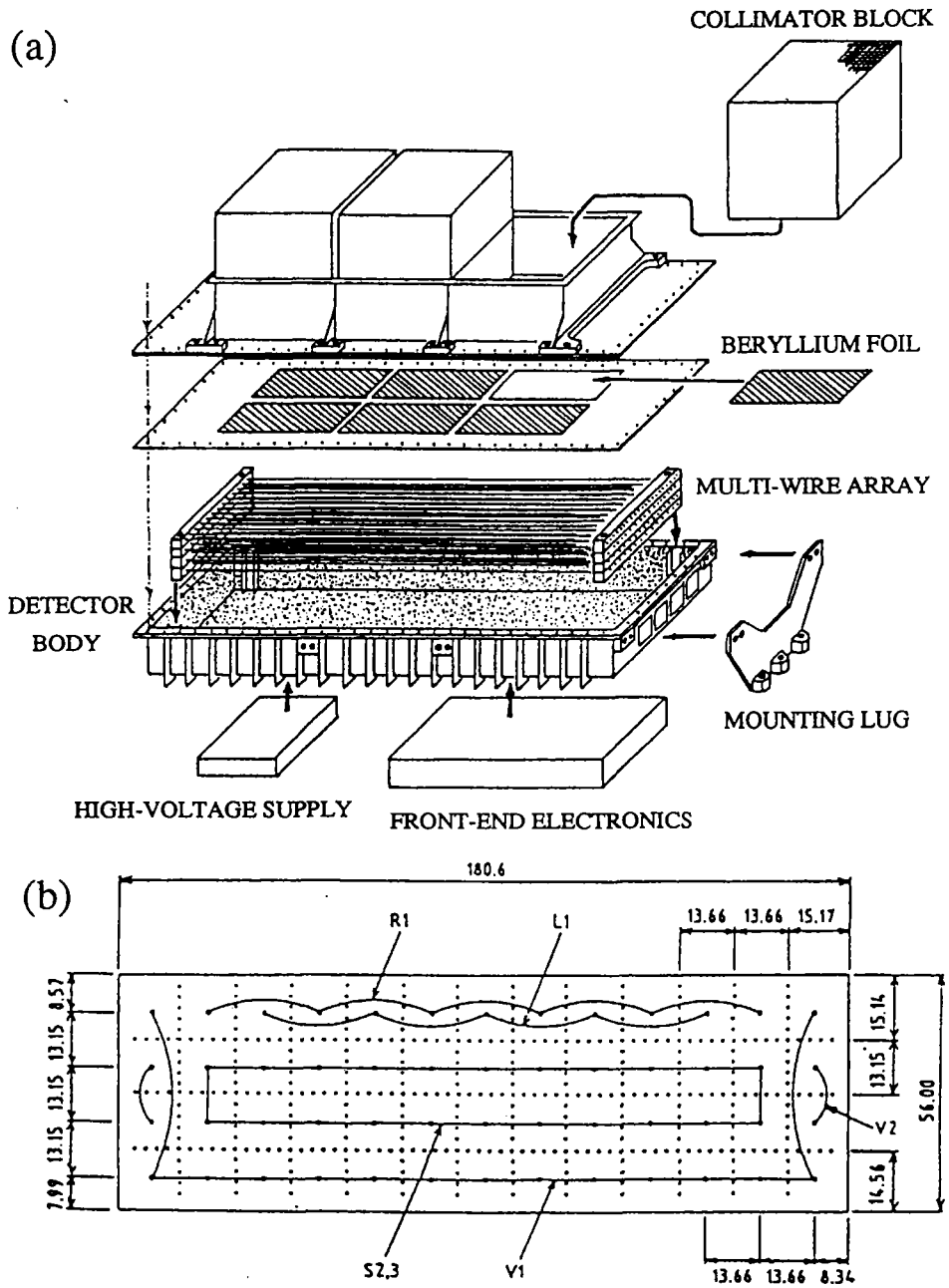

Figure 3.2.1: (a). An exploded view of a LAC detector, showing the components. (b) Cross section of the proportional counter gas cell showing the anode connections. Dimensions are in unit of mm. The figure was adopted from Turner *et al.* 1989.

scale. The gains of each counter and layer were tuned using this silver line throughout the mission about every two weeks, and the gain variance between observations is less than 1%. The effective area at the field of view center was about 500 cm^2 for each detector. The thickness of the window and the effective area were calibrated in orbit using the Crab nebula.

Detector electrodes are of a multi-layer and multi-cell concept which is suitable for achieving gain uniformity and low internal background. There are four anode layers, each layer has 13 anode wires, and each anode wire is surrounded with cathode wires to form a square cell (figure 3.2.1). Of the total 52 anode wires, those in the bottom layer and the outer wires of the other layers formed two groups called V1 and V2. The remaining wires were connected as shown in figure 3.2.1. Eleven anodes in the front layer were connected alternately to form two groups (L1 and R1), while all but the outermost anodes in the second and third layers were connected together to form another group called S23. On both ends of the anode wires near inner wall, so called end guard cathodes were attached, whose signals were connected together to form the 6th group called EV. Each electrode group was connected to a charge-sensitive amplifier. The LAC was operated with the anti-coincidence condition that if any of the two regions are hit, the event is rejected as back ground, because the X-ray is absorbed by the photo-electric process and never hits more than one wire. Of the six electrode groups, L1, R1 and S23 were signal chains, while V1, V2 and EV groups formed guard counters. L1+ R1 signals and S23 signals are referred to as 'top layer' and 'middle layer', respectively. The middle layer is expected to have especially low background, since it is surrounded by anti-coincidence wires in all the direction.

3.2.2 Spectral Response of LAC

The LAC efficiency is shown in figure 3.2.2 as a function of energy for the normal operation condition of anti-coincidence. This curve is determined by the beryllium window at low energies, and by thickness, gas composition and gas pressure at higher energies. Thus the top layer is sensitive to X-rays in the 1.5–40 keV band (where the efficiency of the photo peak $> 1\%$), while the middle layer is sensitive in the range 6–60 keV; it has twice the stopping power of the top layer. The upper broken line is a total efficiency. Although xenon is only 20%, the most photons above 10 keV are absorbed by xenon. There is a remarkable efficiency jump at 34.5 keV, which corresponds to the K absorption edge of xenon. Some detected photons above 34.5keV are followed by the xenon K escape emission, and the pulse height appears less than the true energy by 29.8keV (the energy of the Xe K emission lines).

The solid line is the efficiency of the photo peak, which has the pulse height proportional to the energy. The difference of the total efficiency and the photo peak efficiency is the

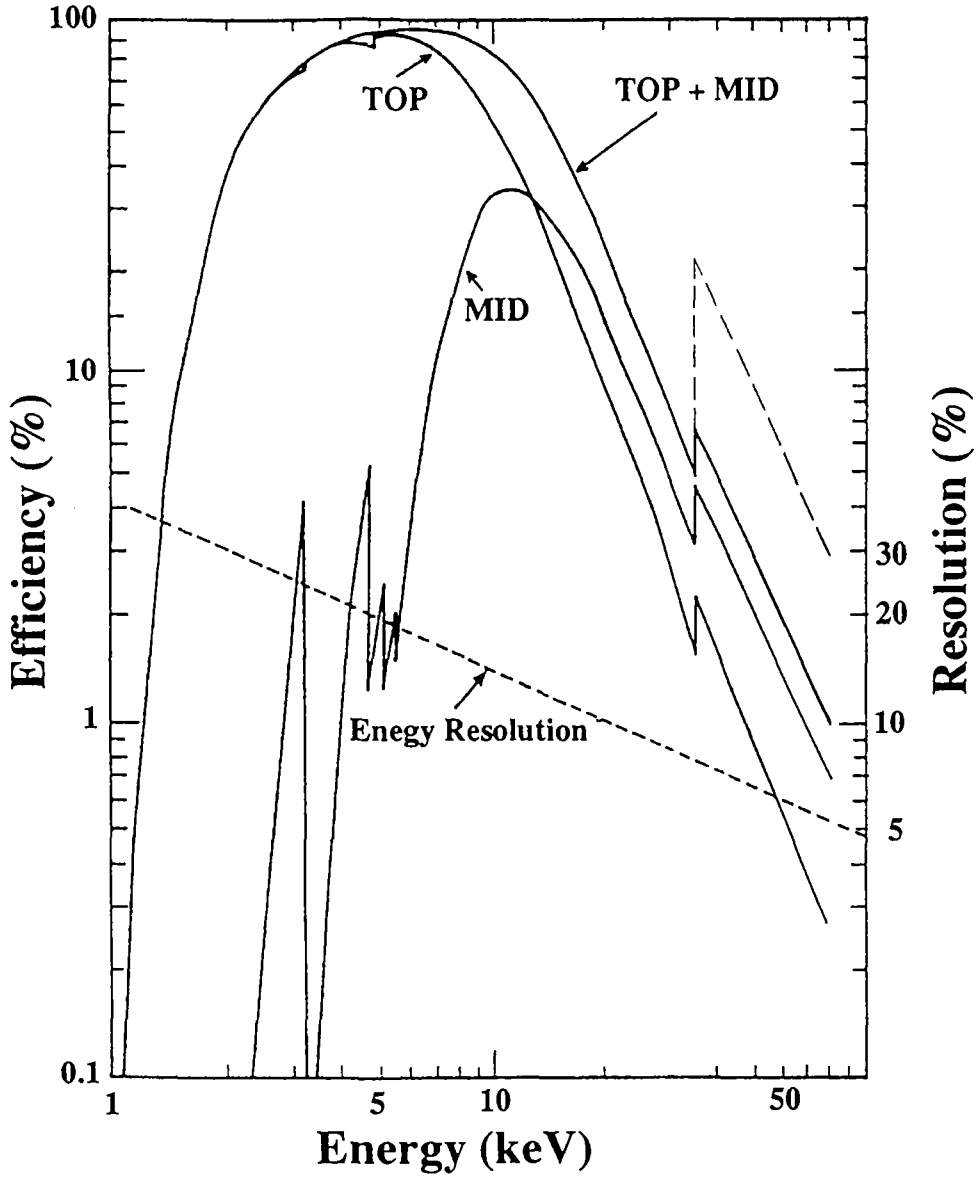

Figure 3.2.2: The photo peak efficiency of the LAC for the top, middle, and top + middle layers (solid curves) and the total efficiency of top + middle layers including escape events (upper broken line) as a function of energy. The energy resolution (dashed line) is also drawn in the figure. The measured energy resolution follows closely the $E^{-0.5}$ law. The figure was adopted from Turner *et al.* 1989.

efficiency of escape events. It is about 2.2 times larger than the normal one, and this factor is almost constant with energy.

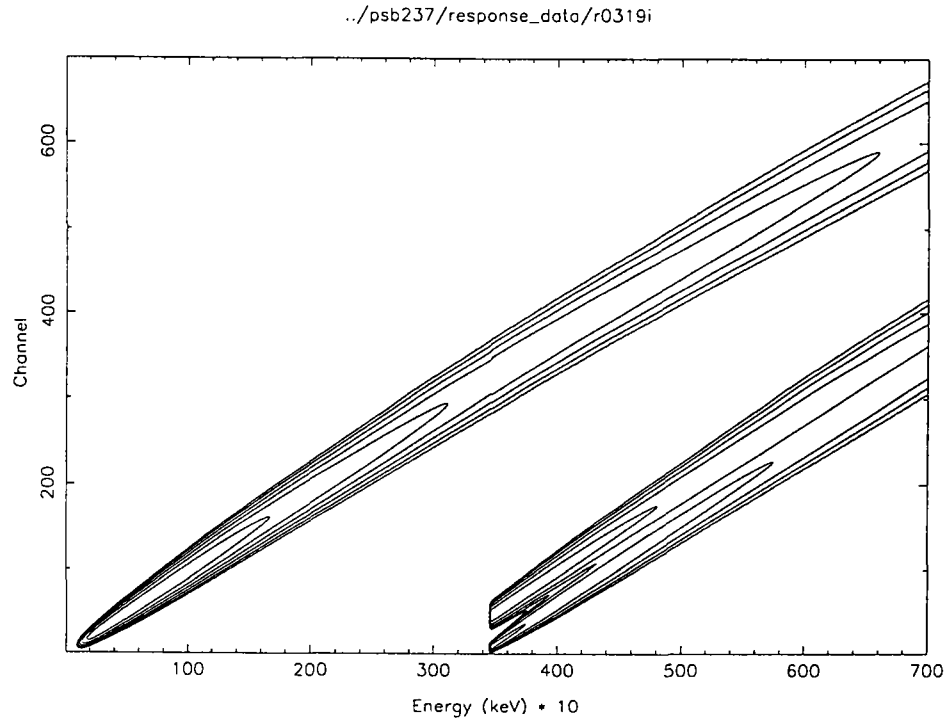

Figure 3.2.3: The contour plot of the 700 × 700 matrix of *Ginga* LAC for top + middle layer used in the standard spectral analysis SPFD (Appendix). The height of the contour represents the detection probability. If one photon with energy E enters the LAC counter, the observed spectrum is the cross section of this contours at Energy of E.

The energy resolution is 18.0% at 6 keV and scales as $E^{-1/2}$ throughout the full energy range. Figure 3.2.3 is the contour plot of the 700 × 700 matrix of *Ginga* LAC response for top + middle layer used in the standard spectral analysis SPFD (Appendix). The height of the contour represents the detection probability. It gets lower toward higher energies. If one photon with energy E enters the LAC counter, the observed spectrum is the cross section of these contours at energy E. The response of the peak is like a single gaussian. If the energy of the incident photon exceeds the xenon K edge, two escape peaks from Kα and Kβ appear in the low energies. The efficiency of the escape events is actually larger than that of the photo peak events as noted above. This efficiency curve was made by Monte-Carlo simulations and confirmed by calibration experiments at some energies on the ground prior to launch and by observations of standard X-ray sources including the Crab Nebula. Fitting the spectrum of Crab nebula has confirmed it to be correct (figure 3.2.4).

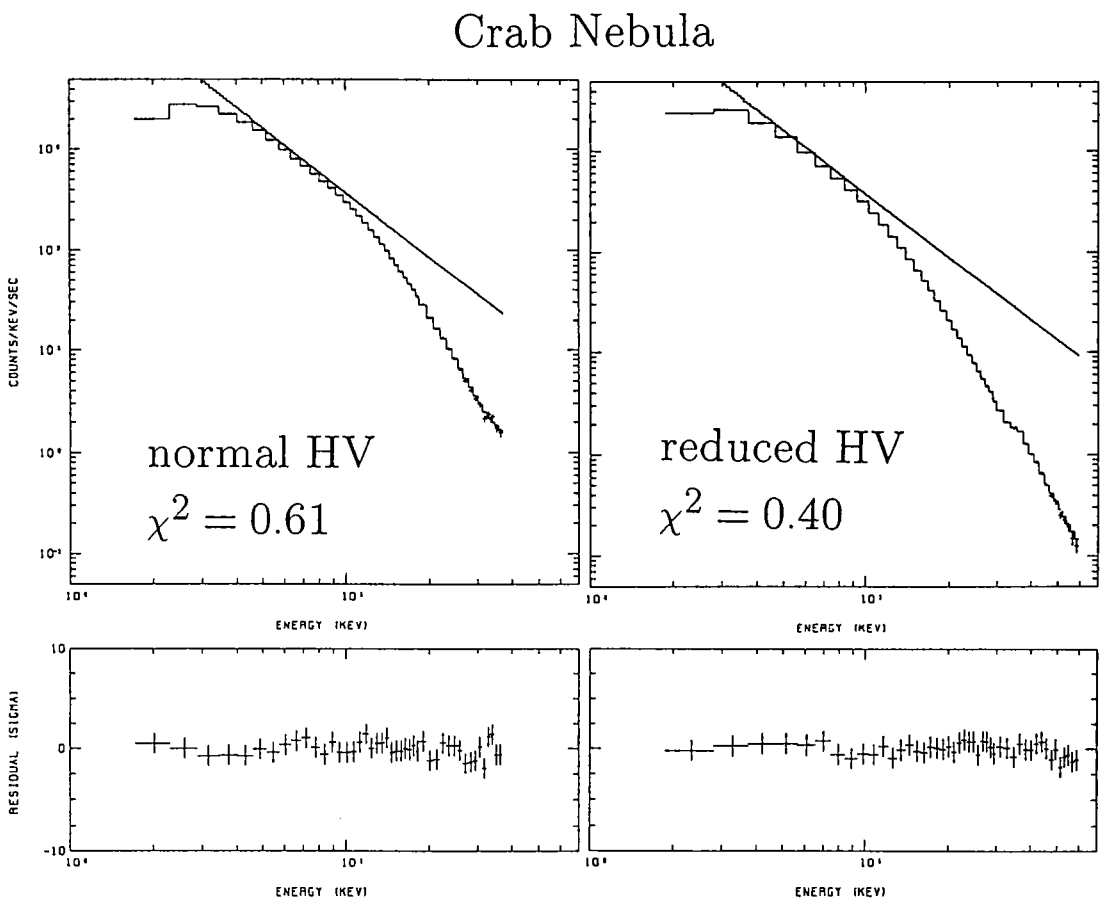

Figure 3.2.4: The spectral fitting for the Crab nebula. The normal and reduced high voltage.

3.2.3 Observation with reduced HV

Normally the high voltage (HV) of the LAC is set at 1830V, which defines an energy range upto 37 keV. This is where the LAC efficiency is high (> 5 %) and the data are mostly free from the Xe K-edge. However the LAC efficiency still remains at a few % even at 60 keV, as shown in figure 3.2.2. Therefore we can utilize a wider energy range of 1.5–60 keV, by reducing the HV by 3 steps from 1830V to 1745V. Such operation mode was sometimes used in observations of bright Galactic sources, including the black-hole candidate Cyg X-1, an LMXB X1608-52, and paticularly X-ray pulsars as will be dealt with in this thesis. We refer to these observations as reduced HV observations.

We need two particular cautions when analyzing the reduced HV data. One is that we must accurately model the effects of the Xe K-edge, since the energy range now covers well beyond 35 keV. This was achieved by ground calibration and Monte-Carlo simulation.

As a result, we were able to fit the LAC spectrum of the Crab Nebula (figure 3.2.4) over the entire 1.8–60 keV range with a single power-law model of photon index 2.09 that is thought to be.

The other is that we need a very accurate understanding of the particle background in the LAC detectors, because the energy range above ~35 keV is generally dominated by background because of the reduced efficiency for signal X-rays. We will review this subject in §3.3.

3.2.4 The LAC electronics and data

The on-board LAC electronics had eight independent but identical processing units, each connected to a fixed detector. The block diagram of a single unit is shown in figure 3.2.5. The energy range of 0 to 37 keV is pulse-height analyzed into 64 digital channels of equal width, and the digital information is sent to the spacecraft DP. The DP counts the number of events in each pulse-height channel for a fixed time interval, and formats the resultant spectrum into telemetry. Depending on combination of the pulse-height spectra, the following four format modes are available for the LAC data. The time resolutions for the modes are summarized in table 3.2.1. The present thesis uses the MPC-1 and -2 data.

Table 3.2.1: Time resolutions of LAC

Mode	Bit-rate			No. of	No. of	No. of	Comments
	High	Medium	Low	bits/ch	channels	spectra	
MPC-1	500 ms	4.0 s	16.0 s	8	48	16	TOP/MID layers × 8 counters
MPC-2	62.5 ms	500 ms	2.0 s	8	48	2	layer added. 4 counters added.
MPC-3	7.81 ms	62.5 ms	250 ms	8	12	1	all added.
PC (H)	1.95 ms	15.6 ms	62.5 ms	4	1	1	4 counters added.
(L)	0.98 ms	7.81 ms	31.3 ms	4	1	1	4 counters added.

The time resolutions in PC mode are different in the energy band (High band and Low band).

1. **MPC-1 mode** : Events are accumulated separately for the top and middle layers of the eight detectors, thus producing 16 separate spectra simultaneously. Each spectrum consists of 48 energy channels; the higher 32 consecutive channels of the original spectrum are rebinned into 16 channels.

2. **MPC-2 mode** : 16 pulse-height spectra in the MPC-1 mode are summed into two. Each spectrum sums over two layers of 4 detectors (LAC 0–3, 4–7). It means eight times compression of the MPC-1 mode, thus allowing an eight times faster time resolution.

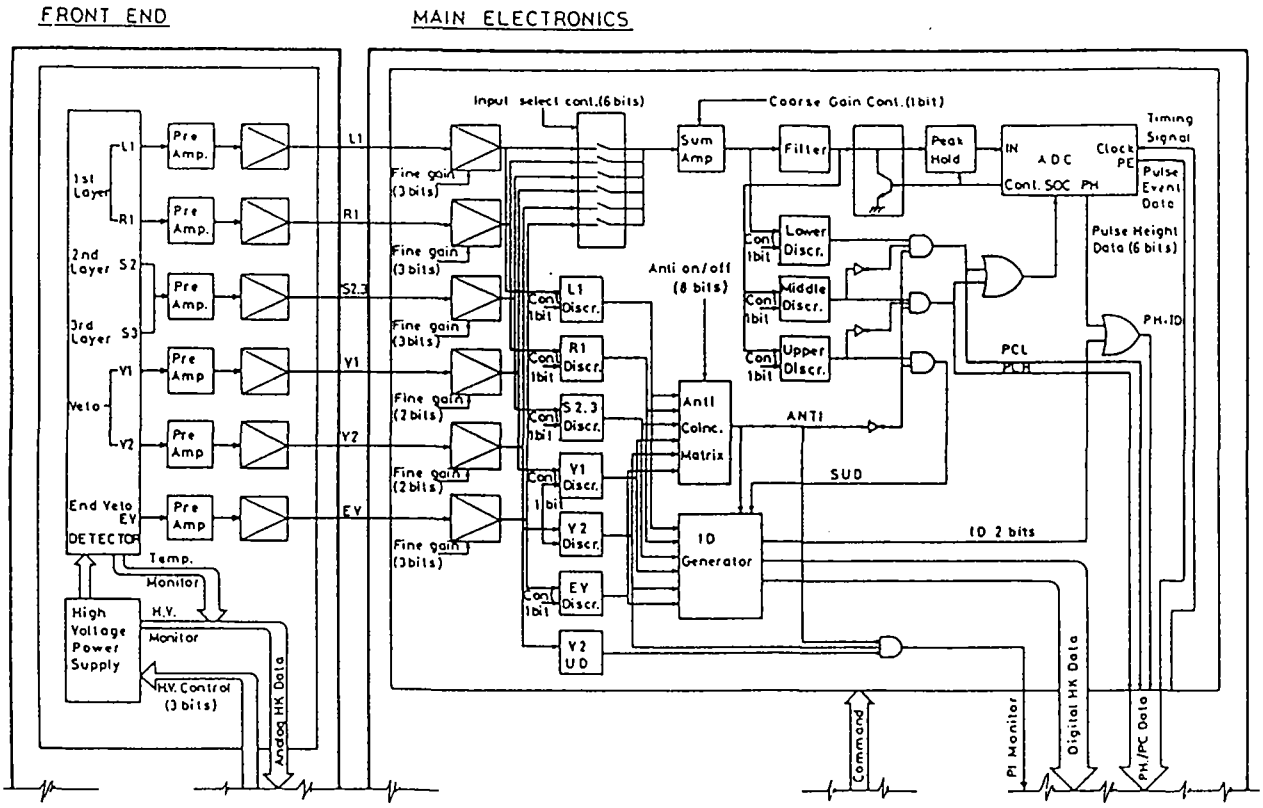

Figure 3.2.5: A block diagram of the on-board electronics

3. **MPC-3 mode** : Data obtained with two layers of eight detectors are accumulated into single 12-channel spectra; each energy channel corresponds to 4 consecutive channels in the MPC-1 or -2 mode.

4. **PC mode** : This mode is used exclusively for fast timing observations of the bright Galactic objects. The ADC is not used to reduce the dead time. The X-ray events are counted in 2 broad energy bands defined by three discriminators.

3.3 Background in the LAC

3.3.1 An overview

Even though the LAC detectors are of extremely low background quality, LAC data are dominated by background events when observing faint objects. Furthermore the LAC was usually operated in pointing modes, and there were no offset detectors available for the live-time background monitoring. Therefore the background subtraction is an essential and delicate process in the LAC data analysis. For the purpose of background subtraction, we usually performed an off-source observation at a nearby blank sky region, immediately before or after each on-source pointing. However, direct subtraction of the off-source data from the on-source data does not work, because the LAC background comprises many different components which are mostly time variable in different and complex ways.

The LAC background is grossly divided into 'internal' (non X-ray) background, and cosmic diffuse X-ray background (CXB) incident through the field of view. The CXB component is about 16 counts s^{-1}, while the internal background varies between $\sim$ 50 counts s^{-1} in the remote orbits and $\sim$ 100 counts s^{-1} in the contact orbits (all expressed in the 1.2-37 keV range and for the top + middle layers of the 8 detectors). An typical spectrum of internal + CXB background is shown in figure 3.3.1. The line around 22 keV is a fluorescent X-ray of silver on the surface of the collimator. The 6.4 keV line is a fluorescent X-ray of iron which is a component of the stainless body of the LAC. Below we will review the behavior of the components of the background, after the work by Hayashida *et al.* (1989).

3.3.2 Background components

The internal background in the LAC detectors comprises the following components.

1. **Cosmic Rays**
   Charged particles passing through the LAC detectors produce spurious events, although most of them are rejected by the anti-coincidence. γ-rays produced in the LAC environment by charged particles can interact with the detector gas via Compton scattering and increase background. These effects depend on the cosmic-ray flux, which scales with the geomagnetic cutoff rigidity (§3.3.3).

2. **Charged particles trapped geomagnetically**
   Their contribution increases in regions such as the South Atlantic Anomaly (SAA), where the earth magnetosphere becomes as low as the satellite orbits. Because of the orbital inclination of 31°, the satellite passes the SAA in 7 orbits per day including all the contact orbits. To protect the detectors against excessive counting rate, the LAC high voltage is turned off during the SAA passage, both manually and automatically.

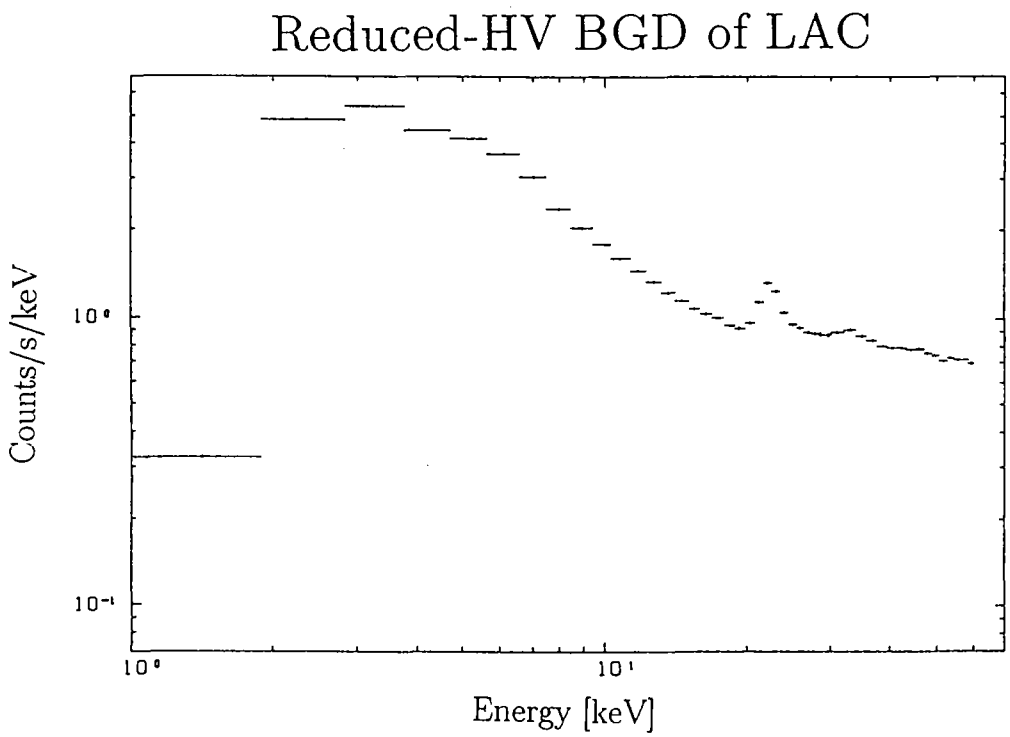

Figure 3.3.1: Typical HV-reduced background spectrum of the LAC

3. **Activation of detector and spacecraft material**
   The LAC internal background remains high for a typical time scale of 5 min after a SAA passage, because materials in the detectors and spacecraft becomes slightly radioactive by interaction with charged particles. There are several components, and the decay time for one is longer than 2 h. The radioactivity decays on various time scales, and resulting γ-rays increases the LAC background. Due to this effect, the internal background is doubled in contact orbits compared with in remote orbits which are free from the SAA.

4. **Penetrating cosmic diffuse hard X-rays**
   Cosmic diffuse X-rays above $\sim$ 35 keV penetrating the detector wall and the collimator cells generate 'X-ray' events, through xenon K-escape process. Pulse height of such an event is shifted towards lower energies by 30 keV (xenon K-line energy), and often falls in the energy range below 37 keV. In order to minimize this effect, the LAC detectors were carefully shielded with 0.2–0.5 mm thick tin foils. This component is mostly constant with time.

3.3.3 Background monitor parameters

There are several auxiliary parameters which are closely correlated with the internal background rate, although none of them is by itself sufficient to determine the background spectrum uniquely. Below we summarize these 'background monitor parameters', which play an important role in the background modeling. The former four parameters are available in the telemetry data, while the latter four are calculated from the satellite position.

1. **SUD**. This refers to the count rate of X-ray-like events whose energy deposit in the LAC surpasses the upper discriminator (UD) which is set at about 37 ch, 24 keV in normal high voltage. We subtract the counts between 37 and 48 ch from UD counts and get Superior Upper Discrimination (SUD) Counts, which is the count above 48ch (= 37 keV in the norml HV and 60 keV in the reduced HV). Since the X-ray efficiency is less than $\sim 3\%$ in the SUD range, it mainly represents the flux of high-energy particles and γ-rays.

2. **MID**. The count rate of lower energy channels (1–5 keV) in the middle layer (S23) of the LAC. This is a good monitor of the internal background below 8 keV, since in this energy region most of the aperture X-rays must be absorbed in the top layer. This monitor item is available only in the MPC-1 mode.

3. **PIM**. Count rate of the V2 electrodes (figure 3.2.1), i.e. anodes which are screened from direct illumination of aperture X-rays but otherwise similar to the other wires.

4. **SOL2**. The count rate of a solid-state detector (PIN diode), a component of the GBD experiment. It is sensitive to particles, especially trapped electrons, and is used as Radiation Belt Monitor (RBM).

5. **RIG**. The geomagnetic cutoff rigidity, defined as the minimum momentum per elementary charge to penetrate the earth magnetosphere to reach a given point of the orbit. Lower rigidity means a higher number of ambient particles.

6. **SAA**. This is a time counter, accumulated with an exponential decay factor, after each satellite passage through the SAA. It represents the effect of radioactive decay as described in §3.3.2. In practice, several different time counters using different decay time constants can be set.

7. **AOP**. The argument of perigee of the satellite orbit. Since the plane of the orbit rotates along the polar axis, this parameter changes with a period of 37 days, The satellite passes the SAA in the contact orbits every day, but the height of the satellite in the SAA passage is different with the AOP. When the apogee is close to the SAA, the satellite is radioactivated by more particles and the LAC internal background increases. The internal background varies significantly with the same period.

8. **Orbital height.** The height of the orbit also effect the background. As the height gets lower year by year, both the SUD counts and the background counts get lower.

3.3.4 Background subtraction

There are mainly three ways to subtract the background of LAC.

1. **Simple subtraction**
   This is the simplest way; just subtracting the background spectrum from the source spectrum. The data should be chosen prior to the subtraction so that the source data and the background data have almost the same values of the parameters as noted in the prior subsection.

2. **SUD sorted method**
   The counting rate of the SUD correlates with the non-X-ray background best of all the parameters. The coefficients of the correlation stayed constant within a few days, but showed periodic 37 d variations with the AOP. Thus the background data obtained from the blank sky regions over a few days or on the same phase in 37 d period are appropriate for the background subtraction. In this method, both on-source and background data are first sorted into several sub-groups accordingly to the SUD rate, the background is subtracted within each sub-group, and finally the subtracted on-source spectra are added together to a single spectrum. When the source is hard and strong, the X-ray from the source may increase the SUD counts. Therefore we must be careful of the X-ray leakage of the source into the SUD when using this method.

3. **Hayashida method**
   The behavior of the internal background of LAC to the parameters was studied by Hayashida *et al.* (1989). From the information of the correlations, we can estimate the background spectrum from the monitoring parameters as

$$BGD(E,t) = F_0(E) + \sum_{i=1}^{N} F_i(E,t) \times P_i$$

   where E is the energy in the spectrum, t is the time from the launch giving the slow changes in the order of months, BGD(E,t) is the background spectrum, $F_0(E)$ is the well-known diffuse X-ray background, $F_i(E,t)$ is the coefficients obtained from the background study, and P_i is the monitoring parameter. The five parameters, SUD, RIG, MID, AOP, PIM, have been found to be sufficient to reproduce the background spectrum.

This method is only for the normal HV, where plenty of backgrounds were observed. It is not established for the reduced HV observation. Moreover, this method cannot produce the galactic ridge background, where most of the X-ray pulsars are distributed.

3.3.5 Background in the reduced HV data

Although the LAC internal background in the normal 1–37 keV energy range has been studied very well (Hayashida *et al.* 1989), that in the 37–60 keV range remained mostly unknown in spite of its importance in the analysis of reduced HV data. We therefore performed a careful study of the internal background in the reduced HV mode, using Her X-1 data in 1989. We have found the behavior of internal background is essentially the same between above and below $\sim$ 37 keV, so that the SUD sorted method for the background subtraction described in §3.3.4 applies as well to the reduced HV data.

An example of the background subtraction in the reduced HV mode is shown as the Crab spectrum of figure 3.2.4. Although the Crab Nebula is a bright and hard source, its signal becomes comparable to the internal background at $\sim$ 40 keV, and falls to 1/8 of the background at 60 keV, The good fit achieved in figure 3.2.4 ensures that the background subtraction has been correct.

Chapter 4

Observation

4.1 Overview

Throughout the mission lifetime of 4 years and 9 months, *Ginga* observed a number of binary X-ray pulsars and related objects. These observations were carried out by many different principal investigators with various scientific objectives. They were performed under different observation categories, including performance-verification-phase (PV) observations, principal-investigator (PI) observations, target-of-opportunity (TOO) observations, and late-phase joint (LJO) observations.

Although results from these observations have already been published in many cases, in the present thesis we will re-analyze a good fraction of these data, in a unified way from the viewpoint of cyclotron resonance effects in the obtained spectra. However, we will not use the data unsuitable for detailed spectral studies, including those taken in high-time-resolution modes (MPC-3 and PC modes), during low intensity states and binary eclipses of the target sources, and so on. In this section, we describe relevant *Ginga* observations.

All the observations dealt with here were performed using the *Ginga* LAC, with the spacecraft attitude mostly in the normal pointing mode. The LAC detectors were normally operated at a high voltage level of 1830 V, which defines the observable energy range up to 37 keV. However as mentioned in chapter 2, most X-ray pulsars are expected to have cyclotron resonances at $\geq$ 20 keV. Therefore those observations which were planned specifically for the study of cyclotron resonance effects were performed in a 'reduced high voltage (HV)' mode, in which an energy range up to 60 keV was achieved by reducing the high voltage level by three steps down to 1745 V (see §3.2.3). In such observations the LAC data were taken in the MPC-1 or MPC-2 modes, in which the full energy range is covered with 48 spectral channels (see §3.2.4). When both the normal-HV and reduced-HV data are available for an object, we will mainly use the reduced-HV data.

We describe observations of persistent sources and transient sources in §4.2 and 4.3

respectively, together with brief information on each object. Table 4.1.1 summarizes date and time of the observation, net exposure time, high voltage level, observation category, and the observed source intensity for each source together with references to the previous publications. Various parameters of the sources, including the pulse period and its change trend, the orbital period, type of the companion star, distance, and the X-ray luminosity, are summarized in Table 4.1.2. Further information on these objects is available in Nagase (1989, 1992) and White *et al.* (1983).

We present background-subtracted and aspect-corrected light curves from these *Ginga* observations in three energy bands, 2–8, 8–20, and 20–37 (or 20–60) keV for some pulsars. These energy bands respectively correspond to the low energy region affected by photoelectric absorption by matter, the medium energy region where the power-law continuum dominates, and the high-energy region where the spectrum falls off steeply.

4.2 Observations of Persistent Sources

Within our Galaxy and the two Magellanic clouds, there are about two dozens of accretion-powered pulsars that are more or less persistently X-ray bright. Most of them have been observed with *Ginga* during its mission lifetime.

4.2.1 4U 1538-52

The 529 s pulsar 4U 1538-52 has a 3.73 d orbit, an eclipse duration of about 0.8 days, and a projected orbital radius of $a_x \sin i = 55$ lt-s. Its optical companion star, QV Nor, is a B0e type supergiant. The pulse period shows a spin down trend on the average ($\dot{P}/P = 2.3 \times 10^{-4}$ yr^{-1}, Makishima *et al.* 1987), on which short-term fluctuation is superposed. This, and a relatively low X-ray luminosity ($\sim 10^{36}$ erg s^{-1} at an estimated distance of 5.5 kpc), suggest that 4U 1538-52 is most likely a wind-fed pulsar.

Ginga observed 4U 1538-52 from 1988 February 29 to March 3, covering a whole orbital cycle, to investigate spectral changes during eclipse transitions. As a by-product of this observation, a cyclotron resonance feature was discovered at 20 keV (Clark *et al.* 1989; Bulik *et al.* 1992). The feature was significantly dependent on the pulse phase and generally appeared in absorption. Clark *et al.* (1989) also discussed possible presence of the second harmonic absorption. This is the third example of cyclotron resonances yet observed from binary X-ray pulsars, and indeed the first of such examples discovered with the *Ginga* LAC. Therefore this observation has become the very start point of a series of investigations to be summarized by the present thesis.

The second observation of this object was carried out on 1990 July 27 in the reduced-HV mode, to search for the second harmonic structure expected around 40 keV. The source was detected at an intensity of 14 mCrab, which is typical of this source, and the 20 keV fundamental structure was reconfirmed. We analyze these reduced-HV data in §5. However, the source intensity was not high enough for a convincing detection of the second harmonic resonance.

Table 4.1.1: Journal of observations of binary X-ray pulsars

Source (P/T)[a]	Start time of observation[b] year	date	[UT]	End time of observation date	[UT]	Exposure Time[c] [s]	H.V.[d]	Flux[e] [mC]	P.I.[f]	Ref. *etc.*
SMC X-1 (P)	88	8/24	22:38	9/ 2	18:21	(505000)	N		DN	Levine 93
	89	7/29	4:30	8/ 3	5:40	(403000)	N		RCN	
Her X-1 (P)	89	5/ 3	17:15	5/ 3	18:54	2200	L	87	MD	one *Ginga* orbit
	89	6/ 3	0:46	6/ 9	2:24	7000	L	91	MD	Mihara 90
	90	7/27	9:59	7/28	9:59	10000	L	125	MMT	
4U0115+63 (T)	90	2/ 9	20:55	2/ 9	23:17	4450	N		TOO	Nagase 91
	90	2/11	19:55	2/11	23:24	8170	L	427	TOO	
	91	4/26	12:38	4/27	23:11	49500	L	70	TOO	
	91	6/17	12:14	6/19	15:13	13000	L	<0.2	TOO	undetected
X0331+53 (T)	89	9/19	21:41	9/20	21:19	6000	N	220	TOO	
	89	10/ 1	18:54	10/ 1	22:21	6400	L	330	TOO	Makishima 90b
Cen X-3 (P)	89	3/21	23:57	3/24	12:24	70000	N	90	Tk	Nagase 92
1E2259+586 (P)	87	6/21	9:46	6/23	10: 8	(174000)	N		PV	Koyama 89
	89	12/14	23: 5	12/19	20:27	(231000)	N		HK	Iwasawa 92
	90	8/ 8	7:44	8/11	2: 1	(238000)	N		LJO	Iwasawa 92
4U1626-67 (P)	90	4/18	12:20	4/21	14:53	26000	L	28	MMT	
GS0834-430 (T)	91	5/28	22:43	5/29	1:30	3213	L	81	TOO	Aoki 93
LMC X-4 (P)	88	3/ 7	5:52	3/10	9:28	(272000)	N		CI	Corbet 91
	89	8/ 3	9:41	8/ 5	23: 3	(220000)	N		RN	Levine 91
GS1843+00 (T)	88	4/19	12:31	4/20	22:57	12000	N	40	TOO	Koyama 90a
OAO1657-415 (P)	88	3/17		in the		126	N	24	K	Kamata 90
	88	4/ 7		scanning		1260	N	30	K	Kamata 90
	89	3/ 4		observations		1400	N	39	K	Kamata 90
EXO2030+375 (T)	89	10/29	22:50	11/ 1	0: 7	21300	N	4	TOO	
Cep X-4 (T)	88	4/ 3	21:55	4/ 4	6:41	10432	N	85	TOO	Koyama 91a
	88	4/ 8	17:48	4/10	11:20	46900	N	70	TOO	and
	88	4/14	13:18	4/15	3:33	17475	N	45	TOO	Mihara 91b
GS1843-02 (T)	89	9/29	10:32	9/29	17:17	6700	N	10	K	Koyama 90b
	89	10/ 3	10:50	10/ 3	14:20	3032	N	10	K	Koyama 90b
A0535+26 (T)	87	10/24	22:42	10/25	10:33	11000	N	2.4	TOO	
	89	4/ 4	6: 6	4/ 4	6:19	660	N	771	TOO	
	90	4/18	16:35	4/19	11: 5	20000	L	1.4	TOO	
Sct X-1 (T)	88	11/14	9: 8	11/14	19:40	~5000	N	2	TOO	Koyama 91b
GX1+4 (P)	87	3/30	16:53	3/30	22: 6	4000	N	2	PV	
	88	3/27	4: 9	3/27	16:49	5400	N	11	TOO	
	89	8/27	11: 9	8/27	21:31	20000	N	13	TOO	
	90	9/ 4	13:47	9/ 5	12:16	6550	N	9	TOO	
	91	9/14	17:24	9/16	1:38	24000	L	2	TOO	

Vela X-1 (P)	90	4/20	14:20	4/22	6:27	50000	L	100	MMT	
1E1145.1-61.41 (T)	91	3/14	1:30	3/16	5:50	61500	L	30	LJO	
X1722-36 (P)	87	10/10	10:30	10/10	21:50	18000	N	0.2–2	PV	Tawara 89
	88	3/29	23:41	4/ 6	12:31	34000	N	1–3	WK	Takeuchi 90
4U1907+09 (P)	90	9/21	8: 6	9/22	22:45	11000	L	13	LJO	
4U1538-52 (P)	88	3/ 2	11:55	3/ 3	19:45	~70000	N	20	Cl	Clark 89
	90	7/27	15:22	7/28	23: 0	60700	L	14	MMT	Bulik 92
GX301-2 (P)	90	6/14	12:38	6/15	18: 2	21440	L	72	MMT	
	91	3/13	20:54	3/14	1:28	15000	L	100	LJO	
X Per (P)	90	1/26	12:19	1/28	19:11	60000	N	12	Robba	
4U1700-37 (P)	91	4/19	22:23	4/20	0: 7	2400	L	235	MMT	

The sources are the incresing order of the pulse period. See table 4.2.

a: Character in the parentheis means,
P : Persistent source,
T : Transient source.

b: The start and end time are for one whole journal of observation. Obervation of another source might be inserted in them. For example, there were three day joint observation of a pulsar in the contact orbit and an AGN for the remote.

c: The exposure time is the total effective time of the obsrvations. Earth occultations and regions of high particle background are excluded. The values with parenthesis () are taken from the *Ginga* observation log, in which the earth occultation etc. are included. The total effective time is roughly 1/3 – 1/4 of it.

d: HV column indicates high voltage condition.
N : normal HV mode (2–37 keV)
L : low HV mode (2–60 keV).

e: The flux is in full energy band, 2–37 keV or 2–60keV in the unit of mCrab. 1 mCrab ~ 1 μJy in this energy band.

f: P.I.(Principal Investigator) notations

Cl : Clark	Co : Corbet	DN : Deeter, Nagase
HK : Halpern, Koyama	LJO : Latter phase Joint Observation	MD : Miyamoto, Deeter
MMT : Makishima, Mihara, Tashiro	PV : Performance Verification	RCN : Rappaport, Clark, Nagase
RN : Rappaport, Nagase	Tk : Takeshima	TOO : Target Of Oppotunity
WK : Warwick, Koyama		

The pulsars below were observed with *Ginga* , but not included in this table.

1E1048-593	The intensity was low (0.8 mCrab). There was a contamination by η Car (Corbet *et al.* 1990).
GX304-1	Under detection limit (< 0.2mCrab).
X1239-599	Under detection limit (< 0.2mCrab).
X0535-668	No pulsations in the twice observations.

Table 4.1.2: Parameters of the sources[a]

Source	Apparent Pulse Period [s]	pulse period changes[b]	Orbital Period [day]	Companion star type	mass [$M_\odot$]	Distance [kpc]	log Lx (2-37(60)keV) [erg/s]
SMC X-1	0.717	↗	3.892	B0		50	38.6
Her X-1	1.24	~	1.700	A9	2	5.8	37.5
4U0115+63	3.6	~	24.31	Be	>5	3.5	37.5, 36.7 [c]
X0331+53	4.37	↘	34.25	Be	(10)	3	37.43, 37.29 [d]
Cen X-3	4.82	↗	2.087	O7		8	37.7
1E2259+586	6.98	↘	<0.08	—	<0.1	3.6	35.2
4U1626-67	7.66	↗↘	0.0228?	—		6	36.9
GS0834-430	12.32	—	111.6	(Be)		—	—
LMC X-4	13.5	↗	1.408	O7	15	50	38.6
GS1843+00	29.5	—	—	(Be)	(10)	(8)	(37.5)
OAO1657-415	37.7	↗	10.444	—		1~5	35.6-37.0
EXO2030+375	41.68	~	46.03	(Be)	(10)	5	35.8
Cep X-4	66.25	—	>23	(Be)	(10)	(3)	(36.6)
GS1843-02	94.9	—	—	(Be)		(8)	(36.9)
A 0535+26	103.4	~	111	B0III	15	1.8-2.6	37.4-37.7
Sct X-1	111.0	—	—	—		—	—
GX 1+4	111.6	↗↘	(304)	M6III		9	36.7 [e]
Vela X-1	283	~	8.965	B0	24	1.4	36.2
1E1145.1-6141	296.90	↗	—	B2I-IIa		(9)	(37.3)
X1722-36	413.08	—	>9	(Be)	>15	—	—
4U1907+09	439.47	↗	8.38	B2III-V	>12	2	35.5
4U1538-52	529	↘	3.73	B0	19	5.5	36.4
GX301-2	683	~	41.5	B1.5Ia	30	1.8	36.7
X Per	837.7	~	(580)	Be	22	0.3	33.6
4U1700-37	—	—	3.41	Of	52	1.8	36.7

a: These values are from observations with *Ginga* . Supplementary information is from Nagase 1989, Nagase 1992, and White *et al.* 1983 *etc.*

b: Gross behavior of the pulse period change is indicated with the following symbols, see figure 2.3.3 and Nagase 1989 in detail.

↗ : relatively monotonic spin up (the spin period getting shorter).

↘ : relatively monotonic spin down (the spin period getting longer).

~ : random fluctuation in pulse period.

— : no detailed information available.

c: In the 1990, 1991 observations, respectively.

d: In the 1989 September 20 and 1989 October 1 observations, respectively.

e: Both in the 1988, 1990 observations.

4.2.2 Her X-1

As reviewed in §2, Her X-1 has been studied extensively throughout the history of X-ray astronomy, from various aspects including the cyclotron resonance effects. Since the cyclotron feature in Her X-1 was considered to be either an emission line at about 60 keV or an absorption trough at about 35 keV, it was essential to operate the LAC in the reduced-HV mode for the study of cyclotron resonance feature in this prototype object.

Motivated by the discovery of the 20 keV cyclotron absorption from 4U 1538-52 by Clark *et al.* (1989), we performed the first reduced-HV *Ginga* observation of Her X-1 on 1989 May 3, when Her X-1 was in a main-on state. The observation was with MPC-1 mode at the sacrifice of the the time resolution (0.5s), because we had to check the gains of all the LAC counters and layers in the reduced-HV mode. Although it was a limited observation lasting only for one *Ginga* orbit with a net exposure time of 2200 s, the cyclotron structure was suggested in the obtained spectrum. Therefore additional reduced-HV observations were attempted for additional 7000 s on the next main-on state, on 1989 June 3 and 6. We used MPC-2 mode this time, whose time resolution was 62.5 ms, and performed the phase resolved analysis. Background was also taken in the neighboring sky on June 3 and 8 (figure 3.3.1). The results from these observations have been published in Mihara *et al.* (1990), in which they suggested that the resonance appears in absorption at about 35 keV rather than in emission.

The third reduced-HV observation was carried out on 1990 July 26–29, in a combination with 4U 1538-52 as a part of the systematic study of cyclotron resonances. Since the purpose of this observation is to take a spectrum with high statistics at high energies, we observed it in the main-on state, and avoided the eclipses. Her X-1 was observed in the contact passes where high bit-rate is available. The 1.24 s pulse period of Her X-1 needs MPC-2 high bit-rate to perform the phase resolved analysis. On the other hand, MPC-1 mode with low bit-rate is enough for the 529 s pulsation of 4U 1538-52, which was observed in the remote orbits. The combination of Her X-1 in the contact orbits and 4U 1538-52 in the remote orbits was repeated for the 3 times. The background for Her X-1 was taken in the contact orbits on July 26, and that for 4U 1538-52 was in the remote orbits on July 29. On-source observation of Her X-1 were carried out on July 27 and 28. The total exposure time was 10000 s. The intensity of Her X-1 was stable on July 27, but it changed violently on July 28. Some dips were observed on July 28. The transient time of the fastest dip is 5 pulses $\sim$ 6 s in 1–10 keV, the fastest ever recorded (figure 4.2.1). The dip was deeper in the lower energies as seen in the figure. Since the dips only affect the low energies, all the data can be summed up for our purpose.

On all these occasions the 2–60 keV source intensity was about 90 mCrab in 1989 observations, and 125 mCrab in 1990, which are typical in the main-on state.

In order to extend and deepen the results of Mihara *et al.* (1990), we combine all these reduced-HV data for the present data analysis. There are in addition a number of normal-HV observations of this object, but most of them are taken in the timing mode and we do not deal with them in the present thesis.

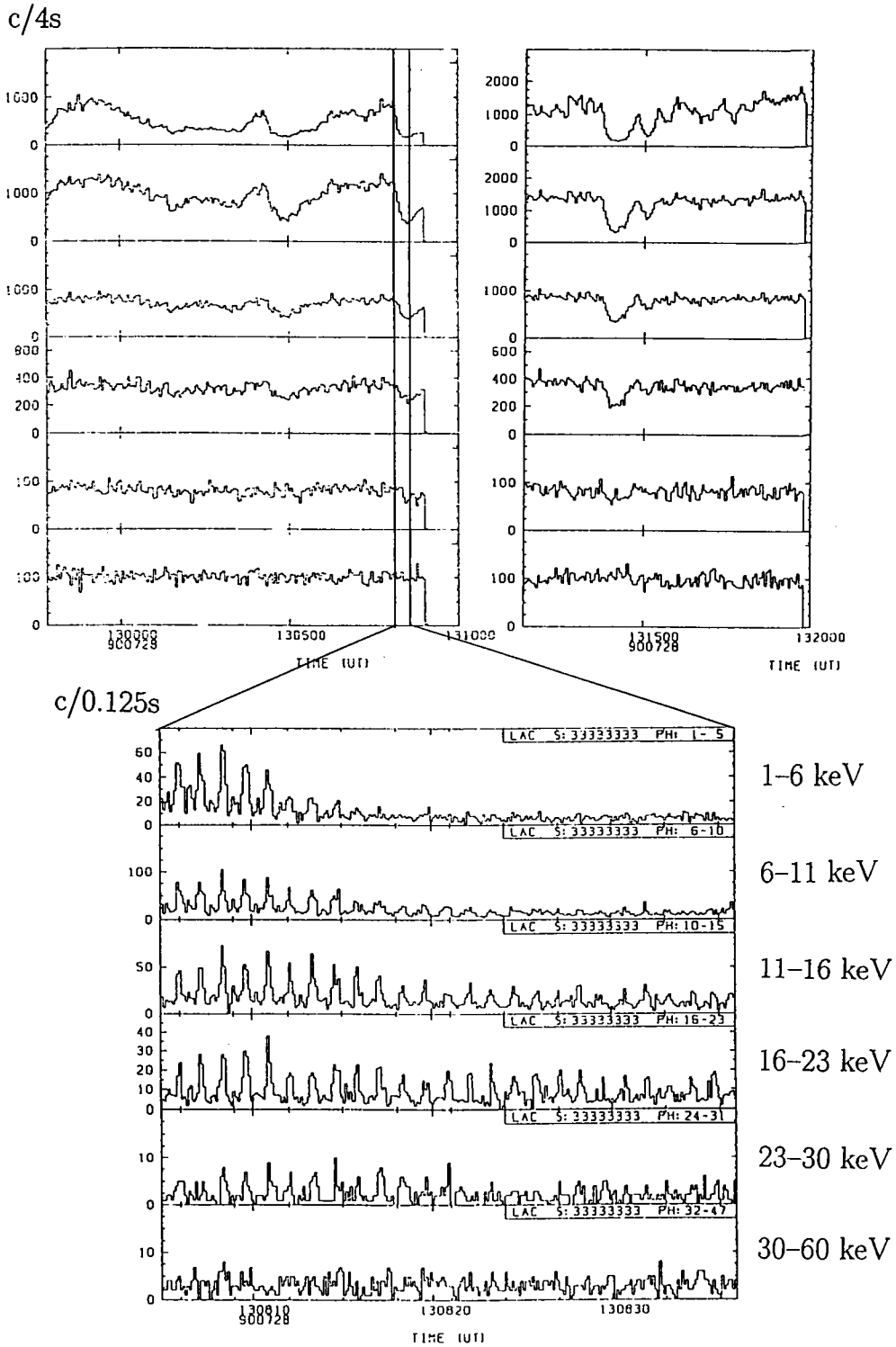

Figure 4.2.1: Some light curves of dips with *Ginga* on 1990 July 27. In the dip shown here, the transition time was 5 pulses $\sim$ 6 s in 1–11 keV, the fastest ever recorded.

4.2.3 Vela X-1

Vela X-1 (4U 0900-40) is a well-studied massive X-ray binary pulsar. The 8.97 day orbital period involves an X-ray eclipse lasting for 1.7 days. The companion star, HD77581, is a B0 type supergiant with an estimated mass of $\sim$24 $M_\odot$. This is a wind-fed system, and the repeated observations with *Hakucho* established that its pulse period changes rather randomly instead of exhibiting a persistent spin-up trend (Nagase *et al.* 1984). The spectra often exhibit pronounced low-energy absorption and intense iron emission lines (Nagae *et al.* 1989; 1992).

The *Ginga* observations of Vela X-1 were conducted in normal HV mode on 1988 February 16 through 23, mainly to study eclipse transitions. The reduced-HV observation was carried out on 1990 April 20 as a part of the systematic search for cyclotron resonances. Vela X-1 was observed in the remote orbits with a low time resolution, and 4U 1626-67 was observed in the contact orbits with a high time resolution. In §5 we will use only these reduced-HV data, to report on a discovery of a cyclotron resonance feature at 25–27 keV. Preliminary results are also described in Makishima and Mihara (1992). Incidentally, Kendziorra *et al.* (1992) reported a discovery of cyclotron structures at 54 keV (and possibly at 27 keV too) from Vela X-1 with *HEXE* on-board Mir space station. The 54 keV feature they detected is most probably the second harmonic resonance, while *Ginga* observed the fundamental resonance.

4.2.4 4U 1907+09

The 8.38 d binary period of 4U 1907+09 was established with *Ariel-V* (Marshall and Ricketts 1980). The 438 s pulsations from this source were discovered with *Tenma* (Makishima *et al.* 1984), and reconfirmed with *EXOSAT* (Cook and Page 1987). The inferred X-ray mass function of $\sim$9 $M_\odot$ implies that the companion is massive. In fact the source has been identified optically with a highly reddened B2 III-V star with emission lines (Iye 1986).

We observed 4U 1907+09 on 1990 September 21 in the reduced-HV mode as a part of the systematic search for cyclotron resonances. LAC 4,5 were switched off during this observation because of a noise trouble. On-source data was taken at the position centered at $(l, b) \sim (43.56, 0.88)$ in the contact passes and the former half of the remote orbits, and the background was taken at $(l, b) \sim (46.48, 4.22)$ in the latter half of the remote orbits. The Galactic diffuse emission at the on-source position is $\sim$ 13 c/s, while that at the background position is less than 2 c/s (Yamauchi, 1991). Therefore the subtracted spectra contain the Galactic diffuse background of 10 c/s/6LAC whose spectrum is explained by a thermal bremsstrahlung with $kT \sim 7.0keV$ with an absorption of $\log_{10} N_H \sim 22.3$. The spectrum of the Galactic diffuse background is fixed and included in the model fitting. The contributions by this background is calculated in the corresponding energy bands and subtracted in the pulse profiles. The source was detected at an intensity level of 13 mCrab, and the apparent pulse period was determined to be 439.47 s. However, as shown in figure 4.2.2, the pulsation sometimes disappeared and there remained a residual flux of order 3 mCrab.

Such 'less-pulsing' state typically lasted for a fraction of an hour, with a duty ratio as large as 50%. A further study found the pulsation even in the 'less-pulsing' state, but the pulse fraction has changed. Figure B.2.1(d) is the folded light curves in the 2-7.5, 7.5-17, and 17-36 keV band. The start time and the period of the folding are the same in the two panels. The pulse fraction has changed as table 4.2.1.

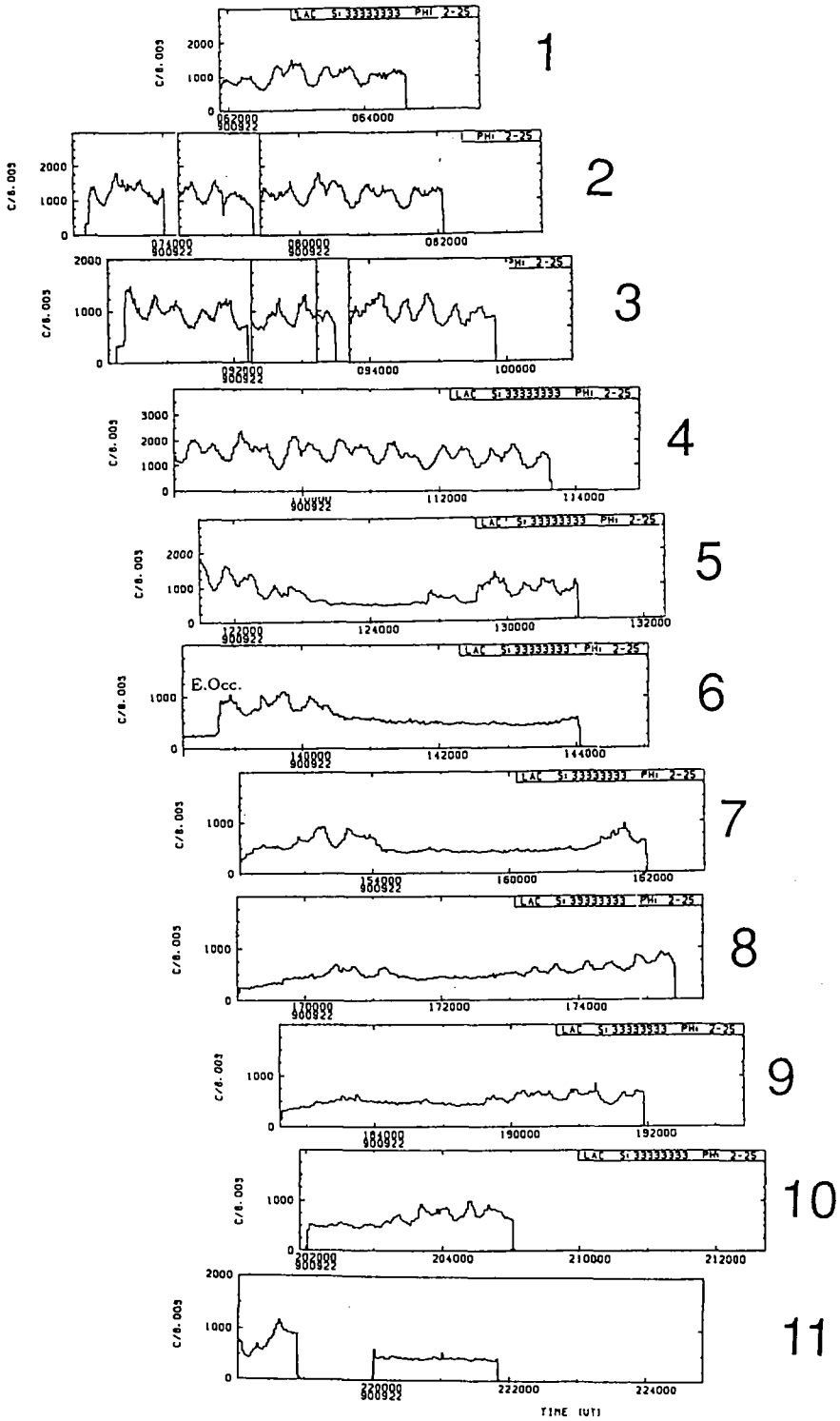

Figure 4.2.2: The raw light curves of 4U 1907+09 in 2–24 keV by each *Ginga* orbit. The particle background in this band is about 200c/8s, and the Galactic diffuse ridge emission is about 80c/8s.

Table 4.2.1: The pulse fractions of 4U 1907+09 in 'pulsing' and 'less-pulsing' states. The pulse fraction has decreased as the intensity drops.

energy range [keV]	pulse fraction [%] 'pulsing' → 'less-pulsing'	error [%]
2 - 7.5	30 → 9	$\pm < 1$
7.5 - 17	48 → 23	$\pm < 1$
17 - 35	43 → 50	$\pm \sim 10$

In §5.5 we analyze the spectra separately for the 'pulsing state' and 'less-pulsing state'. The spectra obtained during the pulsing state are very similar to those of 4U 1538-52 in that there is a clear cyclotron structure at ~20 keV. Furthermore, the residual flux in the 'less-pulsing state' is very likely to be coming from 4U 1907+09 itself.

Following a preliminary report by Makishima and Mihara (1992), these results will be explored in §5. However, it is beyond the scope of this thesis to investigate the cause and mechanism of the transition between the two states.

4.2.5 GX 301-2

GX 301-2 is a typical non-eclipsing wind-fed X-ray binary with an early type massive companion (B2 Ia e, Parkes *et al.* 1980; B1.5 Ia, Bradt *et al.* 1977), Wray 977, and an orbital period of 41.5 d (Sato *et al.* 1986). It flares up in X-rays at the orbital phase of ~1.4 d before the time of periastron passage, probably because at that phase the pulsar crosses the mass outflow from the companion star which is preferentially directed along its rotational equatorial plane. Recent monitoring observations with WATCH on *GRANAT* clearly revealed its orbital dependence (figure 4.2.3, Castro-Tirado 1994). The X-ray spectra of GX 301-2 are characterized by a heavy and variable absorption and a strong iron line (White and Swank 1984; Leahy *et al.* 1988; Leahy *et al.* 1989; Leahy and Matsuoka 1990). The pulse period changes randomly.

We observed GX 301-2 three times with *Ginga* , the first two at orbital phase 0.0 where the intensity is expected to be maximum, and the last at phase 0.56. The first observation occurred on 1987 December 15 with the normal HV setting, and the data were used to study aperiodic intensity variations in X-ray pulsars (Tashiro *et al.* 1991). The latter two were conducted with the reduced high voltage, on 1990 June 14 and on 1991 March 13, as a part of the systematic search for cyclotron resonances. On both these two occasions we observed mean intensities of 70–150 mCrab, and the light curve is shown in figure 4.2.4. We will analyze only the reduced-HV data which have been used only in a preliminary report (Makishima and Mihara 1992).

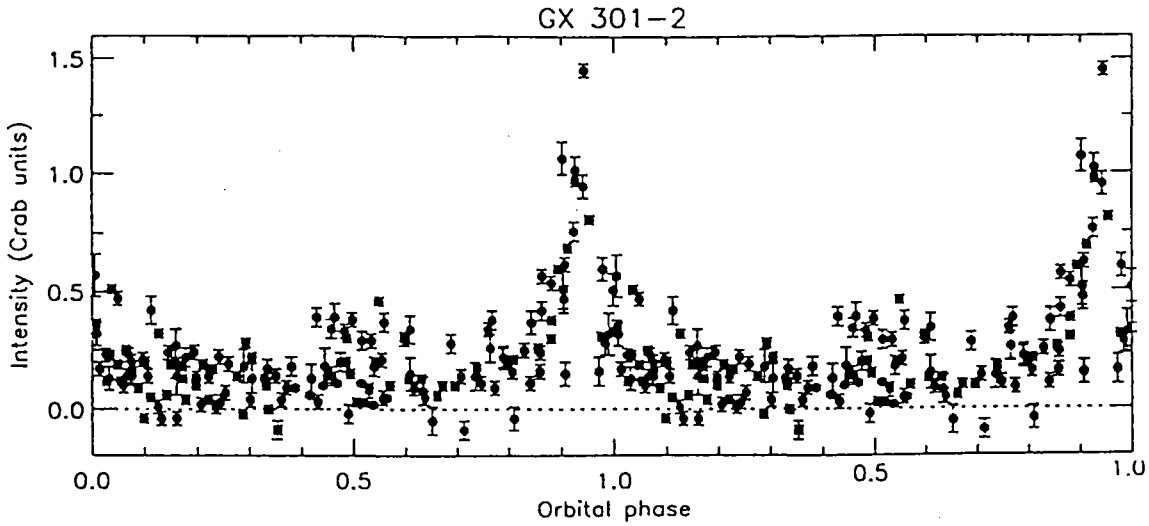

Figure 4.2.3: The GX 301-2 light curve with WATCH on *GRANAT* folded by the 41.5 d orbital period from 1990 January to 1993 March (Castro-Tirado 1994)

4.2.6 4U 1626-67

The 7.7 s X-ray pulsar 4U 1626-67 has been identified optically with a faint blue star KZ TrA, whose optical emission also exhibits the 7.7 s pulsations. There is yet no indication of orbital period either in the X-ray or optical data, nor there is any Doppler delay in pulse arrival times with extremely stringent upper limits. From these facts, this source is considered to have an extremely low-mass ($\sim 0.1\ M_\odot$) companion which fills the Roche-lobe and powers the pulsar. Thus 4U 1626-67 is genetically an extraordinary system, consisting of a strongly magnetized neutron star and a very late type star. Most of the optical emission from this system is considered to be reprocess of X-rays.

The estimated X-ray luminosity of 1.2×10^{37} erg/s, together with a stable spin-up with a constant rate of $\dot{P}/P \simeq -2 \times 10^{-4}$ y^{-1} since the detection of the pulses in 1977, indicates that this pulsar is a disk-fed system. However, it has turned into a spin-down trend soon after this *Ginga* observation; see §4.4.2. This object has been known to exhibit a very complex pulse-phase dependent X-ray spectra. Pravdo *et al.* (1979) found a broad hump around 20 keV in the X-ray spectrum, and if this is a cyclotron structure, the magnetic field becomes 2×10^{12} G. Kii *et al.* (1986), however, proposed a magnetic field of 8×10^{12} G by studying the energy dependence of the pulse profile.

Ginga observed 4U 1626-67 with the normal HV on 1988 July 27. From these data, a 3σ upper limit of $a_x \sin i < 0.008$ lt-s was set on the orbital Doppler delays of the X-ray pulses, and a quasi-periodic oscillation of 0.04 Hz was detected (Shinoda *et al.* 1990). These data were however acquired in the MPC-3 mode so that we will not use them in this thesis. The MPC-2 data with the reduced-HV mode, to be used in the present thesis, were taken on 1990 April 18-21 as a part of the systematic investigation of the cyclotron resonances. These yet unpublished data will be

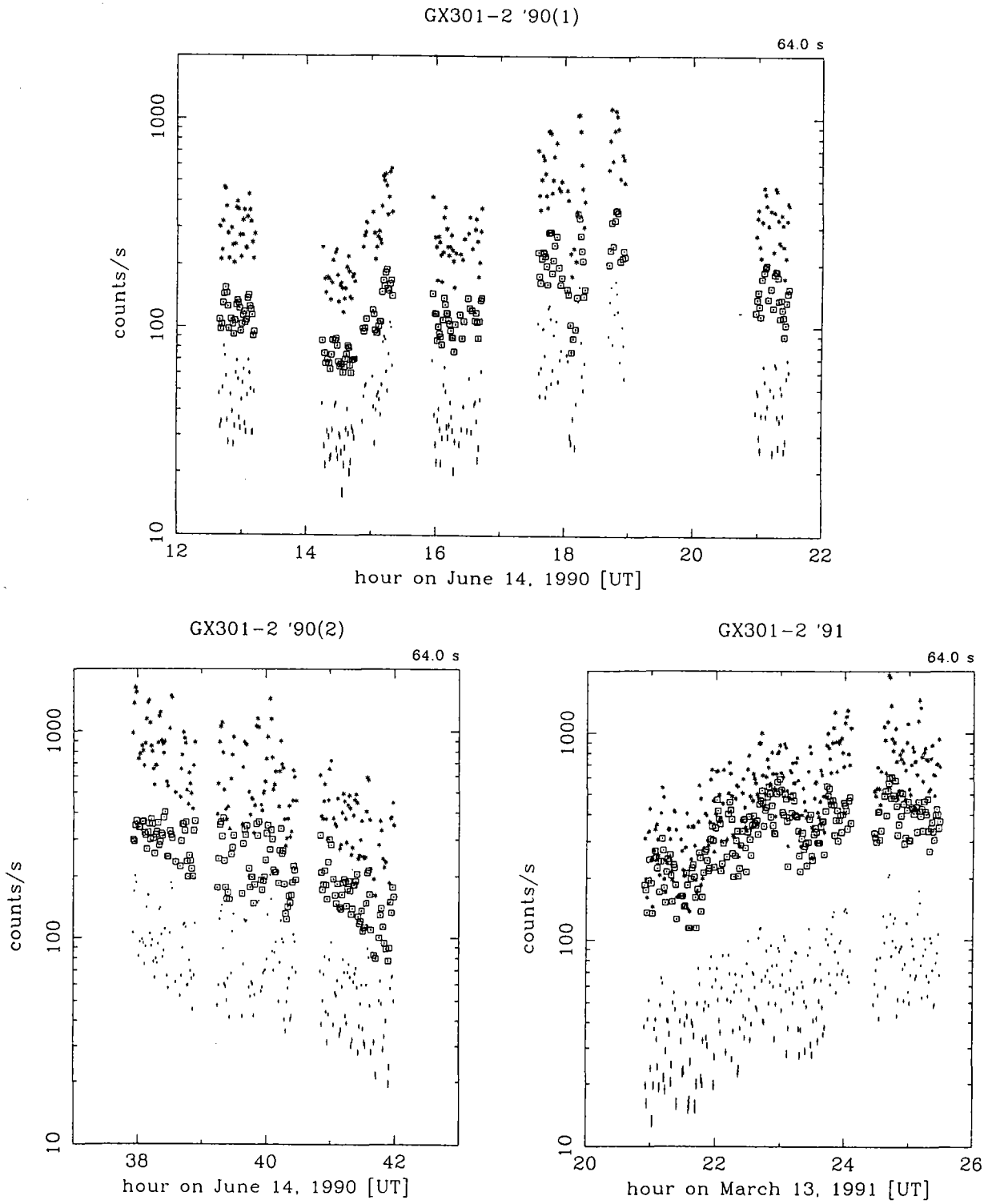

Figure 4.2.4: The GX 301-2 light curves with *Ginga* on 1990 June 14 and 1991 March 13. Since the pulse period (683s) is ten times of binned time (64s), the scatter of the data points is due to the pulsation.

analyzed in §5.11.

4.2.7 1E 2259+586

1E 2259+586 is a 6.98 s X-ray pulsar, discovered with *EINSTEIN* , at the center of a young ($\sim 10^4$yr) supernova remnant G109.1-1.0 (Fahlman *et al.* 1982). The spin down rate, $\dot{P}/P \sim 6 \times 10^{-13}$ s/s, is stable and comparable to that of the Crab pulsar (Koyama *et al.* 1989). It is, however, too small to explain the mean X-ray luminosity of 10^{35} erg/s, because the pulse period is much longer than any other isolated neutron star in a young supernova remnant. Therefore it is likely to be an accretion powered X-ray pulsar. Koyama *et al.* (1989) showed that, if the pulsar has a relatively weak surface field strength of $\sim 5 \times 10^{11}$ G, the observed luminosity and the observed spin-down rate are in good agreement with the accretion torque theory (§2.3.4).

So far, neither an optical counterpart nor any binary indication (e.g. Doppler modulation in X-ray pulse arrival times) has been detected from this object. Therefore the companion, if any, must be an extremely low-mass star. Such a low-mass companion, however, would have been thrown out of the binary system at the supernova explosion. Thus the generation and the mass supply of this pulsar still remain a puzzle. Another peculiar feature of 1E 2259+586 is that its X-ray spectrum is softer than any other binary X-ray pulsar. It is tempting to regard the very soft X-ray spectrum as a result of the inferred weak magnetic field.

Ginga observations of 1E 2259+586 were conducted three times; on 1987 June 21, 1989 December 14 and 17, and 1990 August 8, all in the normal HV mode because of the very soft spectrum. Spectral and timing results from these observations have been published in Koyama *et al.* (1989) and Iwasawa *et al.* (1992). Possible cyclotron lines were reported at about 7 keV and roughly twice this energy, and the inferred magnetic field is in a good agreement with the field value as estimated above (Koyama *et al.* 1989). We will later refer to their work.

4.2.8 4U 1700-37

This is a typical high-mass X-ray binary, with an extreme Of star HD153919 as the optical companion. Its orbital period of 3.41 d involves a well defined X-ray eclipse. Since its discovery, many efforts have been made in search for X-ray pulsations from this source, all without success. The 67 s periodicity claimed by Murakami *et al.* (1984) based on the *Tenma* data was not confirmed with a much longer exposure with *EXOSAT* (Haberl *et al.* 1989) nor with *GRANAT* SIGMA (Laurent *et al.* 1992).

Thus 4U 1700-37 cannot be classified as an X-ray pulsar, but its binary structure is typical of an X-ray pulsar and its X-ray spectrum is very similar to those of other X-ray pulsars; a power-law with absorption in low energy and steep turn over above 20 keV. The compact object in this system is therefore likely to be a magnetized neutron star possibly with aligned rotation and magnetic axes, and the object is worth studying from a view point of cyclotron structure in the spectrum. It is hence included in the present thesis.

We observed this object with *Ginga* on 1991 April 19, with the reduced high voltage. The light curve is shown in figure 4.2.5. The intensity changed violently, but no periodicity was found. In §5.11, we concentrate on the spectral analysis of these unpublished data.

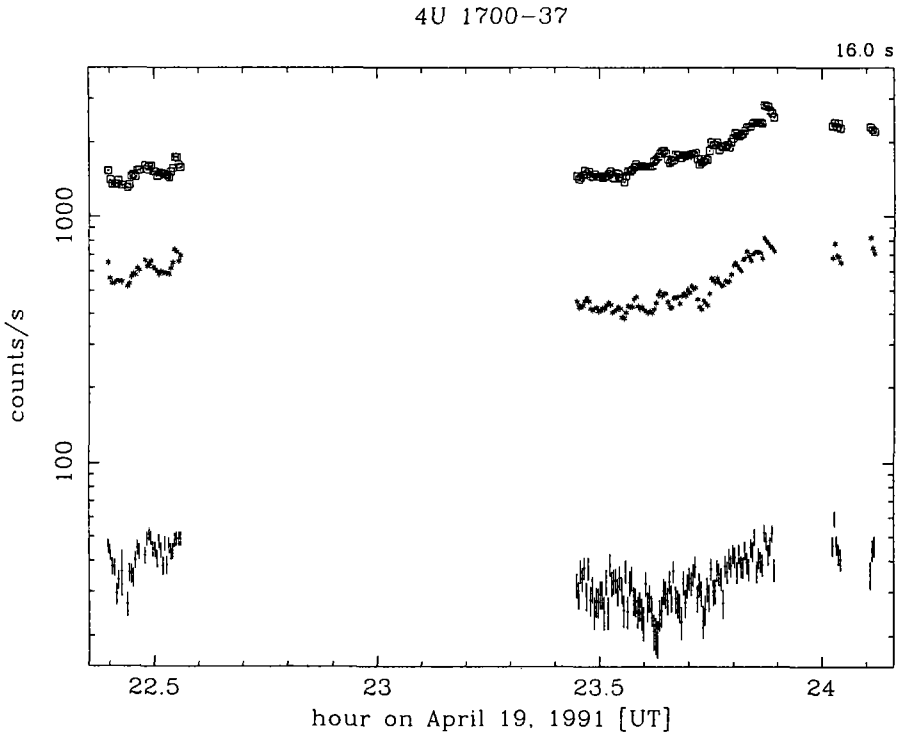

Figure 4.2.5: The 4U 1700-37 light curve with *Ginga* on 1991 April 19.

4.2.9 Other Persistent Sources

Cen X-3 is a luminous ($L_X = 5 \times 10^{37}$ erg/s) X-ray pulsar with an O type companion (see §2.1). *Ginga* observed Cen X-3 in the normal HV mode on 1989 March 22-24, over a complete orbital cycle (Takeshima *et al.* 1991; Nagase *et al.* 1992). The pre-eclipse dips, an eclipse, eclipse ingress and egress were observed. We will use only the data corresponding to the steady high state with a mean intensity of 90 mCrab, and analyze them from the aspect of cyclotron resonance effects in the spectrum.

GX 1+4 is a 111 s pulsar, optically identified with an M6III symbiotic star. Therefore this system is very unusual, consisting of an M giant and a strongly magnetized neutron star. The orbital motion has not been detected. It was one of the brightest sources above 20 keV in the 1970's with the intensity of 200 mCrab and a rapid spin up trend. After it became below the detection limit of *EXOSAT* (< 0.5mCrab) in 1983, *Ginga* re-detected it at 2 mCrab intensity in 1987 March 28-30 (Makishima *et al.* 1988). The subsequent four observations with *Ginga* recorded intensities of 11 mCrab on 1988 March 27, 13 mCrab on 1989 August 27, 9 mCrab on 1990 September 4, and 2 mCrab again on 1991 September 14; that is, still in a low state (Dotani *et al.* 1989; Sakao *et al.* 1990). In a sharp contrast to the behavior in the 1970's, the pulse period-change rate turned into a continuous spin down trend. The *Ginga* spectra show more pronounced absorption than those in the 1970's,

but the increased absorption alone cannot explain the sustained low intensity level. Thus the overall behavior of this object is still full of puzzles. In particular, the spectrum of this pulsar above 20 keV is significantly harder (both in high and low intensity states) than those of other binary X-ray pulsars, suggesting that it has a significantly stronger magnetic field than the others. Because of the source weakness, all the data were acquired in the normal HV mode.

SMC X-1 is a 0.7 s pulsar located in the Small Magellanic cloud (SMC). It forms an eclipsing binary with a 3.89 d period, together with a B0 supergiant Sk 160. Its high X-ray luminosity ($\sim 5 \times 10^{38}$ erg/s), the shortest pulse period among persistent (non-transient) binary X-ray pulsars, and a relatively steady spin-up trend, all indicate a disk-fed accretion. *Ginga* observed SMC X-1 on 1987 May 25–28, 1988 August 25–28, 1988 August 31 – September 2, and 1989 July 29 – August 3, all with the normal HV setting.

LMC X-4 is a 13.5 s pulsar in the Large Magellanic Cloud (LMC) with an O type companion star. The 1.4 d orbital period was first derived from X-ray eclipses. The pulse fraction gets larger during flares, increasing almost by an order of magnitude on time scales of 10 min. The luminosity in the flares even exceeds the Eddington limit by 5 times. There is a report of a 30.4 d intensity variation in this object (Lang *et al.* 1981), which may be caused by a geometrical change of an accretion disk. *Ginga* observed LMC X-4 four times, all in the normal HV mode; in 1987 July, 1987 August, 1988 March, and 1989 August. The last observation was reported in Levine *et al.* (1991). In this thesis we will re-analyze the spectral data.

OAO 1657-415 is a 38 s X-ray pulsar discovered with the *Copernicus* (*OAO-3*) satellite in 1978 (Polidan *et al.* 1978). The optical counterpart has not yet been identified. A large spin up trend, $\dot{P}/P \simeq -10^{-3}$ y^{-1} found with *Tenma* and *Ginga* (Kamata *et al.* 1990), indicates that it is an accreting binary system. *Ginga* observed OAO 1657-415 on 1988 March 17, 1988 April 7, and 1989 March 4, all in the normal HV mode. The *Tenma* and *Ginga* results together were published by Kamata *et al.* (1990). Binary nature has discovered with BATSE on GRO by Chakrabarty 1993.

X Per is a Be star system which is identified with the 837.7 s pulsar 4U 0352+30 with the *EINSTEIN* satellite. Although the pulse period is long and the luminosity is low, $L_X = 2 \times 10^{33}$erg/s, it is thought to be a neutron star binary rather than a white dwarf system, since the pulse period changes largely, for example at a rate of $\dot{P}/P \simeq -2 \times 10^{-4}$ y^{-1} between 1984 and 1986 (Murakami *et al.* 1987). It is even larger than the predictions from the accretion torque theory (§2.3.4). The spectrum is softer than that of a typical X-ray pulsar (Murakami *et al.* 1987; Robba *et al.* 1989). The power-law times exponential cut-off model with $\alpha \sim 1.6$, $E_c \sim 6$ keV and $E_f \sim 5$ keV fits the observed spectrum, but a thermal bremsstrahlung model cannot be ruled out. An optical modulation of 580 d period was reported, but the origin of this modulation is unknown. *Ginga* observed X Per on 1990 January 26–28, in the normal HV mode.

4.3 Observations of Transient Sources

As mentioned in §2, a considerable fraction of binary X-ray pulsars are transient sources, and most of them have Be-type companion stars whose activity cycles control the X-ray outbursts. A number of transient X-ray pulsars have been observed with *Ginga* over its mission lifetime. Some of them are recurrent transients observed at least once with previous missions, whose recurrences were detected with the *Ginga* ASM. Others are new sources discovered either with the ASM or the LAC.

4.3.1 4U 0115+63

This is a typical recurrent transient involving a Be type companion. The X-ray outbursts seem to take place rather irregularly with a typical interval of a few years. The binary orbit has a 24 d period and a significant eccentricity. The pulsation of 3.61 s from this source was discovered with *HEAO-1* in 1978 January (Rose *et al.* 1979) during an outburst reaching about 200 mCrab. Using the data taken on this occasion with the *HEAO-1* A4 experiment (NaI scintillation counters), Wheaton *et al.* (1979) discovered an absorption feature in the spectrum at 20.1 keV, which was supposed to be a cyclotron structure (§2.4.2). From the data taken simultaneously with the *HEAO-1* A2 experiment (proportional counters), White *et al.* (1983) confirmed the structures at 11.5 and 23 keV which appeared in absorption at the pulse peak phase and in emission at the inter-pulse phase.

Three flares were detected from 4U 0115+63 with the ASM while *Ginga* was in orbit; in 1987 March, 1990 February, and 1991 March (figure 4.3.1 from Tamura *et al.* 1992). Pointing observations with the LAC were carried out on 1990 February 9–11, 1991 April 26, and 1991 June 17. The first observation was carried out both with the normal and reduced HV modes, while the second and the third ones were carried out in the reduced HV mode. 4U 0115+63 was in the outburst peak in the first observation with an intensity of 430 mCrab. The second observation covered the declining phase with an intensity of 70 mCrab. The source was not detected in the third observation with an upper limit of 0.2 mCrab.

Using the normal-HV mode data from the first observation, Nagase *et al.* (1991) re-confirmed the two absorption features at 12 and 23 keV. In this thesis we will fully utilize the reduced-HV data for which only very preliminary analysis has been performed so far (Makishima and Mihara 1992).

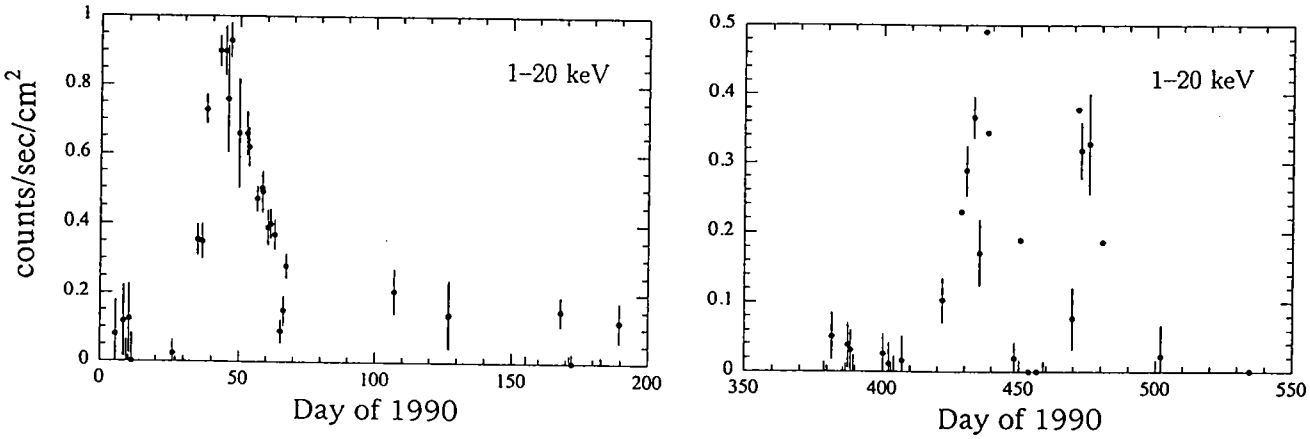

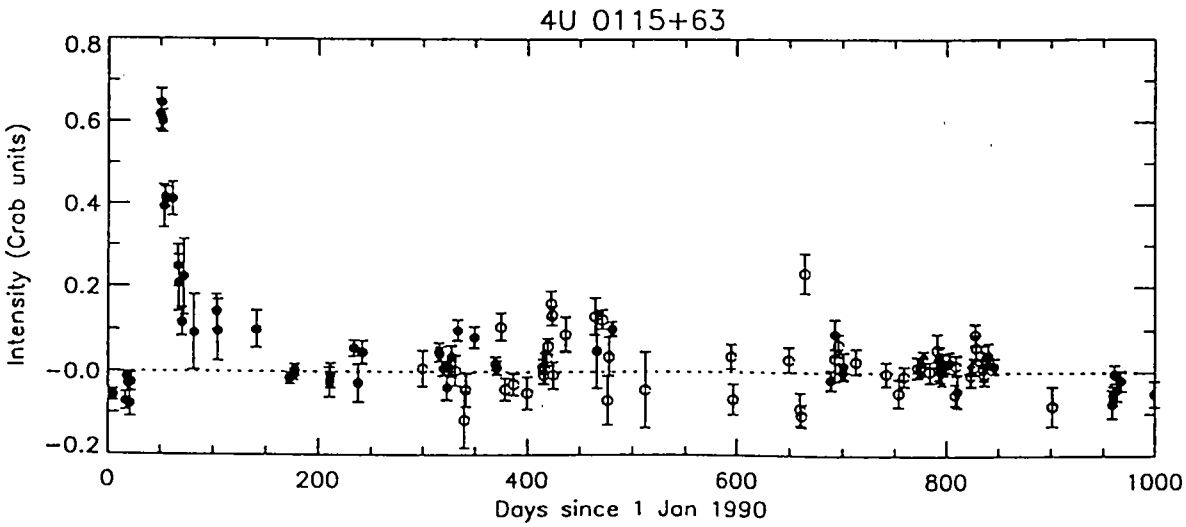

Figure 4.3.1: The light curves of 4U 0115+63. Upper two are the 1990 and 1991 flares with *Ginga* ASM (Tamura 1992 and in *private communication*). Bottom is 1990–1993 with WATCH on *GRANAT* (Castro-Tirado 1994).

4.3.2 X 0331+53

The 4.37 s pulsar X0331+53 (V0332+53) and a Be companion, BQ Cam, form an eccentric binary with an orbital period of 34 days. It was first discovered in 1973 with *Vela 5B* in a bright (~1Crab) outburst (Terrell and Priedhorsky 1984). *Tenma* re-discovered it in 1983 November (Makishima *et al.* 1990a). The flux showed a rapid random variation, and among them, a shallow coherent pulsation was found with *EXOSAT* (Stella *et al.* 1985) which was also confirmed in the *Tenma* data. The spectral fitting of the *Tenma* SPC data suggested a cyclotron structure at 28 keV (Makishima *et al.* 1990a), although the statistics were not high enough to make the result convincing.

An outburst of 200-300 mCrab was detected with the *Ginga* ASM in 1989 middle September. Observations with the LAC were performed on September 19 in the normal high voltage and the obtained data suggested a prominent structure at the highest end of the observable energy range. We therefore reduced the high voltage on October 1, and a clear cyclotron feature at 28.5 keV emerged (Makishima *et al.* 1990b). This has confirmed the *Tenma* suggestion. The light curves are shown in figure 4.3.2. The data on Sep. 20 are taken in MPC-3 high-bit rate, MPC-2 high-bit rate and MPC-1 low-bit rate. The MPC-3 data are excluded in the accumulation because it has poor spectral binning. The MPC-2 data (1600s) are used for the pulse phase-resolved analysis. The background was taken at the neighboring blank sky just before and after the on-source observation on Sep. 20, and just after the on-source observation on Oct. 1.

Most of the reduced-HV data (for 6400 s) were taken in the MPC-1 low-bit-rate mode, with a time resolution of 16 s which did not allow Makishima *et al.* (1990b) to resolve the spectra into pulse phases. However we can here utilize a small amount (400 s) of high-bit-rate data, with a time resolution of 0.5 s, for the pulse phase-resolved analysis.

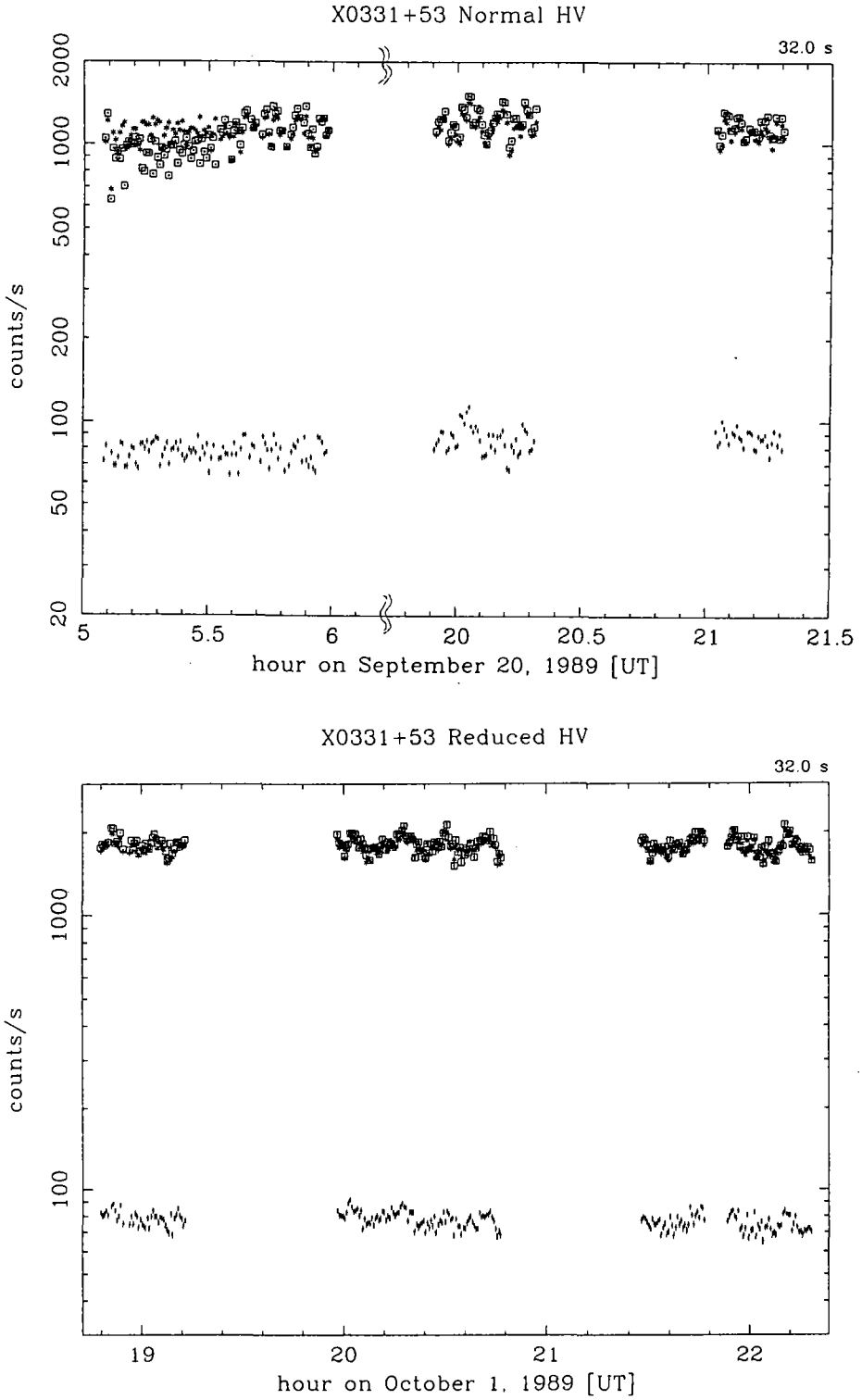

Figure 4.3.2: The X 0331+53 light curves with *Ginga* on 1989 September 20 and 1989 October 1.

4.3.3 Cep X-4

Cep X-4, a transient source listed in the 4U catalog, was re-detected in a ~100 mCrab outburst by the ASM onboard *Ginga* on 1988 March 19, (GS 2138+56: Koyama *et al.* 1991a). The subsequent pointing observations with the LAC on April 3, 8, and 14 showed a gradual decrease of intensity, 85, 70, and 45 mCrab, respectively. Scanning observations with the LAC secured its identification with Cep X-4. The light curves are shown in figure 4.3.3.

A coherent pulsation of 66.25 s was discovered from the LAC pointing observations, and the source has been established as a transient pulsar. Although Cep X-4 is yet to be identified optically, the transient nature, together with results from the pulse timing analysis (Koyama *et al.* 1991a), suggest that it is most likely a Be-star binary. Furthermore, our analysis of the spectra has led to the discovery of a cyclotron resonance structure at 30 keV (Mihara *et al.* 1991b). These results will be re-examined in §5.

4.3.4 A 0535+26

The 103.4 s pulsar A 0535+26 is a typical recurrent transient so far studied extensively. Its companion star is a B0III star, HDE 245770, of about 15 $M_{\odot}$. The reported distance is 1.8–2.6 kpc. An orbital period of 111 d has been established through analysis of the pulse arrival times and outburst recurrence patterns (Nagase *et al.* 1982).

During the *Ginga* lifetime, only one outburst was detected in 1989 March with the ASM. The light curve with ASM is shown in figure 4.3.4. The pointing observation with the LAC was carried out on April 4 only for 11 minutes with the normal high voltage. The intensity was 770 mCrab and the apparent pulse period was 103.43 s. This outburst was also detected with *HEXE* (Kendziorra *et al.* 1992, 1994) on April 8, 9, and 14, and harmonic cyclotron structures at 50 and 100 keV were discovered with their scintillation counters. It was unfortunate that *Ginga* observed it with the normal high voltage with energy range up to 37 keV, because *Ginga* would have detect the fundamental resonance if the high voltage had been reduced (up to 60 keV).

We also observed A 0535+26 on 1990 April 18 with the reduced high voltage as a part of the systematic search for cyclotron resonances. It was, however, in a low state with an intensity of $<$ 1.4 mCrab. Therefore we will not report the data in 1990.

4.3.5 EXO 2030+375

The 41.68 s transient pulsar EXO 2030+375 was discovered with *EXOSAT* on 1985 May 19, at an intensity of 700 mCrab (Parmar *et al.* 1989). It decayed almost linearly to 85 mCrab by July 10, and fell below the *EXOSAT* detection limit ($<$1 mCrab) on August 25. The luminosity dependence of the pulse period was studied by Parmar *et al.* (1989), who showed that it obeys the theory of accretion torque by Ghosh and Lamb (1979) qualitatively but not quantitatively. The pulse profile has also changed during this decay. The spectral change is also investigated using this decay. The cutoff energy decreased as the luminosity decreases (Reynolds *et al.* 1993). They applied cyclotron model to *EXOSAT* observation, but no significant resonance was found. The optical counterpart was identified as a highly reddened early type star with a distance of less than 4 kpc, whose optical characteristics are consistent with those of a Be star. Recently a pulse period of 41.6794 s was

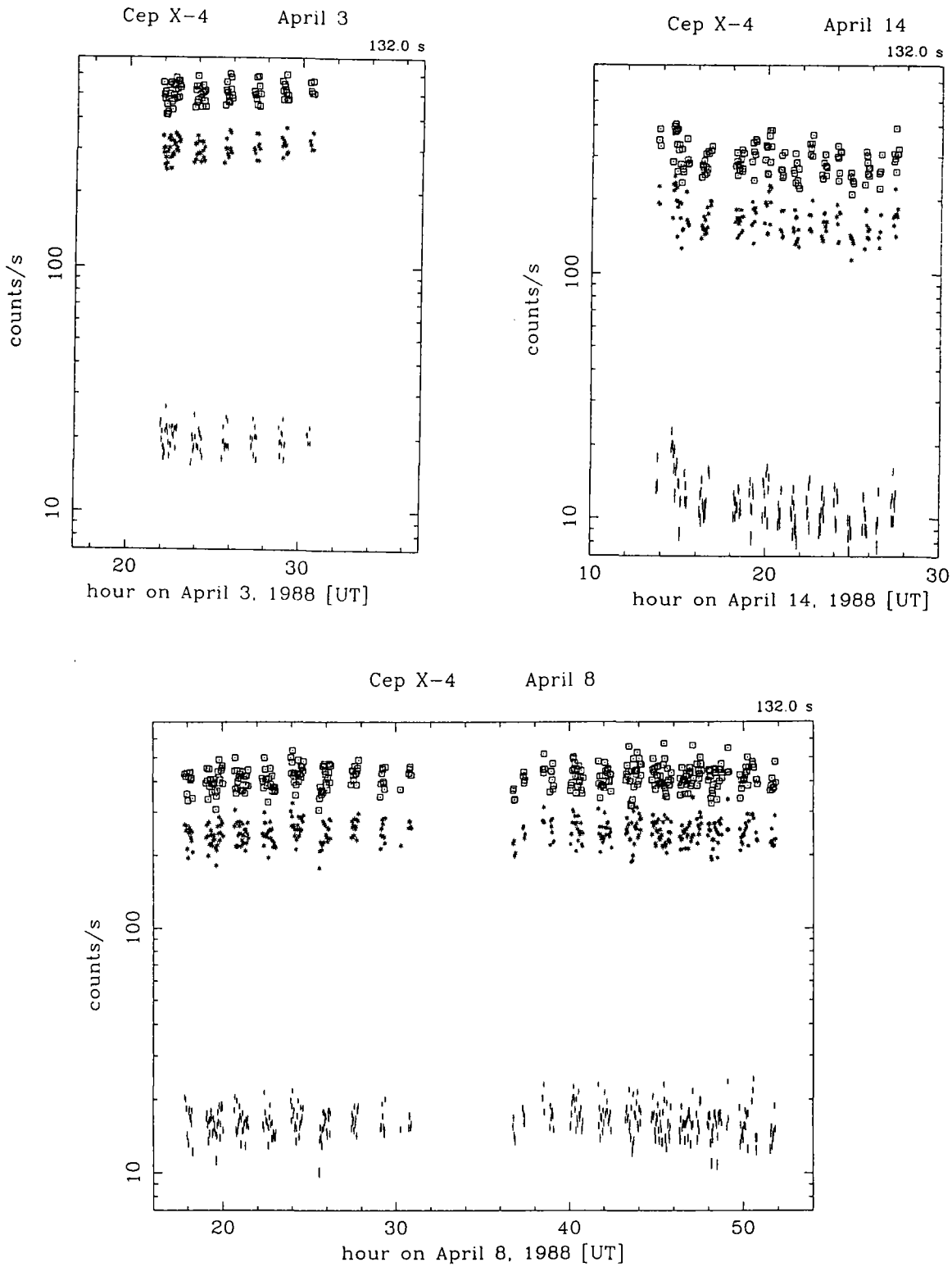

Figure 4.3.3: The Cep X-4 light curves with *Ginga* on 1988 April.

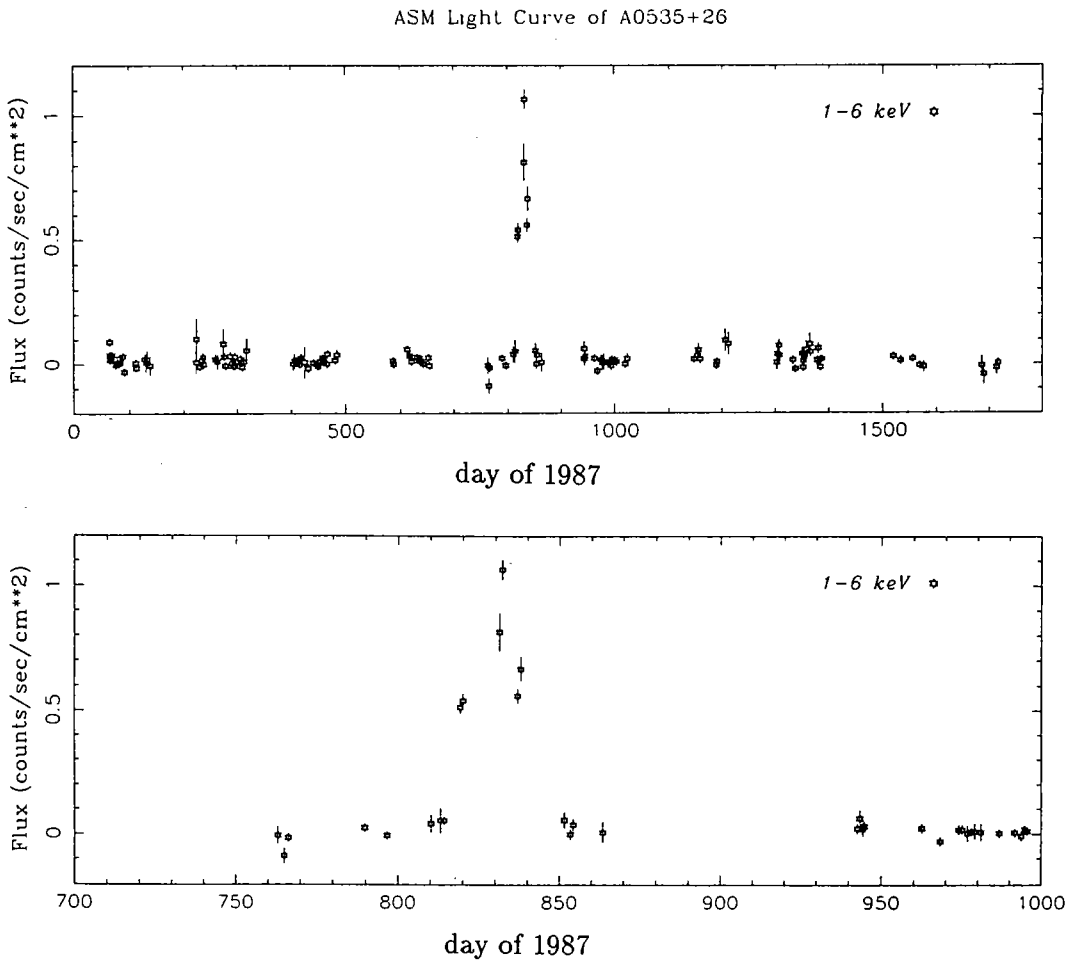

Figure 4.3.4: The light curves with *Ginga* ASM of the 1989 March/April outburst of A 0535+26 (*Ginga* ASM team in *private communication*). LAC observation was carried out on 1989 April 4 (825 day of 1987).

obtained in 1992 February with *GRO* (Wilson *et al.* 1992). The orbital period was calculated to be 46.03 ± 0.01 d (Stollberg *et al.* 1993).

Ginga observed EXO 2030+375 on 1989 October 29, with normal high voltage. The apparent pulse period was 41.7 s, and the intensity was 4 mCrab. This means that the source sometimes maintains a low activity level for an extended period of time.

4.3.6 1E 1145.1-6141

1E 1145.1-6141 is a 296.90 s transient pulsar. It is separated only by 20' from a 292 s transient pulsar 4U 1145-61. The companion of 1E 1145.1-6141 is identified as a B2 I-IIa star, and that of 4U 1145-61 as a B0-1 Ve star, Hen 715. The early confusion of the two sources was resolved by

the imaging observations with *EINSTEIN* (White *et al.* 1980).

Ginga observed this region on 1991 May 15 in the reduced-HV mode. Although the two sources are quite confused in the LAC field of view, the timing analysis revealed only the 296.90 s pulsation as shown in figure 4.4.1. This means that only 1E 1145.1-6141 was active at that time. This pulse period was shorter than any previous measurement of this source, implying that 1E 1145.1-6141 has spun up recently in contrast to the spin down trend observed in the 1970's. The intensity was 30mCrab, which is 40 times larger than previous observations with *OSO 8* , *Ariel-V* , *HEAO-1* , and *EINSTEIN* (White *et al.* 1980). The 2-60keV spectrum was obtained for the first time as shown in figure 5.11.

The recent observations with the ART-P telescope on *GRANAT* in 1992 February showed that only 1E 1145.1-6141 was bright with an intensity of 23±3 mCrab and barycentric period of 296.79±0.09 s, while the one σ upper limit of 4U 1145-61 was 8 mCrab in 6-20 keV (*GRANAT*). These results, both X-ray intensities and pulse period, are quite consistent with the *Ginga* results.

4.3.7 Other Transient Sources

X 1722-36 was discovered with *EXOSAT* during scanning observations along the galactic plane. The 413.9 s pulsation was discovered from this source with *Ginga* (Tawara *et al.* 1989). Takeuchi *et al.* (1990) derived the intrinsic pulse period of 413.08±0.05 s from a follow-up observation. X 1722-36 showed flare like activities, and the mean intensity was 3 mCrab. It was so weak that only a pulse phase averaged spectrum is used in this thesis.

GS 1843+00 is a transient X-ray pulsar discovered with *Ginga* on 1988 April 3, in the Scutum region during galactic plane scanning observations (Koyama *et al.* 1990a). The intensity was about 40 mCrab and the pulse period was 29.5 s, but the pulse fraction, defined as a peak-to-bottom amplitude, was small and only 4% of the mean intensity.

GS 1843-02 was also discovered with *Ginga* by the observation on 1988 September 29 and 1988 October 3 (Koyama *et al.* 1990b) in the Scutum region during galactic plane scanning observations (Koyama *et al.* 1990a). The intensity was 10 mCrab, and the apparent pulse period was 94.9 s. This source was not detected on 1987 Oct. 6, 10, and 1988 Sep. 12 with other scanning observations.

Sct X-1 , previously detected in a sounding-rocket observation in 1973 as an extremely hard source, was also detected with *Ginga* in the scanning observations in October 1987 (Koyama *et al.* 1991b). The 111 s pulsation was discovered during another scanning observation in 1988 September, and confirmed in the pointed observation in 1988 November. The spectrum showed a single steep power law of the photon index of 2.0 with a strong absorption of $N_H = 10^{23.3}$ cm^{-2} plus a 6.4 keV iron line. Since the intensity was 2 mCrab, the acquired spectrum is limited to below 20 keV. This source, together with GS 1843+00 and GS 1843-02, may form a 'colony of pulsars' in the Scutum arm region (Koyama *et al.* 1990c).

GS 0834-430 is a 12.32 s pulsar discovered with *Ginga* in 1990 November. It was only 0.4 degree away from a transient X-ray burster GS 0836-429. The source identifications and episodes with *ROSAT* and *GRANAT* observations are described in Aoki *et al.* (1993) in detail. More than 10 observations were carried out with *Ginga* . The intensity of GS 0834-430 increased to

81 mCrab in the last observation conducted on 1991 May 28. On this occasion we observed it with the reduced high voltage, and we analyze these data in this thesis.

4.4 Pulse Periods and Pulse Profiles

Although the present thesis mainly deals with the study of cyclotron resonance effects in the observed pulsar spectra, in the course of data analysis we must sort the spectra into pulse phase bins in order to study pulse phase dependences of cyclotron resonance parameters. This requires correct knowledge of the current pulse period of each object. Therefore in this section, we briefly describe determinations of the pulse periods for the observed sources, and present the obtained pulse profiles.

4.4.1 Determination of Pulse Periods

In calculating the current pulsation periods of the observed sources, we first correct the times of the light curves for the propagation delay between the satellite and the heliocenter. We then process the light curve using the standard epoch folding method. That is, we fold the time series data with various trial pulse periods near the predicted value, and examine the folded light curve, using chi-square tests, against the hypothesis of 'constant flux across the phase'. The most likely period can be defined as the period value that maximizes the chi-square. Figure 4.4.1 shows an example of the chi-square trace for 1E1145.1−61.41 observation, plotted as a function of the trial period. A clear peak around 296.90 s indicates the most likely apparent pulse period as observed at the heliocenter. Thus we found that the most pulsation came from 1E1145.1−61.41 and 4U1145−61 (P=292s) was not active. The *apparent* heliocentric pulse periods thus derived with *Ginga* are tabulated in table 4.4.1. Here, 'apparent' means that the result is subject to the Dopper effect due to the orbital motion of the neutron star.

For some X-ray pulsars, the pulse periods are highly uncertain due to rapid period changes, very sparse observations, and so on. In such a case we calculate a Fourier power-density spectrum, prior to the folding analysis, over a wide frequency range using the FFT (Fast Fourier Transform) algorithm. Figure 4.4.1 shows the power density spectrum thus calculated for 1145's, where a peak at 296.5 ± 0.7 s indicates the fundamental pulsation. The 3rd 4th 5th ... harmonics of 296s were clearly seen. No harmonics of 292s was detected.

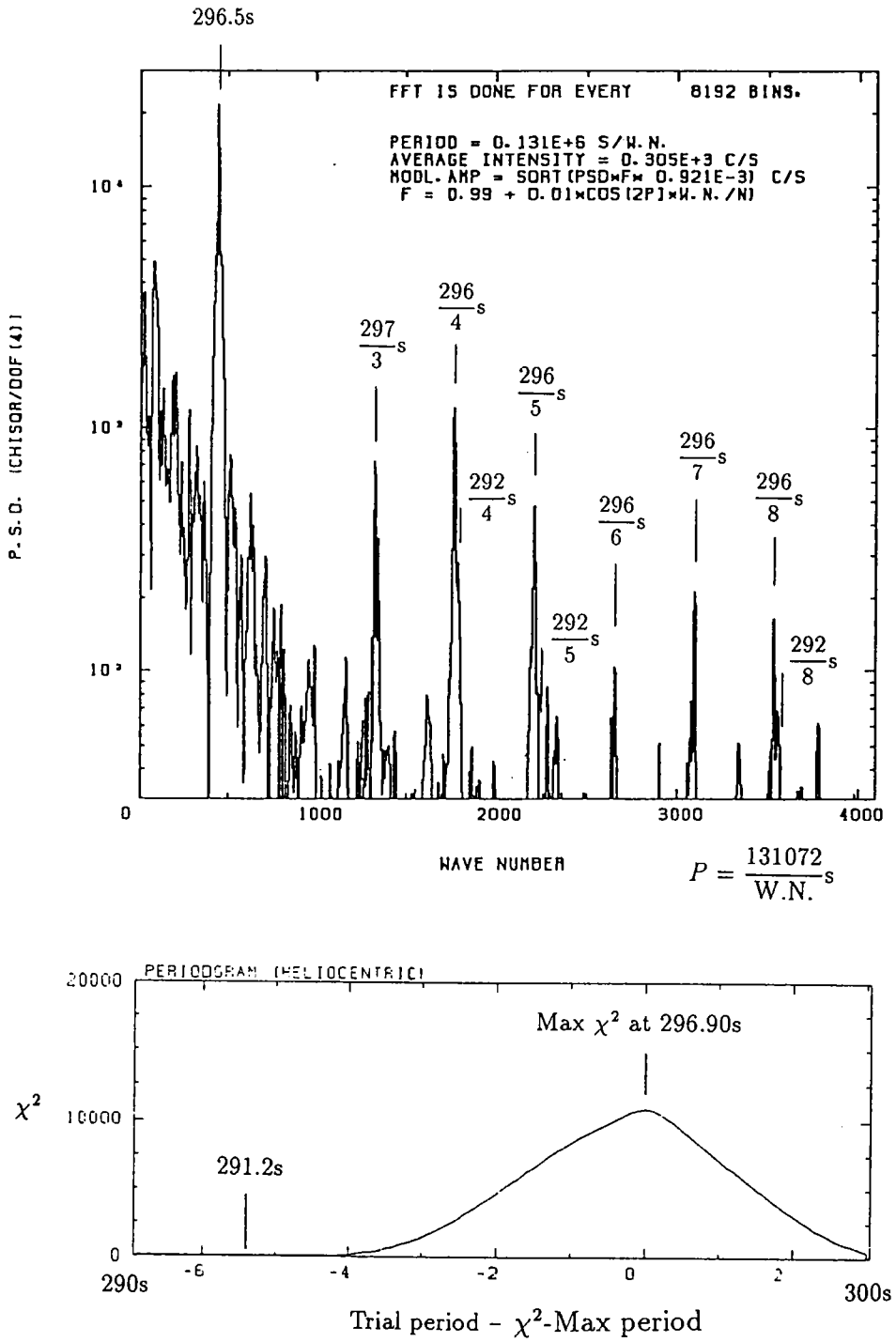

Figure 4.4.1: *upper*: FFT spectrum of 1E 1145.1-6141 and 4U 1145-61 region. *lower*: The chi-square curve for the trial periods. 296.90 s pulse period means that only 1E 1145.1-6141 was active.

Table 4.4.1: Heliocentric pulse periods with *Ginga* without the orbital Doppler correction.

Source	Apparent Period[a] [s]	Epoch date	Epoch [UT]	Reference
SMC X-1	0.710[c]	88/ 8/–	—	Levine 1993
Her X-1	1.23840	89/ 5/ 3	18: 7	
	1.23784	89/ 6/ 3	1:49	
	1.237069	89/ 6/ 6	0:55	
	1.23713	90/ 7/27	10:24	
	1.23706	90/ 7/27	13:33	
	1.23845	90/ 7/28	9:21	
4U0115+63	3.6144	90/ 2/ 9	22:00	Nagase 1991
	3.6148	90/ 2/11	21:42	
	3.6150	90/ 2/12	18:57	
X0331+53	4.37795	89/ 9/20	20:40	
	4.375	89/10/ 1	18:50	
Cen X-3	4.81735	89/ 3/23	3:30	
1E2259+586	6.978759	87/ 6/22	—	Koyama 1989
	6.978789	89/12/15	—	Iwasawa 1992
	6.978795	90/ 8/ 9	—	Iwasawa 1992
4U1626-67	7.66007213[b]	90/ 4/19	1:58	see §4.4.2
	7.66007112[b]	90/ 4/20	0:35	see §4.4.2
	7.66006326[b]	90/ 4/21	0: 4	see §4.4.2
GS0834-430	12.3159	91/ 5/28	—	Aoki 1993
LMC X-4	13.49798[c]	89/ 8/ 3	23:46	Levine 1991
GS1843+00	29.5057	88/ 4/20	6:00	
OAO1657-415	37.747	88/ 3/17	—	Kamata 1990
	37.725	88/ 4/ 7	—	Kamata 1990
	37.713	89/ 3/ 4	—	Kamata 1990
EXO2030+375	41.681	89/10/30	0:45	
Cep X-4	66.251	88/ 4/ 4	2:30	
	66.248	88/ 4/ 9	14:30	
	66.248	88/ 4/14	23:00	

GS1843-02	94.848	88/ 9/29	—	Koyama 1990b
	94.897	88/10/ 3	—	Koyama 1990b
A0535+26	103.43	89/ 4/ 4	6:14	
	103.26	90/ 4/19	1:40	
Sct X-1	111.001	88/ 9/14	—	Koyama 1991b
GX 1+4	110.233	87/ 3/30	—	Sakao 1990
	111.59	88/ 3/27	—	Sakao 1990
	113.626	89/ 8/27	—	Sakao 1990
Vela X-1	283.03	90/ 4/21	0:00	
1E1145.1-6141	296.90	91/ 3/14	5:00	
	296.78	91/ 3/15	17:00	
X1722-36	413.08[b]	88/ 3/30	13:00	Takeuchi 1990
4U1907+09	439.5	90/ 9/22	15:00	
4U1538-52	530.70	90/ 7/28	9:00	
GX301-2	682.9	90/ 6/14	17:00	
	683.4	90/ 6/15	16:00	
	683.5	91/ 3/13	23:00	
X Per	837.5	90/ 1/27	14:00	

a : Apparent heriocentric pulse period.

b : Intrinsic heriocentric pulse period.

c : Intrinsic barycentric pulse period.

These periods were used to obtain pulse-phase sliced spectra.

The apparent pulse periods of some X-ray pulsars change during the observation through Doppler effects caused by the binary motion of the pulsars around their companions. In such cases, we divide the entire data into shorter segments in which the pulse period can be considered constant. Following is an example of Her X-1 as the severest case.

We determined to divide the spectra into 8 phases according to the pulse phase. The apparent pulse period changes with the orbital movement of the neutron star, it may come to a problem in the analysis of the short orbital pulsars. The orbit of Her X-1 is circular, the orbital peiod is 1.7 d, and the orbital radius is 13.19 lt-s (Tananbaum *et al.* 1972). It is clear that we cannot use a common period for the data separated as long as one day. The observations of Her X-1 were in the contact orbits, and the longest observation block was 3.3 hours from the beginning to the end. We estimate the difference of the pulse phase when assuming a mean constant period during the 3.3 hours, and found the difference might be 20 - 200ms (it depends on the position of Her X-1 in the orbit). Comparing that the time resolution of this observation is 62.5 ms and 1/8 phase is 160 ms, it might be a problem in some cases. We folded the light curves by each *Ginga* orbit and checked the pulse period and the phase 0 time. Fortunately they can be considered the same in that 3.3 hour observation. We finally separated the data into 5 blocks : one block for 1989 June 3, one for 1989 June 6, two for 1990 July 27, and one for 1990 July 28. Then we divided the spectrum into 8 phases in each block, subtracted backgroud, and summed up the 5 blocks at the same phases. We took the pulse peak as phase 0.0 and accumulated 0.0–0.125 to the spectrum for phase 1. Spectra obtained in this way will be presented in §5.

To calculate the *intrinsic* pulse periods of the sources, it is necessary to remove the orbital Doppler effects mentioned above. This requires knowledge of the orbital elements of each binary system which, however, have been determined only for a very limited number of objects among our sample. For the purpose of pulse phase-resolved spectroscopy, we only need to know the apparent pulse period. We therefore do not attempt to convert the obtained apparent periods into the intrinsic values.

4.4.2 Pulse Period Changes in 4U 1626-67

Although study of the intrinsic pulse periods and their histories is not our main subject, the case of 4U 1626-67 is worth mentioning. This object used to exhibit the most stable spin-up trend with a characteristic time scale pf $P/\dot{P} = 4800$ years. However observations with the *Compton* gamma-ray observatory (*GRO*) found that it turned into spin down with a rate almost the same in absolute value (Prince *et al.* 1993, Wilson *et al.* 1993).

Table 4.4.2 and figure 4.4.2 summarize heliocentric pulse periods (P) and period derivatives ($\dot{P}$) of 4U 1626-67 during the four-day *Ginga* observations in April 1990. As noticed in §4.2.6, the apparent pulse period is equal to the intrinsic one for this particular object, because no orbital Doppler effect has been detected. Thus 4U 1626-67 was still showing a spin up during the *Ginga* observation, but the obtained values of $-\dot{P}$ were somewhat smaller than the previous values, and P were also a little longer than the extrapolation from previous data points. These results suggest that the *Ginga* observarios of 4U 1626-67 were made during the final phase of its long-term spin up, just before it turns into the spin-down trend.

According to the accretion torque theory (§2.3.4), a fast pulsar would show a spin-up trend when the mass accretion rate is high, and would turn into a spin-down trend when the accretion

rate decreases. However the intensities of 4U 1626-67 we observed are quite typical of this object. It is therefore a big puzzle how a drastic change could have occurred to the long-term $\dot{P}$ trend without accompanied by significant changes in the source intensity. The case of 4U 1626-67 suggests that the accretion torque theory still needs a significant improvement.

Table 4.4.2: Heliocentric Pulse Periods of 4U 1626-67

pulse arrival time of the first peak		Intensity 2–60 keV	pulse numbers	pulse peiord	epoch		$\dot{P}$
date	hour [UT]	[c/s]		[s]	date	hour [UT]	10^{-11}[s/s]
90/ 4/18	14.306656	289					
			10961	7.66007213	4/19	1.968052	
90/ 4/19	13.629448	265					-1.2
		284	10290	7.66007112	4/20	0.576966	
90/ 4/20	11.524484	278					-9.3
			11785	7.66006326	4/21	0.062519	
90/ 4/21	12.600553	280					

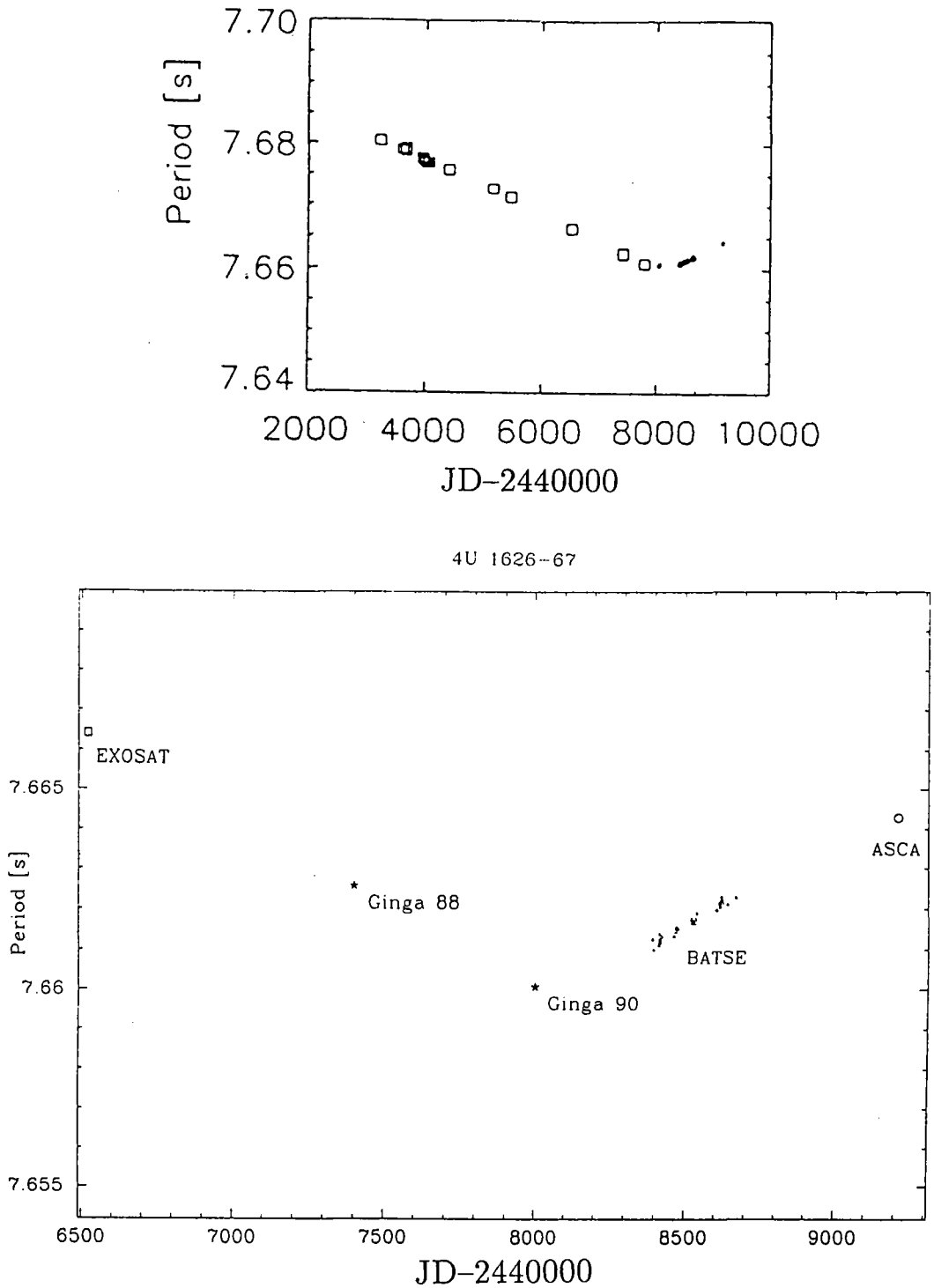

Figure 4.4.2: Heliocentric pulse priod history of 4U 1626-67. *Ginga* data points are plotted on the figure of Wilson *et al.* (1993). *Ginga* observation was during the $\dot{P}$ changing phase, but still showing spin up.

4.4.3 Pulse Profiles in the Whole Energy Band

We show pulse profiles of the observed pulsars in Appendix B.1, integrated over the entire 2–37 keV energy band and folded with the derived periods. These pulse profiles generally agree with previous results (White, Swank and Holt 1983; Nagase 1989).

4.4.4 Energy-Divided Pulse Profiles

It has been known for many years that pulse profiles of X-ray pulsars change considerably with energy, although the degree of energy dependence varies from object to object. There is a general tendency that the pulse profile becomes simpler, either single-peaked or double-peaked, at higher energies. For example, Vela X-1 shows five peaks per one pulse cycle below several keV, but the profile has only two peaks of about euqal heights above $\sim$ 10 keV. The pulse profiles divided by the energy are shown in Appendix B.2.

This sort of energy-dependent pulse profiles result partially from pulse phase-dependent variation in the amount of photoelectric absorption (Nagase *et al.* 1989). However the energy dependence in pulse profile is often observed even for energies well above $\sim$ 5 keV, where the photoelectric absorption would be negligible. Therefore we infer that the pulse profiles are intrinsically energy dependent; in other words, the X-ray emission is fairly anisotropic, and the X-ray beam pattern is energy dependent (§2.7). As argued by many authors (e.g. Kanno 1980; Kii 1986; Meszaros and Nagel 1985a,b), the most likely cause of such an energy dependent beam pattern is the electron cyclotron resonance (see §2.7).

Keeping the above point in mind, in figure B.2.1 we show pulse profiles of some pulsars folded in several energy bands. The energy bands for each object have been selected considering the cyclotron resonance energy described later. These results clearly show that the profile is energy dependent even above 10 keV. We will utilize the information of figure B.2.1 when we try to establish cyclotron resonance features in the observed spectra in §5.

Chapter 5

Data Analysis and Results

In this chapter, we analyze pulse-phase averaged and pulse-phase resolved spectra of the observed sources from the viewpoint of cyclotron resonance effects. In §5.1 we use Cep X-4 as a representative case to explain various analysis techniques employed and to describe the obtained results. Cyclotron resonance features are detected from 12 pulsars altogether. These results are given in sections 5.1 to 5.10. Nondetection of cyclotron structures from the remaining sources are described in the last section of this chapter.

5.1 Cep X-4

Mihara *et al.* (1991b) showed that the 66 s transient X-ray pulsar Cep X-4 (see §4.3.3), re-discovered with *Ginga* , exhibits cyclotron resonance features at about 30 keV. In this section we briefly review the spectral analysis they performed. This will serve as an example for the subsequent data analysis.

5.1.1 Pulse phase averaged spectrum

As a first step, we study pulse phase-averaged normal-HV spectra of Cep X-4. Spectra accumulated for the three days of observations and separately for each day are shown in figure 5.1.1. In obtaining these spectra we used only those data which were acquired in regions of high cut-off rigidity (> 9 GeV) and more than 5 minutes after the exit from the SAA. In this thesis, we use these conditions as standard data selection criteria unless otherwise stated. The SUD sorting method (see §3.3) was used for the background subtraction. The accumulation times are 10100s (Apr.3), 45800s (Apr.8) and 17100s (Apr.14). The background data were taken on April 14, and the accumulation time is 24500s. The same background data were used to produce all the three spectra.

After the background subtraction, all the spectra have been corrected for the aspect effect, which is the decrease of the effective area due to the LAC collimator response when

the source is not in the center of the field of view. Therefore intensities of all the presented spectra are converted to those observed with the 4000 cm^2 effective area.

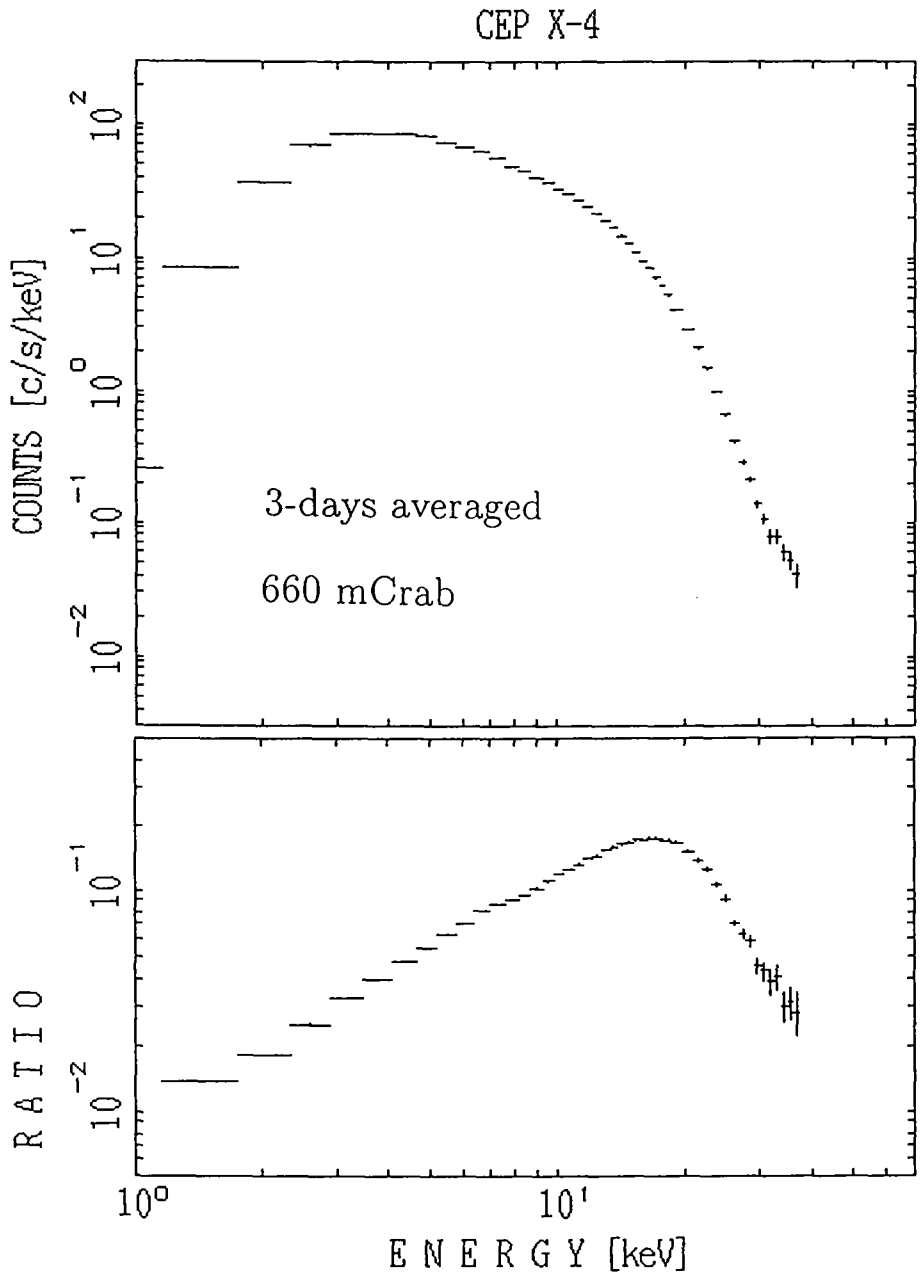

Figure 5.1.1: Pulse phase averaged spectrum of Cep X-4 accumulated for all the 88/4/3, 88/4/8, and 88/4/14 observations. The lower panel is the Crab ratio (PHA ratio to the Crab spectrum).

The three-day average spectrum of Cep X-4 exhibits a noticeable structure (or a cur-

vature change) at about 30 keV, in addition to fluorescent iron K emission line at about 6.4 keV. The 30 keV feature is also visible in each individual spectrum. However it is not obvious at this stage whether the feature is real or instrumental, since the detector response was not yet removed from these spectra. In particular, the LAC spectra generally exhibit instrumental features at Ar-K, Xe-L and Xe-K edges (see §3.2.2). Among them the Xe-K edge feature, at 35 keV, is the most prominent, and close to the energies of interest. Therefore it is of vital importance to examine whether or not the suggested 30 keV feature is simply an artifact due to the instrumental Xe K-edge effect.

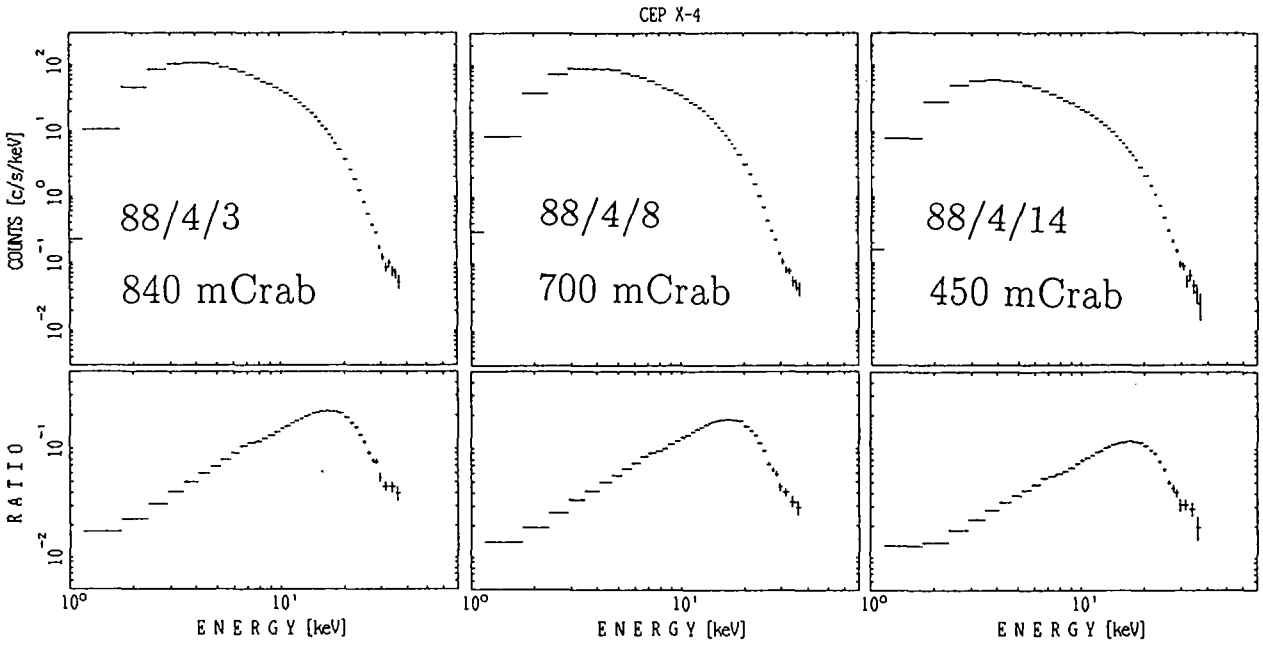

Figure 5.1.1*continued*: Pulse phase averaged spectra and Crab ratios of Cep X-4 of each day.

5.1.2 PHA ratio to the Crab nebula

A direct and model-independent way to approximately remove the effects of the detector response from the observed spectrum is to normalize it, channel by channel, to another spectrum of a standard object acquired with the same instrument. Such ratios between two spectra are called PHA (Pulse Height Analyzer) ratios. When calculating PHA ratios, care must be taken that the two spectra were acquired under the same operational condition of the instrument, including the high voltage setting, the amplifier gain, the anti-coincidence logic, and so on.

The Crab nebula is often used as the standard source, because it is a very bright and

steady X-ray source with a featureless single power-law spectrum. The Crab spectrum has a photon index of 2.10 in the energy range of 2–60 keV, modified by the Galactic absorption of $N_H = 10^{21.5}$ cm^{-2} (Turner *et al.* 1989) (see figure 3.2.4). The PHA ratios calculated against the Crab spectrum will be called 'Crab ratios'.

The lower panel of figure 5.1.1 shows the Crab ratios of the pulse phase averaged spectra of Cep X-4, in which the 30 keV feature is still visible as a significant flux deficit superposed on a smoothly turning-over continuum. Because an instrumental feature would have been canceled out in the Crab ratio, we are confident that there does exist a spectral feature at about 30 keV which is intrinsic to Cep X-4. We tentatively identify it with a cyclotron resonance feature, since no major atomic lines are expected near this energy.

5.1.3 Exponential Cutoff (ECUT) fit

In order to quantitatively evaluate the observed 30 keV feature, we will fit the spectra with model functions that do not have a local feature at about 30 keV. The most conventional and widely used of such models is the power-law times exponential cutoff model (ECUT model) as explained in §2.3.5. Accordingly we first attempted fitting the Cep X-4 spectra over the entire 2–37 keV range, by modifying the ECUT model with the photoelectric absorption factor which becomes significant towards lower energies. In order to simulate the iron emission line, we also added a Gaussian component to the model. The explicit model form thus becomes

$$F(E) = AE^{-\alpha} \times ECUT(E) \times \exp\left(-N_H \sigma_{pe}(E)\right) + Iron\ line.$$

Here N_H is the equivalent hydrogen column density (circum-source plus interstellar), and $\sigma_{pe}(E)$ is the photoelectric absorption cross section (Morrison and McCammon 1983). The exponential cutoff function $ECUT(E)$ has been given in §2.3.5.

We convolved this model through the LAC response matrix and compared the results with the pulse phase averaged spectra of Cep X-4 (figure 5.1.2). The best-fit model parameters are tabulated in the appendix. Thus we obtain $E_c \sim 17$ keV and $E_f \sim 8$ keV, implying that the Cep X-4 spectrum cuts off above ~ 17 keV with the e-folding energy of 8 keV. This is very typical of an X-ray pulsar spectrum. The fit however is unacceptable with significant discrepancies between data and the model as seen in the lower panel of Figure 5.1.2. Similarly ECUT fits for most other pulsars, also tabulated in the appendix, are unacceptable. This indicates that the X-ray pulsar spectra are generally too complex to be described by the above simple model.

Since our purpose is to examine the nature of the 30 keV feature rather than trying to describe the overall spectral shape, we next limited the fit energy range to > 9 keV. This allows us to simplify the fit model by removing the photoelectric absorption factor and the line component. However, as shown in figure 5.1.3(a), the fit has failed again. In fact

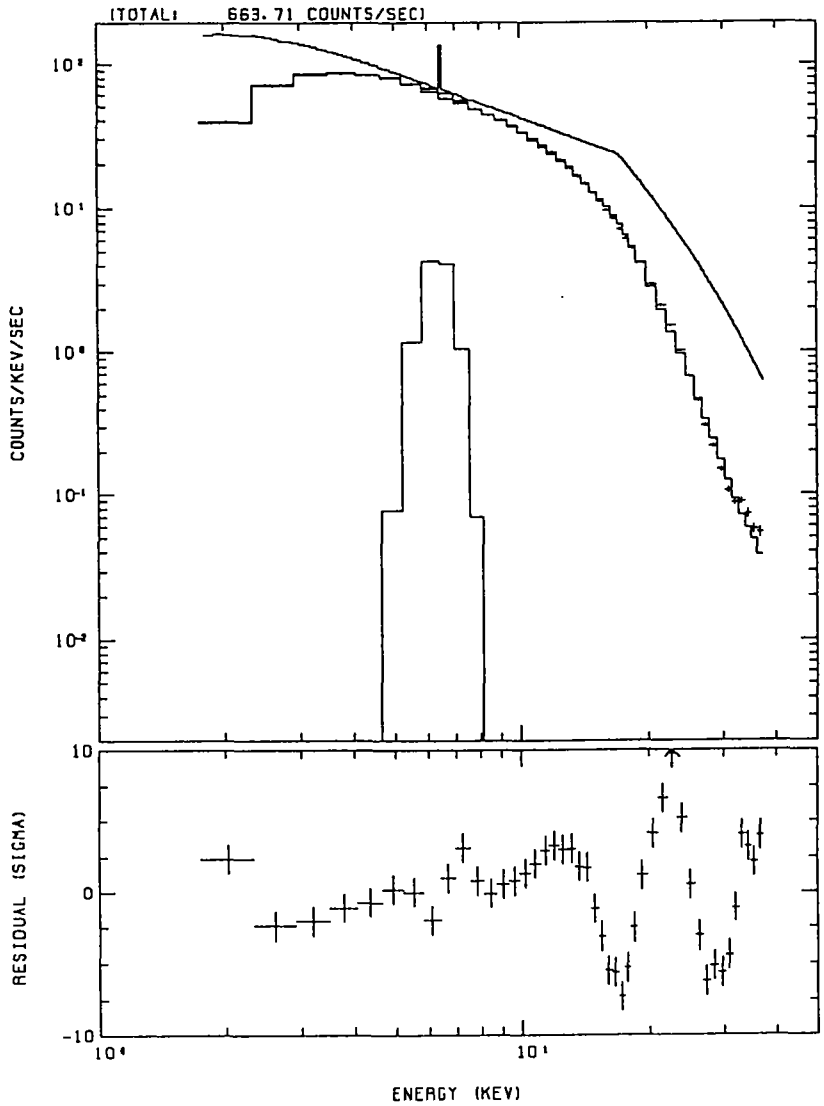

Figure 5.1.2: Pulse averaged spectra with ECUT fitting.

there remain conspicuous fit residuals around 30 keV. Furthermore, a serious discrepancy is also seen at $E \sim E_c$. This is due to the abrupt break at $E = E_c$ where the model value is continuous but its first derivative has a jump (Makishima *et al.* 1990a). Such a model incompleteness would have been of little problem for previous observations with relatively poor data quality, but the *Ginga* LAC has so large an effective area that the data statistics have been improved significantly. These results indicate that the ECUT model is of little use any longer for our purpose.

5.1.4 Fermi-Dirac Cutoff (FDCO) fit

In order to avoid the abrupt break in the ECUT model, we next employ the Fermi-Dirac cutoff (FDCO) model explained in §2.3.5.

$$F(E) = AE^{-\alpha} \times FDCO(E) \times \exp(-N_H \sigma_{pe}(E)) + Iron\ line.$$

$$FDCO(E) = \frac{1}{1 + \exp\{(E - E_c)/E_f\}}$$

We again limit the fit range to > 9 keV. The FDCO fit to the pulse phase averaged spectra of Cep X-4 is shown in figure 5.1.3(b). The obtained value of $E_c \sim 18$ keV is similar to that from the ECUT fits. The fit has in fact been much improved, especially around $E = E_c$, but is still unacceptable. Now the major source of the discrepancy between data and model is the negative residuals at about 30 keV. Since the FDCO model is a smoothly varying function without local structure, we can conclude that the 30 keV dip-like feature is intrinsic to the source and is statistically significant. This greatly reinforces its identification with a cyclotron resonance feature.

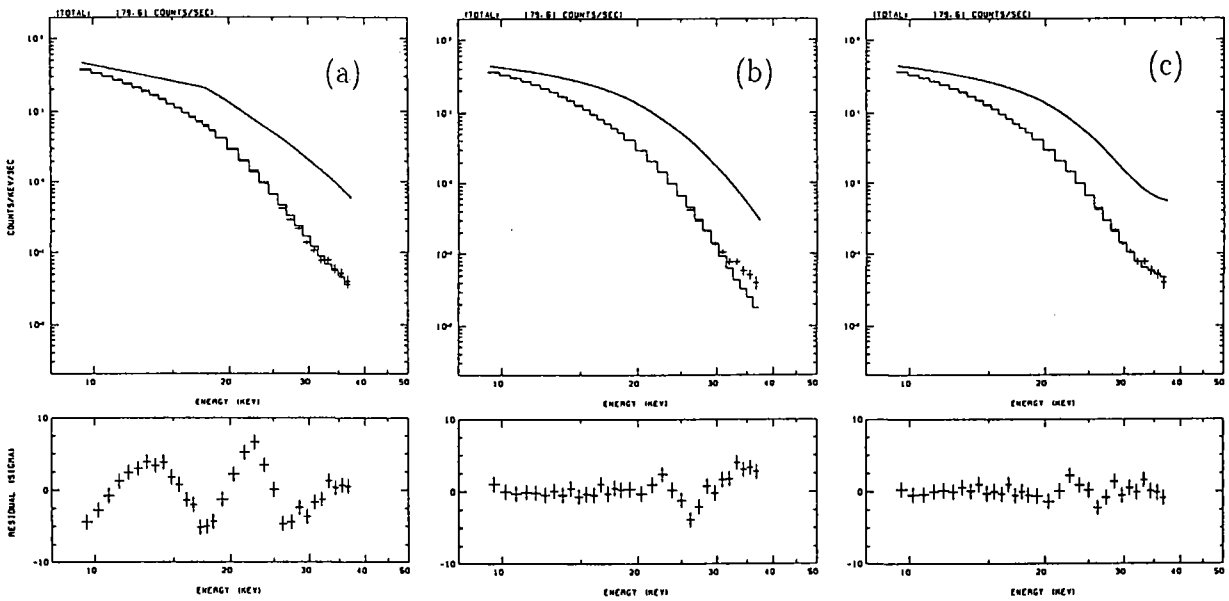

Figure 5.1.3: Fitting of the pulse averaged spectra of Cep X-4 above 9 keV with various models. (a) ECUT: $E_c = 17.5$ keV, $E_f = 7.5$ keV, $\chi^2 = 11.39$, (b) FDCO: $E_c = 18.1$ keV, $E_f = 4.4$ keV, $\chi^2 = 2.86$, (c) CYAB: $E_a = 30.5$ keV, $W = 15.0$ keV, $\tau = 2.93$, $\chi^2 = 0.80$.

5.1.5 Cyclotron Scattering Model (CYAB, CYA2) Fit

Analysis so far conducted in various ways, employing Crab ratios, ECUT fits and FDCO fits, has established that the pulse-phase averaged spectra of Cep X-4 exhibit a dip-like 30 keV feature, which persisted over the three observations. Our next step is to seek its semi-quantitative interpretation in terms of basic physics taking place in plasmas under extremely strong magnetic fields of order 10^{12} G, which are expected for accretion columns of X-ray pulsars.

As noted in §2.7, the photon-electron scattering cross section in magnetized plasmas becomes very large near the cyclotron resonance energy and its harmonic energies. Since pulsed X-rays from X-ray pulsars are thought to be strongly beamed, photons with energies near the resonances will be scattered out of the X-ray propagation direction. Accordingly an absorption feature will be expected if the X-ray beam points toward us. Emission lines will instead be observed at the resonance energies if our line of sight is outside the X-ray beam, although in this case the X-ray intensity would be very low and difficult to detect. The illustration is in figure 5.1.4. We here assume that the X-ray emission region of Cep X-4 has a magnetic field strength of $\sim 2.6 \times 10^{12}$ G, a value very reasonable from a general theoretical viewpoint. Since the fundamental electron cyclotron resonance then appears at 30 keV through eq.(2.5) (neglecting the gravitational redshift), an absorption feature will be formed in the emergent spectrum at $\sim$ 30 keV just as has actually been observed.

We further make a very important assumption after Tanaka (1986) and Makishima *et al.* (1990a); namely we assume that the turn-over of the X-ray pulsar continuum is a phenomenon which is intrinsically and closely related to the cyclotron resonance. More specifically, we regard the turn-over as being caused by the gradually increasing scattering cross section towards the resonance, where the spectrum reaches a local minimum. This assumption is supported by the fact that the ratio of the resonance energy E_a to the cutoff energy E_c is fairly similar, at $\sim$ 1.5, for Her X-1 (E_a = 35 and $E_c \sim$ 20 keV) and 4U 0115+63 (E_a = 12 and $E_c \sim$ 8 keV). If this ratio is indeed well defined, for Cep X-4 having $E_c \sim$ 17 keV we expect $E_a \sim$ 27 keV, close to 30 keV.

In order to quantify the above idea, we try fitting the spectrum with a model which takes into account the effect of electron cyclotron resonance. Although such model spectra have been calculated by many authors, none of them can be used conveniently in a numerical fitting algorithm. We therefore introduce a very simple "cyclotron scattering" (CYAB) model (Tanaka 1986), given as

$$F(E) = AE^{-\alpha} \times e^{-\tau_1}. \tag{5.1}$$

Here $\tau_1 \equiv N_H \sigma_1(E)$ (see §2.6.2) is optical depth of the fundamental cyclotron scattering in a classical cold plasma,

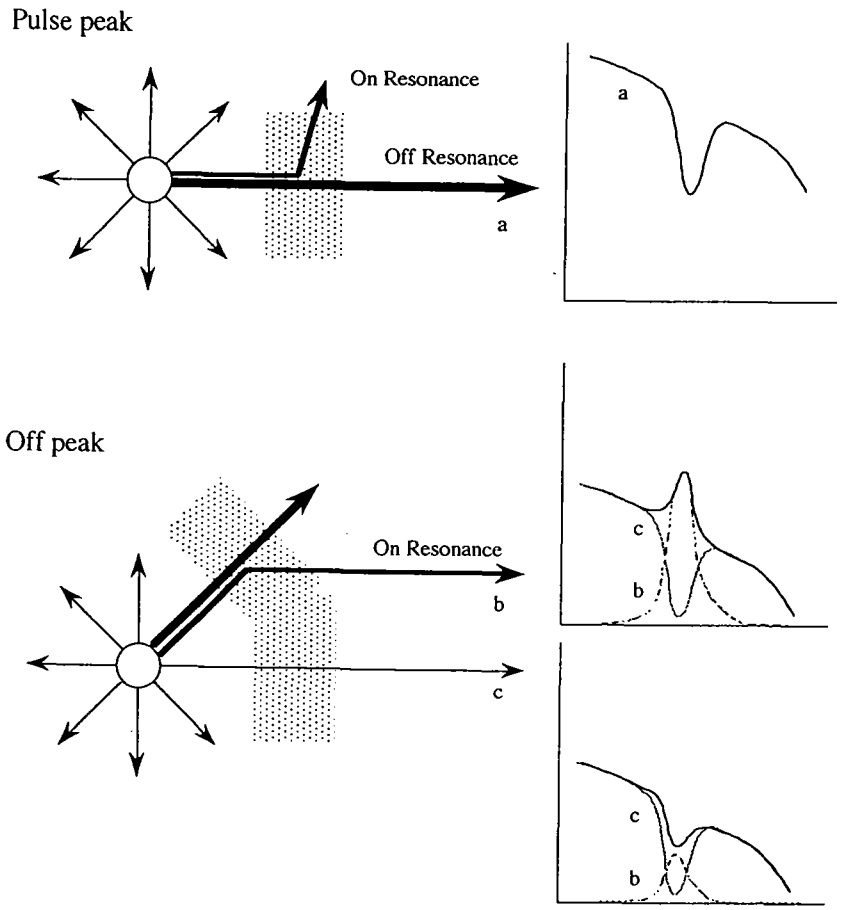

Figure 5.1.4: Geometry of cyclotron scattering which appears as an emission line and an absorption line.

$$\tau_1 \equiv N_H \sigma_1(E) = \frac{D_1(\frac{W}{E_a}E)^2}{(E - E_a)^2 + W^2} \tag{5.2}$$

where E_a is the resonance energy, W is the width of the resonance, and D_1 is the depth of the resonance. As shown in figure 5.1.5, τ_1 has a peak around $E = E_a$, becoming maximum at $E = E_a + W^2/E_a$, and approaches $\tau_1 = D_1(W_1/E_a)^2$ for $E \gg E_a$. See §2.6.2 for detail.

The following "CYA2" model takes the second harmonic into account, as

$$F(E) = AE^{-\alpha} \times e^{-(\tau_1+\tau_2)}. \tag{5.3}$$

$\tau_2 \equiv N_H \sigma_2(E)$ is the second harmonic term. But often, since the resonance energy and the width of the second harmonic cannot be determined independently, they are fixed to

$2E_a$ and $2W$ as

$$\tau_2 \equiv N_H \sigma_2(E) = \frac{D_2(\frac{W}{E_a}E)^2}{(E-2E_a)^2+(2W)^2} \cdot \tag{5.4}$$

Although for generality we include both τ_1 and τ_2, we set $\tau_2 = 0$ in the particular case of Cep X-4 because E_a is expected to appear close to the end of the energy range (37 keV for the normal-HV data) and τ_2 is unlikely to be well constrained by the data. In order to represent a high energy cutoff above the observed energy band we instead use an exponential cut off function with $E_c = 40$ keV and $E_f = 20$ keV in the fitting of Cep X-4.

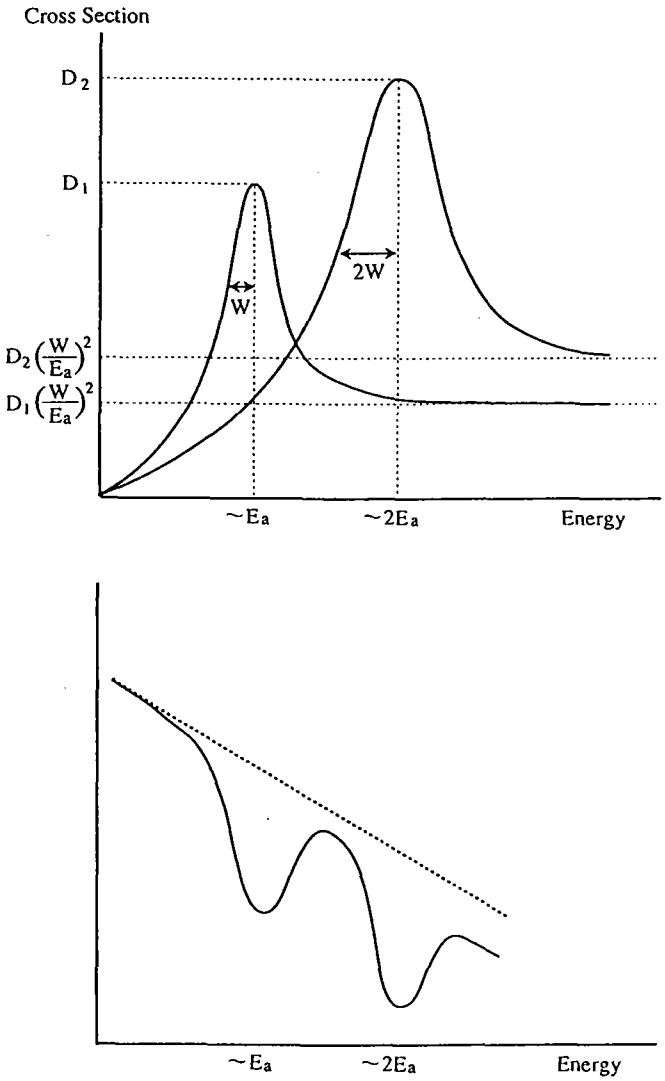

Figure 5.1.5: Energy dependence of τ_1, τ_2 of the cyclotron scattering (CYAB, CYA2) model

The CYAB model introduced above has given completely acceptable fits to the phase-averaged Cep X-4 spectra. The best-fit parameters are summarized in table 5.1.1 together with the phase resolved spectra to be analyzed later. The best-fit parameters for each of the three days observations are also listed in the table 5.1.1. Figure 5.1.3 (c) is the phase averaged spectrum fitted with the cyclotron scattering model. Thus both the spectral break above 17 keV and the 30 keV structure have been described adequately with the CYAB model. As expected, the resonance E_a has turned out to be 30–31 keV, with $W_1 \sim 15$ keV and $D_1 \sim 2.9$. These results are highly convincing evidence for cyclotron resonance at about 30 keV in Cep X-4.

The model 5.1, however, cannot explain the spectrum in the overall energy band of *Ginga* (2–37 keV) as shown in figure 5.1.6 *left*. The continuum will be improved later in this thesis as figure 5.1.6 *right*.

Table 5.1.1: Parameters of CYAB fits for pulse phase averaged and resolved spectra of Cep X-4.

	Cyclotron scattering			Power law		
Pulse Phase	Resonance Ea [keV]	Width W [keV]	Depth1 D_1	Norm. A [ph/s/keV]	photon index α	χ^2_ν
Averaged						
ave.	30.5 ± 0.4	15 ± 2	2.9 ± 0.1	46 ± 1	0.61 ± 0.09	0.80
4/3	30.2 ± 0.5	16 ± 2	2.9 ± 0.1	59 ± 1	0.58 ± 0.10	0.69
4/8	30.6 ± 0.5	15 ± 2	3.0 ± 0.1	49.9 ± 0.7	0.58 ± 0.09	0.67
4/14	31.0 ± 0.7	14 ± 2	2.9 ± 0.2	29.4 ± 0.5	0.69 ± 0.09	0.86
Pulse phase resolved						
1	28.4 ± 2.0	26 ± 7	2.7 ± 0.3	62 ± 5	0.5 ± 0.2	1.11
2	30.2 ± 1.5	23 ± 6	2.6 ± 0.3	37 ± 2	0.5 ± 0.2	0.72
3	29.4 ± 0.9	12 ± 2	2.4 ± 0.3	21.1 ± 0.5	1.0 ± 0.1	1.01
4	28.9 ± 1.1	20 ± 4	2.5 ± 0.2	40 ± 2	0.48 ± 0.16	0.85
5	29.1 ± 0.7	18 ± 2	2.9 ± 0.1	65 ± 2	0.26 ± 0.12	0.44
6	30.7 ± 0.4	11.4 ± 1.1	3.2 ± 0.1	59.4 ± 0.7	0.63 ± 0.07	0.77
7	31.7 ± 0.5	9.3 ± 1.0	4.1 ± 0.3	46.4 ± 0.5	0.63 ± 0.07	1.07
8	31.1 ± 0.8	15 ± 3	3.2 ± 0.3	47.9 ± 1.1	0.7 ± 0.1	1.45

The units of the normalization of the power law are [photons/s/keV] at 10 keV.
ECUT (E_c=40keV, E_f=20keV) is included in this fitting to represent cutoff of high energy photons.

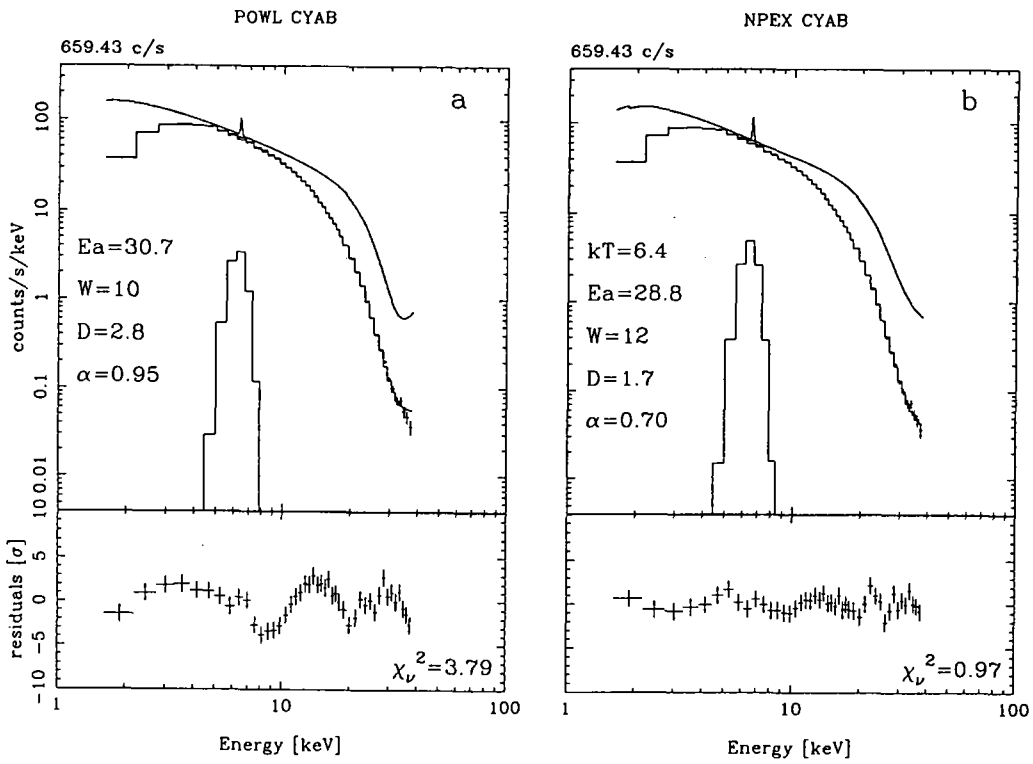

Figure 5.1.6: The spectral fits of Cep X-4 in the overall energy band (2–37 keV). *Left*: POWL × CYAB is unacceptable. *Right*: NPEX (α_2 = 2.0) × CYAB improve the fit. The NPEX parameters are listed in table 5.1.2. ECUT (E_c=40keV, E_f=20keV) is included in the POWL × CYAB fitting to represent cutoff of high energy photons.

5.1.6 Pulse phase resolved spectra

Experiences with Her X-1 (Voges *et al.* 1982; Mihara *et al.* 1990) and 4U 0115+63 (White, Swank and Holt 1983) indicate that the cyclotron resonance features are more or less dependent on the pulse phase. This is very reasonable from theoretical aspects as well, because X-ray pulsation is a direct consequence of anisotropic X-ray emission and such anisotropy is thought to be essential in the formation of cyclotron resonance features.

In order to study pulse-phase dependence of the cyclotron feature in Cep X-4, we divide the entire Cep X-4 data into eight pulse phases of equal width, according to the apparent pulse period and epoch derived in §4. *Ginga* data are generally accumulated for a time interval equal to the time resolution, as explained in §3.2.4. The phase resolved spectra have been accumulated referring to the start time of this data interval. This process requires that the time resolution be shorter than the phase resolving time. This condition is satisfied for the Cep X-4 case, because the phase resolving time of $66.2/8 = 8.3$ s is longer than the time resolution of the data which is mostly 0.5 s (MPC-2 M-bit rate) and partly 2.0 s (MPC-2 L-bit rate). From these raw spectra we subtracted a common background spectrum, as the background variations are in most cases slower than, and not synchronized with, the pulse period.

The pulse-phase resolved spectra of Cep X-4 thus obtained are shown in figure 5.1.7, where phase 0.0 corresponds to the main peak of the pulse. The spectrum changes significantly across the pulse phase, but the 30 keV feature is visible in most pulse phases, becoming most prominent at phases 3, 6, and 7.

5.1.7 Spectral subtraction between pulse phases

To emphasize subtle differences between spectra from different pulse phases, subtraction between two spectra is sometimes useful. In particular such a difference spectrum is least affected by the background uncertainty, because it can be obtained through a direct subtraction of the two spectra before the background is subtracted from them. As an example, figure 5.1.8a shows the phase 2 minus phase 14 spectrum from 16-divided spectra of Cep X-4, where a much sharper structure is seen than before the subtraction. As schematically illustrated in figure 5.1.8b, such a sharp feature can arise near the resonance energy when the cyclotron resonance parameters are significantly dependent on the pulse phases.

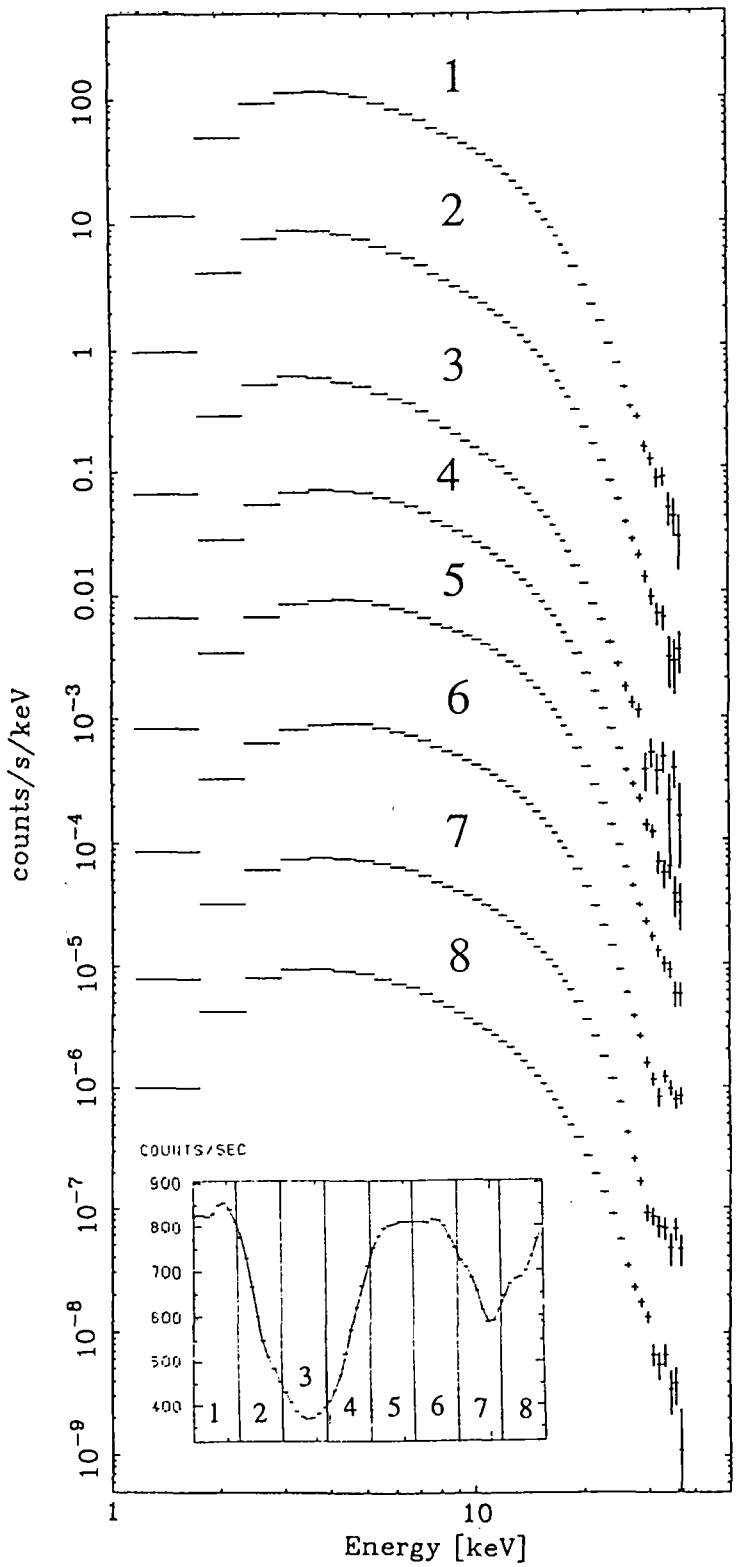

Figure 5.1.7: Phase resolved spectra of Cep X-4. Spectra are shifted downward successively by a factor ten, here and after unless otherwise cited. The values on the vertical axis is for the top curve. The error bars indicate ± one sigma statistical errors.

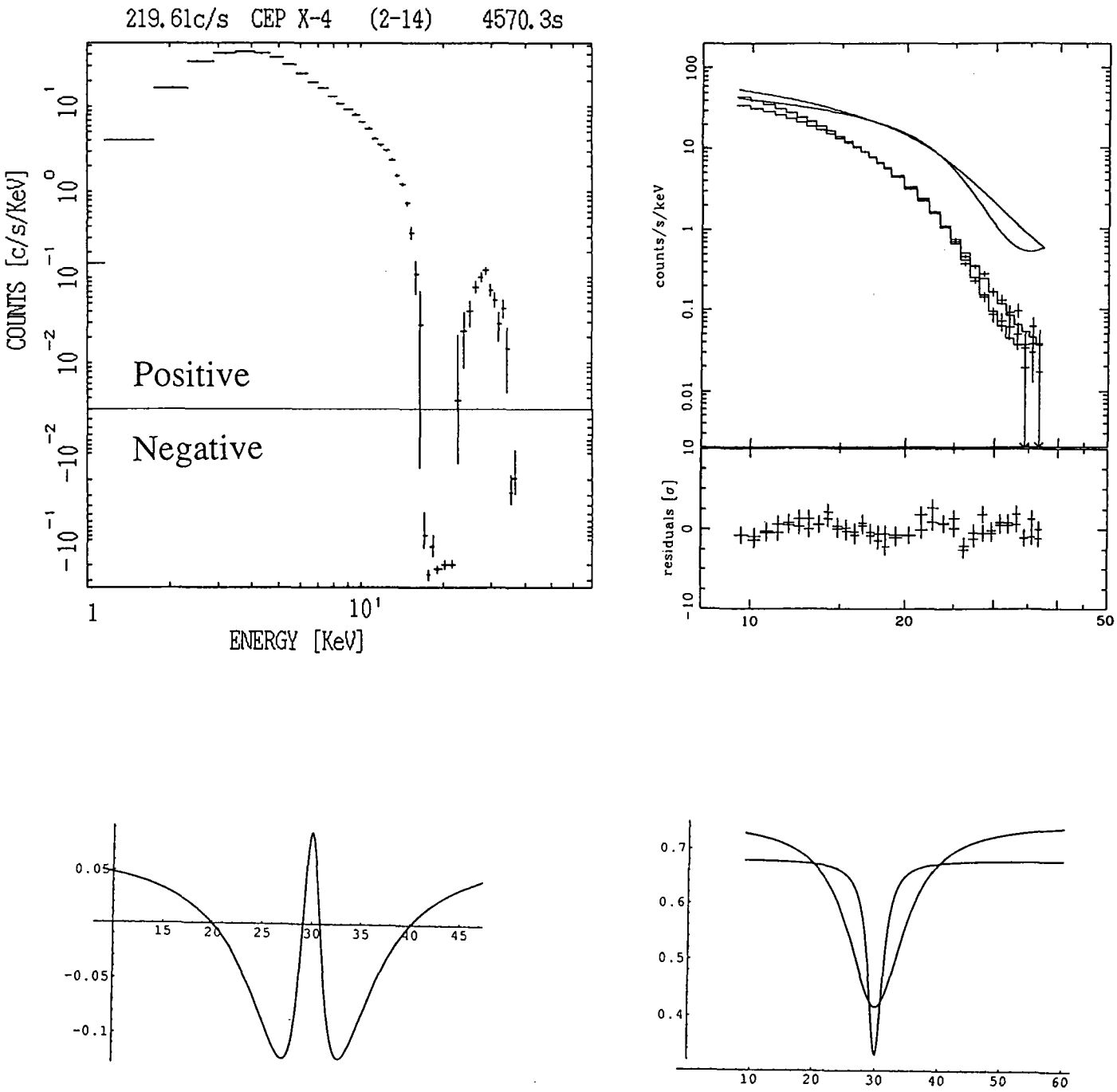

Figure 5.1.8: *Top*: Spectral subtraction of Cep X-4 and overlapped spectra with CYAB fit in phase 2 and 14 of the 16 phases. *Bottom*: Schematic view of spectral subtraction between phases. Wide shallow feature - narrow deep feature makes subtracted spectra.

5.1.8 PHA ratios of pulse phase resolved spectra

Another way of highlighting the phase dependent spectral features is to take PHA ratios of the phase resolved spectra to that of the Crab nebula, as was done for the pulse averaged spectrum in §5.1.2. Figure 5.1.9 shows the Crab ratios of these pulse-phase resolved spectra. The appearance of the cyclotron structure is evident, changing considerably with the pulse phase and becoming most prominent at phase 6 and 7.

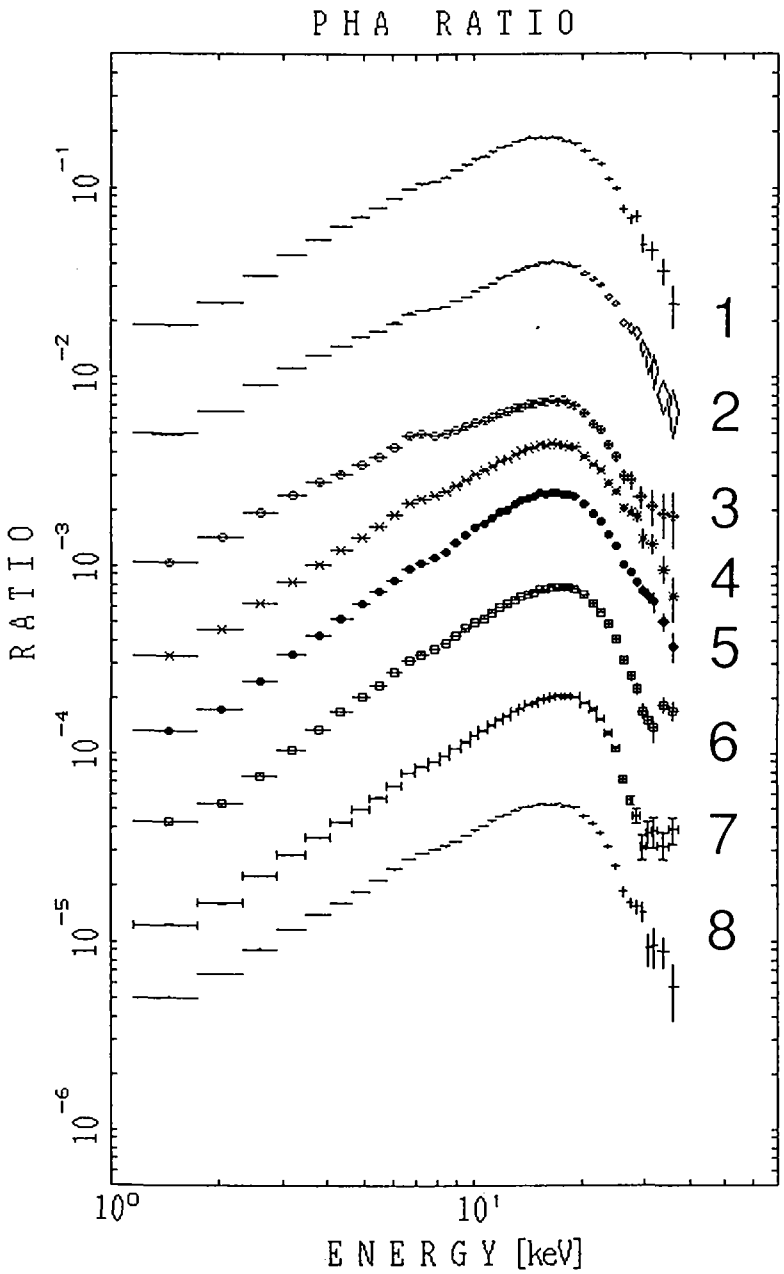

Figure 5.1.9: PHA ratios of pulse phase resolved spectra of Cep X-4 to the Crab nebula. Spectra are shifted downward successively by a factor 3.16 (half order) in this figure.

The Crab ratios have the problem that the continuum slope is rather different between the Crab nebula and the target pulsar, so that the ratio is not very flat as a function of energy. This problem can be avoided by normalizing each phase-resolved spectrum to the phase-averaged spectrum of Cep X-4 instead of the Crab spectrum. However the phase-averaged spectrum used as a denominator contains statistical errors. To further improve on this point, we finally normalized each phase-resolved spectrum to the best-fit FDCO model (convolved through the LAC response) to the phase-averaged spectrum. Figure 5.1.10 show these PHA ratios.

The PHA ratios in figure 5.1.10 exhibit quite conspicuous structures at about 30 keV, exactly corresponding to the cyclotron resonance feature. The feature appears as a prominent dip for phases 6 and 7, while it appears as a shallower dip for phases 1 through 5. This means that the cyclotron dip becomes deeper than the average for phases 6 and 7, while becomes shallower than the average over phases 1–5.

5.1.9 Cyclotron scattering model fitting of the phase resolved spectra

As a final step of the Cep X-4 data analysis, we fitted each phase resolved spectrum (above 9 keV) with the CYAB model (§5.1.5). As summarized in Table 5.1.1 and shown in figure 5.1.11, the model has given acceptable fits for most pulse phases.

The resonance energy E_a thus determined is very well defined, showing at most ± 1 keV scatter around the central value of $\sim$ 30.5 keV. On the other hand, the resonance width W_1 and the resonance depth D_1 are somewhat more phase dependent. The resonance always appears in absorption rather than in emission, since $D_1 > 0$ over the entire pulse phase. The reason why the feature is most prominent at phase 7 can be attributed to the fact that D_1 is largest and W_1 is smallest there. These results are physically very reasonable, and quite self consistent. We are confident that these results have clarified basic properties of cyclotron resonance effects in the spectra of Cep X-4.

After Mihara *et al.* (1991), we briefly examine the reliability of our results. Since the resonance appears rather close to the upper energy boundary, the value of E_a systematically depends on the choice of the fit model by $\sim \pm 2$ keV; for example, inclusion of the 2nd harmonic term generally upshifts the values of E_a by 1–2 keV. However other systematic uncertainties, including those associated with the LAC response and the background determination, are completely negligible. Specifically, the systematic background uncertainty, of order $< 1 \times 10^{-2}$ c s^{-1} keV^{-1}, is much smaller than the photon counting statistics over the entire energy range. Therefore uncertainties in the fit are solely determined by photon counting statistics and are confined within relatively small ranges. This is exemplified in figure 5.1.12 where we show confidence contour maps for some of the fit parameters. The exclusion of the data below 9 keV is well justifiable, because the spectrum below 20 keV depends little on the pulse phase (see figure 5.1.10) except for gradual

changes in the continuum slope and iron line strength. By using the NPEX model, we can fit the spectra in the overall energy band (figure 5.1.13, table 5.1.2). This NPEX model is established through the investigation of Her X-1 spectrum and will be described in detail in the next session.

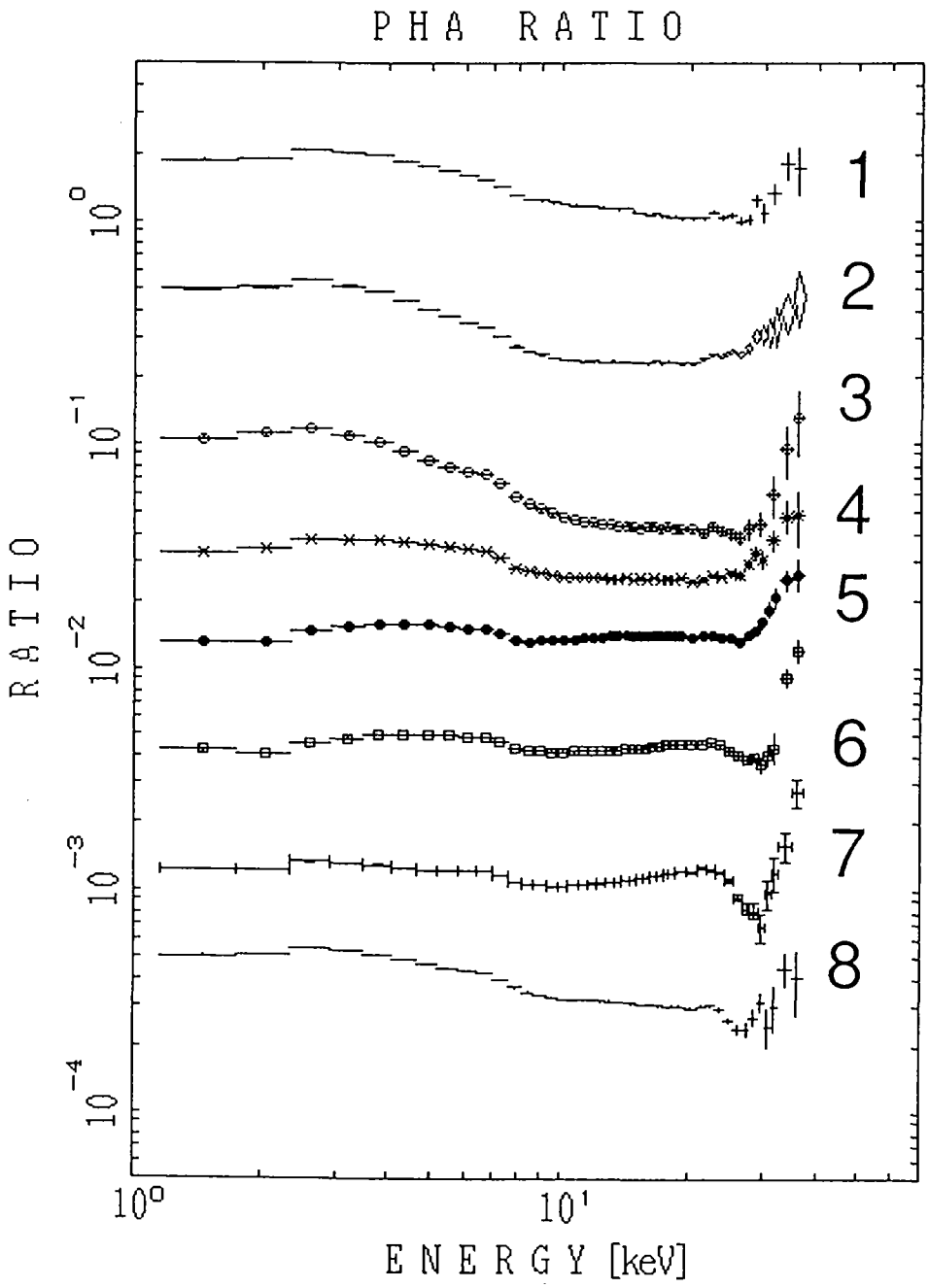

Figure 5.1.10: PHA ratios of the pulse phase resolved spectra of Cep X-4 to the best-fit FDCO model for the averaged spectrum. Spectra are shifted downward successively by a factor 3.16 (half order) in this figure.

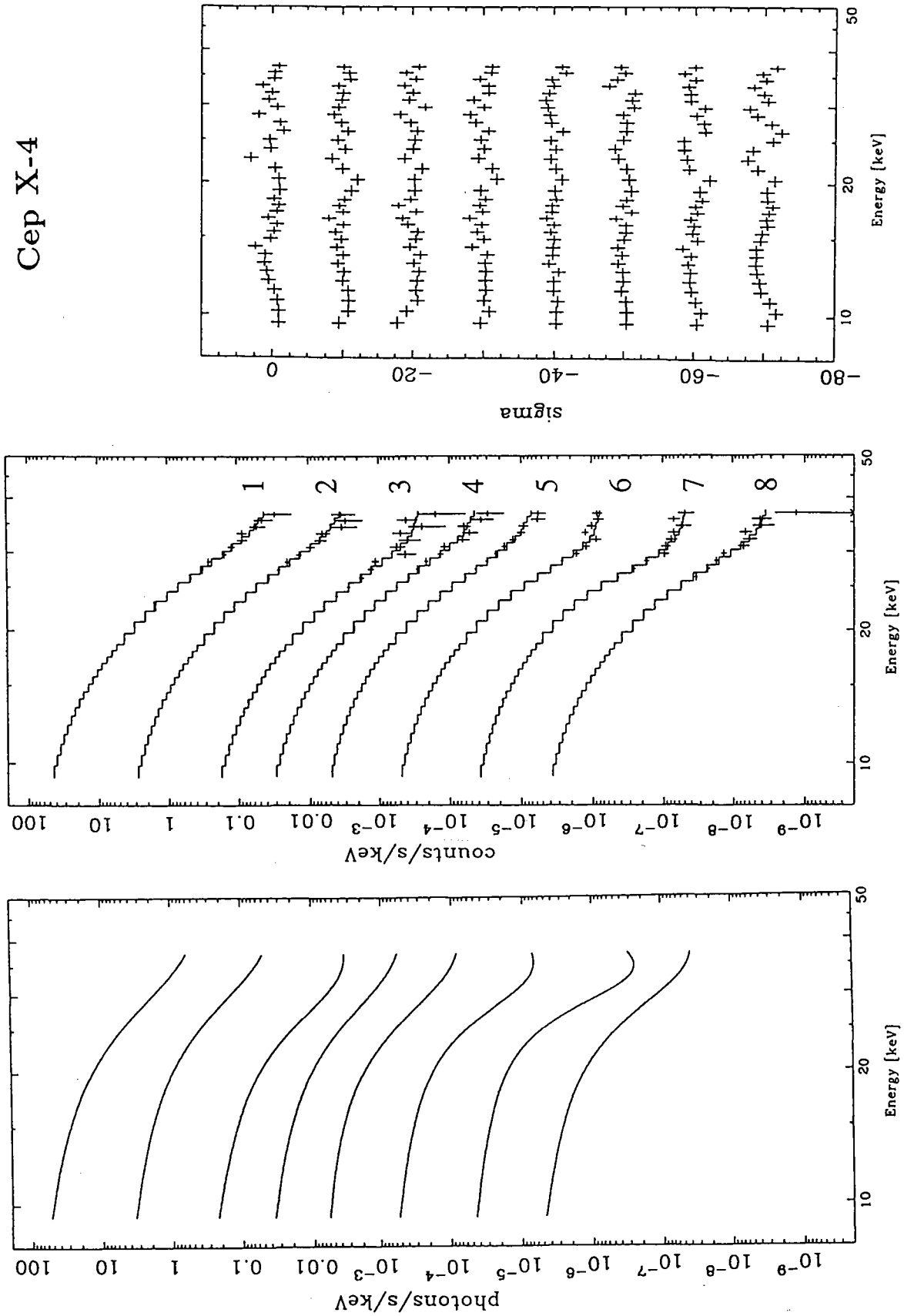

Figure 5.1.11: Fitting the phase resolved spectra with the Power law × CYAB model. The best-fit incident models, data and the best-fit convolved models, and the residuals are shown. Spectra are shifted downward successively by a factor ten. The residuals are shifted downward successively by ten sigma. The values on the vertical axis is for the top curve. The error bars are ± one sigma.

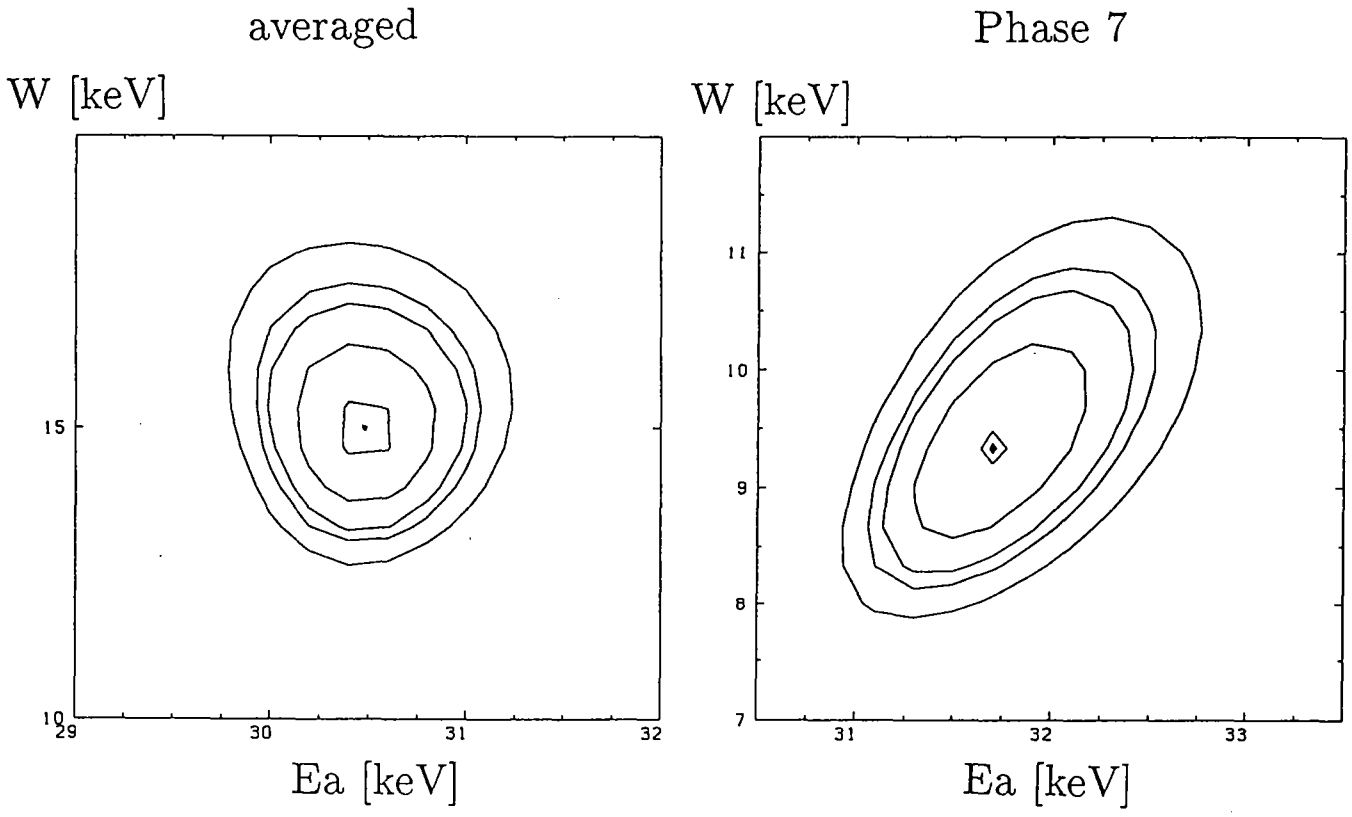

Figure 5.1.12: Contour maps for the fit parameters, Ea and W in phase-averaged and phase 7 spectra with 99, 95, 90, 68, 10 % confidence levels.

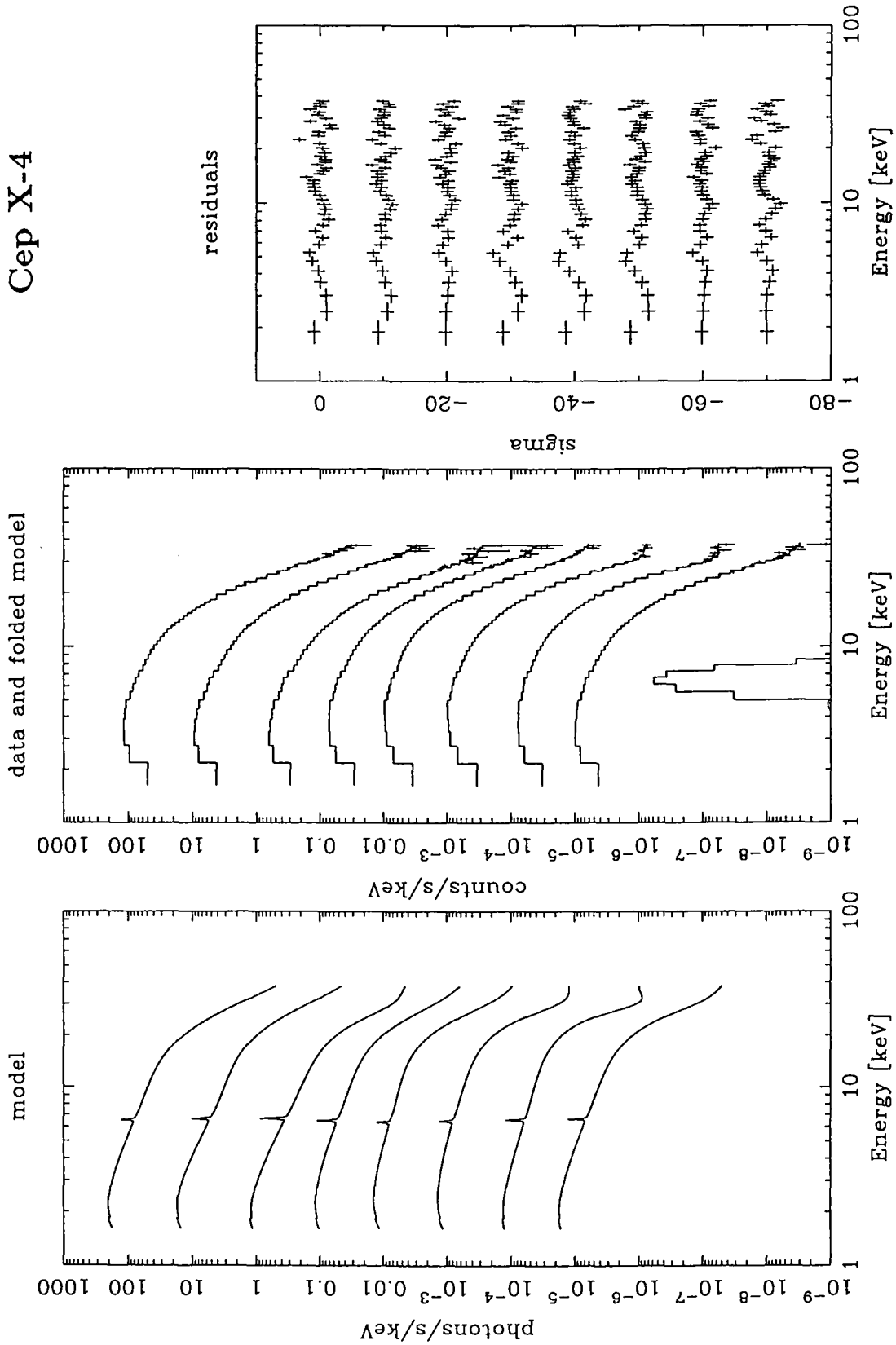

Figure 5.1.13: The NPEX × CYAB fits to the pulse phase resolved spectra of Cep X-4 in the entire energy band (2–37 keV).

Table 5.1.2: The NPEX × CYAB model parameters (figure 5.1.13). This model can fit the entire energy range, and will be introduced in §5.2.4.

pulse phase date	Negative power law Norm. A_1	index α_1	Positive Norm. A_2	Exponential Folding E. kT [keV]	Absorption $\log_{10}N_H$ [cm^{-2}]
ave.	101 ± 13	0.70 ± 0.05	110 ± 59	6.4 ± 1.5	22.01 ± 0.08
4/3	119 ± 37	0.70 ± 0.11	101 ± 92	7.5 ± 3.8	21.99 ± 0.07
4/8	100 ± 18	0.71 ± 0.06	97 ± 60	7.1 ± 2.2	22.01 ± 0.07
4/14	69 ± 11	0.70 ± 0.06	68 ± 43	6.4 ± 1.7	21.87 ± 0.12
1	117 ± 78	0.86 ± 0.24	149 ± 214	6.6 ± 6.3	22.10 ± 0.07
2	69 ± 30	1.14 ± 0.17	83 ± 73	6.9 ± 4.2	22.17 ± 0.05
3	55 ± 20	0.96 ± 0.15	40 ± 39	6.7 ± 3.1	22.04 ± 0.05
4	81 ± 52	0.68 ± 0.25	68 ± 118	7.3 ± 7.3	22.04 ± 0.08
5	107 ± 30	0.63 ± 0.09	124 ± 119	7.7 ± 4.4	22.09 ± 0.08
6	137 ± 20	0.41 ± 0.05	100 ± 78	7.1 ± 2.2	21.98 ± 0.09
7	102 ± 4	0.56 ± 0.07	148 ± 31	5.8 ± 0.4	21.87 ± 0.10
8	120 ± 14	0.69 ± 0.07	144 ± 82	5.7 ± 1.3	21.96 ± 0.12

pulse phase date	Cyclotron scattering Resonance Ea [keV]	Width W [keV]	Depth D	Iron line Flux I_{Fe} [ph/s]	Energy E_{Fe} [keV]	χ^2_ν
ave.	28.8 ± 0.4	12 ± 3	1.7 ± 0.6	7 ± 2	6.5 ± 0.1	0.97
4/3	28.6 ± 0.5	15 ± 5	2.0 ± 1.1	9.1 ± 1.9	6.6 ± 0.1	0.83
4/8	28.9 ± 0.4	14 ± 4	2.0 ± 0.7	7.0 ± 1.5	6.6 ± 0.1	0.79
4/14	29.3 ± 0.8	11 ± 4	1.6 ± 0.7	4.4 ± 1.2	6.5 ± 0.1	1.30
1	26.2 ± 7.0	22.3 ± 21.0	1.6 ± 1.6	6.3 ± 2.3	6.53 ± 0.20	1.33
2	27.6 ± 3.0	19.4 ± 13.0	1.6 ± 1.2	6.8 ± 1.3	6.63 ± 0.11	0.89
3	27.6 ± 0.9	10.5 ± 5.4	1.5 ± 1.1	6.6 ± 0.9	6.67 ± 0.07	0.89
4	27.6 ± 1.1	15.7 ± 12.3	1.7 ± 2.0	7.3 ± 1.7	6.52 ± 0.12	1.39
5	27.7 ± 0.5	15.5 ± 6.1	2.0 ± 1.2	6.5 ± 2.1	6.37 ± 0.17	1.14
6	29.2 ± 0.6	9.5 ± 2.2	2.0 ± 0.7	6.7 ± 2.1	6.46 ± 0.17	1.16
7	29.6 ± 0.3	6.5 ± 0.8	1.9 ± 0.2	7.7 ± 1.3	6.57 ± 0.10	0.75
8	29.3 ± 1.0	10.8 ± 4.1	1.6 ± 0.6	8.2 ± 2.1	6.64 ± 0.14	1.46

The index α_2 of the positive power law is fixed to 2.0.
The unit of the normalizations A is [photons/s/keV] at 10 keV.
The width (σ) of the iron line is fixed to 0.05 keV (narrow).

5.2 Her X-1

Her X-1 is a well-studied cyclotron source (§2.4) and was also observed with *Ginga* in 1989 at the first stage of cyclotron observations. The first observation of Her X-1 was summarized in Mihara *et al.* (1990). Since the observation was almost the first time with reduced-HV, we were very careful in subtracting the background. Thus obtained spectra in 9–60 keV were well fitted by a power law × CYA2 model, which led us to conclude that the structure is an absorption rather than an emission. We observed Her X-1 again in 1990. Here, we add together all the data and report the results with better statistics.

5.2.1 Average spectrum

We had three observations of Her X-1 in 1989 May, 1989 June, and 1990 July. The background data taken in 1989 June and 1990 July were subtracted from the corresponding on-source observations using the SUD method. The background subtracted spectrum, averaged over the three observations and the pulse phase, is shown in figure 5.2.1 together with the Crab ratio. Between 2–15 keV the power law ($\alpha \sim 0.9$) is dominant and the only clear feature is the iron line at $\sim$ 6.5 keV. The spectrum begins to fall off at $\sim$ 20 keV and reaches a minimum at $\sim$ 35 keV. The spectrum appears to stop falling exponentially at 35 keV, and to begin falling like the Crab spectrum (power law with $\alpha \sim 2$) beyond $\sim$ 35 keV. These features are very similar to the 1989 data, but the data statistics have been improved significantly.

We performed model fitting to the > 9 keV spectrum. The data below 9 keV are discarded to avoid the complexity of modeling the iron line. The 9-20 keV region can be described by a power law and the good statistics allow the index to be determined well. First, the FDCO model was applied to the averaged spectrum, but was unsuccessful due to prominent negative residuals centered at $\sim$30 keV ($\chi^2 = 9.99$, figure 5.2.1 bottom left). This is considered to be the cyclotron structure. The CYAB model for the fundamental cyclotron scattering explained the gradual decrease of the flux from 20 keV, and the resonance center converged to 36 keV. However, like in the case of 1989 data alone, it failed to explain the continuous falling off above 40 keV ($\chi^2 = 4.46$), which suggests either that the continuum spectrum itself decreases or that there is second harmonic absorption. Then the CYA2 model (fundamental + second harmonic cyclotron) was tried and gave an acceptable fit ($\chi^2 = 1.26$, figure 5.2.1 bottom right), which suggests the existence of the second harmonic absorption. However, we do not see clear evidence of the second harmonic in the raw spectrum. The depth of the second harmonic D_2 is obtained to be 1.7 times larger than that of the fundamental D_1. The elemental cross section of the fundamental is more than 10 times larger than that of the second harmonic (§2.6.2). However, the radiative transfer could make both features apparently comparable due to

angular dependences of the cross sections and two photon decay process. The resonance energy is $E_a = 33.2$ keV, as listed in table 5.2.1 together with the other parameters. These are consistent with the 1989 observations.

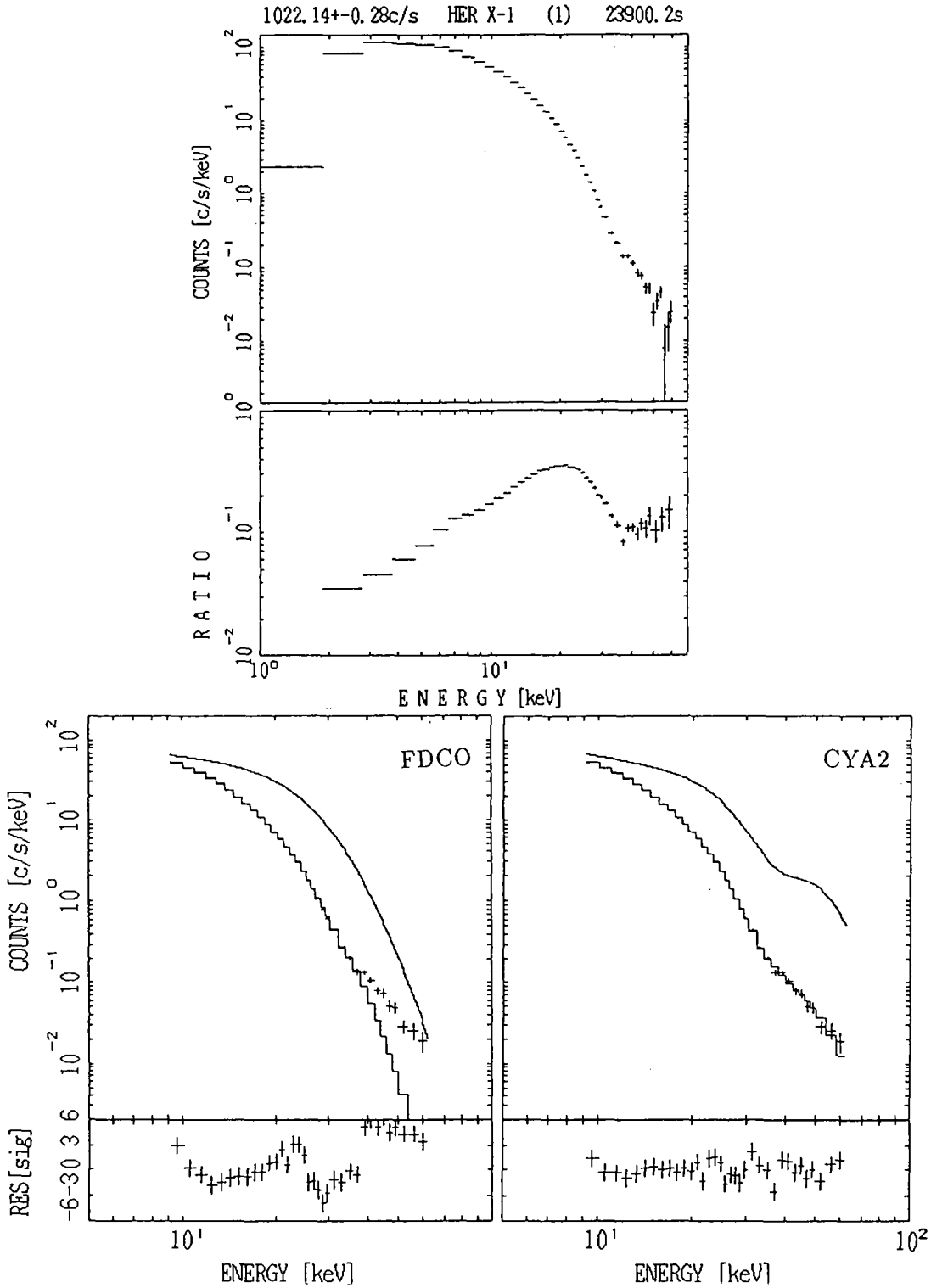

Figure 5.2.1: The observed spectra and FDCO and CYA2 fits of Her X-1 in 1989–1990.

Although we have thus confirmed that Her X-1 exhibit a cyclotron absorption at $\sim$ 34 keV, it is important to examine whether the emission-line model is consistent with the data or not. We have therefore fitted the spectrum with a FDCO continuum and a Gaussian emission line at $\sim$ 45 keV. Although the fit is acceptable as seen in table 5.2.1 (the latter half of the table), the implied exponential fall off is much more rapid than the thermal turn-over. Since we cannot attribute the continuum turn-over to the cyclotron effect in this case, we need to introduce two independent components: a steep falling-off continuum and a cyclotron emission line. Although both fittings are acceptable, the absorption model is physically more simple and natural than the emission model. We conclude that the emission-line interpretation is unlikely.

5.2.2 Phase-resolved spectra

Since the cyclotron structure varies with the pulse phase, we have performed pulse resolved analysis using all of the Her X-1 data. We divided the spectra into the 8 pulse phases in the 5 blocks of observations and summed up the spectra of the same phases as explained in §4.4.1. Figure 5.2.2 is the Crab ratio of the phase-resolved spectra. In all the phases, the spectra show a power law continuum in 2–15 keV. A hump around 6.4 keV is the iron line, which is more prominent in phase 4, 5, and 6, where the intensity is low. This indicates that the iron line intensity is less variable than the continuum. The 35 keV cyclotron feature is clearly observed in phase 1, 2, and 8, which correspond to the pulse peak. In other phases, the spectrum turns over at $\sim$20 keV and changes its slope at $\sim$ 30 keV in a similar way, but the 35 keV feature is less clear.

Next we fit the spectra with the CYA2 model. Figure 5.2.3 is the best-fit models, data and folded models, and the residuals from the best-fit models. The parameters are listed in table 5.2.1 together with those of the average spectrum. Here again all the fits explain the structure well and are acceptable except for phase 8. The resonance energy E_a changes between 29–36 keV with the pulse phases, but the D_1 and D_2 values are significantly larger than zero for all phases, and therefore the cyclotron structure is always significant. The E_a value is $\sim$ 35 keV in phases 1 and 8, which is consistent with the previous observation (Mihara *et al.* 1990), and E_a becomes a little smaller ($\sim$ 30 keV) in phases 3–7 (pulse bottom). The D_1 and D_2 are also large in phases 1, 2, and 8, and about a half those values in phases 3–7. There may be two states of the resonance, and the averaged spectrum is described by the mean parameters of the two states.

Table 5.2.1: The best-fit parameters of Her X-1 in 9–60 keV

No structure POWL×FDCO

	Fermi-Dirac Cut Off		Power law		
	Cut Off Energy	e-folding Energy	Norm.	photon index	χ^2_ν
	Ec	Ef	A	α	
	[keV]	[keV]	[ph/s/keV]		
ave.	20.8 ±—	5.5 ±—	73 ±—	0.33 ±—	9.99

1st + 2nd Absorption POWL×CYA2

	Cyclotron scattering				Power law		
Pulse	Resonance	Width	Depth1	Depth2	Norm.	photon index	χ^2_ν
Phase	Ea	W	D_1	D_2	A	α	
	[keV]	[keV]			[ph/s/keV]		
ave.	33.2 ±0.4	13.2 ±1.0	1.89 ±0.14	3.2 ±0.7	68.1 ±0.7	0.54 ±0.06	1.26
1	34.5 ±0.4	12.4 ±0.9	2.4 ±0.2	5.3 ±1.1	159.8 ±1.7	0.20 ±0.06	1.23
2	32.2 ±0.5	8.9 ±1.1	1.4 ±0.2	8.0 ±1.9	91.9 ±1.0	0.66 ±0.05	1.17
3	30.7 ±1.5	12.8 ±3.0	1.5 ±0.4	4.2 ±2.2	47.6 ±0.8	0.69 ±0.10	0.97
4	29.5 ±1.6	13.5 ±3.4	1.5 ±0.5	3.3 ±1.9	42.3 ±1.0	0.56 ±0.13	1.21
5	28.9 ±1.0	11.8 ±2.3	1.2 ±0.3	4.5 ±1.5	49.3 ±0.8	0.63 ±0.10	0.83
6	29.4 ±1.4	13.2 ±3.1	1.3 ±0.4	4.0 ±1.7	47.0 ±0.9	0.62 ±0.11	0.85
7	29.8 ±1.2	12.0 ±2.6	1.3 ±0.3	4.4 ±1.8	51.7 ±0.8	0.69 ±0.10	1.04
8	35.7 ±0.9	9.5 ±1.7	1.6 ±0.3	8.2 ±3.5	107.5 ±1.4	0.87 ±0.06	1.71

1st Emission POWL×FDCO + emission

Pulse	Gaussian Emission			Fermi-Dirac Cut Off		Power law		
Phase	E_a	σ	Flux	E_c	E_f	A	α	χ^2
	[keV]	[keV]	[ph/s]	[keV]	[keV]	[ph/s/keV]		
ave.	43.7 ± 4.2	13.1 ± 4.9	54 ± 19	24.3 ± 0.5	4.0 ± 0.3	66.6 ± 0.9	0.68 ± 0.08	1.18
1	45.8 ± 5.8	13.1	92 ± 16	24.4 ± 0.5	3.7 ± 0.2	155.1 ± 2.2	0.39 ± 0.07	2.03
2	31.9 ± 3.9	13.1	118 ± 27	25.1 ± 0.3	3.1 ± 0.2	89.2 ± 1.0	0.86 ± 0.06	0.75
3	36.1 ± 13.4	13.1	32 ± 20	22.5 ± 0.9	4.2 ± 0.6	46.8 ± 1.6	0.77 ± 0.13	1.00
4	32.4 ± 11.9	13.1	42 ± 27	21.6 ± 1.0	3.9 ± 0.7	40.9 ± 1.8	0.70 ± 0.17	1.14
5	26.1 ± 7.7	13.1	77 ± 47	21.9 ± 0.6	3.6 ± 0.5	46.8 ± 2.2	0.81 ± 0.14	0.72
6	27.3 ± 9.9	13.1	61 ± 48	21.8 ± 0.7	3.9 ± 0.7	45.1 ± 2.4	0.77 ± 0.16	0.75
7	28.8 ± 9.4	13.1	66 ± 44	22.6 ± 0.7	3.8 ± 0.6	49.9 ± 2.0	0.83 ± 0.14	0.96
8	36.0 ± 5.8	13.1	84 ± 25	27.5 ± 0.3	3.4 ± 0.3	105.7 ± 1.0	1.03 ± 0.05	0.86

The unit of the normalization of the power law A is [photons/s/keV] at 10 keV.
The gaussian σ in the phase resolved spectra in the FDCO + emission fit is fixed to 13.1 keV.
Both 1st+2nd absorption model and 1st emission model are acceptable. However, the exponential fall off in the emission model is much more rapid than the thermal turn-over. Since we cannot attribute the continuum turn-over to the cyclotron effect in this model, the overall interpretation is physically inconsistent. Therefore the emission-line interpretation is unlikely.

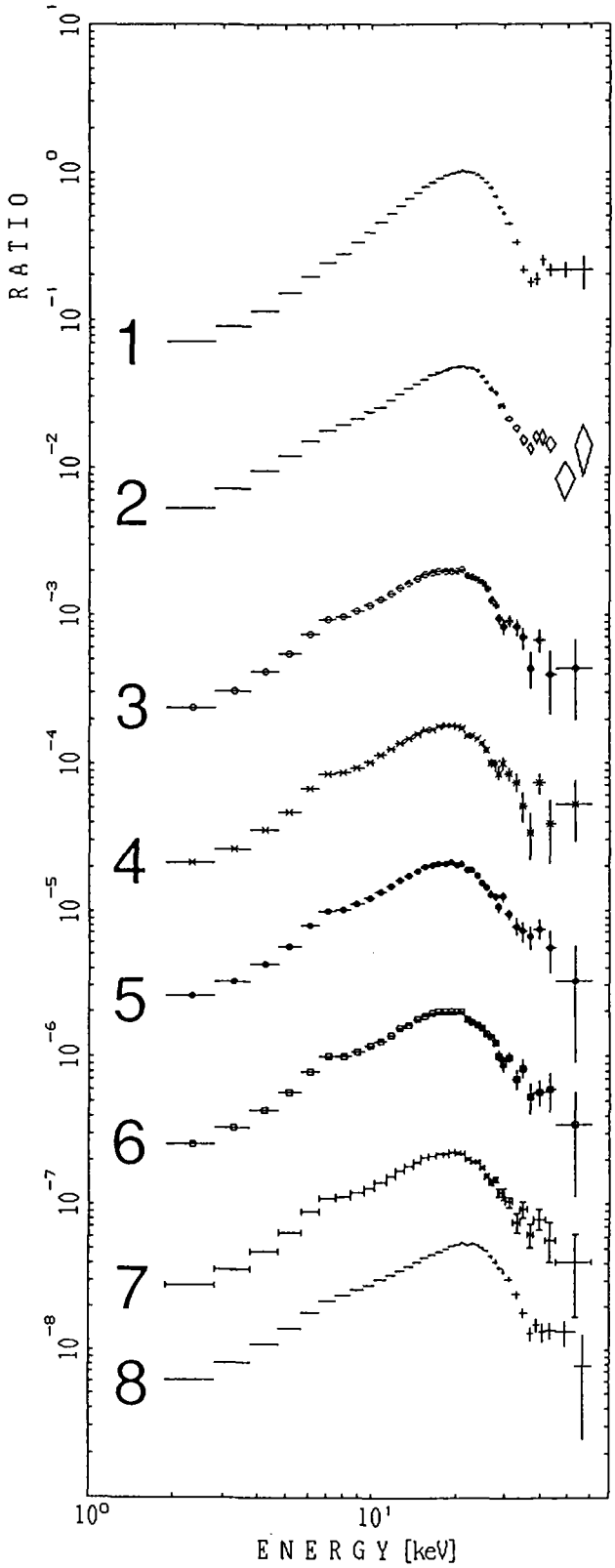

Figure 4.2.2: Crab ratios of the pulse phase resolved spectra of Her X-1 in 1989–1990. The spectrum are shifted downward successively by a factor ten.

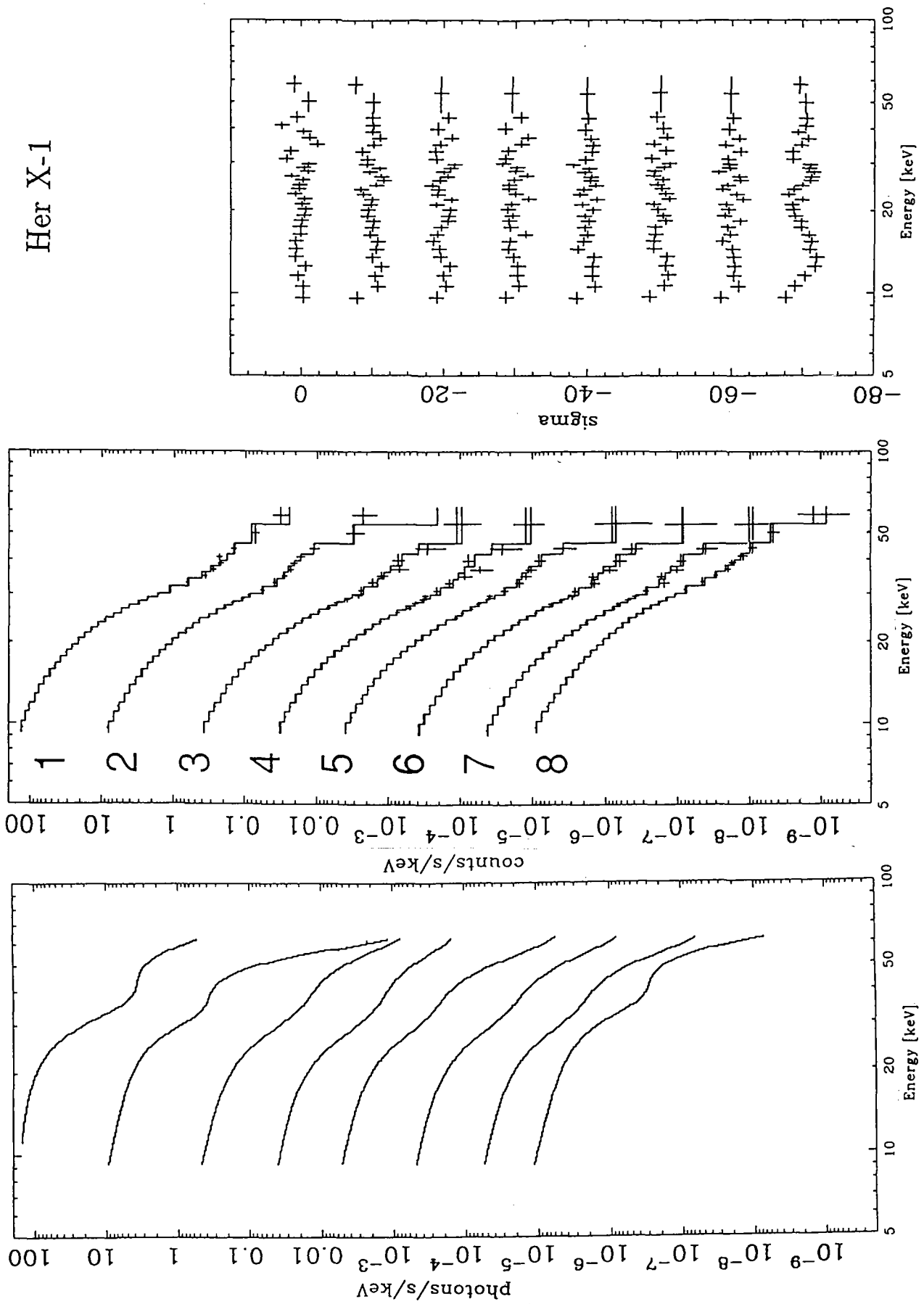

Figure 4.2.3: The CYA2 fits to the pulse phase resolved spectra of Her X-1 in 1989–1990.

5.2.3 Consistency with *HEAO-1* A4 results

The hard X-ray spectra of Her X-1 have been studied with many instruments since the discovery of the cyclotron line. The best quality data obtained so far in 20–100 keV is with the *HEAO-1* A4 instrument (Soong *et al.* 1990, §2.4.1). The pulse shape of Her X-1 was single peaked in the *HEAO-1* A4 energy band (12–180 keV), and the cyclotron structure was observed most clearly in the pulse peak, consistent with the *Ginga* results. We will compare our *Ginga* results with their phase-resolved spectra.

In the spectral fitting of the *HEAO-1* data, Soong *et al.* (1990) used a conventional model for the continuum as

$$F(E) = \begin{cases} I_0 E^{-\alpha} & (E < E_c) \\ I_1 E^{-1} \exp\left(-\frac{E-E_c}{E_f}\right) & (E > E_c) \end{cases} \tag{5.1}$$

together with the continuity condition $I_1 = {E_c}^{-\alpha+1} I_0$. It is similar to our ECUT model, but they fixed the index to -1 above $E = E_c$. They used a gaussian line $G(E)$ as the cyclotron absorption as

$$G(E) = \frac{0.9395}{FWHM} \exp\left\{-2.773\left(\frac{E - E_a}{FWHM}\right)^2\right\}. \tag{5.2}$$

The factor

$$(1 - E_w G(E)) \tag{5.3}$$

was then multiplied by the continuum model of eq. (5.1). E_w becomes an equivalent width since $\int G(E)dE$ is normalized to 1. In order to check the consistency between *HEAO-1* A4 and *Ginga* , we applied this model to the *Ginga* spectra above 9 keV. The fits are not acceptable with $\chi^2 = 3.5$ and 7.02 for the averaged and the pulse-peak spectra, respectively (table 5.2.2), mostly because of the large residual at the ECUT junction ($E = E_c$). The model with such an abrupt cutoff is no longer acceptable with our data. The acquired values, however, agree well with the results by Soong *et al.* (1990).

Next we use a power law × FDCO for the continuum to be free from the junction problem, while retaining the similarity with Soong *et al.* (1990)'s modeling. The gaussian absorption, eq. (5.3), was again used for the cyclotron structure. Although Soong *et al.* (1990) fixed the FWHM of the absorption to 11 keV, we left the FWHM free to vary because otherwise we cannot get an acceptable fit. So we make the FWHM a free parameter. This gives as good fits as the CYA2 model, showing a similar model shape and residuals as figure 5.2.3. However, the two smooth functions, FDCO and gaussian absorption, couple with each other and the errors of the parameters become large. Therefore we tentatively fixed E_c and E_f when estimating the errors of other parameters. The parameters thus obtained are shown in table 5.2.3. The line center is 36 keV at the peak and 31 keV in the interpulse. The α gets smaller (flatter) at the peak. These values and trends are consistent

with the *HEAO-1* results (figure 5.2.4). We therefore conclude that the *HEAO-1* data and the *Ginga* data give consistent results when analyzed in the same way, although the the two observations are separated in 12 years; this means the structure is very stable on this source.

Table 5.2.2: Parameters of the fittings with the Soong (1990) model.

Soong model (eq. 5.1) ×Gaussian absorption (eq. 5.3)

Pulse	Gaussian absorption			Exponential Cut Off		Power law		χ^2_ν
Phase	Equivalent	Center	FWHM	Cut Off	e-folding	Norm.	index	
	E_w[keV]	E_a[keV]	[keV]	E_c[keV]	E_f[keV]	[ph/s/keV]		
ave.	10.3	36.8	15.8	19.2	15.3	66	0.93	3.49
1	8.9	36.9	12.1	19.6	12.6	155	0.63	7.02

The unit of the normalization of the power law is [photons/s/keV] at 10 keV.
The errors are not available because of the large χ^2.
The fits of the phase averaged and the phase 1 spectra with Soong *et al.* (1990) model in 9–60 keV. The fit is not acceptable due to the ECUT junction at $E = E_c$.

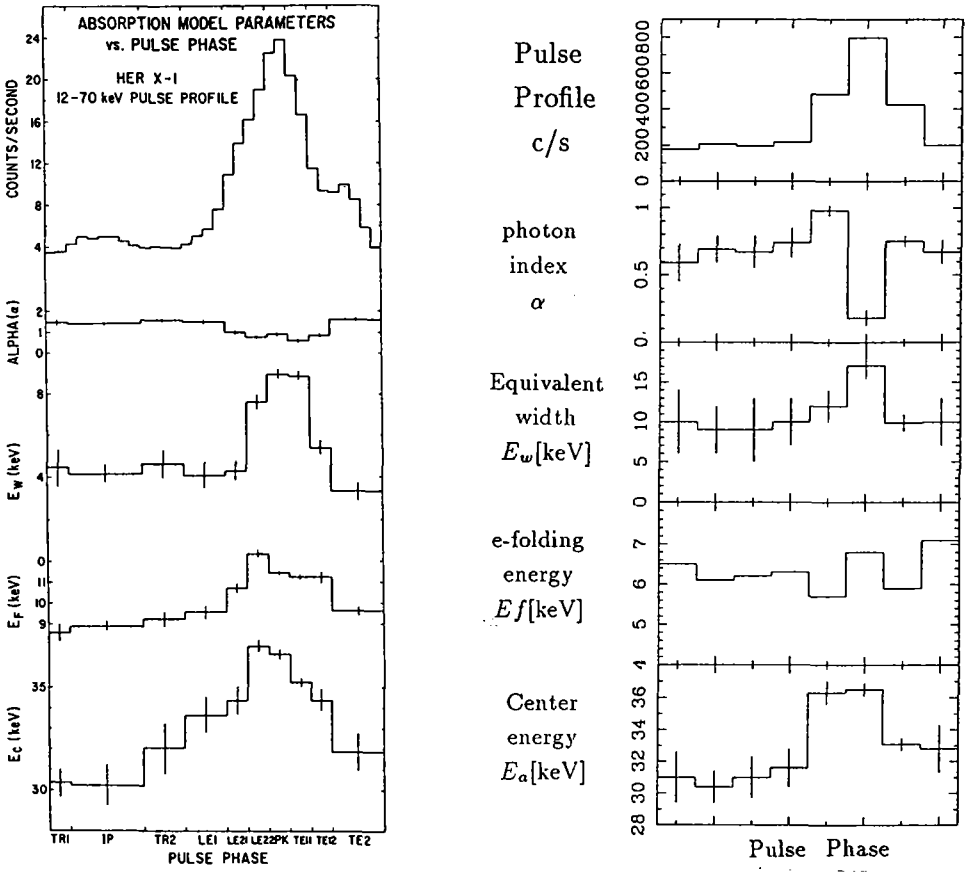

Figure 5.2.4: The pulse phase dependencies of the fitting parameters with *HEAO-1* (left, Soong 1990) and *Ginga* (right, this work). The values and trends are consistent.

Table 5.2.3: Parameters of Her X-1 in 9–60 keV FDCO × gaussian absorption model

Pulse	Gaussian absorption			Fermi-Dirac Cut Off		Power law		χ^2_ν
Phase	Equivalent	Center	FWHM	Cut Off	e-folding	Norm.	index	
	E_w[keV]	E_a[keV]	[keV]	E_c[keV]	E_f[keV]	[ph/s/keV]	α	
ave.	16 ±3	35.6 ±0.5	21 ±2	27.3	7.9	72.3 ±0.9	0.50 ±0.08	1.47
1	17.1 ±1.7	36.5 ±0.4	21 ±2	26.4	6.8	165.2 ±1.6	0.18 ±0.06	1.01
2	9.9 ±1.1	33.1 ±0.4	15 ±1	30.6	5.9	91.6 ±1.0	0.75 ±0.04	0.89
3	10 ±3	32.8 ±1.5	17 ±4	24.3	7.1	50.7 ±0.6	0.67 ±0.09	0.92
4	10 ±4	31.0 ±1.6	17 ±5	24.6	6.5	43.7 ±0.8	0.59 ±0.14	1.20
5	9 ±3	30.4 ±1.0	16 ±3	26.3	6.1	49.8 ±0.6	0.69 ±0.10	0.78
6	9 ±4	31.0 ±1.3	18 ±4	25.8	6.2	47.6 ±0.7	0.67 ±0.12	0.80
7	10 ±3	31.6 ±1.2	17 ±4	27.3	6.3	52.3 ±0.7	0.74 ±0.11	0.98
8	12 ±2	36.3 ±0.7	17 ±2	34.7	5.7	106.5 ±1.2	0.98 ±0.04	1.16

Errors were estimated with E_c and E_f fixed to the best-fit values, in order to avoid unstable coupling between the FDCO parameters and the Gaussian parameters. This model gives as good fits as the CYA2 model (table 5.2.1, figure 5.2.3), but the best-fit parameters are not unique because of coupling parameters. The unit of the normalization of the power law is [photons/s/keV] at 10 keV.

5.2.4 A new continuum model

The successful fittings in §5.2.1 and 5.2.2 with the CYA2 model assume the second harmonic absorption is at $\sim$ 70 keV. This is out of the *Ginga* energy range, but can be checked by the spectra taken with the *HEAO-1* A4. We drew the best-fit models determined with *Ginga* over the deconvolved spectra of *HEAO-1* in the pulse peak where the structure is the most prominent, and in the pulse bottom (figure 5.2.5). The intensities are adjusted arbitrarily to match the two spectra well. Since the deconvolution emphasizes features smaller than the energy resolution, we should compare global shapes. In the *Ginga* energy range upto 60 keV the two curves agree well. However, above that energy, especially >80 keV, *Ginga* model flux increases but the *HEAO-1* data are far below.

In §5.2.1 we had a similar problem when we fitted the Her X-1 spectrum with CYAB model. We introduced the second harmonic to suppress the model recovery above the fundamental harmonic. The same thing happens here. There are two ways that we can choose; putting 3rd and 4th harmonic to reduce the model flux, or assuming that the continuum itself decreases. If we take 3rd and 4th harmonic, their cross sections need to be larger than the 1st or the 2nd ones in order to explain the spectrum. Although the elementary cross section of the fundamental structure is much larger than that of the 2nd harmonic, it can be observed to be smaller than the 2nd one, because the two photons decaying from the second excitation state can almost fill up the fundamental structure. However, the higher harmonics are all absorption and their cross sections become smaller and smaller with the harmonic numbers by orders of magnitude (§2.6). It is not allowed physically that the absorption by the 3rd is larger than that by the 2nd and that the 4th one is larger than the 3rd one. Another unfavorable point is that if the power law with $\alpha \sim 0.7$ extends towards high energies, the total energy implied is infinite. It is physically natural to assume that the spectrum falls off thermally as $\exp(-E/kT)$, where T is the highest temperature of the X-ray emitting plasma.

So let us assume that the continuum falls off exponentially, so that the second harmonic is not always necessary. We search for an improved continuum model which can fit the observed spectra only with the fundamental resonance; that is, we try to express the model photon spectrum as $f(E)\times$CYAB, where $f(E)$ is the new continuum model to be discovered.

First, we tried the simplest formula $f(E) = \exp(-E/kT)$ with CYAB, to fit the phase averaged spectrum in 12–60 keV. This model failed with a large χ^2 of 2.78 (figure 5.2.6a). Next, Boltzmann model; $f(E) = E^{\alpha}\exp(-E/kT)$, was tried. Note that the index of the power low can be either positive or negative. If $\alpha = 2$, this model is identified to be the Wien spectrum which closely resembles the black body spectrum. If $\alpha \sim -1.4$, it represents the thermal bremsstrahlung spectrum. The Boltzmann fit is fairly successful with $\chi^2 = 1.36$ (figure 5.2.6b). The obtained index $\alpha = 0.74 \pm 0.24$ happened to be close to

1 as it was fixed to the Soong model eq.(5.1). However this model is not fully acceptable, because the obtained $\alpha = 0.74$ is definitely different from the index in the low energy part (~ -0.7 for Her X-1). This effect appears below 12 keV in the case of Her X-1. If the energy range is expanded to 9–60 keV, the Boltzmann model is no longer acceptable ($\chi^2 = 2.23$) due to the excess flux of the data in 9–12 keV.

Then we introduce a new continuum model, NPEX model (Negative and Positive power law EXponential model), defined as

$$F(E) = (A_1 E^{-\alpha_1} + A_2 E^{+\alpha_2}) \ \exp(-\frac{E}{kT}). \tag{5.4}$$

This model will be found later in this thesis to be able to express the overall pulsar spectra very well. The first term represents the usual negative-index power law portion which is dominant below $\sim$ 10 keV, while the second term reflects the success achieved with the Boltzmann continuum above 12 keV. A merit of this model is that it can express a slightly concave continuum that is often seen in the pulsar spectra in 2–10 keV range.

We have discovered that the NPEX $\times$ CYAB model can fit the phase-averaged spectrum of Her X-1 very well, not only in the limited 9–60 keV band ($\chi^2 = 1.21$, figure 5.2.6c), but to our surprise, also in the entire 2–60 energy band when a Gaussian iron line is included ($\chi^2 = 1.17$, figure 5.2.6d). The power law $\times$ CYA2 model failed in this energy band ($\chi^2 = 3.37$). Furthermore for the averaged spectrum, the positive index converged to $\alpha_2 = 1.97 \pm 0.26$, which strongly suggests a blackbody. Therefore hereafter in this thesis, we employ $f(E)$ = NPEX $\times$ CYAB as a new model which is improved over the previous power law $\times$ CYA2 model. For simplicity we fix the positive index $\alpha_2 = 2.0$ unless otherwise stated. One possible explanation for the negative power low will be unsaturated comptonization. The physical meaning of NPEX model will be discussed in Chap. 6 in detail.

The NPEX $\times$ CYAB model is also successful in fitting the phase resolved spectra. It can give as good fits as power law $\times$ CYA2 model (figure 5.2.3) in 9–60 keV, and moreover it fits the spectra in 2–60 keV fairly well (figure 5.2.7 and table 5.2.4). The obtained 'temperature' is very constant at 6–9 keV across the pulse phase, suggesting that it has a physical meaning. The normalization of the positive power law, A_2, reflects the pulse light curve very well, which indicates the pulsing component is shaped like a blackbody. It is also supported by Takahama (1992), in which the spectral changes according to the 35d cycle of Her X-1 were reported. They picked out the 'pulsing hard component' from the phase resolved spectral analysis and suggested that it could be fit with a blackbody of $kT = 4.5$ keV with $\log_{10} N_H$ =23.7 in 8–30 keV. The positive power law component in our NPEX model may represent this 'pulsing hard component'.

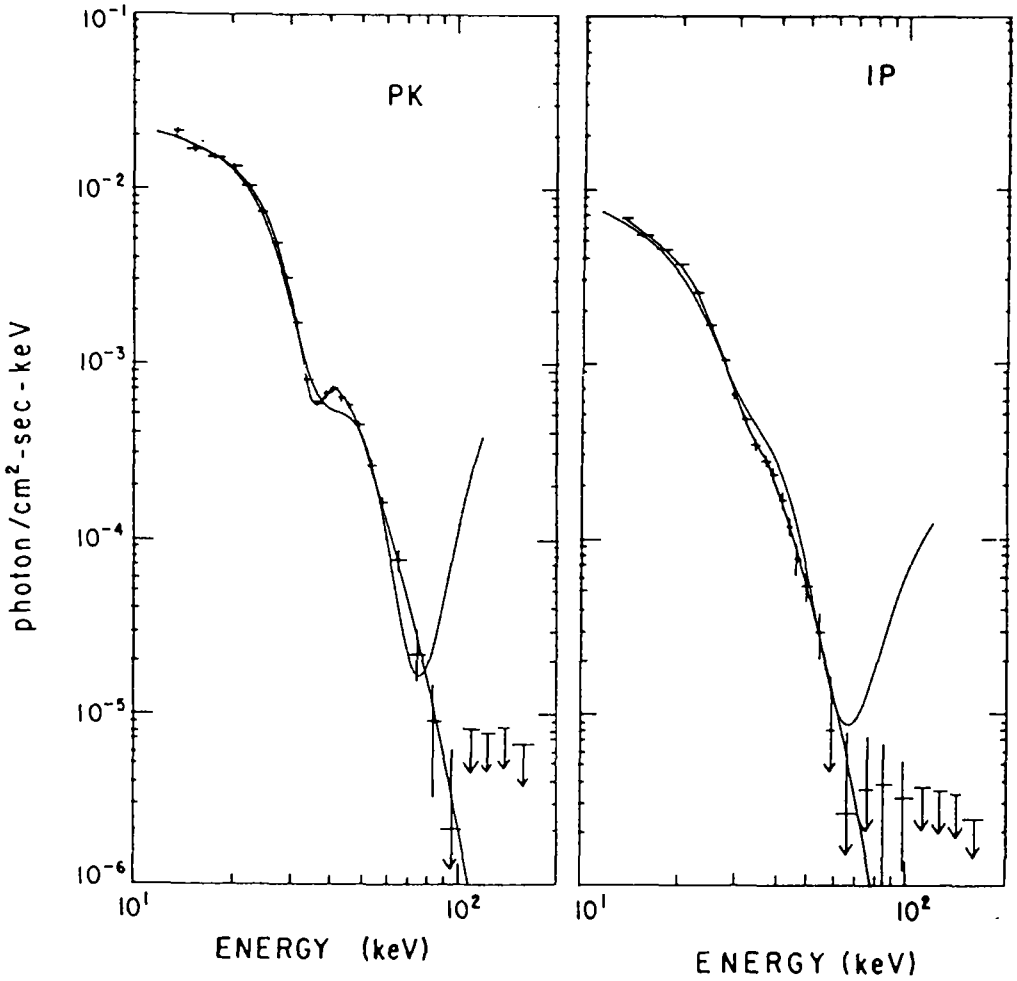

Figure 5.2.5: The incident spectrum with *HEAO-1* A4 (Soong *et al.* 1990) for the pulse peak and bottom overwritten by the best-fit model of *Ginga* for the same pulse phases.

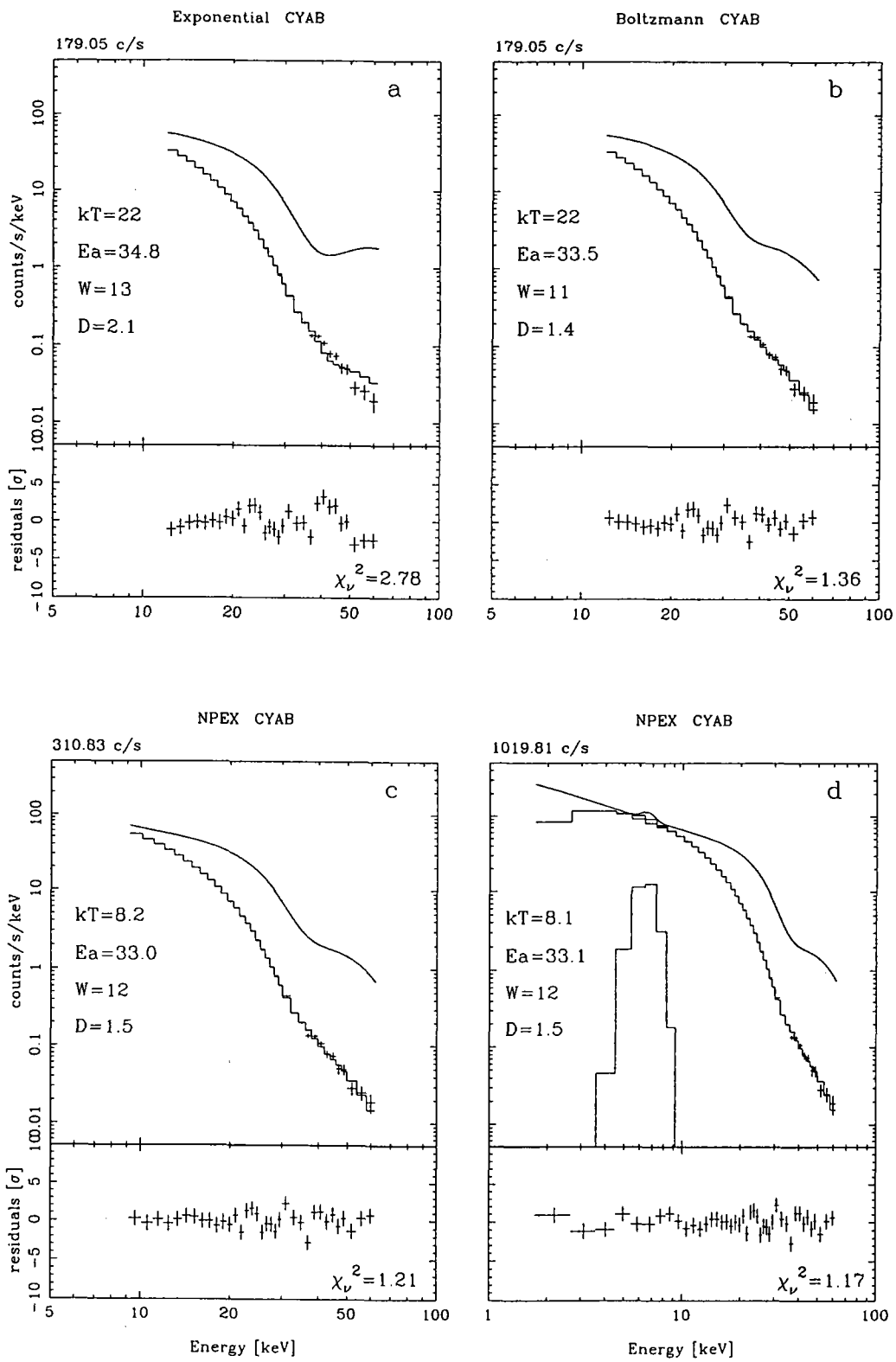

Figure 4.2.6: The fittings to the averaged spectrum with an exponentially-falling continuum, *a*: exponential, *b*: Boltzmann in 12–60 keV, *c*: NPEX in 9–60 keV and *d*: 2–60 keV. Only the fundamental cyclotron scattering is included from the CYAB formula.

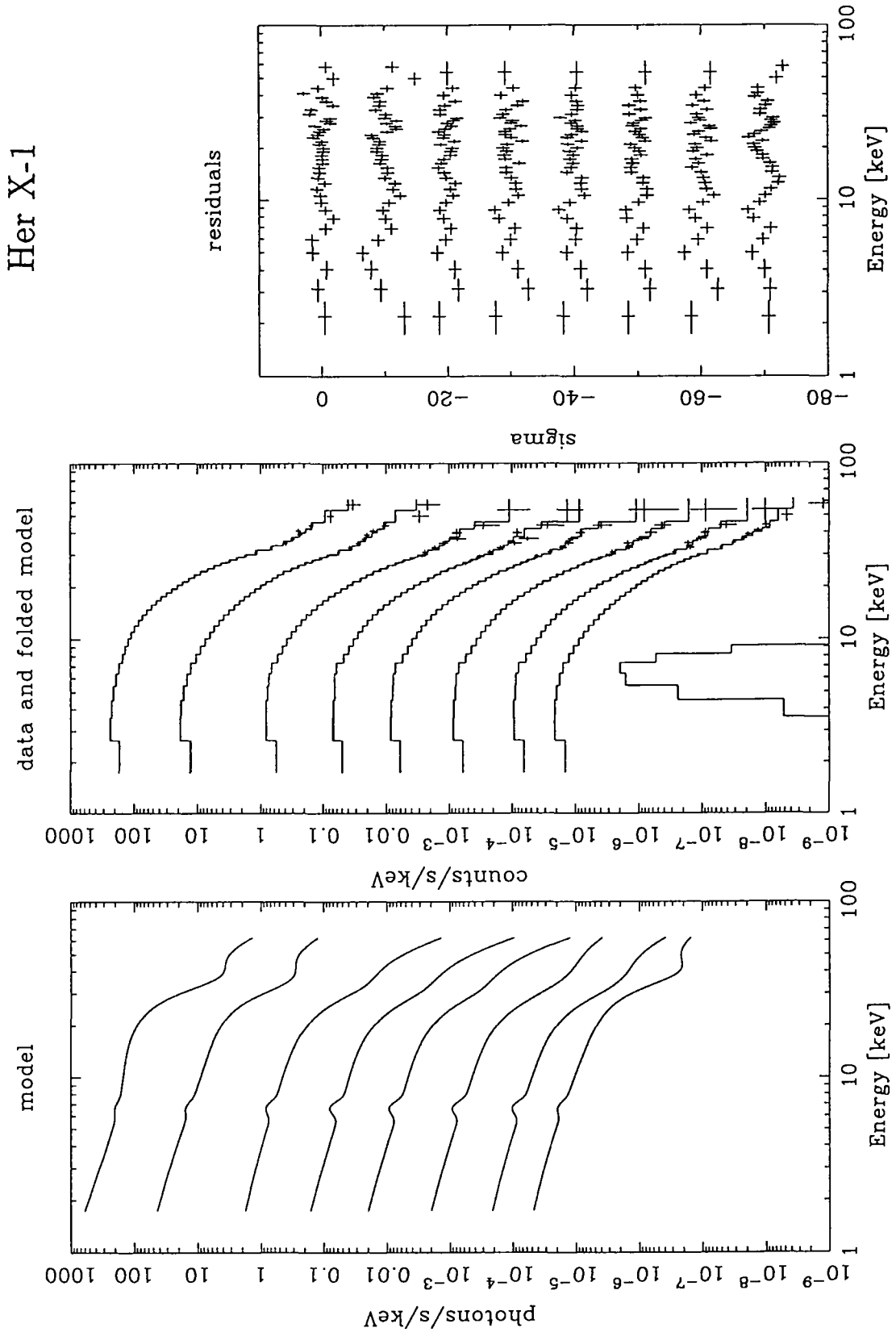

Figure 4.2.7: The NPEX × CYAB fits to the pulse phase resolved spectra of Her X-1 in the entire energy band (2–60 keV).

Table 5.2.4: The model parameters of the fits for the pulse-phase resolved spectra using NPEX continuum and a CYAB factor with an iron line. The absorption by a column density is not included. The corresponding fits are shown in figures 5.2.6d and 5.2.7.

pulse phase	Negative power law Norm. A_1	index α_1	Positive power law Norm. A_2	index α_2	Exponential Folding E. kT [keV]
ave.	133 ±21	0.52 ±0.09	99 ±24	1.97 ±0.26	8.1 ±1.1
ave.	135 ±8	0.51 ±0.03	100 ±23	2.00 fixed	8.0 ±0.8
1	206 ± 9	0.74 ± 0.04	414 ± 49	2.00 fixed	7.2 ± 0.4
2	198 ± 23	0.57 ± 0.05	117 ± 54	2.00 fixed	8.2 ± 1.7
3	117 ± 9	0.39 ± 0.04	113 ± 45	2.00 fixed	6.2 ± 0.9
4	92 ± 8	0.48 ± 0.06	128 ± 56	2.00 fixed	5.9 ± 1.0
5	113 ± 8	0.48 ± 0.04	141 ± 50	2.00 fixed	5.9 ± 0.8
6	95 ± 41	0.53 ± 0.17	61 ± 78	2.00 fixed	8.4 ± 6.1
7	118 ± 32	0.45 ± 0.11	71 ± 68	2.00 fixed	7.7 ± 3.4
8	244 ± 41	0.48 ± 0.07	81 ± 56	2.00 fixed	9.1 ± 2.5

pulse phase	Cyclotron scattering Resonance Ea [keV]	Width W [keV]	Depth D	Iron line Flux I_{Fe} [ph/s]	χ^2_ν (d.o.f.)
ave.	33.1 ±0.5	12.1 ±1.7	1.53 ±0.26	30 ±4	1.17 (34)
ave.	33.1 ±0.3	12.1 ±1.7	1.53 ±0.25	30 ±4	1.14 (35)
1	34.8 ± 0.3	10.0 ± 1.2	1.8 ± 0.2	28 ± 9	1.37
2	33.6 ± 0.8	10.2 ± 2.9	1.6 ± 0.5	30 ± 9	3.08
3	31.0 ± 1.1	9.3 ± 4.5	0.9 ± 0.4	25 ± 3	1.15
4	29.2 ± 1.4	9.5 ± 6.5	0.8 ± 0.5	33 ± 4	1.93
5	29.3 ± 1.0	9.3 ± 4.9	0.7 ± 0.4	35 ± 3	1.32
6	30.3 ± 1.2	16.1 ± 10.3	1.5 ± 1.5	35 ± 4	1.34
7	30.9 ± 1.2	12.9 ± 7.3	1.3 ± 1.0	39 ± 4	1.82
8	36.8 ± 0.9	10.8 ± 3.0	1.9 ± 0.6	46 ± 9	2.31

The unit of the normalizations A is [photons/s/keV] at 10 keV.
The energy and the width (σ) of the iron line are fixed to 6.65 keV and 0.5 keV, respectively.

5.3 4U 0115+63 in 1990 February

4U 0115+63 is the only pulsar from which two cyclotron resonances (presumably fundamental and 2nd harmonics) have been clearly observed with *Ginga* and previous missions. In this section we report the observation on 1990 February 11 when the two features were observed. Figure 5.3.1 is the averaged spectrum of 4U0115+53 on this occasion and its Crab ratio. The Crab ratio obtained on 1990 February 9 is also overlaid in the figure (crosses). The intensity and the spectrum agree well between the two days and the cyclotron dips at ~12 keV and ~23 keV reported by Nagase *et al.* (1991) have also been confirmed by these reduced-HV observations. Figure 5.3.1.right is the PHA ratios of the spectra divided into 8 pulse phases to the FDCO model fitted to the phase-averaged spectrum (figure 5.3.2b). The depths of the harmonics are changing phase by phase. Since there is no structure seen at ~ 6 keV in any phase, 12 keV is considered to be the fundamental resonance. The third harmonic is not observed at any phase.

Figure 5.3.2a is the FDCO fit to the average spectrum in 5–46 keV. The residual plot shows the fundamental and the second dips clearly, but neither the 3rd nor 4th harmonics are seen. If we limit the energy range to 3–20 keV, we can fit the spectrum with a power law × CYA2 model, but this model no longer fits the data in 3–60 keV. The 3rd and 4th harmonics or a falling continuum is necessary as was the case of Her X-1, but the former is not justified here, since there is no sign of the 3rd or 4th harmonics. Thus we employ the exponentially falling continuum.

In order to better define the underlying continuum, we have next limited the energy range so as not to be affected by the cyclotron scattering. Figure 5.3.2b is the best-fit FDCO model thus obtained over the 3–46 keV range, but excluding 7.6-29 keV. The spectral modification from the smooth FDCO curve is shown well in the residuals. The power law index became smaller, $\alpha = -0.13$, which means a positive power law. This particular set of parameters of the FDCO model was used as the denominator of the PHA ratio in figure 5.3.1.

Figure 5.3.2b indicates that we may be able to fit the spectrum in terms of a moderately falling continuum, multiplied by two CYAB functions. For example, Nagase *et al.* (1990) employed a power law × ECUT continuum. To avoid the junction problem, however, we prefer using the power law × FDCO continuum, and fit the data with

"Power law × FDCO × CYAB($E_a \sim 12$ keV) × CYAB($E_a \sim 22$ keV) + Iron Line",

As shown in figure 5.3.2c, this fit is acceptable in the 4–46 keV range. The reason why we used two CYAB factors instead of a CYA2 factor is that the data require the two sets (1st and 2nd) of resonance parameters to be adjusted independently. After our experience with Her X-1 (§5.2.5), we may alternatively use the NPEX continuum. Indeed, the model

"NPEX($\alpha_2 = 2.0$ fixed) × CYAB($E_a \sim 12$keV) × CYAB($E_a \sim 22$keV) + Iron Line",

gives an acceptable fit (figure 5.3.2d) over the widest energy range of 3–46 keV. The best-

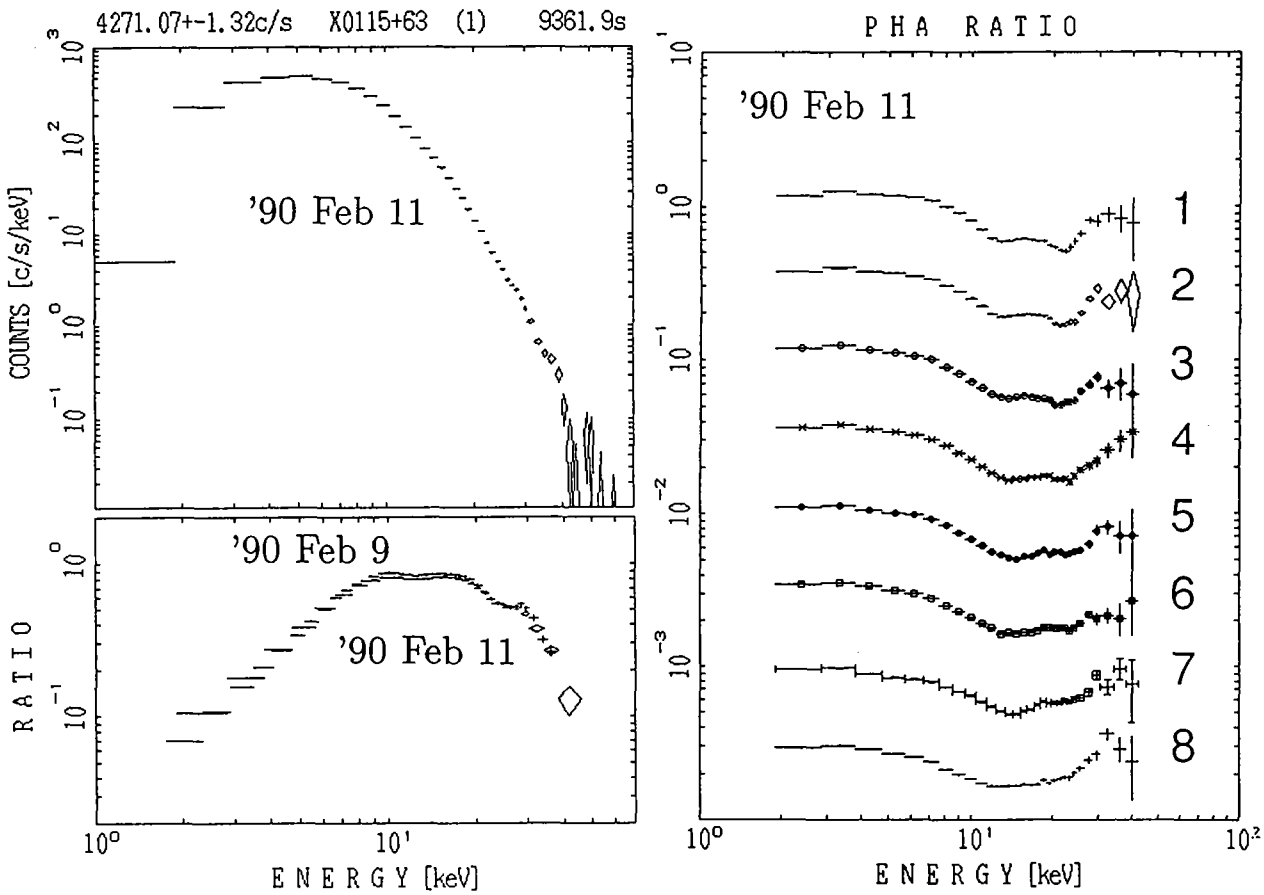

Figure 5.3.1: The averaged spectrum and its Crab ratio of 4U 0115+63 on 1990 Feb. 11 and the PHA ratios of the phase resolved spectra to the FDCO model in figure 5.3.2b. In the Crab ratio, observation on 1990 Feb. 9 with normal HV is overplotted.

fit parameters are given in table 5.3.1. We have thus confirmed again the new continuum model, NPEX, gives an excellent fit to the observed spectra when properly combined with the CYAB factors. The obtained resonance energies are 11.3 ± 0.6 keV and 22.1 ± 0.4 keV, whose ratio 1.96 ± 0.11 is consistent with that of the second and the fundamental harmonics, 1.98, from the relativistic consideration (§2.6.1). The obtained width and the depth of the two absorptions are nearly equal, similar to those observed from γ-ray bursts with *Ginga* (Murakami *et al.* 1988) and can be qualitatively interpreted under some geometrical conditions (§2.4.3).

Here we multiply the two CYAB factors by the continuum, assuming that the emission region is single and two CYAB work on the same continuum. There might be another configuration with two separate emission regions, such as the 'north' and 'south' poles or

multipoles like the sun spots, which are affected by CYAB factors with different resonances for each. Such fit is statistically successful but physically unlikely, since the obtained depth is $D_1 > 5.0$, which is 10 times larger than D_2, and such a large depth has never been observed from any other pulsars.

We have further conducted fitting of the pulse-phase resolved spectra with the above model in terms of the NPEX continuum. As shown in figure 5.3.3 and table 5.3.1, the fits have mostly been successful and there is no significant indication of the $\sim$ 6 keV or 30 keV resonances. The obtained $kT \sim 4.9$ keV is almost constant throughout the pulse phase. It is also stable in Her X-1 but at $\sim$ 7 keV. Thus kT possibly indicates a physical value particular to the system.

The two absorptions are significantly detected in all the phases, since the three parameters Ea, W, and D are well determined. The X-ray intensity with *Ginga* was as strong as that with *HEAO-1* A2 (White *et al.* 1983, §2.4.2) and the two absorptions were detected at the consistent energies. However, it is inconsistent that the structure appeared as absorptions throughout the pulse phase, while White *et al.* (1983) reported that the feature was an absorption at the pulse peak and an emission at the inter-pulse. Thus the spectral feature of 4U0115+63 would be very variable. In fact, it was more variable between the two observations with *Ginga* , and these results will be presented in the next section.

The center energies range from 10–12 keV and 17–23 keV, varying as much as $\pm \sim 10$ %. The ratios of the two center energies change as 1.6 - 2.2, but the error bars enable us to consider it constant $\sim$ 1.9. When we fit the spectra with the fixed energy ratio of 2.0, the χ^2 increases less than about 20 % in most of the phases except for 40% in the phase 6 and 70% in phase 7. The F-test shows that 20% increase in one parameter omission occurs with a probability of a few %. Since the two apparent absorption dips are consistent with the harmonics relation in most of the phases, they can be interpreted as the fundamental and the second harmonics. The relation also confirms that the structures are due to the cyclotron scattering resonances and not by the other mechanisms.

We must be careful since the NPEX $\times$ CYAB model needs low energy part to determine the negative power law, and higher part above the cyclotron resonance to determine kT and the resonance parameters. If the energy band was limited to above the E_c, 10–46 keV, the slope of the power law converged to a very steep value, $\sim$3. It is, however, definitely wrong, because Crab ratio (figure 5.3.1) shows that the true power law appears at 4–10 keV. As will be shown in §5.10.4, 1E 2259+586 shows a steep (index = 4.0) power law in the *Ginga* band (2–15 keV). The same thing might have been happened with 1E 2259+586; the true power law region may be at lower energy than *Ginga* is sensitive to and failed to be observed, and only the exponentially falling part with a cyclotron structure is observed.

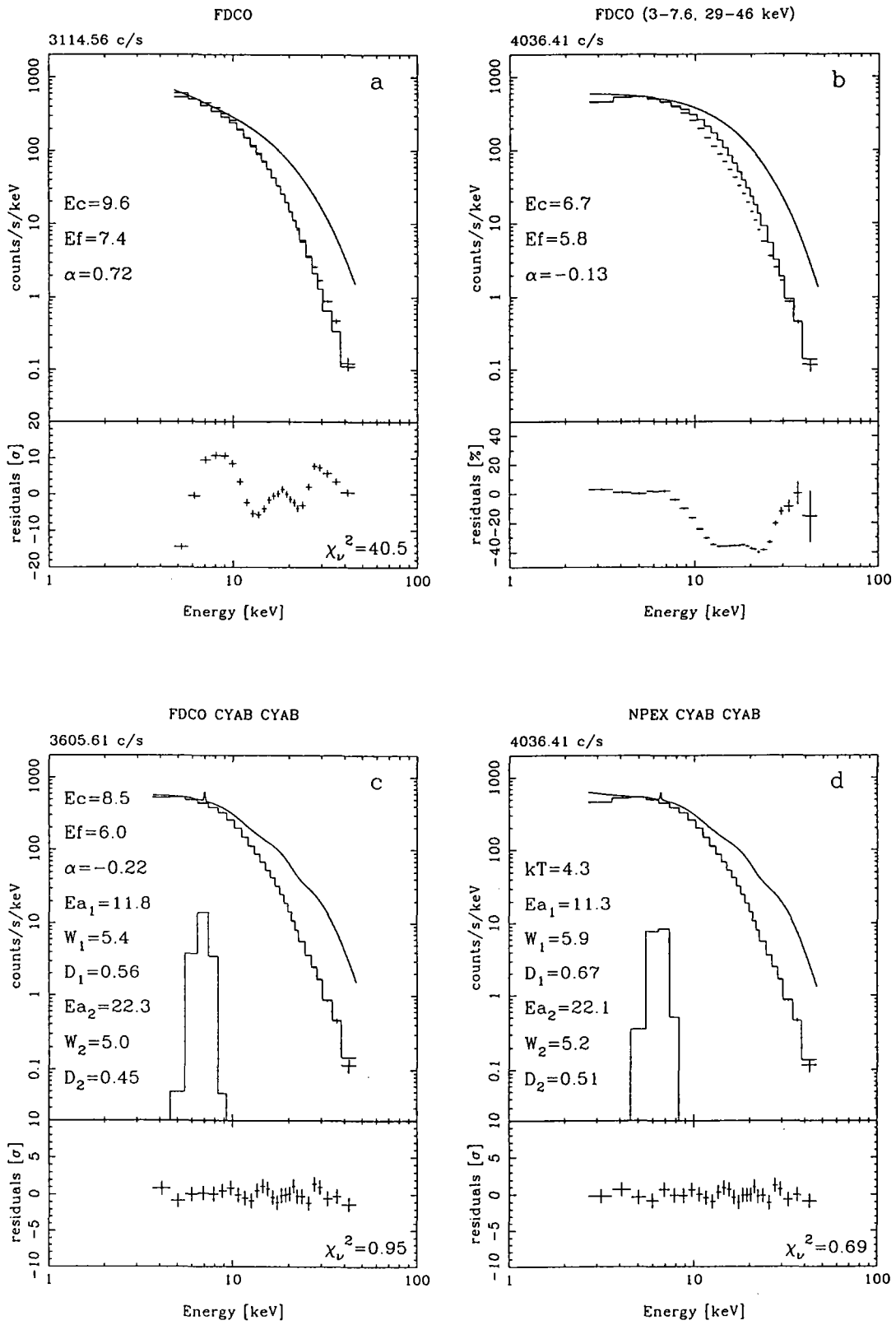

Figure 5.3.2: Fits to the averaged spectrum of 4U 0115+63 on 1990 Feb. 11. *a*: 5–46 keV with FDCO. *b*: 3–7.6, 29–46 keV with FDCO. *c*: 4–46 keV with FDCO × CYAB × CYAB + Iron line. *d*: 3–46 keV with NPEX × CYAB × CYAB + Iron line. The unit of the residuals in the figure *b* is % of the model.

Table 5.3.1: Parameters for the spectra of 4U 0115+63 on 1990 Feb. 11 in 3–50 keV

Pulse Phase	The fundamental Resonance1 Ea_1 [keV]	Width1 W_1 [keV]	Depth1 D_1	The second Resonance2 Ea_2 [keV]	Width2 W_2 [keV]	Depth2 D_2	2nd/1st ratio Ea_2/Ea_1
ave.	11.25 ± 0.62	5.9 ± 0.8	0.67 ± 0.08	22.10 ± 0.40	5.2 ± 1.0	0.51 ± 0.07	1.96 ± 0.11
1	10.78 ± 0.91	6.1 ± 1.3	0.80 ± 0.17	22.75 ± 1.71	9.3 ± 3.9	0.69 ± 0.27	2.11 ± 0.24
2	9.55 ± 2.31	7.0 ± 2.4	0.66 ± 0.26	21.38 ± 2.84	9.2 ± 4.5	0.53 ± 0.27	2.24 ± 0.62
3	10.96 ± 0.89	3.2 ± 2.1	0.23 ± 0.17	17.43 ± 1.59	9.4 ± 2.0	0.73 ± 0.24	1.59 ± 0.19
4	12.41 ± 0.57	4.8 ± 1.5	0.61 ± 0.17	21.34 ± 1.20	8.1 ± 1.8	1.03 ± 0.16	1.72 ± 0.12
5	12.47 ± 0.41	4.7 ± 0.9	0.72 ± 0.10	22.99 ± 0.69	7.4 ± 1.7	1.03 ± 0.16	1.84 ± 0.08
6	11.44 ± 0.31	4.4 ± 0.6	0.79 ± 0.10	20.65 ± 0.79	8.9 ± 1.3	1.15 ± 0.12	1.81 ± 0.08
7	11.41 ± 0.32	3.3 ± 0.8	0.64 ± 0.14	19.31 ± 0.91	8.4 ± 1.6	1.06 ± 0.15	1.69 ± 0.09
8	11.24 ± 0.37	4.6 ± 0.7	0.72 ± 0.12	20.63 ± 0.78	8.1 ± 1.4	0.87 ± 0.12	1.84 ± 0.09

pulse phase	Negative power law Norm. A_1	index α_1	Positive Norm. A_2	Exponential Folding E. kT [keV]	Iron line Flux I_{Fe} [ph/s]	χ^2_ν
ave.	491 ± 326	0.41 ± 0.48	4960 ± 1220	4.25 ± 0.10	17 ± 18	0.69
1	600 ± 420	0.31 ± 0.49	3070 ± 1780	4.87 ± 0.50	34 ± 18	0.86
2	520 ± 610	0.32 ± 0.80	2770 ± 2790	5.05 ± 0.45	30 ± 18	0.91
3	1240 ± 590	-0.26 ± 0.33	1350 ± 1700	5.47 ± 0.68	34 ± 22	1.04
4	1100 ± 770	-0.18 ± 0.49	3520 ± 1970	5.10 ± 0.42	27 ± 34	1.90
5	640 ± 350	0.20 ± 0.41	3540 ± 1100	4.96 ± 0.33	13 ± 26	1.66
6	450 ± 230	0.44 ± 0.38	3630 ± 930	5.04 ± 0.29	20 ± 19	0.75
7	970 ± 550	-0.02 ± 0.41	3030 ± 1570	4.86 ± 0.41	31 ± 28	1.54
8	750 ± 350	0.20 ± 0.33	3520 ± 1250	4.66 ± 0.26	27 ± 17	0.57

The index of the positive power law is fixed to $\alpha_2 = 2.0$.
The unit of the normalization of the power law is [photons/s/keV] at 10 keV.
The width of the iron line is fixed to narrow, $\sigma = 0.05$ keV.
The energy of the iron line are fixed to 6.6 keV.

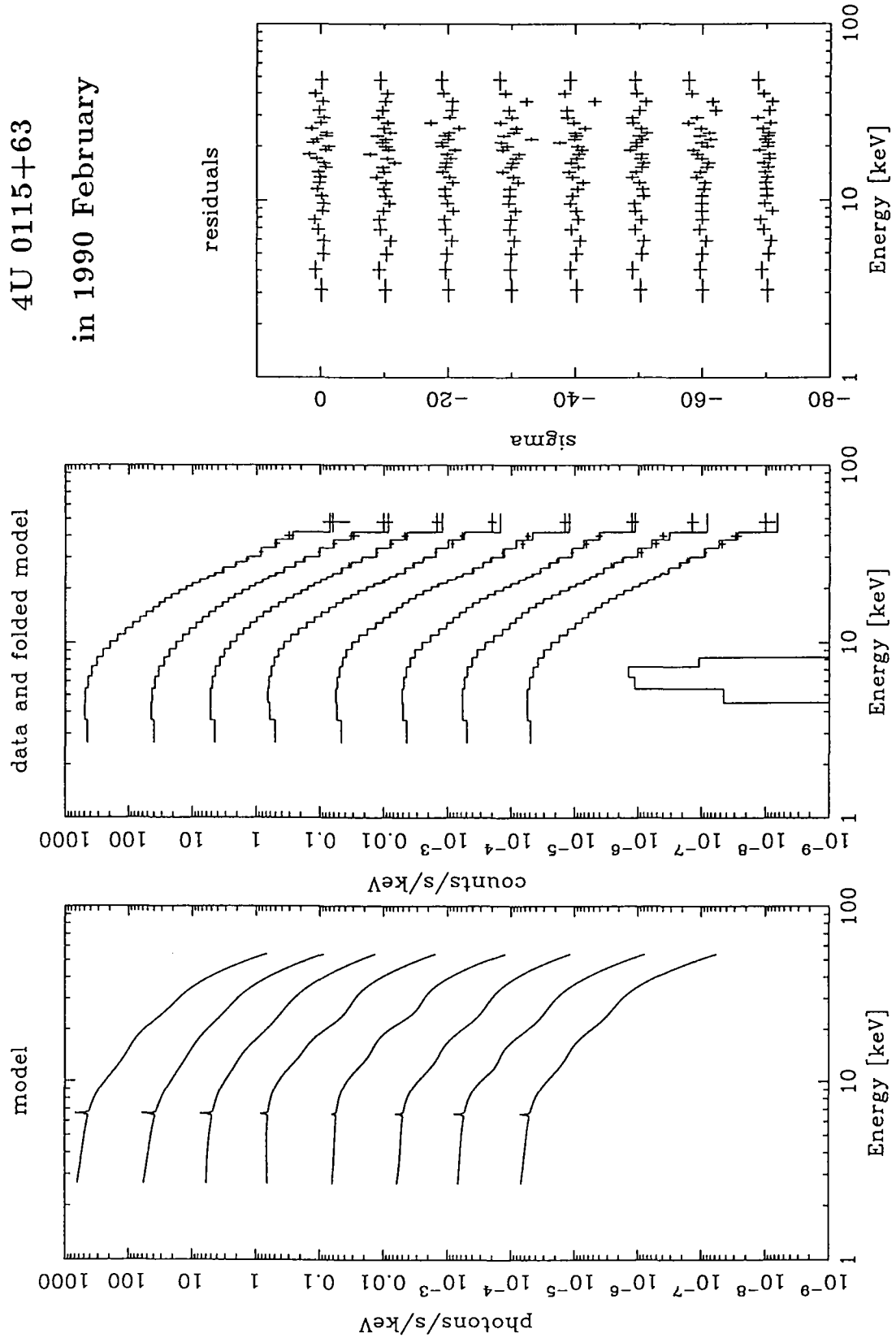

Figure 5.3.3: The NPEX × CYAB × CYAB fitting in 3–50 keV to the phase resolved spectra of 4U 0115+63 in 1990.

5.4 4U 0115+63 in 1991 April

The observation of 4U 0115+63 in 1991 April was a very surprise. As shown in figure 5.4.1 left, the absorption feature appears to be single, while it was double in the previous year (§5.3). Figure 5.4.1 right are the PHA ratios of the 8 phase resolved spectra to the FDCO model in figure 5.4.2b. The cyclotron structures are detected deeply at ~17 keV throughout the pulse phase, although the shape and depth are changing with the pulse phase. The energy is just between the 1st and the 2nd harmonics observed in 1990, and therefore it is not clear whether it is the 1st or the 2nd harmonic. There might be a shallow hollow seen at $\sim$ 8 keV in phases 6 and 7 but it is not clear in other phases. No feature is apparent at $\sim$ 34 keV.

We tried the FDCO model in 5–55 keV to the averaged spectrum (figure 5.4.2) as was performed in §5.3. We can see a single huge dip at $\sim$ 17 keV in the residual plot but no second one at $\sim$ 34 keV. Next in order to look for the underlying continuum, the energy range is limited so as not to be affected by the cyclotron scattering. Figure 5.4.2b is the best-fit FDCO model in 3–55 keV, but 10–32 keV is excluded from the fitting. The absorption-like structure from the smooth FDCO curve is well seen in the residuals. This set of the parameters of the FDCO model was used as the denominator of the PHA ratio in figure 5.4.1.

We try fittings with models including cyclotron resonance. Neither the model "Power law × CYAB" nor "Power law × CYA2" can fit the spectrum in 5–55 keV, suggesting an additional 'exponentially falling factor' may be necessary. Therefore we employ the FDCO model as an exponential continuum as

$$\text{“Power law} \times \text{FDCO} \times \text{CYAB}(E_a \sim 16\text{keV})\text{”}.$$

The iron line is not included, because of its absence in the residuals. Figure 5.4.2c is the best-fit in 5–55 keV. This model has given a good fit, but we further use the NPEX model to expand the energy range to 3–55 keV as

$$\text{“NPEX}(\alpha_2 = 2.0 \text{ fixed}) \times \text{CYAB}(E_a \sim 16\text{keV})\text{”}$$

which is also successful (figure 5.4.2d). The obtained kT of 4.34 ± 0.14 keV agrees very well with the 1990 data, (4.25 ± 0.10 keV), which suggests that kT could be intrinsic to the pulsar and NPEX model is excellent to represent the pulsar spectrum.

The NPEX model is also applied to the pulse phase resolved spectra. The fits are good but are not acceptable in the phase 1, 2, 7, and 8 (figure 5.4.3). The resonance energies are obtained between 14–17 keV. Although the resonance energy is low in phase 3, it means that the absorption gets wide rather than that the resonance energy is shifted. In such phases (phase 3 and 4) the exponential fall of the continuum and broad cyclotron function conflict with each other and the parameters are not well determined.

In phase 1 and 2 the residuals appear like an emission at 9 keV. If we add an broad gaussian emission centered at 9 keV, the fits are improved to $\chi^2 = 1.84$ and 2.13 in phase

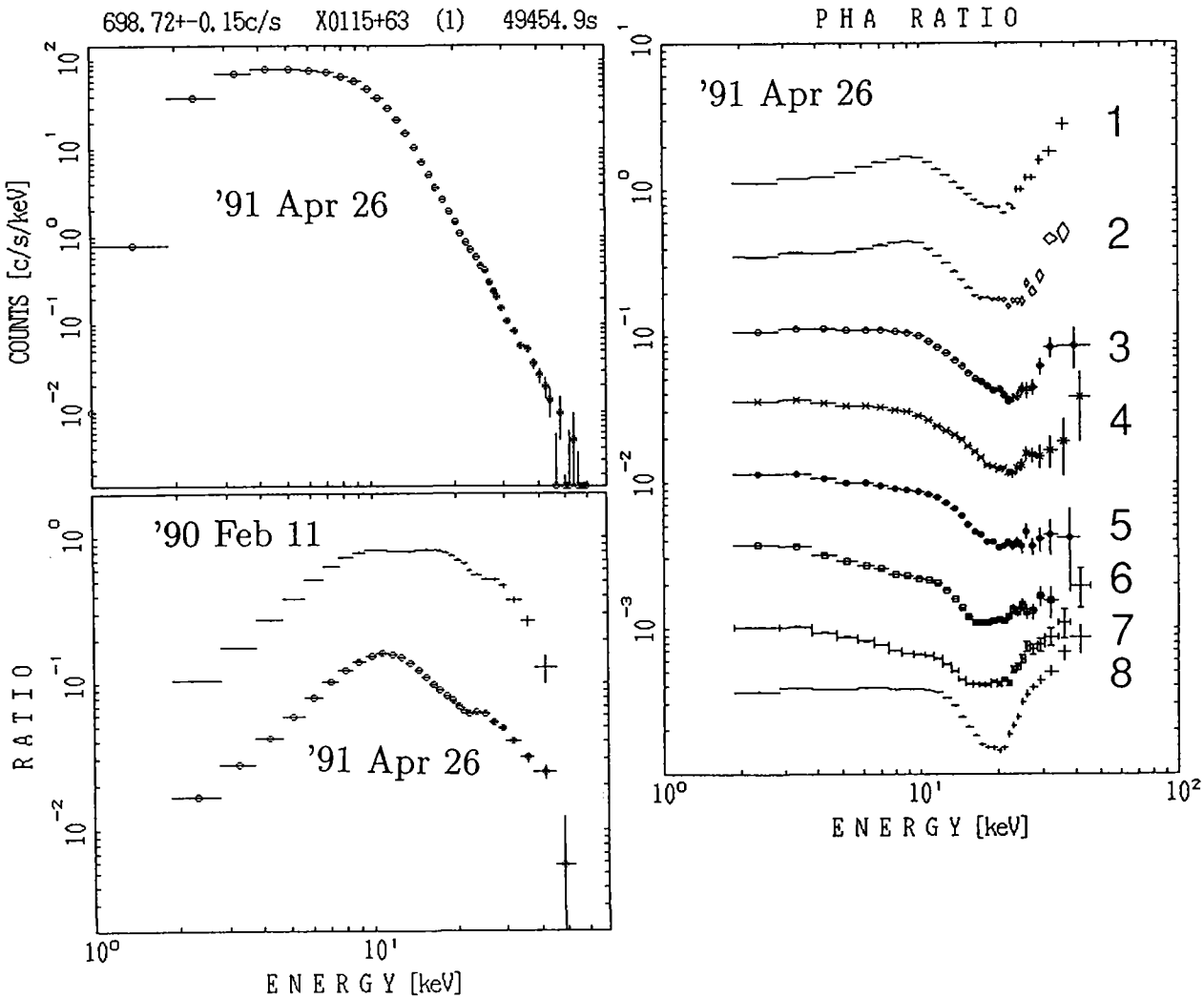

Figure 5.4.1: The averaged spectrum and its Crab ratio of 4U 0115+63 on 1991 April 26. The right panel is the PHA ratios of the phase resolved spectra to the FDCO model in figure 5.4.2b. In the Crab ratio, observation on 1990 Feb. 11 (§5.3) is also plotted for comparison.

1 and 2, respectively. The line energy is almost half of the absorption center energy. Therefore the emission line is the fundamental harmonic, and the deep absorption might be the second harmonic. However, since such emission-like residuals are also seen in phase 6, 7, and 8 in different energies and the features are near the iron line and edge energies, the significance should not be so high and we would like to conclude that the 16 keV is more likely to be the fundamental harmonic.

The resonance energy has changed from 11.3 keV in 1990 to 15.6 keV in 1991. But the

pulse profiles did not change so much suggesting that the emission beam pattern or viewing angle did not change dramatically. The simplest understanding is that the magnetic field strength in the scattering region increased by 40 % as the luminosity decreased to 16 %. If we attribute this change to the height of the scattering region from the neutron star surface, the region is $\sim$ 1.1 km lower in 1991 than in 1990, where we assume the magnetic field is dipole ($B \propto r^{-3}$) and the radius of the neutron star r_{NS} is 10 km. If the magnetic field is quadrupole such as proposed by Ruderman (1991), the difference can be smaller, but still as much as 700m.

The Ghosh and Lamb theory predicts that a change of $\dot{M}$ would cause a change the accreting point on the surface, which may accompany a change of the magnetic field. Since the Alfven radius r_A is $\propto \dot{M}^{-2/7}$ (§2.3.4), 16 % decrease of $\dot{M}$ causes 1.7 times increase of r_A. If the field is a perfect dipole, the angular separation θ of the accreting point on the neutron star surface from the magnetic pole is given as $\sin\theta \sim \sqrt{r_{NS}/r_A}$. Assuming $r_A = 10^8$ cm, θ changes from 5.7° to 4.4° with the decrease of $\dot{M}$, which implies the distance change from 1 km to 0.77 km. This change follows an increase of magnetic field strength of the accreting point. However, this process cannot explain the phenomenon since the change of the magnetic field is as small as 0.2 % to the θ direction, which is proportional to $\sqrt{1 + 3\cos^2\theta}$.

Thus the change of the resonance energy would be strongly related to the structure of the accretion column, the magnetic field distribution on the surface of the neutron star, and so on; we will discuss this further in §6.3. An important point is that although the cyclotron structure is the direct measurement of the magnetic fields of the X-ray pulsars, the obtained strength of the magnetic fields has an uncertainty of about ±50 %, which would depend on the various conditions.

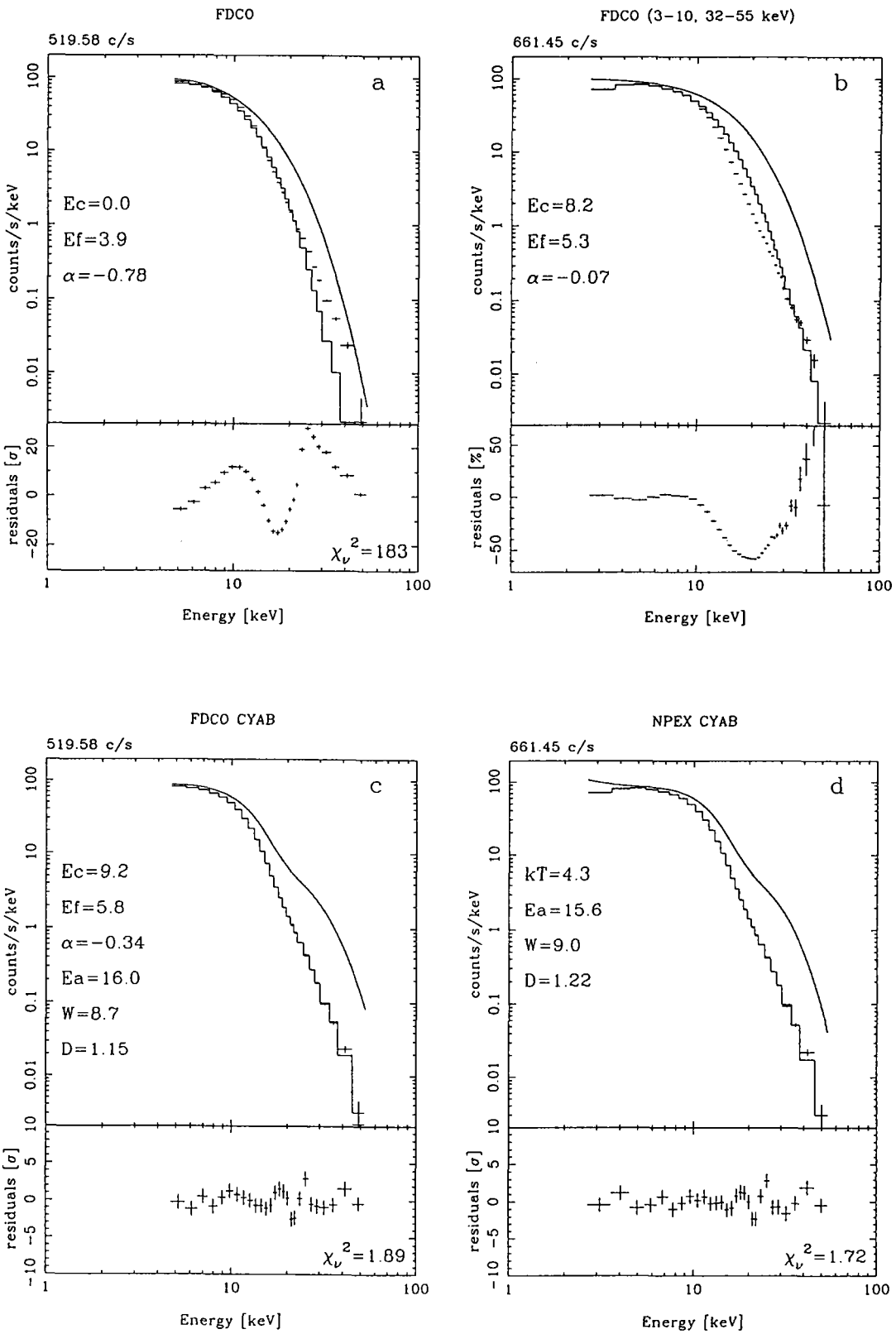

Figure 5.4.2: Some fits to the averaged spectrum of 4U 0115+63 on 1991 April 26. *a*: 5–55 keV with FDCO. *b*: 2–10, 32–55 keV with FDCO. *c*: 5–55 keV with FDCO × CYAB. *d*: 3–55 keV with NPEX × CYAB. The unit of the residuals in the figure*b* is % of the model.

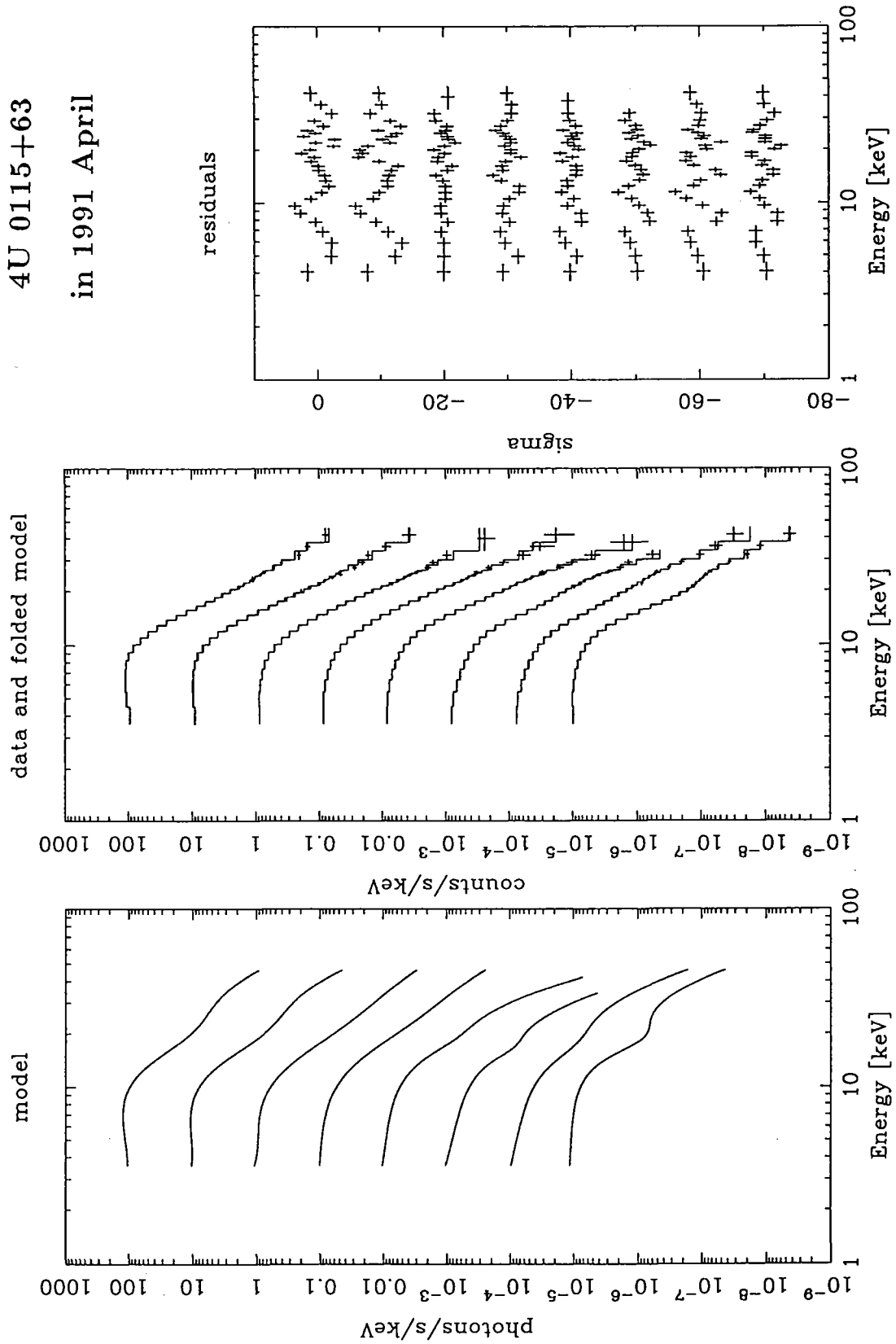

Figure 5.4.3: The NPEX × CYAB fitting in 3–50 keV to the phase resolved spectra of 4U 0115+63 in 1991.

Table 5.4.1: Parameters for the spectra of 4U 0115+63 on 1991 Apr. 26 in 3–50 keV. The corresponding figure is figure 5.4.3. The resonance energies are obtained in 14–17 keV.

Pulse Phase	Resonance1 Ea_1 [keV]	Width1 W_1 [keV]	Depth1 D_1
ave.	15.61 ± 0.37	9.00 ± 0.61	1.22 ± 0.06
1	14.6 ± 0.7	11.0 ± 1.3	1.6 ± 0.1
2	14.5 ± 1.1	11.0 ± 2.3	1.6 ± 0.3
3	10.0 ± 3.4	16.2 ± 3.1	1.1 ± 0.3
4	13.1 ± 5.2	15.9 ± 6.3	1.2 ± 0.3
5	17.0 ± 0.4	6.2 ± 1.6	0.7 ± 0.2
6	16.0 ± 0.3	3.9 ± 0.8	0.7 ± 0.1
7	15.7 ± 1.0	6.5 ± 2.1	0.8 ± 0.2
8	17.3 ± 0.2	5.9 ± 0.6	1.5 ± 0.1

pulse phase	Negative power law Norm. A_1	index α_1	Positive Norm. A_2	Exponential Folding E. kT [keV]	χ^2_ν
ave.	62 ± 22	0.65 ± 0.29	785 ± 58	4.34 ± 0.14	1.72
1	9 ± 2	2.00 fixed	1128 ± 108	5.4 ± 0.7	3.43
2	11 ± 3	2.00 fixed	1082 ± 210	5.0 ± 1.1	5.60
3	12 ± 13	2.08 ± 1.01	843 ± 204	6.6 ± 3.2	0.83
4	142 ± 145	-0.01 ± 0.74	436 ± 281	6.0 ± 3.7	1.43
5	96 ± 49	0.53 ± 0.49	991 ± 198	3.5 ± 0.2	1.23
6	113 ± 46	0.55 ± 0.40	712 ± 118	3.5 ± 0.1	1.90
7	141 ± 87	0.21 ± 0.57	345 ± 177	4.4 ± 0.4	4.21
8	159 ± 79	0.06 ± 0.46	651 ± 140	4.6 ± 0.2	2.16

The index α_2 of the positive power law is fixed to 2.0.
The unit of the normalization of the power law is [photons/s/keV] at 10 keV.
No iron line is included.

5.5 4U 1538-52

As shown in §5.1–4, the detection of the second harmonic resonance has become an important issue. One reason is because the presence or absence of the 2nd harmonic leads to different continuum models, and another reason is because we can measure the optical depth of the scattering region using the 2nd harmonic which is a pure absorption. Since the resonance energies of Her X-1 are higher than 30 keV where the detector efficiency is low, we could not confirm the second harmonic even in the HV-reduced observations. On the other hand, 4U 0115+63 showed two clear absorptions with similar depths in 1990, but one large absorption in 1991. Therefore the second harmonic is still to be investigated further.

From the persistent X-ray pulsar 4U 1538-52, the cyclotron resonance at 20 keV was discovered by Clark *et al.* (1989). The phase resolved spectra with CYA2 fits are shown in figure 5.5.1. The resonance energies are distributed in 19 – 22 keV across the pulse phases. Though the flux is only 20 mCrab, its fundamental resonance was observed with a high significance because of the higher efficiency of the X-ray detector at the low resonance energy. The cyclotron feature is cross-confirmed by the pulse shape sliced by the energy range in figure 4.4.4e. The second peak has almost disappeared in the resonance center, while it appears in the lower and higher energy bands. Although Clark *et al.* (1989) employed the power law × CYA2 model for the first time to reproduce the flux decrease above the resonance, presence of the 2nd harmonic was not confirmed in their data covering up to 37 keV.

In order to search for the suggested second harmonic, the second observation of 4U 1538-52 was carried out with the reduced HV. Below we concentrate on the analysis of these reduced HV data. The left panel of figure 5.5.2 is the pulse averaged spectrum and the Crab ratio obtained on this occasion. The Crab ratio shows a clear dip at $\sim$ 20 keV, which is the same cyclotron resonance discovered by Clark *et al.* (1989) in the previous *Ginga* observation. The ratio then falls off sharply above 30 keV, and reaches the background uncertainty level at 40 keV. The spectrum in 2–12 keV is a power law with an hump due to the iron line. The right panel shows the Crab ratios of the phase resolved spectra. The cyclotron feature is most prominent at phase 3, 4, and 5, which correspond to the second peak of the pulse profiles shown in figure 4.4.4f. The second peak has disappeared at the resonance center $\sim$ 20 keV, consistently with the first observation (figure 4.4.4e). However, the second peak never recovers in the high energy band. In fact only one peak is observed in the 37.6–45.1 keV band which is the highest energy band with good statistics, and there is no sign of the second peak. Since the statistics of the first observation were poor in the 30.6–38.2 keV band, the first and the second observations are consistent and the recovery of the second peak is not certain. In the phase 4 of the Crab ratios there is an emission-line like structure at 28 keV, and similar feature is also seen in the data in

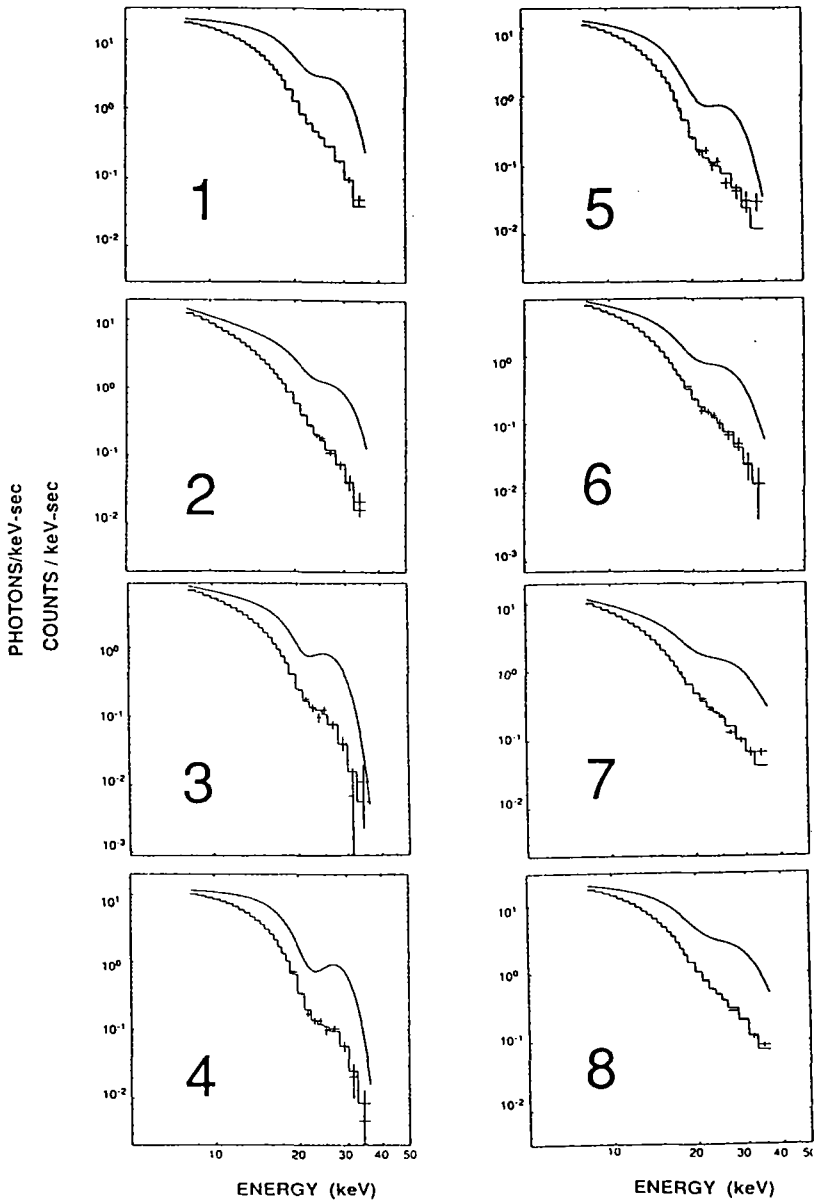

—Pulse-height spectra (counts keV^{-1} s^{-1}) of 4U 1538 − 52 in eight equal phase intervals of the pulse cycle. Above each histogram of counting rates is the fitted incident energy spectrum (photons keV^{-1} s^{-1}) before convolution with the LAC response function.

TABLE

PARAMETERS OF THE TRIAL FUNCTION (EQ. 1) FITTED TO THE PULSE HEIGHT SPECTRA

	PHASE CENTER $I \times 10^{*}$								
bin	phase	ph s^{-1} keV^{-1}	α	A_1	E_c (keV)	W (keV)	ew (keV)	A_2	χ^2/DOF
1.....	0.06	20.7 ± 1.0	0.17 ± 0.08	1.16 ± 0.09	21.6 ± 0.3	5.4 ± 0.6	10.8 ± 0.5	8.1 ± 1.8	1.47
2.....	0.19	11.7 ± 0.6	1.15 ± 0.08	0.77 ± 0.17	22.2 ± 0.9	4.7 ± 1.6	7.5 ± 1.3	7.9 ± 5.9	1.07
3.....	0.31	7.2 ± 0.3	0.74 ± 0.11	1.22 ± 0.20	20.7 ± 0.5	3.6 ± 0.9	8.6 ± 1.1	12.6 ± 8.1	0.80
4.....	0.44	12.1 ± 0.6	0.07 ± 0.10	2.07 ± 0.21	21.4 ± 0.3	4.3 ± 0.6	13.3 ± 0.7	13.9 ± 5.5	1.40
5.....	0.56	12.8 ± 0.6	0.41 ± 0.15	1.87 ± 0.29	20.3 ± 0.6	5.4 ± 1.2	13.3 ± 0.8	7.3 ± 3.8	1.36
6.....	0.69	5.9 ± 0.3	0.72 ± 0.21	1.01 ± 0.21	19.4 ± 0.7	5.3 ± 1.8	9.0 ± 1.3	4.2 ± 2.5	0.93
7.....	0.81	10.1 ± 0.5	0.84 ± 0.18	0.81 ± 0.12	19.1 ± 0.6	6.0 ± 1.6	8.2 ± 0.8	2.5 ± 0.8	2.39
8.....	0.94	20.2 ± 1.0	0.24 ± 0.11	1.07 ± 0.08	20.1 ± 0.4	6.7 ± 0.8	10.7 ± 0.4	4.0 ± 0.8	1.73

Figure 5.5.1: The CYA2 fits to the phase resolved spectra of 4U 1535-52 in 1988 (Clark *et al.* 1989). The cyclotron absorption were discovered at 19-22 keV.

the normal high voltage data (figure 4.4.4e, phase 3 and 4). Since the cyclotron feature is deepest in the phase 4, the emission like structure may have some relation to the cyclotron structure, but its statistical significance is too low to be discussed.

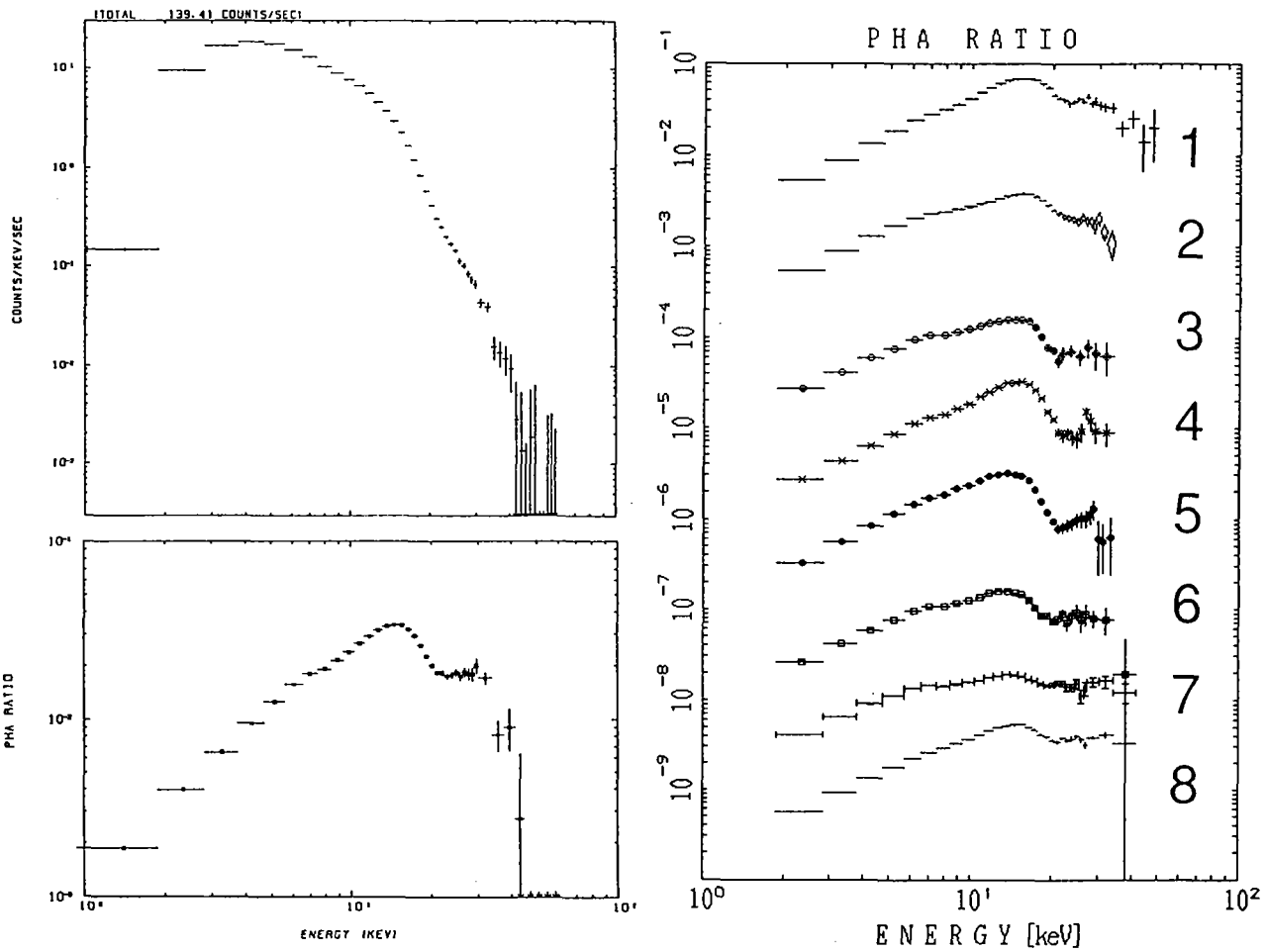

Figure 5.5.2: *Left*: The averaged spectrum of 4U 1538-52 and its Crab ratio obtained in the reduced HV observation. *Right*: The Crab ratios of the pulse phase resolved spectra of 4U 1538-52.

We have analyzed the pulse averaged spectrum of 4U 1538-52 in a similar way as Her X-1 and 4U 0115+63, and the results are shown in figure 5.5.3. Panel a is the FDCO fit above 9 keV, in which the cyclotron resonance is clearly revealed as a deep dip at $\sim$ 20 keV, but evidence for the 2nd harmonic is inconclusive. The power law $\times$ CYA2 fit (panel b) is acceptable with $\chi^2 = 1.02$ in the 9–60 keV range, thus confirming the modeling first employed by Clark *et al.* (1989). However, this fit cannot be extended to lower energies ($\chi^2 = 7.21$) as presented in panel c. On the contrary, the entire spectrum has been fitted fairly well ($\chi^2 = 1.58$) with the NPEX $\times$ CYAB model (panel d), which assumes an intrinsic turn over in the continuum instead of the 2nd harmonic absorption. This implies that the 2nd harmonic is not statistically significant in the spectrum of 4U 1538-52.

We have sorted the spectrum into 8 pulse phases. The spectra were first fitted with the power law $\times$ CYA2 model, for comparison with Clark *et al.* (1989). All the obtained parameters agree very well with those in the first observation (figure 5.5.1), though the two observations are separated by 2 years and 5 months. The cyclotron feature is thus inferred to be very stable from 4U 1538-52 as well as from Her X-1. Figure 5.5.4 is the NPEX $\times$ CYAB fit to the phase resolved spectra with the best-fit parameters listed in table 5.5.1. The model has reproduced the spectra reasonably well, although the fit is not good in several phases, particularly phase 4.

Amazingly, the determined resonance energies agree with those derived by Clark *et al.* (1989) within an rms scatter of 0.2 keV over the 8 phases, in spite of the difference in the observation epoch and the difference of the spectral model. This indicates that the cyclotron resonance in this pulsar is a very well defined phenomenon, in contrast to the case of 4U 0115+63. The obtained 'temperature' in the NPEX model has turned out to be very constant ($kT = 4 - 5.5$ keV) across the pulse phase, and in addition, is very similar to those obtained for Her X-1 (6 – 9 keV) and 4U 0115+63 ($\sim$ 5 keV). This reinforces the physical reality of the NPEX continuum.

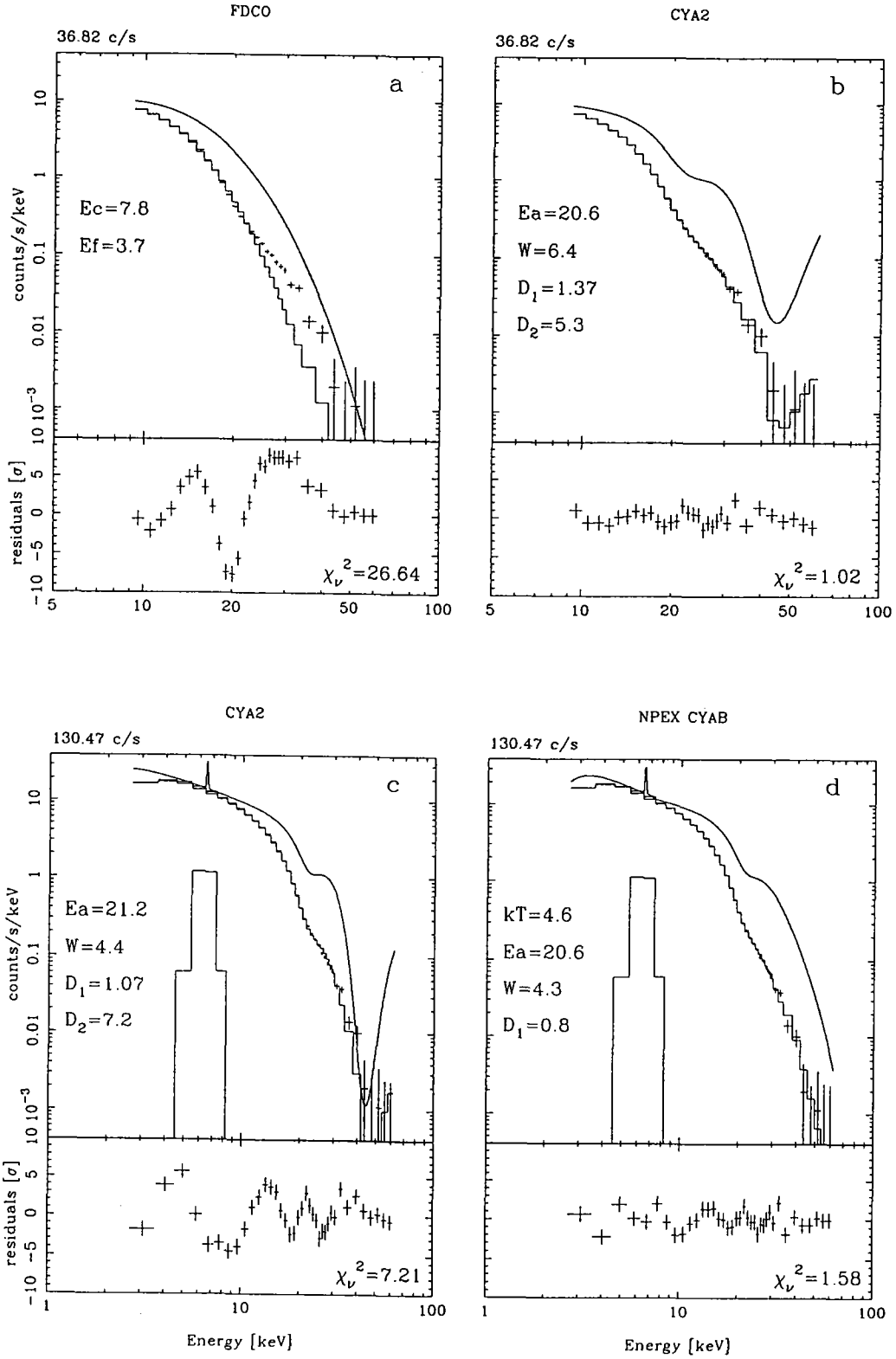

Figure 5.5.3: Model fitting to the averaged spectrum of 4U 1538-52 with the reduced HV. *a*: 9–60 keV with FDCO. *b*: 9–60 keV with Powerlaw × CYA2. *c*: 3–60 keV with Powerlaw × CYA2. *d*: 3–60 keV with NPEX × CYAB.

Table 5.5.1: Parameters of the NPEX fits to the 4U 1538-52 spectra in 3–60 keV. This model is successful in the entire energy band of *Ginga* LAC.

Pulse Phase	Resonance Ea [keV]	Width W [keV]	Depth D
ave.	20.6 ± 0.2	4.3 ± 0.6	0.8 ± 0.1
1	21.5 ± 0.3	3.9 ± 0.8	0.7 ± 0.1
2	21.6 ± 0.6	2.7 ± 1.6	0.6 ± 0.2
3	20.4 ± 0.5	2.1 ± 1.1	1.1 ± 0.3
4	21.8 ± 0.6	3.5 ± 1.4	2.0 ± 0.5
5	20.4 ± 0.3	3.2 ± 0.9	1.5 ± 0.2
6	18.9 ± 0.5	3.5 ± 1.4	1.0 ± 0.2
7	18.8 ± 0.8	5.2 ± 2.4	0.6 ± 0.2
8	19.9 ± 0.3	6.0 ± 0.9	0.9 ± 0.1

pulse phase	Negative power law Norm. A_1	index α_1	Positive Norm. A_2	Exponential Folding E. kT [keV]	Absorption $\log_{10} N_H$ [cm^{-2}]	χ^2_ν
ave.	19 ± 2	1.5 ± 0.2	68 ± 8	4.6 ± 0.2	22.81 ± 0.07	1.58
1	24 ± 3	1.6 ± 0.2	118 ± 15	4.8 ± 0.2	22.84 ± 0.08	1.92
2	36 ± 4	1.1 ± 0.2	68 ± 24	4.5 ± 0.5	22.74 ± 0.11	3.31
3	15 ± 2	1.2 ± 0.3	40 ± 17	4.2 ± 0.5	22.73 ± 0.12	1.84
4	7 ± 2	2.4 ± 0.7	60 ± 24	4.9 ± 0.8	22.98 ± 0.15	6.28
5	15 ± 3	1.8 ± 0.5	110 ± 35	4.0 ± 0.4	22.91 ± 0.11	2.00
6	11 ± 2	1.6 ± 0.3	42 ± 15	4.4 ± 0.5	22.81 ± 0.10	1.98
7	19 ± 3	1.3 ± 0.2	23 ± 7	5.4 ± 0.6	22.71 ± 0.10	2.12
8	26 ± 3	1.3 ± 0.2	73 ± 9	5.5 ± 0.3	22.70 ± 0.10	1.61

The index α_2 of the positive power law is fixed to 2.0.
The unit of the normalization of the power law is [photons/s/keV] at 10 keV.
The flux, energy, width of the iron line are fixed to 2.5 [photons/s], 6.50 keV, $\sigma = 0.05$ keV (narrow), respectively.

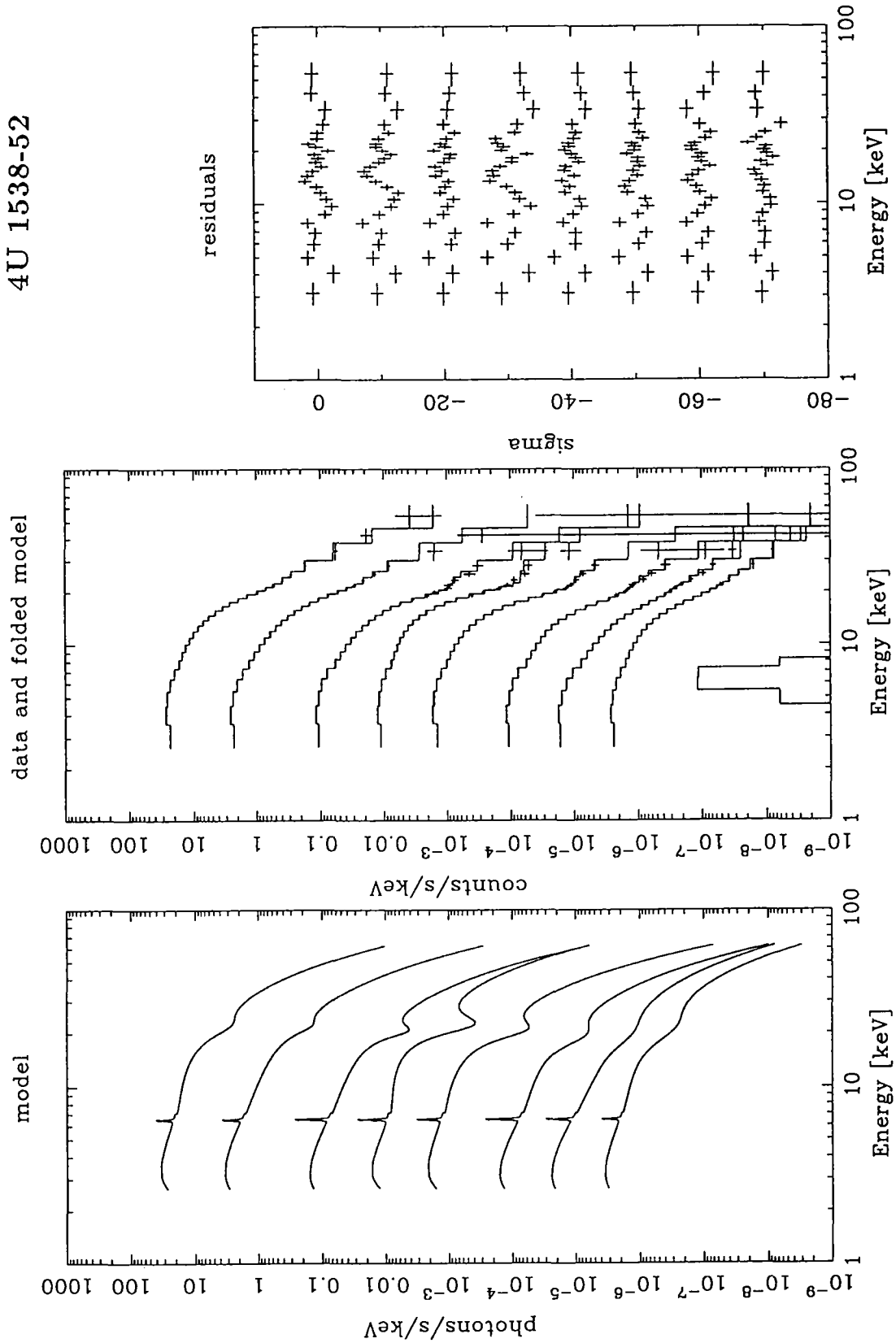

Figure 5.5.4: The NPEX × CYAB fitting in 3–60 keV to the phase resolved spectra of 4U 1538-52 in 1990.

5.6 4U 1907+09

The spectrum of 4U 1907+09 is very similar to that of 4U 1538-52, not only in the shape but also in the flux level. The pulse-averaged spectra in 'pulsing' and 'less-pulsing' states are both shown in figure 5.6.1 together with the Crab ratios. The 'pulsed' spectrum shows a dip at 20 keV, which is likely to be a cyclotron structure, as expected from the similarity to 4U 1538-52. On the other hand, the 'less-pulsing' spectrum does not show it clearly.

The 20 keV feature is obvious in the fitting with the FDCO model for the 'pulsing' state spectrum (figure 5.6.2a). An additional fixed model component in the middle of the figure represents contamination by the Galactic diffuse emission.

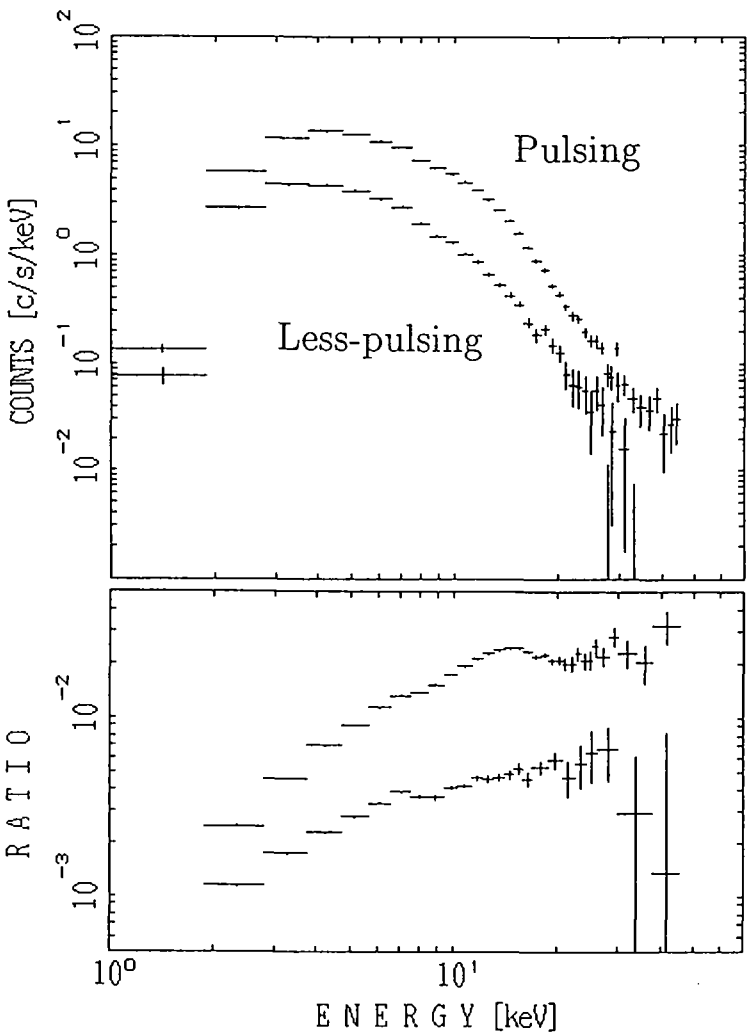

Figure 5.6.1: The averaged spectrum and its Crab ratio of 4U 1907+09.

The 'pulsing' state spectrum exhibits dips at 9 and 20 keV in the residuals, just like the 1st and the 2nd harmonics. However, we regard the 9 keV feature as spurious. In the residual plot the depths of the two features look similar, but since their statistics are much different, the absolute discrepancy from the model of the 9 keV dip is actually small. In fact the 9 keV feature can be explained by an iron edge and a concave continuum and finally disappears in figure 5.6.2d. In the limited energy range above 9 keV, the CYA2 model can fit well the spectrum including the 20 keV dip (figure 5.6.2b). However, in the wider energy band of 3–45 keV, CYA2 no longer gives a good fit (figure 5.6.2c), while the NPEX model can perfectly fit the observed data (figure 5.6.2d). Therefore 4U 1907+09 exhibits no clear evidence of the 2nd harmonic, either.

The 'less-pulsing' state spectrum does not have any feature in the Crab ratio. It is fitted well either by the FDCO model or by the NPEX model in 3-45 keV without the cyclotron structure (figure 5.6.3). Adding a CYAB structure with the same parameters as in the 'pulsing' state in fact increases the $\chi^2(0.98 \rightarrow 1.23)$. Therefore the absence of the structure is real rather than due to poor statistics.

Figure 5.6.4 left is the Crab ratios of the 'pulsing' state spectra resolved into 8 phases. The cyclotron feature is most prominent in phase 1, 2, and 8, which correspond to the peak of the pulse profile. We sorted the 'less-pulsing' state spectrum into 8 phases (figure 5.6.4 right), in a similar way utilizing the pulse-phase information determined in the 'pulsing' state. Although the feature was not significant in the averaged spectrum in the 'less-pulsing' state, a hint of the flux deficit around 20 keV is suggested in the same phase, 1, 2, and 8 as in the 'pulsing' state. This and the same column densities suggest that most of the X-rays come from 4U 1907+09 even in the 'less-pulsing' state. These spectra are consistent with the fact that the pulse fraction is the largest in the 7.5-17 keV band in the 'less-pulsing' state (figure 4.4.4d).

Finally we performed fitting of the phase resolved spectra. Figure 5.6.5 shows fitting with NPEX $\times$ CYAB model for the 'pulsing' state, and figure 5.6.6 with NPEX model for the 'less-pulsing' state. The CYAB is not included in the 'less-pulsing' state, since the data do not require it. In the 'pulsing' state, the cyclotron resonance energy was determined to be $\sim$ 20 keV except for at phase 6 where E_a is not well constrained due to weakness of the feature. The NPEX 'temperature' has again turned out to be almost phase independent, at $\sim$ 5 keV which is very close to that obtained for 4U 1538-52. The kT in the averaged spectrum in the 'less-pulsing' state is consistent with that in the 'pulsing' state, suggesting kT to be an intrinsic parameter of the system. The kT in the phase resolved spectra are small but not convincing because of the relatively poor statistics and undefined normalizations.

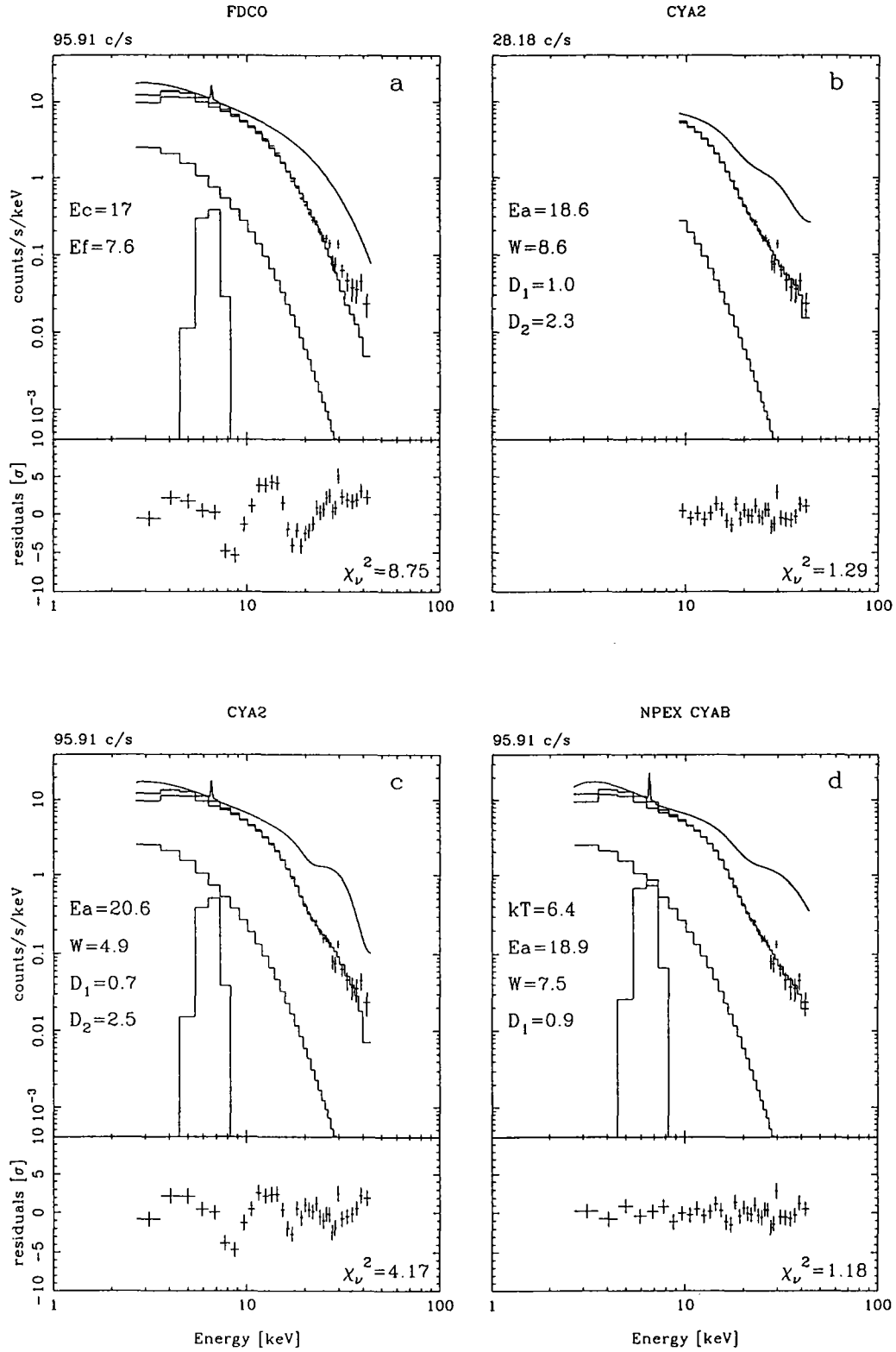

Figure 5.6.2: Model fittings to the averaged spectrum of 4U 1907+09 in the 'pulsing' state. *a*: 3–45 keV with FDCO. *b*: 9–45 keV with Powerlaw × CYA2. *c*: 3–45 keV with Powerlaw × CYA2. *d*: 3–45 keV with NPEX × CYAB. The contamination by the Galactic ridge emission is included in the fitting (shown as a histogram in the figures) as a thermal bremsstrahlung model with kT = 7 keV, $\log_{10}N_H$ = 22.3 and the intensity of 10 c/s/6LAC without an iron line. The model spectrum (smooth curve on the top) includes it.

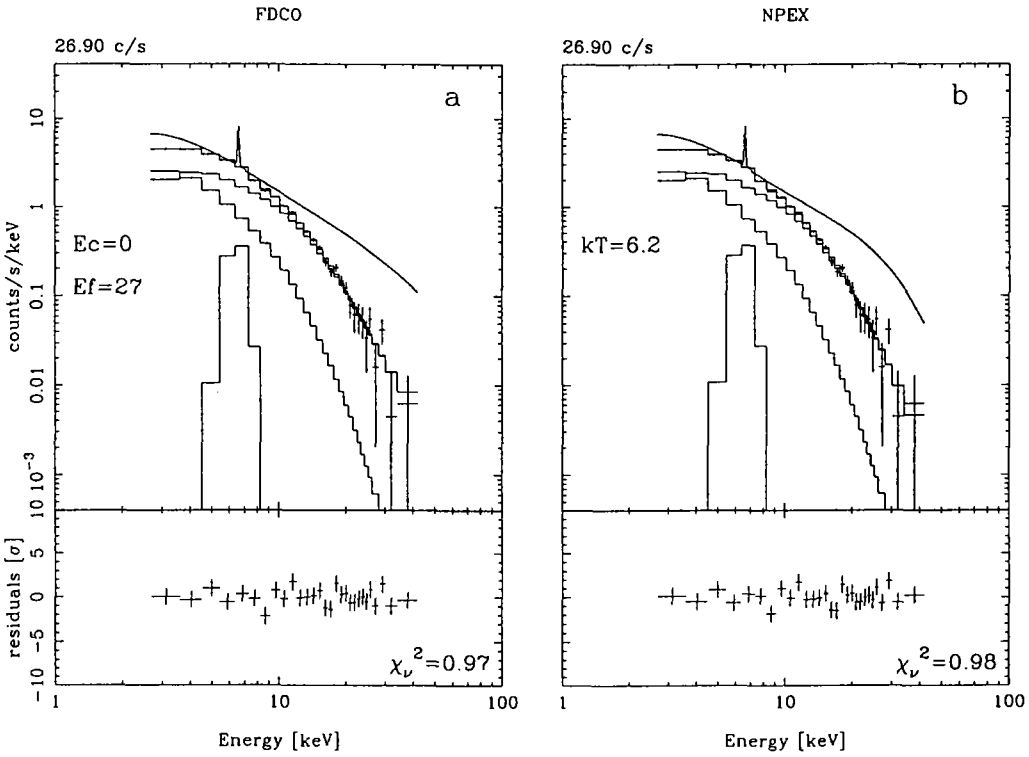

Figure 5.6.3: Model fittings to the averaged spectrum in the 'less-pulsing' state. *a*: 3–30 keV with FDCO. *b*: 3–30 keV with NPEX. The contamination by the Galactic ridge emission is included in the fitting as a thermal bremsstrahlung model of kT = 7 keV, $\log_{10}N_H$ = 22.3 and the intensity of 10 c/s/6LAC without an iron line (shown as a histogram in the figures).

Table 5.6.1: Parameters of the NPEX fits in the 'pulsing' state in 3–45 keV, and the 'less-pulsing' state in 3–30 keV. The CYAB is not included in the fittings of the 'less-pulsing' state.

Pulse Phase	Resonance Ea [keV]	Width W [keV]	Depth D
'pulsing' state			
ave.	18.9 ± 0.7	7.5 ± 2.1	0.9 ± 0.2
1	21.2 ± 0.6	7.1 ± 1.3	1.7 ± 0.2
2	21.2 ± 0.7	5.8 ± 2.5	1.4 ± 0.5
3	20.7 ± 0.9	5.1 ± 3.1	0.6 ± 0.3
4	20.0 ± 0.7	4.3 ± 2.4	0.5 ± 0.2
5	19.2 ± 0.9	4.5 ± 2.8	0.4 ± 0.1
6	9.5 ± 14.8	10.3 ± 6.0	0.4 ± 0.2
7	16.9 ± 0.7	3.8 ± 2.1	0.4 ± 0.1
8	18.9 ± 0.8	5.8 ± 3.3	1.0 ± 0.5

pulse phase	Negative power law Norm. A_1	index α_1	Positive Norm. A_2	Exponential Folding E. kT [keV]	Absorption $\log_{10} N_H$ [cm^{-2}]	Iron line Flux I_{Fe}[ph/s]	χ^2_ν
'pulsing' state							
ave.	11 ± 2	1.4 ± 0.3	25 ± 5	6.4 ± 0.7	22.86 ± 0.08	1.7 ± 0.5	1.18
1	10 ± 2	1.9 ± 0.4	53 ± 5	5.5 fixed[a]	23.02 ± 0.07	1.9 ± 0.7	1.19
2	10 ± 2	2.0 ± 0.4	48 ± 22	5.3 ± 1.1	23.01 ± 0.09	2.1 ± 0.8	1.74
3	15 ± 2	1.1 ± 0.2	34 ± 13	5.0 ± 0.7	22.85 ± 0.07	1.6 ± 0.4	0.58
4	12 ± 2	1.6 ± 0.4	64 ± 18	4.6 ± 0.5	22.95 ± 0.09	1.9 ± 0.6	1.04
5	23 ± 4	0.7 ± 0.3	28 ± 9	5.5 ± 0.5	22.73 ± 0.10	1.5 ± 0.6	0.98
6	6 ± 4	2.3 ± 1.2	37 ± 47	5.6 ± 1.2	22.96 ± 0.23	1.6 ± 0.4	0.78
7	9 ± 2	1.4 ± 0.3	19 ± 5	5.0 ± 0.4	22.82 ± 0.09	1.5 ± 0.3	0.41
8	9 ± 3	1.6 ± 0.5	37 ± 20	4.8 ± 1.1	22.87 ± 0.12	1.4 ± 0.5	0.93
'non-pulsing' state							
ave.	3.8 ± 0.5	0.64 ± 0.25	2.3 ± 2.5	6.2 ± 1.8	22.64 ± 0.19	0.7 ± 0.2	0.98
1	1 ± 2	3.46 ± 3.40	35 ± 28	3.3 ± 0.6	23.24 ± 0.42	0.7 ± 0.6	2.31
2	3 ± 3	1.51 ± 1.95	15 ± 16	3.8 ± 0.9	22.98 ± 0.41	0.6 ± 0.4	1.55
3	4 ± 1	1.01 ± 0.72	4 ± 6	5.2 ± 2.1	22.86 ± 0.27	0.8 ± 0.4	1.32
4	1 ± 1	3.52 ± 2.12	24 ± 13	3.6 ± 0.5	23.22 ± 0.28	0.9 ± 0.4	1.37
5	3 ± 2	1.71 ± 1.37	13 ± 10	4.0 ± 0.7	23.04 ± 0.26	1.0 ± 0.4	0.96
6	2 ± 3	1.95 ± 2.22	17 ± 17	3.6 ± 0.8	22.97 ± 0.47	0.8 ± 0.5	1.76
7	3 ± 1	0.61 ± 0.28	1 ± 4	6.2 ± 3.9	22.55 ± 0.28	0.9 ± 0.2	0.49
8	2 ± 4	2.29 ± 4.07	40 ± 41	3.0 ± 0.6	23.06 ± 0.67	0.5 ± 0.5	1.75

a: Fixed, otherwise kT couples with the CYAB parameters and becomes about twice as large as those in the other phases.

The index of the positive power law α_2 is fixed to 2.0.

The unit of the normalization of the power law is [photons/s/keV] at 10 keV.

The energy and width of the iron line are fixed to 6.60 keV and $\sigma = 0.05$ keV (narrow), respectively.

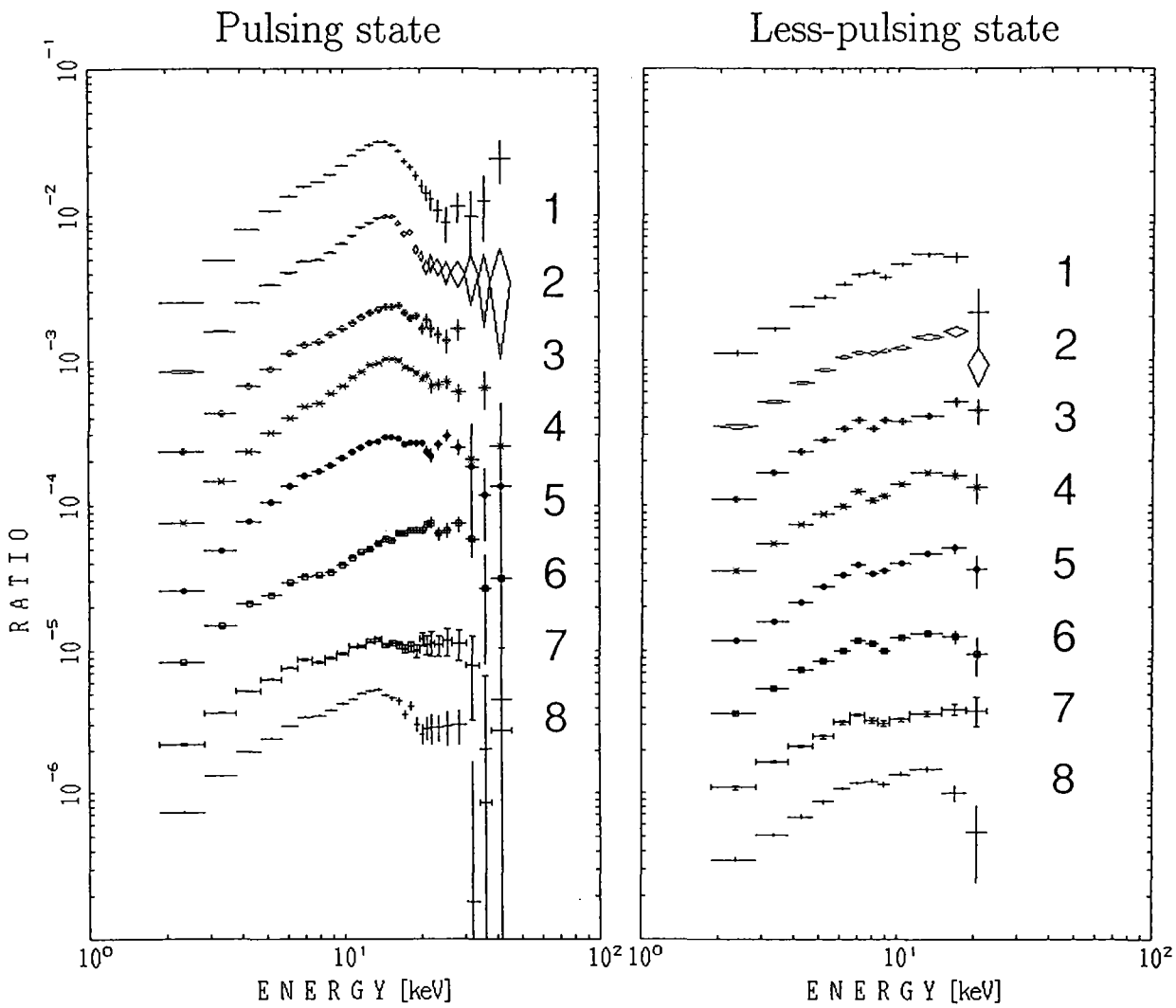

Figure 1.6.4: The Crab ratios of the phase resolved spectra of 4U 1907+09. Spectra are shifted downward successively by a factor 3.16 (half order) in this figure.

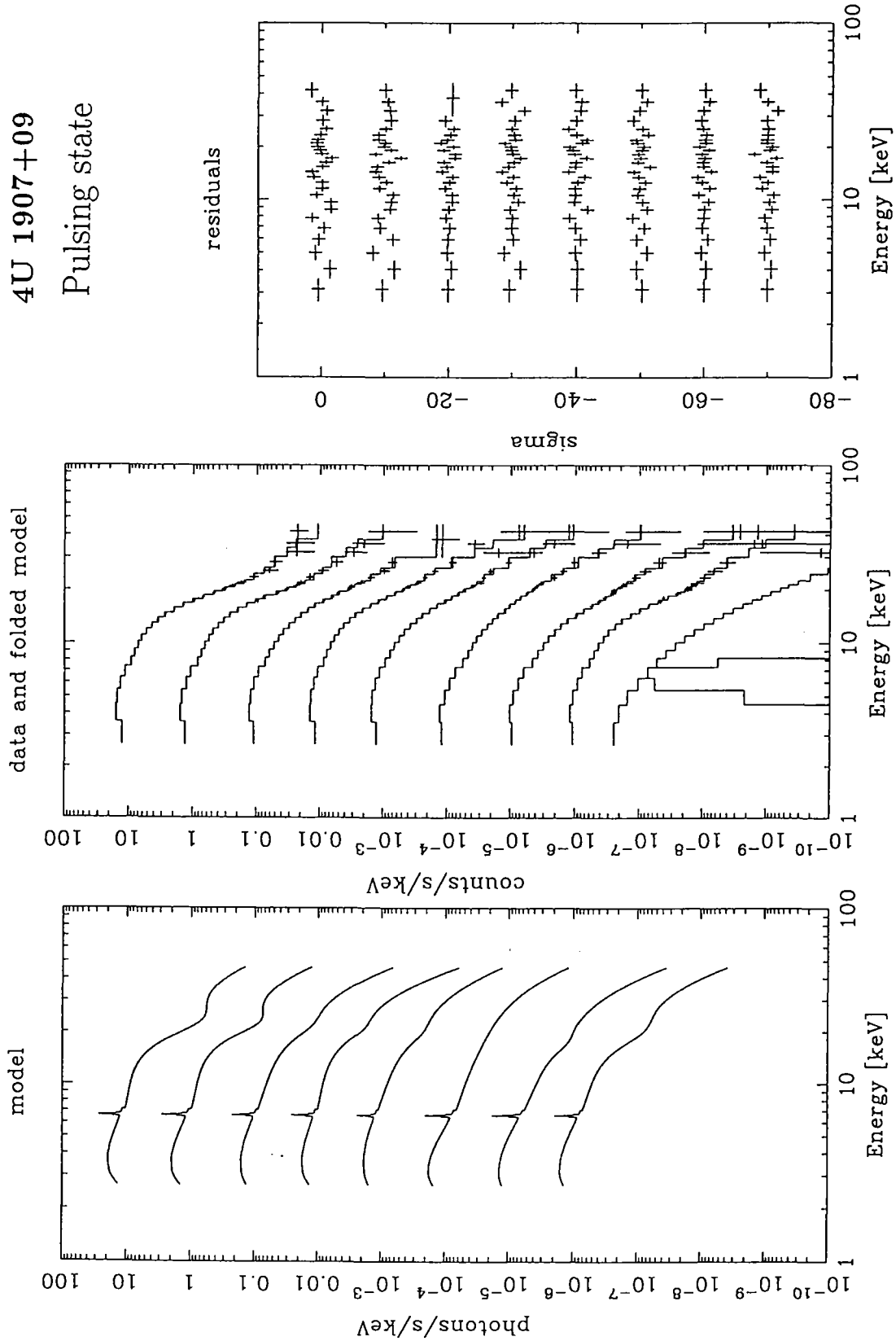

Figure 5.6.5: The NPEX × CYAB fittings in 3–45 keV to the phase resolved spectra of 4U 1907+09 in the 'pulsing' state.

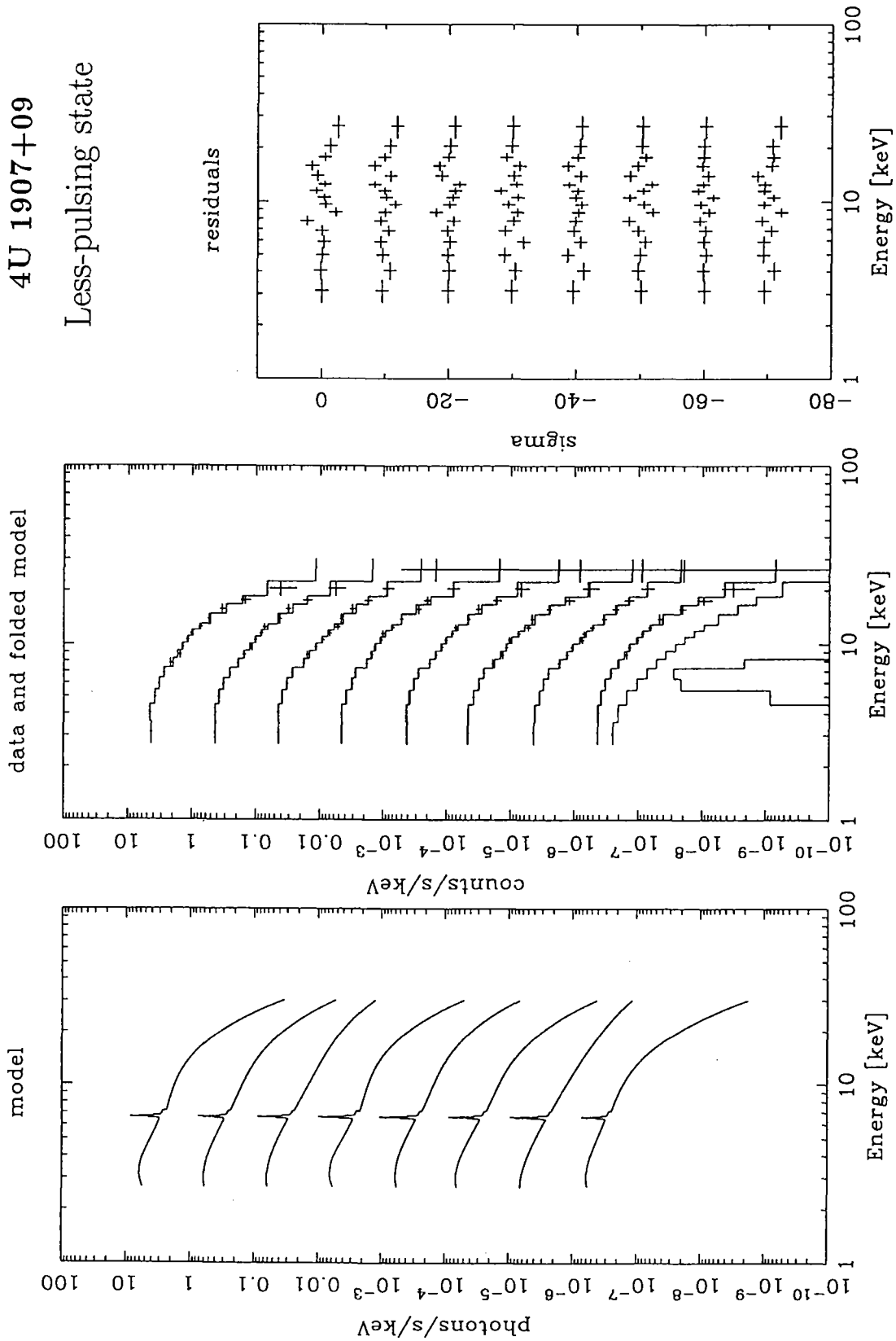

Figure 5.6.6: The NPEX fittings in 3–30 keV to the phase resolved spectra of 4U 1907+09 in the 'less-pulsing' state.

5.7 X 0331+53

5.7.1 Pulse-phase-averaged spectra

The 1989 outburst of the transient pulsar X0331+53 has provided basically two sets of data (§4.3.2); the normal HV data taken on 1989 September 20 duration 1600 s, and the reduced HV data obtained on 1989 October 1 duration 6400 s. Over the 10 day interval, the X-ray intensity increased by about 40% from 2410 c/s on September 20 to 3360 c/s on October 1.

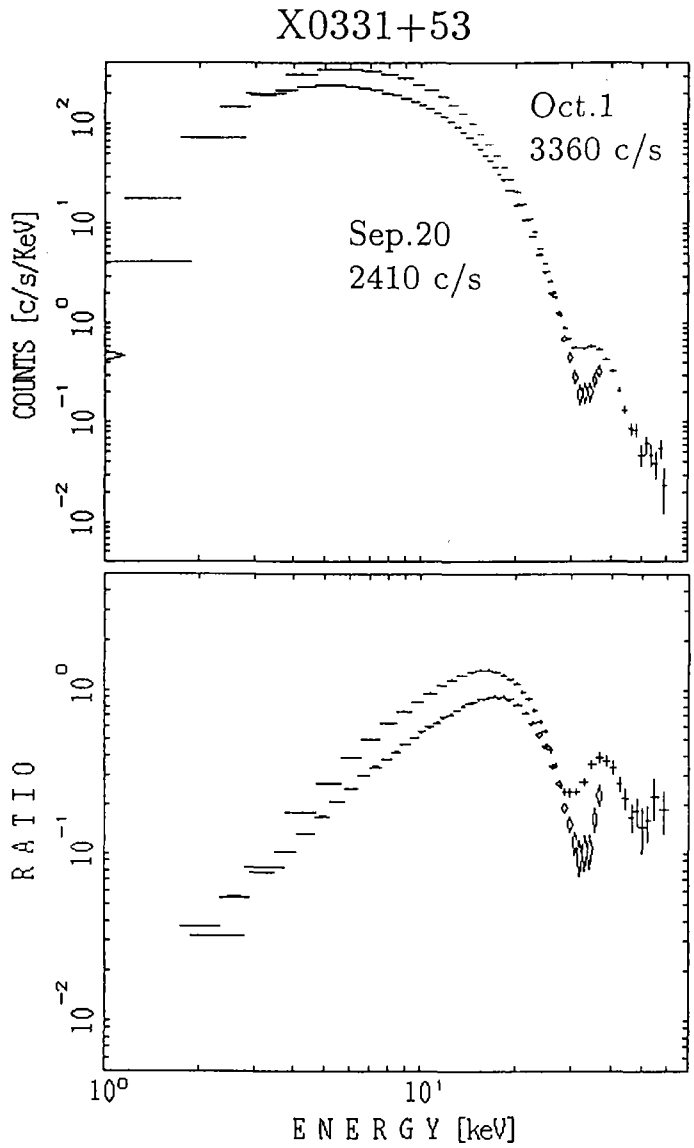

Figure 5.7.1: The averaged spectra and the Crab ratios of X 0331+53.

Analyzing the latter data set, Makishima *et al.* (1990) discovered a prominent cyclotron resonance feature which turned out to be the best-quality example ever obtained of the cyclotron resonance phenomenon. Here we analyze the entire data set, including the normal-HV data as well. A significant fraction of the reduced-HV data was taken in the low-bit-rate mode, in which the top-layer data suffered from overflow of on-board scalars in the 3–10 keV energy range because the source flux exceeded the limit of 256 c/16s/ch/(1 LAC top layer) $\sim$ 200 c/s/keV/(8LAC top+mid) (§3.2.4). We have therefore corrected the data for the scalar overflow and show it in figure 5.7.1. However, in order for accuracy, we use the data taken only in the high bit-rate mode to fit in the overall energy band. The data taken in the low bit-rate mode are used in §5.7.3, where we study the cyclotron structure in detail with the spectrum in 9–60 keV.

Figure 5.7.1 shows the pulse-phase-averaged spectra and their Crab ratios obtained on the two occasions. In both spectra the cyclotron resonance structure is observed as a sharp dip at about 30 keV, which is far more prominent than could be explained by any instrumental effect (Makishima *et al.* 1990). Although the resonance in the normal-HV data appears near the upper bound of the spectral range, there is no doubt that this is the same feature as was discovered in the reduced-HV data by Makishima *et al.* (1990). However we notice a slight decrease in the resonance energy over the time interval of 10 days, presumably in correlation with the flare evolution.

As shown in figure 5.7.1 we have fitted the reduced-HV spectrum with several spectral models that have been employed so far. As was usually the case with previous pulsars, the power-law $\times$ FDCO fit is totally unacceptable, while the NPEX $\times$ CYAB fit is the most favored one. The power-law $\times$ CYA2 fit (as originally employed by Makishima *et al.* 1990) is intermediate, in the sense that it can trace the feature fairly well but it fails to reproduce the overall (2–60 keV) continuum shape. We thus reconfirm our conclusion made previously for several pulsars, that the continuum is likely to be turning over intrinsically across the energy region where the cyclotron resonance is present. However the NPEX model is not completely acceptable, and we come back to this issue later in §5.7.3.

The same analysis was performed on the normal-HV data. The results presented in figure 5.7.3 are basically very similar to those obtained for the reduced-HV data. However, these results clearly indicate that the cyclotron resonance energy decreased by about 10% from $\sim$ 30.0 keV in September to $\sim$ 27.2 keV in October. The resonance depth also decreased from 2.3 to 1.6, while the resonance width remained roughly constant at 10–11 keV. For confirmation we re-analyzed the reduced-HV data over the energy range below 37 keV corresponding to the energy range of the normal-HV data, but the results turned out to be the same as before. Therefore the shift of resonance energy is real and is not attributed to an artifact due to the difference in the energy band. This provides valuable information about the dependence of the cyclotron resonance characteristics on the mass

accretion rate.

Utilizing the superior signal-to-noise ratio, we would like to examine here again whether the spectra are really incompatible with the concept of cyclotron line emission. In fact, the residuals to the FDCO fit in figure 5.7.2 suggest an emission line at 35 keV. We have therefore fitted again the 9–60 keV portion of the reduced-HV spectrum using a broad Gaussian model for the emission line, and either the power-law × FDCO model or the Boltzmann model for the continuum. As shown in figure 5.7.4, both fits failed. While the Boltzmann continuum cannot reproduce the very steep continuum break above 20 keV, the FDCO model underpredicts the flux above 50 keV. We therefore conclude that the high-quality data on X0331+53 exclude an interpretation in terms of the cyclotron emission line.

5.7.2 Pulse-phase-resolved spectra

Although Makishima *et al.* (1990) did not perform the pulse-phase resolved analysis, we can in fact utilize a small amount of high-bit-rate data, 1600 s on September 20 and 400 s on October 1, for this purpose. We have accordingly sorted these data into 8 pulse phase-resolved spectra, and their Crab ratios are shown in figure 5.7.5. The cyclotron resonance persists throughout the pulse phase, with little dependence on the pulse phase. This result may be related to the very small pulse fraction of X0331+53 (12% peak-to-bottom vs. average, in 2–37 keV; Figure 4.4.3).

The NPEX × CYAB model has been applied to the phase-resolved spectra, as shown in figure 5.7.6 for the October data and 5.7.7 for the September data. The best-fit parameters are listed in table 5.7.1. The fits are mostly acceptable, and the fit parameters show little dependence on the pulse phase.

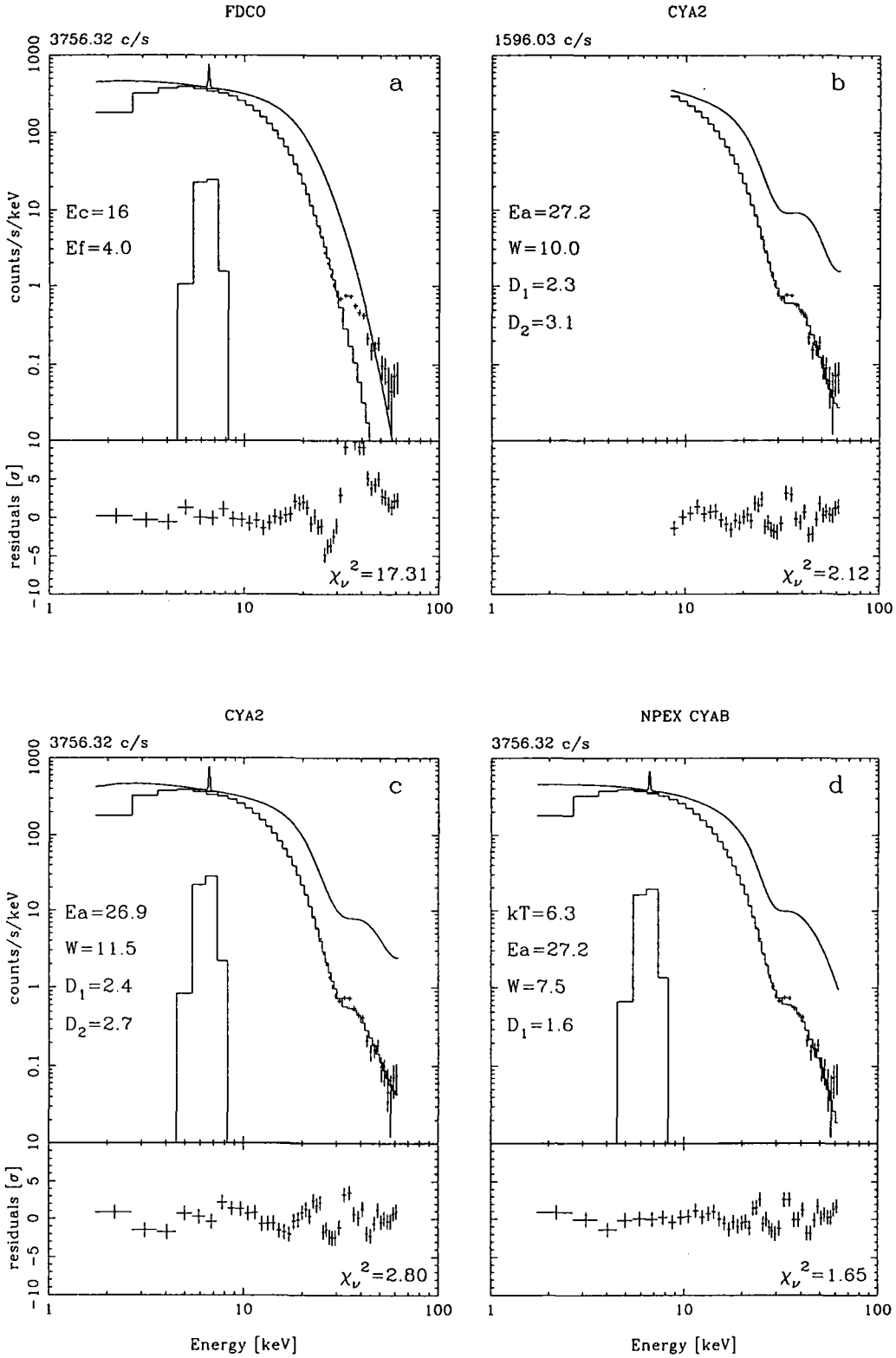

Figure 5.7.2: Model fitting to the averaged spectrum with the reduced HV in high bit-rate. *a*: 2–60 keV with FDCO. *b*: 9–60 keV with Powerlaw × CYA2. *c*: 2–60 keV with Powerlaw × CYA2. *d*: 2–60 keV with NPEX × CYAB.

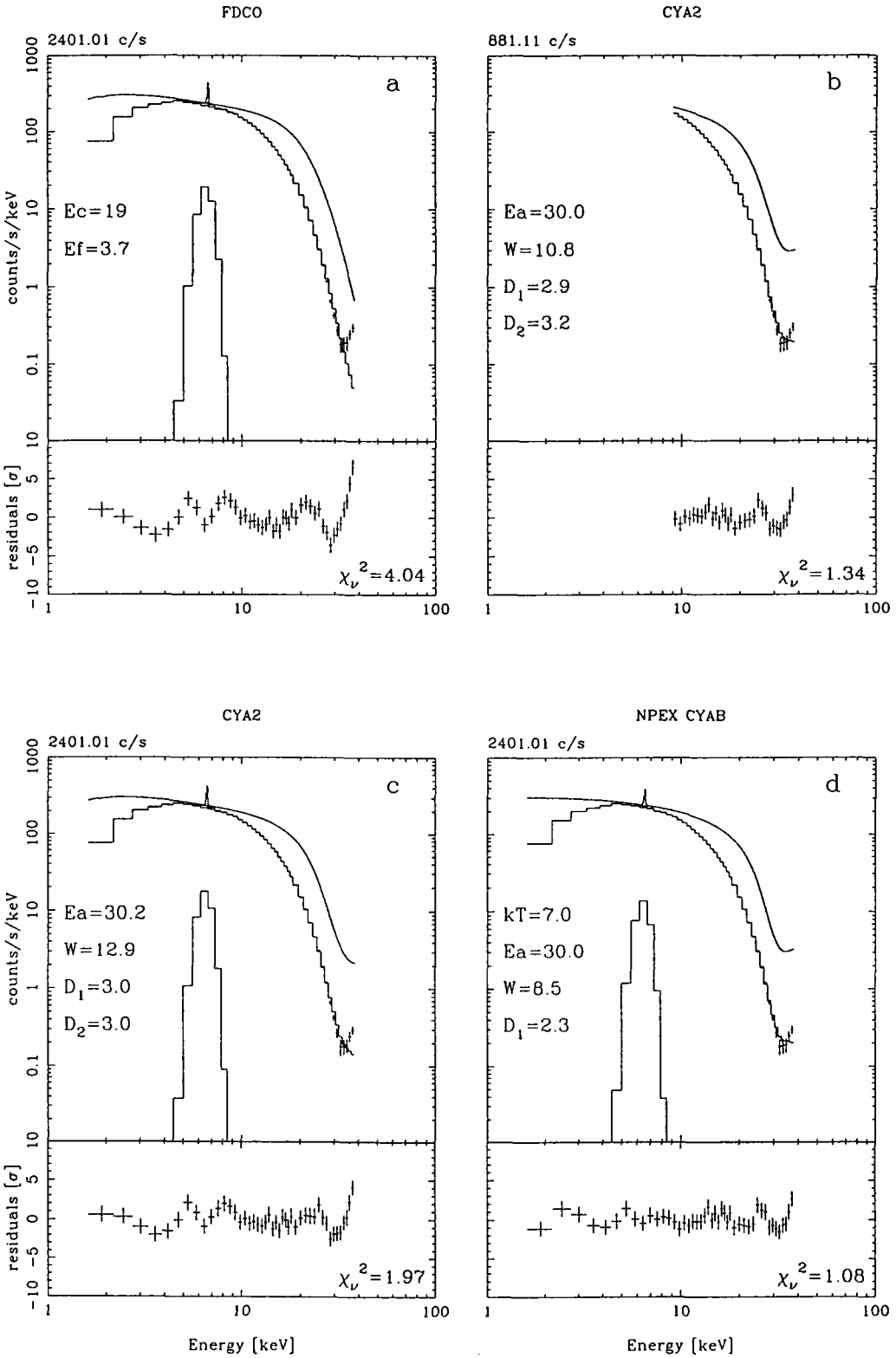

Figure 5.7.3: Model fitting to the averaged spectrum with the normal HV in high bit-rate. *a*: 2–37 keV with FDCO. *b*: 9–37 keV with Powerlaw × CYA2. *c*: 2–37 keV with Powerlaw × CYA2. *d*: 2–37 keV with NPEX × CYAB.

Table 5.7.1: Parameters of the NPEX fits of reduced HV and of the normal HV spectra.

Pulse Phase	Resonance Ea [keV]	Width W [keV]	Depth D	Resonance Ea [keV]	Width W [keV]	Depth D
	reduced HV			normal HV		
ave.	27.2 ± 0.3	7.5 ± 0.9	1.6 ± 0.2	30.0 ± 0.5	8.5 ± 1.4	2.3 ± 0.5
1	27.5 ± 0.6	6.3 ± 1.4	1.7 ± 0.3	29.2 ± 0.6	8.2 ± 1.9	2.0 ± 0.5
2	27.3 ± 0.6	8.2 ± 1.9	1.6 ± 0.3	29.5 ± 0.4	7.4 ± 1.2	2.2 ± 0.3
3	28.6 ± 1.0	10.5 ± 1.9	2.2 ± 0.5	29.4 ± 1.2	7.7 ± 2.1	2.3 ± 1.2
4	27.2 ± 0.7	7.3 ± 2.3	1.5 ± 0.4	29.4 ± 0.7	8.3 ± 2.3	1.9 ± 0.6
5	25.8 ± 0.6	8.6 ± 2.6	1.3 ± 0.4	29.5 ± 1.0	8.9 ± 2.8	2.1 ± 0.9
6	26.1 ± 0.8	8.5 ± 3.6	1.3 ± 0.5	29.4 ± 0.9	9.2 ± 3.1	1.7 ± 0.6
7	27.1 ± 0.6	7.3 ± 1.6	1.8 ± 0.3	30.0 ± 1.5	9.7 ± 3.5	2.3 ± 1.4
8	27.2 ± 0.6	7.3 ± 1.6	1.8 ± 0.3	29.0 ± 0.5	6.9 ± 1.5	1.9 ± 0.3

pulse phase	Negative power law Norm. A_1	index α_1	Positive Norm. A_2	Exponential Folding E. kT [keV]	Iron line Flux I_{Fe}[ph/s]	χ^2_ν
reduced HV						
ave.	930 ± 63	-0.27 ± 0.05	633 ± 171	6.3 ± 0.5	38 ± 16	1.65
1	1084 ± 83	-0.32 ± 0.05	563 ± 323	6.3 ± 0.9	48 ± 16	0.97
2	989 ± 89	-0.27 ± 0.06	571 ± 323	6.5 ± 1.1	57 ± 15	0.87
3	820 ± 137	-0.24 ± 0.08	185 ± 229	9.0 ± 2.9	36 ± 15	0.85
4	827 ± 73	-0.23 ± 0.07	820 ± 452	5.8 ± 1.0	37 ± 15	1.14
5	729 ± 64	-0.15 ± 0.07	1034 ± 454	5.6 ± 0.9	54 ± 13	0.78
6	791 ± 92	-0.19 ± 0.10	1029 ± 655	5.6 ± 1.2	27 ± 18	1.39
7	776 ± 67	-0.17 ± 0.07	802 ± 335	6.2 ± 0.9	38 ± 16	1.22
8	950 ± 85	-0.27 ± 0.06	614 ± 330	6.5 ± 1.0	32 ± 17	1.12
normal HV						
ave.	532 ± 38	-0.19 ± 0.03	314 ± 239	7.0 ± 1.6	19.0 ± 5.7	1.08
1	551 ± 47	-0.19 ± 0.03	341 ± 290	6.8 ± 1.8	20.8 ± 5.6	0.78
2	532 ± 24	-0.16 ± 0.02	359 ± 179	6.8 ± 1.1	16.6 ± 4.4	0.50
3	546 ± 147	-0.20 ± 0.09	199 ± 451	7.8 ± 5.1	21.3 ± 6.0	0.85
4	532 ± 47	-0.17 ± 0.04	351 ± 307	6.8 ± 1.9	18.0 ± 6.3	1.05
5	509 ± 91	-0.17 ± 0.06	263 ± 382	7.4 ± 3.5	18.7 ± 6.2	1.03
6	535 ± 43	-0.20 ± 0.04	403 ± 350	6.5 ± 1.8	21.2 ± 6.5	1.14
7	481 ± 130	-0.16 ± 0.09	226 ± 447	7.8 ± 5.3	19.4 ± 6.5	1.14
8	548 ± 23	-0.20 ± 0.04	455 ± 231	6.2 ± 0.9	20.4 ± 5.6	0.84

The index of the positive power law α_2 is fixed to 2.0.
The unit of the normalization of the power law is [photons/s/keV] at 10 keV.
The energy and width of the iron line are fixed to 6.59 keV and $\sigma = 0.05$ keV (narrow), respectively.

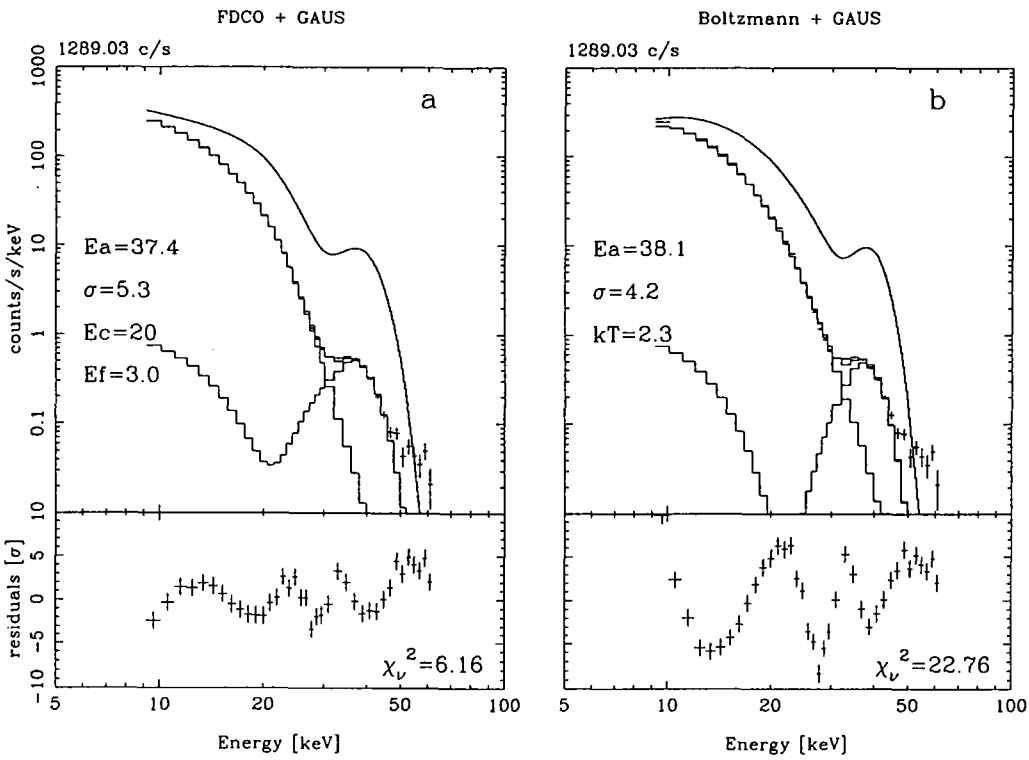

Figure 5.7.4: Gaussian emission fits to the averaged spectrum of X 0331+53. *a*: FDCO continuum. *b*: Boltzmann continuum. Since both fits are unsuccessful, the emission model is unlikely.

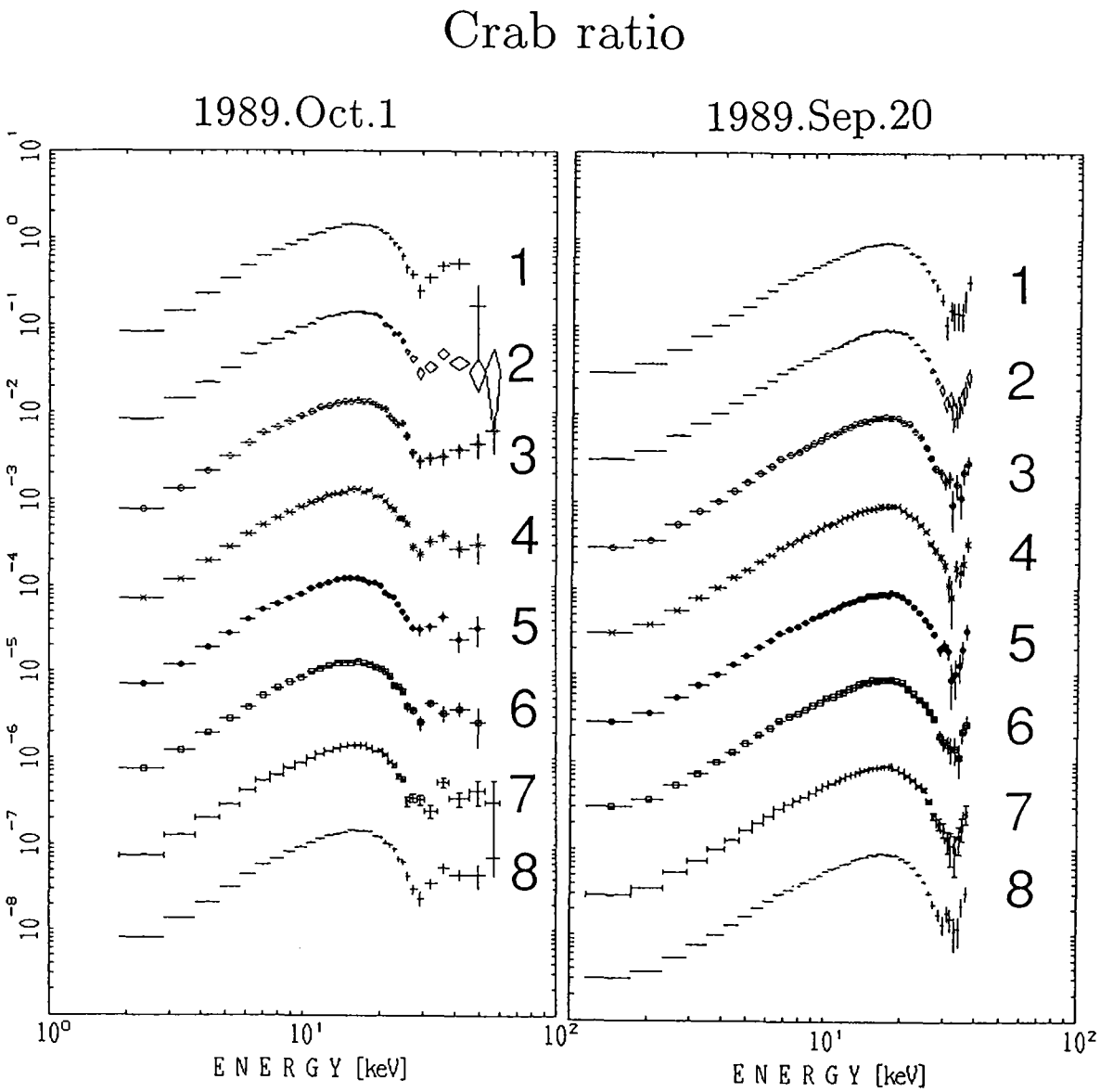

Figure 5.7.5: The Crab ratios of the phase resolved spectra of X 0331+53.

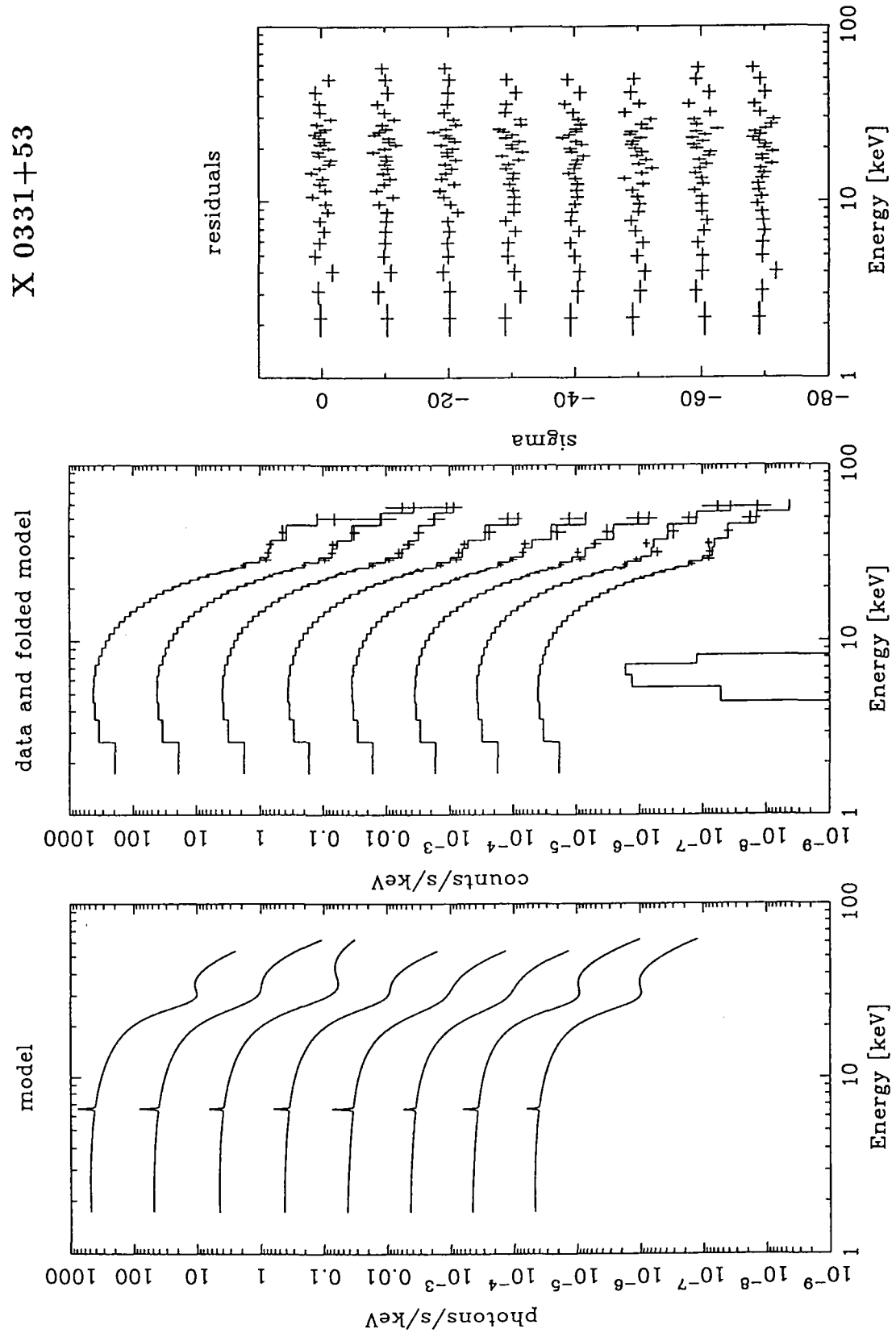

Figure 5.7.6: The NPEX × CYAB fits to the phase resolved spectra on 1989 Oct. 1.

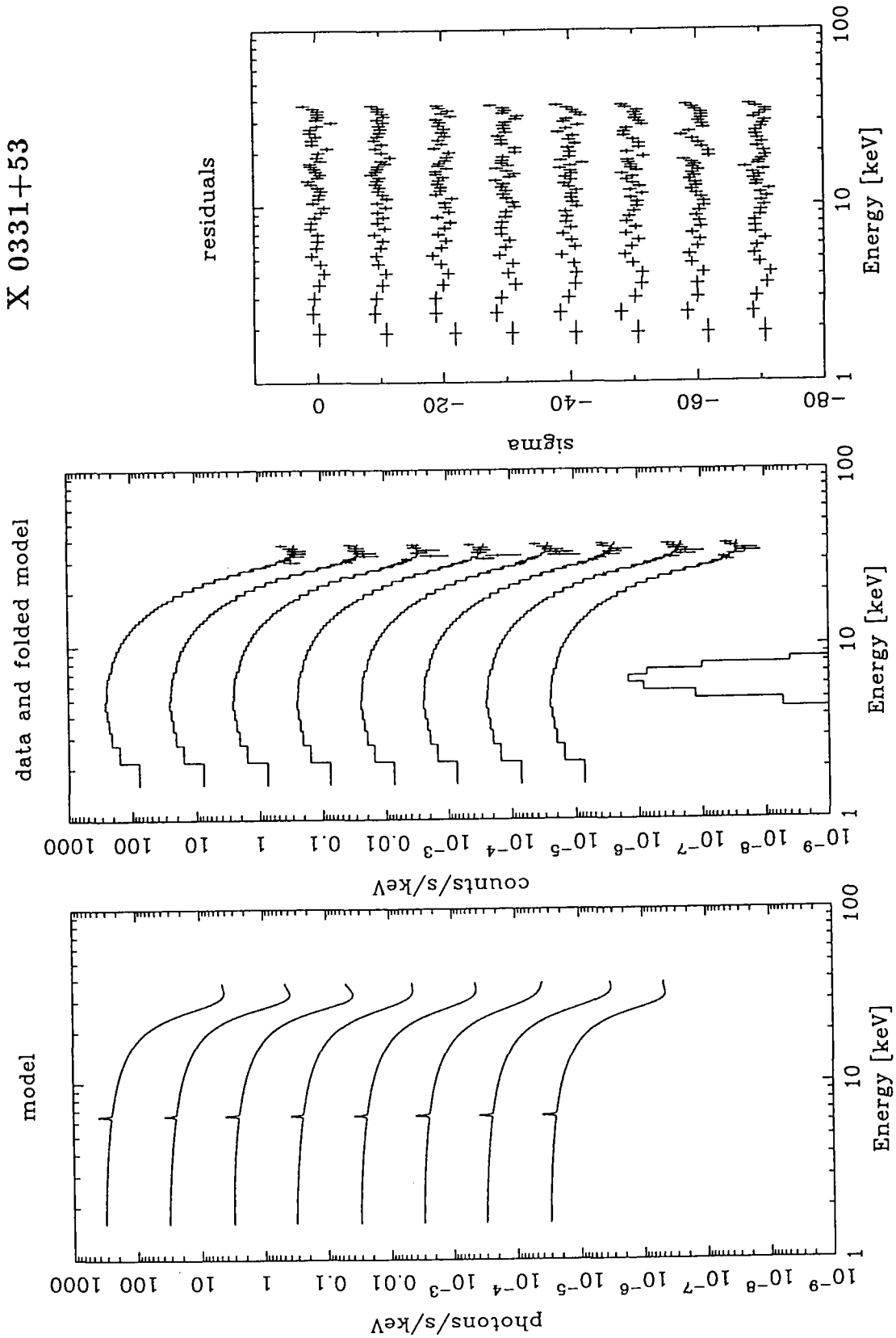

Figure 5.7.7: The NPEX × CYAB fits to the phase resolved spectra on 1989 Sep. 20.

5.7.3 The shape of the structure

The NPEX fit in figure 5.7.2d expresses the overall spectrum of X 0331+53 fairly well, but a close look at the residuals around the cyclotron structure shows a systematic structure. Since the X 0331+53 data has good statistics, it is the best source to investigate the fine structure of the resonance. We limit the energy range to above 9 keV, and use all the data in high and low bit-rate. We apply the CYAB model to describe the cyclotron structure, and the FDCO model or Boltzmann model to describe the continuum instead of the NPEX model, since the NPEX model needs the low energy part to determine the low energy index and it is nearly equivalent to the Boltzmann model in this energy band for this source. Top panels in figure 5.7.8 give the resultant fits, and both models show similar residuals; these are more likely to be caused by inadequate modeling of the resonance rather than that of the continuum.

To improve the fit, we replaced the CYAB factor with the CYA2 model, but the fit does not improve at all. Then we try various models for the fundamental cyclotron structure; Gaussian absorption ($\exp(-Gaus.)$ and $(1 - Gaus.)$), Lorentzian absorption, and Voigt function, which is a sharp intrinsic Lorentzian profile convolved with a Gaussian function due to the Doppler effect of the electrons (Mihalas 1978, Yoshida 1989). However, as shown in figure 5.7.8, most of these are not successful leaving zigzag residuals centered at the resonance. Lorentzian absorption is the best model among them. The $(1 - Gaus.)$ model is good, but this is the 1st order expansion of the $\exp(-Gaus.)$ and physically not meaningful, since the $\exp(-Gaus.)$ fails.

The residuals of CYAB and $\exp(-Gaus.)$ models suggest a sharper resonance at the center. Therefore, we add another sharp Gaussian absorption ($\exp(-Gaus.)$) to the model, where the resonance centers of the two absorptions (energy at the max τ of the CYAB model, and the center energy of the Gaussian model) are constrained to be the same (figure 5.7.8). The fits are improved significantly. The fits are not affected by whether the sharp absorption is Gaussian ($\exp(-Gaus.)$) or Lorentzian. But in the CYAB $\times$ Gaussian fit, the Gaussian broadens and the CYAB represents the sharp resonance.

The two absorption model also gives a good fit to the normal-HV data. Figure 5.7.9a shows the Boltzmann $\times$ CYAB fit, which leaves systematic residuals similar to those in the reduced HV mode. Adding a sharp gaussian absorption flattens the residuals very well (figure 5.7.9b). In particular, it fits the rising part at the high energy end well. Contrary to the reduced-HV case, the CYAB remains wide and the Gaussian represents the sharp resonance.

Therefore, to fit the the spectrum of X 0331+53, Lorentzian absorption, CYAB $\times$ sharp absorption, or Gaussian absorption ($\exp(-Gaus.)$) $\times$ sharp absorption are suitable. The comparisons with other pulsars will be discussed in Chap. 6.2.

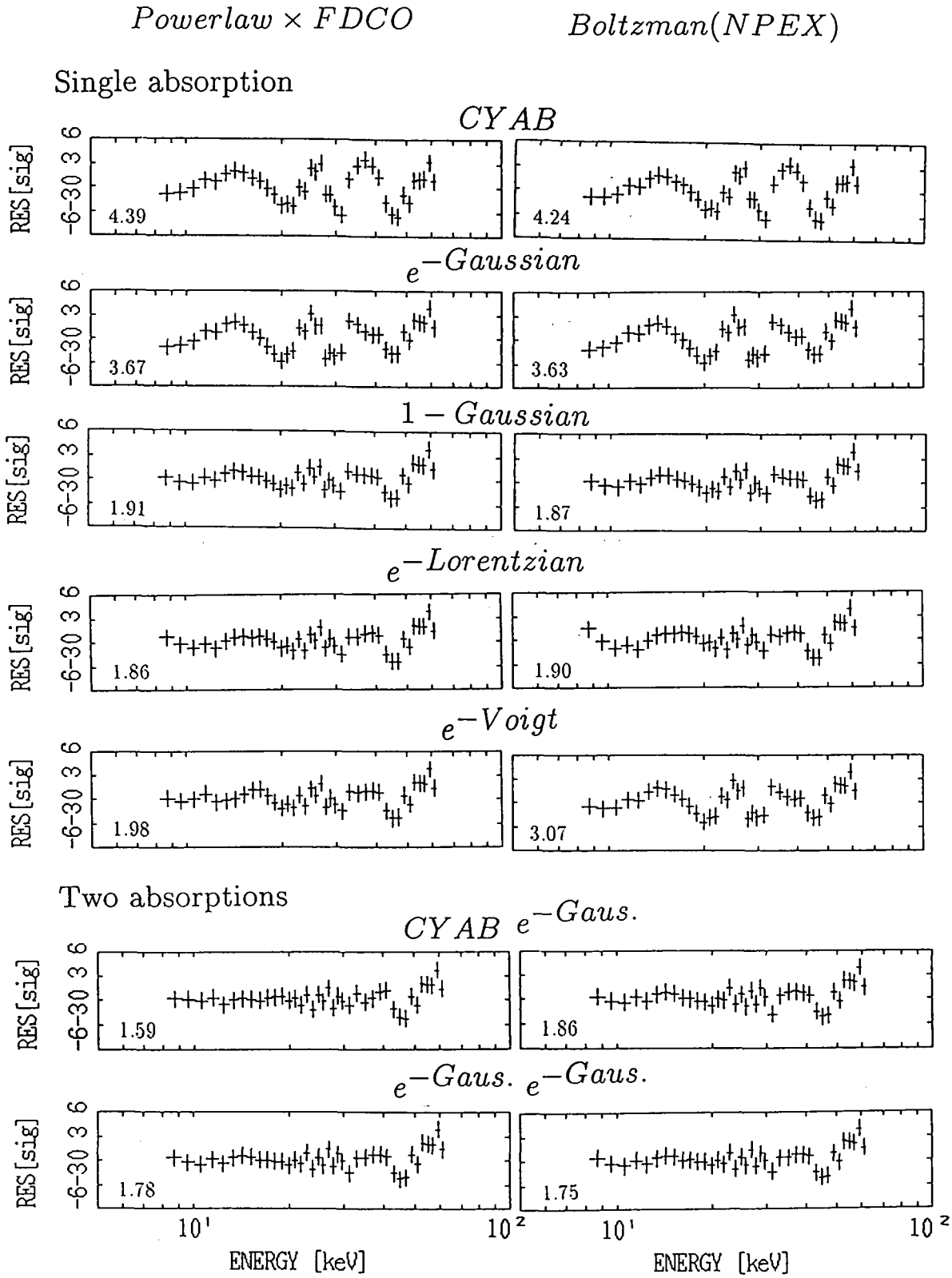

Figure 5.7.8: Fit residuals in 9–60 keV by the various resonance models with the FDCO and the Boltzmann models as the continuum. All the reduced-HV data, taken in both low and high bit-rates, are summed to maximize the statistics. The χ^2_ν of the fits are written in the figures.

Table 5.7.2: Parameters of various model fittings for the resonance of X0331+53 in figure 5.7.8. FDCO (F) or Boltzmann (B) are used as a continuum.

model		Resonance Ea [keV]	Lore. Width Γ [keV]	Gaus. Width W, σ [keV]	Depth D	χ^2_ν
CYAB	F	$29.0^{(a)}$ ±—	5.8 ±—		1.54 ±—	4.39
	B	$29.0^{(a)}$ ±—	5.8 ±—		1.55 ±—	4.24
exp(−*Gaus.*)	F	29.3 ±—		4.4 ±—	14.1 ±—	3.67
	B	29.3 ±—		4.4 ±—	14.4 ±—	3.63
(1 − *Gaus.*)	F	29.2 ±0.2		5.4 ±0.3	10.3 ±0.6	1.91
	B	29.2 ±0.2		5.5 ±0.3	10.5 ±0.6	1.87
exp(−*Loren.*)	F	29.2 ±0.2	5.5 ±0.4		28.5 ±3.1	1.86
	B	29.2 ±0.2	5.4 ±0.3		28.6 ±2.3	1.90
exp(−*Voigt*)	F	29.2 ±0.2	4.9 ±0.3	1.3 ±0.4	26.4 ±1.8	1.98
	B	29.3 ±0.2	1.2 ±3.4	3.8 ±1.1	16.6 ±10.3	3.07
CYAB	F	$29.6^{(a)}$ ±0.2	11.8 ±1.3		1.2 ±0.4	1.59
exp(−*Gaus.*)				3.1 ±0.4	6.9 ±2.3	
	B	$29.1^{(a)}$ ±0.2	2.6 ±1.3		0.6 ±0.2	1.86
				5.1 ±0.4	12.1 ±2.0	
exp(−*Gaus.*)	F	29.2 ±0.2		5.2 ±0.8	13.0 ±1.3	1.78
exp(−*Gaus.*)				2.2 ±0.7	2.5 ±1.9	
	B	29.2 ±0.2		5.2 ±0.5	13.4 ±1.2	1.75
				2.2 ±0.7	2.4 ±1.6	

model		Cut Off E. Ec [keV]	e-folding E. Ef, kT [keV]	Norm. A [ph/s/keV]	index α
CYAB	F	−2.3 ±—	7.3 ±—	1980 ±—	−0.5 ±—
	B		6.9 ±—	1310 ±—	0.79 ±—
exp(−*Gaus.*)	F	−0.5 ±—	6.5 ±—	1800 ±—	−0.5 ±—
	B		6.1 ±—	1567 ±—	0.90 ±—
(1 − *Gaus.*)	F	1.9 ±23.7	6.5 ±1.5	1400 ±4200	−0.5 ±1.4
	B		5.9 ±0.2	1643 ±70	1.0 ±0.1
exp(−*Loren.*)	F	8.5 ±6.7	6.5 ±0.4	770 ±440	−0.4 ±0.5
	B		5.5 ±0.1	2087 ±96	1.3 ±0.1
exp(−*Voigt*)	F	4.3 ±14.0	6.2 ±1.0	1170 ±2000	−0.7 ±1.1
	B		6.0 ±0.8	1640 ±508	1.0 ±0.6
CYAB exp(−*Gaus.*)	F	24.4 ±7.4	6.6 ±1.0	368 ±51	0.25 ±0.22
	B		6.0 ±0.2	1618 ±82	1.0 ±0.1
exp(−*Gaus.*) exp(−*Gaus.*)	F	2.8 ±27.4	6.5 ±1.7	1230 ±4210	−0.5 ±1.7
	B		5.9 ±0.2	1658 ±84	1.1 ±0.1

(a): The energy at the maximum τ.

In the CYAB and exp(−*Gaus.*) fits, the errors of the parameters are not certain because of large χ^2. If Ec is fixed to 0.0, it is identical to the Boltzmann fits.

The unit of the normalization of the power law is [photons/s/keV] at 10 keV.

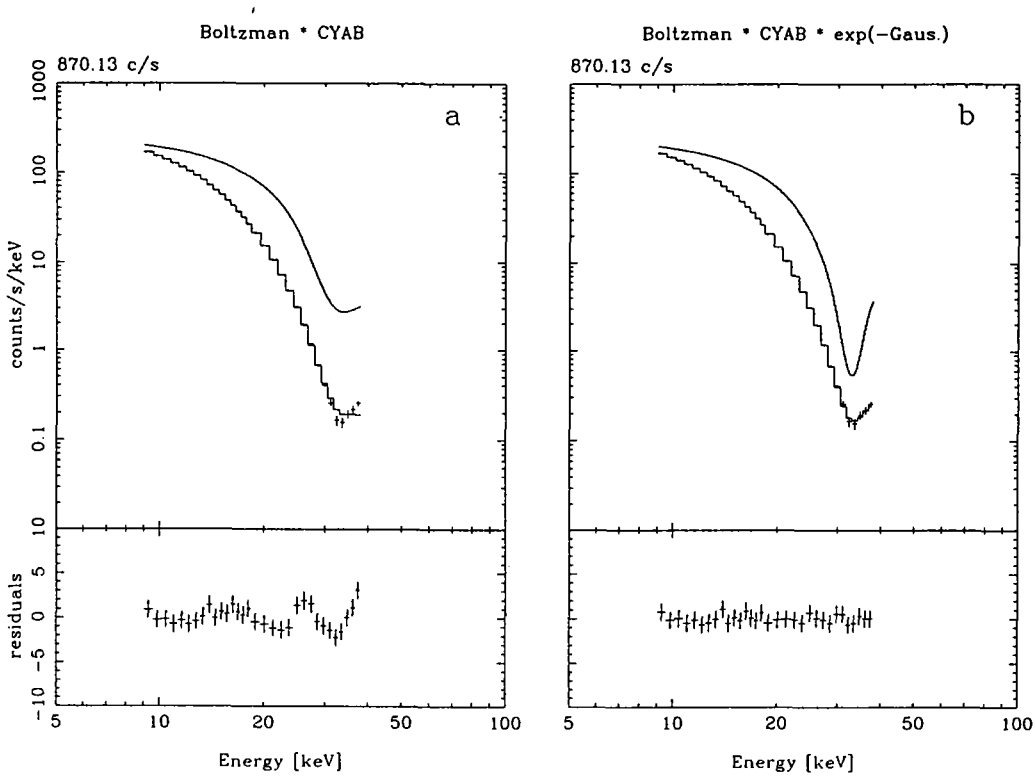

Figure 5.7.9: Fitting the cyclotron structure in the normal HV mode. *a*: Boltzmann × CYAB model, *b*: Boltzmann × CYAB × narrow gaussian absorption model.

Table 5.7.3: Parameters of fittings of the cyclotron structure in the normal HV mode. Boltzmann × CYAB × narrow gaussian absorption model improve the fits.

model	Cyclotron scattering			Boltzmann			χ^2_ν
	Resonance	Width	Depth	e-folding	Norm.	index	
	$Ea'^{(a)}$	σ, Γ	D	kT	A	α	
	[keV]	[keV]		[keV]	[ph/s/keV]		
CYAB	32.3 ±1.0	7.7 ±1.2	2.2 ±0.5	8.6 ±0.4	627 ±270	0.66 ±0.50	1.64
CYAB	32.9 ±0.2	10.1 ±0.5	2.4 ±0.3	15.8 ±4.1	379 ±59	0.18 ±0.17	0.28
exp(−*Gaus.*)		2.4 ±0.3	12.3 ±6.7				

(a): The energy at the maximum τ is used here to deal equally with the gaussian absorption. The unit of the normalization of the power law is [photons/s/keV] at 10 keV.

5.8 Vela X-1

The averaged spectrum and the Crab ratio of Vela X-1 are shown in figure 5.8.1 after subtracting background taken in the day following the on-source observation. The spectrum starts deviating from a power-law above $\sim$ 20 keV, and falls off steeply above $\sim$ 40 keV, in agreement with published results (e.g. White *et al.* 1983). The lack of high energy flux above $\sim$ 40 keV is obvious in the spectrum when it is compared with the spectra of the Crab nebula (figure 3.2.4). No particular feature is, however, recognized in the spectrum except for the iron K-emission line at 6.4 keV and an instrumental Xe K-edge feature at $\sim$ 35 keV, the latter being canceled out in the ratio to the Crab spectrum.

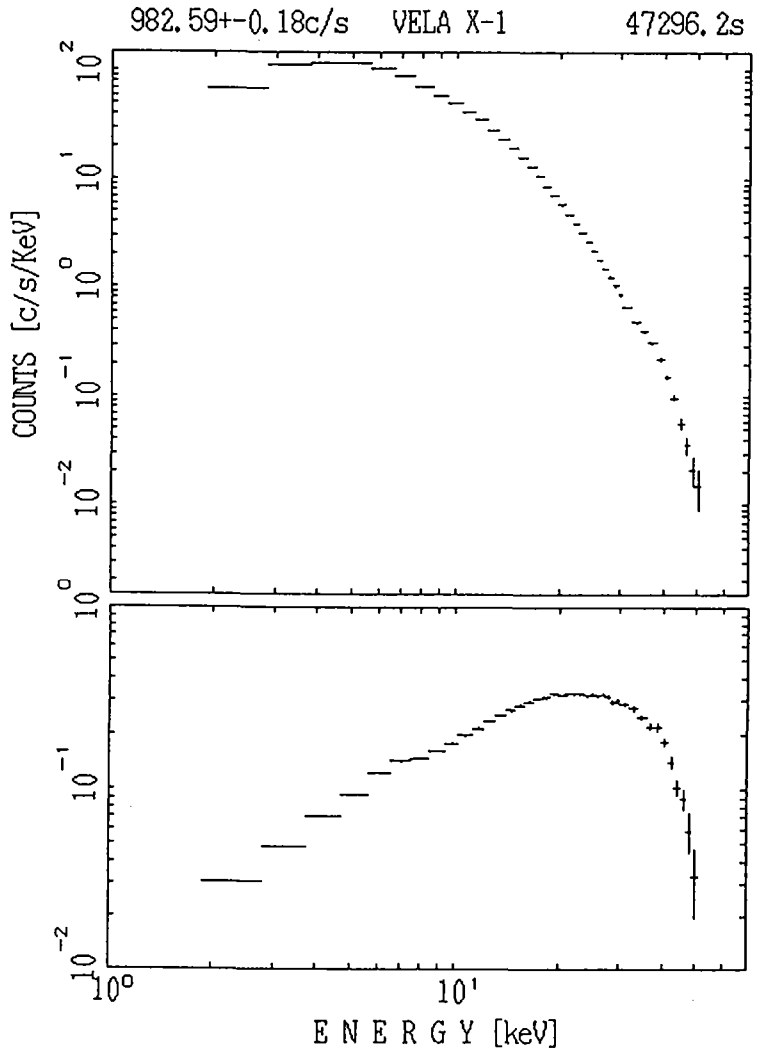

Figure 5.8.1: The averaged spectrum and the Crab ratio of Vela X-1.

We have applied the FDCO fit to the spectrum to search for small but significant deviations from the smooth curve (figure 5.8.2a). Two dips appear in the residuals at $\sim$ 25 keV and $\sim$ 50 keV, which might be considered as the first and the second cyclotron structures. This prompted us to apply the power law $\times$ CYA2 model above 9 keV (figure 5.8.2b), and the two dips were mostly removed. The best-fit parameters indicate the resonance energy of 25.5 keV and the width of 10.3 keV. However, the depth of the 50 keV feature $D_2 = 3.0$, which is >10 times larger than the 25 keV one ($D_1 = 0.24$). We later come back to this issue. Even when we expand the CYA2 model to the overall energy band, the fit remains acceptable ($\chi^2 = 1.04$) but shows wavy residuals (figure 5.8.2c). The NPEX model with CYA2 can fit the spectrum much better (figure 5.8.2d). The width of the resonances becomes smaller and cyclotron structures are localized, while the global fall off is explained by the e-folding energy kT=6.5 keV. The depth of the second harmonic is $D_2 = 0.8$, which is still >10 times larger than the first one ($D_1 = 0.07$), but the absolute difference in exp(−depth) becomes smaller.

Figure 5.8.3 *left* is the Crab ratios of the spectra resolved by the pulse phase into 8 phases, while figure 5.8.3 *right* shows residuals from the best-fit NPEX model without including the cyclotron resonance factor. The two structures detected in the averaged spectrum are mostly present throughout the pulse phase, becoming most prominent in phase 1, 7, 8, which correspond to the main peak. The 25 keV feature appears in the energy-sorted pulse shapes as the lack of flux in 23–30 keV (figure 4.4.4c). The depths of the first and the second harmonics are not always correlated. In phases 2–5 only the second harmonic is observed, whereas in phases 6 and 7 the fundamental is prominent.

Figure 5.8.4 show the NPEX fits for the phase-resolved spectra with the CYA2 model, and the fit parameters are listed in table 5.8.1. We fixed the width of the resonance when it coupled with other parameters and could not be well determined. In all phases the fits are acceptable and the fundamental resonance energy ranges between 22–26 keV. From the successful fits of the two dips in harmonic relation, we can conclude that these dips are the fundamental and the second harmonics of the cyclotron resonance.

We remark that a cyclotron structure was reported at $\sim$ 54 keV independently by Kendziorra *et al.* (1992) in *HEXE* data. The energy and the depth of the cyclotron resonance are consistent with the 50 keV dip found in the *Ginga* observations. The cyclotron feature was detected at the same phase that *Ginga* detected the 50 keV feature most significantly. From these results, we conclude that the 54 keV feature observed with the *HEXE* is the same second harmonic as we have discovered.

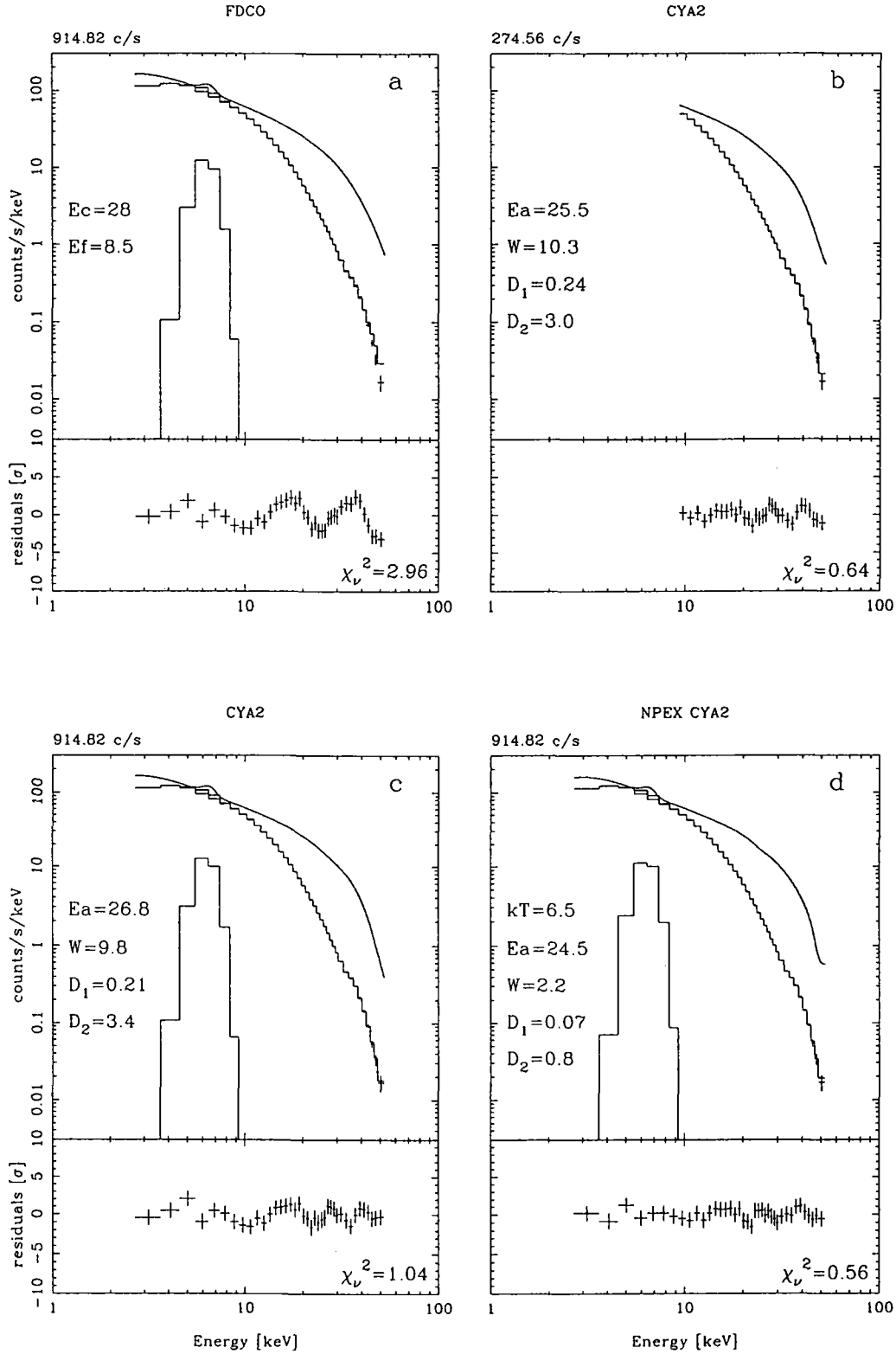

Figure 5.8.2: Model fitting to the averaged spectrum of Vela X-1. *a*: 2–52 keV with FDCO. *b*: 9–52 keV with Power law × CYA2. *c*: 2–52 keV with Power law × CYA2. *d*: 2–52 keV with NPEX × CYA2.

Table 5.8.1: Parameters of the NPEX × CYA2 fits of Vela X-1.

Pulse Phase	Resonance Ea_1 [keV]	Width W_1 [keV]	Depth D_1	Depth D_2	Iron line Flux I_{Fe}[ph/s]	χ^2_ν
ave.	24.5 ± 0.5	2.2 ± 1.0	0.065 ± 0.015	0.80 ± 0.26	26.6 ± 3.1	0.56
1	24.2 ± 0.4	3.55 ± 1.46	0.14 ± 0.03	0.9 ± 0.2	31.7 ± 4.9	0.84
2	24.0 ± 1.8	2.17 fixed	0.03 ± 0.03	0.8 ± 0.7	23.5 ± 3.4	0.99
3	23.7 ± 1.5	1.39 ± 2.18	0.02 ± 0.02	0.8 ± 0.8	23.8 ± 2.5	0.51
4	23.7 ± 1.8	3.44 ± 4.42	0.03 ± 0.03	0.4 ± 0.2	28.9 ± 3.5	0.67
5	24.3 ± 1.4	2.17 fixed	0.01 ± 0.02	0.8 ± 0.5	28.2 ± 3.4	0.64
6	22.4 ± 1.1	2.86 ± 3.17	0.07 ± 0.05	1.4 ± 0.8	23.4 ± 2.7	0.99
7	24.2 ± 0.5	2.15 ± 1.34	0.13 ± 0.03	1.9 ± 1.2	27.3 ± 3.5	0.66
8	25.9 ± 0.5	3.55 fixed	0.17 ± 0.03	0.6 ± 0.5	30.4 ± 4.6	0.85

pulse phase	Negative power law Norm. A_1	index α_1	Positive Norm. A_2	Exponential Folding E. kT [keV]	Absorption $\log_{10} N_H$ [cm^{-2}]
ave.	171 ± 4	0.61 ± 0.05	123 ± 8	6.4 ± 0.1	22.41 ± 0.06
1	227 ± 13	0.28 ± 0.06	46 ± 14	8.6 ± 0.7	21.77 ± 0.32
2	140 ± 3	0.76 ± 0.06	73 ± 7	6.6 ± 0.2	22.45 ± 0.08
3	173 ± 3	0.33 ± 0.04	79 ± 11	6.5 ± 0.2	22.28 ± 0.09
4	164 ± 4	0.58 ± 0.06	132 ± 21	6.9 ± 0.4	22.48 ± 0.07
5	151 ± 4	0.76 ± 0.06	174 ± 8	6.4 ± 0.1	22.48 ± 0.06
6	101 ± 6	0.97 ± 0.07	79 ± 22	6.1 ± 0.6	22.54 ± 0.07
7	201 ± 7	0.72 ± 0.05	96 ± 15	6.2 ± 0.3	22.48 ± 0.06
8	214 ± 8	0.54 ± 0.08	234 ± 22	5.8 ± 0.1	22.39 ± 0.09

The index of the positive power law α_2 is fixed to 2.0.
The unit of the normalization of the power law is [photons/s/keV] at 10 keV.
The widths of the iron line are fixed to $\sigma = 0.5$ keV (broad). The best fit energy of the iron line in the average spectrum is 6.52 ± 0.09 keV, and those of the phase resolved spectra are fixed to that value.

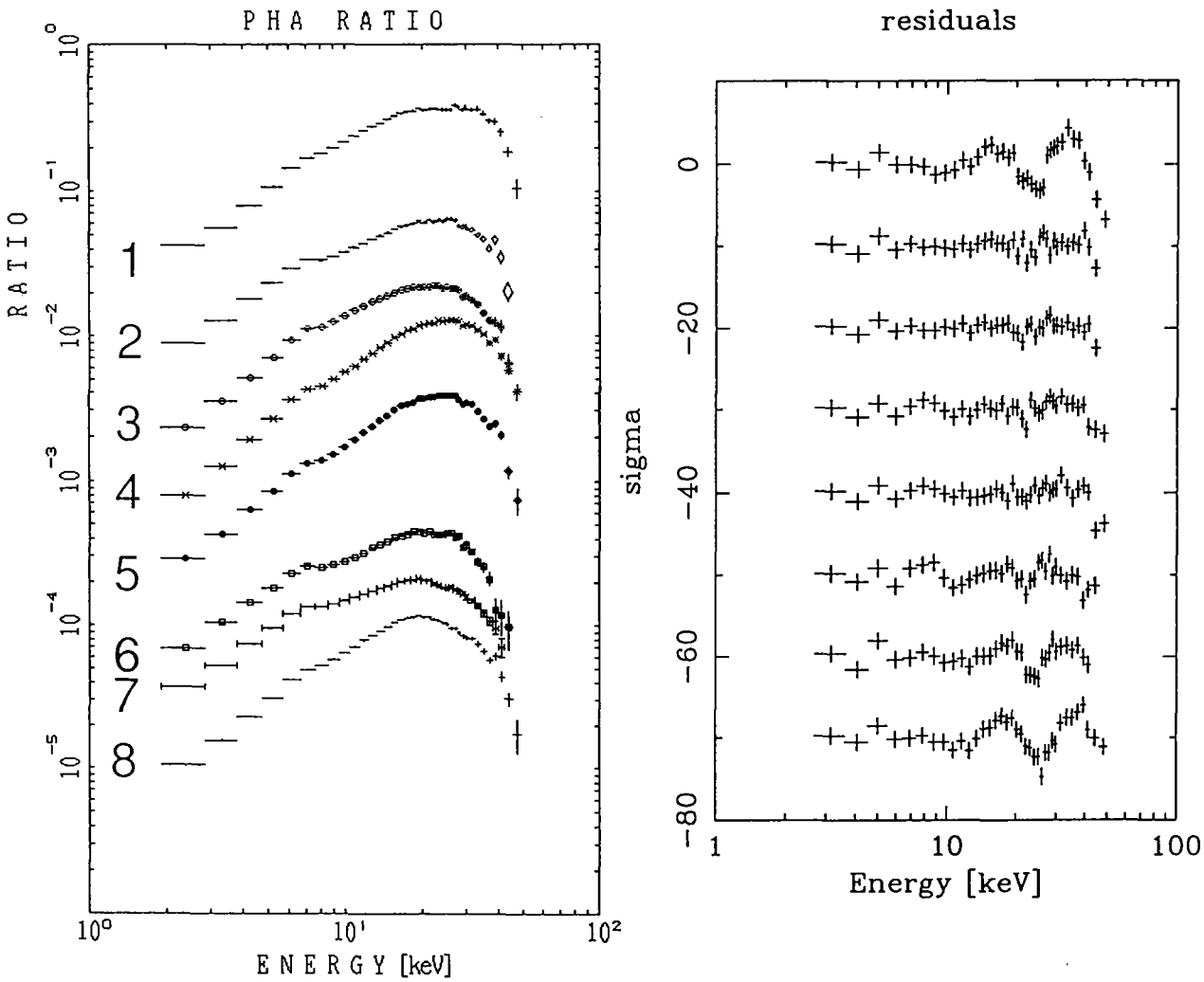

Figure 5.8.3: The Crab ratios and the residuals from the NPEX model of the phase resolved spectra of Vela X-1. The fit model does not involve any cyclotron resonance factor.

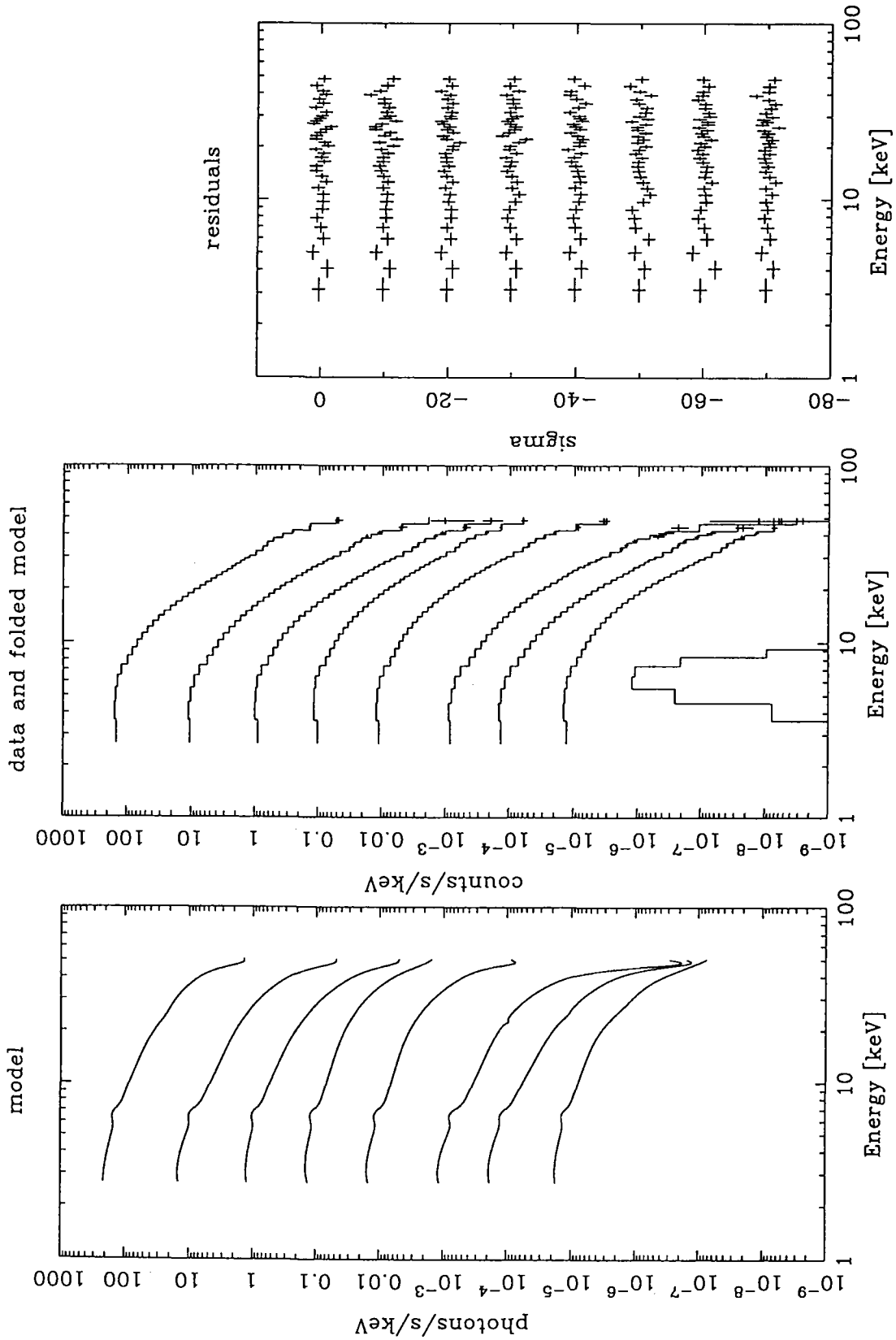

Figure 5.8.4: The NPEX × CYA2 fits to the phase resolved spectra of Vela X-1.

5.9 GX 301-2

5.9.1 The averaged spectrum

The spectra and the Crab ratios of GX 301-2 obtained in the two observations are shown in figure 5.9.1, where the data from the 1991 March observation are shifted downward by a factor ten. Since GX 301-2 is right on the Galactic plane $(l,b) = (300.1, -0.1)$, the spectrum is contaminated by the Galactic ridge emission. Background from the same galactic latitude is desirable, but due to the attitude limits of the satellite, the background data were taken on the successive days at $(l,b) = (299.0, -3.8)$ in 1990 and (301.4, 2.9) and (304.6, 4.0) in 1991, where the ridge emission is significantly lower than the on-source position. Therefore we did not fully subtract the ridge emission. However, it is much softer and weaker then GX 301-2 itself above 10 keV where our interest lies. The spectrum of GX 301-2 falls rapidly at low energies due to large photoelectric absorption. A strong iron line at $\sim$ 6.4 keV has been observed, which has been inferred to be as the fluorescent iron K-line from the absorber. The Crab ratio reaches its maximum at around 20 keV, 60 % of the Crab, and falls exponentially toward higher energies. The bottom figure is the PHA ratio between the two observations. The count rate in the whole energy band is 757c/s in the 1990 data, and 995c/s in the 1991 data. However, the difference is mainly caused by the absorption, as $\log_{10} N_H = 23.59$ in 1990 and 23.24 in 1991. The spectral difference between the two observations is small in the high energy band, and therefore, the two observations are added together to get good statistics (figure 5.9.1).

We fitted the spectrum above 10 keV with the FDCO model including photoelectric absorption, because the large column density of GX 301-2 affects the spectrum even above 10 keV. The overall fit is good ($\chi^2 = 0.98$, figure 5.9.2a), but the residuals show a shallow dip at 40 keV, which is suggestive of the cyclotron structure.

To investigate the significance of this feature we resolved the spectra into 8 pulse phases in each year. Figure 5.9.3 is their PHA ratios to the best-fit FDCO model for the average spectrum summed from both observations (figure 5.9.2b). In the lower panels of figure 5.9.3, the pulse profiles in 16–36 keV are shown. The pulse profile consists of a larger peak and a smaller peak in 1990, and two peaks with almost the same height in 1991. Such changes of the pulse profiles have been reported from GX 301-2, for example from comparing the pulse profiles in White *et al.* (1983) and Tashiro *et al.* (1991). We defined the phase 0 epoch at the larger peak in 1990. The varying feature is clearly seen at $\sim$ 40 keV, and is obvious in phases 1, 2, and 3 (figure 5.9.3 left). Phase 0 in 1991 is chosen at the one of the two peaks where the dip is observed more clearly (figure 5.9.3 center). The 40 keV dip is also clear in phases 1, 2, 3, and 4. The significant detections in the two observations make the dip feature very confident. Therefore we conclude the 40 keV dip is a cyclotron structure. The two sets of the phase-resolved spectra are summed in phase

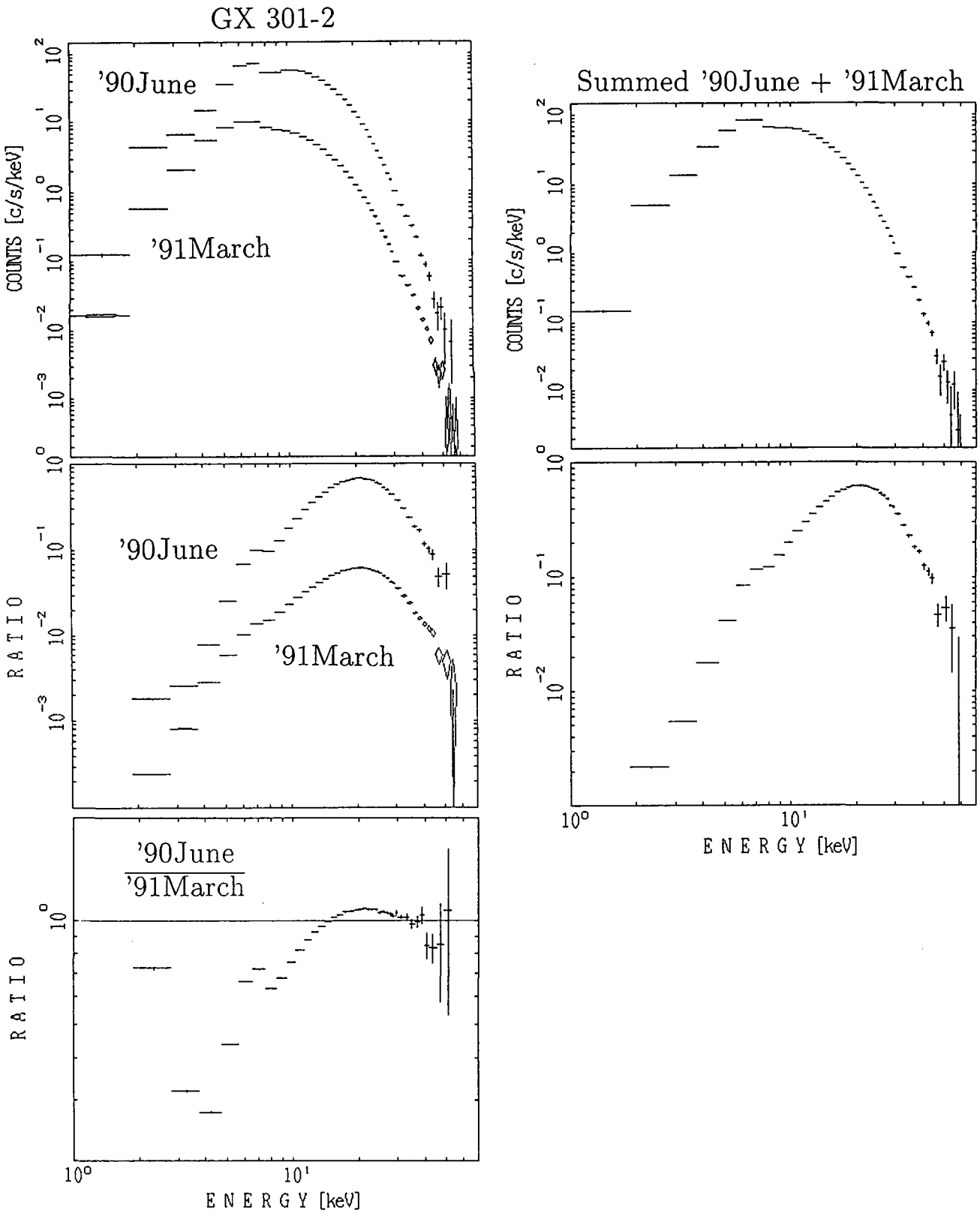

Figure 5.9.1: The averaged spectra and their Crab ratios of GX 301-2. The spectrum and ratio of 1991 March observation are shifted downward by a factor of ten.

and used for the analysis (figure 5.9.3 right).

We fit the average spectrum with the CYAB model. The fit is improved with $\chi^2_\nu = 0.73$ (figure 5.9.2b), but the CYAB parameters have been determined so as to explain the global exponential fall off rather than the 40 keV feature. The values of $E_a = 37.0 \pm 0.9$ keV and the width $W = 37 \pm 4$ keV mean that the cross section of the CYAB function has the maximum at 74 keV, and the sharp feature at 40 keV is not modeled, and becomes smaller but is still visible in the residuals. Furthermore, the fit cannot be extended successfully to the lower energy range including the iron line.

We can replace the FDCO or the above CYAB models with the NPEX model representing exponential continuum in 3.5–60 keV (figure 5.9.2c). However the data require the index of the positive power law α_2 to be free to vary. The clear 40 keV feature is fit with the CYAB factor successfully with $\chi^2_\nu = 0.57$ leaving very flat residuals (figure 5.9.2d). Since the width W and the depth D are not well determined, we fix $W = 16.4$ keV in order to get errors. The index α_2 approaches 2.0 when the CYAB factor is included, but is still larger than 2.0. We will discuss on this problem later.

We perform fitting of the phase resolved spectra using the NPEX model (α_2 free) without CYAB factor (table 5.9.1 and the residuals in figure 5.9.4). The fits are acceptable in the phases 3–8, but not acceptable in phases 1 and 2 mostly because of the dip feature. When the CYAB model is included in phases 1–4, all the fits are improved and become acceptable (figure 5.9.5, table 5.9.2). The positive index α_2 is generally smaller than those obtained without CYAB, but it is still significantly larger than 2.0 in some phases.

We have successfully fit the spectra of other pulsars with fixed $\alpha_2 = 2.0$, which represents the Wien peak and therefore is physically meaningful. So we searched for a possible model with $\alpha_2 = 2.0$. The most probable way is by introducing the leaky absorber model which has been often applied to GX 301-2 and Vela X-1 (eg. Nagase 1986). A heavy absorption by the column density N_H has been included in the fittings of GX 301-2. However, a single column density may be a too simple assumption, and in fact there would be a mixture of various column densities. We used two column densities representing the continuous distribution (leaky absorber model). This model is the most likely for GX 301-2 compared with any other pulsars, since it has the largest column density among the pulsars. The fits using the NPEX ($\alpha_2 = 2.0$) model with the leaky absorber ($\log_{10} N_H = 23.48$ and 24.77) are shown in figure 5.9.6a. The 40 keV dip is seen in the residuals without being affected by the leaky absorber. Adding the CYAB factor improves the fit as in figure 5.9.6b. We also applied the leaky absorber model to the phase resolved spectra and have obtained acceptable fits with similar χ^2 as in table 5.9.2. Thus by using the leaky absorber model, we can fit the spectra of GX 301-2 with the same NPEX $\times$ CYAB model with $\alpha_2 = 2.0$, keeping the physical meaning of the positive power law.

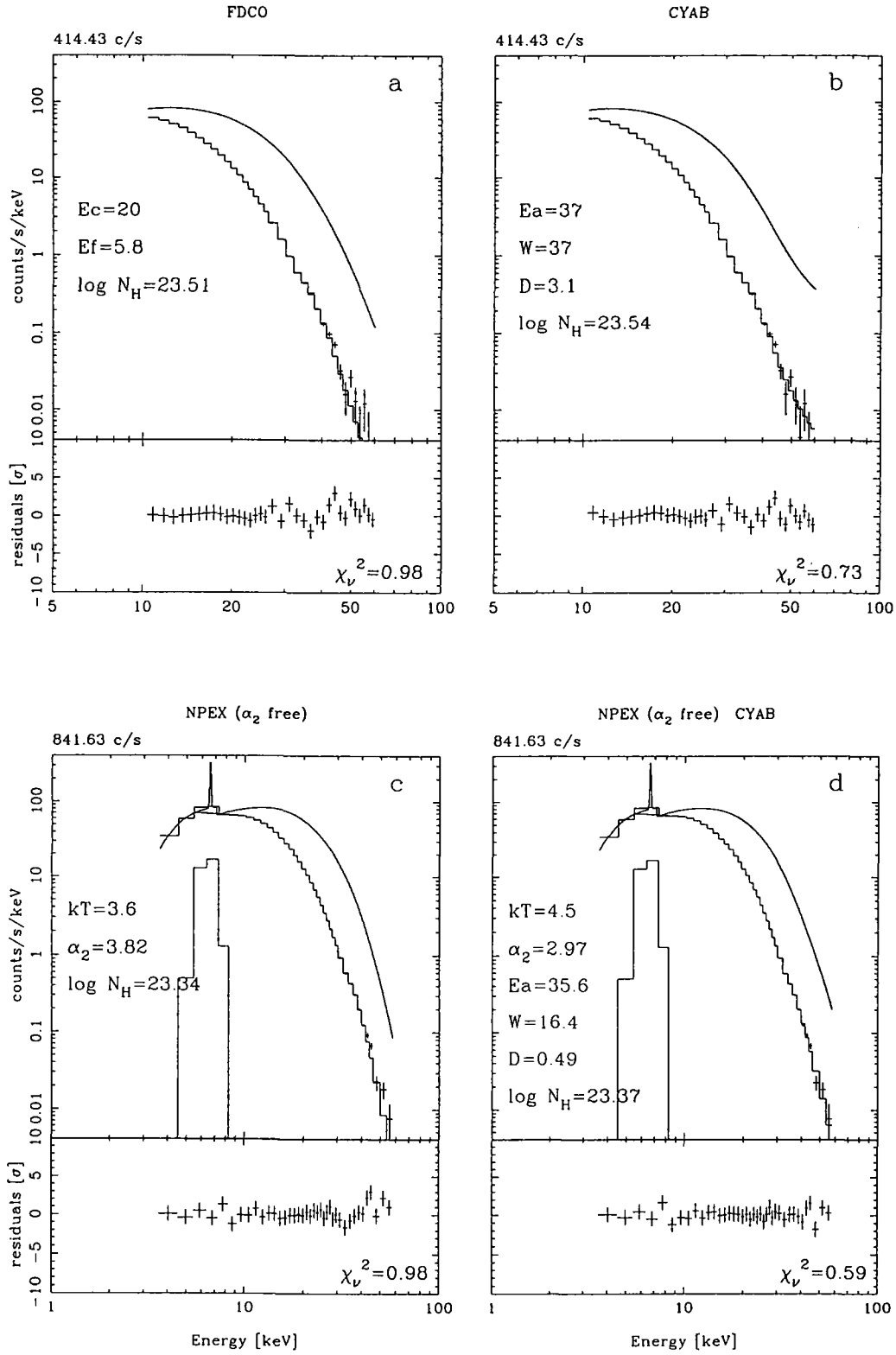

Figure 5.9.2: Model fitting to the average spectrum of GX 301-2 summed over the two observations. *a*: 10–60 keV with FDCO. *b*: 10–60 keV with Powerlaw × CYA2. *c*: 3.5–60 keV with NPEX. *d*: 3.5–60 keV with NPEX × CYAB.

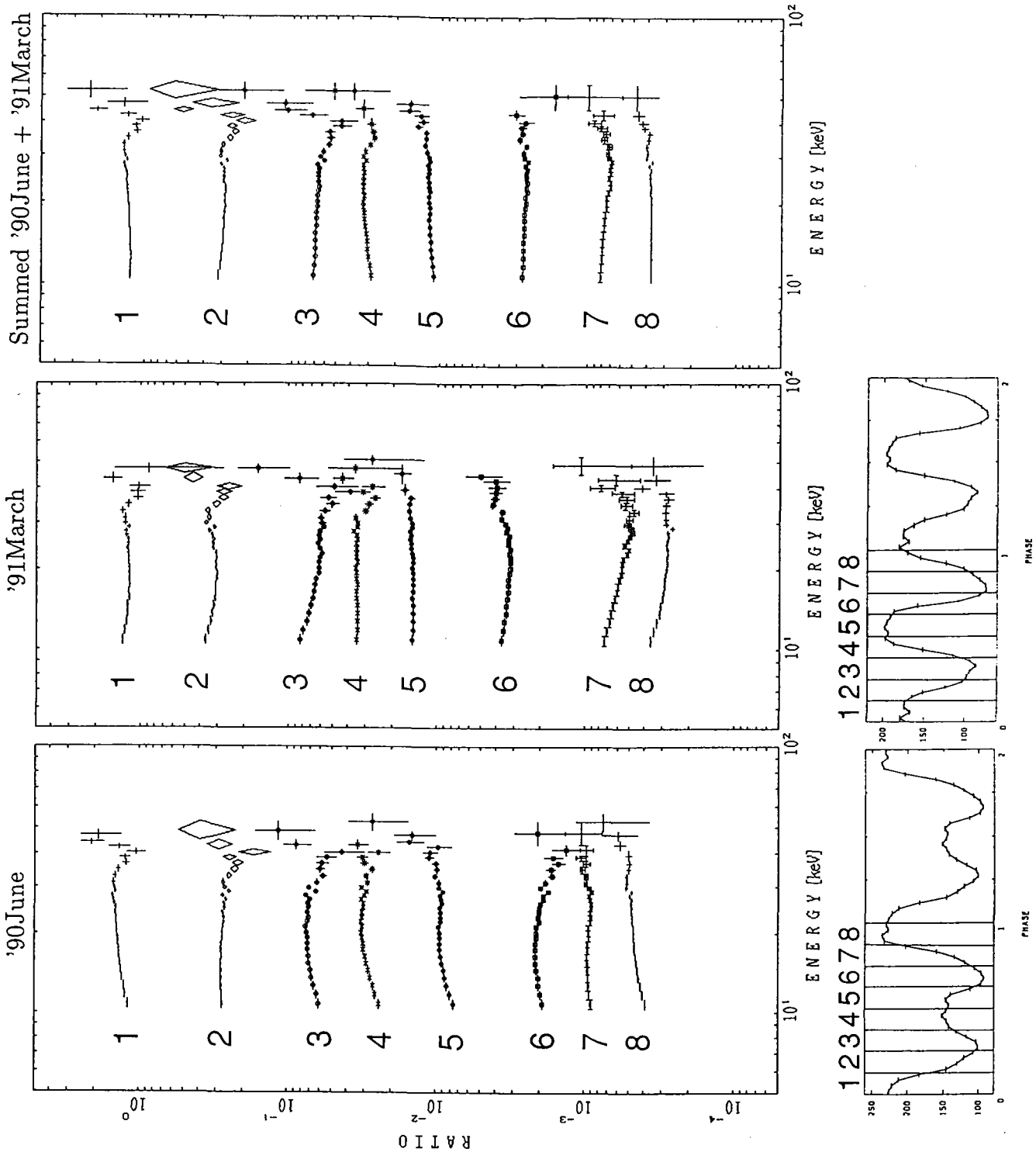

Figure 5.9.3: The Crab ratios and the residuals from the NPEX model of the phase resolved spectra of GX 301-2.

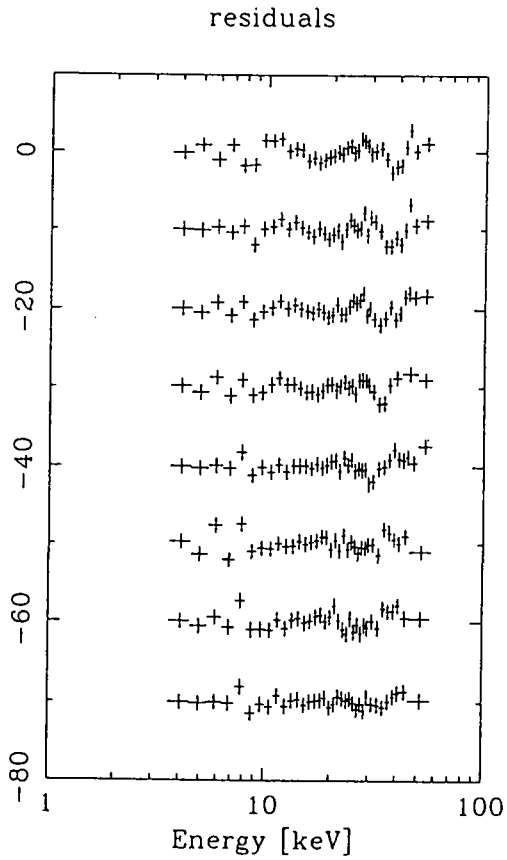

Figure 5.9.4: The residuals of NPEX fit without CYAB factor to the phase resolved spectra of GX 301-2.

Table 5.9.1: Parameters of the NPEX fits of GX 301-2 without CYAB model. The fits will be improved by adding the CYAB model (table 5.9.2).

pulse phase	Negative power law Norm. A_1	index α_1	Positive power law Norm. A_2	index α_2	Exponential Folding E. kT [keV]	Absorption $\log_{10} N_H$ [cm^{-2}]	Iron line Flux I_{Fe}[ph/s]	χ^2_ν
ave.	555 ± 93	-0.25 ± 0.23	1026 ± 30	3.82 ± 0.18	3.6 ± 0.1	23.34 ± 0.04	32.1 ± 3.4	0.98
1	880 ± 207	-0.69 ± 0.31	1303 ± 66	4.24 ± 0.30	3.4 ± 0.1	23.30 ± 0.06	23.0 ± 5.3	1.72
2	893 ± 216	-1.00 ± 0.30	856 ± 55	4.30 ± 0.36	3.4 ± 0.2	23.16 ± 0.07	26.6 ± 4.5	1.51
3	663 ± 140	-0.41 ± 0.28	870 ± 56	4.33 ± 0.30	3.3 ± 0.1	23.34 ± 0.05	37.5 ± 3.4	1.23
4	740 ± 124	-0.41 ± 0.23	1327 ± 57	4.52 ± 0.21	3.2 ± 0.1	23.41 ± 0.04	39.1 ± 3.2	0.99
5	426 ± 97	0.11 ± 0.30	1177 ± 44	3.58 ± 0.21	3.8 ± 0.1	23.40 ± 0.04	33.2 ± 3.8	1.09
6	387 ± 117	-0.20 ± 0.37	821 ± 42	3.50 ± 0.31	3.8 ± 0.2	23.29 ± 0.06	36.2 ± 3.6	1.31
7	303 ± 87	0.60 ± 0.37	801 ± 42	3.03 ± 0.28	4.0 ± 0.2	23.48 ± 0.04	37.1 ± 3.7	1.30
8	593 ± 95	-0.38 ± 0.21	1088 ± 31	3.73 ± 0.18	3.7 ± 0.1	23.27 ± 0.04	21.6 ± 2.9	0.57

The units of the normalization of the power law are [photons/s/keV] at 10 keV.
The energy and the width of the iron line are fixed to 6.60 keV and $\sigma = 0.05$ keV (narrow), respectively.

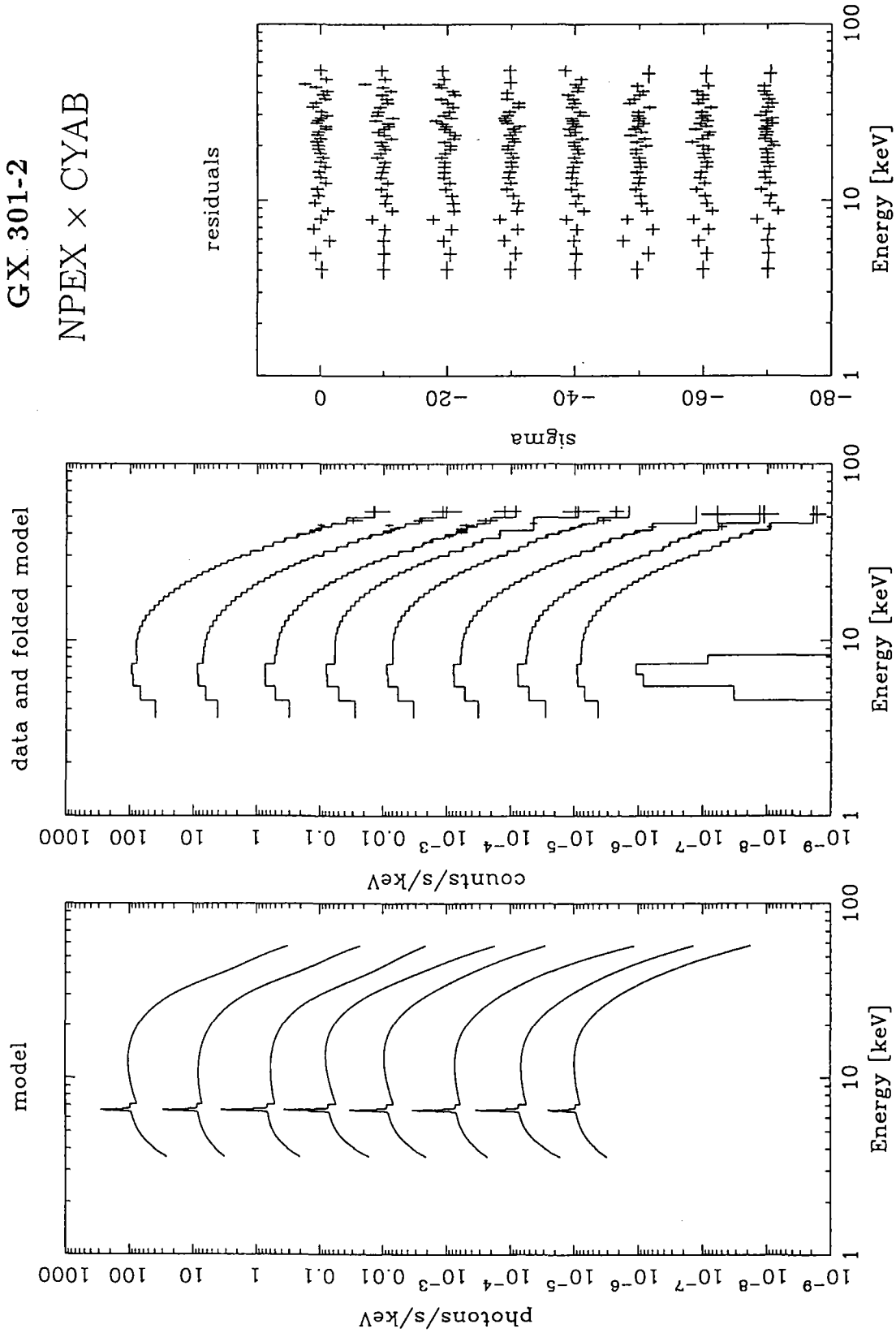

Figure 5.9.5: The NPEX × CYAB fits to the phase resolved spectra of GX 301-2.

Table 5.9.2: Parameters of the NPEX×CYAB fits of GX 301-2. The cyclotron structure is very significant in phases 1, 2, and 3 with large τ. The widths of the resonance are fixed to W = 16.4 keV, the best-fit value for the averaged spectrum.

Pulse Phase	Resonance Ea [keV]	Width W [keV]	Depth D	Iron line Flux I_{Fe}[ph/s]	χ^2_ν
ave.	35.6 ± 1.6	16.4 ± 15.4	0.49 ± 0.80	32.3 ± 2.6	0.59
ave.	35.5 ± 1.4	16.4 fixed	0.48 ± 0.18	32.2 ± 2.6	0.57
1	40.0 ± 1.4	16.4 fixed	1.2 ± 0.3	24.2 ± 3.6	0.81
2	40.0 ± 2.2	16.4 fixed	1.1 ± 0.5	27.6 ± 3.7	1.04
3	36.5 ± 1.5	16.4 fixed	1.2 ± 0.5	38.2 ± 2.9	0.91
4	36.0 ± 1.3	16.4 fixed	0.8 ± 0.3	39.7 ± 2.8	0.73
5	31.4 ± 2.2	16.4 fixed	0.4 ± 0.1	32.7 ± 2.7	0.56
6	22.8 ± 8.5	16.4 fixed	0.2 ± 0.1	35.5 ± 3.5	1.16
7	26.8 ± 3.7	16.4 fixed	0.3 ± 0.1	36.4 ± 2.9	0.76
8	33.7 ± 2.7	16.4 fixed	0.3 ± 0.2	21.6 ± 2.8	0.52

pulse phase	Negative power law Norm. A_1	Negative power law index α_1	Positive power law Norm. A_2	Positive power law index α_2	Exponential Folding E. kT [keV]	Absorption $\log_{10}N_H$ [cm^{-2}]
ave.	269 ± 220	0.36 ± 0.67	659 ± 383	2.97 ± 0.88	4.5 ± 1.4	23.37 ± 0.04
ave.	277 ± 102	0.34 ± 0.38	667 ± 96	3.00 ± 0.39	4.5 ± 0.4	23.37 ± 0.04
1	116 ± 89	1.26 ± 0.81	598 ± 129	2.12 ± 0.57	5.8 ± 1.1	23.41 ± 0.05
2	148 ± 178	0.52 ± 1.06	407 ± 118	2.11 ± 1.04	5.8 ± 1.8	23.26 ± 0.07
3	123 ± 100	1.06 ± 0.77	310 ± 116	2.23 ± 0.86	5.8 ± 1.7	23.42 ± 0.05
4	223 ± 116	0.69 ± 0.54	636 ± 163	3.08 ± 0.56	4.6 ± 0.7	23.46 ± 0.04
5	312 ± 113	0.27 ± 0.39	819 ± 116	3.21 ± 0.38	4.3 ± 0.4	23.39 ± 0.04
6	552 ± 356	−0.64 ± 0.67	747 ± 162	4.00 ± 1.01	3.7 ± 0.5	23.25 ± 0.07
7	315 ± 141	0.38 ± 0.48	596 ± 105	3.10 ± 0.57	4.3 ± 0.5	23.46 ± 0.04
8	392 ± 161	−0.07 ± 0.40	807 ± 138	3.24 ± 0.46	4.3 ± 0.5	23.28 ± 0.04

The unit of the normalization of the power law is [photons/s/keV] at 10 keV.
The energy and the width of the iron line is fixed to 6.60 keV and σ = 0.05 keV (narrow), respectively.

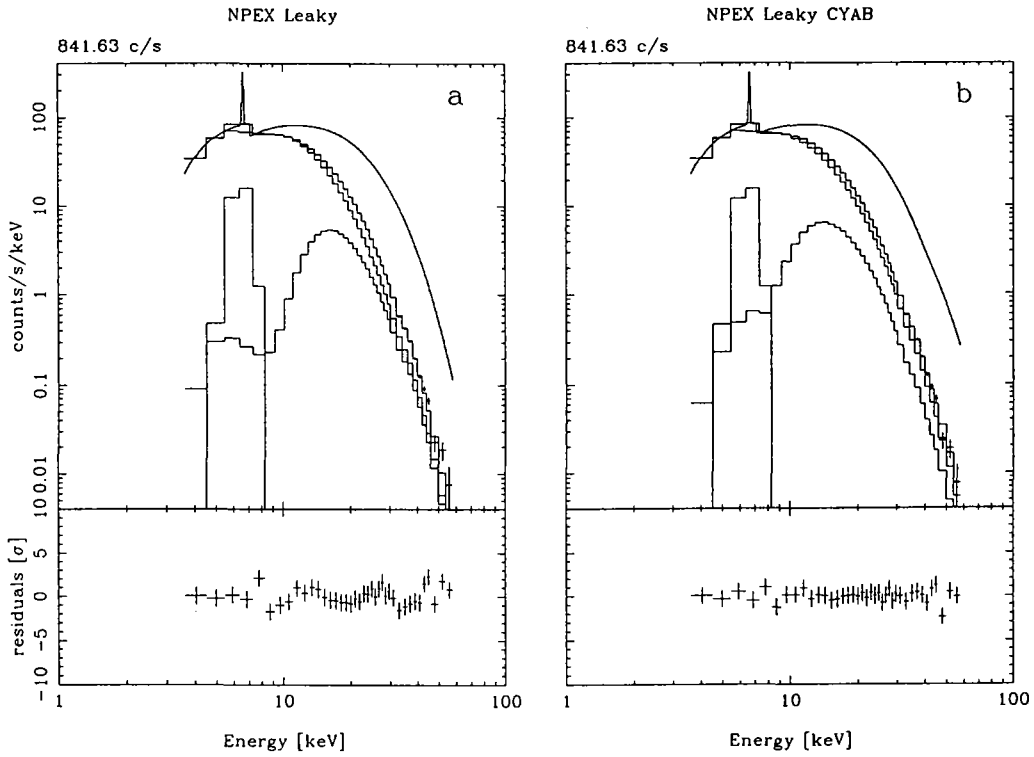

Figure 5.9.6: Model fitting to the averaged spectrum by NPEX (α_2 = 2.0 fixed). Acceptable fits are available using the leaky absorber model. *a*: 3.5–60 keV with NPEX with leaky absorber. *b*: 3.5–60 keV with NPEX × CYAB with leaky absorber.

	Resonance Ea [keV]	Width W [keV]	Depth D	Iron line I_{Fe}[ph/s]	χ^2_ν
a	—	—	—	31.2 ± 3.6	1.16
b	37.6 ± 1.1	16.4 fixed	0.65 ± 0.17	30.6 ± 3.1	0.56

	Negative power law Norm. A_1	index α_1	Positive Norm. A_2	Exponential Folding-e kT [keV]	Absorption$_1$ $\log_{10}N_{H1}$ [cm^{-2}]	Factor	Absorption$_2$ $\log_{10}N_{H2}$ [cm^{-2}]
a	68 ± 16	2.19 ± 0.41	954 ± 66	4.42 ± 0.06	23.48 ± 0.05	0.84 ± 0.10	24.77 ± 0.06
b	135 ± 71	0.80 ± 0.85	485 ± 184	5.4 ± 0.3	23.37 ± 0.07	0.38 ± 0.26	24.44 ± 0.22

(Absorption$_1$ + Factor×Absorption$_2$) is multiplied by the above NPEX model (α_2 = 2.0 fixed).
The width of the resonance is fixed to 16.4 keV.
The unit of the normalization of the power law is [photons/s/keV] at 10 keV.
The energy and the width of the iron line is fixed to 6.60 keV and σ = 0.05 keV (narrow), respectively.

5.10 Possible cyclotron sources

In this section we discuss 4 pulsars as possible cyclotron sources. A 0535+26 is reported to have cyclotron resonance at 50 keV with HEXE instrument. Since it was above the *Ginga* energy range, *Ginga* did not detect the feature. 1E 2259+586 is a 'peculiar' pulsar with a steep power law. *Ginga* detected a varying feature in the spectra, but did not confirm it to be a cyclotron feature, since the significance was not large and the structure was different from the other 'common' cyclotron structures. GS 1843+00 is a transient pulsar with a very low pulse fraction. LMC X-4 is a persistent pulsar, but the pulsation is detected only in the flare state. The spectra of both pulsars are very hard and concave in log-log scale. The cyclotron structures were found in the residuals of the NPEX model.

5.10.1 A 0535+26

The pulse-averaged spectrum of A 0535+26 and its Crab ratio are shown in the left top panel of figure 5.10.1. Although the observation was only 11 minutes, the statistics of the spectrum were very good. The flare was strong as the flux exceeds that of the Crab nebula in 8-37 keV as the ratio shows. The spectrum gradually changes its slope around 20 keV and gets steeper toward high energies. There is an indication of the soft excess below 2 keV. Although the energy band is affected by the absorption of the Be entrance window, the amount of the excess is much larger than background level and therefore significant. We discarded this energy range because our interest is the high energy part. The FDCO model with an iron line gives an acceptable fit above 2 keV ($\chi^2 = 0.50$), which indicates that there is no prominent structure between 2–37 keV. The residuals are shown in the right panel of figure 5.10.1. The CYAB model also gives a good fit ($\chi^2_\nu = 0.52$). However, the width becomes so large ($W = 99$ keV) that the CYAB function represents only an exponentially-falling function. In such a case the obtained resonance energy is not valid.

The left bottom panel of figure 5.10.1 is an efficiency-corrected spectrum taken with the TTM and HEXE instruments on Mir space station on 1989 April 8-14 (cross points, Kendziorra *et al.* 1994) together with the best-fit CYAB model obtained with *Ginga* (solid curve). The spectra from *Ginga* and TTM/HEXE agree well in the 7–37 keV range. The two arrows show cyclotron absorption structures which were reported. The best-fit model in Kendziorra *et al.* (1994) is a power law × ECUT with two narrow (fixed to $W = 2$ keV) absorption features. According to this model, the curve of the spectrum in the *Ginga* band is just a power law with ECUT. However, fitting the *Ginga* data with the ECUT model failed with $\chi^2_\nu = 6.38$ and left wavy residuals shown in figure 5.10.1.

The spectrum would be well described by a power law with the Fermi-Dirac Cut-off function and two absorption features whose widths are narrower than the spectral resolution of scintillation counters. These features are similar to those in the spectrum

of 4U 0115+63 in 1990 February. The NPEX model (without CYAB) is also successful ($\chi^2_\nu = 0.46$) in fitting the global exponential fall off with the positive index fixed to $\alpha_2 = 2.0$ (figure 5.10.1).

Figure 5.10.2 shows the PHA ratios of the phase resolved spectra to the pulse averaged spectrum. Phases 2 and 3 have hollows at 9 keV and 6 keV, respectively. The NPEX fits are shown in figure 5.10.3, and the best-fit parameters are listed in table 5.10.1. The hollows prevent acceptable fits in phases 2 and 3. Most phases show an iron line above the smooth continuum, though the phase 3 has no apparent iron line due to this hollow. Probably, this hollow is not be a cyclotron structure, since it appears only in two pulse-phases and the energies change very much over 1/8 pulse phase.

Table 5.10.1: Parameters of NPEX fits for the averaged and pulse-phase resolved spectra of A 0535+26

pulse phase	Negative power law Norm. A_1	index α_1	Positive Norm. A_2	Exponential Folding E. kT [keV]	Absorption $\log_{10} N_H$ [cm^{-2}]	Iron line Flux I_{Fe}[ph/s]	χ^2_ν
ave.	1504 ± 16	0.20 ± 0.03	736 ± 51	6.91 ± 0.09	21.68 ± 0.13	64 ± 11	0.46
1	1445 ± 32	0.23 ± 0.05	790 ± 116	6.4 ± 0.2	21.64 ± 0.24	59 ± 17	0.97
2	992 ± 46	0.62 ± 0.09	974 ± 118	6.7 ± 0.2	22.25 ± 0.10	114 ± 26	2.45
3	1404 ± 38	0.31 ± 0.03	1111 ± 110	6.6 ± 0.2	15.00 fixed	—	1.92
4	1789 ± 23	0.14 ± 0.03	705 ± 99	6.9 ± 0.2	21.56 ± 0.21	94 ± 17	0.62
5	1496 ± 24	0.14 ± 0.04	520 ± 107	7.1 ± 0.3	21.72 ± 0.19	63 ± 18	1.01
6	1598 ± 26	0.08 ± 0.04	521 ± 118	7.2 ± 0.3	22.03 ± 0.10	73 ± 19	1.02
7	1674 ± 31	0.12 ± 0.04	745 ± 120	7.0 ± 0.2	21.52 ± 0.30	76 ± 20	0.92
8	1450 ± 25	0.17 ± 0.04	601 ± 100	7.3 ± 0.2	21.55 ± 0.28	50 ± 18	0.97

The index α_2 of the positive power law is fixed to 2.0.
The energy of iron line is $E_{Fe} = 6.50 \pm 0.11$ keV for the averaged spectrum and fixed to this value for the resolved spectra.
The units of the normalization of the power law are [photons/s/keV] at 10 keV.
The energy of the iron line is fixed to $\sigma = 0.05$ keV (narrow).

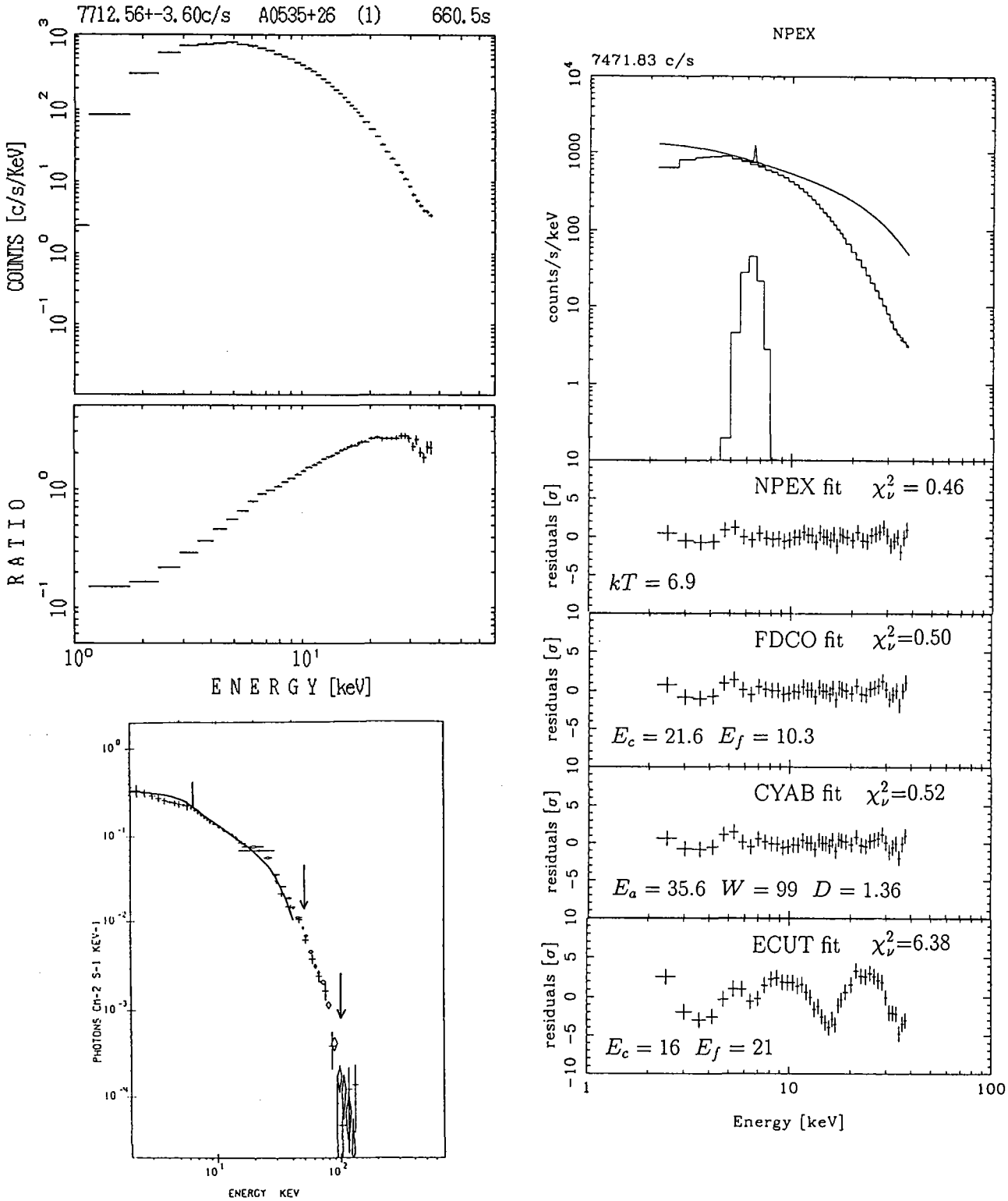

Figure 5.10.1: The left top panel is the averaged spectrum and the Crab ratio of A 0535+26. The right panel is the fit residuals from various models. The left bottom panel is the spectrum with A 0535+26 with TTM/HEXE of the same flare (Kendziorra *et al.* 1992, 1994 and private communication). The best-fit CYAB model with *Ginga* is superposed with the solid curve.

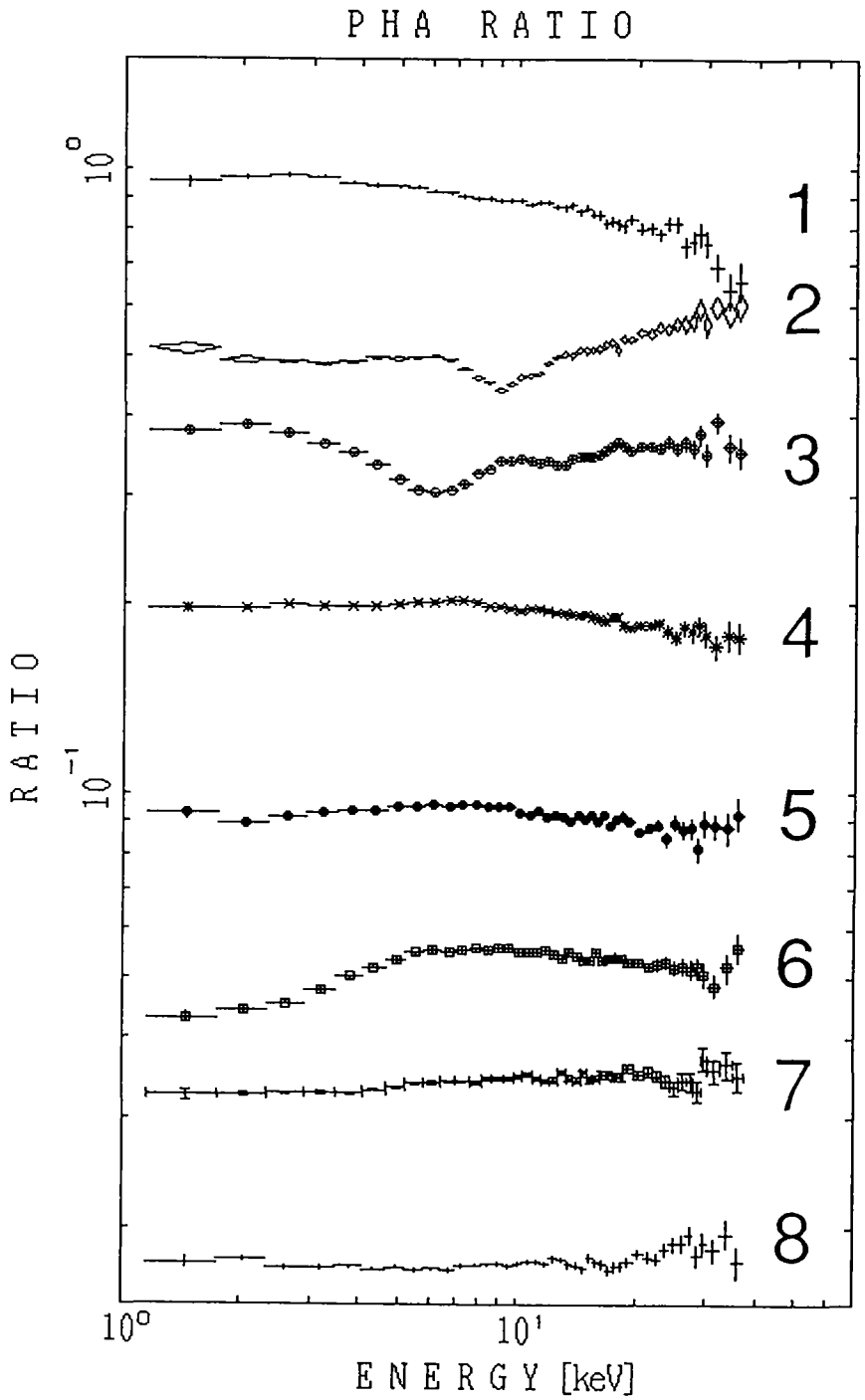

Figure 5.10.2: The PHA ratios of the phase resolved spectra of A 0535+26 to the averaged one. Spectra are shifted downward successively by a factor 0.562 (quarter order) in this figure.

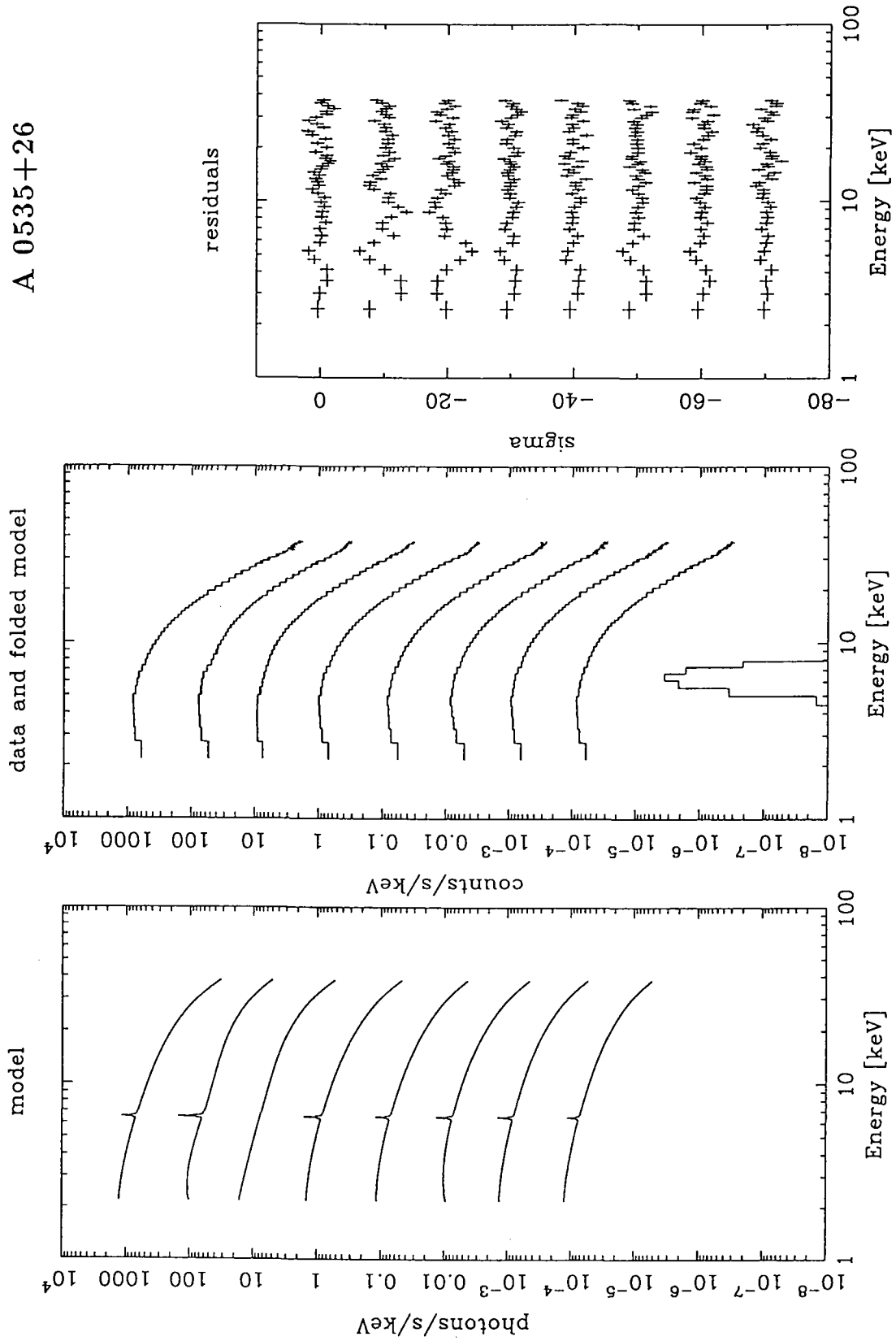

Figure 5.10.3: The NPEX fits to the phase resolved spectra of A 0535+26.

5.10.2 1E 2259+586

Three *Ginga* observations of 1E 2259+586 were analyzed and published by Koyama *et al.* (1989) and Iwasawa *et al.* (1992). Here we first describe their analysis. The pulse averaged spectra are shown in figure 5.10.4. It cannot be described by a single component model due to the structure between 5–10 keV. The rough power law index is 4.0, steeper than the other X-ray pulsars. The hump around 6–8 keV observed in 1987 can be fitted by an emission line with an energy of 7.2 ± 0.1 keV. Since the pulsed component also has the 7.2 keV emission line structure, it must be emitted from the region near the neutron star. The energy of this structure exceeds the iron line energy of any ionization state. In order to investigate the structure in more detail, spectrum is divided into four phases. Figure 5.10.5 is the PHA ratios to the best-fit two power law model. In the spectra from 1989, although the absorption structure at 5–6 keV is seen in all pulse phases, it is most clear in phase 1. In 1990, the dip structure is more complicated and is strongly pulse-phase dependent. Two dips at about 6 and 10 keV are found in phase 3. These structures might be the fundamental and the second harmonics of cyclotron resonant scattering. However, a simple cyclotron model is rejected.

1E 2259+586 is slowly spinning down, but the spin down rate cannot power the X-ray luminosity. Therefore, it is thought to be an accreting binary neutron star. Assuming that the rotation is in the equilibrium (the Alfvén radius = the co-rotation radius) and applying the theory by Ghosh and Lamb (1978, 1979a, b), a magnetic field of $B \sim 5 \times 10^{11}$ G at the surface of the neutron star was derived. If the 7.2 keV emission is the fundamental cyclotron emission, the magnetic field becomes 6×10^{11} G. On the other hand, if the dip at 6 keV is attributed to the cyclotron absorption line, the magnetic field was estimated to be 5×10^{11} G. These values are consistent with the value obtained from the pulse period and X-ray luminosity.

We should note that the steep (index = 4.0) power law of 1E 2259+586 might be an artifact from the energy band it is observed in. If the energy band is limited to the exponentially falling part of X-ray pulsar and the POWL $\times$ CYAB model is applied, the slope of the power law converges to a very steep value. An example was shown in the case of 4U 0115+63 in 1990 (§5.3). When the energy band was limited to 10–46 keV, the index converged to $\alpha \sim 3$, which is definitely wrong, as the Crab ratio suggests that the true flat power law appeared in the lower band 4–10 keV. 1E 2259+586 might be in a similar situation. The true power law region may be lower than the *Ginga* band, and only the exponentially falling part with a cyclotron structure might be observed. The contamination by the SNR may contribute to the steep power law to some extent. However, we will perform a unified fitting to 1E 2259+586.

Figure 5.10.6 is the averaged spectrum and its Crab ratio in the 1990 observation. The ratio shows that the lowest 2 bins are as flat as the Crab spectrum, but the spectrum

above 2.5 keV falls off faster than the Crab spectrum until the 7 keV emission like feature. Above 8 keV the spectrum flattens a little again. The lowest 2 bins might be the power law region slightly affected by the exponential fall off. The fit by the NPEX model was applied, but NPEX model could not describe the steep fall off and flattening above 8 keV. The concave region between 3–10 keV might be expressed by the cyclotron structure. The NPEX × CYAB model was applied and could fit the global spectrum well (figure 5.10.6, table 5.10.2). The χ^2 is large but the residuals look scattered at random on a smaller scale than the energy resolution. The positive index α_2 was already fixed to 2.0, but the parameters, kT, negative index α_1, optical depth τ, and width W were correlated with each other and the errors were not determined well. This means that the continuum and cyclotron structure are not separated well in the fitting. Therefore, the continuum temperature was fixed to the best-fit value $kT = 2.1$ keV and the errors were determined again. Thus we obtained the resonance $E_a = 4.2 \pm 0.6$ keV and $W = 2.0 \pm 0.9$ keV.

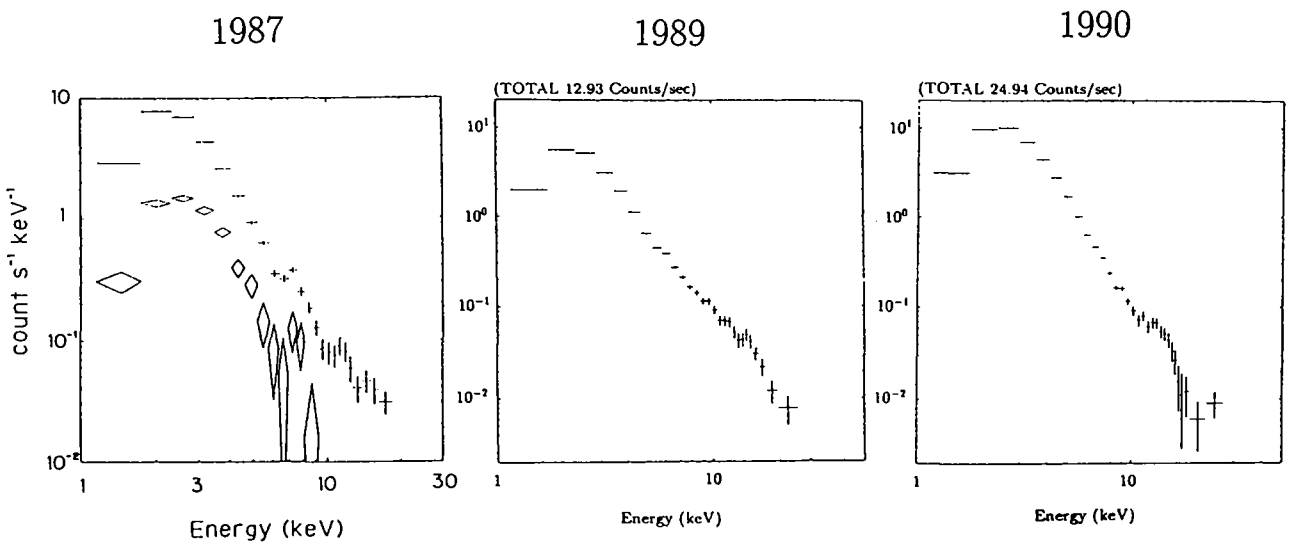

Figure 5.10.4: The averaged spectra of 1E 2259+586. *Left* : The spectrum in 1987. Spectrum of the surrounding supernova remnant G 109.1-1.0 is contaminated. The spectrum of the pulsed component is shown by diamonds (Koyama *et al.* 1989). *Middle* and *Right* : In 1989 and 1990, respectively (Iwasawa *et al.* 1992).

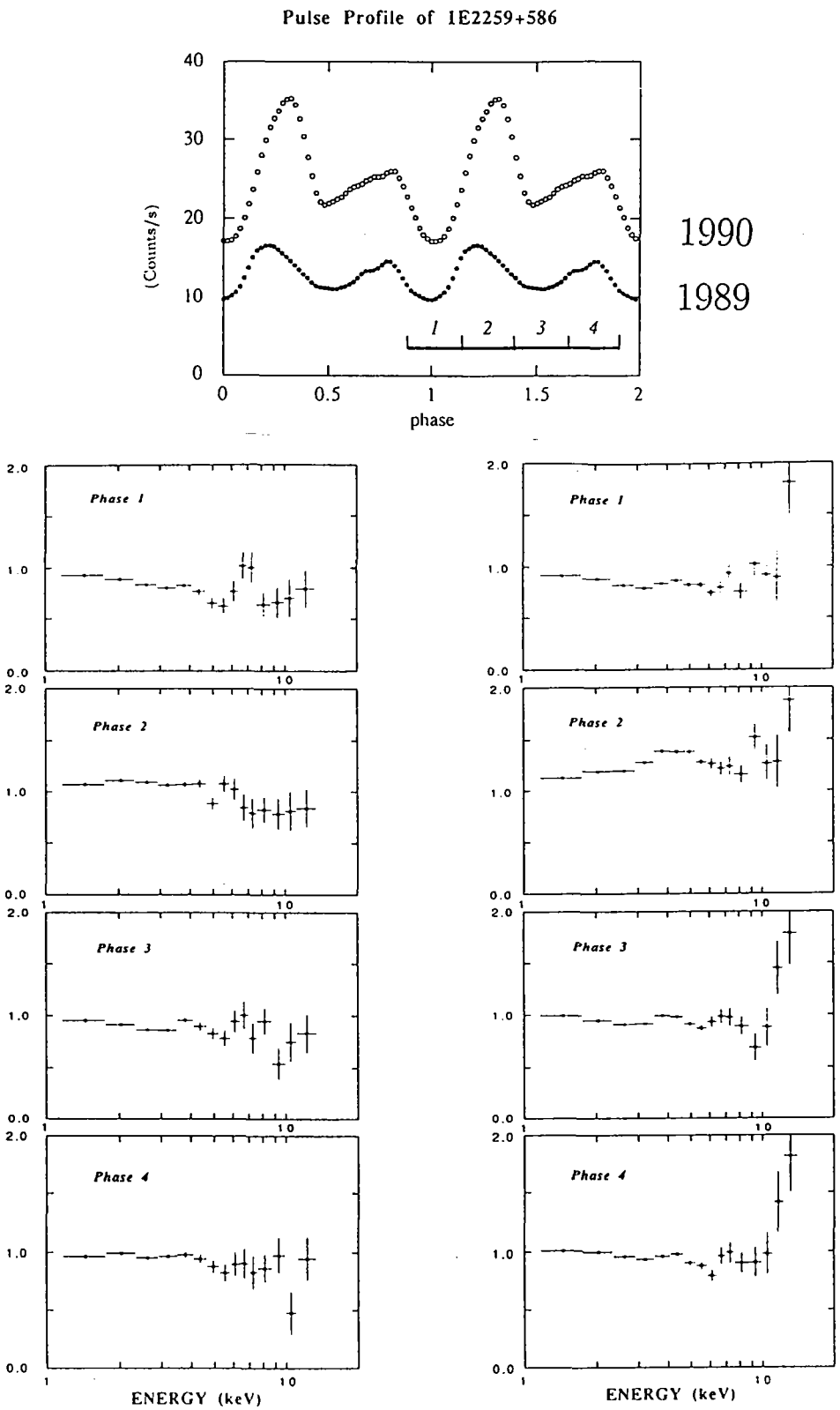

Figure 5.10.5: The ratios of the phase resolved spectra of 1E 2259+586 to the best-fit two power law models in 1989 (*left*), and 1990 (*right*). The *upper* panel is the pulse profiles in 1.2–14 keV (Iwasawa *et al.* 1992).

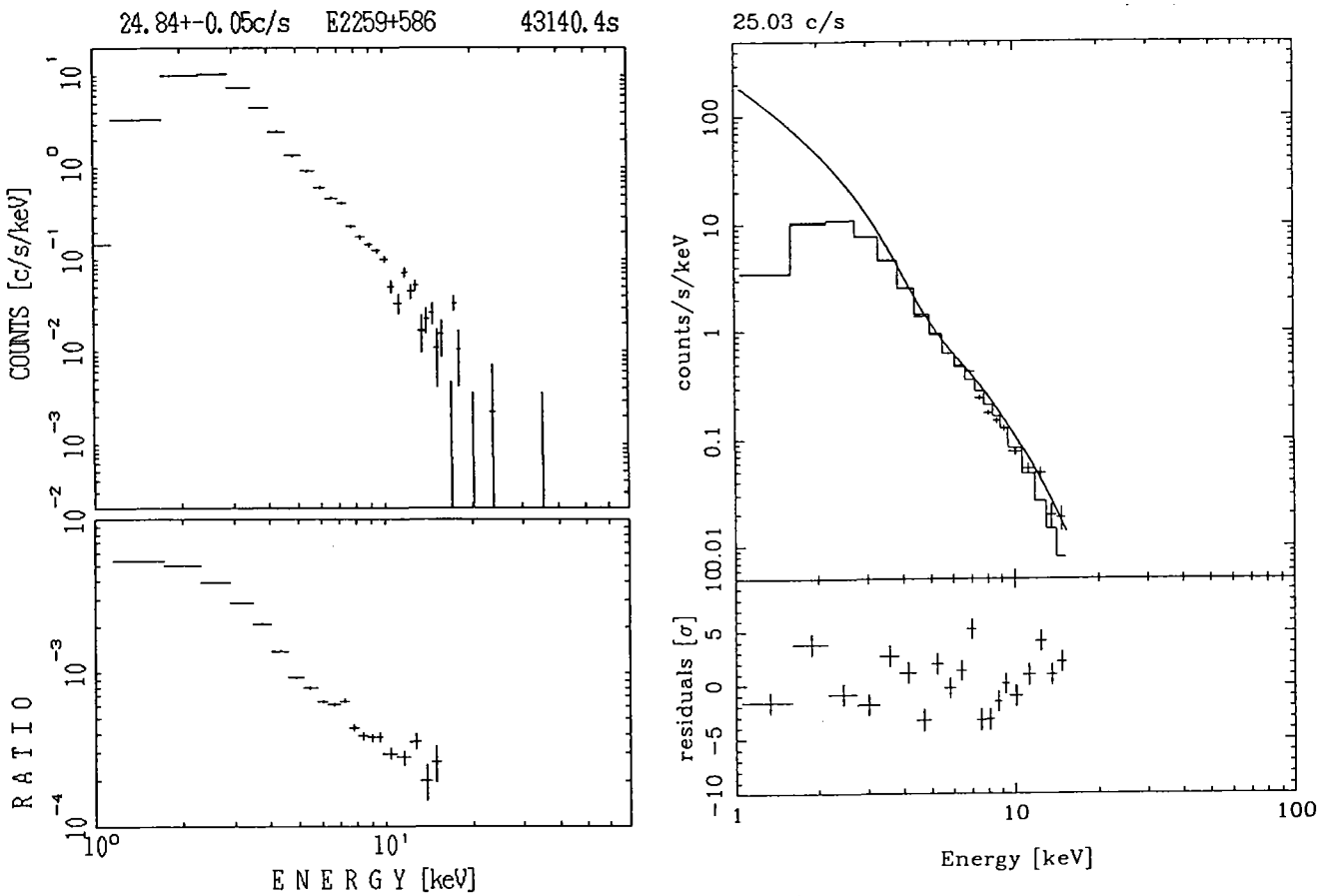

Figure 5.10.6: The averaged spectrum and the Crab ratio of 1E 2259+586 in 1990. The right panel is the fits by the NPEX × CYAB model.

Table 5.10.2: Parameters of NPEX × CYAB fit for the averaged spectrum of 1E2259+586

Resonance	Width	Depth	Negative power law		Positive	folding-e	χ^2_ν
Ea [keV]	W [keV]	D	A_1	α_1	A_2	kT [keV]	
4.2 ± 0.6	2.0 ± 0.9	0.86 ± 0.27	13 ± 12	1.4 ± 0.5	9.2 ± 7.2	2.1 fixed	8.71

The index α_2 of the positive power law is fixed to 2.0.
Absorption by the column density is not included in the fitting.
Since the parameters, kT, α_1, τ, and W were correlated with each other, their errors were obtained by temporarily fixing kT to the best-fit value of 2.1 keV.
The units of the normalization of the power law are [photons/s/keV] at 10 keV.

5.10.3 GS 1843+00

GS 1843+00 shows a very hard spectrum as the curve in the Crab ratios increases monotonically between 2–37 keV (figure 5.10.8). Since the spectrum is concave between 8-20 keV in a log-log scale, ECUT and CYAB models are not appropriate. However, the NPEX model can reproduce the spectrum well as shown in figure 5.10.8. The obtained temperature of 8.3 keV is high compared with other pulsars, e.g. A0535+26 (6.9 keV), and as high as Her X-1 (8keV). The residuals show two dips at 8 and 24 keV. The absolute deviations of these dips are small, but the good statistics mean they are significant. Both of the dips cannot be real in the average spectrum, since if we put a CYAB factor at 20 keV then the 8 keV structure disappears and vice versa. The difference appears when we fit the phase resolved spectra. The CYAB factor at 20 keV can fit the spectra in all phases; on the other hand, the 8 keV CYAB cannot fit the spectra so well as the χ^2 are large especially in phases 3, 7, and 8. Therefore we conclude the 20 keV CYAB is correct for GS 1843+00 (figure 5.10.9 and table 5.10.3). The phase phase dependency of the parameters is small, consistent with the small pulse fraction. The resonance energies are obtained between 18–22 keV and the optical depths are small ($D = 0.1 - 0.2$). Since this shallow feature is strongly coupled with the continuum model, we classify GS 1843+00 a possible cyclotron source.

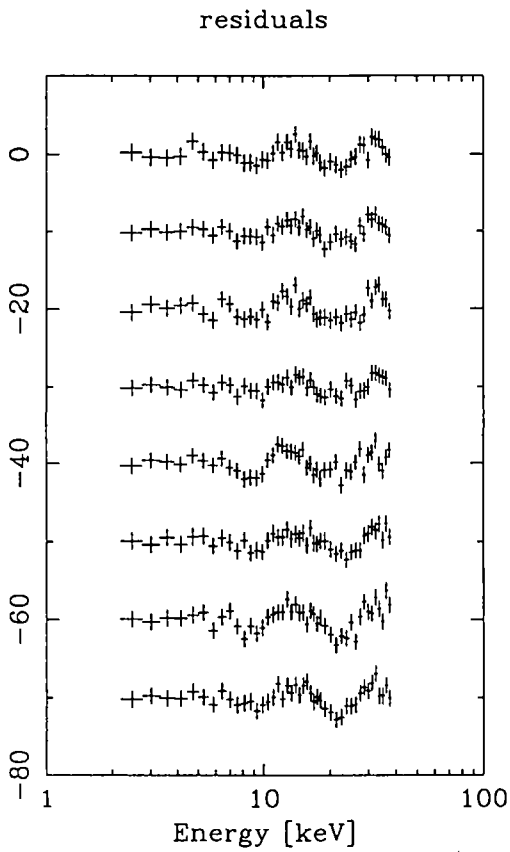

Figure 5.10.7: The residuals of the NPEX model of the phase resolved spectra of GS 1843+00. The 8 keV and 20 keV dips are seen in all the phases. Adding a CYAB factor at 20 keV flattens the residuals (figure 5.10.9).

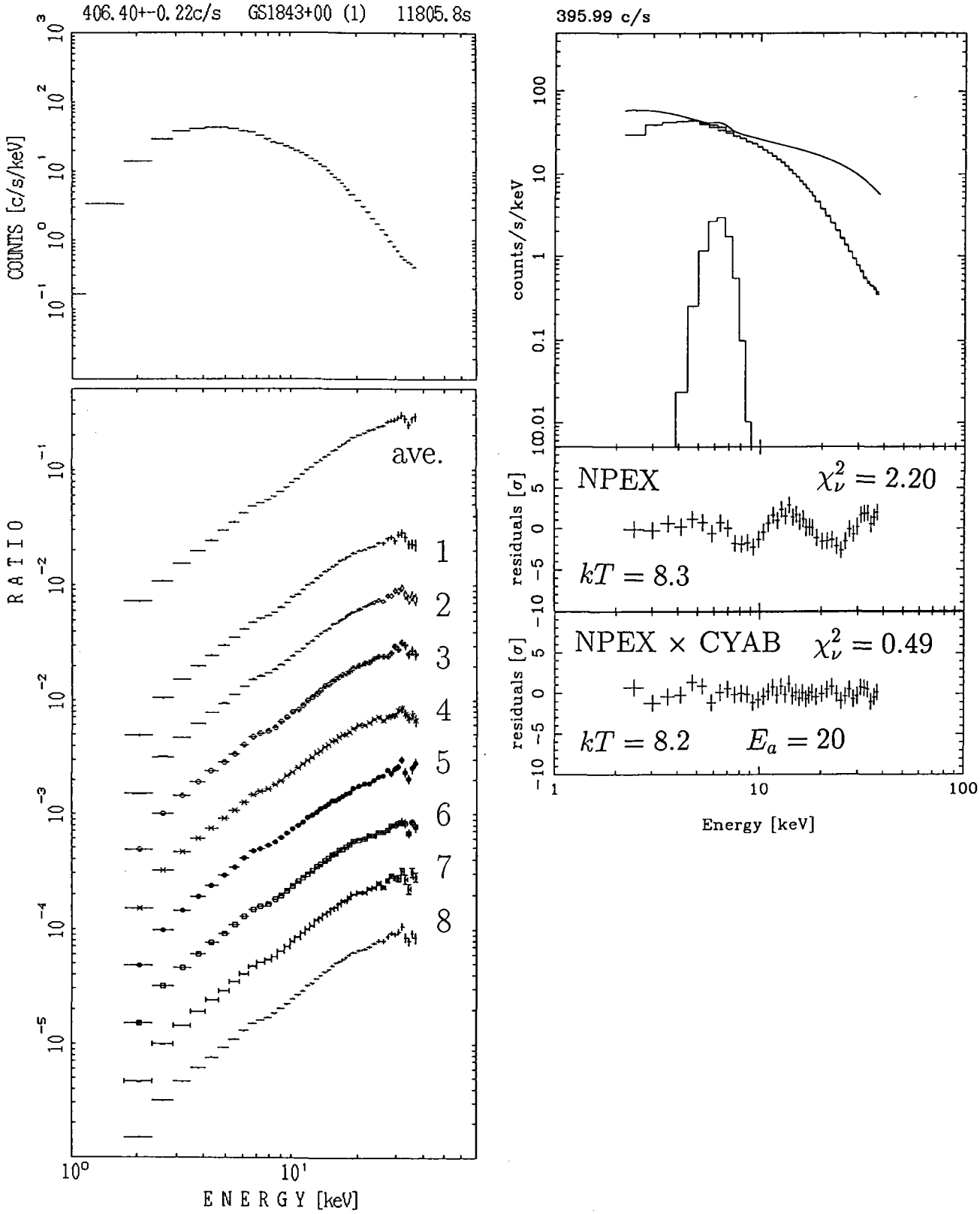

Figure 5.10.8: The left panel is the spectra and the Crab ratios of GS 1843+00. The right panel is the NPEX fit and the residuals of NPEX × CYAB fit. The residuals of the NPEX fit shows two dips, but the 20 keV one is more likely to be the cyclotron feature.

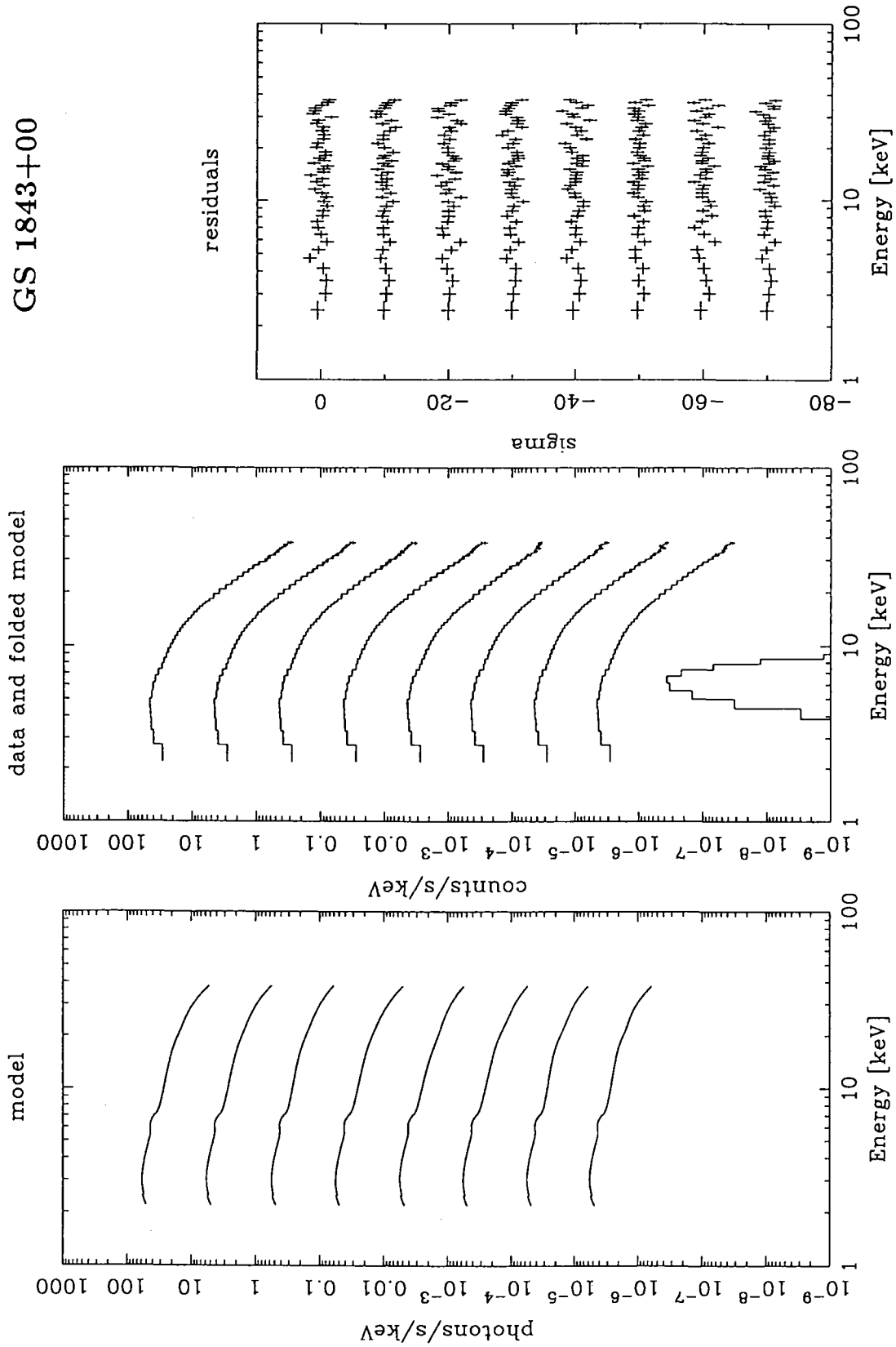

Figure 5.10.9: The NPEX × CYAB fits to the phase resolved spectra of GS 1843+00.

Table 5.10.3: Parameters of the NPEX × CYAB fits of GS 1843+00.

Pulse Phase	Resonance Ea [keV]	Width W [keV]	Depth D	χ^2_ν
ave.	19.8 ± 2.1	9.9 ± 3.6	0.16 ± 0.05	0.49
1	20.9 ± 1.4	5.5 ± 3.8	0.10 ± 0.04	0.77
2	20.0 ± 2.2	7.5 ± 5.0	0.12 ± 0.06	0.64
3	19.6 ± 3.7	9.9 ± 7.6	0.18 ± 0.12	1.17
4	20.1 ± 4.1	9.6 ± 9.4	0.12 ± 0.10	0.70
5	17.6 ± 3.5	9.2 ± 5.3	0.22 ± 0.13	1.16
6	22.9 ± 1.2	6.8 ± 3.8	0.14 ± 0.06	0.50
7	21.6 ± 1.4	7.4 ± 4.1	0.19 ± 0.07	1.07
8	21.3 ± 0.8	4.7 ± 2.1	0.12 ± 0.03	0.58

pulse phase	Negative power law A_1	α_1	Positive A_2	e-folding kT [keV]	Absorption $\log_{10} N_H$	Iron line I_{Fe}[ph/s]
ave.	45 ± 3	0.73 ± 0.08	47 ± 5	8.2 ± 0.2	22.29 ± 0.05	7.6 ± 0.9
1	49 ± 3	0.76 ± 0.08	54 ± 5	7.6 ± 0.2	22.40 ± 0.05	6.7 ± 1.2
2	48 ± 3	0.74 ± 0.09	50 ± 6	7.9 ± 0.2	22.40 ± 0.05	6.6 ± 1.2
3	43 ± 6	0.81 ± 0.15	53 ± 9	8.1 ± 0.6	22.41 ± 0.08	6.8 ± 1.6
4	47 ± 5	0.73 ± 0.11	49 ± 7	7.8 ± 0.5	22.38 ± 0.06	6.3 ± 1.2
5	45 ± 7	0.78 ± 0.18	47 ± 14	8.1 ± 0.4	22.42 ± 0.09	6.4 ± 1.6
6	49 ± 2	0.68 ± 0.06	40 ± 4	8.2 ± 0.3	22.36 ± 0.04	6.0 ± 0.9
7	43 ± 4	0.83 ± 0.11	56 ± 6	7.9 ± 0.4	22.43 ± 0.06	6.8 ± 1.4
8	45 ± 2	0.82 ± 0.07	53 ± 3	7.9 ± 0.1	22.44 ± 0.04	7.4 ± 1.0

The index of the positive power law α_2 is fixed to 2.0.
The unit of the normalization of the power law is [photons/s/keV] at 10 keV.
The energy and width of the iron line are fixed to 6.40 keV and $\sigma = 0.50$ keV (broad), respectively.

5.10.4 LMC X-4

LMC X-4 also has a hard spectrum as shown in the Crab ratios (figure 5.10.11). Since the ratio indicates a soft excess, we limit the fitting range to 3–37 keV. The spectrum is also concave between 8-20 keV, and therefore the ECUT and CYAB models fail, but the NPEX model successfully represents the continuum with $kT = 7.1$ keV (figure 5.10.11). The residuals show a dip at around 20 keV. Again the absolute deviation of the dip is small but significant. The 20 keV dip is seen in some phase resolved spectra (figure 5.10.10). The feature is deep in phases 6, 7, and 8, at the rising tail of the peak. But the discrepancies are smaller than those from GS 1843+00, and the confidence is lower for the feature in LMC X-4. However, when we add the CYAB factor, the fits to the average spectrum and those in the phase 6, 7 are significantly improved (figure 5.10.12 and table 5.10.4). Therefore we conclude the 20 keV dip in the spectra of LMC X-4 is a candidate for the cyclotron structure. The resonance energy is determined to be between 19–23 keV which is very similar to that of GS 1843+00. The optical depth is similarly small as $D \sim 0.1$. Thus LMC X-4 and GS 1843+00 are very similar systems in small pulse fraction (LMC X-4 shows the pulsation only in the outbursts), hard spectra, and shallow possible cyclotron features at 20 keV.

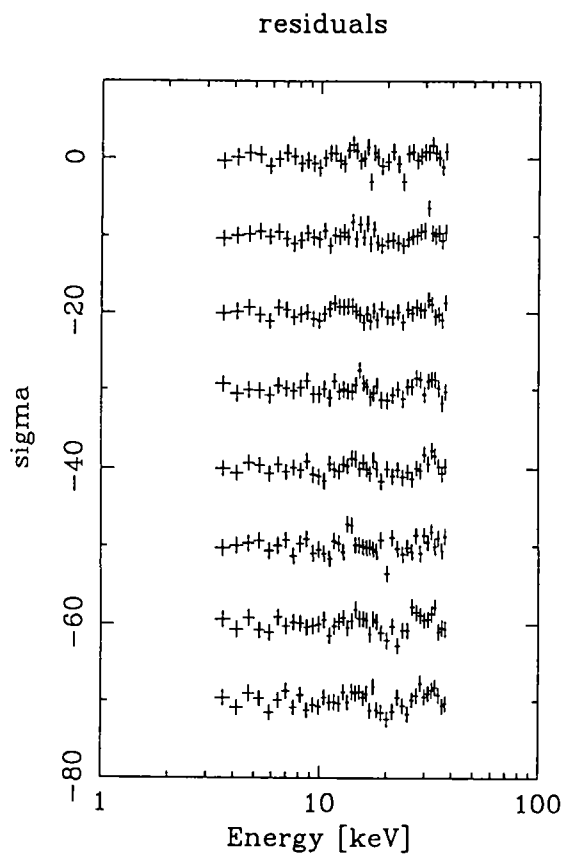

Figure 5.10.10: The residuals of the NPEX model of the phase resolved spectra of LMC X-4. The 20 keV dips are obvious in the phase 6, 7, and 8. CYAB factor at 20 keV resonance improve the fits (figure 5.10.12).

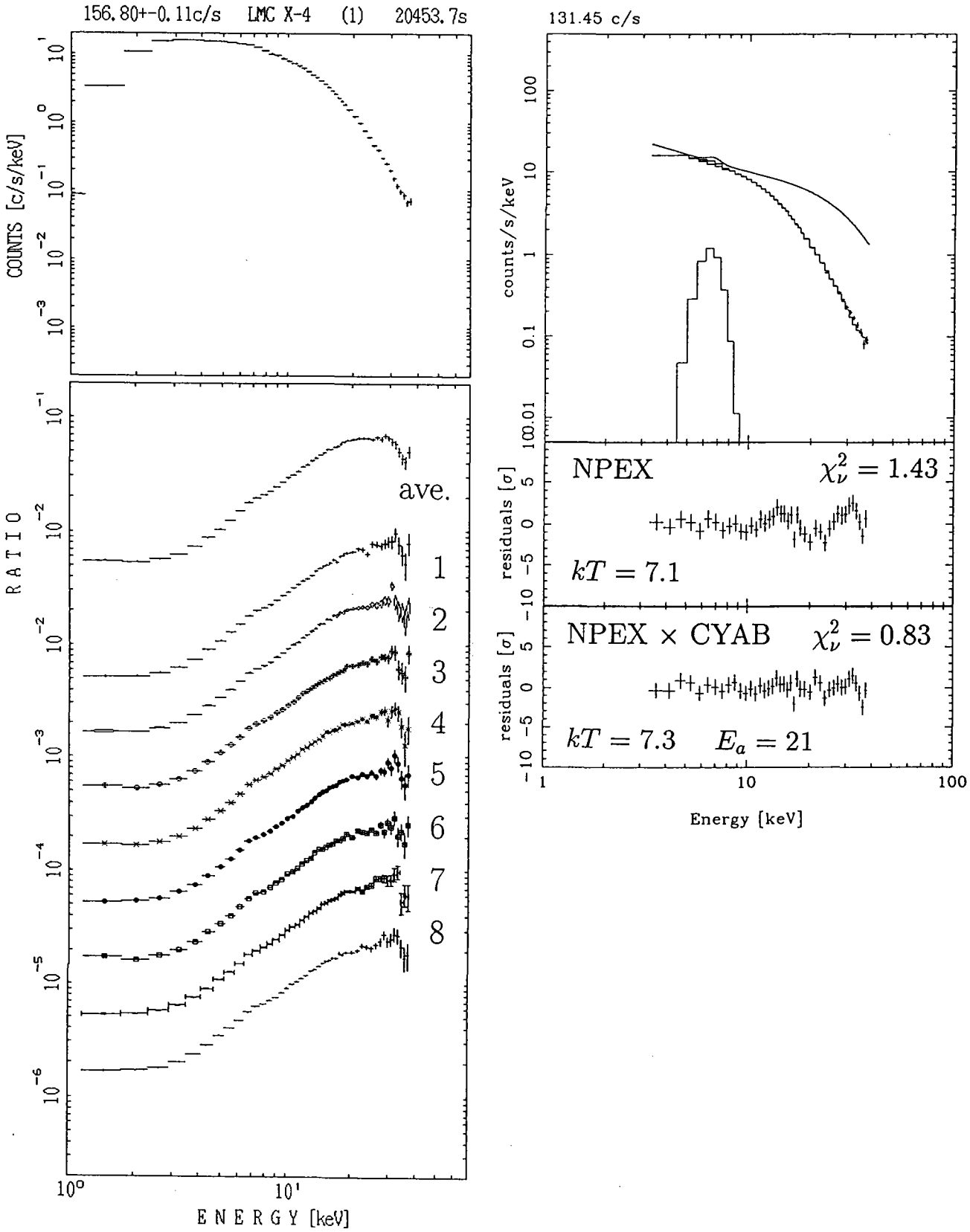

Figure 5.10.11: The left panel is the spectra and the Crab ratios of LMC X-4. The right panel is the NPEX fit and the residuals of NPEX × CYAB fit. The residuals of the NPEX fit shows a dip at 20 keV which is a candidate for the cyclotron structure.

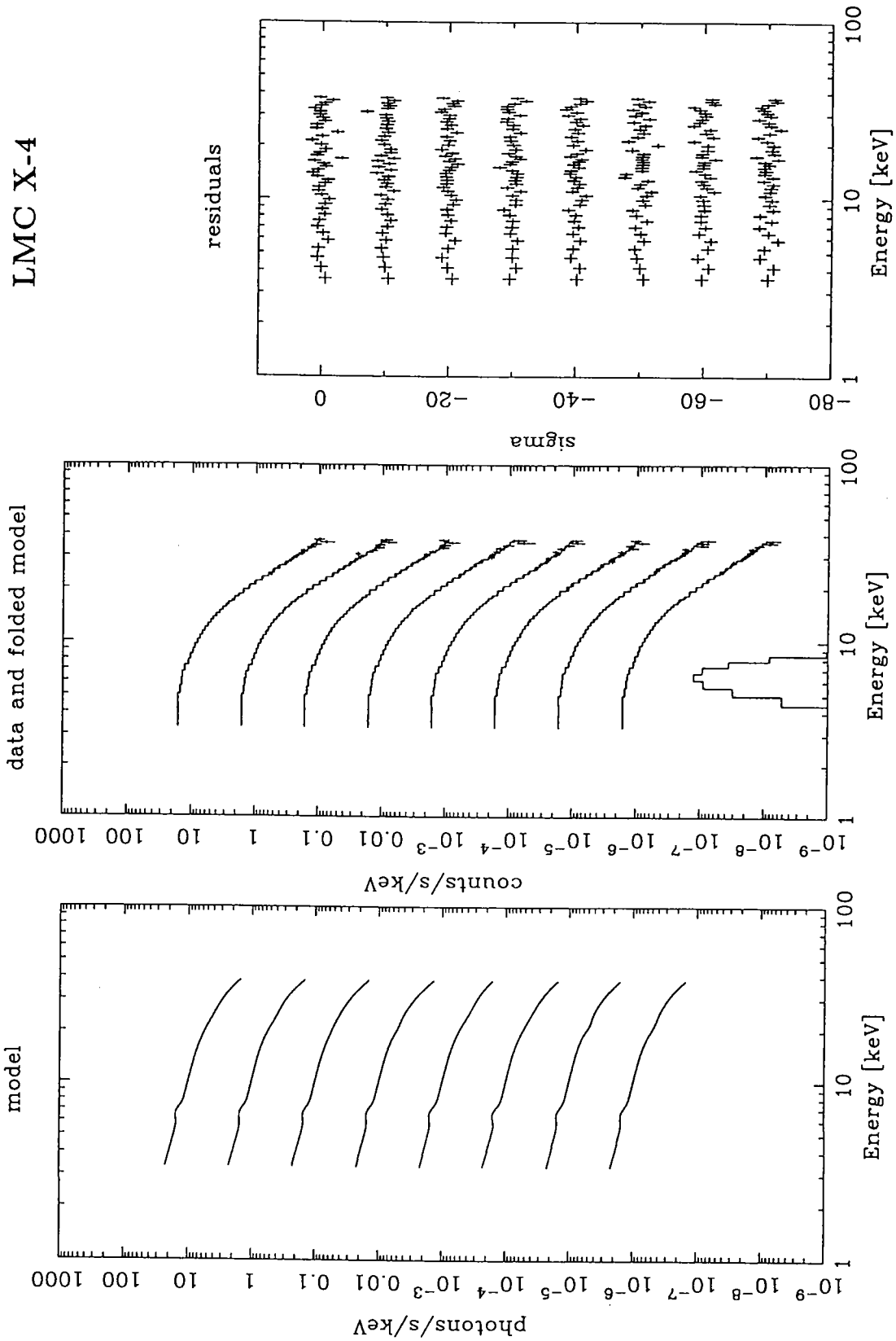

Figure 5.10.12: The NPEX × CYAB fits to the phase resolved spectra of LMC X-4.

Table 5.10.4: Parameters of the NPEX × CYAB fits of LMC X-4 in 3–37 keV.

Pulse Phase	Resonance Ea [keV]	Width W [keV]	Depth D	χ^2_ν
ave.	21.4 ± 1.2	5.1 ± 3.8	0.11 ± 0.05	0.83
1	22.1 ± 3.4	6.4 ± 12.0	0.10 ± 0.14	1.06
2	22.3 ± 1.6	4.5 ± 5.0	0.12 ± 0.08	0.76
3	18.7 ± 3.8	7.1 ± 9.6	0.08 ± 0.09	0.55
4	20.5 ± 1.4	2.6 ± 3.6	0.08 ± 0.04	0.72
5	23.3 ± 2.1	6.7 ± 8.0	0.16 ± 0.15	0.70
6	21.7 ± 3.3	7.3 ± 12.3	0.13 ± 0.19	1.31
7	21.5 ± 1.0	2.5 ± 2.5	0.13 ± 0.06	0.90
8	21.2 ± 1.3	3.6 ± 3.5	0.13 ± 0.06	0.98

pulse phase	Negative power law A_1	α_1	Positive A_2	e-folding kT [keV]	Iron line I_{Fe}[ph/s]
ave.	21 ± 1	0.43 ± 0.06	19 ± 2	7.3 ± 0.3	2.7 ± 0.4
1	21 ± 2	0.41 ± 0.09	17 ± 4	7.5 ± 0.7	2.6 ± 0.6
2	21 ± 1	0.43 ± 0.07	20 ± 3	7.2 ± 0.4	2.6 ± 0.5
3	20 ± 2	0.45 ± 0.10	21 ± 4	7.2 ± 0.4	2.4 ± 0.5
4	21 ± 1	0.40 ± 0.06	19 ± 3	7.1 ± 0.3	2.6 ± 0.5
5	21 ± 2	0.40 ± 0.07	16 ± 4	7.7 ± 0.8	2.8 ± 0.5
6	20 ± 3	0.50 ± 0.12	20 ± 5	7.3 ± 0.9	3.1 ± 0.7
7	21 ± 1	0.41 ± 0.06	18 ± 3	7.4 ± 0.3	2.6 ± 0.6
8	21 ± 1	0.41 ± 0.07	18 ± 3	7.4 ± 0.4	2.5 ± 0.6

The index of the positive power law α_2 is fixed to 2.0.
The unit of the normalization of the power law is [photons/s/keV] at 10 keV.
The energy of the iron line in the average spectrum is 6.6 ± 0.1 keV with fixed width $\sigma = 0.50$ keV. The energy and width in the phase resolved spectra are fixed to 6.60 keV and $\sigma = 0.50$ keV (broad), respectively.

5.11 Other sources

Ginga observed 10 X-ray binary pulsars and 1 binary pulsar candidate with good statistics other than the 12 pulsars shown in the previous sections in this chapter. The spectra of the pulsars from which the cyclotron resonance has not been discovered (non-cyclotron pulsars) are well fitted by the NPEX model except for Cen X-3 and 4U1626-67, which are potential cadidates for cyclotron pulsars. In this section, we present the spectra, the Crab ratios, and NPEX fits of Cen X-3 and 4U1626-67. Those of other pulsars are shown in the appendix in the order of increasing pulse period. The best-fit parameters are also summarized in the appendix.

5.11.1 Cen X-3

Cen X-3 is one of the two pulsars which NPEX model cannot fit well with $\alpha = 2.0$. The multiplication of the CYAB model with the fixed resonance energy E_a at 36 keV improves the fit. When the α_2 of the NPEX model is set free, the fit is improved as well.

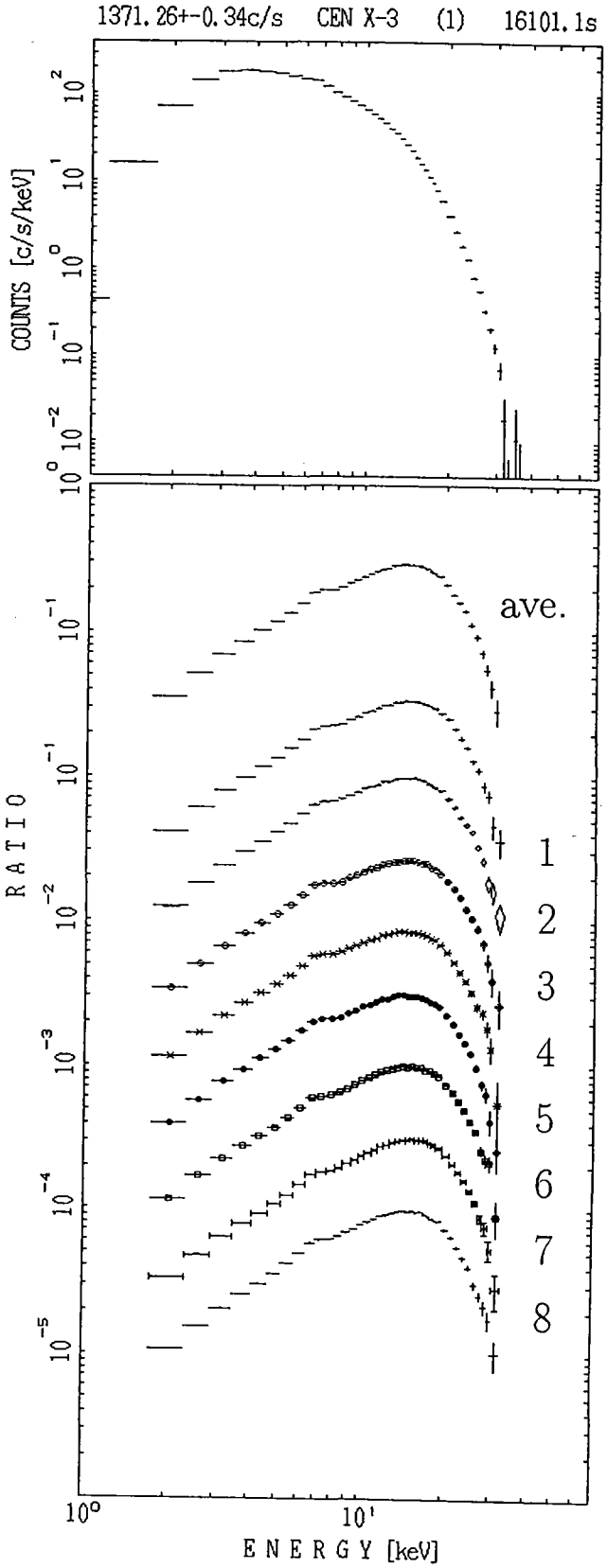

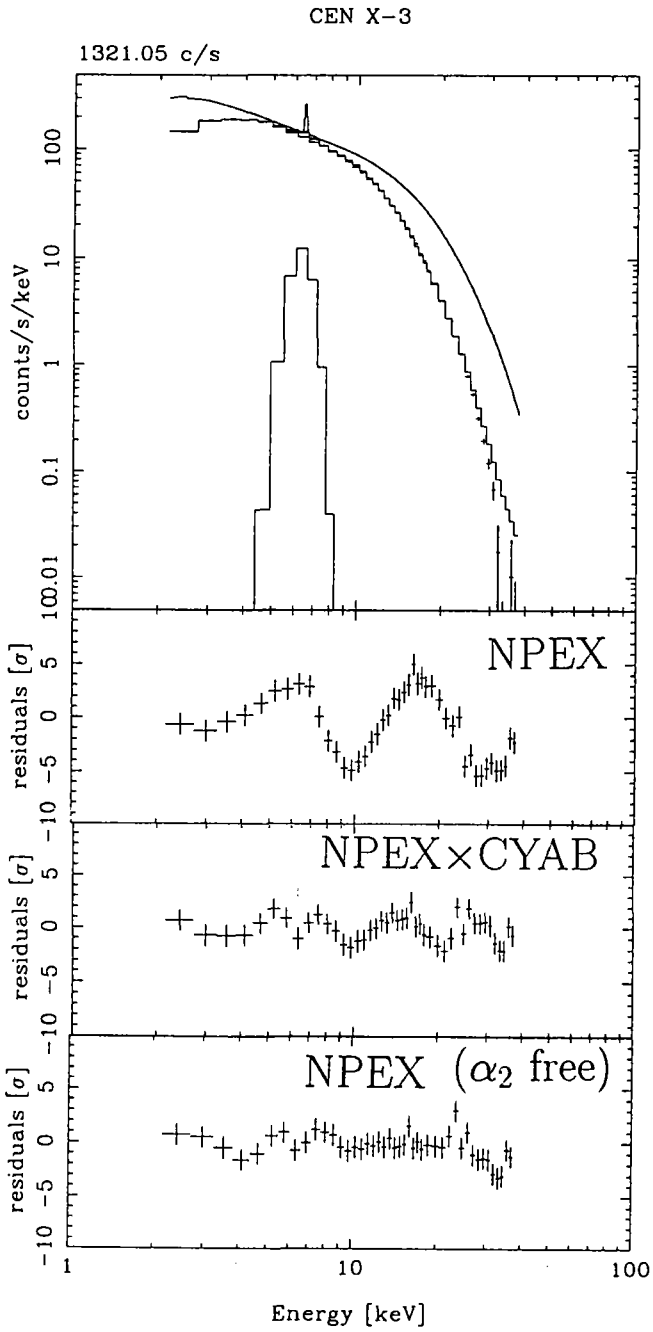

5.11.2 4U 1626-67

4U 1626-67 is the other of the two pulsars which the NPEX model cannot fit well. When α_2 is set free, it still failed to fit the spectrum. If a emission line is added at $\sim$ 20 keV, the fit becomes better, but the wavy residuals still remain.

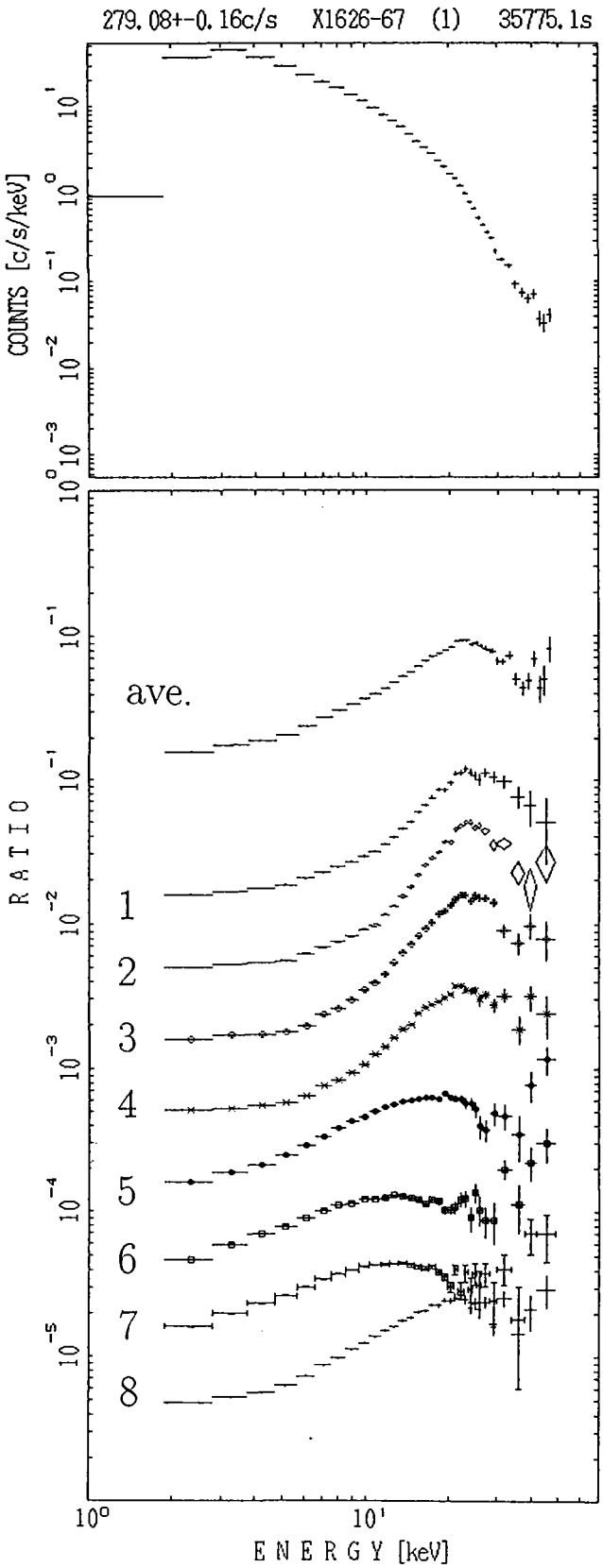

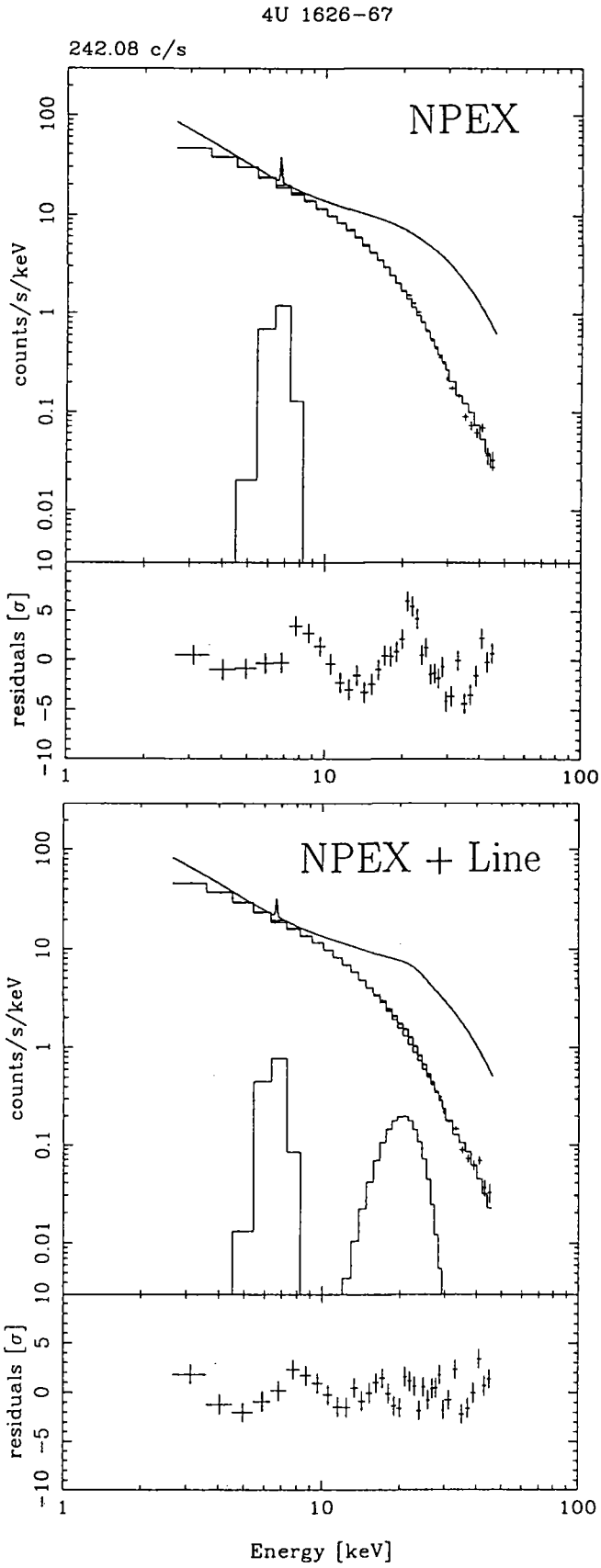

Chapter 6

Discussion

In Chapter 4, we described the reduced HV observations of some X-ray pulsars to get broad band spectra up to 60 keV. In Chapter 5, we analyzed the *Ginga* data of a total of 23 X-ray binary pulsars (including a candidate), and discovered two major facts;

1. The NPEX model, which was introduced through the considerations of the Her X-1 spectra in §5.2, was able to, for the first time, successfully fit the spectra of all the pulsars very well in the overall energy band.

2. Cyclotron resonances were found from 11 pulsars, two of which were newly discovered in this thesis by applying the NPEX continuum. Adding one pulsar with cyclotron resonances discovered with *HEXE* , a total of 12 pulsars, half of the X-ray binary pulsars observed with *Ginga* , were revealed to have the magnetic fields of $4 \times 10^{11} - 5 \times 10^{12}$ G.

The best-fit parameters with NPEX ($\times$ CYAB) model for the pulse averaged spectra are summarized in table 6.1.1 and 6.1.2. In this Chapter we derive a physical interpretation of the NPEX model, some information on the accretion column, and properties of the pulsar magnetic fields.

6.1 Interpretation of NPEX model

6.1.1 X-ray spectra of pulsars

The spectra of X-ray pulsars have been a mystery since their discovery. Pioneers applied the empirical ECUT model for the continuum, but the physical meaning was uncertain (White *et al.* 1983). Some pulsars with gentle fall-off might have thermal origin but some showed a steeper cutoff (Tanaka 1986). The discovery of the cyclotron resonance gave a hint for the understanding of the cutoff, as the exponential cutoff might be caused by

Table 6.1.1: The best-fit parameters with NPEX model for the pulse averaged spectra.

sources	Negative power law Norm. A_1 [ph/s/keV]	index α_1	Pos. POWL Norm. A_2 [ph/s/keV]	Exponential folding-e kT [keV]	Absorption $\log_{10} N_H$ [cm^{-2}]
Cyclotron Sources					
Her X-1	135 ± 8	0.51 ± 0.03	100 ± 23	8.0 ± 0.8	—
4U0115+63 (90)	491 ± 326	0.41 ± 0.48	4960 ± 1220	4.2 ± 0.1	—
4U0115+63 (91)	62 ± 22	0.65 ± 0.29	785 ± 58	4.3 ± 0.1	—
X0331+53	930 ± 63	-0.27 ± 0.05	630 ± 170	6.3 ± 0.5	—
1E2259+586	13 ± 12	1.42 ± 0.47	9 ± 7	2.1 fixed	—
LMC X-4	21 ± 1	0.43 ± 0.06	19 ± 2	7.3 ± 0.3	—
GS1843+00	45 ± 3	0.73 ± 0.08	47 ± 5	8.2 ± 0.2	22.29 ± 0.05
Cep X-4	101 ± 13	0.70 ± 0.05	110 ± 59	6.4 ± 1.5	22.01 ± 0.08
Vela X-1	171 ± 4	0.61 ± 0.05	123 ± 8	6.4 ± 0.1	22.41 ± 0.06
4U1907+09	11 ± 2	1.39 ± 0.29	25 ± 5	6.4 ± 0.7	22.86 ± 0.08
4U1538-52	19 ± 2	1.47 ± 0.20	68 ± 8	4.6 ± 0.2	22.80 ± 0.07
GX301-2	135 ± 71	0.80 ± 0.85	485 ± 184	5.4 ± 0.3	23.37 ± 0.07
	Leaky absorber, Norm $\times 0.38 \pm 0.26$				24.44 ± 0.22
Non-cyclotron Sources					
SMC X-1	67 ± 1	0.38 ± 0.04	18 ± 4	6.1 ± 0.2	22.00 ± 0.15
Cen X-3	256 ± 38	0.92 ± 0.14	1350 ± 120	3.5 ± 0.1	22.30 fixed
Cen X-3 [a]	2200 ± 300	-0.70 ± 0.09	3340 ± 370	2.4 ± 0.1	—
Cen X-3 [b]	302 ± 34	0.67 ± 0.19	761 ± 201	4.0 ± 0.3	22.21 ± 0.16
4U1626-67	27 ± 2	1.16 ± 0.09	38 ± 5	6.4 ± 0.2	—
4U1626-67 [c]	30 ± 2	1.07 ± 0.07	38 ± 4	6.2 ± 0.2	—
GS0834-430	163 ± 3	0.16 ± 0.06	65 ± 12	7.2 ± 0.3	21.92 ± 0.26
OAO1657-415	102 ± 3	0.31 ± 0.05	28 ± 9	7.2 ± 0.4	22.92 ± 0.03
EXO2030+375	3.1 ± 1.5	1.50 ± 0.33	0.1 ± 0.3	16.0 ± 15.0	22.60 ± 0.06
GX1+4 1988	26 ± 46	0.36 ± 1.00	2.4 ± 25.4	7.2 ± 12.9	22.62 ± 0.11
GX1+4 1990	15 ± 8	0.81 ± 0.35	0.9 ± 2.5	10.0 ± 6.6	22.94 ± 0.09
1E1145.1-61.41	44 ± 13	0.75 ± 0.23	1.2 ± 2.3	12.8 ± 5.5	22.75 ± 0.09
X1722-36	3.2 ± 0.9	0.39 ± 0.16	0.4 ± 0.8	9.6 ± 4.2	23.05 ± 0.44
X Per	27 ± 13	0.89 ± 0.25	4.4 ± 7.8	5.0 ± 1.6	22.09 ± 0.07
4U1700-37	364 ± 19	0.83 ± 0.04	37 ± 11	8.5 ± 0.5	22.43 ± 0.06

α_2 is fixed to 2.0. The units of the normalization of the power laws are [photons/s/keV] at 10 keV. Errors are in 90% confidence level.

a) The positive index α_2 is 4.4 ± 0.2.

b) CYAB function is multiplied (E_a is fixed to 36 keV, $D = 2.4 \pm 1.1$, and $W = 11.3 \pm 3.9$ keV).

c) A gaussian emission line of $I = 7.2 \pm 2.9$ [photons/s] at $E = 21.7 \pm 0.6$ keV with $\sigma = 2.8 \pm 0.9$ keV is added.

Table 6.1.2: The best-fit CYAB parameters with NPEX continuum for the pulse averaged spectra.

sources		CYAB Resonance E_a [keV]	CYAB Width W [keV]	CYAB Depth D
Her X-1		33.1 ± 0.3	12.1 ± 1.7	1.53 ± 0.25
4U0115+63 (90)	1st	11.3 ± 0.6	5.9 ± 0.8	0.67 ± 0.08
	2nd	22.1 ± 0.4	5.2 ± 1.0	0.51 ± 0.07
4U0115+63 (91)		15.6 ± 0.4	9.0 ± 0.6	1.22 ± 0.06
X0331+53		27.2 ± 0.3	7.5 ± 0.9	1.62 ± 0.15
1E2259+586		4.2 ± 0.6	2.0 ± 0.9	0.86 ± 0.27
LMC X-4		21.4 ± 1.2	5.1 ± 3.8	0.11 ± 0.05
GS1843+00		19.8 ± 2.1	9.9 ± 3.6	0.16 ± 0.05
Cep X-4		28.8 ± 0.4	12.1 ± 3.1	1.67 ± 0.59
Vela X-1	1st	24.5 ± 0.5	2.2 ± 1.0	0.065 ± 0.015
	2nd	$2E_{a1}$ fixed	$2W_1$ fixed	0.80 ± 0.26
4U1907+09		18.9 ± 0.7	7.4 ± 2.1	0.87 ± 0.21
4U1538-52		20.6 ± 0.2	4.2 ± 0.6	0.83 ± 0.08
GX301-2		37.6 ± 1.1	16.4 fixed	0.65 ± 0.17

Errors are in 90% confidence level.
See §2.6.2 and 5.1.5 for the CYAB formula.

the cyclotron resonance (Clark *et al.* 1989). However, they still assumed a power law for the underlying continuum. In the previous chapter, we found that the spectral fall-off of Her X-1 was explained not only by the cyclotron resonance but also by a thermal fall-off. Since the fitting revealed that the high energy spectrum is similar to a blackbody ($\propto E^2 \exp(-E/kT)$), we added a negative index power law function to explain the flat power law in the low energies. Thus the NPEX (Negative Positive power law EXponential) model was introduced as

$$NPEX(E) = (A_1 E^{-\alpha_1} + A_2 E^{+\alpha_2}) \exp\left(-\frac{E}{kT}\right),$$

where α_1 was a negative power index and the positive power index α_2 was fixed to 2.0. We found that the NPEX model can reproduce the slightly concave pulsar spectra very well with the same number of parameters as the ECUT or FDCO models, and the cyclotron structures were recognized clearly as the deviation from the NPEX model. By applying a CYAB factor to the NPEX continuum, the spectra of all the binary pulsars are fitted well in the overall *Ginga* energy band for the first time, as shown in Chapter 5.

6.1.2 Superposing spectra

Thus the NPEX model is an excellent model for the continuum spectra of X-ray pulsars. Let us consider a physical interpretation of this model. It would be natural to assume that kT is the highest temperature of the X-ray emitting plasma. In order to investigate the roles of the other parameters, we normalize the spectra with the energy of kT after correcting for the detector efficiency. The flux level is normalized by the flux at $E = kT$. The normalized spectra for the non-cyclotron and cyclotron sources are shown in figure 6.1.1 (see Appendix D for the NPEX fittings of non-cyclotron sources). The effect of the absorption by the intervening matter is also corrected in this figure.

In the simple case of the non-cyclotron sources, the spectra obey a power law in the low energies, although the indices are different, and make a round shoulder at around $E = 3kT$. In the NPEX model, the low energy power law is represented by the negative power law component, and the round shoulder is modeled by the positive power law component. As the power law flattens, the hump at $E = 3kT$ increases, suggesting the existence of one hidden parameter which determines the shape of the continuum. The hidden parameter is also suggested from the pulse profiles sliced by energy band. Since the pulse shapes do not change between below kT and above kT, the two power laws cannot be independent, but are coupled by a hidden parameter.

In the case of the cyclotron sources, the curves are more complicated. However, the overall curves are similar to those of the non-cyclotron sources. The difference is that the spectrum show a steep fall off at some energies, which is caused by the cyclotron resonance. The locations of the resonances are not the same for each source in this figure.

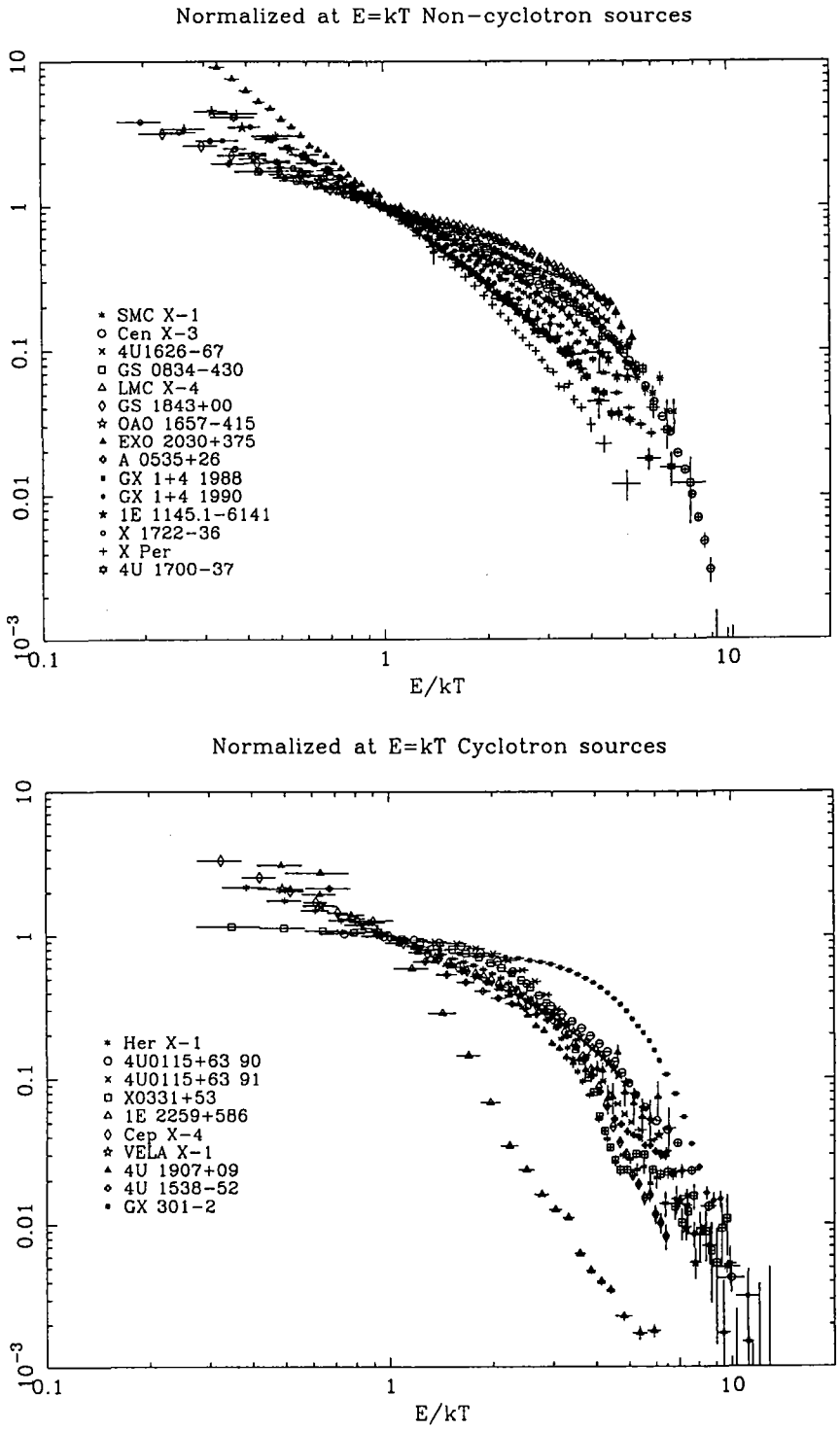

Figure 6.1.1: The efficiency-corrected continuum spectra of the non-cyclotron (*upper*) and cyclotron (*lower*) sources normalized by the energy kT and by the flux at $E = kT$. 1E2259+586 might have a contamination of SNR in the soft energy. GX 301-2 might have a leaky absorber making a large hump. Those two should be excluded from consideration.

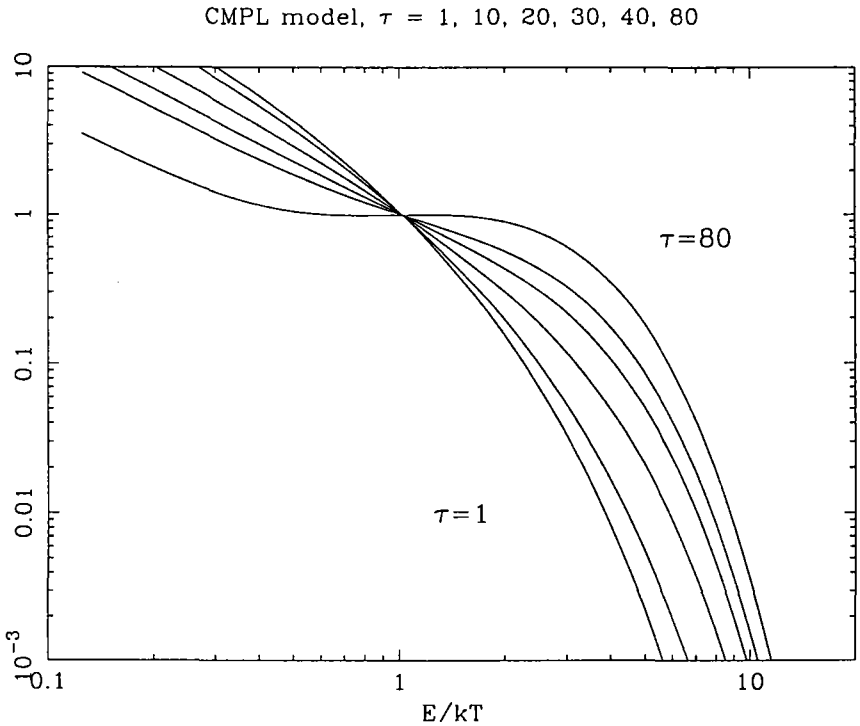

Figure 6.1.2: Comptonization by Lamb and Sanford model (1979) (CMPL model) for the comptonized spectra with input bremsstrahlung spectrum. The spectral shape is determined by the optical depth τ. The changes of the spectra are very similar to the observed changes.

6.1.3 Possible models

Let us consider a model which is a power law in the low energy region and falls like a blackbody in the high energies. The multi-blackbody model would be a candidate, which was proposed for the LMXB and black hole candidates. The spectral index was determined by the areas which have the temperatures. If the area is given by a power law as $S(E) = AE^{-\eta}$, the observed spectral index becomes $\alpha = \eta - 3$. We can make any power law with the slope of $\alpha > -2$, but we cannot make a concave spectrum under this assumption. To make a concave structure, a function with greater dependency on the energy than a power law is necessary. It may be a defect of the multi-blackbody model, since the largest advantage of the NPEX model is the ability to fit the concave spectrum.

Another candidate is the Comptonization model. The changes of the spectra in figure 6.1.1 reminds us the comptonized spectra for different optical depth τ. In this model τ can be the hidden parameter. If a soft photon goes into the hot electron plasma, where scattering is a more dominant process than absorption, the photon gains energy by the inverse-compton mechanism and comes out with a larger energy. A power law spectrum

results for small τ, and a Wien peak for large τ. An analytic approximate calculation was done by Sunyaev and Titarchuk (1980) for the given soft photon input. The emergent photon spectrum is given as $(E^2+o(E^2))\exp(-E/kT)$, where $o(E^2)$ means the polynomials with lower order than 2. For example, when the photon index of the high energy wing is $\alpha = -2$, the photon spectrum $F(x)$ is expressed as

$$F(x) \propto e^{-x}\left(\frac{x^2}{24}+\frac{x}{6}+\frac{1}{2}+\frac{1}{x}+\frac{1}{x^2}\right),$$

where $x \equiv E/(kT)$. This function is almost the same as the NPEX model.

Figure 6.1.2 shows another comptonization model by Lamb and Sanford (1979), referred as CMPL (CoMPtonization by Lamb *et al.*) model here and after, which assumes a bremsstrahlung spectrum for the photon input. The shape of the spectrum is determined only by the optical depth τ, and the change of spectral shape as a function of τ mimics various observed spectra shown in figure 6.1.1. Moreover, the CMPL model can represent the various concave spectra. Thus a comptonization model is a very possible candidate.

6.1.4 Comptonization model fits

We choose the CMPL model for the comptonized spectrum, since it does not include integration and is easily calculated. We performed fitting of the phase average spectra with CMPL model for the non-cyclotron pulsars, and with CMPL × CYAB model for the cyclotron pulsars. The figures and the best-fit parameters are summarized in Appendix E. A0535-26 is included as a non-cyclotron pulsar since it shows no sign of the cyclotron structure in the observed energy range.

The CMPL model can reproduce the pulsar spectra approximately, but the fits are slightly worse than with the NPEX model. Especially bad fits are found for Cen X-3, 4U 1626-67, and 1E 2259+586, which the NPEX model also failed to fit. The parameters of the CYAB factor also take similar values in the two continuum models. We compare parameters of the NPEX and CMPL models. The kT of the CMPL model becomes a little higher, but the the kT's in both models are correlated proportionally (Appendix E.3). The τ is well correlated with the intensity ratio of the two power laws of the NPEX model, i.e. (positive power law)/(negative power law), at $E = kT$. A large τ makes a spectrum much like a blackbody, as expected. Thus τ can be considered the hidden parameter which determines the shape of the spectra.

We should remark that kT and τ are in good agreement between the two observations of 4U 0115+63 in 1990 and 1991. But these spectra are apparently quite different as shown in §5.3 and §5.4. The intensities are different by a factor of 6, the cyclotron resonances have changed from double to single, and the resonance energies have changed. The agreement of kT and τ indicates that the CMPL model represents the underlying continuum correctly, suggesting the propriety of the model.

Then what is the soft photon input to the comptonization region? The CMPL model assumes soft photons produced by the bremsstrahlung of the comptonizing plasma itself, and Sunyaev and Titarchuk (1980) model assumes soft photon input. However, since these two models are similar and give as good fits as the other, we cannot judge by the spectral fittings. The bremsstrahlung of the CMPL model would not be sufficient to make high luminosity. The accretion column must be optical thick to emit as high luminosity as the 'Eddington limit'. Then the center of the column might be the thickest, emit a black body radiation of lower temperature and input these photons to the surface comptonizing region. This is one candidate. Another considerable source of soft photons is the boundary region of the accretion column and the surface of the neutron star. Since a half of the X-ray emission goes to the surface of the neutron star, it might be heated up to emit soft photons.

A reason of the χ^2 increase in the CMPL model could be because it is not the proper comptonization model for the accretion column of pulsars, and another reason could be that the averaged spectrum is a mixture from different τ's and cannot be simply modeled with a single τ. In the case of the pulsar, the viewing angle of the accretion column changes with the pulsar rotation and the optical depth changes for different polarizations of the photons. Considering these factors, it may be surprising that the CMPL model can fit the spectra so well. Thus an interpretation of the NPEX model is the comptonized spectrum.

6.1.5 Optical depth, temperature, and resonance energy

We have found the pulsar continuum are approximately described by two parameters, kT and τ. Here we study the relationship between the obtained parameters to find some rules. Instead of τ, kT, and E_a in the CMPL model, we use the pos./neg. intensity ratio, kT, and E_a in the NPEX model, respectively, because the fitting with the NPEX model is better than that with the CMPL model.

Figure 6.1.3 shows the remarkable correlation of pos./neg. intensity ratio and kT. They are well anti-correlated regardless of the existence of the cyclotron structure. If a neutron star emits an isotropic blackbody radiation at the Eddington luminosity, the temperature should become 2 keV. The obtained kT are higher than this value and ranging 4–14 keV. A simple understanding of the relationship is that when the blackbody is superior to the negative power law (pos./neg. ratio is large), the emission increases and the temperature decreases down to 2 keV, since the blackbody emission is the most effective emission mechanism.

Then what determines the temperature or τ? X-ray luminosity L_x would be a candidate. However, as shown in figure 6.1.4, kT does not depend on L_x. Therefore L_x is unlikely. Burnard *et al.* (1983) suggested that luminosity and spin period may be related

to the temperature, but kT does not depend on the period, either. The next candidate would be the magnetic field strength. Figure 6.1.5 shows the E_a dependencies of kT. Although the data points are only from the cyclotron sources, there is a weak positive correlation between E_a and kT. The bottom figure of figure 6.1.5 shows the $E_a - kT$ relation of the phase resolved spectra. The data points are clustered by each pulsar, and this shows that kT is as characteristic for each pulsar as E_a. Thus the magnetic field might determine the temperature.

Let us consider the energy flow in the accretion column. Protons in the accreting matter have most of the gravitational energy. Electrons receive energy from protons and give it to photons. The time scale in which protons give energy to electrons is

$$t_{col} = 5 \times 10^{-5}\ n_{20}^{-1} \left(\frac{kT}{10\ \mathrm{keV}}\right)\ [\mathrm{s}]$$

(Gould 1982). Here n_{20} is the density in the unit of 10^{20} cm^{-3}. On the other hand, the time scale in which electron lose energy by the comptonization is estimated by

$$t_{comp} = 1 \times 10^{-15} \left(\frac{kT}{10\ \mathrm{keV}}\right)^{-4}\ [\mathrm{s}]$$

(Rybicki and Lightman 1979). Here compton cross section is assumed to be $10^4\sigma_T$ near the cyclotron resonance. Therefore electrons and photons interact much more strongly than protons and electrons, and electrons may be cooled down by giving energy to photons by comptonization.

If comptonization takes place under a strong magnetic field, the temperature of the electrons would be given as $kT = 0.25E_a$ from the equilibrium of the nonrelativistic Kompaneets equation, as derived below. The energy change by a Compton scattering of an input photon in a cloud of nonrelativistic thermal electrons is given by

$$\Delta E = \frac{E}{mc^2}(4kT - E), \tag{6.1}$$

for example, by Rybicki and Lightman (1979). If the cloud is optically thick for scattering, the energy of the photon saturates to

$$E = 4kT. \tag{6.2}$$

In the case of the pulsar, the free falling electrons would be thermalized to a very high temperature at the top of the accretion column, mostly by the radiative shock. Since the high temperature fully ionizes the atoms, photoelectric absorption is no longer effective and the main electron-photon interactions are Thomson/Compton (cyclotron) scattering and free-free absorption/emission, where the former has a larger cross section. At the center of the accretion column, the matter would be optically thick for both scattering and absorption and photons would radiate like a blackbody. However, at the surface of

the accretion column, there is a region which is optical thick to scattering but thin for absorption, where we can apply the above theory. Since the cross section of the scattering is very large at the cyclotron resonance, the Compton interactions mainly occur with the photons of approximately the cyclotron energy. Consequently the temperature of the electrons is 'adjusted' to satisfy equation 6.2. Thus

$$kT = 0.25E_a \tag{6.3}$$

is obtained. Monte-Carlo simulations of optically thick media by Lamb *et al.* (1990) find $kT \approx 0.27E_a$, and it is applied to the γ-ray bursts. The $kT = 0.25E_a$ relation is shown in figure 6.1.5 and is in rough agreement with the data points. Thus the magnetic field may determine the temperature. At the same time, the relation may confirm the comptonization model for X-ray pulsars.

From the $E_a - kT$ relation one important suggestion can be deduced. Figure 6.1.3 shows that pulsars have kT between 4–14 keV, which might indicate the cyclotron resonance energies are fairly constant within 10-60 keV. Moreover the temperatures of the non-cyclotron sources are relatively higher than those of the cyclotron sources. The magnetic fields of non-cyclotron sources, therefore, might be slightly stronger than those of the cyclotron sources. The higher kT values suggest that the resonances are nearly at the higher end of the energy range of *Ginga* and therefore they might not be detected.

Cen X-3 has a low temperature and is the only exception among the non-cyclotron sources, which suggests that it could have a cyclotron structure as strong as those of the cyclotron sources. It is consistent with the considerations from the spectrum (§5.11.1).

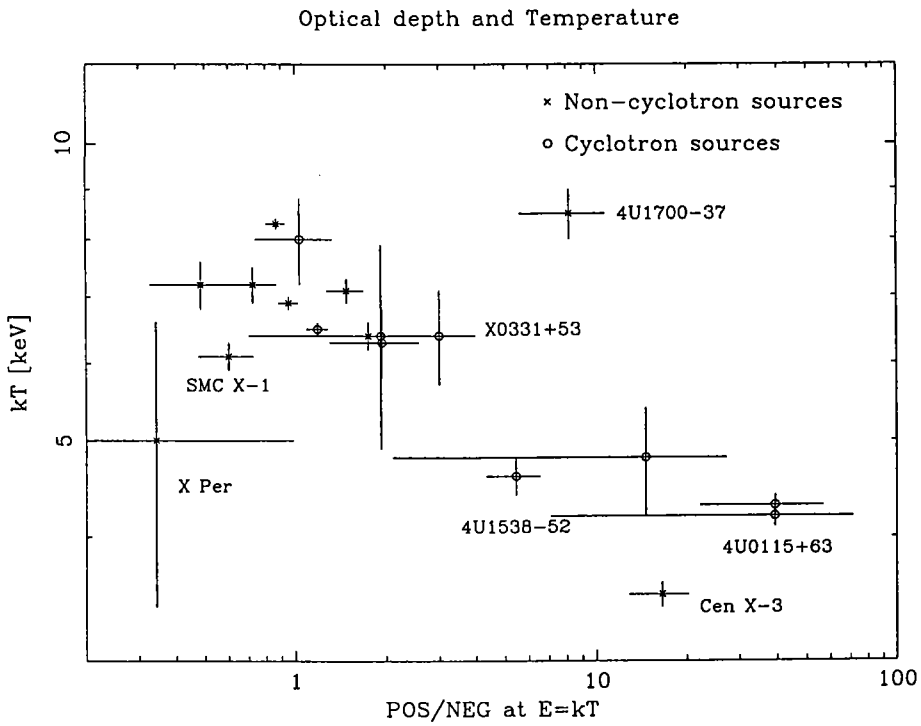

Figure 6.1.3: The plot of the the pos./neg. intensity ratio (optical depth) at $E = kT$ and kT with the NPEX model. There is an anti-correlation, which would caused by the efficient cooling at the large optical depth.

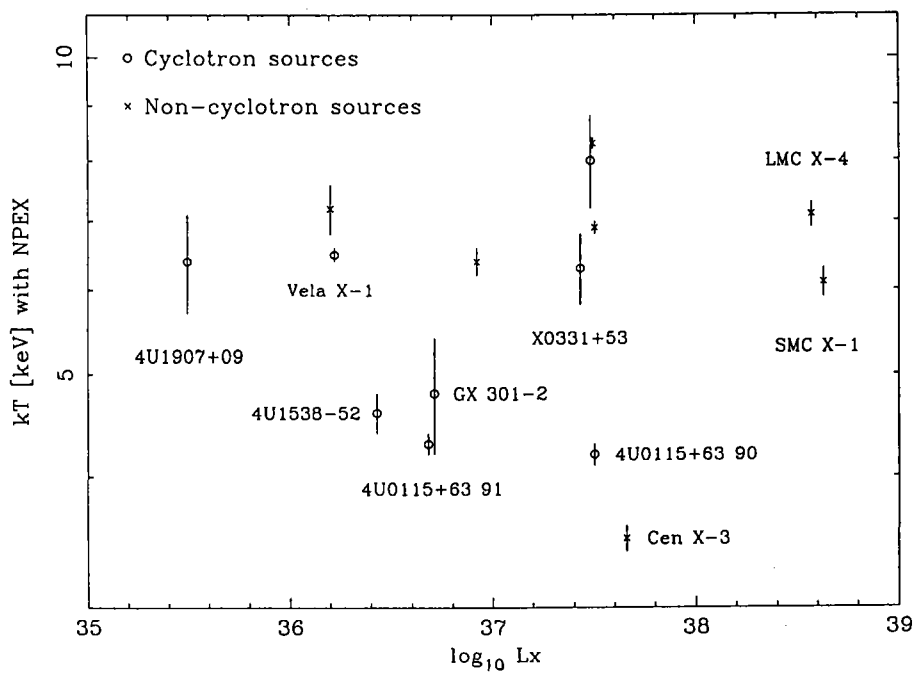

Figure 6.1.4: The L_x dependencies of the kT in the NPEX model. No dependency is seen.

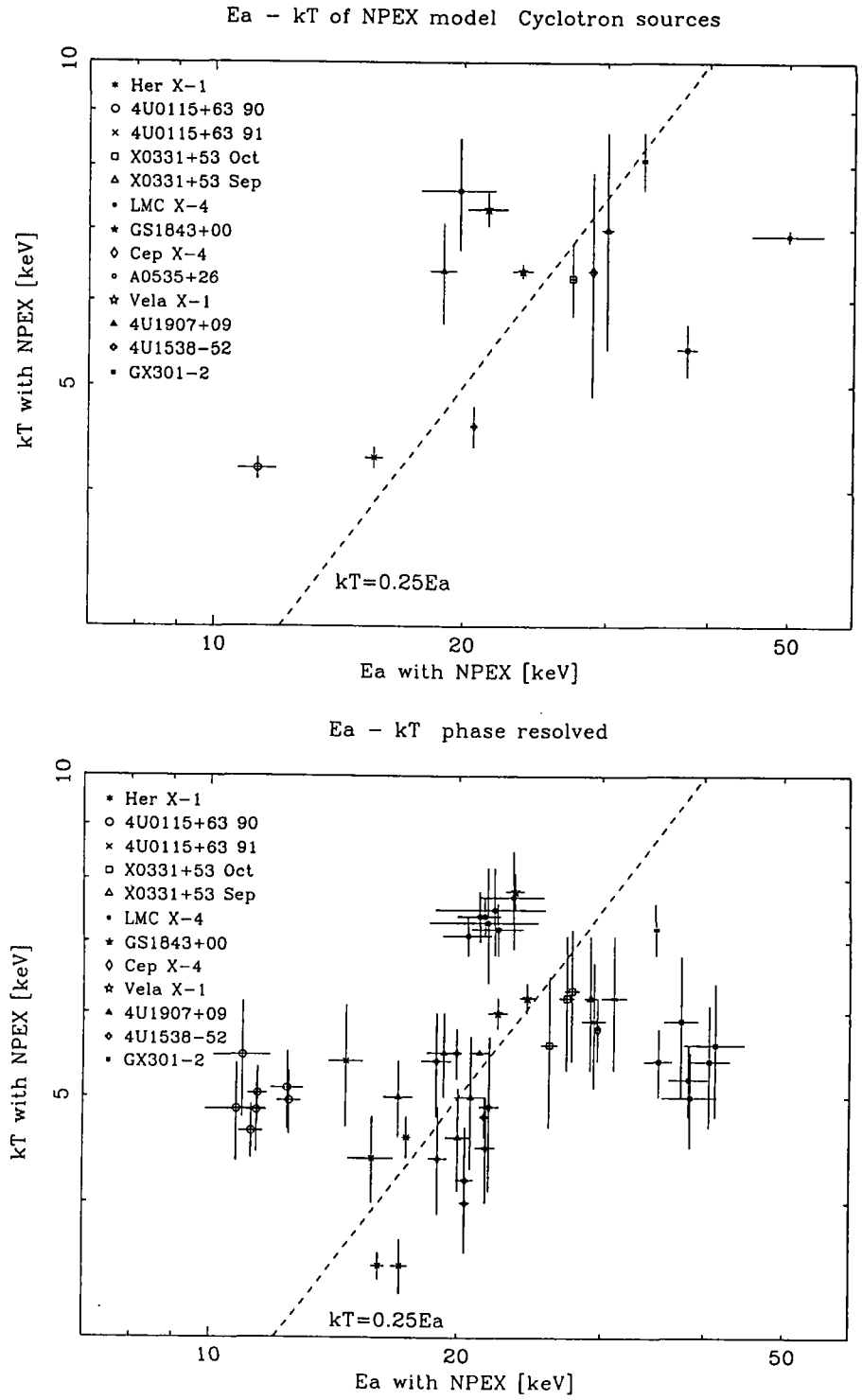

Figure 6.1.5: The E_a dependencies of the kT in the NPEX model of the average spectra (*top*) and phase resolved spectra (*bottom*). If the comptonization takes place, $kT = 0.25E_a$ is expected, which is consistent with the data.

6.2 Resonance shape

In §5.7, we investigate the shape of the cyclotron structure using a good quality data of X0331+53. Here we summarize the shapes of the cyclotron structures together with the other pulsars.

6.2.1 Superposing spectra

The NPEX × CYAB(s) model can fit the spectra of binary X-ray pulsars very well as shown in Chapter 5. In order to investigate the shapes of the resonance, we superpose the spectra normalized by the energy E_a (figure 6.2.1) after correcting the fall-off by kT and low energy absorption, and subtracting the iron emission line. We can see a variety of depths of the resonances; Vela X-1 is the shallowest and other pulsars appear as clusterized at minimum values of 0.4 and 0.2. Since the energy resolution of LAC is much better than the widths of the resonances as indicated in the figure, the widths are really broad with FWHM ranging 0.5–0.8 E_a. The origin of the broad width will be discussed in §6.2.2.

The shapes may look asymmetric, but it is not certain because the symmetry strongly depends on the continuum model. Since we used CYAB function, the global shape is like the CYAB function, but we will find the CYAB factor is the best model to express all the cyclotron pulsars except for X0331+53. The sharper structure seen in the curve of X0331+53, which is not expressed well by a single CYAB factor, but needs an additional sharper structure at the center (§5.7.2).

We try various models to find out the shape of the cyclotron structure. Candidate cross sections of resonance are CYAB, Gaussian, Lorentzian, and Voigt function (Mihalas 1978). The factor exp(− cross section) is multiplied to the continuum. We use the NPEX model as the continuum, since we have known that the models for the continua do not affect the shape of the resonance so much, from the study on X0331+53 in §5.7.2. We pick up 6 observations with good statistics, i.e. X0331+53 (in §5.7.2), Her X-1, 4U0113+63 in 1990 and 1991, Cep X-4, and 4U1538-52. The figure and parameters of the fittings are summarized in Appendix F.

Any of the four models cannot fit consistently all the pulsars. However, except for X0331+53, CYAB is the best model which gives rough fits to all the other pulsars. We should note that the CYAB model is not perfect and the fits are not always acceptable, as the residuals still have some wavy structures. Thus the resonance shape is not so simple that it can be expressed by a single analytic function. Radiative transfer and geometry would make it complicated, as suggested in the next section.

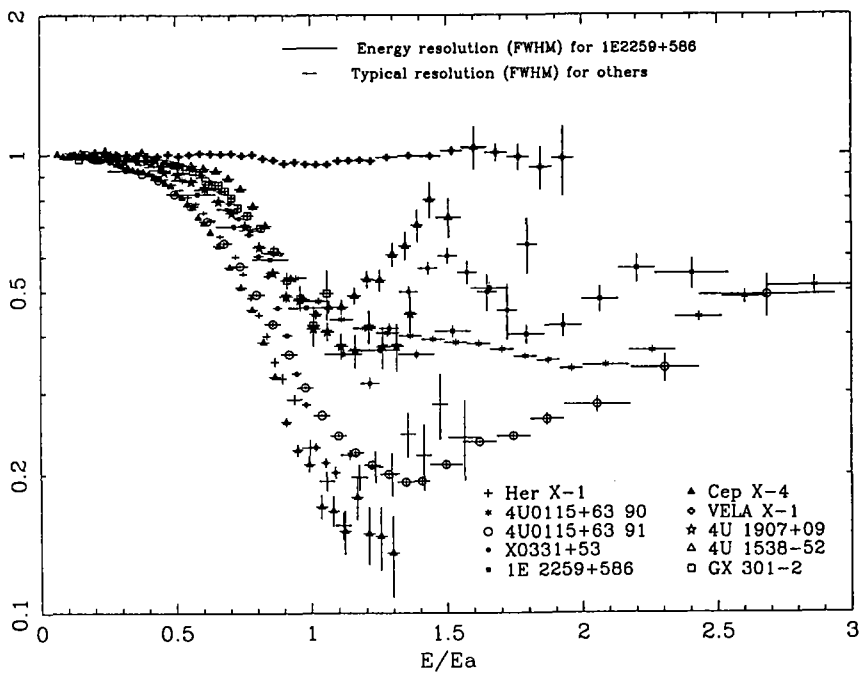

Figure 6.2.1: The superposed spectra corrected the fall-off by kT of the NPEX model with the energy normalized by E_a.

6.2.2 The width of the resonance

The energy resolution of *Ginga* LAC was good enough to reveal the fact that the cyclotron structures are broad (figure 6.2.1). Several reasons are considered as the origins of the width of the resonance (e.g. Bulik *et al.* 1992). One is the thermal Doppler effect. If the electron has a temperature kT, the energy of the scattered photon distributes as the Voigt function (Mihalas 1978), which has a gaussian-like peak with

$$\sigma = E_a \sqrt{\frac{kT}{m_e c^2}} \tag{6.4}$$

and a lorentzian-like tails which originates from the natural line profile. But as shown in Appendix F, the Voigt function does not give good fits in general. Another reason is geometrical effect. Since the cyclotron scattering region (nearly equals X-ray emitting region) has finite size, there would be a gradation of the magnetic fields in it. The most considerable case is the $1/r^3$ dependence of the dipole magnetic fields. We would observe a mixture of different magnetic fields, and the structure is observed to be broad. If this is the case, the broadening is not easy to be estimated since we must know the structure of the accretion column and the emission distribution.

We plot in figure 6.2.2 W/E_a versus kT taken from the best-fit NPEX parameters

in table 6.1.1 and 6.1.2. If the width is the thermal origin, $W/E_a = 1.2\sqrt{kT/511\text{keV}}$ is expected from eq. 6.4, since W in CYAB function is approximately HWHM ($W \sim 1.2\sigma$). The observed W/E_a, however, does not show a clear correlation with kT in figure 6.2.2. Most of the observed widths are $2 \sim 4$ times larger than those estimated from eq. 6.4. Therefore, the geometrical broadening would make a larger contribution to broadening the structure.

If the geometry determines the shape of the resonance, the width might have a relation to the X-ray luminosity L_X, since the luminosity would affect the beam pattern of the pulsars (White *et al.* 1983). However, as figure 6.2.3 shows, any dependency on the L_x was not found. The Luminosity is not the crucial parameters, but other geometrical parameters such as the angles between line of sight and magnetic axis, and between rotation axis and magnetic axis would play important roles.

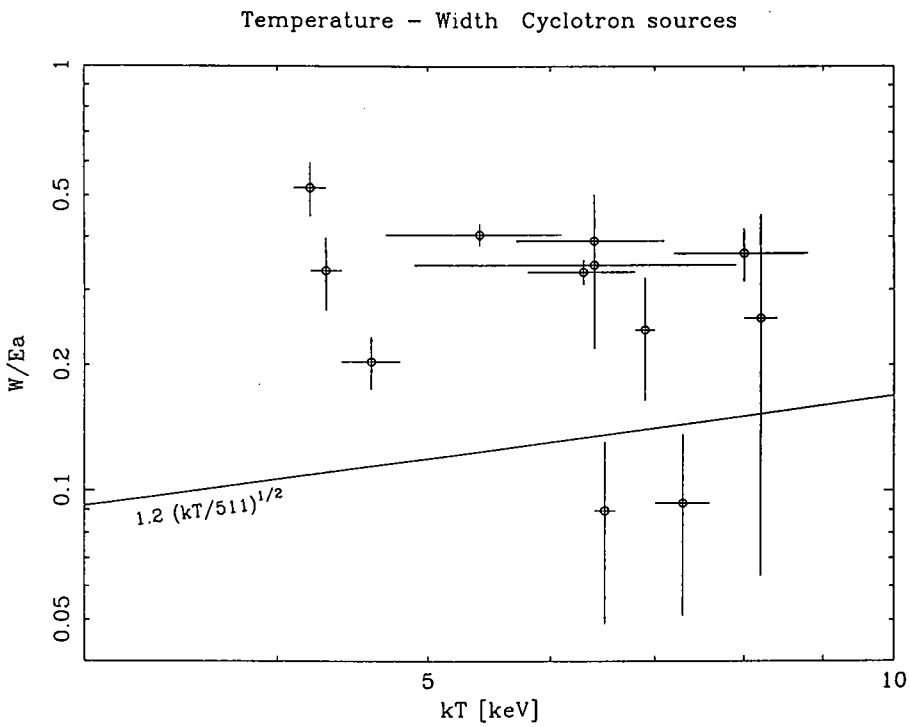

Figure 6.2.2: The relation between W/E_a and kT of the best-fit NPEX parameters in log-log scales. The line is the expected W/E_a from the thermal Doppler broadening. The observed W/E_a are larger than this line in general, which suggests that the thermal process would not be significant.

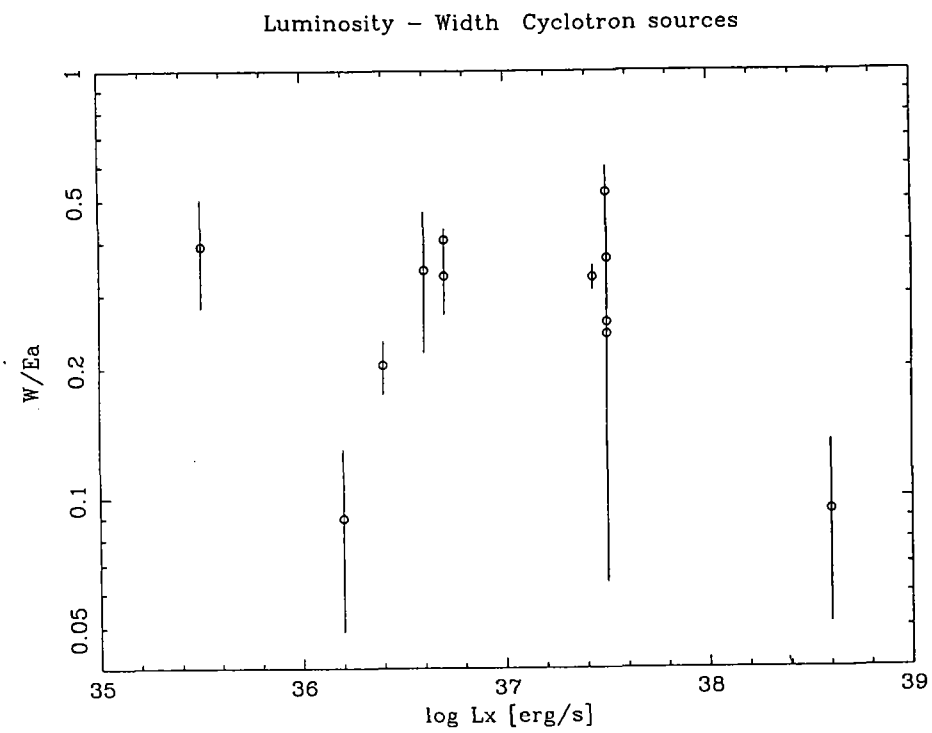

Figure 6.2.3: The width of the resonance W/E_a and the X-ray luminosity L_X plot. There is no correlation.

6.3 Resonance energy and Luminosity

6.3.1 Observation summary

We have observed some sources on several occasions with different intensities; those are 4U 0115+63, X0331+53, Cep X-4, Her X-1, and 4U 1538-52 (see §5 for each source). We summarize the intensities and resonance energies of these objects in table 6.3.1. In §5.4, 4U 0115+63 showed a remarkable change of the resonance energy with the intensity and we pointed out the possibility that the column height changes with the luminosity. We tentatively attribute the change of E_a to the height change of the scattering region ($E_a \propto r^{-3}$) and calculate the height difference in the table 6.3.1 assuming r in the weaker state is equal to the radius of the neutron star $R_{NS} = 10$ km. We discuss here the changes of resonance energies with other objects to obtain the general explanation.

6.3.2 Accretion column height

We estimate the height of the accretion column to examine whether the change in height cited in table 6.3.1 is reasonable or not, referring to the modeling by Burnard *et al.* (1991). Let us assume a dipole magnetic field and axisymmetric accretion onto a circular polar cap of area $\pi(\theta_c R_{NS})^2$. Here R_{NS} is the radius of the neutron star and θ_c is the opening angle of the polar cap, which is given as $\theta_c = \sqrt{R_{NS}/r_A} \sim 0.1$ by the Ghosh and Lamb theory. The mass flow is assumed to be constant within the polar cap and zero outside. The falling matter forms a 'mound' on the polar cap, whose radius is almost fixed to $\theta_c R_{NS}$ by the magnetic field and the height is determined by the luminosity L_X, such that the mound emits all of the gravitational energy released.

Since the cross section of electrons in a strong magnetic field depends on the direction of the magnetic field, we define two Eddington luminosities L_{Edd}^{eff} and L_1 for the two directions along and across the magnetic field. L_{Edd}^{eff} is defined to be the flux along the magnetic axis in balance with the accretion flow,

$$L_{Edd}^{eff} = L_{Edd} \frac{\pi\ (\theta_c R_{NS})^2}{4\pi\ R_{NS}^2} H_{||} = \frac{L_{Edd}\ \theta_c^2\ H_{||}}{4}.$$

Here $H_{||} = \sigma_T/\sigma_B$ is the ratio of the Thomson cross section σ_T to the Rosseland averaged scattering cross section σ_B for the radiation flow along B. Rosseland averaged opacity appears since the structure of the flow and of radiation field is determined by the diffusion of radiation along and across the magnetic field. $H_{||}$ is determined by the ratio of cyclotron energy and the temperature of plasma, which is described in Arons *et al.* (1987). Since the temperature kT and the cyclotron energy E_a in the emission region are comparable, $H_{||}$ and $H_\perp$ are approximately unity; $H_{||}$ and $H_\perp \sim 1$ when $E_a/kT < 2$. Here $H_\perp$ is the ratio of the Thomson cross section and the Rosseland averaged cross section for the

Table 6.3.1: Parameters of the cyclotron resonance energy and luminosity. The Δheight is calculated by assuming $E_a \propto r^{-3}$ with r in the weaker state equal to the radius of the neutron star R_{NS} = 10 km. $H_{\|}$ is a function of E_a/kT and obtained from Arons *et al.* 1987. H_s is the height of the column calculated by eq. (6.5) from L_X and $H_{\|}$ assuming $M_{NS} = 1.4\ M_{\odot}$.

sources date	count rate [c/s]	E_a [keV]	kT [keV]	$\log_{10} L_X$ [erg/s]	Δheight [m]	$H_{\|}$, $H_{\perp}$	H_s [m]
4U 0115+63	3–50 keV						
1990/2/11	4036	11.3 ± 0.6	4.25 ± 0.10	37.50	1100 ± 220	1.23	1280
1991/4/26	661	15.6 ± 0.4	4.34 ± 0.14	36.68	0		203
X0331+53	3–37 keV						
1989/10/1	3586	27.2 ± 0.3	6.3 ± 0.5	37.43	330 ± 70	1.44	930
1989/9/20	2271	30.0 ± 0.5	7.0 ± 1.6	37.29	0		674
Cep X-4	2–37 keV						
1988/4/3	834	28.58 ± 0.5 $(\pm 0.05)^a$	7.5 ± 3.8	36.67^b	82 ± 109 (± 14)	1.38	170^b
1988/4/8	692	28.94 ± 0.4 $(\pm 0.05)^a$	7.1 ± 2.2	36.59^b	40 ± 102 (± 14)		140^b
1988/4/14	450	29.29 ± 0.8 $(\pm 0.11)^a$	6.4 ± 1.7	36.40^b	0		90^b
Her X-1	3–60 keV						
1990/7/27	1154	34.1 ± 0.4	8.1 ± 1.2	37.53	-160 ± 140	1.35	1250
1989/6/3	857	32.5 ± 1.0	10.3 ± 3.2	37.44	0 ± 110		1020
1989/6/6	792	32.5 ± 0.4	8.2 ± 0.9	37.40	0		930
1989/5/3	739	33.9 ± 1.2	9.7 ± 5.2	37.37	-140 ± 123		860
4U 1538-52	3–37 keV						
1988/3/2	184	20.6 ± 0.2	4.7 ± 0.3	36.56	0 ± 50	1.47	120
1990/7/27	130	20.6 ± 0.2	4.6 ± 0.2	36.43	0		91

a: single parameter error, when other parameters than E_a are fixed to their best-fit values.
b: estimated in this work assuming observed height changes are equal to H_s changes. They would have very large errors because of the large fitting errors of E_a. The most probable distance to Cep X-4 is 3.0 kpc.

radiation flow across B and appears in the expression of L_1 below. L_{Edd} is the conventional Eddington Luminosity by the Thomson scattering given as

$$L_{Edd} = 2.01 \times 10^{38} \left(\frac{\kappa}{0.35\ \mathrm{cm}^2/\mathrm{g}}\right)^{-1} \left(\frac{M_{NS}}{1.4M_\odot}\right)\ \mathrm{ergs/s},$$

where κ is the electron scattering opacity, $\kappa = 0.2(1+X)\ \mathrm{cm}^2/\mathrm{g}$ and X is the mass fractional hydrogen abundance. For matter with cosmic abundances, $X = 0.73$ and $\kappa = 0.35\ \mathrm{cm}^2/\mathrm{g}$. Since radiation can escape from the side of the flow in the X-ray pulsars, $L_X > L_{Edd}^{eff}$ does not always means a cessation of flow. The Eddington luminosity across the magnetic field is defined as

$$L_1 = \theta_c L_{Edd} H_\perp.$$

The derivation of the equation is shown in Burnard *et al.* (1991) and Basko and Sunyaev (1976), but an intuitive understanding would be follows. The radiation pressure across the magnetic field produces the pressure towards the accretion flow, since globally the magnetic field lines are open upwards with an angle θ_c. The component of the pressure along the magnetic field is given by the factor of the opening angle θ_c.

In fact many pulsars satisfy

$$L_X \gg L_{Edd}^{eff} \sim 10^{35.7} \left(\frac{\theta_c}{0.1}\right)^2 \left(\frac{M_{NS}}{1.4M_\odot}\right) H_\parallel\ \mathrm{ergs/s}$$

and

$$L_X > L_1 \sim 10^{37.3} \frac{\theta_c}{0.1} \left(\frac{M_{NS}}{1.4M_\odot}\right) H_\perp\ \mathrm{ergs/s}$$

Accretion flow with the luminosity of this magnitude yields a mound which is no longer a flat patch on the surface. Let us assume the mound is as tall as it is wide ($R_{NS}\theta_c$), when it emits the Eddington luminosities, i.e. L_{Edd}^{eff} upward and L_1 sideways. When $L_X \sim L_1$, the height of the mound H_s would change in proportion to L_X. Thus the height of the mound becomes

$$H_s \approx \frac{L_X}{L_1} R_{NS}\theta_c = \frac{L_X}{L_{Edd} H_\perp} R_{NS} \tag{6.5}$$

above the surface. Detailed calculations by Burnard *et al.* (1991) and Basko and Sunyaev (1976) justify this relation showing that the height H_s is the place where the radiation-dominated shock at Thomson optical depth $\tau \sim 4-9$ transforms free fall matter into the subsonically settling on the mound. When $L_X \gtrsim L_1$ the mound is at least as tall as it is wide. This has significant consequences for the nature of the spectrum and pulse profiles.

6.3.3 Comparisons of observation and theory

We choose kT of the NPEX model as the temperature, assume R_{NS} = 10 km and M_{NS} = 1.4 $M_{\odot}$, and calculate $H_{\perp}$ and H_s listed in table 6.3.1 and shown in figure 6.3.1. The predicted H_s agree very well with the observations for X0331+53 and 4U 0115+63. The values of 4U 1538-52 are also consistent, since the low luminosity makes a low mound which reduces the change of the resonance energy by the 1.3 times the luminosity change. The measured magnetic field of 4U 1538-52 is almost that on the surface of the neutron star. We should mention that we do not always observe the magnetic field at the top of the mounds, but the height of the cyclotron scattering region should be proportional to the height of the mound H_s. The good agreement of the observations and predictions support the assumption that the change of the resonance energy is caused by the height change by the luminosity and the dipole dependency of the magnetic field.

Let us assume simply H_s to be the height in table 6.3.1 and apply it to Her X-1 and Cep X-4. This assumption is justified by the good agreement between X0331+53, 4U 0115+63, and 4U 1538-52. Her X-1 does not appear to obey the relation, and E_a is changing independently of L_X. The E_a in 1989/6/3 and 1989/6/6 were observed at similar values, which might indicate that the E_a is constant during the main-on of the same 35 d cycle. If E_a represents the column height, we can conclude that the intensity change of the 35 d cycle is not caused by the $\dot{M}$ change but by other geometrical reasons, such as an increase of the scattering gas, occultation by the accretion disk, change of the X-ray beam and so on. This is consistent with the fact that optical data shows X-ray heatings even in the low state of the 35 d cycle (Bahcall 1972, 1978, see §2.4.1).

In Cep X-4 we cannot calculate H_s since we do not know the distance of this source. But by assuming the relation (eq. 6.5), we can obtain a rough distance of Cep X-4. Since we have three observations, we get two independent solutions of, for example, H_s on 1988/4/14, which are 95 m and 85 m. Although the fitting errors of E_a are large, the good agreement between the two values may show that the E_a values are more reliable, presumably because such fitting parameters as kT, W, and D may couple with each other and make the error of the well defined E_a larger. In fact when we fix the parameters except for E_a, the errors of H_s get as small as 20 m which is comparable to the scatter of the results and reasonable. We use this value for the error. If we take the mean value 90 m for H_s on 1988/4/14, those on 4/3 and 4/8 are calculated to be 170 m and 140 m, respectively, and also the luminosities of the three days to be $\log_{10}L_X$ = 36.67, 36.59, and 36.40 with errors of $\pm$ 0.06. From these results we have obtained the distance to Cep X-4 of 3.0 $\pm$ 0.2 kpc. Therefore, this can be a new method to estimate the distance to a pulsar.

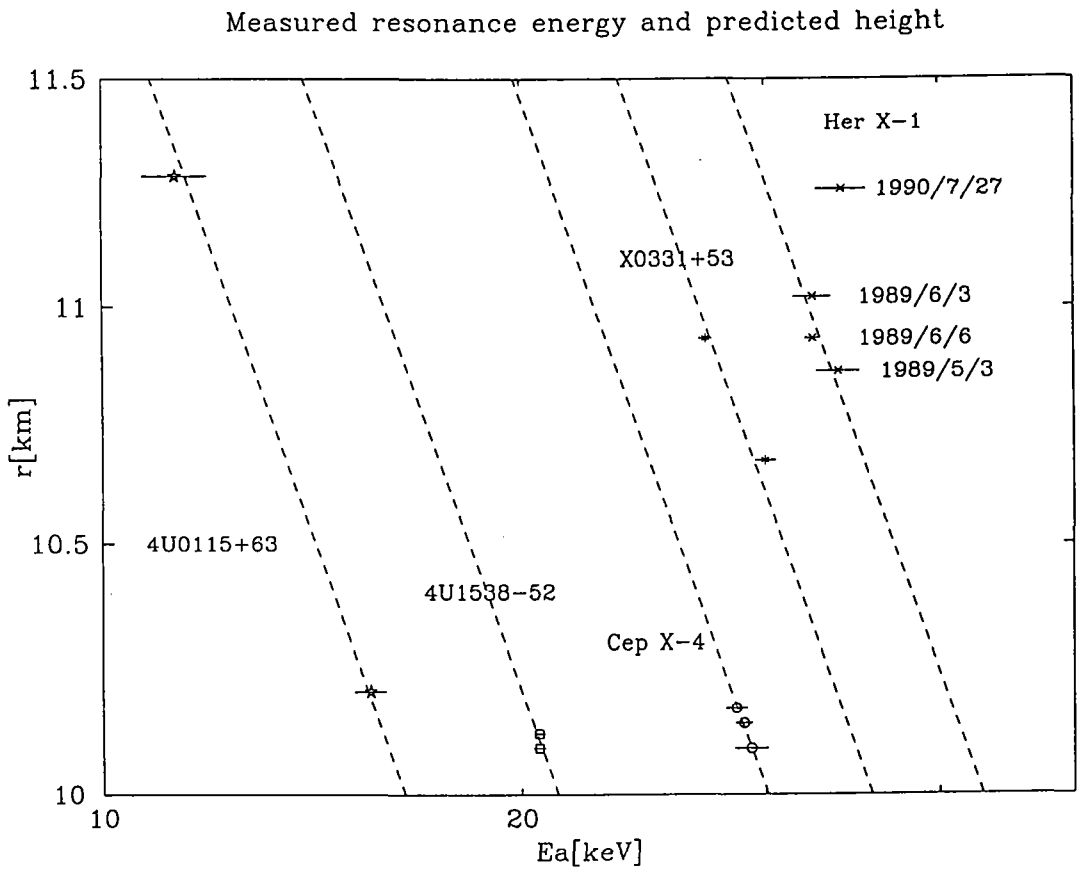

Figure 6.3.1: The observed resonance energy and the height of the accretion column estimated by a simple theory (eq. 6.5). The dashed line indicates $1/r^3$ dependencies for each source. 4U0115+63, 4U1538-52, and X0331+53 obey the simple r^{-3} well. Her X-1 does not obey this law, in which another mechanism to change the intensity would exist as has been proposed for the reason of the 35 d cycle. Assuming the r^{-3} relation, the luminosities of Cep X-4 is calculated, which leads the distance to Cep X-4 to be 3.0 kpc.

6.3.4 A problem of the height interpretation

In the previous section we attribute the change of the resonance energy to the height change of the accretion column produced by the change of the luminosity. All the 5 pulsars are explained successfully, and therefore the interpretation seems to be correct. However, a problem with this interpretation arises in the pulse phase resolved spectra of low luminosity pulsars.

We have summarized the pulse phase dependencies of the NPEX $\times$ CYAB model parameters in Appendix G. The resonance energy changes as much as $\pm$ 10 % in most of the pulsars. In luminous pulsars such as Her X-1, the above interpretation is successful. The high resonance energy at the pulse peak can be understood if we are observing the most luminous bottom of the column, and therefore the beam pattern is fan-beam as expected. The wide width can be interpreted by the variation of the magnetic fields when we observed from the side of the column. A problem is that the resonance depth is large at the pulse peak, while the basic angular dependency of the cyclotron cross section is smaller when viewing from the side than when viewing from the top. However, it is not a serious problem since we do not take the radiation transfer into account.

The above interpretation fails in the low luminosity pulsars, such as 4U 1538-52 and 4U 1907+09. Basically the accretion columns of these pulsars are considered to be low like a flat patch on the surface. Therefore we cannot expect a change of the magnetic field due to the height change in the accretion column. The relativistic resonance energy in §2.6.1 has a θ dependence. It is, however, not large enough to explain the 10% change. These pulsars show as large widths as luminous pulsars, which is also hard to explain. The problem was also discussed by Clark *et al.* (1989) and Bulik *et al.* (1992) for 4U 1538-52, but remains unsolved. Recently Bulik *et al.* (1995) introduced asymmetric magnetic fields to explain this phenomenon.

Therefore we should mention that the interpretation shown in this section is not established yet.

6.4 Magnetic fields of pulsars

The magnetic fields have been measured from 12 X-ray binary pulsars using the cyclotron resonance. In this section we compare the derived magnetic fields with other parameters of the system.

6.4.1 Pulse period and Luminosity against Resonance energy

As shown in Chapter 5, about a half of the pulsars show the cyclotron structures in their spectra and the other half do not. We plot the resonance energies against pulse periods and luminosities in Figure 6.4.1. Although the P and L_X change by 3 orders of magnitude, the resonance energies do not show any clear dependencies, indicating they are not determined by the external factors such as pulse period and luminosity.

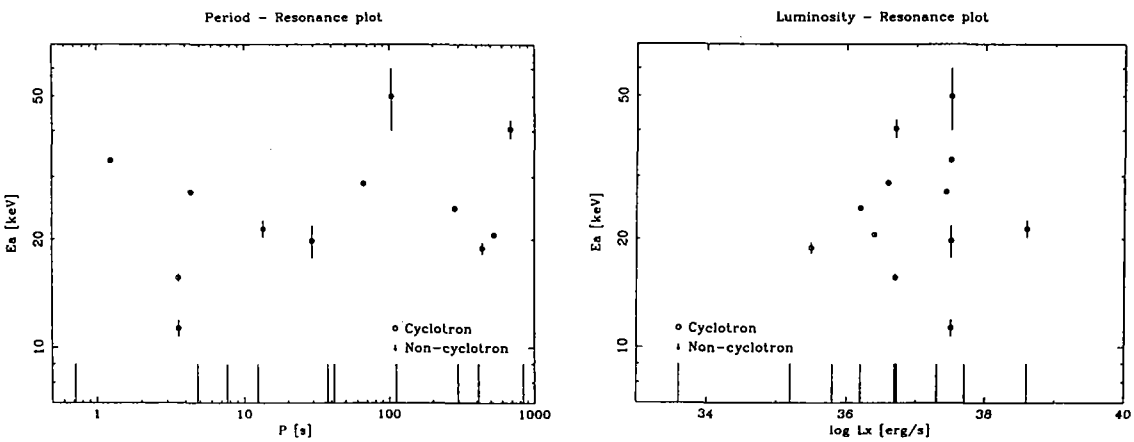

Figure 6.4.1: The existence of the resonance and the resonance energy E_a shows no dependencies against pulse periods P and luminosities L_X. Short lines on the horizontal axis are the non-cyclotron sources.

6.4.2 Spin equilibrium and resonance energy

The pulsars get or loose angular momentum by the accretion at $r = 0.52r_A$ (r_A : Alfven radius) according to the Ghosh Lamb theory (see §2.3.4). If the accretion continues constantly, the pulsar rotation finally reaches an 'equilibrium' state, which satisfies the equation

$$\left(\frac{B_{eq}}{10^{12}\mathrm{G}}\right) = 0.434\left(\frac{P}{1\mathrm{s}}\right)^{7/6}\left(\frac{L_X}{10^{37}\mathrm{erg/s}}\right)^{1/2}.$$

We have obtained the magnetic field B_{cy} from the cyclotron resonance, and compare B_{cy} and B_{eq} in figure 6.4.2. A pulsar in the equilibrium state should be located on the diagonal line $B_{cy} = B_{eq}$. Four fast-rotating pulsars; Her X-1, 4U0115+63, X0331+53, and

1E2259+586 are found to be almost in the equilibrium state. However, all the other pulsars are in the $B_{cy} < B_{eq}$ region, where theory predicts the pulsars to spin up, but it does not agree with observations. Most of the pulsars are not in rotation equilibrium, which may be because of the transient nature, wind-fed accretions, young age, or incompleteness of the theory.

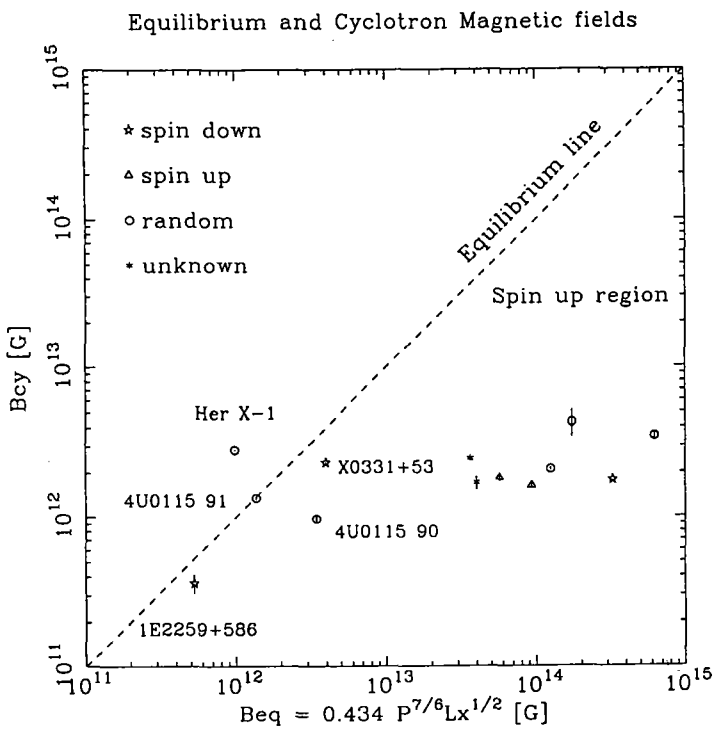

Figure 6.4.2: The equilibrium magnetic field B_{eq} predicted by Ghosh Lamb theory and the true field B_{cy} from the cyclotron resonance. A pulsar in the equilibrium state should be on the diagonal line $B_{cy} = B_{eq}$. Four fast-rotating pulsars (Her X-1, 4U0115+63, X0331+53, and 1E2259+586) are almost in the equilibrium state. The other pulsars are in the $B_{cy} < B_{eq}$ region, where the theory predicts the pulsars to spin up but it does not agree with the observation.

6.4.3 Age of neutron star and magnetic field

Magnetic field decay is an important problem concerning the neutron star interior and evolution of the neutron star binaries. The age estimated as $P/\dot{P} = 10^2 - 10^6$ y (e.g. Nagase 1989) is not correct for the age of the neutron star in the X-ray binaries, since the accretion is intermittent and strongly depends on the binary evolution. Instead, the lifetime of the optical companion would be helpful. Statistically speaking, half the main sequence lifetime of the companion would be the age of the system. Figure 6.4.3 summarize the observed cyclotron energies as a function of the optical companion masses. The figure suggests that the magnetic fields of X-ray pulsars do not decay, at least on the typical

lifetime of massive binary systems ($\sim 10^7$ y). In particular, Her X-1, thought to have an age of $\gg 10^8$ y has a strong field of 3×10^{12} G, while 1E2259+586, thought to be a young pulsar in SNR, seems have $\sim 5 \times 10^{11}$ G.

From these results, we consider the following possibilities as a scenario of magnetic field evolution of neutron stars.

1. Strongly and weakly magnetized neutron stars are intrinsically different and the fields do not decay or decay very slowly on a longer time scale of $> 10^9$ y.

2. The field decay occurs under some conditions, such as a large amount of mass accretion.

3. At some critical field intensity, the neutron star makes a sudden phase transition such as between ferromagnetic and paramagnetic states of neutron spin alignment, although alignment of the spin is not likely in the fluid neutron.

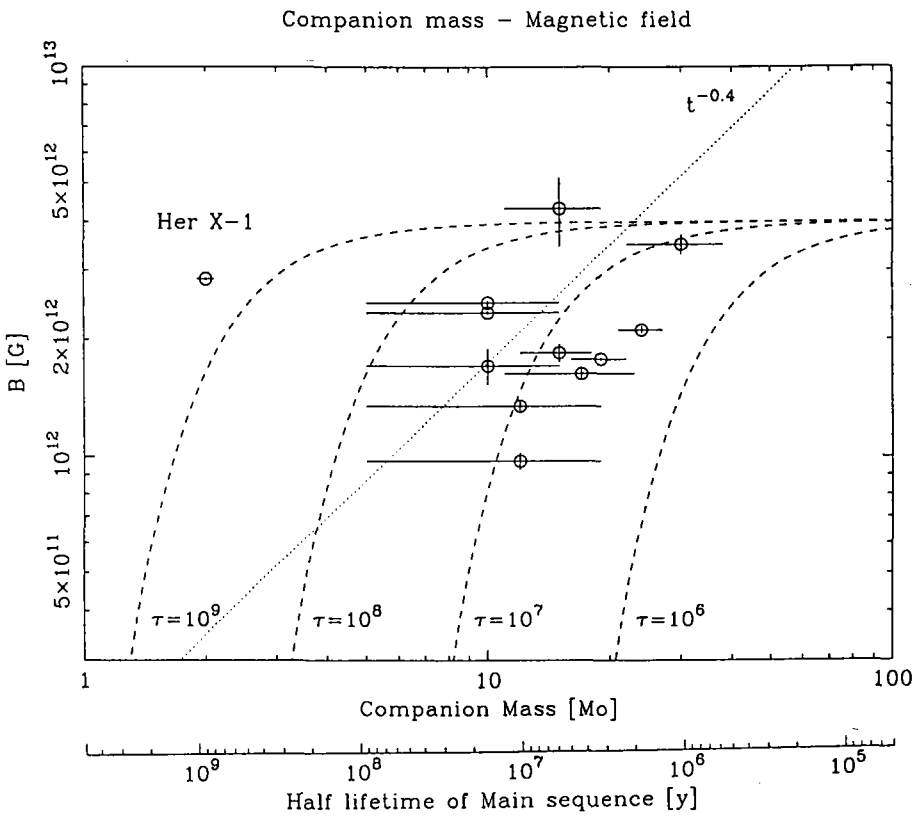

Figure 6.4.3: The observed cyclotron energies and the optical companion masses. Statistically speaking, half of the main sequence lifetime of the companion gives the age of the system.

6.4.4 Magnetic fields distributions and future prospects

We show the magnetic fields distribution of X-ray binary pulsars in figure 6.4.4. The magnetic fields range between $3 \times 10^{11} - 4 \times 10^{12}$ G, which is similar to the age-corrected distribution of the radio pulsars (*bottom dotted line*), ranging between $10^{11} - 10^{13}$ G with a peak at $2 - 3 \times 10^{12}$ G. In this figure the distribution of X-ray pulsars is different from that of the *observed* radio pulsars (*bottom solid line*) without age correction, which might indicate that the magnetic fields of the X-ray pulsars do not decay within a characteristic time scale of the radio pulsars ($10^6 - 10^7$ y). This is consistent from the results estimated by the companion masses in the previous section. Moreover, the magnetic fields by the radio observations are obtained assuming the magnetic dipole radiation. The multipole components would not contribute to the radio emission. Therefore the magnetic fields measured by the radio observations are only the dipole component. However, those measured by the X-ray cyclotron structure are near the surface of the neutron star. The agreement of the two indicates that the magnetic fields of the neutron star is dipole, and not multipole.

Here, we should discuss the selection effect. We expect that a pulsar with a cyclotron resonance less than a few keV would show a steep power law of $\alpha \sim 3$ in the *Ginga* energy range, as does 1E2259+586. But all the other pulsars have shown a flat power law in 2–10 keV range and the pulsar with $E_a \lesssim 2$ keV does not seem to exist. The temperatures with the NPEX model give information on the possibilities of high magnetic field pulsars. So far A0535+26 has the strongest magnetic field with resonance at 50 keV. However, the $E_a - kT$ relation predicts all the pulsars would have the cyclotron resonances in 4–50 keV. Therefore the pulsars with more than 50 keV resonances are not likely to exist.

Thus the magnetic field of X-ray binary pulsars are likely to really cluster between $3 \times 10^{11} - 4 \times 10^{12}$ G. One of the possible explanations would be as follows. The strong magnetic field of a neutron star is considered to be the frozen-in magnetic fluxes of the progenitor core in the supernova explosion. The problem of the field similarity of the neutron stars is then replaced by the field similarity of the progenitor core. The progenitors of the neutron stars are OB stars which do not have convective zones, sunspots and local magnetic fields. The magnetic field in the core might be the frozen-in magnetic fields at the star formation. If the star is late-type, the magnetic field inside diffuses out during its lifetime. However OB stars might keep the flux in the stellar core until the ends of their short lives. We should note that there is an idea that a stellar core has a convection and magnetic fields are produced through equipartition (Ruderman and Sutherland 1973). However, this would cause multipoles rather than a dipole and would not explain the observed results.

If we assume the star is formed from the gas with the interstellar magnetic field of 100 μG, the flux conservation law requires $(10^6 \text{ cm})^2 10^{12}\text{G} = (10^{11} \text{ cm})^2 10^2\text{G} = (10^{14}$

cm)$^2 10^{-4}$G, for the pulsar, the progenitor, and the disk in the star formation, respectively. The required radius for 100 μG interstellar magnetic field is as large as the Jupitarian orbit. The collapsing gas in the star formation would be limited by the interstellar magnetic field, when it becomes ionized. If the magnetic field is too strong, the gas cannot gather together to be a star. Thus the magnetic fields of the neutron star might be selected by these processes to have similar values.

For future observations, it is important to detect of X-ray pulsars with magnetic fields weaker than 4×10^{11} G or stronger than 5×10^{12} G. The former would be performed by the observatories which are sensitive in the low energy range, such as ASCA. The latter would be carried out by the observatories sensitive in 10-200 keV, such as XTE and Astro-E.

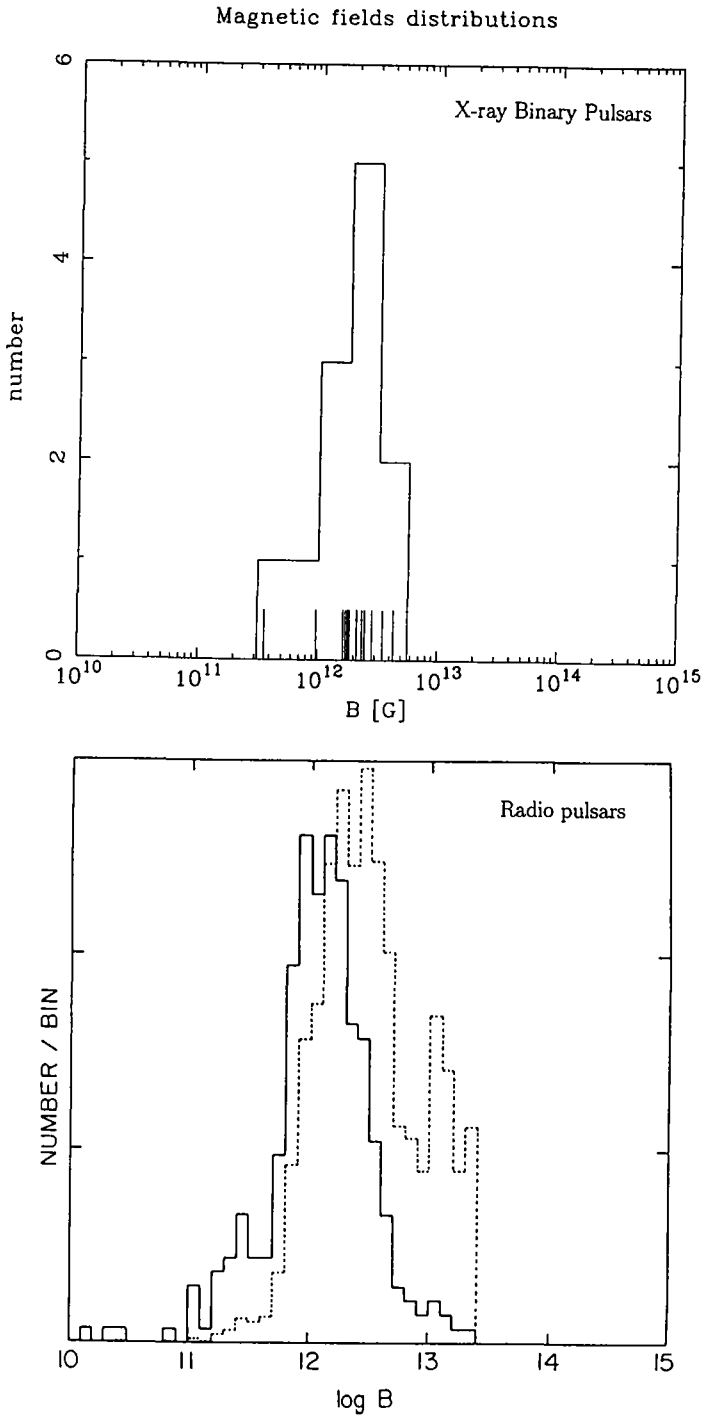

Figure 6.4.4: The magnetic fields distribution of X-ray binary pulsars measured by the cyclotron resonances (*top*). The data magnetic fields of all the 12 pulsars are indicated by the short lines on the horizontal axis. It is similar to the age-corrected distribution of the radio pulsars (*bottom dotted line*), ranging in $10^{11} - 10^{13}$ G with a peak at $2 - 3 \times 10^{12}$ G. The solid line in the bottom figure is the distribution of the observed radio pulsars, which does not agree with that of X-ray pulsars.

Chapter 7

Conclusions

We have investigated X-ray spectra of binary pulsars observed with *Ginga*. In order to detect the cyclotron structures, we performed reduced high voltage observations for some pulsars and discovered new cyclotron structures. In this thesis, confirming the previous results, we analyzed all the data systematically.

1. We introduced a new model for continua, NPEX model (Negative Positive power law EXponential), which is given as

$$NPEX(E) = (A_1 E^{-\alpha_1} + A_2 E^{+\alpha_2}) \exp\left(-\frac{E}{kT}\right),$$

   where kT is the typical temperature of the X-ray emitting plasma, and α_1 and α_2 are the negative and positive power-law indices, respectively.

   From the study of the spectra of Her X-1, the α_2 was found to be 2.0 ± 0.3, which expresses the high energy part of the blackbody; i.e., Wien spectrum. Therefore α_2 was fixed to 2.0 and used for the whole analysis.

   - Using the NPEX model for the continuum and the CYAB factor (Cyclotron Scattering Model; §2.6.2 and 5.1.5) for the cyclotron resonance, we successfully fit the spectra of all the pulsars with the same model. For sources without cyclotron structure, only the NPEX model was used, and for those with the second harmonic, another CYAB factor was multiplied.
   - A possible physical meaning of the NPEX model is the Comptonized spectra, whose temperature might be determined by the magnetic field with the relation of $kT \approx 0.25 E_a$.

2. The NPEX model is a smooth function and can represent the slightly concave spectra of X-ray pulsars; hence, the model is also favorable to detect line-like spectral structures.

- We have found the cyclotron structures from 11 sources among a total of 23 X-ray pulsars and pulsar-candidates of which *Ginga* made good quality observations. Adding one from which *HEXE* discovered the cyclotron line, the cyclotron structures have been detected from 12 pulsars which are about a half of the 23 sources.
- The magnetic fields were discovered in the range of $4 \times 10^{11} - 5 \times 10^{12}$ G, and the distribution was shown for the first time. The distribution of the magnetic fields is remarkably similar to that of radio pulsars, which might indicate that the magnetic fields of the X-ray pulsars do not decay within a characteristic time scale of the radio pulsars ($10^6 - 10^7$ y) and the magnetic fields of the neutron star is dipole, and not multipole.

3. About the cyclotron structures and resonance energies, we have found;

- Second harmonics are observed from 4U 0115+63 in the 1990 observation and possibly from Vela X-1.
- However, the cyclotron structure of 4U 0115+63 changed to a single structure in 1991. The resonance energy also increased by 40 %. If we attribute this change to the height of the scattering region in a dipole magnetic field, the difference is as much as $\sim$ 1.1 km.
- Changes of the resonance energies with luminosities for 5 pulsars are well explained by the accretion column height model. However, the same model does not explain the changes of the resonance energies in different pulse phases of the low luminosity pulsars.
- The widths of the cyclotron structures are as wide as $W \sim 0.4E_a$, and are larger than those expected from the thermal broadening by the plasma with temperature kT which is obtained from the NPEX model fittings. This possibly indicates that a geometrical broadening is taking place.
- The CYAB model can represent line shape better than other analytic functional forms like Gaussian, Lorentzian, and Voigt function with an exception of X0331+53, for which the data show an additional sharp structure near the resonance center.

Appendix A

SPFD & SPFC

SPFD is Spectral Fitting Double precision program written in FORTRAN and running on a FACOM mainframe computer : M380 M770 M780. It was written by Dr. Ohashi and some colaboration of *Ginga* team. It can handle binning selection and fitting model easily. All the fitting of *Ginga* data were done by this program.

The fitting has two stages, first Simplex method which serches χ^2 minimum in a grobal scale, second the linearization method which is commonly used for minimum χ^2 fitting.

The response matrixes of *Ginga* are 700 $\times$ 700 single precision for three layer patterns : TOP, MIDDLE and TOP + MIDDLE with normal high voltage 1830V. 1 unit of the matrix corresponds to 0.1keV. The first number 1 unit is for integrated flux between 0 and 0.1 keV. So the matrix is for 0–70 keV. Although the observational energy range is up to 37 keV in the normal HV and 60 keV in the reduced HV, there is Xe K escape event, which appears 30keV below the true peak. The rate of the escape event is about two times more than the normal event. Thus 0–70 keV matrix fully covers 0–40 keV. Since the stopping efficiency drops exponentially in the high energies, the matrix is effective for a little higher energy up to 60keV.

The 700 $\times$ 700 matrix is summed to 700 $\times$ 48 matrix in SPFD, because the LAC has 48 energy channels. The summation evaluates a calibration energy scale, the reflection inside the colimeter, the pulse height jump at Xenon L edge and the space charge effect. They take the width of the 64 ADC channels to be equal, which is justified by the ground calibrations of electronics. All the calibration uncertainties are pushed into the systematic error, which is 1% of the data counts. The systematic error and the statistical error are added together and used for the fitting. The value of the systematic error was determined to give reasonable fits to many targets in the PV phase or of early observations, but it is sometimes too large for the bright source, for Crab or some pulsars dealt in this thesis. We did not change the error value to keep the consistency.

Recently work stations have become popular and we have transported the core of the

SPFD to the work stations (SPFC), where a part of the program was rewritten in the C language. Most of the analysis appeared in this thesis was performed using SPFC on DEC α work stations.

The response matrix is also transrated for XSPEC, which is commonly used in the spectral fitting in the X-ray astronomy.

Appendix B

Pulse Profiles

B.1 Whole Energy Band

In figure B.1.1, we show pulse profiles of the observed pulsars, integrated over the entire 2–37 keV energy band and folded with the derived periods. These pulse profiles generally agree with previous results (White, Swank and Holt 1983; Nagase 1989). The pulse profiles of 4U0115+63 in 1990 and 1991, which exhibited a remarkable change in the spectra are shown in B.1.2.

B.2 Energy-Divided

The pulse profiles of X-ray pulsars change considerably with energy, although the degree of energy dependence varies from object to object. There is a general tendency that the pulse profile becomes simpler, either single-peaked or double-peaked, at higher energies. For example, Vela X-1 shows five peaks per one pulse cycle below several keV, but the profile has only two peaks of about euqal heights above $\sim$ 10 keV (figure B.2.1). A reason of this change is the amount of photoelectric absorption (Nagase *et al.* 1986).

However, the energy dependence in the pulse profile is often observed even above $\sim$ 5 keV, where the photoelectric absorption would be negligible. Therefore we infer that the pulse profiles are intrinsically energy dependent; in other words, the X-ray emission is fairly anisotropic, and the X-ray beam pattern is energy dependent (§2.7). The most likely cause of such an energy dependent beam pattern is the electron cyclotron resonance (see §2.7).

Keeping the above point in mind, in figure B.2.1 we show pulse profiles of some pulsars folded in several energy bands. The energy bands for each object have been selected considering the cyclotron resonance energy described later. These results clearly show that the profile is energy dependent even above 10 keV.

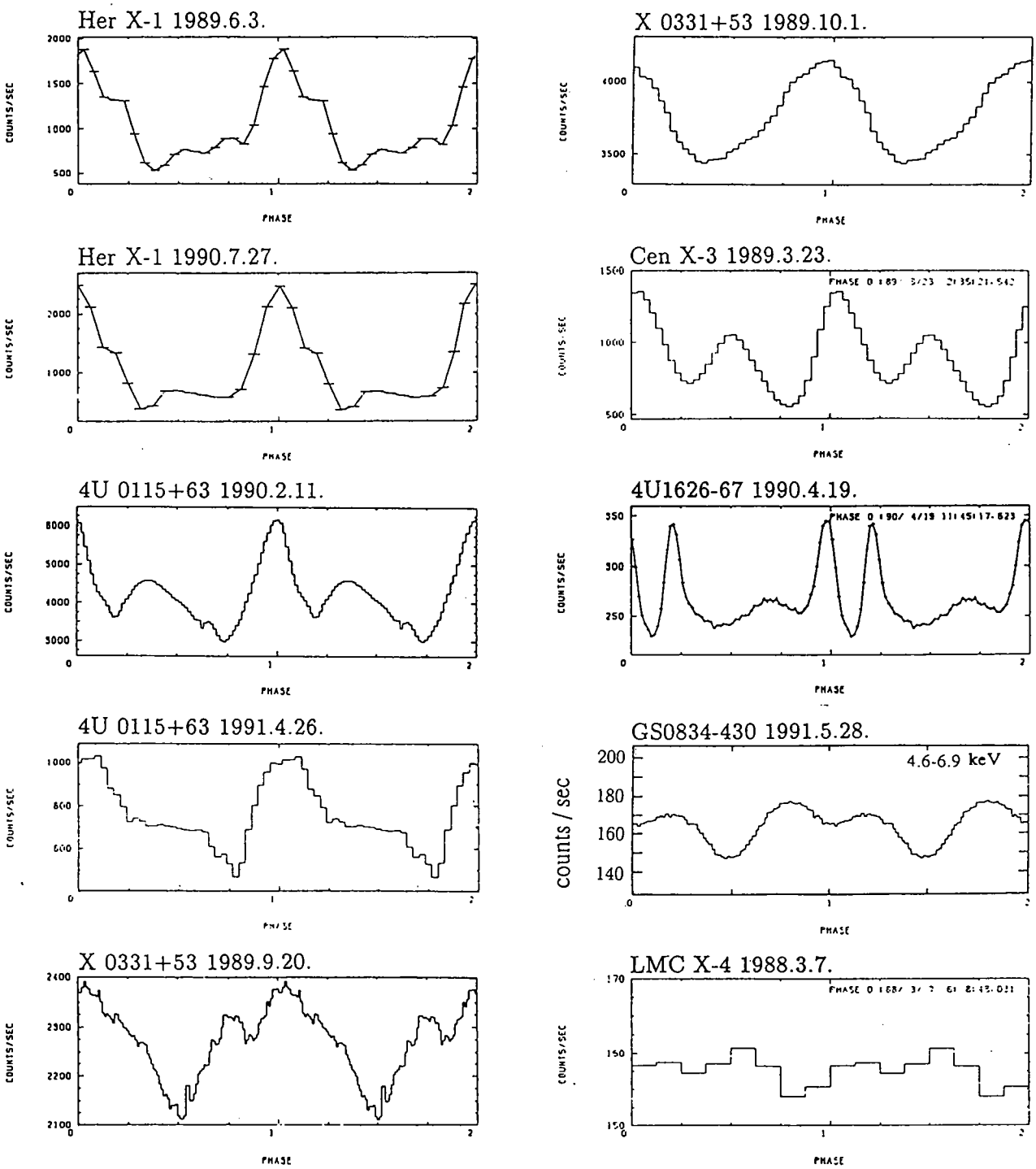

Figure B.1.1: Pulse profiles in the total energy band, otherwise noted (*to be continued*).

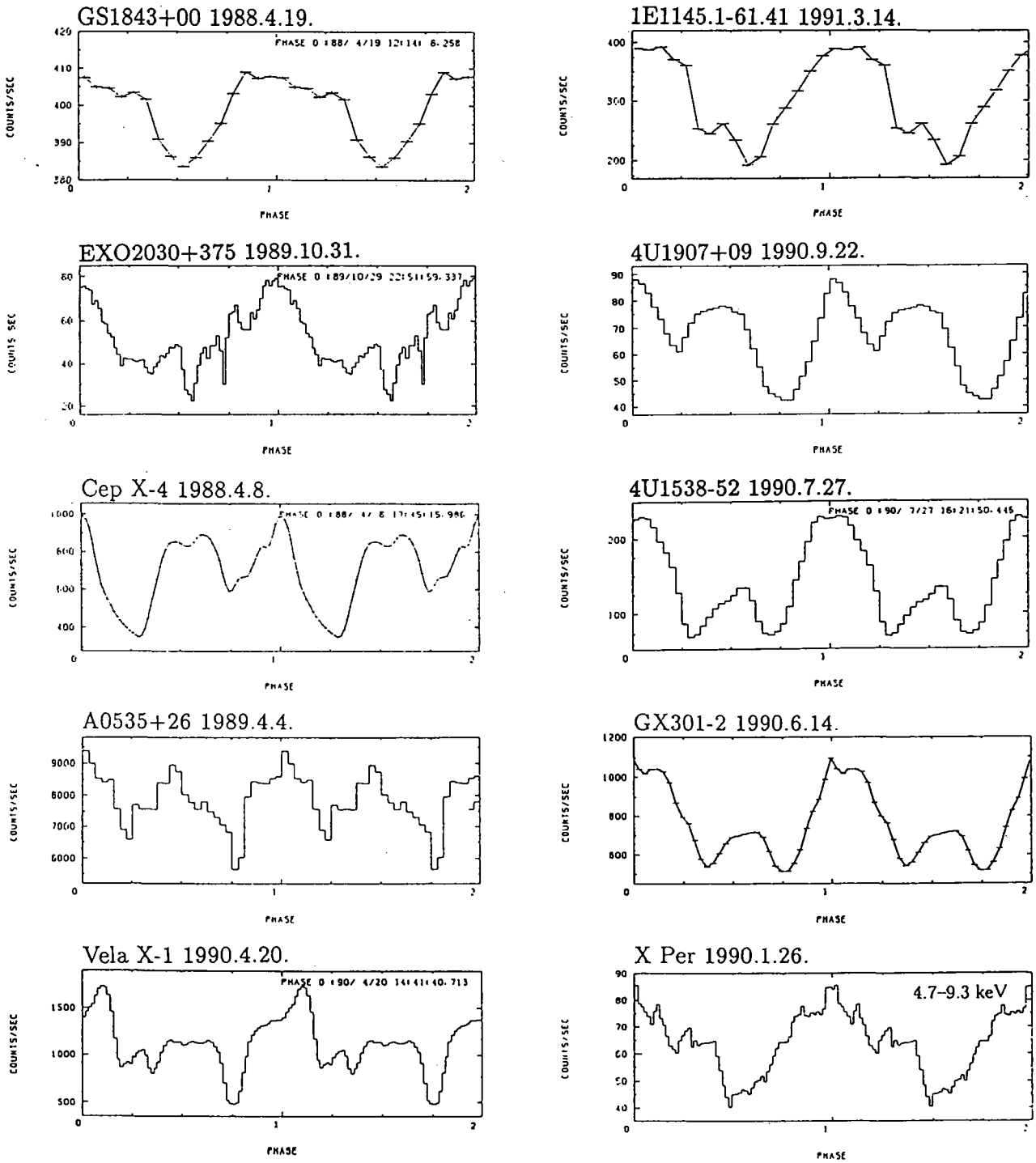

Figure B.1.1 (*continued*): Pulse profiles in the total energy band, otherwise noted.

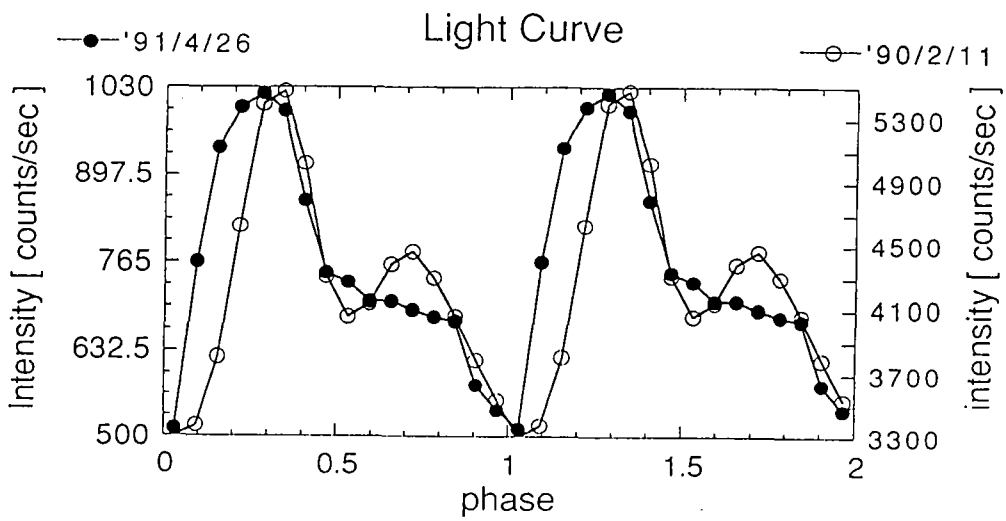

Figure B.1.2: The similar pulse profiles of 4U0115+63 in 1990 and 1991, which exhibited a remarkable change in the spectra.

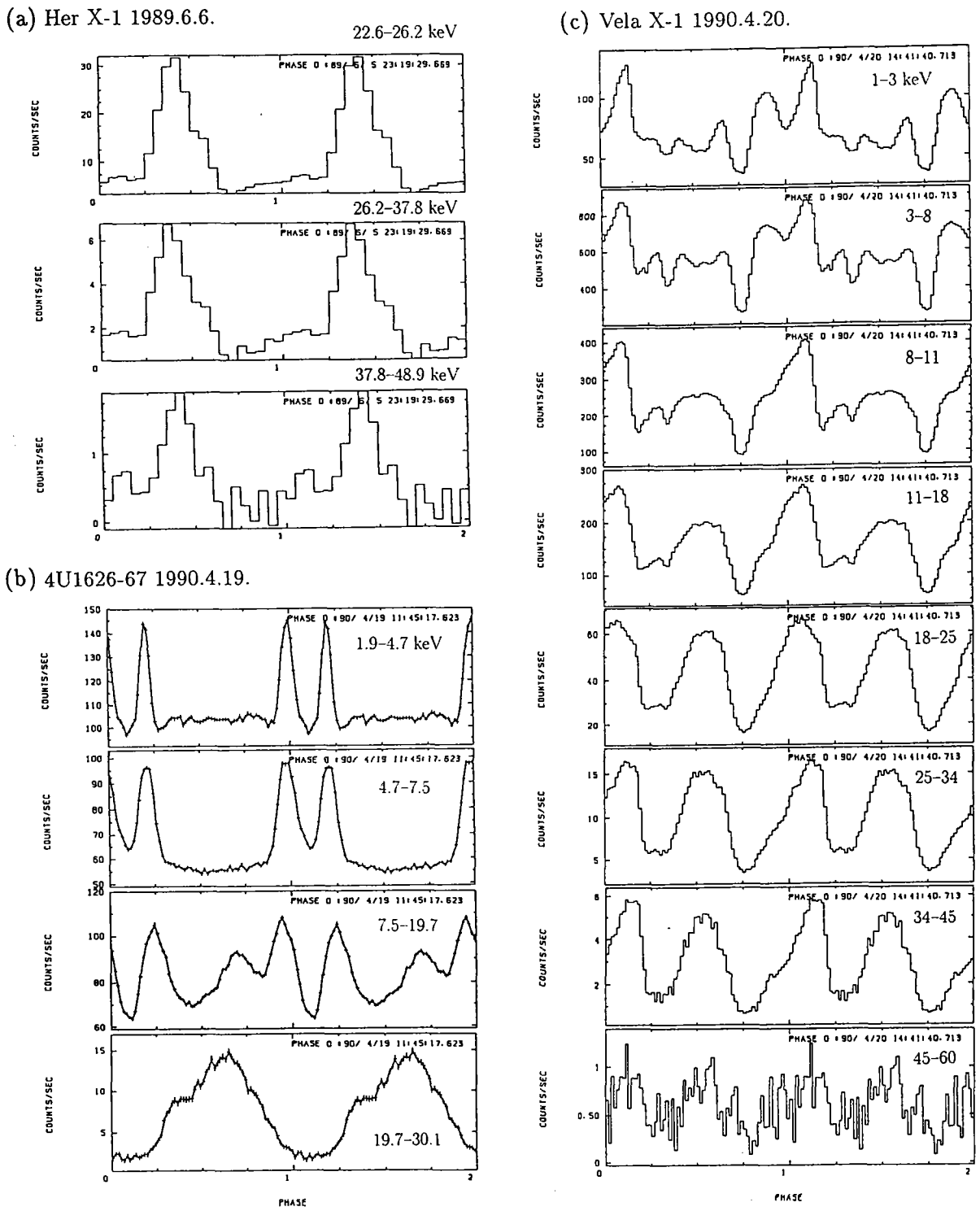

Figure B.2.1: Pulse profiles of X-ray pulsars divided into several energy bands. (a) Her X-1, (b) 4U 1626-67, (c) Vela X-1.

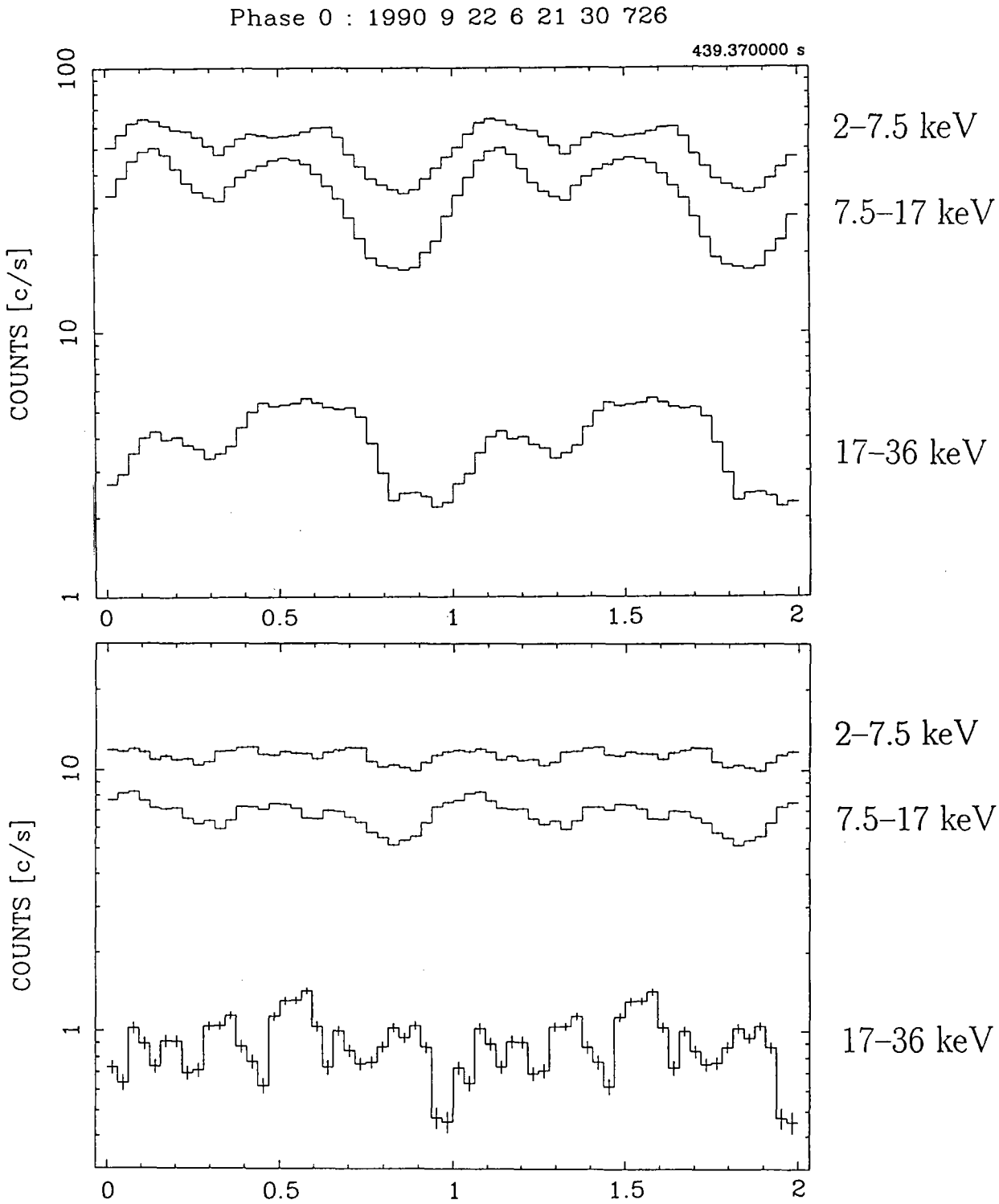

Figure B.2.1 (d) : Pulse profiles of 4U 1907+09 in 'pulsing state' (upper) and 'non-pulsing state' (lower) in 2–7.5, 7.5–17, 17–36 keV bands. The particle and Galactic ridge background are subtracted.

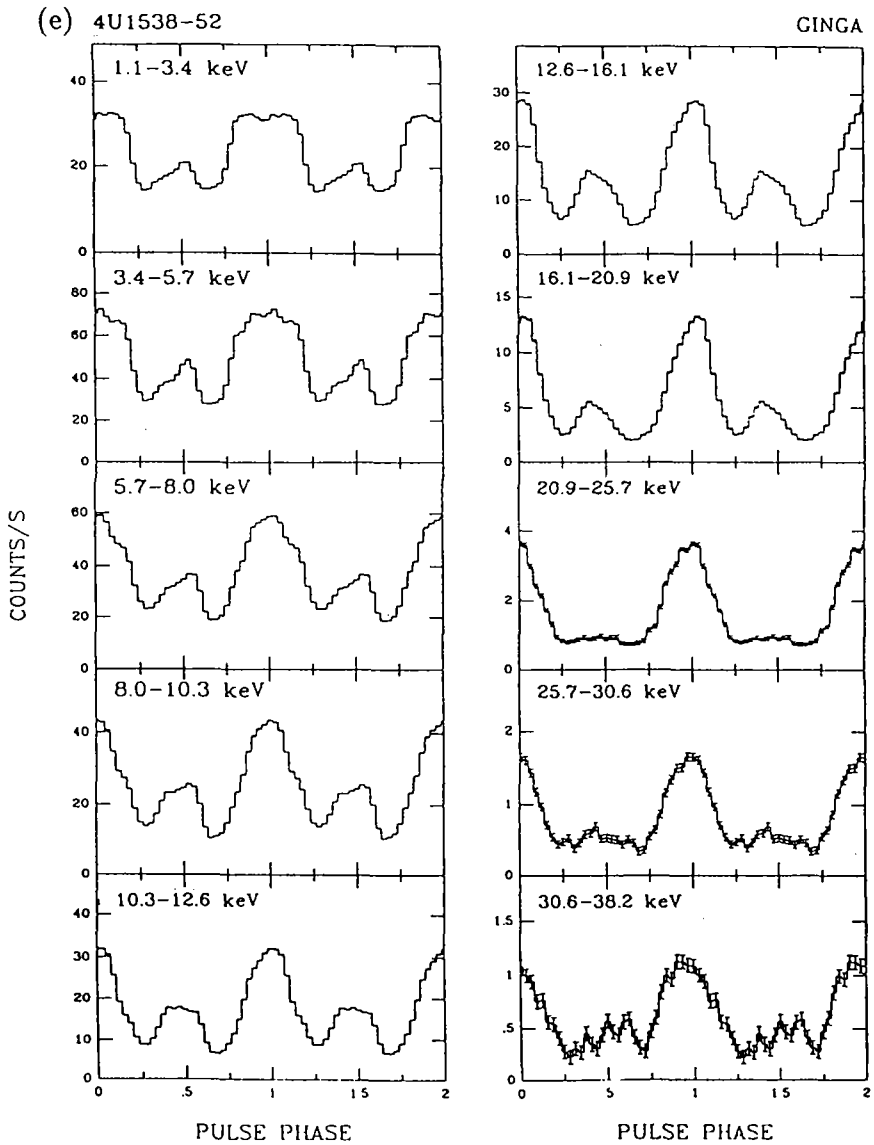

Figure B.2.1 (e) : Pulse profiles of 4U 1538-52 (1988) in ten pulse height intervals. The disappearance of the second peak at 20.9–25.7 keV band reflects the presence in the sepctrum of an absorption line which has a maximum equivalent width near phase 0.5.

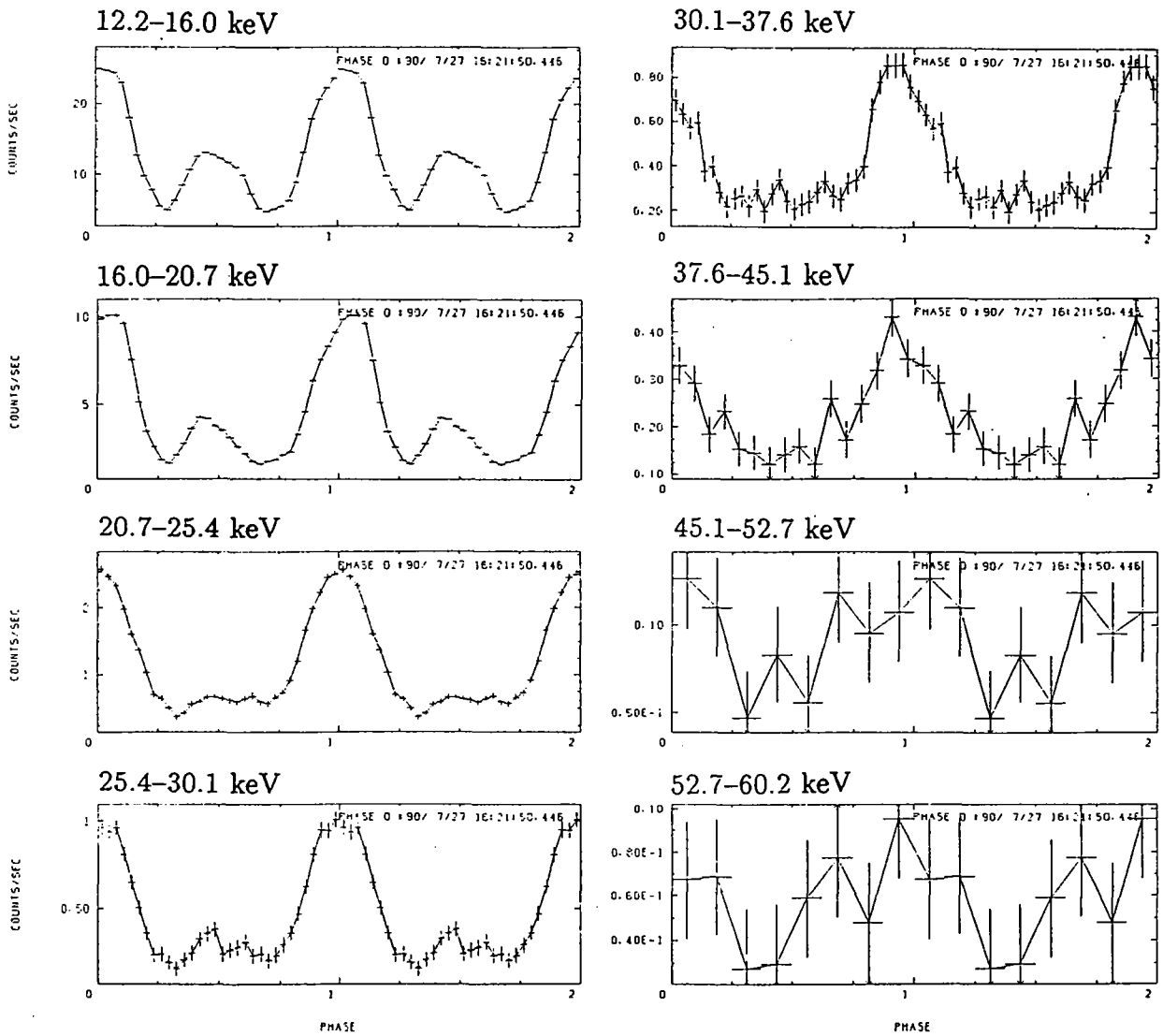

Figure B.2.1 (f) : Pulse profiles of 4U 1538-52 (1990) with the reduced HV. The disappearance of the second peak is consitent with 1988 observation in figure (e), but the second peak does not appear at higher energies.

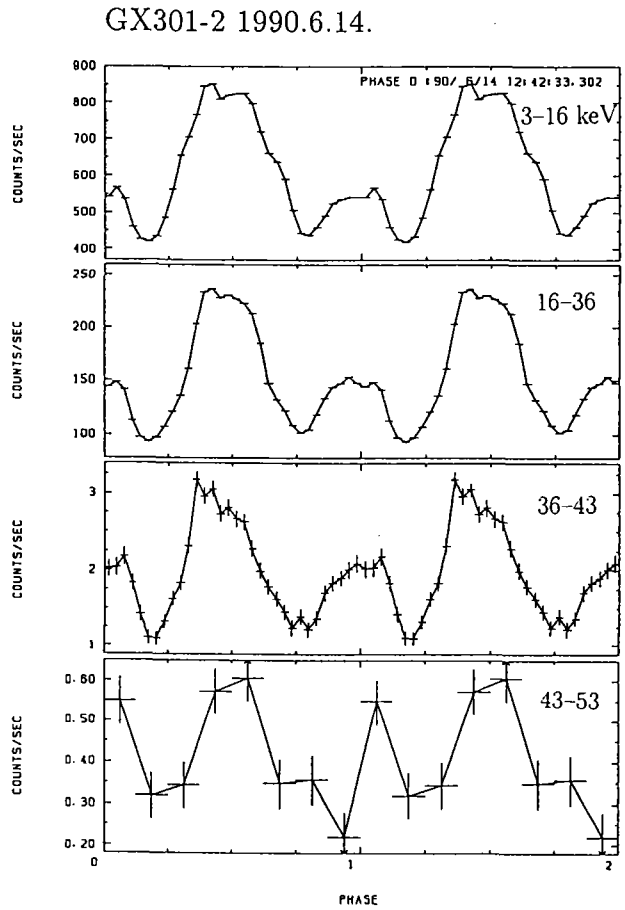

Figure B.2.1 (g) : Pulse profiles of GX 301-2 (1990) with the reduced HV.

Appendix C

ECUT parameters

Here we summarize the parameters of the ECUT model to the averaged *Ginga* spectra in the overall energy band. The photon flux spectrum $F(E)$ of an X-ray pulsar has been fitted traditionally with 'power-law × exponential cutoff (ECUT)' model (White, Swank and Holt 1983), of the form

$$F(E) = AE^{-\alpha} \exp(-N_H \sigma(E)) \times \begin{cases} 1 & (E < E_c) \\ \exp\{-(E - E_c)/E_f\} & (E > E_c). \end{cases}$$

Here E is the X-ray energy, α is the photon index which is typically in the range 0.2–1.0, E_c (typically 10–20 keV) is the energy where the high-energy cutoff starts, E_f (typically 5–30 keV) represents the steepness of the cutoff, N_H is the equivalent hydrogen column density, and $\sigma(E)$ is the cross section of photoelectric absorption due to cold matter of cosmic abundance (Morrison and McCammon 1983). In addition to the continuum, the X-ray pulsar spectrum very often shows fluorescent iron K-lines (Kα at 6.40 keV and Kβ at 7.05 keV) (Makishima 1986).

However, the ECUT model failed to give acceptable fits to the *Ginga* data because of the discontinuity at $E = E_c$. We listed the 'best-fit' parameters in the table. When the χ^2 is large, the errors are not always correct.

Table C.1.1: parameters of the ECUT fit for pulse averaged spectra.

Source	Exponential cut-off		Power law Norm.	Phton index	Absorption
	Ec [keV]	Ef [keV]	A [ph/s/keV]	α	$\log_{10} N_{\mathrm{H}}$ [cm^{-2}]
SMC X-1	5.0 ± 0.4	13.0 ± 0.4	24.4 ± 0.9	0.72 ± 0.03	—
HER X-1	20.0 ± 0.5	9.0 ± 0.6	65.6 ± 1.7	0.93 ± 0.06	22.05 ± 0.36
4U0115+63 ('90)	7.7 ± 1.3	8.5 ± 1.1	397 ± 68	0.52 ± 0.25	22.13 ± 0.26
4U0115+63 ('91)	8.8 ± 0.9	5.5 ± 0.5	68 ± 10	0.37 ± 0.19	—
X0331+53	13.9 ± 0.6	6.1 ± 0.5	297 ± 13	0.37 ± 0.06	—
Cen X-3	14.8 ± 0.4	6.9 ± 0.4	81.4 ± 1.7	1.27 ± 0.05	22.26 ± 0.08
4U1626-67	24.0 ± 2.6	14.8 ± 6.8	14.9 ± 0.3	1.12 ± 0.04	—
GS0834-430	15.1 ± 0.7	23.3 ± 1.7	56.4 ± 0.7	0.92 ± 0.04	22.40 ± 0.10
LMC X-4	16.1 ± 0.5	26.4 ± 1.7	10.0 ± 0.1	0.72 ± 0.01	—
GS1843+00	19.8 ± 1.1	33.3 ± 3.3	27.1 ± 0.2	0.74 ± 0.02	22.01 ± 0.06
OAO1657-415	5.0 ± 0.9	17.2 ± 1.8	43.8 ± 3.1	0.63 ± 0.11	22.97 ± 0.13
EXO2030+375	—	—	1.77 ± 0.03	1.85 ± 0.04	22.63 ± 0.03
Cep X-4	17.6 ± 0.4	6.2 ± 0.5	42.8 ± 0.7	0.93 ± 0.04	21.95 ± 0.14
A0535+26	15.1 ± 0.7	21.0 ± 1.3	517 ± 7	0.86 ± 0.03	22.04 ± 0.09
GX 1+4 ('88)	5.8 ± 0.9	13.1 ± 2.7	9.9 ± 1.3	0.81 ± 0.20	22.60 ± 0.08
GX 1+4 ('90)	6.8 ± 1.4	17.2 ± 4.6	6.7 ± 0.8	0.93 ± 0.22	22.53 ± 0.15
Vela X-1	18.8 ± 0.8	19.3 ± 1.7	59.2 ± 1.0	1.51 ± 0.04	22.65 ± 0.07
1E1145.1-61	8.7 ± 0.9	25.9 ± 2.4	21.3 ± 0.6	1.09 ± 0.07	22.58 ± 0.06
X1722-36	14.2 ± 2.9	50 ± 24	1.2 ± 0.5	1.11 ± 0.43	23.00 ± 0.65
4U1907+09	14.2 ± 0.5	5.5 ± 0.8	8.8 ± 0.1	1.01 ± 0.05	22.51 ± 0.05
4U1538-52	14.2 ± 0.6	7.6 ± 0.8	9.3 ± 0.3	1.10 ± 0.10	22.37 ± 0.23
GX301-2	19.6 ± 0.8	9.1 ± 0.8	102 ± 7	0.75 ± 0.14	23.39 ± 0.07
X Per	5.7 ± 0.3	13.0 ± 1.1	6.1 ± 0.3	1.70 ± 0.07	22.23 ± 0.04
4U1700-37	6.6 ± 1.3	31.3 ± 4.3	138 ± 7	1.45 ± 0.08	22.53 ± 0.06

Source	Iron Line Intensity I_{Fe} [photon/s]	Iron Line Energy E_{Fe} [keV]	Iron Line Width σ_{Fe} [keV]	χ^2_ν	Energy range [keV]
SMC X-1	2.9 ± 1.1	6.5 ± 0.3	0.50	1.34	2 – 37
HER X-1	20.8 ± 12.3	6.7 ± 0.5	0.50	11.19	3 – 60
4U0115+63 ('90)	47.9 ± 79.1	6.6 fixed	0.05	9.78	2 – 46
4U0115+63 ('91)	—	—	—	39.32	3 – 46
X0331+53	114 ± 67	6.6 fixed	0.05	39.32	2 – 60
Cen X-3	31.1 ± 13.2	6.4 fixed	0.05	18.83	2 – 37
4U1626-67	—	—	—	27.81	3 – 46
GS0834-430	6.3 ± 4.4	6.4 fixed	0.05	2.55	3 – 60
LMC X-4	2.3 ± 0.4	6.6 ± 0.2	0.50	1.18	3 – 37
GS1843+00	6.0 ± 0.0	6.4 fixed	0.50	3.86	2 – 37
OAO1657-415	9.9 ± 1.6	6.7 ± 0.1	0.05	1.23	2 – 37
EXO2030+375	0.6 ± 0.2	6.4 fixed	0.05	2.99	2 – 37
Cep X-4	6.2 ± 5.3	6.7 ± 0.5	0.05	16.41	2 – 37
A0535+26	98.7 ± 42.9	6.6 ± 0.3	0.05	7.37	2 – 37
GX 1+4 ('88)	2.6 ± 0.6	6.6 ± 0.1	0.05	0.75	2 – 33
GX 1+4 ('90)	3.2 ± 0.5	6.4 fixed	0.05	2.55	3 – 37
Vela X-1	25.7 ± 9.2	6.4 fixed	0.50	4.32	3 – 50
1E1145.1-61	4.5 ± 1.3	6.4 fixed	0.05	1.24	3 – 58
X1722-36	2.7 ± 0.3	6.7 ± 0.1	0.33	1.55	2 – 30
4U1907+09	1.5 ± 0.0	6.6 fixed	0.05	3.07	2 – 37
4U1538-52	2.5 ± 0.0	6.5 fixed	0.05	16.54	3 – 42
GX301-2	8.1 ± 13.9	6.4 fixed	0.05	20.83	4 – 54
X Per	—	—	—	0.73	2 – 28
4U1700-37	37.3 ± 8.7	6.5 ± 0.1	0.05	1.10	3 – 60

All these values are from *Ginga* observations.
The width (σ of the gaussian) of the iron line is fixed to the tabulated value.
When the χ^2 is large, the errors are not always correct.
The unit of the normalization of the power law A is [photons/s/keV] at 10 keV.

Appendix D

Non-cyclotron sources

The spectra of non-cyclotron pulsars from which the cyclotron resonance has not been discovered are shown here. We present the spectra, the Crab ratios, and NPEX fits for each pulsar in the order of the pulse period. The best-fit parameters are summarized in the table following the figures.

D.1 SMC X-1

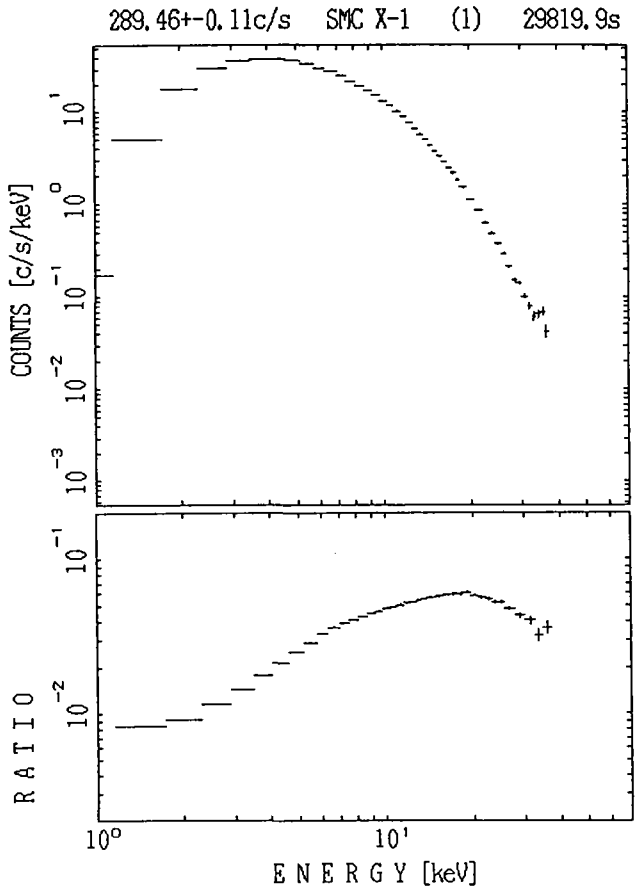
289.46+-0.11c/s SMC X-1 (1) 29819.9s
COUNTS [c/s/keV]
RATIO
ENERGY [keV]

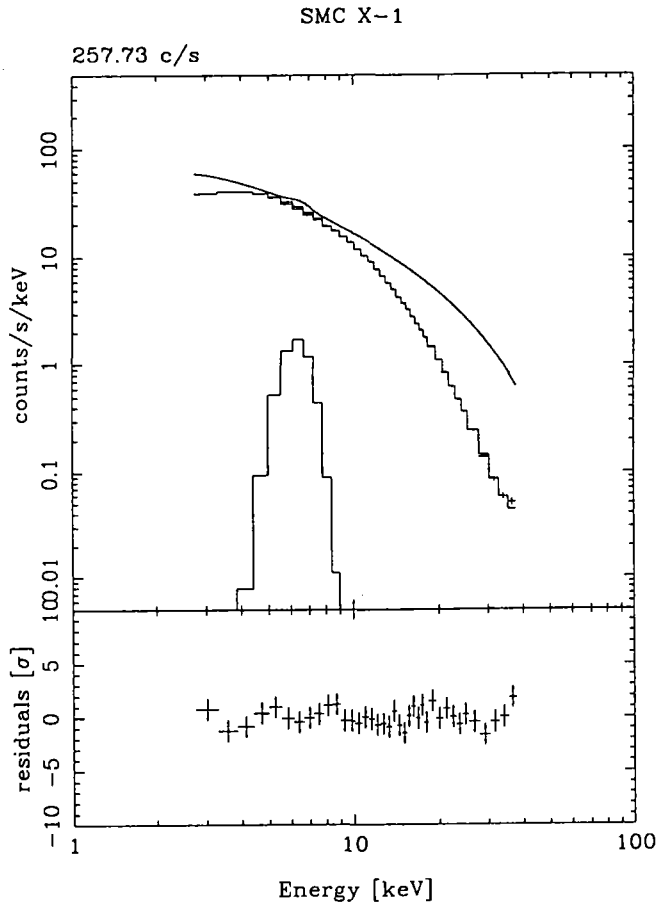
SMC X-1
257.73 c/s
counts/s/keV
residuals [σ]
Energy [keV]

D.2 GS 0834-430

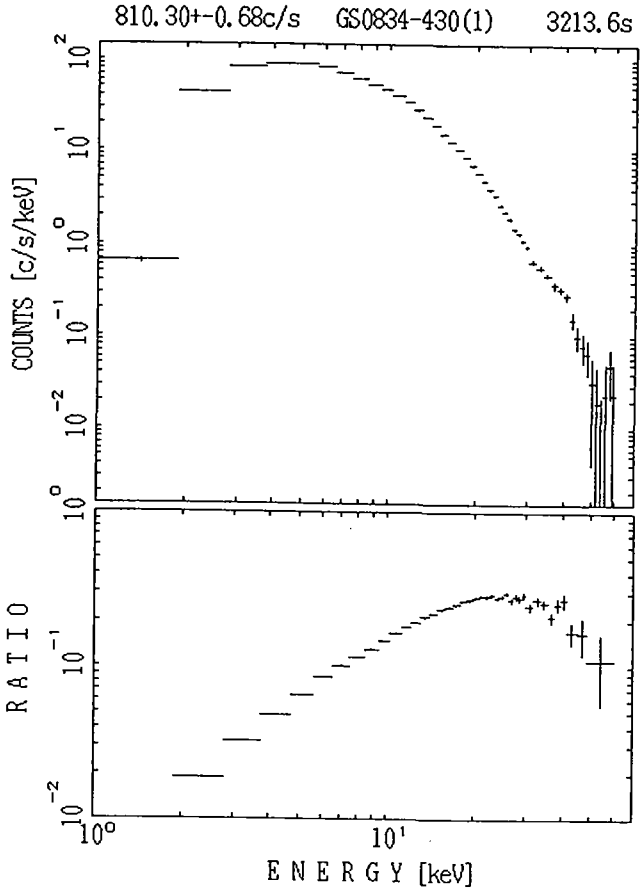

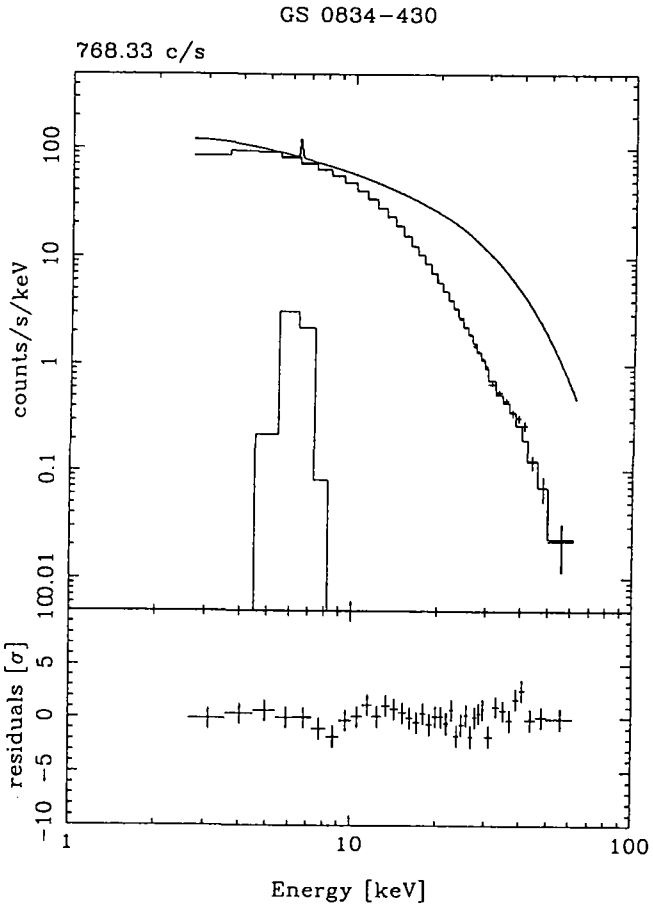

D.3 OAO 1657-415

The Galactic ridge emission is already subtracted in the spectrum shown below.

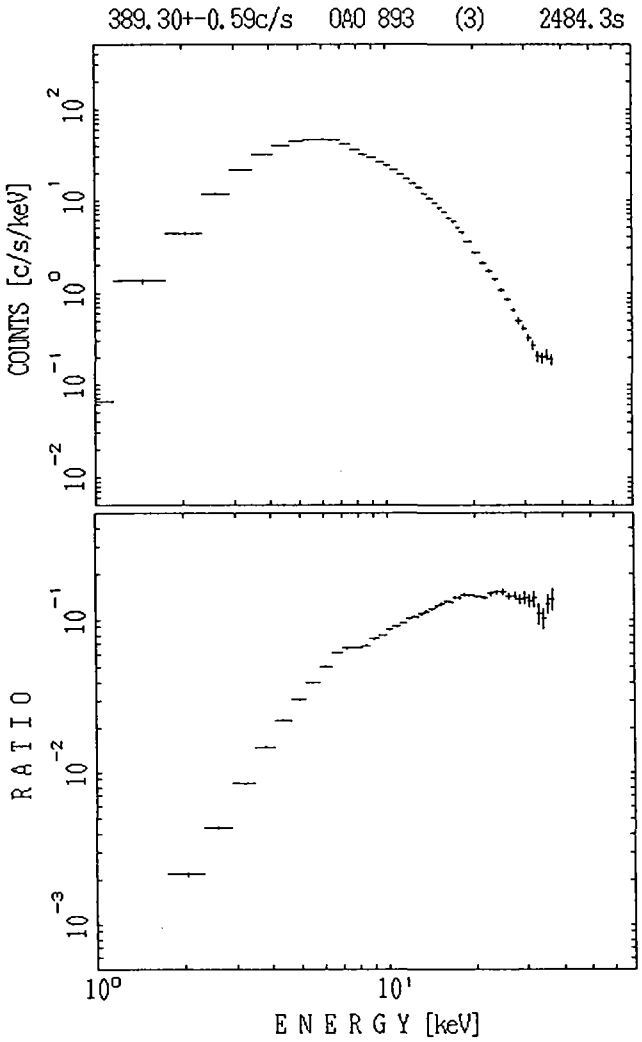

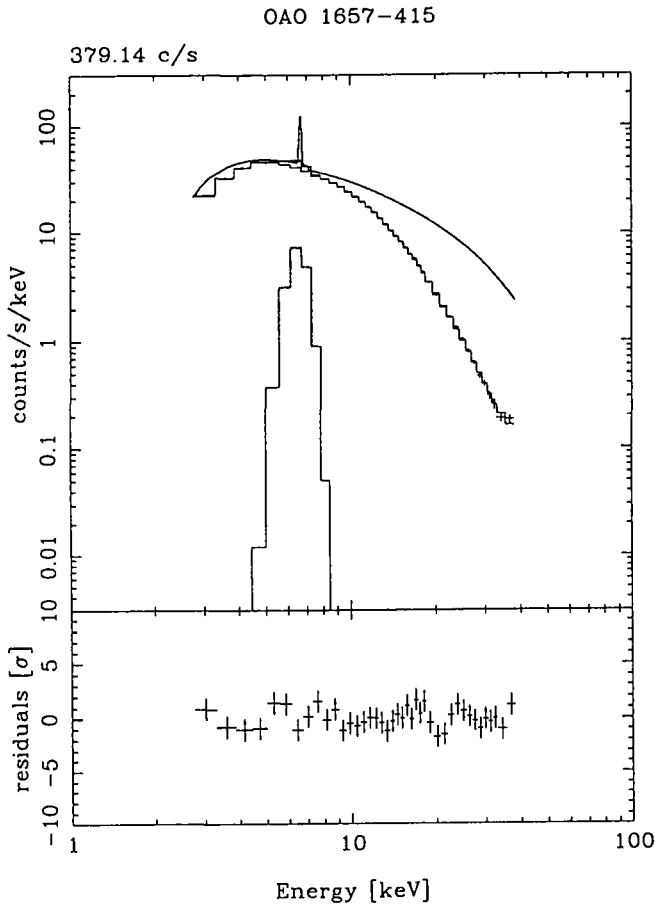

D.4 EXO 2030+375

A spectral flattening above 25 keV might be due to the incorrect background subtraction, although the NPEX fit the spectrum well.

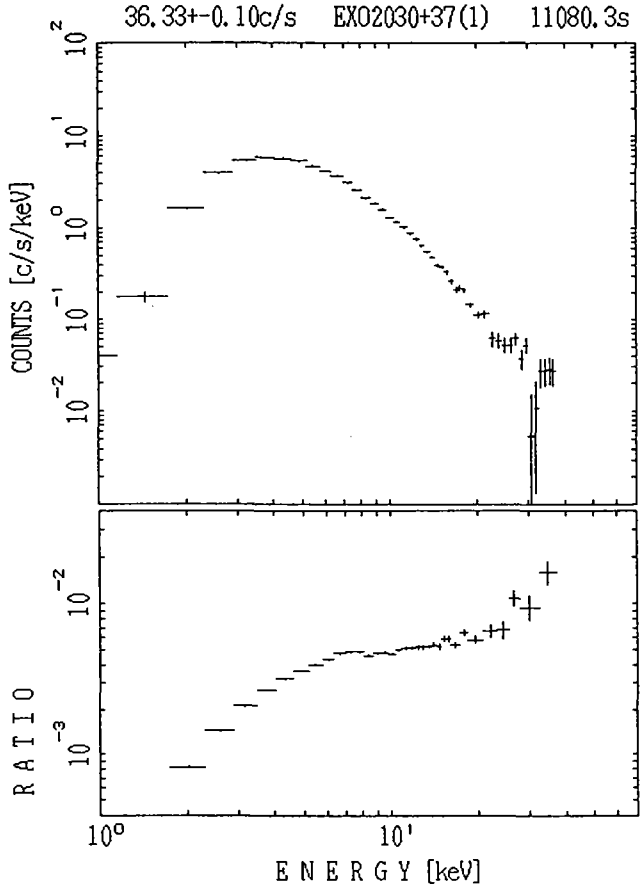

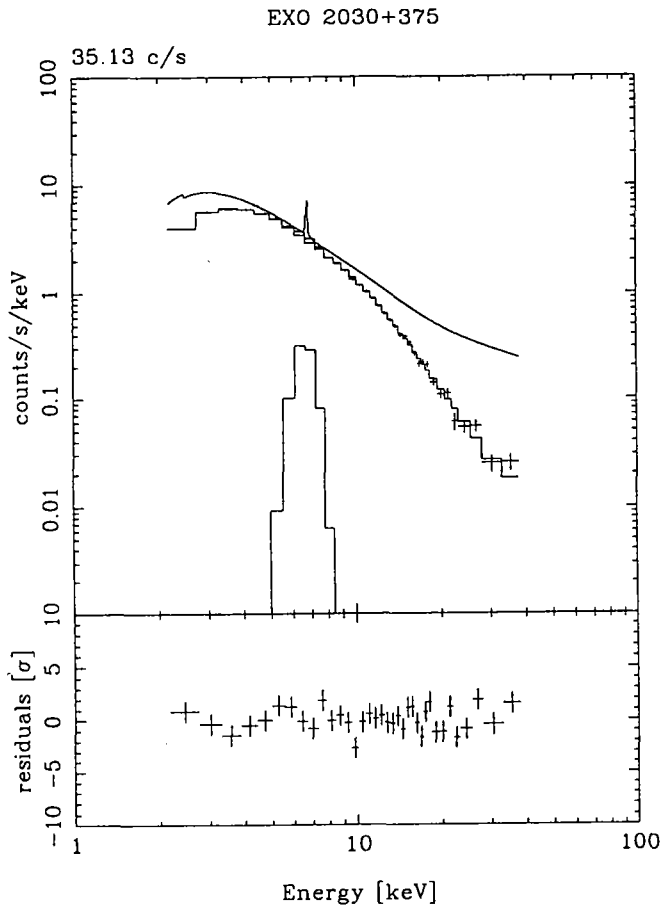

D.5 GX 1+4 in 1988

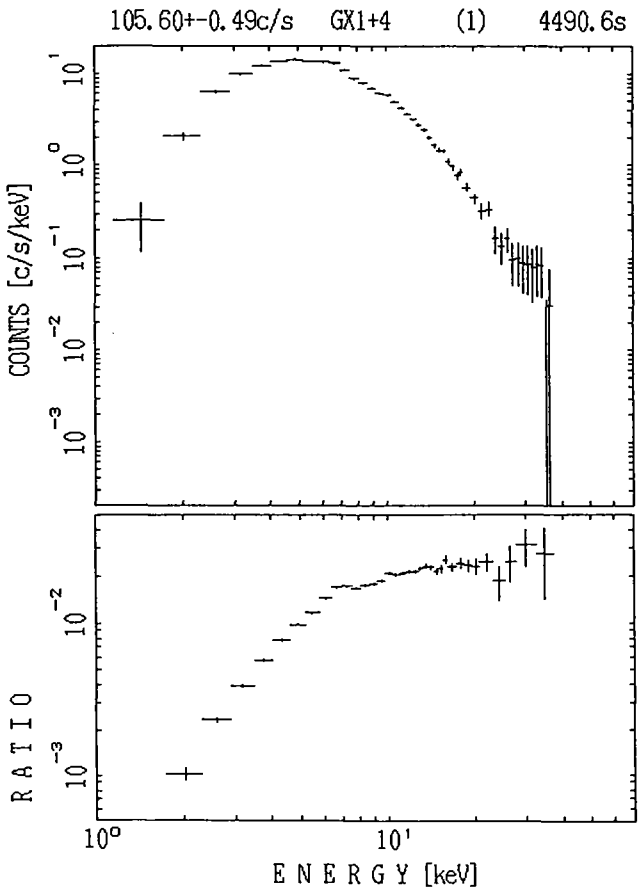

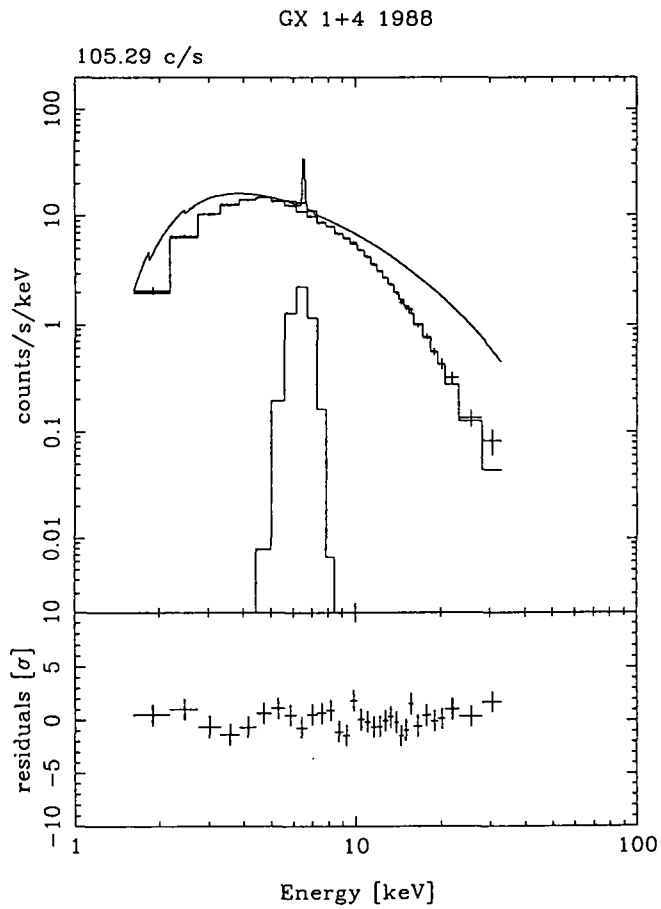

D.6 GX 1+4 in 1990

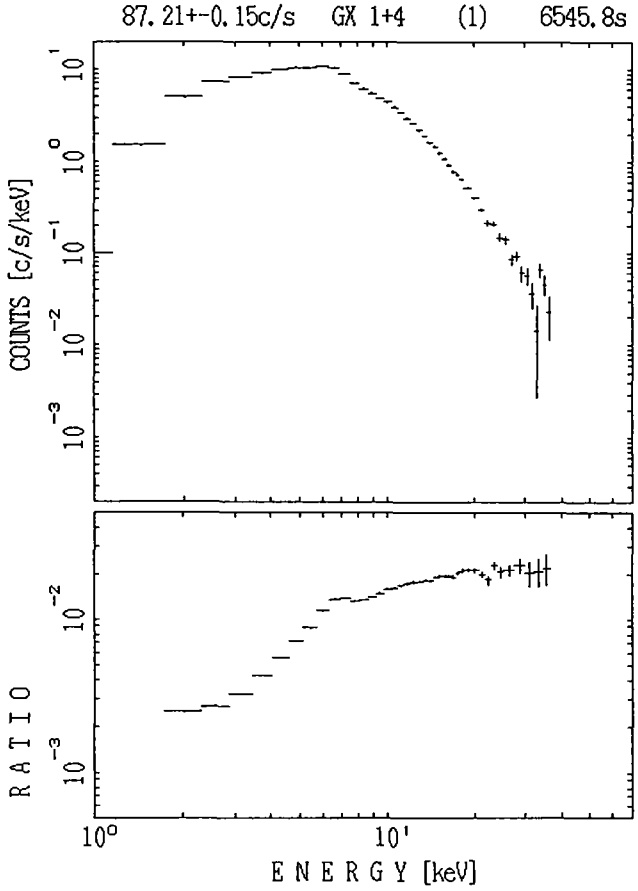

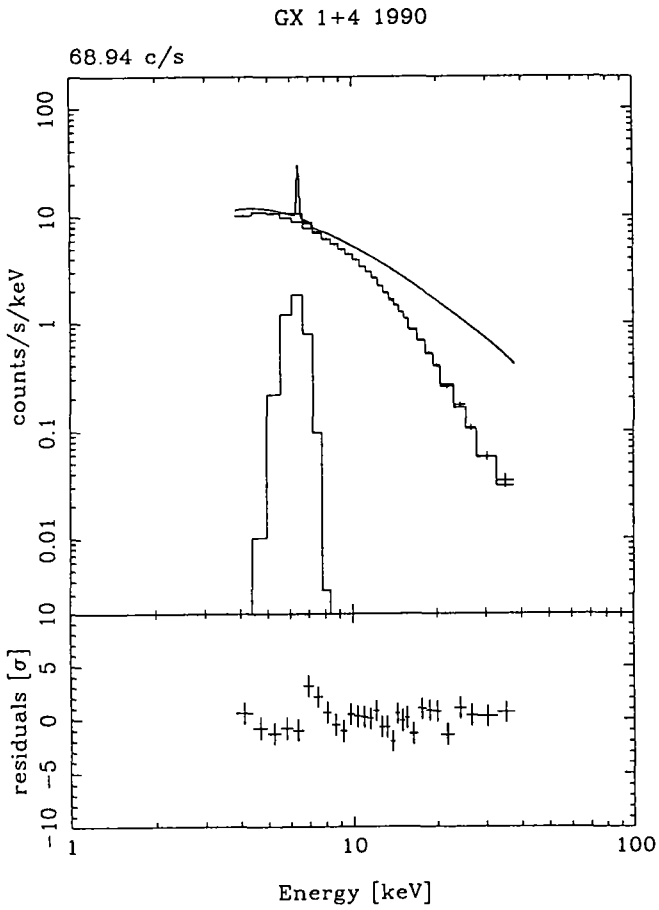

D.7 1E 1145.1-6141

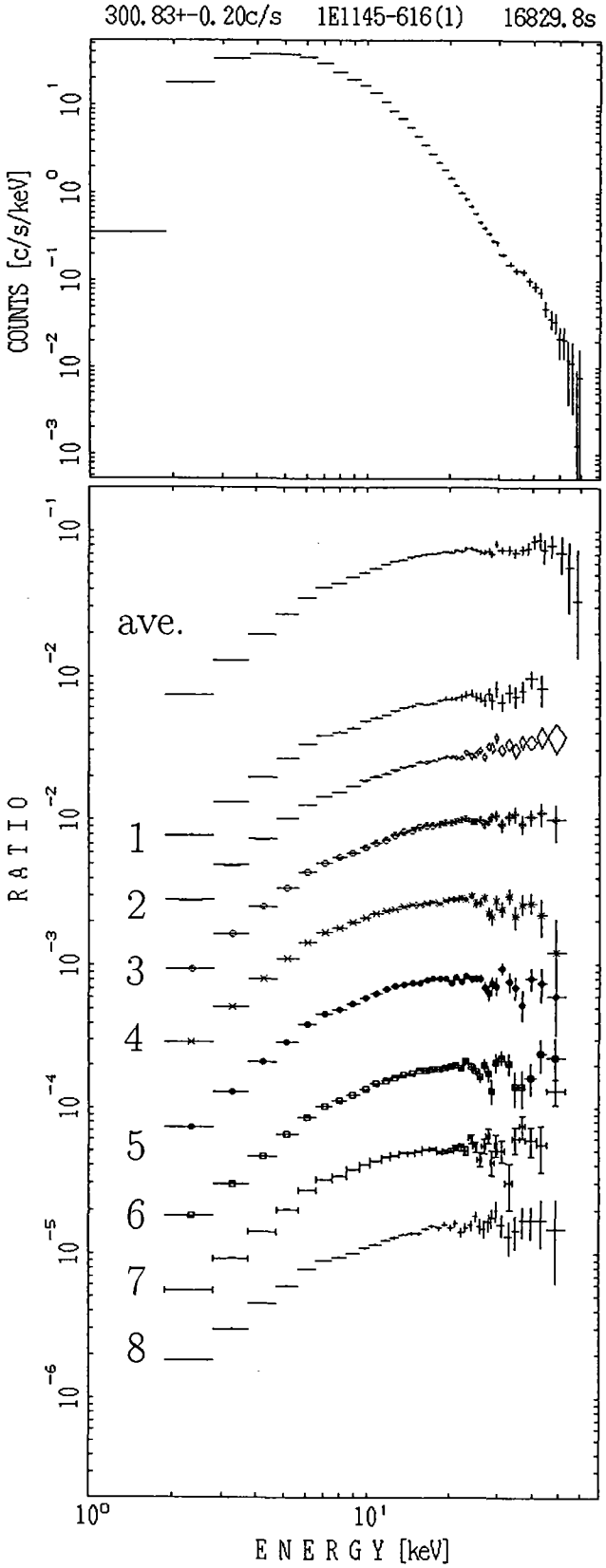

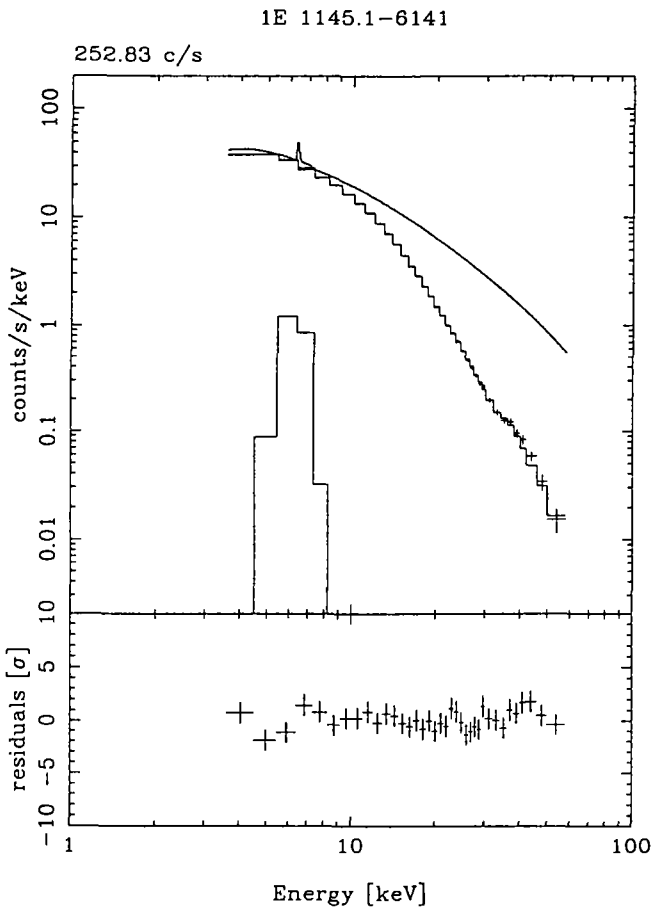

D.8 X 1722-36

A prominent iron line is observed in the Crab ratio, but most of it comes from the Galactic ridge emisison. The background was subtracted by Hayashida method. Therefore the spectrum contains the ridge emisison. The amount of the contamination was estimated from Ymauchi 1991 and added in the spectral fitting. As the component curve shows in the fitting plot, the X-ray from X 1722-36 is heavily absorbed, and most of the emisison below 7 keV is the ridge emission.

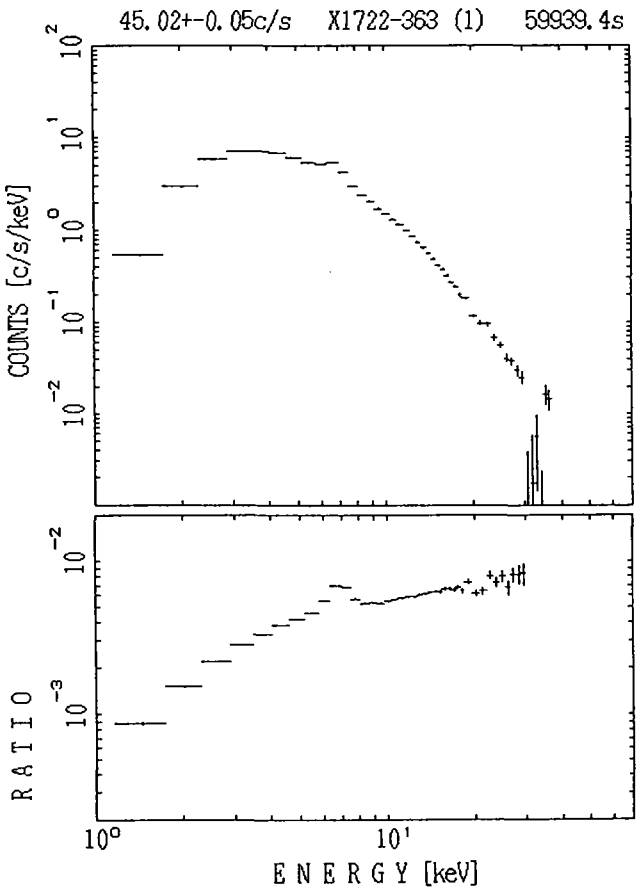

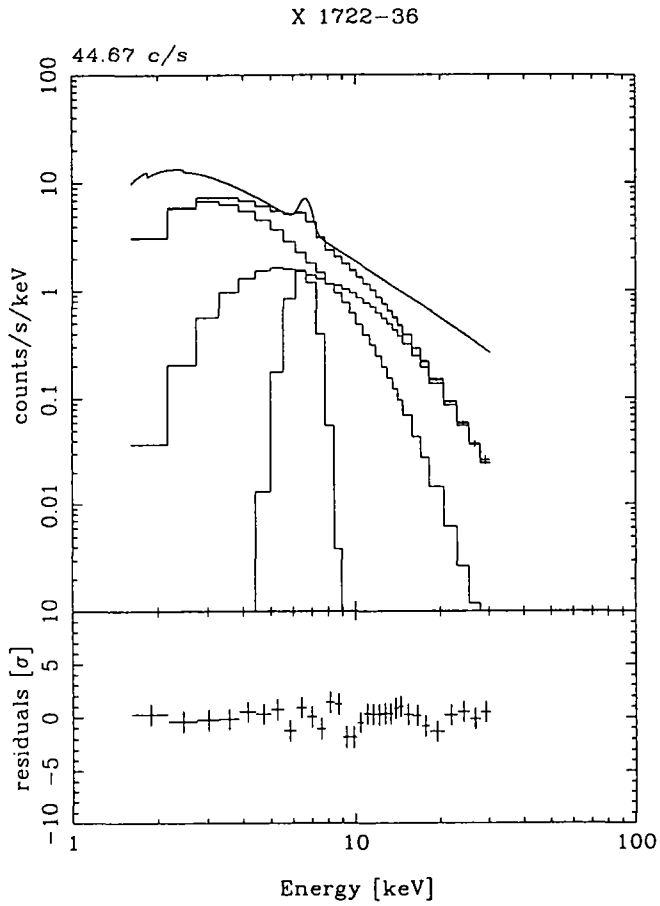

D.9 X Per

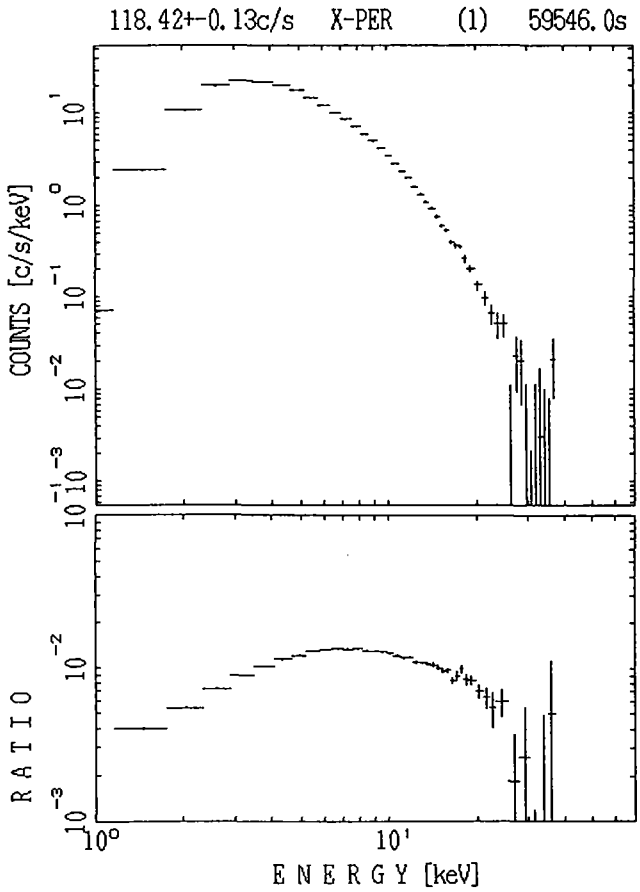
118.42+-0.13c/s X-PER (1) 59546.0s
COUNTS [c/s/keV]
RATIO
ENERGY [keV]

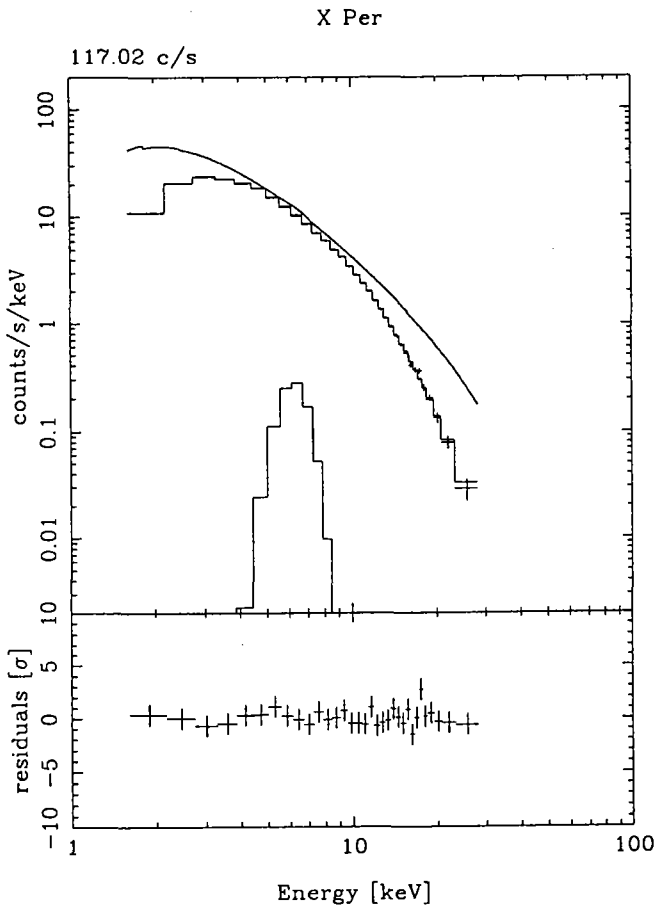
X Per
117.02 c/s
counts/s/keV
residuals [σ]
Energy [keV]

D.10 4U 1700-37

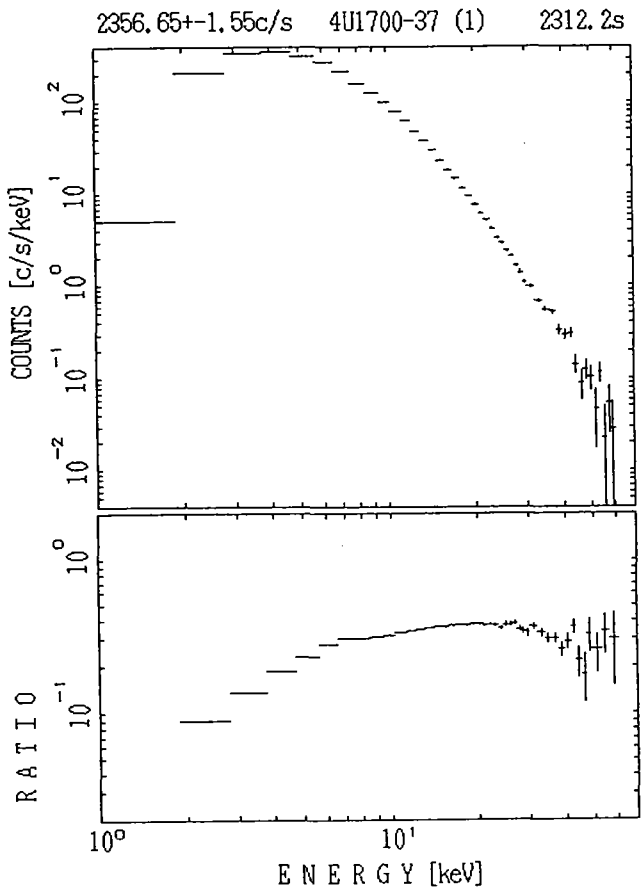

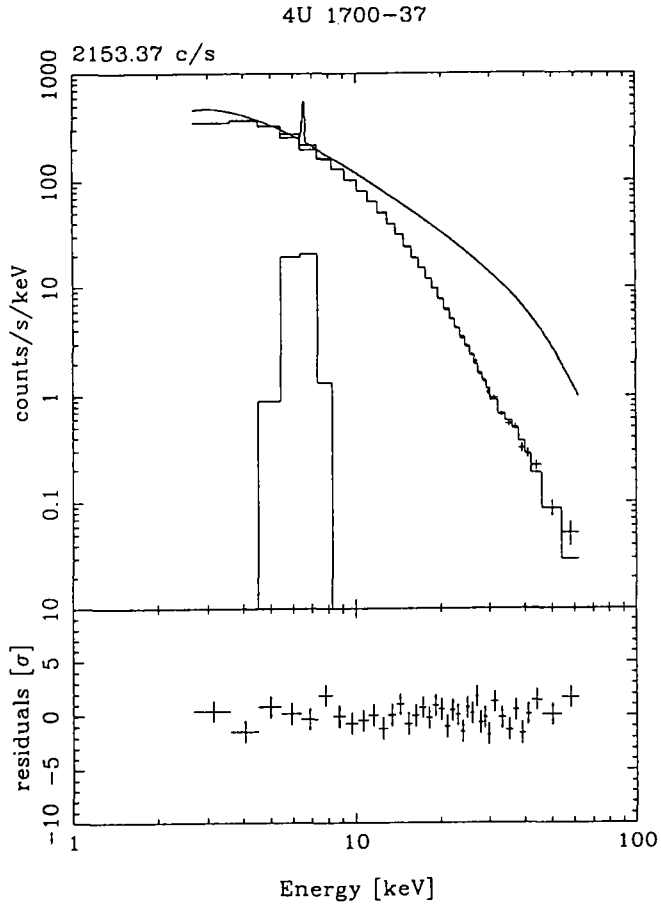

Table D.1.1: Parameters of NPEX fits for the non-cyclotron sources.

source	Negative power law		Positive power law		Exponential
	Norm. A_1 [ph/s/keV]	index α_1	Norm. A_2 [ph/s/keV]	index α_2	folding-e kT [keV]
SMC X-1	67 ± 1	0.38 ± 0.04	18 ± 4	2.00 fixed	6.1 ± 0.2
Cen X-3	256 ± 38	0.92 ± 0.14	1350 ± 120	2.00 fixed	3.5 ± 0.1
Cen X-3 [a]	2200 ± 300	-0.70 ± 0.09	3340 ± 370	4.4 ± 0.2	2.4 ± 0.1
Cen X-3 [b]	302 ± 34	0.67 ± 0.19	761 ± 201	2.00 fixed	4.0 ± 0.3
4U1626-67	27 ± 2	1.16 ± 0.09	38 ± 5	2.00 fixed	6.4 ± 0.2
4U1626-67 [c]	30 ± 2	1.07 ± 0.07	38 ± 4	2.00 fixed	6.2 ± 0.2
GS0834-430	163 ± 3	0.16 ± 0.06	65 ± 12	2.00 fixed	7.2 ± 0.3
OAO1657-415	102 ± 3	0.31 ± 0.05	28 ± 9	2.00 fixed	7.2 ± 0.4
EXO2030+375	3.1 ± 1.5	1.50 ± 0.33	0.1 ± 0.3	2.00 fixed	16.0 ± 15.0
GX1+4 1988	26 ± 46	0.36 ± 1.00	2.4 ± 25.4	2.00 fixed	7.2 ± 12.9
GX1+4 1990	15 ± 8	0.81 ± 0.35	0.9 ± 2.5	2.00 fixed	10.0 ± 6.6
1E1145.1-61.41	44 ± 13	0.75 ± 0.23	1.2 ± 2.3	2.00 fixed	12.8 ± 5.5
X1722-36 [d]	3.2 ± 0.9	0.39 ± 0.16	0.4 ± 0.8	2.00 fixed	9.6 ± 4.2
X Per	27 ± 13	0.89 ± 0.25	4.4 ± 7.8	2.00 fixed	5.0 ± 1.6
4U1700-37	364 ± 19	0.83 ± 0.04	37 ± 11	2.00 fixed	8.5 ± 0.5

a) α_2 is set free.

b) CYAB function is multiplied. $D = 2.4 \pm 1.1$, $W = 11.3 \pm 3.9$ keV. The resonance energy E_a is fixed to 36 keV.

c) A gaussian emission line of $I = 7.2 \pm 2.9$ [photons/s] at $E = 21.7 \pm 0.6$ keV with $\sigma = 2.8 \pm 0.9$ keV is added.

d) The Galactic ridge emission is included in the fitting of X1722-36, whose spectrum is a bremsstrahlung of kT=6.0 keV (fixed), $\log_{10} N_H$=22.357 and 28.5 c/s (best-fit values) without an iron line. The tabulated iron line includes the one from the Galactic ridge emission.

The units of the normalization of the power law are [photons/s/keV] at 10 keV.

Table D.1.1 *continued.*

source	Iron line			Absorption	χ^2_ν
	Flux	Energy	Width		
	I_{Fe}	E_{Fe}	σ_{Fe}	$\log_{10} N_H$	
	[ph/s]	[keV]	[keV]	[cm^{-2}]	
SMC X-1	3.4 ± 0.8	6.49 ± 0.18	0.50 fixed	22.00 ± 0.15	0.80
Cen X-3	17.0 fixed	6.47 ± 0.36	0.05 fixed	22.30 fixed	10.99
Cen X-3 [a]	26.6 ± 4.4	6.57 ± 0.10	0.05 fixed	—	1.70
Cen X-3 [b]	27.3 ± 4.5	6.52 ± 0.09	0.05 fixed	22.21 ± 0.16	1.66
4U1626-67	2.1 ± 1.8	6.70 fixed	0.05 fixed	—	7.09
4U1626-67 [c]	1.4 ± 1.1	6.70 fixed	0.05 fixed	—	2.54
GS0834-430	5.6 ± 2.7	6.40 fixed	0.05 fixed	21.92 ± 0.26	0.99
OAO1657-415	10.3 ± 1.2	6.66 ± 0.07	0.05 fixed	22.92 ± 0.03	0.98
EXO2030+375	0.5 ± 0.1	6.77 ± 0.16	0.05 fixed	22.60 ± 0.06	1.51
GX1+4 1988	3.1 ± 0.5	6.54 ± 0.09	0.05 fixed	22.62 ± 0.11	1.04
GX1+4 1990	2.6 ± 0.4	6.40 fixed	0.05 fixed	22.94 ± 0.09	1.46
1E1145.1-61.41	2.2 ± 1.2	6.40 fixed	0.05 fixed	22.75 ± 0.09	0.94
X1722-36 [d]	2.7 ± 0.2	6.65 ± 0.04	0.33 fixed	23.05 ± 0.44	0.94
X Per	0.6 ± 0.3	6.40 fixed	0.50 fixed	22.09 ± 0.07	0.69
4U1700-37	42.5 ± 8.6	6.55 ± 0.11	0.05 fixed	22.43 ± 0.06	1.09

Appendix E

CMPL fits

The CMPL, Comptonization by Lamb and Sanford (1979), model fits are presented. It is a physical model instead of the phenomenological NPEX model. The non-cyclotron sources are fitted by the NPEX model, and the cyclotron sources are by NPEX $\times$ CYAB model. The best-fit parameters are summarized in the table following the figures.

E.1 Cyclotron sources

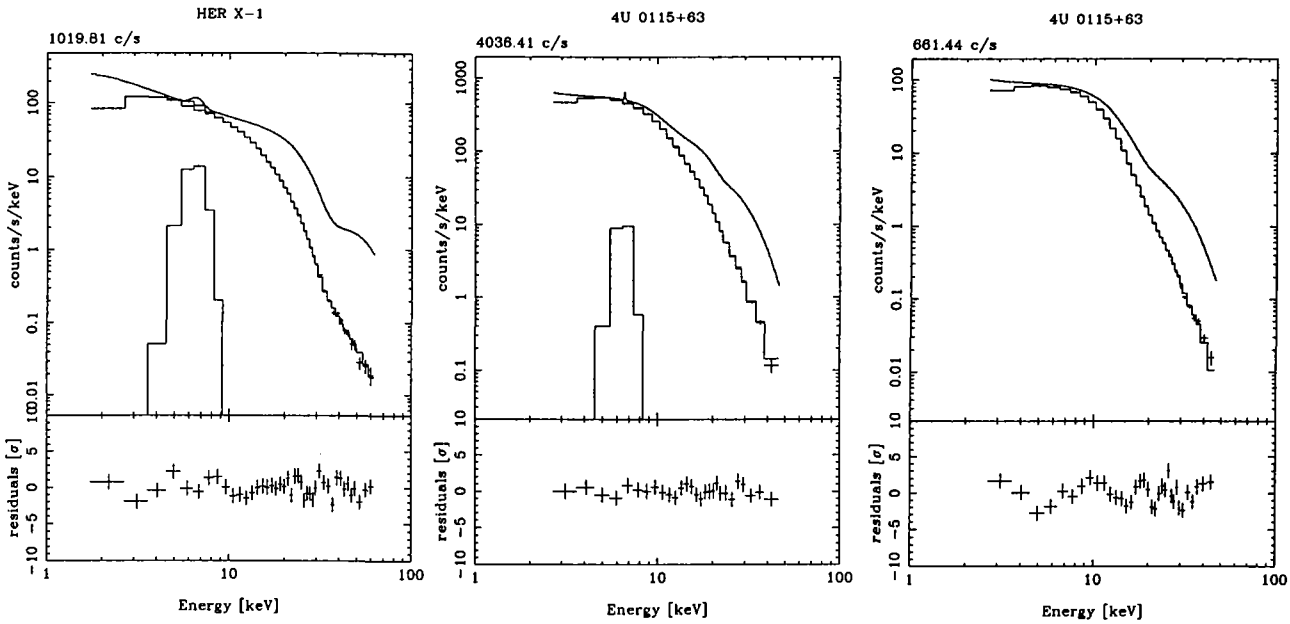

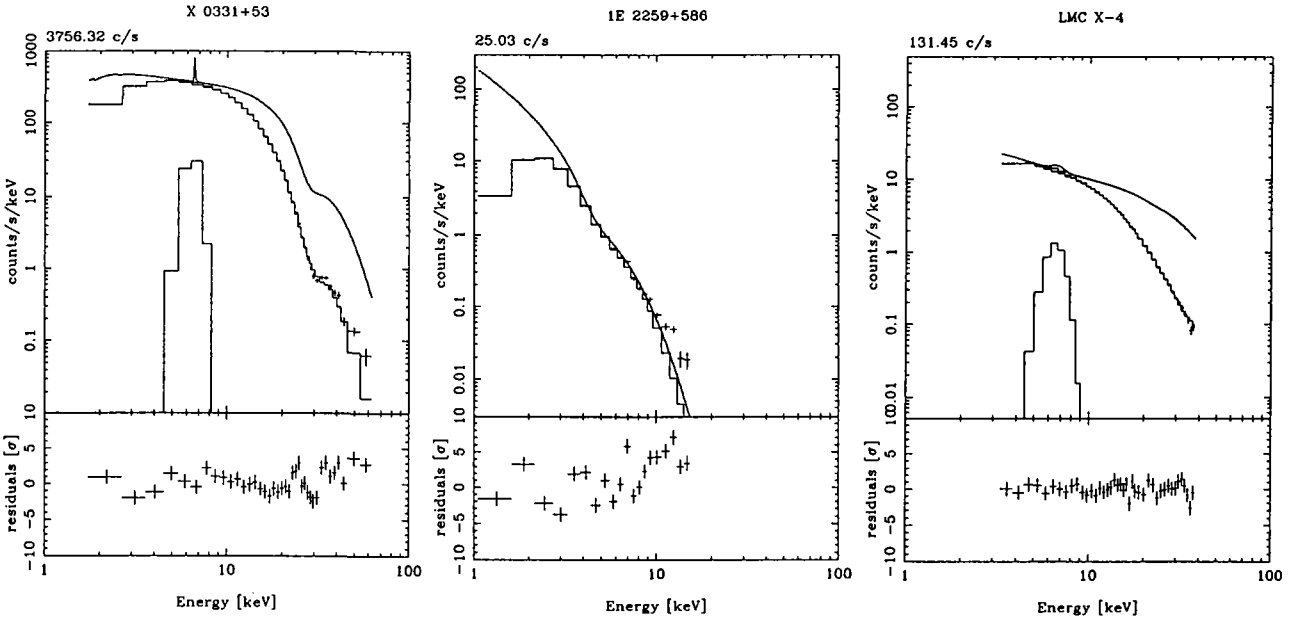

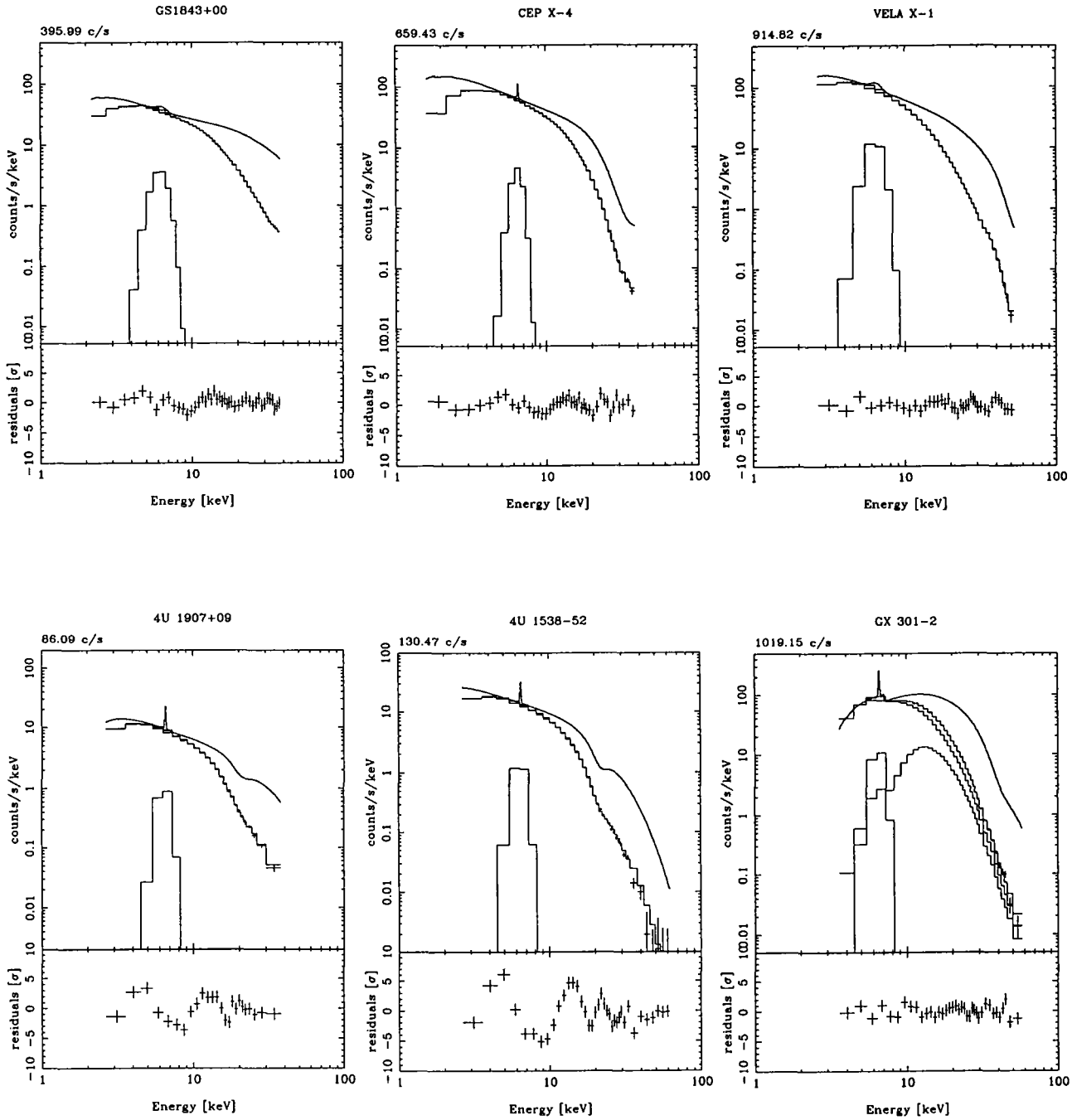
GS1843+00
395.99 c/s
CEP X-4
659.43 c/s
VELA X-1
914.82 c/s
4U 1907+09
86.09 c/s
4U 1538-52
130.47 c/s
GX 301-2
1019.15 c/s
counts/s/keV
residuals [σ]
Energy [keV]

E.2 Non-cyclotron sources

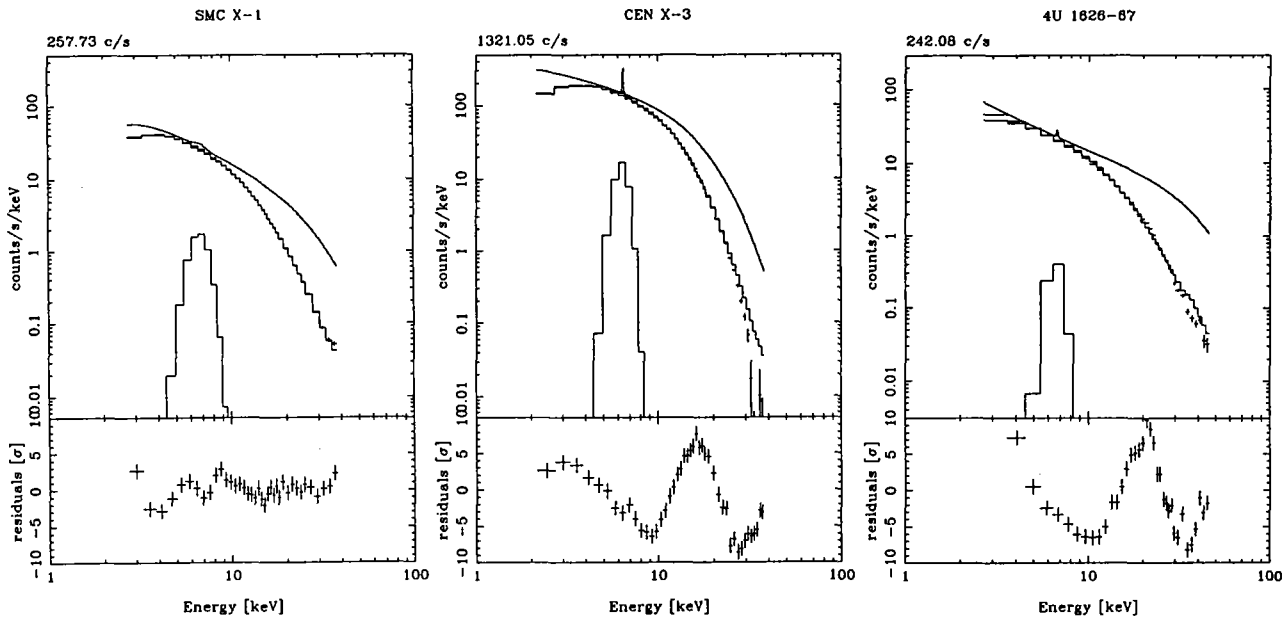

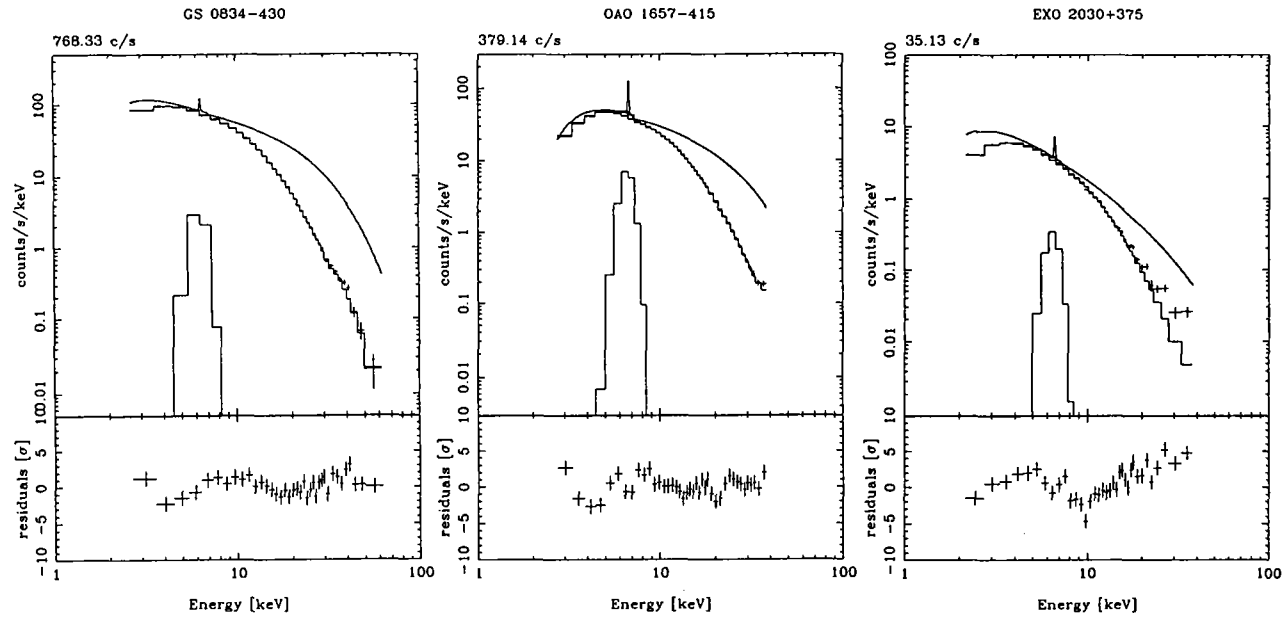

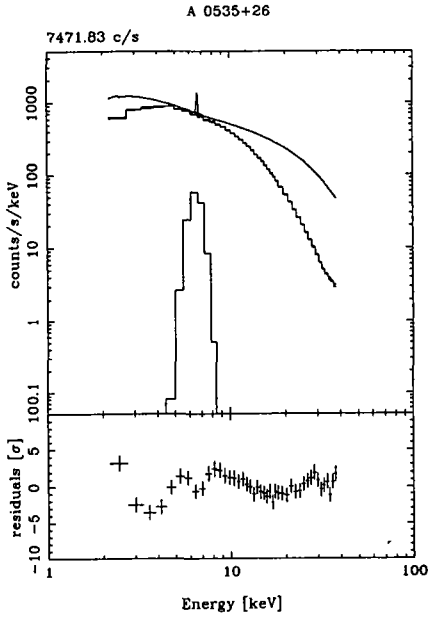
A 0535+26
7471.83 c/s
counts/s/keV
residuals [σ]
Energy [keV]

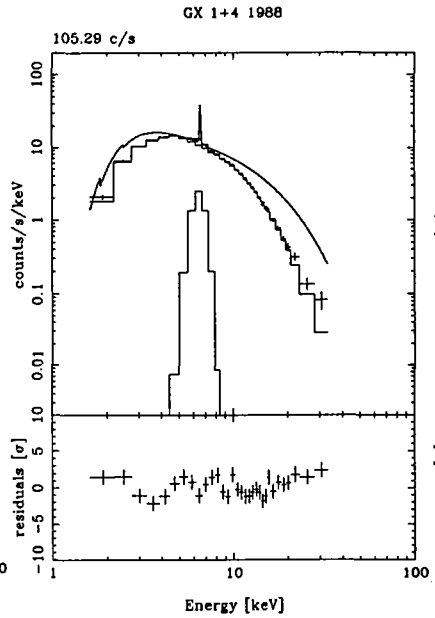
GX 1+4 1988
105.29 c/s
counts/s/keV
residuals [σ]
Energy [keV]

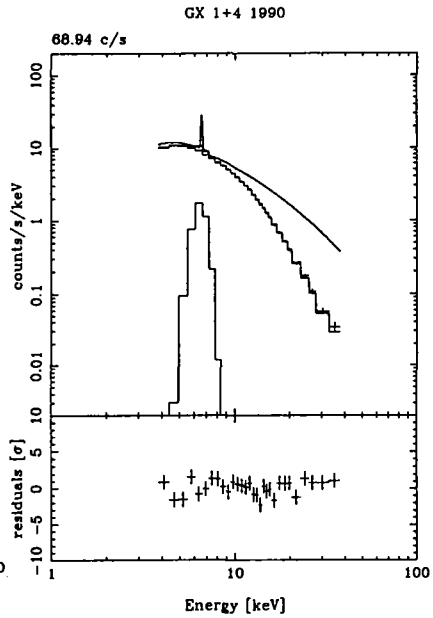
GX 1+4 1990
68.94 c/s
counts/s/keV
residuals [σ]
Energy [keV]

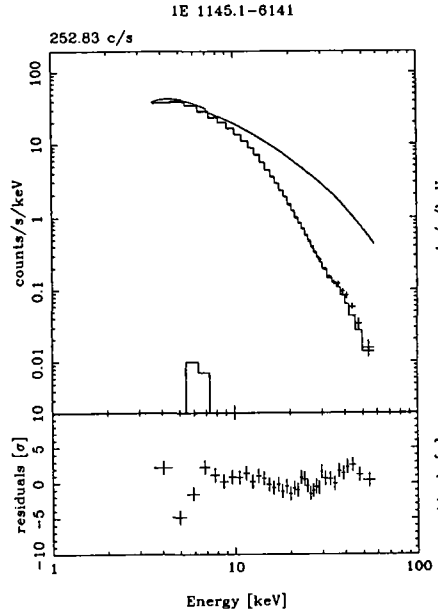
1E 1145.1−6141
252.83 c/s
counts/s/keV
residuals [σ]
Energy [keV]

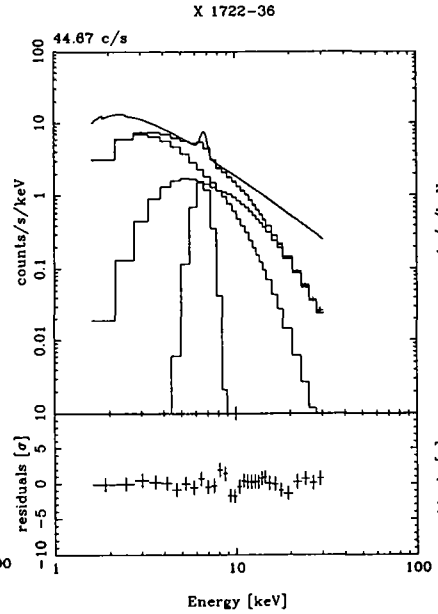
X 1722−36
44.67 c/s
counts/s/keV
residuals [σ]
Energy [keV]

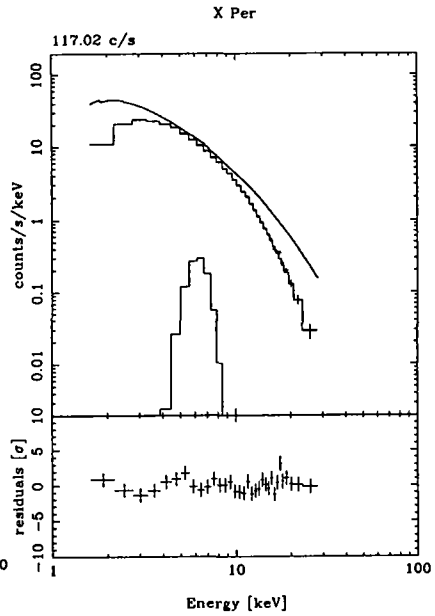
X Per
117.02 c/s
counts/s/keV
residuals [σ]
Energy [keV]

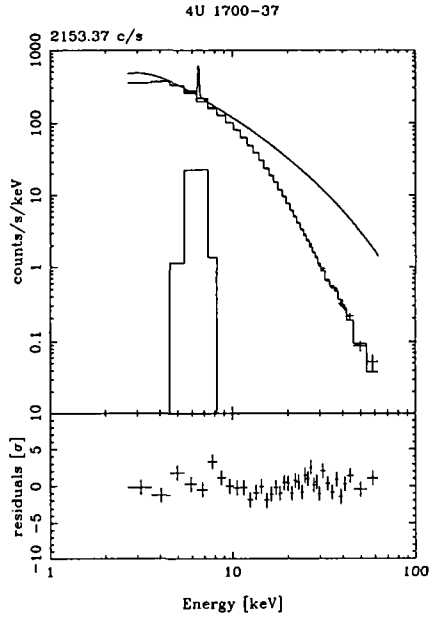
4U 1700−37
2153.37 c/s
counts/s/keV
residuals [σ]
Energy [keV]

Table E.1.1: Parameters of CMPL fits to the cyclotron sources.

sources	Resonance Ea [keV]	CYAB Width W [keV]	Depth D
Her X-1	33.6 ± 0.4	11.5 ± 1.6	1.6 ± 0.2
4U0115+63 1990	11.6 ± 0.3	5.4 ± 0.5	0.57 ± 0.03
4U0115+63 1990 (2nd)	22.0 ± 0.4	5.0 ± 0.9	0.47 ± 0.06
4U0115+63 1991	16.3 ± 0.3	8.2 ± 0.7	1.10 ± 0.06
X0331+53	26.8 ± 0.4	6.6 ± 1.3	1.3 ± 0.2
1E2259+586	4.2 ± 0.3	1.7 ± 0.4	0.83 ± 0.10
LMC X-4	22.0 ± 1.3	3.8 ± 3.8	0.08 ± 0.04
GS1843+00	23.6 ± 1.8	4.7 ± 4.8	0.05 ± 0.02
Cep X-4	30.3 ± 0.7	14.0 ± 2.9	2.8 ± 0.6
Vela X-1	25.6 ± 0.9	7.2 ± 2.6	0.12 ± 0.09
Vela X-1 (2nd)	fixed to 2 × above values		1.6 ± 0.5
4U1907+09	20.0 ± 1.0	4.1 ± 2.6	0.6 ± 0.2
4U1538-52	21.2 ± 0.4	3.6 ± 1.2	0.8 ± 0.2
GX301-2	—	11.7 ± 1.3	1.0 ± 0.2

Table E.1.2: Table E.1.1 *continued.*

sources	CMPL model		
	Norm. A [ph/s/keV]	Temperature kT [keV]	optical depth τ
Her X-1	291 ± 7	9.33 ± 0.85	14.5 ± 0.4
4U0115+63 1990	577 ± 37	4.67 ± 0.09	33.8 ± 1.6
4U0115+63 1991	93 ± 6	4.67 ± 0.17	34.0 ± 1.4
X0331+53	773 ± 68	5.80 ± 0.38	22.9 ± 1.3
1E2259+586	205 ± 14	2.00 fixed	0.241 ± 0.003
LMC X-4	43 ± 2	8.61 ± 0.30	15.1 ± 0.5
GS1843+00	117 ± 2	10.10 ± 0.19	14.3 ± 0.2
Cep X-4	222 ± 18	13.57 ± 4.61	12.2 ± 0.8
Vela X-1	394 ± 12	9.62 ± 1.96	10.8 ± 0.9
4U1907+09	38 ± 3	7.99 ± 1.68	12.6 ± 1.3
4U1538-52	52 ± 6	5.86 ± 0.58	15.1 ± 1.4
GX301-2	296 ± 55	6.44 ± 0.40	21.0 ± 2.4

source	Iron line			Absorption	χ^2_ν
	Flux I_{Fe} [ph/s]	Energy E_{Fe} [keV]	Width σ_{Fe} [keV]	$\log_{10} N_H$ [cm^{-2}]	
Her X-1	33.2 ± 4.4	6.60 fixed	0.50 fixed	21.85 ± 0.09	1.63
4U0115+63 1990	19.6 ± 15.5	6.60 fixed	0.05 fixed	—	0.74
4U0115+63 1991	—	—	—	—	2.52
X0331+53	56.8 ± 21.8	6.59 fixed	0.05 fixed	22.21 ± 0.08	3.32
1E2259+586	—	—	—	—	15.23
LMC X-4	2.6 ± 0.5	6.68 ± 0.12	0.50 fixed	22.14 ± 0.16	0.88
GS1843+00	7.3 ± 1.1	6.33 ± 0.11	0.50 fixed	22.34 ± 0.03	0.90
Cep X-4	6.4 ± 1.5	6.53 fixed	0.05 fixed	22.11 ± 0.02	1.15
Vela X-1	27.6 ± 3.5	6.53 ± 0.10	0.50 fixed	22.43 ± 0.05	0.71
4U1907+09	1.7 fixed	6.60 fixed	0.05 fixed	22.59 ± 0.08	4.42
4U1538-52	2.5 fixed	6.50 fixed	0.05 fixed	22.21 ± 0.23	8.86
GX301-2	20.6 ± 4.0	6.60 fixed	0.05 fixed	23.33 ± 0.04	1.01

The units of the normalization of the power law are [photons/s/keV] at 10 keV.

Table E.2.1: Parameters of CMPL fits to the non-cyclotron sources.

sources	CMPL model		
	Norm. A [ph/s/keV]	Temperature kT [keV]	optical depth τ
SMC X-1	164 ± 5	6.83 ± 0.21	9.7 ± 0.4
Cen X-3	496 ± 36	4.06 ± 0.10	18.4 ± 0.9
4U1626-67	91 ± 5	9.88 ± 1.25	10.6 ± 1.0
GS0834-430	308 ± 13	7.65 ± 0.18	13.3 ± 0.4
OAO1657-415	231 ± 9	7.67 ± 0.32	11.1 ± 0.5
EXO2030+375	24 ± 112	14 ± 217	2.7 ± 100.3
A0536-26	2671 ± 75	7.49 ± 0.11	14.0 ± 0.3
GX1+4 1988	63 ± 5	5.16 ± 0.48	12.8 ± 1.3
GX1+4 1990	55 ± 3	20.00 ± 0.01	2.6 ± 0.3
1E1145.1-61.41	194 ± 68	13.58 ± 0.04	5.3 ± 0.6
X1722-36	10 ± 1	10.66 ± 2.35	8.6 ± 1.7
X Per	112 ± 29	8.36 ± 7.60	2.2 ± 9.8
4U1700-37	1184 ± 883	19.98 ± 50.57	2.4 ± 13.0

sources	Iron line			Absorption	χ^2_ν
	Flux I_{Fe} [ph/s]	Energy E_{Fe} [keV]	Width σ_{Fe} [keV]	$\log_{10} N_H$ [cm^{-2}]	
SMC X-1	3.6 ± 1.1	6.92 ± 0.24	0.50 fixed	22.48 ± 0.04	1.93
Cen X-3	23.0 ± 0.0	6.44 fixed	0.05 fixed	22.00 fixed	24.62
4U1626-67	0.7 ± 0.0	6.70 fixed	0.05 fixed	—	34.21
GS0834-430	5.4 ± 3.5	6.40 fixed	0.05 fixed	22.55 ± 0.05	1.65
OAO1657-415	10.6 ± 1.7	6.75 ± 0.09	0.05 fixed	23.04 ± 0.02	1.90
EXO2030+375	0.5 ± 0.3	6.55 ± 0.36	0.05 fixed	22.47 ± 0.25	5.98
A0536-26	84.8 ± 24.9	6.69 ± 0.17	0.05 fixed	22.36 ± 0.04	2.34
GX1+4 1988	3.5 ± 0.7	6.56 ± 0.12	0.05 fixed	22.75 ± 0.04	1.96
GX1+4 1990	2.4 ± 0.4	6.58 ± 0.09	0.05 fixed	23.04 ± 0.08	1.32
1E1145.1-61.41	0.0 ± 2.2	6.40 fixed	0.05 fixed	22.98 ± 0.08	2.34
X1722-36	2.4 ± 0.2	6.68 ± 0.03	0.26 ± 0.07	23.22 ± 0.20	0.92
X Per	0.6 ± 0.3	6.40 fixed	0.50 fixed	22.21 ± 0.02	1.05
4U1700-37	48.8 ± 9.7	6.52 ± 0.11	0.05 fixed	22.51 ± 0.08	1.62

The Galactic ridge emission is included in the fitting of X1722-36 as a bremsstrahlung without an iron line.

The units of the normalization of the power law are [photons/s/keV] at 10 keV.

E.3 Comparison of parameters

Here we compare the parameters of the NPEX and CMPL models. Figure E.3.1 is the kT's by the two models. The CMPL model has a little higher kT, but their relation is almost proportional. The kT of the CMPL model represents that of the NPEX model well.

The τ of the CMPL model is considered to represent the intensity ratio (positive power law)/(negative power law) of the NPEX model. Figure E.3.3 is τ in the CMPL model vs. the ratio of the components (pos./neg.) at $E = kT$ in the NPEX model. The data points with large errors are excluded in the figure (eg. EXO 2030+375, X Per, 1E 2259+586, etc.) The figure shows a good correlation. Thus τ defines the ratio of the power law and the blackbody Wien peak.

If τ means the number of the scatterings, the of the negative power law is expected to be larger (steeper) for smaller τ. Figure E.3.2 is the plot of the τ and the negative index α_1. Although the data points scatter, the global trend is consistent as expected.

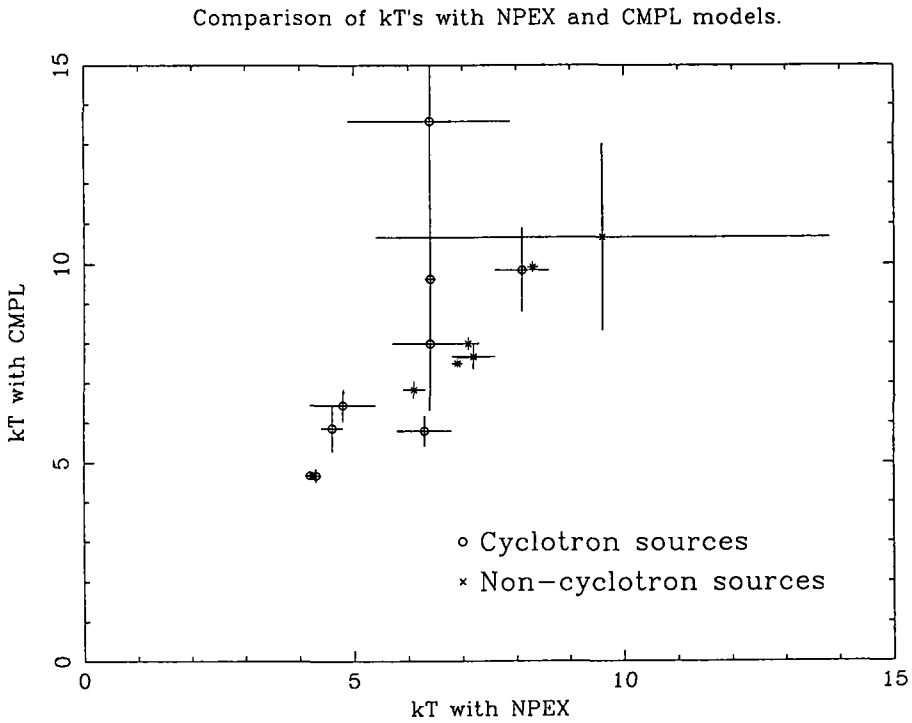

Figure E.3.1: The kT values by the NPEX and the CMPL models. The CMPL model has a little higher kT, but the relation is almost proportional.

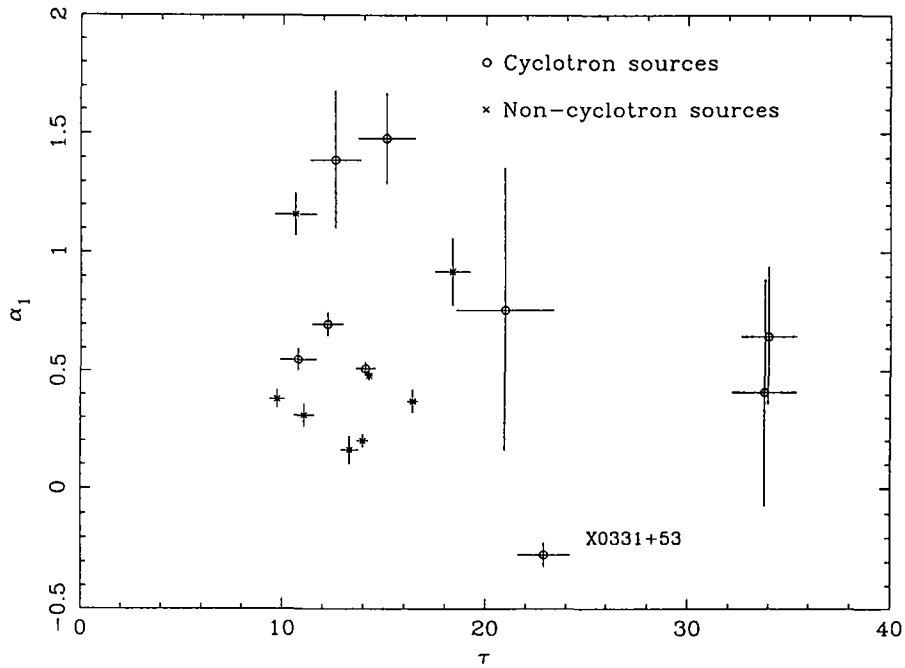

Figure E.3.2: The plot of the τ of the CMPL model and the negative index α_1 in the NPEX model.

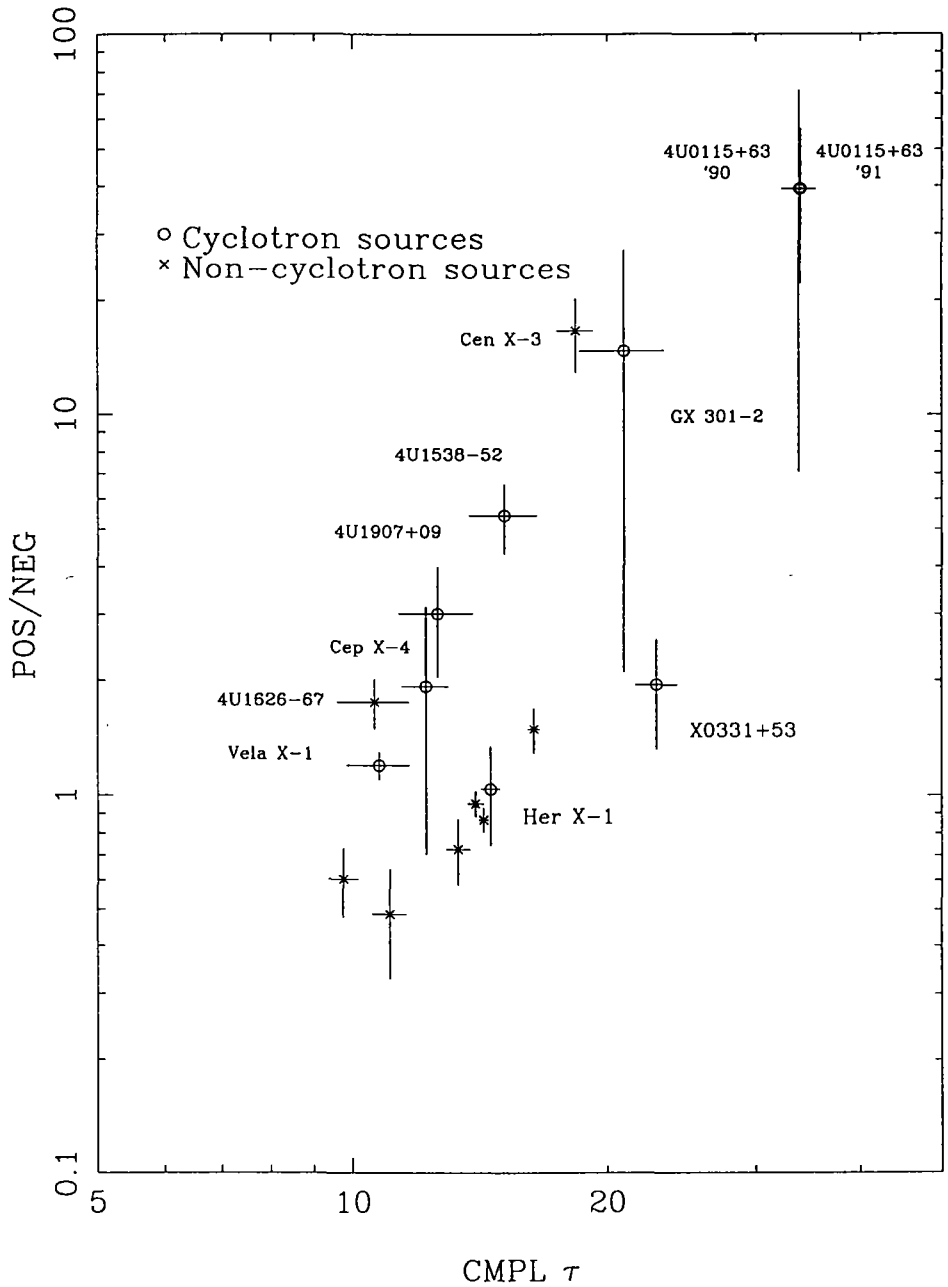

Figure E.3.3: τ in the CMPL model vs. the ratio of positive power law and negative power law at $E = kT$ in the NPEX model. The data points with large errors are excluded in the figure (eg. EXO 2030+375, X Per, 1E 2259+586, etc.) The figure shows that these two values are well correlated.

Appendix F

Resonance shape

We try various models and study the shape of the cyclotron structure by the fittings. The cross section of resonance models are given as CYAB, Gaussian, Lorentzian, and Voigt function (Mihalas 1978). The factor exp(− cross section) is multiplied to the continuum. As studied on X0331+53 in §5.7.2, the kinds of the continua does not affect the shape of the resonance so much. Therefore we use the NPEX model as the continuum. We pick up 6 observations with good statistics, ie. X0331+53 (in §5.7.2), Her X-1, 4U0113+63 in 1990 and 1991, Cep X-4, and 4U1538-52.

Figure F.1.4 are the residuals of the model fittings to their averaged spectra. The χ^2 shows that all the models are acceptable in 4U0115+63 in 1990 and Cep X-4, but CYAB is the only good model in 4U0115+63 in 1991. The Her X-1 and 4U1538-52 are the middle case; CYAB and Gaussian are good, but Lorentzian is not acceptable. Considering the X0331+53 results that only the Lorentzian was good (figure 5.7.9), none of the four models cannot fit all the pulsars by themselves. Thus the shape of the resonance is not the simple. However, except for X0331+53, CYAB is the best model to give 'good' fits to all the other pulsars. We should note that the CYAB model is not perfect and cannot give 'acceptable' fits to all the pulsars, as the residuals in figure F.1.4 still have some wavy structures. There might be two interpretation of X0331+53; that the spectral shape of X0331+53 is not CYAB but Lorentzian, or that the CYAB is not complete and another function like Gaussian is necessary.

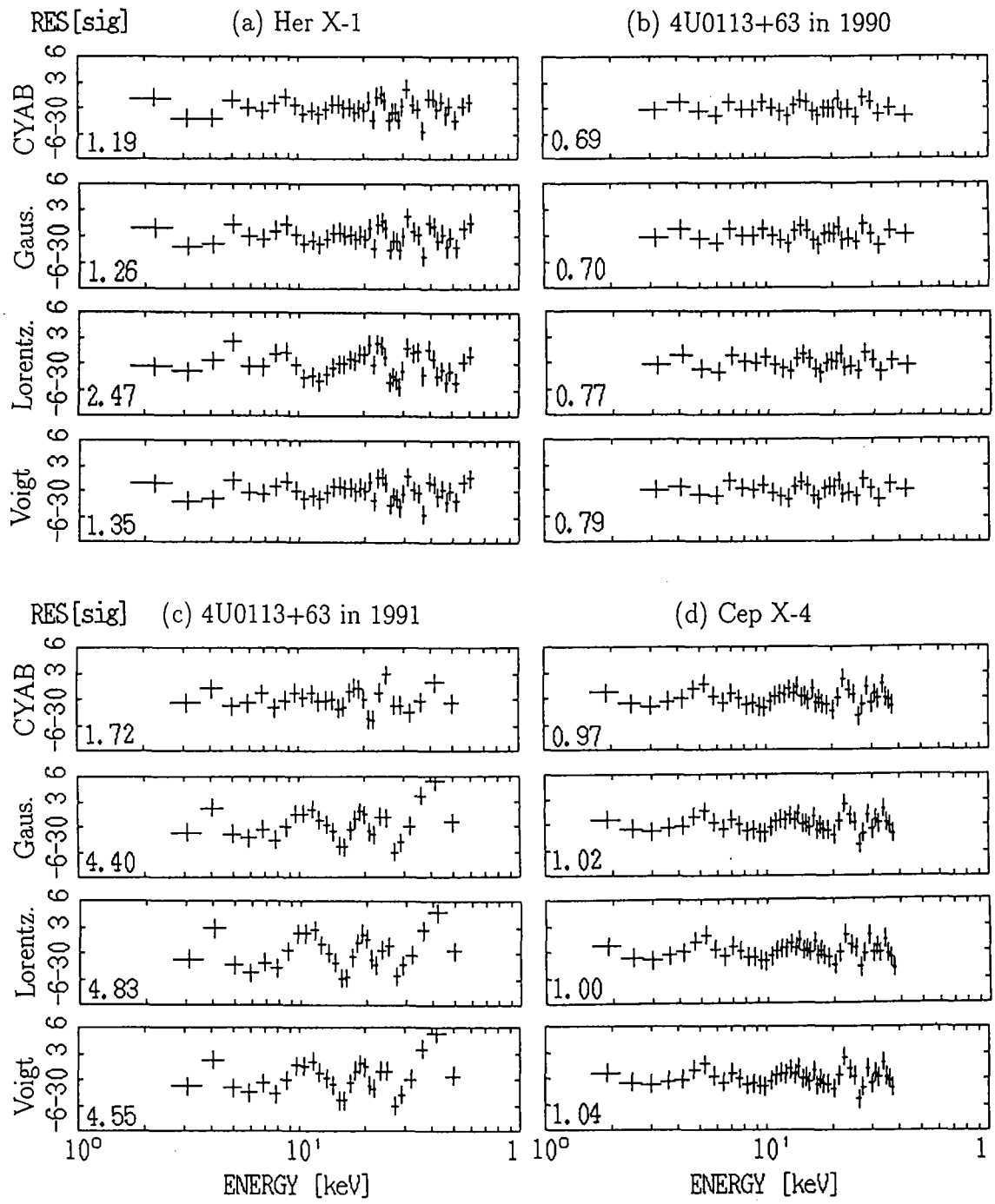

Figure F.1.4: The residuals of the NPEX × resonance model fittings to the averaged spectra of (a) Her X-1, (b,c) 4U0113+63 in 1990 and 1991, (d) Cep X-4, and (e) 4U1538-52. The χ^2_ν of the fittings are written in the figures.

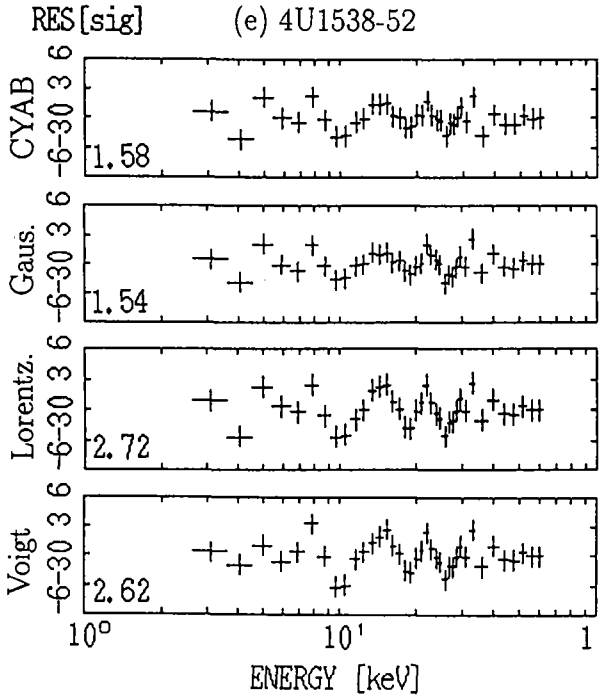

Figure F.1.4 *continued.*

Table F.1.1: Parameters of figure F.1.4.

sources	model	Cyclotron scattering				χ^2_ν
		Resonance Ea [keV]	Lore. Width Γ [keV]	Gaus. Width W, σ [keV]	Depth D	
Her X-1	CYAB	37.5[a] ±1.3	12.1 ±1.7		1.54 ±0.26	1.21
	Gaussian	36.5 ±0.8		7.1 ±0.7	19.9 ±4.6	1.26
	Lorentzian	36.3 ±0.8	9.0 ±1.5		44 ±14	2.47
	Voigt	36.4 ±3.5	0.1 ±—	7.1 ±—	20 ±5	1.35
4U0115+63 in 1990	CYAB	14.4[a] ±0.5	5.9 ±0.8		0.67 ±0.08	0.69
		23.3[a] ±0.4	5.2 ±1.0		0.51 ±0.07	
	Gaussian	13.0 ±0.3		3.3 ±0.5	4.6 ±1.9	0.70
		22.2 ±0.4		4.9 ±0.6	9.2 ±1.9	
	Lorentzian	13.0 ±0.2	5.7 ±1.0		15 ±6	0.77
		22.8 ±0.4	7.4 ±1.1		22 ±6	
	Voigt	13.0 ±—	0.05 ±—	3.2 ±—	4.5 ±—	0.76
		22.2 ±—	0.04 ±—	5.0 ±—	9.7 ±—	
4U0115+63 in 1991	CYAB	20.8[a] ±0.5	9.0 ±0.6		1.22 ±0.06	1.72
	Gaussian	19.5 ±0.3		5.6 ±0.5	14.9 ±2.5	4.40
	Lorentzian	19.4 ±0.3	8.8 ±1.0		42 ±9	4.83
	Voigt	19.5 ±—	1.7 ±—	5.0 ±—	18 ±—	4.55
Cep X-4	CYAB	33.8[a] ±2.6	12 ±3		1.64 ±0.57	0.97
	Gaussian	33.5 ±2.3		7.8 ±1.9	33.8 ±28.2	1.02
	Lorentzian	33.9 fixed	10.5 ±0.7		127 ±7.2	1.00
	Voigt	33.9 ±—	1.2 ±—	7.7 ±—	42 ±—	1.04
4U1538-52	CYAB	21.5[a] ±0.3	4.3 ±0.6		0.83 ±0.08	1.58
	Gaussian	21.7 ±0.3		3.1 ±0.3	5.5 ±0.9	1.54
	Lorentzian	21.6 ±0.3	3.8 ±0.7		10.2 ±2.8	2.72
	Voigt	21.6 ±—	3.8 ±—	0.6 ±—	10.4 ±—	2.62

(a): The energy at the maximum τ.

—: The parameters are coupled and not well determined.

Table F.1.1 *continued*

sources	model	NPEX continuum				
		Norm. A_1 [ph/s/keV]	index α_1	Norm. A_2 [ph/s/keV]	index α_2	e-folding kT [keV]
Her X-1	CYAB	135 ±8	0.51 ±0.03	100 ±23	2.0 fixed	8.0 ±0.9
	Gaussian	149 ±5	0.47 ±0.03	150 ±21	2.0 fixed	6.6 ±0.3
	Lorentzian	151 ±8	0.54 ±0.05	192 ±19	2.0 fixed	6.7 ±0.4
	Voigt	150 ±7	0.47 ±0.04	153 ±22	2.0 fixed	6.5 ±0.3
4U0115+63 in 1990	CYAB	490 ±330	0.41 ±0.48	4960 ±1220	2.0 fixed	4.25 ±0.10
	Gaussian	518 ±415	0.40 ±0.57	5260 ±1720	2.0 fixed	3.95 ±0.16
	Lorentzian	310 ±320	0.92 ±0.82	10200 ±3200	2.0 fixed	3.80 ±0.13
	Voigt	610 ±—	0.28 ±—	4900 ±—	2.0 fixed	3.99 ±0.46
4U0115+63 in 1991	CYAB	62 ±22	0.65 ±0.29	785 ±58	2.0 fixed	4.34 ±0.14
	Gaussian	27 ±25	1.3 ±0.8	1210 ±133	2.0 fixed	3.56 ±0.06
	Lorentzian	13 ±17	2.1 ±1.1	1980 ±290	2.0 fixed	3.54 ±0.06
	Voigt	25 ±—	1.4 ±—	1300 ±—	2.0 fixed	3.56 ±—
Cep X-4	CYAB	102 ±12	0.70 ±0.05	112 ±59	2.0 fixed	6.3 ±1.4
	Gaussian	109 ±17	0.66 ±0.06	116 ±79	2.0 fixed	6.0 ±1.7
	Lorentzian	134 ±3	0.73 ±0.05	149 ±23	2.0 fixed	7.7 ±0.5
	Voigt	105 ±—	0.67 ±—	104 ±—	2.0 fixed	6.4 ±—
4U1538-52	CYAB	18.7 ±1.7	1.5 ±0.2	68 ±8	2.0 fixed	4.6 ±0.2
	Gaussian	20.3 ±1.9	1.4 ±0.2	74 ±8	2.0 fixed	4.4 ±0.1
	Lorentzian	17.0 ±2.3	1.76 ±0.28	92 ±10	2.0 fixed	4.3 ±0.1
	Voigt	16.7 ±—	1.79 ±—	93 ±—	2.0 fixed	4.3 ±—

An iron line is added except for 4U0115+63 in 1991, whose parameters are not listed, since they are not important here.
The unit of the normalization of the power law is [photons/s/keV] at 10 keV.
—: The parameters are coupled and not well determined.

Appendix G

Pulse phase dependencies

We summarize pulse phase dependencies of various parameters of the NPEX × CYAB model together with their features, interpretations and problems. The parameter tables are shown in Chapter 5 for each pulsar.

Resonance depth

The depth of the cyclotron structure changes with pulse phases. It generally becomes most obvious at the pulse peak. The deepest depth D appears at around the main peak for Her X-1, 4U0115+63, 4U0331+53, 4U1907+09, and Vela X-1, and at the second peak for 4U1538-52 and the 2nd harmonic of 4U0115+63. The low flux in the off-pulse phases is not a reason of the small depths, because the statistics are enough even in the off-pulse phases. The emission from the accretion column would have a strong angular dependency, as the fundamental and the second harmonic cross section have the dependencies of $(1+\cos^2\theta)$ and $(1+\cos^2\theta)\sin^2\theta$, respectively, where θ is the angle between the magnetic field and direction of input photon. In case of 4U0115+63, it is consistent with fan beam as the optical depth of the 2nd harmonic of 4U0115+63 shows the maximum at the pulse bottom. However, in general, the optical depth is at the maximum at the pulse peak. The simple understanding is that the emission pattern is like a pencil beam, which would be consistent with the low luminosity pulsars such as 4U1907+09. However, it is unlikely for Her X-1 because of the change of the resonance energies in the next paragraph and because of the large luminosity as discussed §6.3. It would not be straightforward, and we might need a solution of radiation transfer.

Resonance energy

$E_a/\langle E_a\rangle$ is the resonance energies normalized by the weighted mean of the resonance energies along the pulse phases. The resonance energies vary as much as ± 10% in most pulsars. The exceptional flat dependency is X0331+53 in 1989 September and

Cep X-4. The simple understanding is that the change of the resonance energy is attributed to the change of the observing place on the column. As viewing angle to the accretion column changes with the rotation of the neutron star, the column surface facing toward us would also change, which accompanies the resonance energy change. The E_a is the largest at the pulse peak (phase 1 and 8) in most pulsars, which suggests that the column bottom emits the strongest X-ray, we are observing sideways and the emission pattern is so-called fan beam. It is consistent in the luminous pulsars such as Her X-1 which have tall accretion columns, and emit most of the flux toward the side (§6.3). The problem is low luminosity pulsars, which have negligibly low accretion columns compared to the width. They cannot change the magnetic field strength by the viewing angle. On the contrary, low luminosity pulsars such as 4U1907+09 and 4U1538-52 show significant change of the resonance energies. The problem was also discussed by Clark *et al.* (1990) and Bulik *et al.* (1992) but still remains unsolved.

Resonance width

In the figure, W or W/E_a do not show a systematic dependency with the pulse phase but almost constant. As shown in §6.2 the width is larger than the thermal broadening. The geometrical broadening is the most possible candidate. If we observe the column from the side, emission from many different heights would cause broadening the resonance. If the column is as high as 1 km such as Her X-1, the difference is as much as 1.3 E_a, which is enough to explain the broad widths. This model is consistent with the constant widths along the pulse phase. A problem is also for the low luminosity pulsars, in which the model predicts narrow widths because of the low column height. However, W/E_a does not depend on the luminosity as shown in §6.2. Other explanation is necessary at least for low luminosity pulsars.

Temperature in the NPEX model

kT of the NPEX model is constant within $\pm$ 20 % with the pulse phase in all the pulsars, but is different by pulsar and pulsar. Therefore kT is proper to each pulsar. The values of kT are 4–8 keV in the cyclotron pulsars ranging in the narrow range of a factor of two, which might be related to the narrow range distribution of the magnetic field of the neutron star. The E_a and kT variations are approximately consistent with $kT = 0.25E_a$ relation. Therefore the idea introduced in §6.1 can be applied here too, that kT is the temperature of electrons on the surface of the accretion column, and determined by the magnetic field.

POS/NEG ratio in the NPEX model

The intensity ratio of the positive and negative power laws at $E = kT$ can be interpreted as approximately representing the Comptonization optical depth τ (§6.1). Large value means that the spectrum is near to the blackbody. Her X-1 shows a high value at the main peak, which suggests that high flux needs large number of Comptonizations. However, many other pulsars show higher value at the inter-pulse, which is contrary to the above simple idea.

Negative power law index α_1 in the NPEX model

The index of the negative power law gets large at the pulse peak in such pulsars as Her X-1, Cep X-4, 4U1907+09, and GX301-2. Utilizing the interpretation of Comptonization, The steep index shows either an increase of the input soft photons or the decrease of the Comptonizing optical depth. High intensity at the peak prefers the former idea; an increase of the input soft photons forms the pulse peak. It accompanies a decrease of the number of the Comptonizing electrons, since the cooling would more efficient, which is consistent with the large POS/NEG ratio at the inter-pulse.

Thus the accretion column height theory introduced in §6.3 can qualitatively explain the phase dependency of luminous pulsars. But the low luminosity pulsars need other explanations.

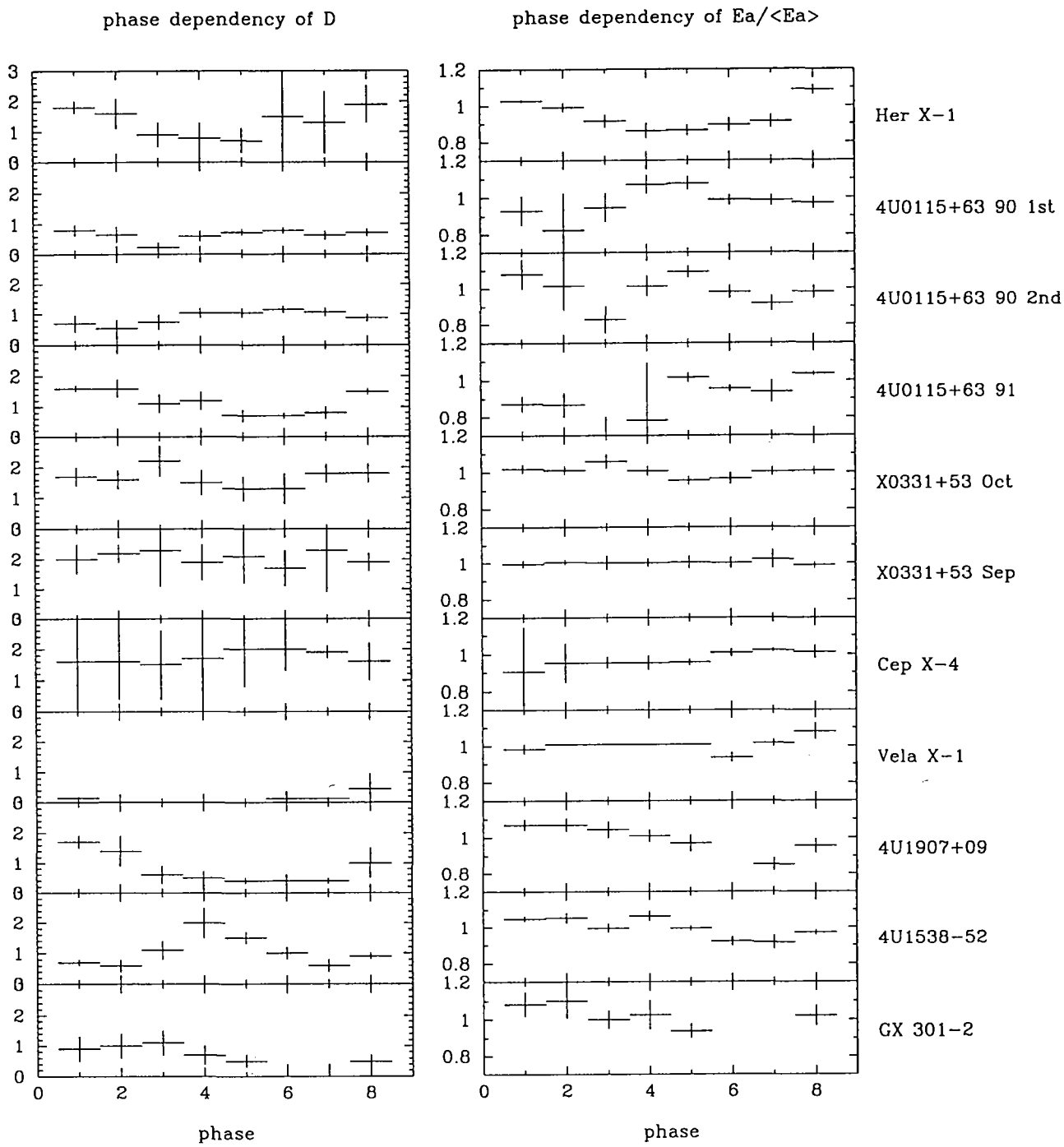

Figure G.1.1: Pulse phase dependencies of the resonance depth D and the resonance energy E_a. E_a is normalized by the weighted mean over the phases, and plotted in the same scale.

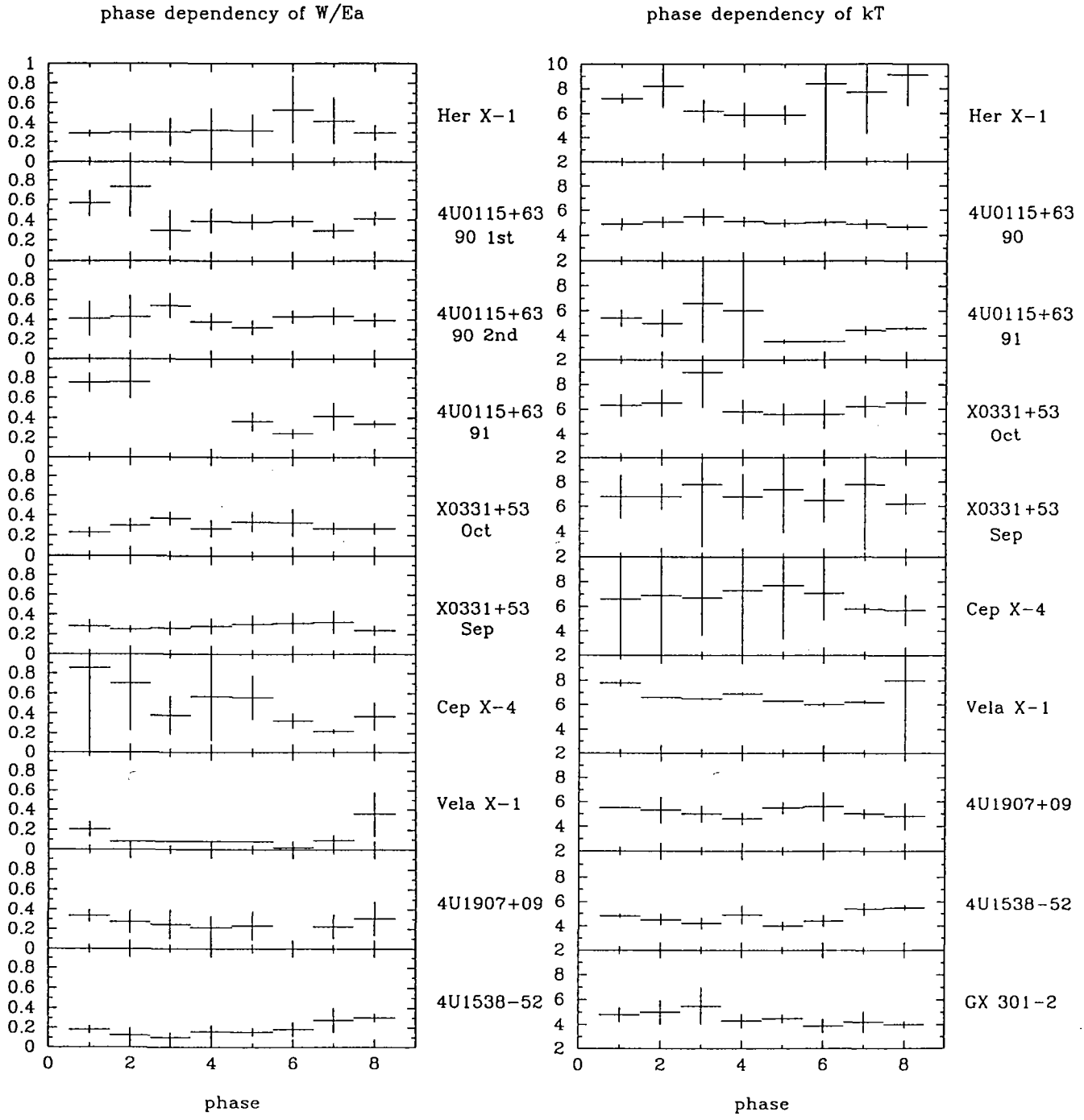

Figure G.1.2: Pulse phase dependencies of the resonance width W and the NPEX temperature kT. W is normalized by E_a to show the relative broadness of the resonance.

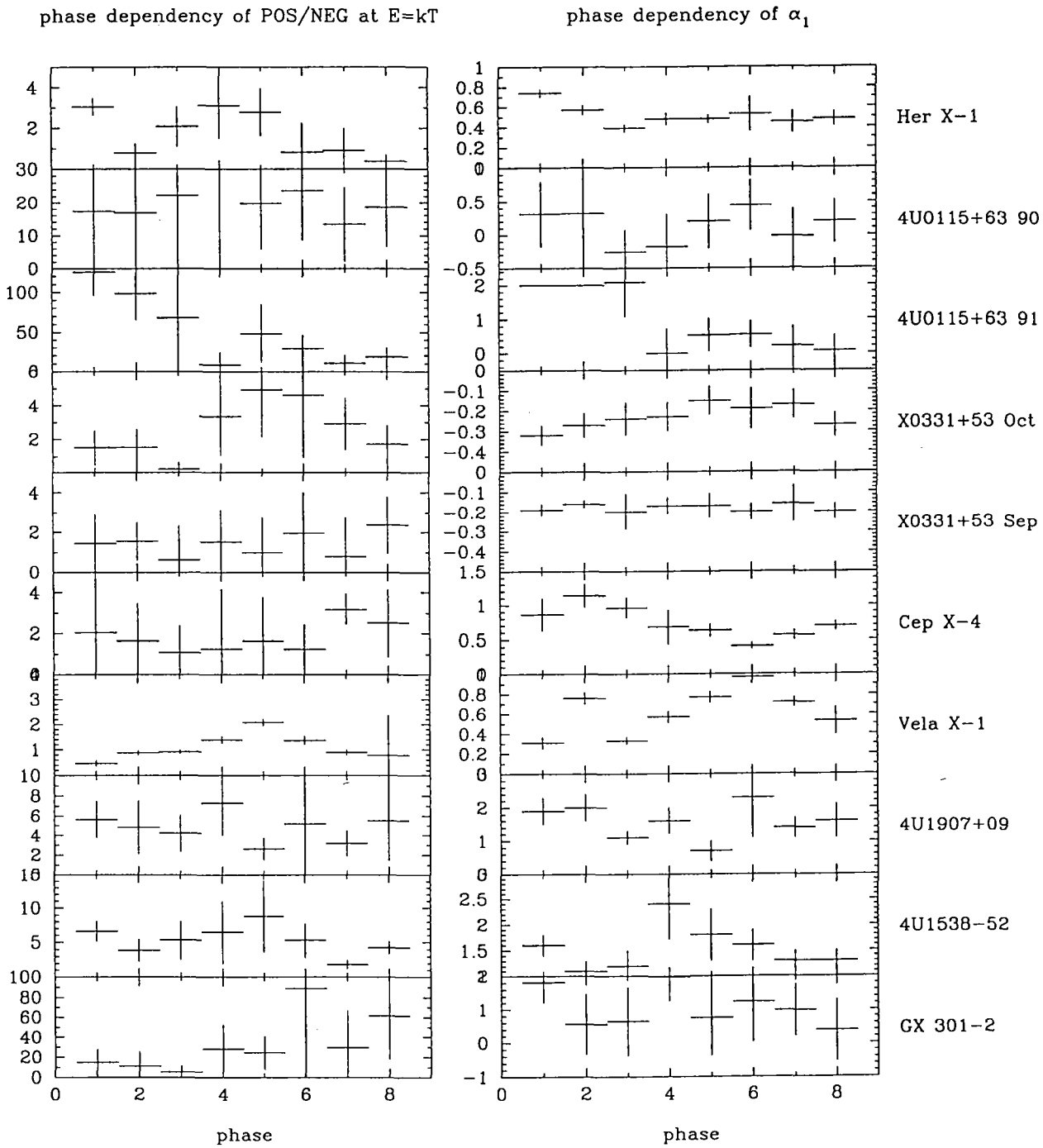

Figure G.1.3: Pulse phase dependencies of the intensity ratio of positive and negative power laws at $E = kT$, which corresponds to the optical depth τ in the Compton model, and the negative power law α_1.

Acknowledgement

I am grateful to Prof. K. Makishima for his continuous guidance and encouragement throughout the 4 years of my graduate course and successive 3 years before completion of this thesis. He guided me to the world of X-ray Astronomy and offered me the splended theme for my thesis.

I am much indebted to Prof. M. Matsuoka, Prof. F. Nagase, Prof. N. Shibazaki, and Dr. A. Yoshida for their valuable discussions, suggestions and support on this work. I would like to express my gratitude to Dr. N. Kawai, Dr. S. Kumagai, Dr. M. Tashiro, Dr. K. Ebisawa and Dr. T. Takeshima, and Prof. T. Ohashi for their discussions and continuous encouragement.

I acknowledge Dr. K. Leighly for her careful reading of the manuscript.

I wish to thank Prof. F. Makino and all the members of the *Ginga* team who led the *Ginga* mission successfully.

Special thanks to Dr. K. Asai for her help to preparing some figures for the manuscript and her heartful encouragement. I would like to thank all the members in Makishima Laboratory in University of Tokyo, in Cosmic Radiation Laboratory in RIKEN, and in ISAS for their help and all the enjoyable times.

Finally I would like to bless the *Ginga* satellite for the excellent performance throughout the mission of 4 years and 9 months.

References

Alexander, S. and Meszaros, P. 1989, *Astrophys. J.*, **344**, L1.

Alexander, S. and Meszaros, P. 1991a, *Astrophys. J.*, **372**, 554.

Alexander, S. and Meszaros, P. 1991b, *Astrophys. J.*, **372**, 565.

Aoki, T. *et al.* , 1992, *Publ. Astr. Soc. Japan* , **44**, 641.

Arons, J., Klein, R. I., and Lea, S. M., 1987, *Astrophys. J.*, **312**, 666.

Avni, Y. and Bahcall, J. N., 1974, *Astrophys. J.*, **192**, L139.

Avni, Y. and Bahcall, J. N., 1975, *Astrophys. J.*, **197**, 675.

Baade, W. and Zwicky, F., 1934, *Phys. Rev.*, **45**, 138.

Bahcall, J.N., and Bahcall, N.A., 1972, *Astrophys. J.*, **178**, L1.

Bahcall, J.N., 1978, *Physics and Astrophysics of Neutron Stars and Black Holes*, p63, ed. R. Giacconi and R.Ruffini, North-Holland Publishing Company, Amsterdam.

Band *et al.* , Proceedings of the Huntsville Gamma-ray burst workshop, eds. Fishman, G.J., Brainerd, J.J., Hurley, K.

Basko, M. M., and Sunyaev, R. A., 1976, *Mon. Not. Roy. Astr. Soc.*, **175**, 395.

Blandford, R., Applegate, J., and Hernquist, L. 1983, *Mon. Not. Roy. Astr. Soc.*, **204**, 1025.

Bonazzola, S., Heyvaerts, J., and Puget, J. L. 1979, *Astron. & Astrophys.*, **78**, 53.

Bradt, H.V. *et al.* 1977, *Nature* , **269**, 21.

Bradt, H. V., Remillard, R. A., Tuohy, I. R., Buckley, D. A. H., Brissenden, R., Schwartz, D. A. & Roberts, W., 1988, *Proc. of the symposium on the Physics of Neutron Star and Black Holes*, Tokyo, ed.Tanaka, Y., Universal Academic Press Inc., Tokyo.

Bulik, T., Meszaros P., Woo J.W., Nagase F., Makishima K., 1992, *Astrophys. J.*, **395**, 564.

Bulik, T. *et al.* , 1995, *Astrophys. J.*, **444**, 405.

Burnard, D. J., Lea, S. M., and Arons, J., 1983, *Astrophys. J.*, **266**, 175.

Burnard, D. J., Arons, J., and Klein, R. I., 1991, *Astrophys. J.*, **367**, 575.

Canuto, V. and Ventura, V. 1977, Fund. Cosmic Phys. **2**, 203.

Castro-Tirado, A. J., 1994, Ph.D. thesis for the science degree of University of Copenhagen.

Chakrabarty, D. *et al.* , 1993, *Astrophys. J.*, **403**, L33.

Chanmugam, G., 1992, *Annual Review of Astronomy and Astrophysics*, **30**, 143.

Clark, G. W. *et al.* , 1989, *Astrophys. J.*, **353**, 274.

Coe, M. J. *et al.* , 1977, *Nature* , **268**, 508.

Cook M. C. and Page C. G., 1987, *Mon. Not. Roy. Astr. Soc.*, **225**, 381.

Corbet, R. H. D. and Day, C. S. R., 1990, *Mon. Not. Roy. Astr. Soc.*, **243**, 553.

Corbet, R. H. D., Nagase, F., and Woo, J. H., 1991, in preparation.

Cropper, M. *et al.* , 1988, *Mon. Not. Roy. Astr. Soc.*, **231**, 597.

Daugherty, J. K. and Harding, A. K., 1986, *Astrophys. J.*, **309**, 362.

Dotani, T. *et al.* , 1989, *Publ. Astr. Soc. Japan* , **41**, 427.

Fahlman G.G., Hickson P., Richer H.B., Gregory P.C., Middledich J., 1982, *Astrophys. J.*, **261**, L1.

Fenimore, E. E. *et al.* , 1988, *Astrophys. J.*, **335**, L71.

Ford, L. A. *et al.* , 1992, *Compton Gamma-ray Observatory*, pp 887, ed. Friedlander, M. Gehrels, N., and Macomb, D. J., AIP Conference Proceedings 280. American Institute of Physics Press.

Ghosh, P. and Lamb, F. K., 1978, *Astrophys. J.*, **223**, L83.

Ghosh, P. and Lamb, F. K., 1979a, *Astrophys. J.*, **232**, 259.

Ghosh, P. and Lamb, F. K., 1979b, *Astrophys. J.*, **234**, 296.

Gould, R. J., 1982, *Astrophys. J.*, **254**, 755.

Giacconi, R. *et al.* , 1962, *Phys. Rev. Lett.*, **9**, 439.

Giacconi, R. *et al.* , 1971, *Astrophys. J.*, **167**, L67.

Graziani, C. *et al.* , 1992, *Compton Gamma-ray Observatory*, pp 897, ed. Friedlander, M. Gehrels, N., and Macomb, D. J., AIP Conference Proceedings 280. American Institute of Physics Press.

Grindlay, J. *et al.* , 1976, *Astrophys. J.*, **205**, L127.

Haberl, F., White, N. E., and Kallman, T. R., 1989, *Astrophys. J.*, **343**, 409.

Harding, A. K. and Preece, R. D., 1989, *Astrophys. J.*, **338**, L21.

Hayashida, K. *et al.* , 1989, *Publ. Astr. Soc. Japan* , **41**, 373.

Hewish, A. *et al.* , 1968, *Nature* , **217**, 709.

Inoue, H. 1975, *Publ. Astr. Soc. Japan* , **27**, 311.

Iwasawa, K. *et al.* , 1992, *Publ. Astr. Soc. Japan* , **44**, 9.

Iye, M., 1986, *Publ. Astr. Soc. Japan* , **38**, 463.

Jones, P. B., 1991, *Mon. Not. Roy. Astr. Soc.*, **253**, 279.

Joss, P. C. and Rappaport, S. A., 1976, *Nature* , **264**, 219.

Kamata, Y. *et al.* , 1990, *Publ. Astr. Soc. Japan* , **42**, 785.

Kanno, S., 1980, *Publ. Astr. Soc. Japan* , **32**, 105.

Kendziorra, E. *et al.* , 1992, *Frontiers of X-ray Astronomy*, p51, ed. Tanaka, Y. and Koyama, K., Universal Academic Press Inc., Tokyo.

Kendziorra, E. *et al.* , 1994, *Astron. & Astrophys.*, **291**, L31.

Kii, T. *et al.* , 1986, *Publ. Astr. Soc. Japan* , **38**, 751.

Krzemiński, W., 1974, *Astrophys. J.*, **192**, L135.

Koyama, K. *et al.* , 1984, *Publ. Astr. Soc. Japan* , **36**, 659.

Koyama, K. *et al.* , 1989, *Publ. Astr. Soc. Japan* , **41**, 461.

Koyama, K. *et al.* , 1990a, *Astrophys. J.*, **356**, L47.

Koyama, K. *et al.* , 1990b, *Publ. Astr. Soc. Japan* , **42**, L59.

Koyama, K. *et al.* , 1990c, *Nature* , **343**, 148.

Koyama, K. *et al.* , 1991a, *Astrophys. J.*, **366**, L19.

Koyama, K. *et al.* , 1991b, *Astrophys. J.*, **370**, L77.

Lamb, D. Q. and Lamb, F. K., 1978, *Astrophys. J.*, **220**, 291.

Lamb, D. Q., Wnag, C. L. and Wassweman, I. M., 1990, *Astrophys. J.*, **363**, 670.

Lamb, F. K., 1991, *Frontiers of Stellar Evolution*, ed. Lambert, D. L., Astronomical Society of the Pacific, pp. 299-388.

Lamb, P. and Sanford, P. W., 1979, *Mon. Not. Roy. Astr. Soc.*, **188**, 555.

Lang, F.L., Levine, A.M., Bautz, M., Hauskins, S, Howe, S., Primini, F.A., Lewin, W.H.G., Baity, W.A., Knight, F.K., Rothschild, R.E., and Petterson, J.A., 1981, *Astrophys. J.*, **246**, L21.

Laurent, P. *et al.* , 1992, *Astron. & Astrophys.*, **260**, 237.

Leahy, D.A. *et al.* , 1988, *Publ. Astr. Soc. Japan* , **40**, 197.

Leahy, D.A. *et al.* , 1989, *Mon. Not. Roy. Astr. Soc.*, **236**, 603.

Leahy, D.A., Matsuoka M., 1990, *Astrophys. J.*, **355**, 627.

Levine, A., Rappaport, S., Putney, A., Corbet, R., and Nagase, F., 1991, *Astrophys. J.*, **381**, 101.

Levine, A. *et al.* , 1993, *Astrophys. J.*, **410**, 328.

Lewin, W. H. G. and Joss, P. C., 1983, *Accretion-driven Stellar X-ray Sources* pp. 41 ed. Lewin, W. H. G. and van den Heuvel, P. J., Cambridge university press.

Lyne, A. G., Manchester, R. N. and Taylor, J. H., 1985, *Mon. Not. Roy. Astr. Soc.*, **213**, 613.

Lyne, A. G. and Graham-Smith, F., 1990, *Pulsar astronomy*, Cambridge Astrophysics Series 16, Cambridge university press.

Lyne, A. G., 1995 *The Lives of the Neutron Stars*, pp. 213, ed. Alpar, M. A., Kiziloglu, U. and van Paradijs, J., Kluwer Academic Publishers.

Marshall, N. and Ricketts, M. J., 1980, *Mon. Not. Roy. Astr. Soc.*, **193**, 7p.

Mazets, E. P. *et al.* , 1981, *Nature* , **290**, 378.

Makishima, K. *et al.* , 1984, *Publ. Astr. Soc. Japan* , **36**, 679.

Makishima, K. *et al.* , 1987, *Astrophys. J.*, **314**, 619.

Makishima, K. *et al.* , 1988, *Nature* , **333**, 746.

Makishima, K. *et al.* , 1990a, *Publ. Astr. Soc. Japan* , **42**, 295.

Makishima, K. *et al.* , 1990b, *Astrophys. J.*, **365**, L59.

Makishima K., and Mihara T., 1992, *Frontiers of X-ray Astronomy*, p23, ed. Tanaka, Y. and Koyama, K., Universal Academic Press Inc., Tokyo.

Manchester, R. N. and Taylor, J. H., 1977, *Pulsars* San Francisco : Freeman.

Melrose, D.B. and Parle, A.J., 1983, *Aust. J. Phys.*, **36**, 799.

Meszaros P., and Nagel W., 1985a, *Astrophys. J.*, **298**, 147.

Meszaros P., and Nagel W., 1985b, *Astrophys. J.*, **299**, 138.

Meszaros P., 1992, *High-Energy Radiation from Magnetized Neutron Stars*, The University of Chicago Press.

Michel, F. C., 1991, *Theory of Neutron Star Magnetospheres*, The University of Chicago Press.

Mihalas, D., 1978, *Stellar Atmospheres 2nd Ed.*, by Freeman and Company.

Mihara, T. *et al.* , 1990, *Nature* , **346**, 250.

Mihara, T. *et al.* , 1991a, *Publ. Astr. Soc. Japan* , **43**, 501.

Mihara, T. *et al.* , 1991b, *Astrophys. J.*, **379**, L61.

Mitsuda, K. *et al.* , 1984, *Publ. Astr. Soc. Japan* , **36**, 741.

Morrison, R., and McCammon, D., 1983, *Astrophys. J.*, **270**, 119.

Murakami, T. *et al.* , 1984, *Publ. Astr. Soc. Japan* , **36**, 691.

Murakami, T. *et al.* , 1987, *Publ. Astr. Soc. Japan* , **39**, 253.

Murakami, T. *et al.* , 1988, *Nature* , **335**, 234.

Murakami, T. *et al.* , 1989, *Publ. Astr. Soc. Japan* , **41**, 405.

Nagase, F. *et al.* , 1982, *Astrophys. J.*, **263**, 814.

Nagase, F. *et al.* , 1984, *Astrophys. J.*, **280**, 259.

Nagase, F. *et al.* , 1986, *Publ. Astr. Soc. Japan* , **38**, 547.

Nagase, F., 1989, *Publ. Astr. Soc. Japan* , **41**, 1.

Nagase, F. *et al.* , 1991, *Astrophys. J.*, **375**, L49.

Nagase, F., Corbet, R. H. D., Day, C. S. R., Inoue, H., Takeshima, T., Yoshida, K., and Mihara, T., 1992, *Astrophys. J.*, **396**, 147.

Nagel, W., 1980, *Astrophys. J.*, **236**, 904.

Nagel, W., 1981a, *Astrophys. J.*, **251**, 278.

Nagel, W., 1981b, *Astrophys. J.*, **251**, 288.

Nishimura, O., 1992, *Publ. Astr. Soc. Japan* , **44**, 109.

Ostriker, J. P. and Gunn, J. E., 1969, *Nature* , **223**, 817.

Palmer, D. M. *et al.* , 1992, *Compton Gamma-ray Observatory*, pp 892, ed. Friedlander, M. Gehrels, N., and Macomb, D. J., AIP Conference Proceedings 280. American Institute of Physics Press.

Parmar, A. N. *et al.* , 1989, *Astrophys. J.*, **338**, 359.

Parkes, G. E., Mason K.O., Murdin P.G., Culhane J.L., 1980, *Mon. Not. Roy. Astr. Soc.*, **191**, 547.

Pravdo, S. H. *et al.* , 1978, *Astrophys. J.*, **225**, 988.

Pravdo, S. H. *et al.* , 1979, *Astrophys. J.*, **231**, 912.

Prince, T. A. *et al.* , 1993, *The Evolution of X-ray Binaries*, pp. 235, ed. Holt S.S. and Day C.S., AIP conference proceedings 308.

Polidan, R. S., Pollard, G. S. G., Sanford, P. W., and Locke, M. C., 1978, *Nature* , **275**, 296.

Rappaport, S. A. and Joss, P. C., 1983, *Accretion-driven Stellar X-ray Sources*, pp. 1 ed. Lewin, W. H. G. and van den Heuvel, E. P. J. (Cambridge University Press, Cambridge)

Reynolds, A. P., 1993, *Astrophys. J.*, **414**, 302.

Robba, N. R., 1989, *Astrophys. J.*, **346**, 469.

Rose, L.A. *et al.* , 1979, *Astrophys. J.*, **231**, 919.

Ruderman, M. A. and Sutherland, P. G., 1973, *Nature physical science*, **246**, 93.

Ruderman, M. A., 1991, *Astrophys. J.*, **366**, 261.

Rybicki, G. R. and Lightman, A. P., 1979, *Radiative Processes in Astrophysics*, John Wiley & Sons, Inc.

Sakao, T. *et al.* , 1990, *Mon. Not. Roy. Astr. Soc.*, **246**, *Short Comm.*, 11.

Sang, Y. and Chanmugam, G., 1987, *Astrophys. J.*, **323**, L61.

Sang, Y. and Chanmugam, G., 1990, *Astrophys. J.*, **363**, 597.

Sato, N. *et al.* , 1986, *Astrophys. J.*, **304**, 241.

Schreier, E. *et al.* , 1972, *Astrophys. J.*, **172**, L79.

Shinoda, K., 1990, *Publ. Astr. Soc. Japan* , **42**, L27.

Soong, Y. *et al.* , 1990, *Astrophys. J.*, **348**, 641.

Srinivasan, G. *et al.* , 1990, *Curr. Sci.*, **59**, 31.

Stella L. *et al.* , 1985, *Astrophys. J.*, **288**, L45.

Stollberg, M. T. *et al.* , 1993, *The Evolution of X-ray Binaries*, pp. 255, ed. Holt S.S. and Day C.S., AIP conference proceedings 308.

Sunyaev, R. A. and Titarchuk, L. G., 1980, *Astron. & Astrophys.*, **86**, 121.

Takahama, S., 1992, Master thesis in the physics department of Osaka University (in Japanese).

Takeshima, T., Dotani T., Mitsuda K., Nagase F., 1991, *Publ. Astr. Soc. Japan* , **43**, L43.

Takeuchi, Y., Koyama, K., and Warwick, R. S., 1990, *Publ. Astr. Soc. Japan* , **42**, 287.

Tamura, K. *et al.* , 1992, *Astrophys. J.*, **389**, 676.

Tanaka, Y. *et al.* , 1984, *Publ. Astr. Soc. Japan* , **36**, 641.

Tanaka, Y., 1986, *Radiation Hydrodynamics in Stars and Compact Objects*, p.198 ed. Mihalas, D. Winkler, K. H. (Springer, Berlin)

Tananbaum, H., Gursky, H., Kellogg, E.M., Levinson, R., Schreier, E., and Giacconi, R., 1972, *Astrophys. J.*, **174**, L143.

Tashiro M., Makishima K., Ohashi T., Sakao T., and Sansom A.E., 1991, *Mon. Not. Roy. Astr. Soc.*, **252**, 156.

Tawara, Y., Yamauchi, S., Awaki, H., Koyama, K., and Nagase, F., 1989, *Publ. Astr. Soc. Japan* , **41**, 473.

Terrell, J., and Priedhorsky, W. C., 1984, *Astrophys. J.*, **285**, L15.

Thompson, C., and Dunkan, R., 1993, *Astrophys. J.*, **408**, 194.

Trümper, J. *et al.* , 1978, *Astrophys. J.*, **219**, L105.

Tsunemi, H. *et al.* , 1989, *Publ. Astr. Soc. Japan* , **41**, 391.

Turner, M. J. L. *et al.* , 1989, *Publ. Astr. Soc. Japan* , **41**, 345.

van den Heuvel, E. P. J., 1991, *Neutron stars : theory and observation*, pp. 171 ed.Ventura, J. and Pines, D., Kluwer Academic Publishers, Netherlands.

van den Heuvel, E. P. J., 1992, *X-ray Binaries and Recycled Pulsars*, pp. 233 ed. E.P.J. van den Heuvel and S.A. Rappaport, NATO ASI Series, Kluwer Academic Publishers.

Ventura, J., 1979, *Physical Rev. D*, **19**, 1684.

Visvanathan, N. and Wickramasinghe, D. T., 1979, *Nature*, **281**, 47.

Voges, W. *et al.* , 1982, *Astrophys. J.*, **263**, 803.

Wakatsuki, S. *et al.* , 1992, *Astrophys. J.*, **392**, 628.

Wang, J. C. L. *et al.* , 1989, *Physical Review Letters*, **63**, 1550.

Wang, J. C. L. *et al.* , 1993, *Astrophys. J.*, **414**, 815.

Wheaton, W. A., 1979, *Nature* , **282**, 240.

Whilson, R. B. *et al.* , 1992, *IAU Circ.*, no.5454, 1.

White, N. E. and Pravdo, S. H., 1979, *Astrophys. J.*, **233**, L121.

White, N. E. *et al.* , 1980, *Astrophys. J.*, **239**, 655.

White, N. E., Swank, J. H., and Holt S. S., 1983, *Astrophys. J.*, **270**, 711.

White, N. E., Swank, J. H., 1984, *Astrophys. J.*, **287**, 856.

Wilson, R. B. *et al.* , 1992, *I.A.U. circ.*, **5454**, 1.

Wilson, R. B. *et al.* , 1993, *Astrophys. J.submitted.*

Woltjer, L., 1964, *Astrophys. J.*, **140**, 1309.

Yamauchi, S., 1991, Ph.D. thesis for the science degree of Nagoya University.

Yoshida, A. *et al.* , 1991, *Publ. Astr. Soc. Japan* , **43**, L69.

Yoshida, A., 1989, Ph.D. thesis for the physics degree of University of Tokyo.